BEILSTEIN JOURNAL OF ORGANIC CHEMISTRY

Multivalency as a chemical organization and action principle

Edited by Rainer Haag

Imprint

Beilstein Journal of Organic Chemistry
www.bjoc.org
ISSN 1860-5397
Email: journals-support@beilstein-institut.de

The *Beilstein Journal of Organic Chemistry* is published by the Beilstein-Institut zur Förderung der Chemischen Wissenschaften.

Beilstein-Institut zur Förderung der Chemischen Wissenschaften
Trakehner Straße 7–9
60487 Frankfurt am Main
Germany
www.beilstein-institut.de

BEILSTEIN JOURNAL OF ORGANIC CHEMISTRY

Multivalency as a chemical organization and action principle

Rainer Haag

Editorial

Open Access

Address:
Institute for Chemistry and Biochemistry, Freie Universität Berlin, Takustr. 3, 14195 Berlin, Germany

Email:
Rainer Haag - haag@chemie.fu-berlin.de

Keywords:
glycoarchitectures; supramolecular chemistry; multivalency; multivalent protein inhibitors; pathogen binding

Beilstein J. Org. Chem. **2015,** *11,* 848–849.
doi:10.3762/bjoc.11.94

Received: 06 May 2015
Accepted: 07 May 2015
Published: 19 May 2015

This article is part of the Thematic Series "Multivalency as a chemical organization and action principle".

Guest Editor: R. Haag

Multivalency is a key principle in nature to establish strong, but also reversible chemical interactions between two units, e.g., a receptor and a ligand, viruses and host cells, or between two cell surfaces. Multivalent binding is based on multiple simultaneous molecular recognition processes and plays an important role in the self-organization of matter, in biological recognition processes as well as in signal transduction in biological systems. The targeted development of multivalent molecules is not only used for the strong inhibition of proteins and prevention of pathogen infections, but also allows for the selective production of functional molecular architectures and surface structures as well as the controlled interaction of multivalent surfaces. The chemical and biological mechanisms and the influence of scaffold architectures with different dimensions for multivalent interactions have not been comprehensively explored. Thus, the experimental and theoretical understanding of defined oligovalent binding systems requires further detailed understanding in the gas phase, in solution and on surfaces.

Frequently the interaction of a single ligand with an acceptor (monovalent interaction) in many cases can be quantitatively understood. This, however, is completely different, when several covalently linked ligands of the same or of a similar nature bind to an ensemble of acceptors (multivalent interactions) [1]. Due to the multiple additive (in some cases cooperative) interactions the equilibrium will shift and bond reinforcement occurs (Figure 1). Also, the kinetically controlled dissociation can become very slow to almost non-existent. Multivalency is also dependent on the size, shape and flexibility of the scaffold architecture, especially for the interfacial interaction with biological systems.

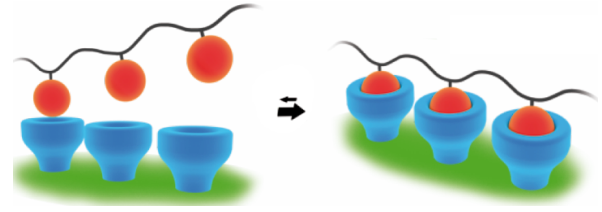

Figure 1: Multivalent interactions shift the equilibrium and enhance the binding strength. Reprinted with permission from [1]. Copyright 2012 Wiley-VCH.

In order to obtain a deeper understanding of multivalent interactions this Thematic Series in the *Beilstein Journal of Organic Chemistry* puts its focus to unravel new cellular interactions that

are highly relevant [2] and systematically combines theoretical exploration of defined multivalent supramolecular interactions [3] as well as new supramolecular designer systems [4,5]. The influence of spacer length and flexibility on the binding affinity of ligands [6] will be examined as well as the mechanical stability of complexes [7]. Furthermore, the Thematic Series covers the synthesis of various new glycoarchitectures for multivalent interactions [8-12] and studies the scope of multivalent lectin-glycointeractions in galectins [13], with iminosugars [14] and carbohydrate mimetics [15]. This Thematic Series in the *Beilstein Journal of Organic Chemistry* also investigates the enhanced multivalent binding of protein scaffolds [16], peptide–polymer interactions [17-20] tripodal-catecholates [21] and polycatechol–surface interactions [22] as well as multivalent organocatalyts [23]. Finally, multivalent dendritic poly(arginine/histidine)-siRNA complexes are evaluated regarding their transfection efficiency [24].

In the future a deeper understanding of multivalent interactions at all length scales from the nanometer to the micrometer range is crucial for solving important problems and for the development of new systems in the fields of life and materials science. In order to address this highly complex and long-term challenge, the interdisciplinary cooperation of scientists with different expertise ranging from biochemistry to theory is essential.

Rainer Haag

Berlin, May 2015

References

1. Fasting, C.; Schalley, C. A.; Weber, M.; Seitz, O.; Hecht, S.; Koksch, B.; Dernedde, J.; Graf, C.; Knapp, E.-W.; Haag, R. *Angew. Chem.* **2012,** *124,* 10622–10650. doi:10.1002/ange.201201114 *Angew. Chem., Int. Ed.* **2012,** *51,* 10472–10498. doi:10.1002/anie.201201114
2. Wei, Q.; Pohl, T. L. M.; Seckinger, A.; Spatz, J. P.; Cavalcanti-Adam, E. A. *Beilstein J. Org. Chem.* **2015,** *11,* 773–783. doi:10.3762/bjoc.11.87
3. Achazi, A. J.; Mollenhauer, D.; Paulus, B. *Beilstein J. Org. Chem.* **2015,** *11,* 687–692. doi:10.3762/bjoc.11.78
4. Lohse, M.; von Krbek, L. K. S.; Radunz, S.; Moorthy, S.; Schalley, C. A.; Hecht, S. *Beilstein J. Org. Chem.* **2015,** *11,* 748–762. doi:10.3762/bjoc.11.85
5. Benkhäuser, C.; Lützen, A. *Beilstein J. Org. Chem.* **2015,** *11,* 693–700. doi:10.3762/bjoc.11.79
6. Liese, S.; Netz, R. R. *Beilstein J. Org. Chem.* **2015,** *11,* 804–816. doi:10.3762/bjoc.11.90
7. Gensler, M.; Eidamshaus, C.; Taszarek, M.; Reissig, H.-U.; Rabe, J. P. *Beilstein J. Org. Chem.* **2015,** *11,* 817–827. doi:10.3762/bjoc.11.91
8. Bantzi, M.; Rigol, S.; Giannis, A. *Beilstein J. Org. Chem.* **2015,** *11,* 604–607. doi:10.3762/bjoc.11.67
9. Ciuk, A. K.; Lindhorst, T. K. *Beilstein J. Org. Chem.* **2015,** *11,* 668–674. doi:10.3762/bjoc.11.75
10. Schmidt, S.; Wang, H.; Pussak, D.; Mosca, S.; Hartmann, L. *Beilstein J. Org. Chem.* **2015,** *11,* 720–729. doi:10.3762/bjoc.11.82
11. Lai, C.-H.; Hahm, H. S.; Liang, C.-F.; Seeberger, P. H. *Beilstein J. Org. Chem.* **2015,** *11,* 617–621. doi:10.3762/bjoc.11.69
12. Novoa, A.; Winssinger, N. *Beilstein J. Org. Chem.* **2015,** *11,* 707–719. doi:10.3762/bjoc.11.81
13. Cousin, J. M.; Cloninger, M. J. *Beilstein J. Org. Chem.* **2015,** *11,* 739–747. doi:10.3762/bjoc.11.84
14. Lepage, M. L.; Mirloup, A.; Ripoll, M.; Stauffert, F.; Bodlenner, A.; Ziessel, R.; Compain, P. *Beilstein J. Org. Chem.* **2015,** *11,* 659–667. doi:10.3762/bjoc.11.74
15. Salta, J.; Dernedde, J.; Reissig, H.-U. *Beilstein J. Org. Chem.* **2015,** *11,* 638–646. doi:10.3762/bjoc.11.72
16. Mühlberg, M.; Hoesl, M. G.; Kuehne, C.; Dernedde, J.; Budisa, N.; Hackenberger, C. P. R. *Beilstein J. Org. Chem.* **2015,** *11,* 784–791. doi:10.3762/bjoc.11.88
17. Henning, L. M.; Bhatia, S.; Bertazzon, M.; Marczynke, M.; Seitz, O.; Volkmer, R.; Haag, R.; Freund, C. *Beilstein J. Org. Chem.* **2015,** *11,* 701–706. doi:10.3762/bjoc.11.80
18. Schöne, D.; Schade, B.; Böttcher, C.; Koksch, B. *Beilstein J. Org. Chem.* **2015,** *11,* 792–803. doi:10.3762/bjoc.11.89
19. Lauster, D.; Pawolski, D.; Storm, J.; Ludwig, K.; Volkmer, R.; Memczak, H.; Herrmann, A.; Bhatia, S. *Beilstein J. Org. Chem.* **2015,** *11,* 589–595. doi:10.3762/bjoc.11.65
20. Koschek, K.; Durmaz, V.; Krylova, O.; Wieczorek, M.; Gupta, S.; Richter, M.; Bujotzek, A.; Fischer, C.; Haag, R.; Freund, C.; Weber, M.; Rademann, J. *Beilstein J. Org. Chem.* **2015,** *11,* 837–847. doi:10.3762/bjoc.11.93
21. Klitsche, F.; Ramcke, J.; Migenda, J.; Hensel, A.; Vossmeyer, T.; Weller, H.; Gross, S.; Maison, W. *Beilstein J. Org. Chem.* **2015,** *11,* 678–686. doi:10.3762/bjoc.11.77
22. Krysiak, S.; Wie, Q.; Rischka, K.; Hartwig, A.; Haag, R.; Hugel, T. *Beilstein J. Org. Chem.* **2015,** *11,* 828–836. doi:10.3762/bjoc.11.92
23. Pecchioli, T.; Muthyala, M. K.; Haag, R.; Christmann, M. *Beilstein J. Org. Chem.* **2015,** *11,* 730–738. doi:10.3762/bjoc.11.83
24. Mehrabadi, F. S.; Zeng, H.; Johnson, M.; Schlesener, C.; Guan, Z.; Haag, R. *Beilstein J. Org. Chem.* **2015,** *11,* 763–772. doi:10.3762/bjoc.11.86

License and Terms

BEILSTEIN JOURNAL OF ORGANIC CHEMISTRY

Potential of acylated peptides to target the influenza A virus

Daniel Lauster[*1], Damian Pawolski[1], Julian Storm[1], Kai Ludwig[2], Rudolf Volkmer[3], Henry Memczak[4], Andreas Herrmann[1] and Sumati Bhatia[*5]

Letter

Open Access

Address:
[1]Humboldt-Universität zu Berlin, Institute of Biology, Invalidenstr. 42, 10115 Berlin, Germany, [2]Freie Universität Berlin, Research Center of Electron Microscopy, Fabeckstr. 36a, 14195 Berlin, Germany, [3]Charité Universitätsmedizin Berlin, Institute of Immunology, Charitéplatz 1, 10117 Berlin, Germany, [4]Fraunhofer Institute for Cell Therapy and Immunology, Am Mühlenberg 13, 14476 Potsdam, Germany and [5]Freie Universität Berlin, Institute of Chemistry and Biochemistry, Takustr. 3, 14195 Berlin, Germany

Email:
Daniel Lauster* - daniel.lauster@hu-berlin.de; Sumati Bhatia* - sumatichem@gmail.com

* Corresponding author

Keywords:
amphiphilic peptide; antiviral; influenza virus; multivalency; self-assembled structures

Beilstein J. Org. Chem. **2015,** *11,* 589–595.
doi:10.3762/bjoc.11.65

Received: 03 March 2015
Accepted: 24 April 2015
Published: 29 April 2015

This article is part of the Thematic Series "Multivalency as a chemical organization and action principle".

Guest Editor: R. Haag

Abstract

For antiviral drug design, especially in the field of influenza virus research, potent multivalent inhibitors raise high expectations for combating epidemics and pandemics. Among a large variety of covalent and non-covalent scaffold systems for a multivalent display of inhibitors, we created a simple supramolecular platform to enhance the antiviral effect of our recently developed antiviral Peptide B (PeB^{GF}), preventing binding of influenza virus to the host cell. By conjugating the peptide with stearic acid to create a higher-order structure with a multivalent display, we could significantly enhance the inhibitory effect against the serotypes of both human pathogenic influenza virus A/Aichi/2/1968 H3N2, and avian pathogenic A/FPV/Rostock/34 H7N1 in the hemagglutination inhibition assay. Further, the inhibitory potential of stearylated PeB^{GF} (C18-PeB^{GF}) was investigated by infection inhibition assays, in which we achieved low micromolar inhibition constants against both viral strains. In addition, we compared C18-PeB^{GF} to other published amphiphilic peptide inhibitors, such as the stearylated sugar receptor mimicking peptide (Matsubara et al. 2010), and the "Entry Blocker" (EB) (Jones et al. 2006), with respect to their antiviral activity against infection by Influenza A Virus (IAV) H3N2. However, while this strategy seems at a first glance promising, the native situation is quite different from our experimental model settings. First, we found a strong potential of those peptides to form large amyloid-like supramolecular assemblies. Second, in vivo, the large excess of cell surface membranes provides an unspecific target for the stearylated peptides. We show that acylated peptides insert into the lipid phase of such membranes. Eventually, our study reveals serious limitations of this type of self-assembling IAV inhibitors.

Introduction

Annually influenza A virus infections cause up to 500.000 deaths worldwide, and are therefore a serious threat, and burden to humans [1]. Hence, research and development of new affordable influenza antivirals are an important task to combat not only seasonal epidemics, but also devastating pandemics. For therapy of infected patients, several pharmaceuticals targeting influenza neuraminidase (oseltamivir, zanamivir) or the proton channel protein M2 (amantadine, rimantadine) are available. However, the efficiencies of these drugs are competing with fast and continuously changing phenotypes of the influenza virus [2].

Among different strategies to block virus entry [3], several multivalent inhibitors preventing binding of the influenza virus to the host cell proved to be potent drug candidates [4-9]. Those inhibitors bind to the virus envelope spike protein hemagglutinin (HA) which is organized as a homotrimer. In particular, inhibitors competing for the highly conserved binding site for sialic acid, which is the natural receptor presented on the host cell surface have been applied. Essentially, these approaches revealed that an efficient block of virus binding requires a multivalent interaction between virus and inhibitors. This can be rationalized by the fact that a stable binding of influenza virus to the host cell is mediated by a multivalent interaction between HA binding pockets and cell surface receptors as a monovalent interaction is too weak for stable binding [10,11].

Peptide-based self-assembled nanostructures can be used as the simplest platform for the multivalent display of ligands, although this approach has not been explored much in the context of virus inhibition. There are only a few reports on using peptide based self-assembly for influenza virus inhibition [12-14].

The entry blocker (EB) which is a peptide fragment derived from the fibroblast growth factor signal sequence 4 (FGF) has a rather broad antiviral activity among several influenza strains in the micromolar range [14]. It has been shown that EB can bind to HA, and causes viral aggregation, which has been ascribed to multimerization of EB monomers providing a multivalent surface [15,16]. However, the inhibitory mechanism has not been elucidated in detail.

Matsubara et al. introduced a sugar mimetic peptide, which binds to the sialic acid binding pocket of HA [13]. In order to increase the inhibitory capacity of the peptide, a stearyl group has been attached to the mimetic peptide, presumably leading to the formation of a supramolecular assembly, which allows multivalent interactions. By that, multivalent inhibitors could be designed with antiviral activity in the low micromolar range.

Recently, we identified an antiviral peptide, which we derived from the paratope region of an antibody directed against HA binding to the sialic acid binding pocket. The peptide was shown to bind still to this site, and inhibits different influenza A virus strains in binding, and infection being superior to other antiviral peptides. We demonstrated inhibitory performance in the micromolar range against the serotypes of human pathogenic influenza A/Aichi/2/1968 H3N2 (X31) and avian pathogenic A/FPV/Rostock/34 H7N1. Inspired by the strategy of Matsubara et al. we attached a C18 fatty acid chain to this peptide, called PeB^{GF}, to assemble multivalent structures which enhanced the antiviral potential compared to the monomeric form. In this study, stearylated PeB^{GF} (C18-PeB^{GF}) has been compared with EB, the stearylated sialic acid mimetic (C18-s2s), and the stearylated control peptide with the reverse amino acid sequence (C18-rs2s) in respect to their potential to inhibit virus mediated hemagglutination, and to lyse red blood cells.

Results and Discussion

Peptide synthesis and characterization

Peptide synthesis was performed using a rink amide resin on an automatic synthesizer by the Fmoc/*tert*-butyl strategy [17,18]. The *N*-terminus of the *N*-terminal free resin bound peptide was acylated with stearic acid using *O*-(benzotriazol-1-yl)-*N*,*N*,*N*',*N*'-tetramethyluronium tetrafluoroborate (TBTU) as coupling reagent in the presence of diisopropylethylamine (DIPEA) in DMF. Peptides summarized in Table 1 were explored for influenza A virus inhibition.

Table 1: Peptide sequences and modifications.

Name	Structure
C18-s2s	$C_{17}H_{35}CO$-**ARLPRTMV**-$CONH_2$
C18-s2s-TAMRA	$C_{17}H_{35}CO$-**ARLPRTMV**-βA-βA-TAMRA
C18-rs2s	$C_{17}H_{35}CO$-**VMTRPLRA**-$CONH_2$
C18- PeB^{GFa}	$C_{17}H_{35}CO$-**XXXXXXXXXXXXXX**-$CONH_2$
Entry blocker (EB)	**RRKKAAVALLPAVLLALLAP**-$CONH_2$

[a]Patent application is in progress [19]. The sequence will be revealed soon, by a publication in another journal.

Acylated and other amphiphilic peptides are well known to self-assemble into supramolecular structures [20,21]. Stearylated peptides, closely related to C18-s2s, C18-rs2s and C18-PeB^{GF} assemble as supramolecular structures with a critical micelle concentration (CMC) between 0.8–0.9 μM and a size between 0.2 and 2.3 μm depending on the peptide concentration [12]. The rather large size indicates the formation of rather large

structures different from a simple sphere-like micelle. To verify and characterize the assembly of our peptides into higher-order structures, we studied exemplarily the organization of C18-PeB^{GF} by dynamic light scattering (DLS) and transmission electron microscopy (TEM).

First, the size of the supramolecular nanostructures formed by C18-PeB^{GF}, C18-s2s, and C18-rs2s was analyzed by DLS at low concentration of 20 µM in PBS (10 mM, pH 7.4). For the analysis of C18-PeB^{GF}, we observed a hydrodynamic diameter of 16.7 nm (PDI = 0.454) along with 10–15% bigger supramolecular structures with hydrodynamic diameters of 184.3 nm and 573.1 nm as per volume distribution profile (Figure 1). We observed much bigger aggregates in the case of C18-rs2s with a hydrodynamic diameter of 818.8 nm (PDI = 0.328). The volume size distribution was multimodal for C18-s2s showing higher-order aggregates of different sizes at 20 µM concentration (see Supporting Information File 1).

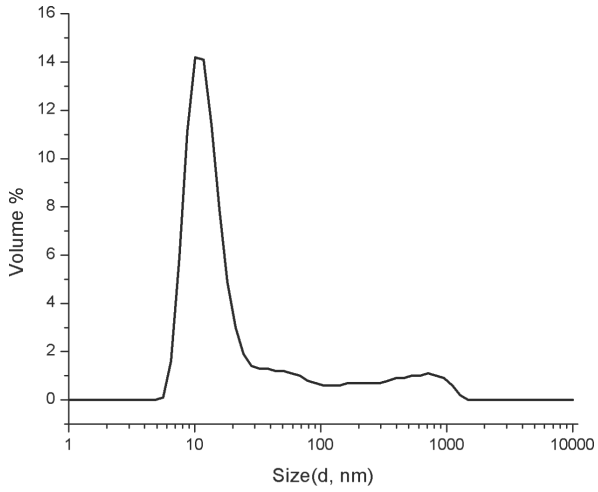

Figure 1: Volume size distribution profile of C18-PeB^{GF} at a concentration of 20 µM in PBS (10 mM, pH 7.4).

To address if the tendency of C18-PeB^{GF} to form larger supramolecular structures becomes prominent at higher concentrations, we analyzed C18-PeB^{GF} in DLS measurements at a concentration of 100 µM, too. Indeed, under those conditions we observed supramolecular aggregates with a size larger than 1 µm indicating the strong potential of C18-PeB^{GF} to organize as rather large assemblies. To visualize the organization of those assemblies, we employed TEM. To facilitate the structure identification, we used an even higher concentration of C18-PeB^{GF}. We found a fibrillar supramolecular arrangement being up to several hundred nanometers long at 2 mM peptide concentrations (Figure 2). These fibers appeared predominantly as single, rather elongated structures. However, we found sheet like structures, possibly from a side-by-side assembly of these fibers, too. Importantly, cryo-TEM provides the same results (not shown) showing that formation of the large assemblies is

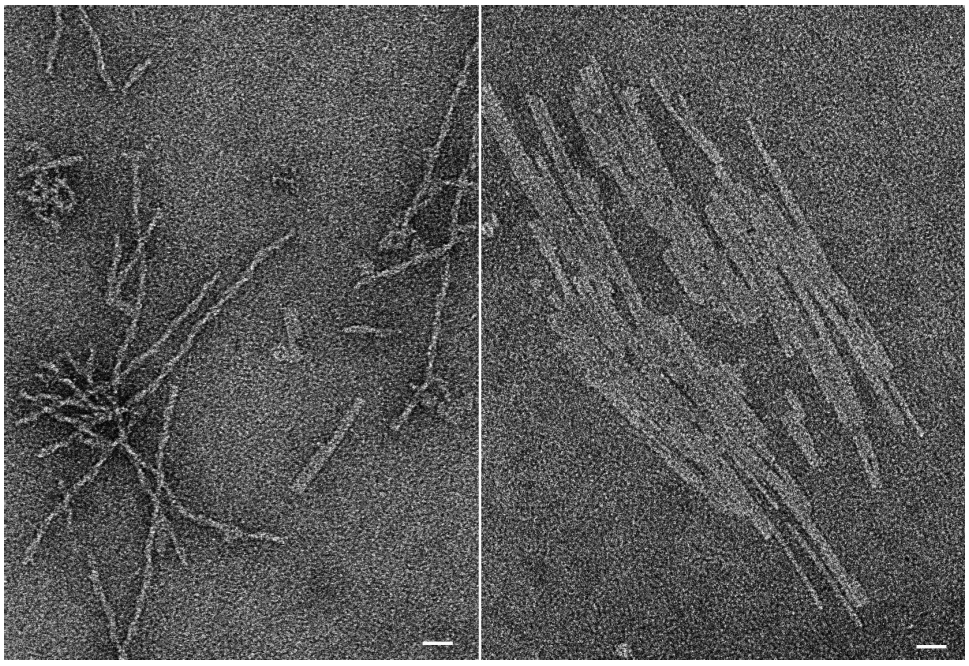

Figure 2: Negative staining transmission electron micrographs (TEM) of fibrillar (left) and sheet-like structures (right) of C18-PeB^{GF} (2 mM in PBS), scale bars correspond to 25 nm.

not caused by contrast material. Preliminary TEM studies indicate similar assemblies for the other peptides used here.

Our results indicate that the amphiphilic peptides do not behave like typical micelle-forming molecules. Although we found smaller supramolecular assemblies at 20 µM C18-PeB^{GF}, there is a strong tendency to form larger and stable supramolecular arrangements. Indeed, our TEM images implicate a rather amyloid-like character of C18-PeB^{GF} and other amphiphilic peptides used here. Notably, such larger structures are consistent with the observation of Matsubara et al. at least with respect to the dimension. Although the authors did not visualize the morphology of their structures, the DLS data of this report indicate different sized assembly forms even in the µm range.

Amphiphilic peptides cause aggregation of viruses

For the stearylated peptide s2s and the polar peptide EB binding to influenza HA has been demonstrated [13,14]. In accordance with the study of Matsubara et al. we used the reverse peptide rs2s from the sialic acid mimetic as a control which does not recognize the sialic acid binding pocket and thus does not bind to HA.

To prove whether stearylated PeB^{GF} is able to interfere with influenza virus activity, we first investigated its potential to aggregate viruses and compared it with that of other amphiphilic peptides (Table 1). To this end, fluorescently labeled influenza A virus X31 has been incubated with amphiphilic inhibitors at 100 µM concentrations and shortly centrifuged. For all inhibitors, but the control compound C18-rs2s a higher fluorescent signal in the pellet compared to the supernatant was observed, indicating not only binding to viruses but also aggregation of viruses caused by the inhibitors (Figure 3). Jones et al. suggested that the inhibitory mechanism of action of EB is based on its viral aggregation potential, which has been supported by density gradient and electron microscopy analysis [15]. Indeed aggregation of viruses can only be explained by the formation of a supramolecular arrangement of amphiphilic peptides forming a surface with multiple ligands recognizing HA but not by a monomeric organisation of amphiphilic peptides.

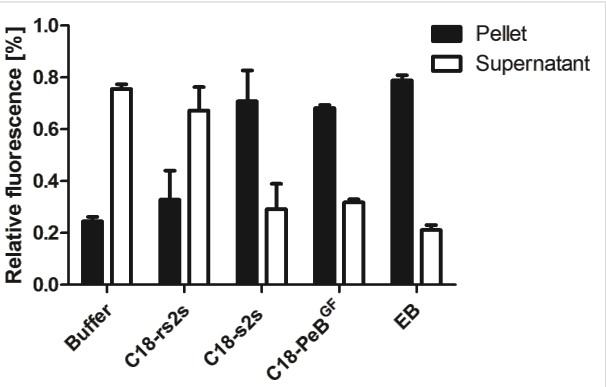

Figure 3: Amphiphilic inhibitors induce aggregation of viruses. R18 labeled influenza virus was incubated without or with inhibitors at 100 µM for 20 min at room temperature and subsequently centrifuged. To supernatant and pellet, respectively, Triton-X100 was added, and their fluorescence signal was recorded. Relative fluorescence indicates fluorescence from pellet and supernatant in relation to the total signal before centrifugation. Error bars represent the standard error of the mean (SEM) of at least three independent experiments.

Amphiphilic peptides interfere with virus binding to cells

The potential to inhibit binding of influenza viruses to cells can be investigated by the well-established hemagglutination inhibition assay (HAI) [22]. All peptides, but the control peptide C18-rs2s were able to inhibit Aichi H3N2 virus mediated hemagglutination already at low micromolar concentrations (Table 2). For EB an IC_{50} of 20 µM against Aichi H3N2 in the HAI has been determined, however at higher viral titer than we used [14].

However, we noted that inhibitors by themselves can trigger unspecific hemagglutination. To quantify this behaviour, we introduced another inhibitor constant (K_iA), which represents the minimum concentration to cause inhibitor triggered human erythrocyte agglutination. While the multivalent organized peptidic inhibitors inhibited virus mediated agglutination

Table 2: Inhibition constants for inhibition of virus mediated hemagglutination (K_iHAI) and for inhibitor caused agglutination (K_iA).

Compound	C18-PeB^{GF}	C18-s2s	C18-rs2s	EB
K_iHAI $_{(Aichi\ H3N2)}$ [µM]	1.2 ± 0.0	0.8 ± 0.5	no effect	1.6 ± 0.3
K_iHAI $_{(Rostock\ H7N1)}$ [µM]	2.8 ± 0.9	n.d.	n.d.	n.d.
K_iA [µM]	100.0 ± 0.0	7.0 ± 0.8	4.1 ± 2.1	8.6 ± 7.0

The K_iHAI represents the lowest concentration needed for full hemagglutination inhibition. The K_iA value reflects the minimum concentration for agglutination caused by the inhibitor itself. The shown values represent the mean of at least three independent experiments. Extended values represent the standard error of the mean (SEM). n.d. (not determined).

already at low micromolar concentrations of about 1 µM, onset of unspecific agglutination was observed at much higher concentrations being in the range from 7 to 100 µM. It is important to note that the unspecific interaction of our compounds with cells can reduce the efficiency of compounds to prevent virus binding to cells, possibly even by incorporation into the lipid phase of membranes (see below).

In addition to the human pathogenic influenza A model strain X31 (Aichi H3N2), we asked whether our inhibitor is able to inhibit hemagglutination caused by the avian pathogenic strain Rostock H7N1, too. Indeed, C18-PeB^{GF} was able to inhibit H7N1 completely at 2.8 µM concentrations (Figure 4). Thus, by attaching stearyl to the N-terminus of the PeB^{GF} sequence, we could decrease the K_iHAI value up by 10 fold for H7N1 and by 20 fold for Aichi H3N2 respectively (data not shown, see patent [19]).

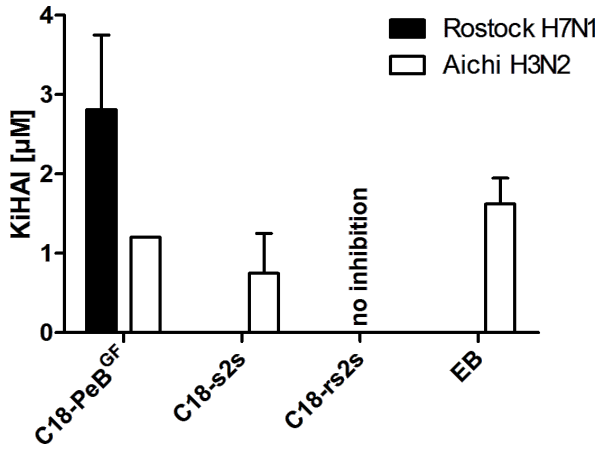

Figure 4: Inhibition constants K_iHAI of C18-PeB^{GF}, C18-s2s, C18-rs2s and EB against Aichi H3N2 and Rostock H7N1 virus. The K_iHAI reflects the lowest concentration needed for full hemagglutination inhibition. Error bars indicate the standard error of the mean (SEM) of at least three independent experiments.

Protection from virus infection by acylated peptide PeB^{GF}

Next, we determined the potential of stearylated peptide PeB^{GF} for infection inhibition of MDCK cells by Aichi H3N2 and Rostock H7N1. We found that C18-PeB^{GF} inhibited the infection of cells at MOI 0.05 (1,500 pfu) with IC_{50} values of 84 µM against Rostock H7N1, and 5.9 µM against Aichi H3N2 (Figure 5). In comparison to unmodified PeB^{GF} the inhibitory potential could be enhanced by approx. 5 fold against Aichi H3N2, while the inhibition against Rostock H7N1 did not increase (data not shown, see patent application [19]). These results are in the same molar range found for the multivalent assemblies of C18-s2s and EB. Jones et al. determined for EB

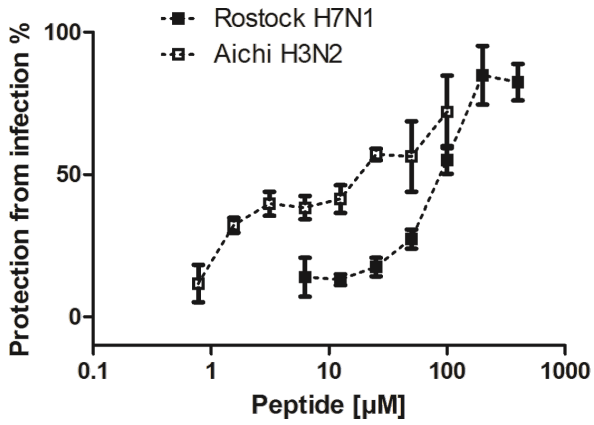

Figure 5: C18-PeB^{GF} mediated protection from infection of MDCK cells by Rostock H7N1 and Aichi H3N2. MDCK II cells were incubated with viruses at an MOI of 0.05 for 24 h at 37 °C. Error bars indicate the standard deviation of three experiments.

an IC_{50} of 4.5 µM against Hongkong H5N1 at an MOI of 0.05 48 h post infection.

Interaction with lipid membranes

Although the above presented data may be promising in terms of efficient inhibition of influenza virus binding and, thus, infection, we have to take into account that the conditions of these experiments do not match the in vivo situation. Typically, such antiviral compounds will be applied intravenously or by inhalation to allow a systemic distribution or a tissue specific targeting within the infected host. However, in those cases amphiphilic peptides are in an environment of cell membrane surfaces being in excess to viruses. Thus, the majority of peptides will be incorporated into cell membranes. This would be of significant negative consequences for application of those peptides as antiviral drugs, because the multivalent presentation of the peptides would be prevented and one may speculate that cell surface membrane associated peptides may act as an additional receptor for virus attachment to the host cell surface.

Therefore, we studied the interaction of amphiphilic peptides with membranes. To this end, we repeated our hemagglutination inhibition experiments, but we incubated the peptides with 100 nm large unilamellar vesicles (LUV) containing 6.25 nmol DOPC for 30 minutes before virus and erythrocytes were added. In that case the K_iHAI increased by a factor of 2–4 (data not shown; notably, a similar increase was found for K_iA). This suggests that the potential of inhibitors to prevent hemagglutination must have been partially neutralized by the liposomes, either by attachment and/or incorporation into the lipid bilayer. Very likely, in case of stearylated peptides, we surmise incorporation into the bilayer via the fatty acyl chain.

To verify the association with lipid membranes exemplarily, we synthesized the s2s construct with a terminal rhodamine fluorophore. This compound was mixed with DOPC giant unilamellar vesicles (GUV) or human erythrocytes. In both cases clear membrane labeling could be detected (Figure 6).

To assess how strong membrane incorporation of these peptides can perturb membranes we measured their cell lytic activity in a titration experiment with human erythrocytes. Apart from compound C18-s2s which acted extremely hemolytic above concentrations of 20 µM, all peptides showed only low hemolytic activity (Figure 7). For EB the same has been reported by Jones et al. [16].

These results show that acylated peptides, e.g., C18-PeB^{GF}, could readily insert into biological membranes. As we observed association with the plasma membrane of red blood cells we surmise that those peptides could also insert into the virus envelope.

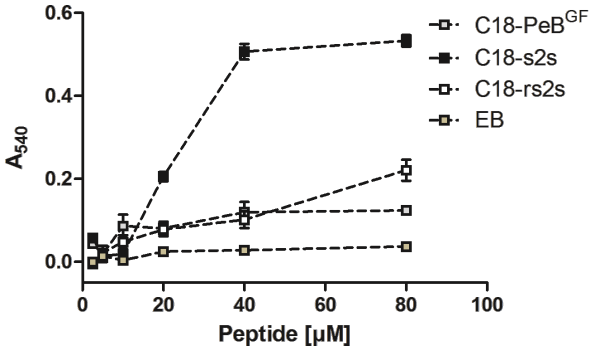

Figure 7: Hemolytic activity of stearylated peptides and EB. 2% human erythrocytes were incubated for one hour with peptides at 37 °C. After centrifugation, the hemolytic activity was assessed by absorption measurement of the supernatant at 540 nm. Error bars indicate the SEM of three titration experiments.

Conclusion

Here, we investigated the potential of a stearylated HA antibody derived peptide, entitled C18-PeB^{GF} to inhibit virus binding to red blood cells, and to prevent from viral infection of MDCK II cells. Based on the known capability of amphiphilic peptides to organize as supramolecular structures, we intended to enable a multivalent presentation of virus binding ligands with enhanced antiviral activity. Although DLS analysis indicated the presence of nanostructures at lower concentrations, as the majority of detected objects showed an average diameter of 16.7 nm, we found already at 20 µM concentrations the formation of rather large supramolecular structures which are even more prominent at higher concentrations. Structural analysis by TEM revealed the presence of stable fiberlike assemblies, which can further arrange side-by-side as sheets. Thus, acylated peptides as C18-PeB^{GF} cannot be considered as micelle forming molecules as it would be expected from the C18 chain. We surmise that the peptide is an important structural determinant leading to a rather amyloid-like assembly. This is certainly a serious disadvantage for the application of those acylated peptides as antiviral drugs.

Nevertheless, only the multiple presentations of antiviral peptides, and the binding of peptides to HA can explain the observed ability to aggregate viruses, which has been demonstrated for all peptides except for the control peptide C18-rs2s. We found that C18-PeB^{GF} was able to inhibit Aichi H3N2 and Rostock H7N1 virus induced hemagglutination at 1.2 µM and 2.8 µM, respectively. In comparison to unmodified PeB^{GF} the inhibitory potential was increased by 10 fold for Rostock H7N1 and by 20 fold for Aichi H3N2. In addition, we found enhanced infection inhibition of C18-PeB^{GF} compared to its non-acylated form. Against Aichi H3N2 and Rostock H7N1 we determined

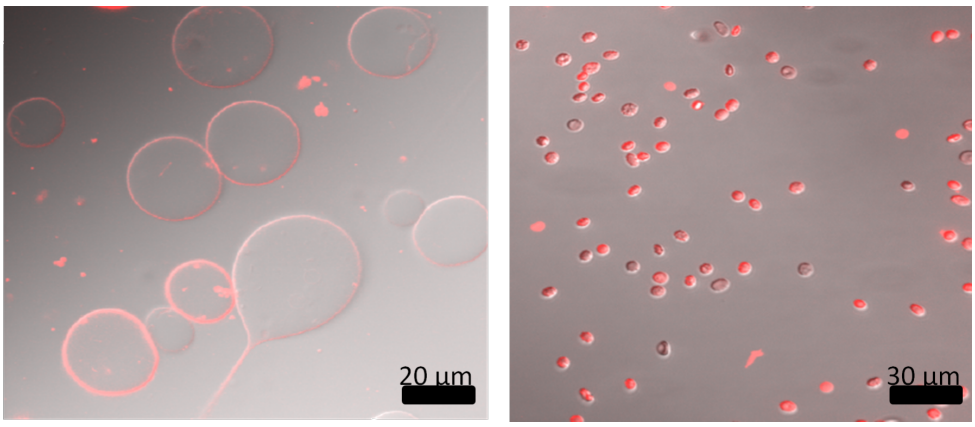

Figure 6: Fluorescence microscopy images of GUVs (left) and human erythrocytes (right) after incubation with C18-s2s-TAMRA. The overlap of DIC and rhodamine channels demonstrate the labeling of membranes by the fluorescent stearate peptide. Scale bars are in black.

IC_{50} values of 5.9 μM and 84 μM, respectively. Compared to the monomeric peptide we could reduce the IC_{50} value by 5 fold against Aichi H3N2, whereas we did not observe enhanced inhibitory potential in the infection experiments with Rostock H7N1.

However, despite the principal potential of acylated antiviral peptides such as C18-PeB^{GF} to inhibit virus interaction with cells, our observation of a strong affinity of those structures to membranes, and also to incorporate into membranes are serious disadvantages for their application as therapeutics. Indeed, we found that the inhibition of virus mediated hemagglutination by acylated antiviral peptides was drastically reduced in the presence of additional membranes (here liposomes). Taken into consideration that the in vivo situation is characterized by an excess of cell membrane surfaces serving as targets for the amphiphilic peptides, the multivalent presentation of antiviral peptides by respective nanostructures will be perturbed or even inhibited.

In conclusion, the acylation of those peptides as used in our study, and in previous studies does not resemble an advantage over other strategies of multivalent presentations.

Supporting Information

Supporting Information File 1

Experimental part.
[http://www.beilstein-journals.org/bjoc/content/supplementary/1860-5397-11-65-S1.pdf]

Acknowledgements

The project was supported by the DFG (SFB 765).

References

1. Kuiken, T.; Riteau, B.; Fouchier, R. A. M.; Rimmelzwaan, G. F. *Curr. Opin. Virol.* **2012,** *2,* 276. doi:10.1016/j.coviro.2012.02.013
2. van der Vries, E.; Schutten, M.; Fraaij, P.; Boucher, C.; Osterhaus, A. *Adv. Pharmacol.* **2013,** *67,* 217. doi:10.1016/B978-0-12-405880-4.00006-8
3. Vanderlinden, E.; Naesens, L. *Med. Res. Rev.* **2014,** *34,* 301. doi:10.1002/med.21289
4. Papp, I.; Sieben, C.; Ludwig, K.; Roskamp, M.; Böttcher, C.; Schlecht, S.; Herrmann, A.; Haag, R. *Small* **2010,** *6,* 2900. doi:10.1002/smll.201001349
5. Papp, I.; Sieben, C.; Sisson, A. L.; Herrmann, A.; Haag, R. *J. Controlled Release* **2010,** *148,* e114. doi:10.1016/j.jconrel.2010.07.086
6. Papp, I.; Sieben, C.; Sisson, A. L.; Kostka, J.; Böttcher, C.; Ludwig, K.; Herrmann, A.; Haag, R. *ChemBioChem* **2011,** *12,* 887. doi:10.1002/cbic.201000776
7. Tuzikov, A. B.; Chinarev, A. A.; Gambaryan, A. S.; Oleinikov, V. A.; Klinov, D. V.; Matsko, N. B.; Kadykov, V. A.; Ermishov, M. A.; Demin, I. V.; Demin, V. V.; Rye, P. D.; Bovin, N. V. *ChemBioChem* **2003,** *4,* 147. doi:10.1002/cbic.200390025
8. Lees, W. J.; Spaltenstein, A.; Kingery-Wood, J. E.; Whitesides, G. M. *J. Med. Chem.* **1994,** *37,* 3419. doi:10.1021/jm00046a027
9. Mammen, M.; Dahmann, G.; Whitesides, G. M. *J. Med. Chem.* **1995,** *38,* 4179. doi:10.1021/jm00021a007
10. Mammen, M.; Choi, S.-K.; Whitesides, G. M. *Angew. Chem., Int. Ed.* **1998,** *37,* 2754. doi:10.1002/(SICI)1521-3773(19981102)37:20<2754::AID-ANIE2754>3.0.CO;2-3
11. Fasting, C.; Schalley, C. A.; Weber, M.; Seitz, O.; Hecht, S.; Koksch, B.; Dernedde, J.; Graf, C.; Knapp, E.-W.; Haag, R. *Angew. Chem., Int. Ed.* **2012,** *51,* 10472. doi:10.1002/anie.201201114
12. Matsubara, T.; Sumi, M.; Kubota, H.; Taki, T.; Okahata, Y.; Sato, T. *J. Med. Chem.* **2009,** *52,* 4247. doi:10.1021/jm801570y
13. Matsubara, T.; Onishi, A.; Saito, T.; Shimada, A.; Inoue, H.; Taki, T.; Nagata, K.; Okahata, Y.; Sato, T. *J. Med. Chem.* **2010,** *53,* 4441. doi:10.1021/jm1002183
14. Jones, J. C.; Turpin, E. A.; Bultmann, H.; Brandt, C. R.; Schultz-Cherry, S. *J. Virol.* **2006,** *80,* 11960. doi:10.1128/JVI.01678-06
15. Jones, J. C.; Settles, E. W.; Brandt, C. R.; Schultz-Cherry, S. *Vaccine* **2011,** *29,* 7696. doi:10.1016/j.vaccine.2011.07.133
16. Jones, J. C.; Settles, E. W.; Brandt, C. R.; Schultz-Cherry, S. *Antimicrob. Agents Chemother.* **2011,** *55,* 1810. doi:10.1128/AAC.01428-10
17. Carpino, L. A.; Sadat-Aalaee, D.; Chao, H. G.; DeSelms, R. H. *J. Am. Chem. Soc.* **1990,** *112,* 9651. doi:10.1021/ja00182a041
18. Tu, R. S.; Tirrell, M. *Adv. Drug Delivery Rev.* **2004,** *56,* 1537. doi:10.1016/j.addr.2003.10.047
19. Memczak, H.; Stöcklein, W.; Ehrentreich-Förster, E. Peptides for binding of influenza viruses and inhibition of influenza infections. Eur. Pat. Appl. 14193922.3, Nov 7, 2014.
20. Cui, H.; Webber, M. J.; Stupp, S. I. *Biopolymers* **2010,** *94,* 1. doi:10.1002/bip.21328
21. Cavalli, S.; Albericio, F.; Kros, A. *Chem. Soc. Rev.* **2010,** *39,* 241. doi:10.1039/B906701A
22. Hirst, G. K. *J. Exp. Med.* **1942,** *76,* 195. doi:10.1084/jem.76.2.195

License and Terms

BEILSTEIN JOURNAL OF ORGANIC CHEMISTRY

Synthesis of a hexasaccharide partial sequence of hyaluronan for click chemistry and more

Marina Bantzi[1], Stephan Rigol[1,2] and Athanassios Giannis[*1]

Full Research Paper

Open Access

Address:
[1]Universität Leipzig, Institut für Organische Chemie, Johannisallee 29, 04103 Leipzig, Germany and [2]Current address Rice University, Department of Chemistry, BioScience Research Collaborative, 6100 Main Street, Houston, Texas 77005, USA

Email:
Athanassios Giannis[*] - giannis@uni-leipzig.de

* Corresponding author

Keywords:
azide; click chemistry; extracellular matrix; hexasaccharide; hyaluronan; multivalency

Beilstein J. Org. Chem. **2015,** *11,* 604–607.
doi:10.3762/bjoc.11.67

Received: 19 February 2015
Accepted: 27 April 2015
Published: 30 April 2015

This article is part of the Thematic Series "Multivalency as a chemical organization and action principle".

Associate Editor: J. S. Dickschat

Abstract

In the present work, the synthesis of a hexasaccharide partial sequence of hyaluronan equipped with a terminal azido moiety is reported. This hexasaccharide can be used for the attachment on surfaces by means of click chemistry and after suitable deprotection for biophysical studies.

Introduction

Much effort has been exerted during the last years to refine current knowledge about the biology of the extracellular matrix (ECM) [1]. While in the past, it was only regarded as a "space filler" among the cells, nowadays it is well known that the ECM composes the ideal microenvironment for cells in order to interact with each other and also for supporting signaling between ECM macromolecules and intracellular components [2]. Besides water, the ECM consists of electrolytes, amino acids, monosaccharides, fibrous proteins (collagens), glycosaminoglycans (GAGs), and proteoglycans (PGs). The latter are complex proteins containing at least one covalently bound glycosaminoglycan part [3]. GAGs are long, unbranched polysaccharides comprising repeating disaccharide units, which are constituted of a hexosamine and an uronic acid. These repeating disaccharide units are used for the classification of GAGs [4].

Hyaluronic acid, a member of the GAG family, owes its name to the Greek word "ὕαλος" (= glass) since it was first isolated in 1934 from the vitreous body of the bovine eye [5]. Its structure was elucidated in 1954 [6] and since 1986 it is known as "hyaluronan" (HA) [7]. HA is an unbranched polysaccharide, whose disaccharide repeating unit consists of *N*-acetylglucosamine and D-glucuronic acid conjoined through β-(1→3) and β-(1→4)-glycosidic bonds. Hyaluronan has an average size of 15–20 kDa and does not form PGs, in contrast to the other

GAGs, which are synthesized in the Golgi apparatus or the endoplasmic reticulum [8]. HA is enzymatically produced by three glycosyltransferases (HA synthases: HAS 1, 2 and 3) in the cellular plasma membrane and its chain can reach a mass of 10^2–10^4 kDa [9]. Despite its simple structure HA can trigger many signaling pathways depending on its fragments' size, thus representing an interesting target in pharmacotherapy. It is involved in tissue repair and wound healing; it serves as space

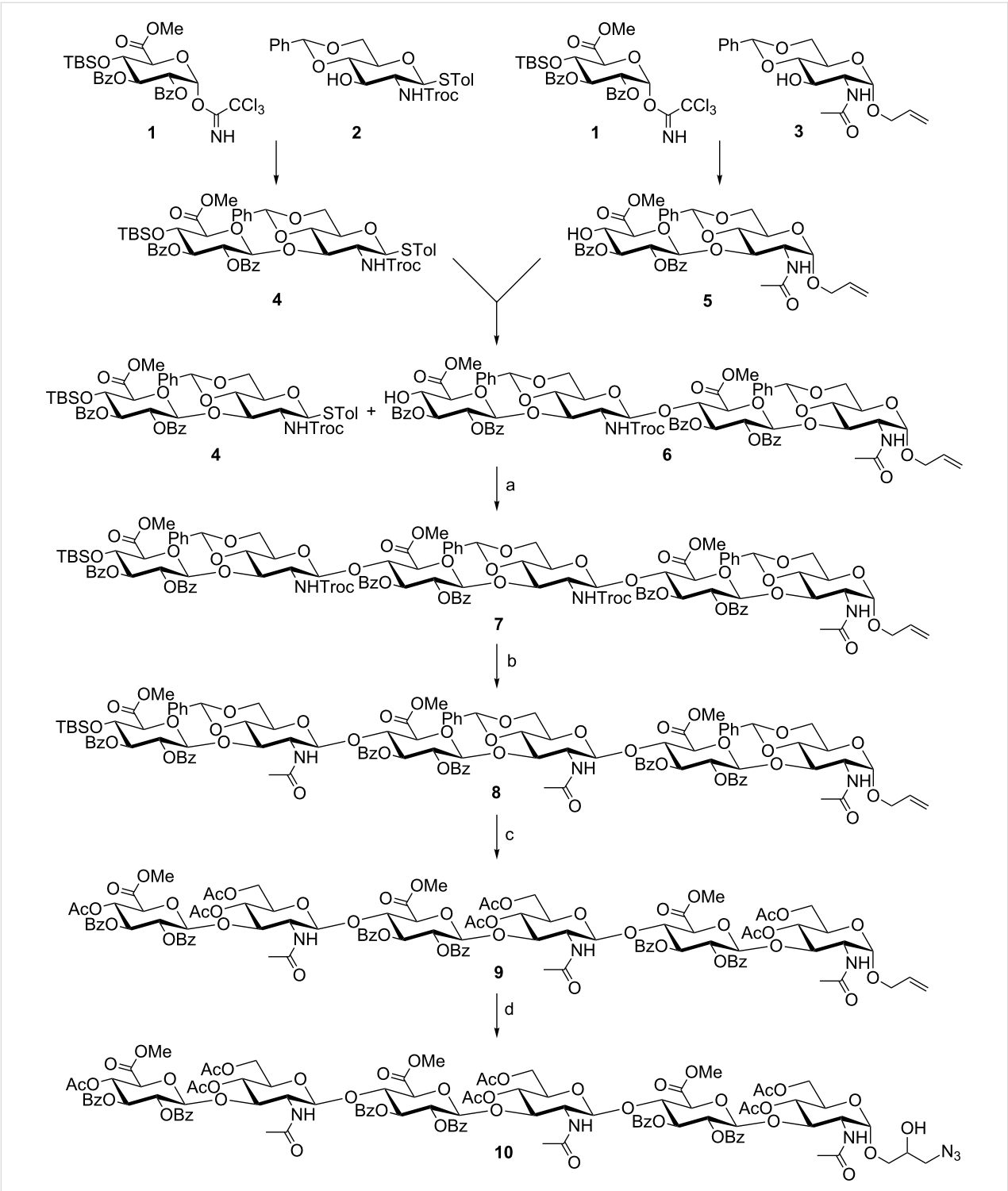

Scheme 1: Synthesis of hexasaccharide **10**. Conditions: a) TfOH, NIS, 4 Å molecular sieves, DCM, 0 °C to rt; b) 1. Zn, AcOH; 2. Ac_2O, pyridine, 50% (over 2 steps); c) 1. HF·pyridine; 2. Ac_2O, pyridine, 70%; d) 1. DMDO, acetone, −78 °C to rt; 2. NaN_3, DMF, 70%.

filler, lubricant, protector of the joints and water storage [4]. In addition, HA is able to interact with three major classes of cell surface receptors, namely CD44 (cluster of differentiation 44), RHAMM (receptor for HA-mediated motility) and ICAM-1 (intracellular adhesion molecule-1) [10,11]. CD44 is a heterogeneous, transmembrane glycoprotein which is overexpressed on the surface of cancer stem cells [11,12] and plays a crucial role in the development of different types of cancer [13]. It seems that short fragments of HA (3–25 disaccharides) cause a pro-angiogenic effect in contrast to longer ones depending on the activity of this receptor [9]. Hence, well-defined oligomers related to HA are highly desired as novel pharmacotherapy targets.

Syntheses of HA disaccharides appear for the first time in literature in 1962 from Jeanloz et al. [14] and Takanashi et al. [15]. Since then, many efforts have been done in this field resulting in the synthesis of longer HA fragments which were bearing either a free reducing end or a non-functionalized aglycone [16-18]. In 2007, a study focusing on the synthesis of HA sequences which could be functionalized and used for biological studies yielded oligosaccharides bearing an alkyl-azide [19]. Besides the results of this work as well as that from Hsieh-Wilson et al. [20] and van der Marel et al. [21] both published *O*-1-allyl-equipped HA subunits, we reported recently the first synthesis of a ^{13}C-labeled HA tetramer for ongoing biophysical studies [22]. Different methodologies were used to establish the glycosidic linkages; most important was the reaction's stereochemical outcome. Elongation of the synthesized oligosaccharides was easily done, since the TBS-protection is selectively cleavable. The anomeric allyl moiety permits varieties of feasible modifications including the introduction of an azido group. In the frame of a research project aiming the investigation of protein–GAG binding a convergent synthesis of a HA hexamer with a suitably modified aglycone is described herein.

Results and Discussion

The synthetic cascade to the desirable hexasaccharide **10** is presented in Scheme 1. Trichloroacetimidate **1** [20,23] was linked with glycosyl acceptor **2** [24,25] using TMSOTf as promoter to obtain disaccharide **4** in 90% yield. Likewise, reaction of glycosyl donor **1** with monosaccharide **3** [26] and subsequent *O*-TBS group cleavage with Olah's reagent [27], afforded disaccharide **5** in 86% yield. Thence, both disaccharides were coupled through initial activation of **4** with NIS and TfOH to furnish the corresponding protected tetrasaccharide. Furthermore, treatment of the glycosylation product with Olah's reagent and an additional amount of pyridine generated the tetrasaccharide glycosyl acceptor **6** by removal of the TBS group at O-4''' in 59% yield [22]. The excess amount of pyridine is necessary in order to avoid cleavage of the benzylidene acetals. Following the same concept, fully protected hexasaccharide **7** was synthesized. Therefore, thioglycoside **4** was activated with NIS and TfOH and subsequently combined with tetrasaccharide **6**. The underlying protecting group pattern with a selectively cleavable silyl group at the non-reducing end of the saccharide sequence permits the further elongation by additional iterative cycles based on the presented methodology. Then, the *N*-Troc groups were cleaved under mild reducing conditions (Zn, AcOH) [28] and subsequently the liberated amino groups were acetylated to furnish compound **8**. Eventually, the silyl group and all benzylidene moieties were removed by treatment with Olah's reagent to give, after acetylation, derivative **9**. Finally, oxidation of the terminal olefinic double bond with Murray's reagent [29,30] yielded the analogous epoxide that was treated with NaN_3 in order to afford the desired azido-modified hexasaccharide **10**.

Conclusion

In conclusion, hexasaccharide **10** was successfully prepared in 26 steps and is readily equipped with a terminal azido group. Thus, allowing it to be used for surface modification via click chemistry. After suitable deprotection it can be used for biophysical studies by interaction with an alkyne group of suitably prepared proteins or proteoglycans giving the opportunity to gain deeper insights into ECM processes. Eventually, this knowledge can be employed during the development of artificial extracellular matrices for basic research in the field of wound healing in skin and bone injuries.

Supporting Information

Supporting Information File 1

Experimental details, analytical data and copies of ^{1}H and ^{13}C NMR spectra for the newly synthesized compounds.
[http://www.beilstein-journals.org/bjoc/content/supplementary/1860-5397-11-67-S1.pdf]

Acknowledgements

This work was partially supported by the Deutsche Forschungsgemeinschaft (Transregio 67, project Z3). We thank Dr. Lothar Hennig, Universität Leipzig, for his general help and especially for recording NMR spectra and interpreting the 2D NMR spectra.

References

1. Kim, S.-H.; Turnbull, J.; Guimond, S. *J. Endocrinol.* **2011,** *209,* 139–151. doi:10.1530/JOE-10-0377
2. Hynes, R. O. *Science* **2009,** *326,* 1216–1219. doi:10.1126/science.1176009

3. Theocharis, A. D.; Gialeli, C.; Bouris, P.; Giannopoulou, E.; Skandalis, S. S.; Aletras, A. J.; Iozzo, R. V.; Karamanos, N. K. *FEBS J.* **2014,** *281,* 5023–5042. doi:10.1111/febs.12927
4. Gandhi, N. S.; Mancera, R. L. *Chem. Biol. Drug Des.* **2008,** *72,* 455–482. doi:10.1111/j.1747-0285.2008.00741.x
5. Meyer, K.; Palmer, J. W. *J. Biol. Chem.* **1934,** *107,* 629–634.
6. Weissmann, B.; Meyer, K. *J. Am. Chem. Soc.* **1954,** *76,* 1753–1757. doi:10.1021/ja01636a010
7. Balazs, E. A.; Laurent, T. C.; Jeanloz, R. W. *Biochem. J.* **1986,** *235,* 903.
8. Fraser, J. R. E.; Laurent, T. C. *J. Intern. Med.* **1997,** *242,* 25–26. doi:10.1046/j.1365-2796.1997.00169.x
9. Vigetti, D.; Karousou, E.; Viola, M.; Deleonibus, S.; De Luca, G.; Passi, A. *Biochim. Biophys. Acta* **2014,** *1840,* 2452–2459. doi:10.1016/j.bbagen.2014.02.001
10. Chen, W. Y. J.; Abatangelo, G. *Wound Repair Regener.* **1999,** *7,* 79–89. doi:10.1046/j.1524-475X.1999.00079.x
11. Arpicco, S.; Lerda, C.; Pozza, E. D.; Costanzo, C.; Tsapis, N.; Stella, B.; Donadelli, M.; Dando, I.; Fattal, E.; Cattel, L.; Palmieri, M. *Eur. J. Pharm. Biopharm.* **2013,** *85,* 373–380. doi:10.1016/j.ejpb.2013.06.003
12. Eliaz, R. E.; Szoka, F. C. *Cancer Res.* **2001,** *61,* 2592–2601.
13. Wang, H.; Tan, M.; Zhang, S.; Li, X.; Gao, J.; Zhang, D.; Hao, Y.; Gao, S.; Liu, J.; Lin, B. *Int. J. Mol. Sci.* **2015,** *16,* 3391–3404. doi:10.3390/ijms16023391
14. Jeanloz, R. W.; Flowers, H. M. *J. Am. Chem. Soc.* **1962,** *84,* 3030. doi:10.1021/ja00874a045
15. Takanashi, S.; Hirasaka, Y.; Kawada, M.; Ishidate, M. *J. Am. Chem. Soc.* **1962,** *84,* 3029. doi:10.1021/ja00874a044
16. Slaghek, T.; Nakahara, Y.; Ogawa, T. *Tetrahedron Lett.* **1992,** *33,* 4971–4974. doi:10.1016/S0040-4039(00)61248-0
17. Slaghek, T. M.; Hyppönen, T. K.; Ogawa, T.; Kamerling, J. P.; Vliegenthart, J. F. G. *Tetrahedron Lett.* **1993,** *34,* 7939–7942. doi:10.1016/S0040-4039(00)61517-4
18. Blatter, G.; Jacquinet, J. C. *Carbohydr. Res.* **1996,** *288,* 109–125. doi:10.1016/S0008-6215(96)90785-5
19. Dinkelaar, J.; Codée, J. D. C.; van den Bos, L. J.; Overkleeft, H. S.; van der Marel, G. A. *J. Org. Chem.* **2007,** *72,* 5737–5742. doi:10.1021/jo070704s
20. Tully, S. E.; Mabon, R.; Gama, C. I.; Tsai, S. M.; Liu, X.; Hsieh-Wilson, L. C. *J. Am. Chem. Soc.* **2004,** *126,* 7736–7737. doi:10.1021/ja0484045
21. Walvoort, M. T. C.; Volbeda, A. G.; Reintjens, N. R. M.; van den Elst, H.; Plante, O. J.; Overkleeft, H. S.; van der Marel, G. A.; Codée, J. D. C. *Org. Lett.* **2012,** *14,* 3776–3779. doi:10.1021/ol301666n
22. Rigol, S.; Xia, L.; Giannis, A. *Bioorg. Med. Chem.* **2013,** *21,* 733–741. doi:10.1016/j.bmc.2012.11.025
23. France, R. R.; Compton, R. G.; Davis, B. G.; Fairbanks, A. J.; Rees, N. V.; Wadhawan, J. D. *Org. Biomol. Chem.* **2004,** *2,* 2195–2202. doi:10.1039/b316728c
24. Wang, Z.; Zhou, L.; El-Boubbou, K.; Ye, X.-s.; Huang, X. *J. Org. Chem.* **2007,** *72,* 6409–6420. doi:10.1021/jo070585g
25. Geng, Y.; Zhang, L.-H.; Ye, X.-S. *Tetrahedron* **2008,** *64,* 4949–4958. doi:10.1016/j.tet.2008.03.103
26. Izumi, M.; Fukase, K.; Kusumoto, S. *Biosci., Biotechnol., Biochem.* **2002,** *66,* 211–214. doi:10.1271/bbb.66.211
27. Olah, G. A.; Nojima, M.; Kerekes, I. *Synthesis* **1973,** 779–780. doi:10.1055/s-1973-22297
28. Schultz, M.; Kunz, H. *Tetrahedron: Asymmetry* **1993,** *4,* 1205–1220. doi:10.1016/S0957-4166(00)80230-X
29. Murray, R. W.; Singh, M.; Rath, N. *J. Org. Chem.* **1997,** *62,* 8794–8799. doi:10.1021/jo971339f
30. Murray, R. W.; Singh, M. *Org. Synth.* **1997,** *74,* 91–100. doi:10.15227/orgsyn.074.0091

License and Terms

BEILSTEIN JOURNAL OF ORGANIC CHEMISTRY

Automated solid-phase synthesis of oligosaccharides containing sialic acids

Chian-Hui Lai[1], Heung Sik Hahm[1,2], Chien-Fu Liang[1] and Peter H. Seeberger[*1,2,§]

Full Research Paper

Open Access

Address:
[1]Department of Biomolecular Systems, Max-Planck-Institute of Colloids and Interfaces, Am Mühlenberg 1, 14476 Potsdam, Germany and [2]Freie Universität Berlin, Institute of Chemistry and Biochemistry, Arnimallee 22, 14195 Berlin, Germany

Email:
Peter H. Seeberger[*] - peter.seeberger@mpikg.mpg.de

* Corresponding author
§ Fax: +49 30 838-59302; Tel: +49 30 838-59301

Keywords:
α-sialylation; automated synthesis; glycosylation; sialic acid; solid-phase synthesis

Beilstein J. Org. Chem. **2015,** *11,* 617–621.
doi:10.3762/bjoc.11.69

Received: 11 February 2015
Accepted: 20 April 2015
Published: 04 May 2015

This article is part of the Thematic Series "Multivalency as a chemical organization and action principle".

Associate Editor: S. Flitsch

Abstract

A sialic acid glycosyl phosphate building block was designed and synthesized. This building block was used to prepare α-sialylated oligosaccharides by automated solid-phase synthesis selectively.

Introduction

N-Acetylneuraminic acid (sialic acid, Neu5Ac) is an important component of mammalian glycans and key to many recognition events of biomedical relevance including cell–cell recognition, signaling, and the immune response [1]. Sialic acids are present in tumor-associated carbohydrate antigens (TACAs) such as the sialyl-Tn antigen (sTn) [2]. Neu5Ac is often the terminal residue and is usually linked via an α-(2,3) or α-(2,6) linkage to galactose (Gal) (Figure 1) [3].

Automated glycan assembly enables rapid access to structurally defined oligosaccharides [4,5] including glycopeptides [6], glycosaminoglycans [7-9], and chains as long as 30-mers [10]. Key to automated assembly is the identification of reliable monosaccharide building blocks to construct particular linkages. To date, α-(2,3)- and α-(2,6)-sialylated glycans have been accessible by automation only via incorporation of sialic acid–galactose disaccharide building blocks [5,11]. Here, we describe a sialic acid building block that can be utilized for automated glycan assembly.

Results and Discussion

Sialylating oligosaccharides in high yield and α-selectivity was challenging since the presence of a C-1 carboxyl electron-withdrawing group at the quaternary anomeric center decreases the reactivity. In addition, no participating group on C-3 can be used to direct the stereochemistry at the anomeric carbon (C-2)

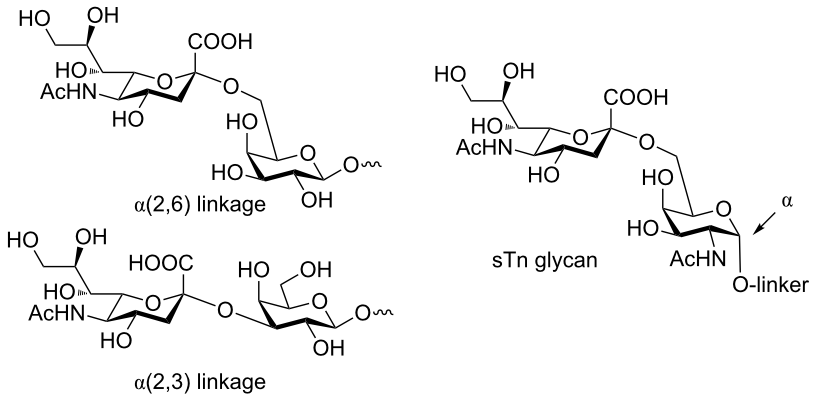

Figure 1: Terminal sialic acids are typically α-(2,3) or α-(2,6) linked to galactose (Gal) such as in the tumour-associated antigen sialyl Tn (sTn).

[2]. Efficient chemical sialylation reactions utilize the cyclic 4*O*,5*N*-oxazolidinone protecting group [12-15], where the *trans*-fused cyclic protecting group in the glycosylation transition state likely stabilizes the positive charge on the intermediate acetonitrile adduct and decreases the generation of a positive charge at the anomeric center by their strong dipole moment [2,16,17].

Based on these considerations sialyl phosphate building blocks **4** and **5** [14] were selected for automated glycan assembly using monosaccharides (Scheme 1). The synthesis of building block **4** commenced with the placement of a C-9 Fmoc protecting group on thioglycoside **1** [14] to produce **2**. Installation of *O*-chloroacetyl groups on C-7 and C-8 for better α-stereoselectivity [12] produced **3**. An α-anomeric phosphate leaving group was chosen since it had previously shown high reactivity [14,18] and selectivity [15]. Building block **4** was obtained in 54% yield over three steps from **1**.

"Approved building blocks" for automated glycan assembly have to be accessible in sufficient quantities, stable for storage and activated at a specific temperature to provide the desired linkage in high yield. The optimal glycosylation temperature was determined to ensure fast and efficient reactions at the highest possible temperature [19,20]. Rather than slowly warming a reaction mixture as is done in solution phase, on the automated synthesizer, the building block will be delivered at the optimal temperature and reacted for a predetermined time. For sialic acid building block **4**, the activation temperature was determined to be −20 °C (Table S1 in Supporting Information File 1). The synthesis of trisaccharides **14** illustrates how optimization of the activation temperature resulted in increased yields (Table S4 in Supporting Information File 1).

Six di- and trisaccharides (**12**–**17**, Scheme 2) served as targets to develop an automated method for chemical sialylation. Monosaccharide building blocks **4**, **5** [14], **6**, **7** [21], **8**, **9** [21],

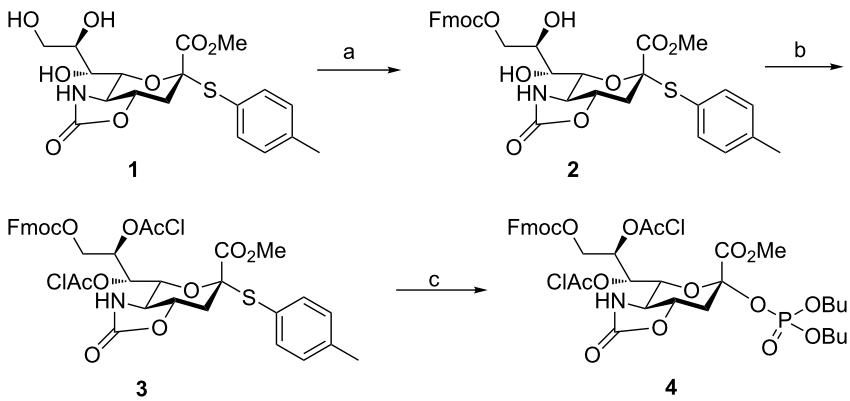

Scheme 1: (a) FmocCl, py, CH_2Cl_2, rt, 4 h, 77%, (b) 2-chloroacetyl chloride, py, CH_2Cl_2, 0 °C to rt, 3 h, 88%, (c) $HOPO(OBu)_2$, NIS, TfOH, 4 Å MS, CH_3CN/CH_2Cl_2, −78 °C to 0 °C, 2 h, 80%.

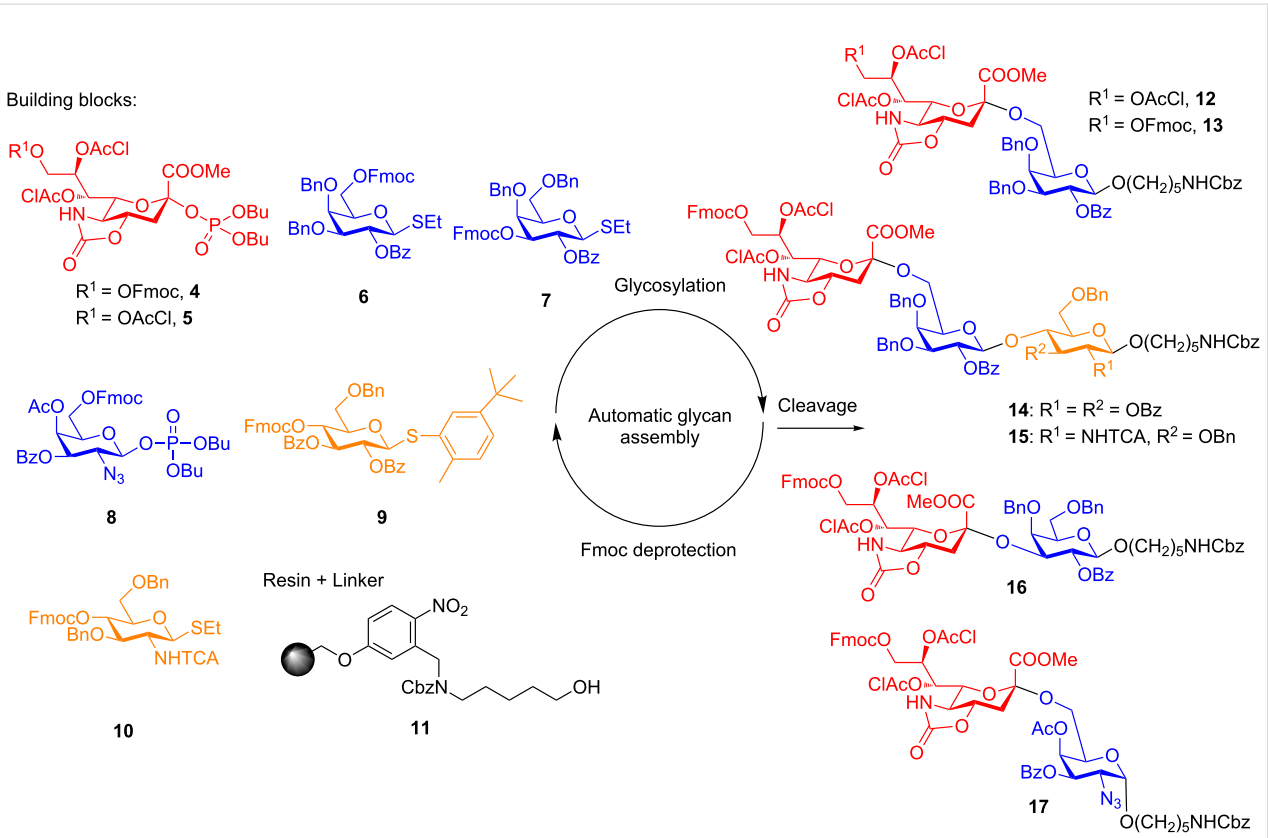

Scheme 2: Automated synthesis of oligosaccharides with α(2,3)-, α(2,6)-sialic acid linkages. Glycosylations: a) 2 × 5 equiv TMSOTf, ACN/DCM (1:1), −50 °C (5 min), −30 °C (10 min), −20 °C (80 min), −10 °C (10 min), 0 °C (10 min) for **4** and **5**. b) 2 × 5 equiv TfOH, NIS, DCM, −40 °C (5 min), −20 °C (30 min) for **6** and **7**. c) 2 × 5 equiv TMSOTf, DCM/dioxane (3:2), 20 °C (90 min), for **8**. d) 2 × 5 equiv TfOH, NIS, DCM, −30 °C (5 min), −10 °C (25 min) for **9** and **10**. Fmoc Deprotection: e) 3 × 20% NEt_3 in DMF, 5 min. Photocleavage: f) UV irradiation using a continuous flow reactor, DCM, rt. Synthesis of **12** or **13**: (1) **6**, b, (2) e, (3) **4** or **5**, a (4) f, 30% for four steps to yield **12**, 40% for four steps to yield **13**; synthesis of **14**: (1) **9**, d, (2) e, (3) **6**, b, (4) e, (5) **4**, a, (6) f, 22% for six steps; synthesis of **15**: (1) **10**, d, (2) e, (3) **6**, b, (4) e, (5) **4**, a, (6) f, 7% for six steps; synthesis of **16**: (1) **7**, b, (2) e, (3) **4**, a, (4) f, 19% for four steps; synthesis of **17**: (1) **8**, c, (2) e, (3) 3 × Ac_2O, py, 25 °C for 60 min, (4) **4**, a, (5) f, 10% for five steps.

and **10** [5] were employed for these syntheses. Merrifield polystyrene resin equipped with a photocleavable linker, **11**, was placed in the reaction chamber of the automated synthesizer and the coupling cycles were initiated following programmed maneuvers. Each cycle starts with a TMSOTf acidic wash at −20 °C to ensure that no base from previous deprotection reactions remains and quenches the subsequent coupling. This problem had been observed earlier (data not shown) and can be overcome by this extra washing step. In addition, TMSOTf eliminates any moisture that may have resided on the resin or in the reaction vessel.

Glycosylations were carried out using the optimized temperatures for each building block using twice five equivalents of building block and activator. Removal of the Fmoc protecting group with triethylamine uncovered the hydroxy group to serve as the nucleophile in the next coupling. Participating protecting groups at the C2 position of building blocks **6**, **7**, **9** and **10** ensured selective formation of β-glycosidic linkages during the glycosylations. These building blocks resulted in complete conversion as determined by Fmoc quantification [5] and HPLC analysis.

Sialyl phosphate building blocks **4** and **5** resulted in good α-selectivity for the installation of α-(2,6)-linkages in disaccharides **12** and **13**, both sialyl phosphate building blocks **4** and **5** showed exclusive α-selectivity. However, building block **4** was more reactive than **5** as the synthesis of disaccharide **13** resulted almost in full α-sialylation as observed by HPLC analysis of the crude product following photocleavage from the resin that showed only one peak while **12** was not the only product. Disaccharide **12** was obtained in 30% and **13** in 40% overall yield for four steps based on resin loading. The absolute anomeric configurations of glycans that contain sialylic acid were determined by recording the long-range coupling constants of C1 with axial H3 (^3J C-1,H-3_{ax}) using 1D coupled HMQC experiments. Coupling constant higher than 5 Hz correspond to α-configurations [12].

Two trisaccharides (**14** and **15**) that are α-(2,6)-sialylated were obtained in 22% and 7% yield after HPLC purification based on resin loading for six steps. The sialylation proceeded with α-stereoselectivity in both cases. The synthesis of **14** was higher yielding than **15**. The major structural difference of **14** and **15** is the first sugar attached on the resin. The *N*-protecting TCA group of glucosaminoside has more electron-withdrawing character in the synthesis of **15** than the benzoate ester groups of the glucoside in the synthesis of **14** which resulted in a less favorable sialylation for **15**.

To demonstrate that α-(2,3)-sialylations are possible, model disaccharide **16** was synthesized in 19% yield. The secondary C3 hydroxy group in galactose is less reactive and consequently, even after optimization, the chemical sialylation of the C3 position of galactose did not result in a satisfactory yield and demonstrates a current limitation of the automated glycan assembly approach. Recently, placement of an isothiocyanate moiety on the C5 position was reported to be an effective method to construct alpha linkages [22] and may prove useful for solid-phase synthesis in the future as well.

The tumor associated sTn carbohydrate antigen (Neu5Ac-α(2,6)GalNAc-α(1,1)linker) disaccharide **17**, that resembles the sTn antigen glycan framework (Neu5Ac-α(2,6)GalNAc-α(1,1)Ser/Thr) was synthesized. In order to install the *cis*-glycoside formed by the union of the galactosamine and the linker, galactosamine building block **8** relies on remote participating protecting group effects of esters at C3 and C4 [23,24]. The selectivity of the *cis*-glycosylation improved with higher reaction temperatures due the strongly deactivating effect of three electron withdrawing ester and carbonate protecting groups [23,25]. The addition of dioxane to CH_2Cl_2 resulted in preferred formation of the α-anomer, an effect that is well known from solution phase syntheses [26] (Table S6, Figure S1 in Supporting Information File 1). When five equivalents of building block **8** were used at 20 °C for 90 min with a solvent ratio of CH_2Cl_2 and dioxane of 3:2, mainly the desired α-anomer was obtained (2:1). A double coupling of building block **8** to install the α-galactosamine linker was followed by a capping step. Incorporation of building block **4**, cleavage from the resin and purification by HPLC yielded disaccharide **17** in 10% yield.

Conclusion

In summary, we demonstrated that a 5*N*,4*O*-carbonyl-7,8-di-*O*-chloroacetyl-9-*O*-Fmoc-protected sialic acid phosphate building block **4** can be used to install α(2,6)-sialic acid linkages efficiently, while it did not give satisfactory results for α(2,3)-sialylations. The latter linkage has to be incorporated either by using a preformed sialic acid–Gal disaccharide building block [11] or by enzymatic sialylation [27] following the cleavage and deprotection of an oligosaccharide.

Supporting Information

Supporting Information File 1

Experimental part.
[http://www.beilstein-journals.org/bjoc/content/supplementary/1860-5397-11-69-S1.pdf]

Acknowledgements

We thank the Max Planck Society and the ERC (Advanced Grant AUTOHEPARIN) for very generous financial support. We thank Dr. Fabian Pfrengle, Dr. Mattan Hurevich and Mr. Frank Schuhmacher for assistance in operating the synthesizer, HPLC and fruitful discussions.

References

1. Varki, A.; Cummings, R. D.; Esko, J. D.; Freeze, H. H.; Stanley, P.; Bertozzi, C. R.; Hart, G. W.; Etzler, M. E. *Essentials of glycobiology,* 2nd ed.; Cold Spring Harbor Laboratory Press: New York, 2009.
2. Adak, A. K.; Yu, C.-C.; Liang, C.-F.; Lin, C.-C. *Curr. Opin. Chem. Biol.* **2013,** *17,* 1030–1038. doi:10.1016/j.cbpa.2013.10.013
3. Varki, A. *Nature* **2007,** *446,* 1023–1029. doi:10.1038/nature05816
4. Plante, O. J.; Palmacci, E. R.; Seeberger, P. H. *Science* **2001,** *291,* 1523–1527. doi:10.1126/science.1057324
5. Kröck, L.; Esposito, D.; Castagner, B.; Wang, C.-C.; Bindschädler, P.; Seeberger, P. H. *Chem. Sci.* **2012,** *3,* 1617–1622. doi:10.1039/c2sc00940d
6. Hurevich, M.; Seeberger, P. H. *Chem. Commun.* **2014,** *50,* 1851–1853. doi:10.1039/c3cc48761j
7. Eller, S.; Collot, M.; Yin, J.; Hahm, H. S.; Seeberger, P. H. *Angew. Chem., Int. Ed.* **2013,** *52,* 5858–5861. doi:10.1002/anie.201210132
8. Kandasamy, J.; Schuhmacher, F.; Hahm, H. S.; Klein, J. C.; Seeberger, P. H. *Chem. Commun.* **2014,** *50,* 1875–1877. doi:10.1039/c3cc48860h
9. Walvoort, M. T. C.; Volbeda, A. G.; Reintjens, N. R. M.; van den Elst, H.; Plante, O. J.; Overkleeft, H. S.; van der Marel, G. A.; Codée, J. D. C. *Org. Lett.* **2012,** *14,* 3776–3779. doi:10.1021/ol301666n
10. Calin, O.; Eller, S.; Seeberger, P. H. *Angew. Chem., Int. Ed.* **2013,** *52,* 5862–5865. doi:10.1002/anie.201210176
11. Esposito, D.; Hurevich, M.; Castagner, B.; Wang, C.-C.; Seeberger, P. H. *Beilstein J. Org. Chem.* **2012,** *8,* 1601–1609. doi:10.3762/bjoc.8.183
12. Lin, C.-C.; Lin, N.-P.; Sahabuddin, L. S.; Reddy, V. R.; Huang, L.-D.; Hwang, K. C.; Lin, C.-C. *J. Org. Chem.* **2010,** *75,* 4921–4928. doi:10.1021/jo100824s
13. Tanaka, H.; Nishiura, Y.; Takahashi, T. *J. Am. Chem. Soc.* **2006,** *128,* 7124–7125. doi:10.1021/ja0613613
14. Chu, K.-C.; Ren, C.-T.; Lu, C.-P.; Hsu, C.-H.; Sun, T.-H.; Han, J.-L.; Pal, B.; Chao, T.-A.; Lin, Y.-F.; Wu, S.-H.; Wong, C.-H.; Wu, C.-Y. *Angew. Chem., Int. Ed.* **2011,** *50,* 9391–9395. doi:10.1002/anie.201101794

15. Hsu, C.-H.; Chu, K.-C.; Lin, Y.-S.; Han, J.-L.; Peng, Y.-S.; Ren, C.-T.; Wu, C.-Y.; Wong, C.-H. *Chem. – Eur. J.* **2010,** *16,* 1754–1760. doi:10.1002/chem.200903035
16. Kancharla, P. K.; Navuluri, C.; Crich, D. *Angew. Chem., Int. Ed.* **2012,** *51,* 11105–11109. doi:10.1002/anie.201204400
17. Kancharla, P. K.; Kato, T.; Crich, D. *J. Am. Chem. Soc.* **2014,** *136,* 5472–5480. doi:10.1021/ja501276r
18. Weishaupt, M. W.; Matthies, S.; Seeberger, P. H. *Chem. – Eur. J.* **2013,** *19,* 12497–12503. doi:10.1002/chem.201204518
19. Seeberger, P. H. *Chem. Soc. Rev.* **2008,** *37,* 19–28. doi:10.1039/B511197H
20. Ratner, D. M.; Murphy, E. R.; Jhunjhunwala, M.; Snyder, D. A.; Jensen, K. F.; Seeberger, P. H. *Chem. Commun.* **2005,** 578–580. doi:10.1039/B414503H
21. Hofmann, J.; Hahm, H. S.; Seeberger, P. H.; Pagel, K. submitted for publication.
22. Mandhapati, A. R.; Rajender, S.; Shaw, J.; Crich, D. *Angew. Chem., Int. Ed.* **2015,** *54,* 1275–1278. doi:10.1002/anie.201409797
23. Kalikanda, J.; Li, Z. *J. Org. Chem.* **2011,** *76,* 5207–5218. doi:10.1021/jo1025157
24. Ngoje, G.; Addae, J.; Kaur, H.; Li, Z. *Org. Biomol. Chem.* **2011,** *9,* 6825–6831. doi:10.1039/c1ob05893b
25. Park, J.; Kawatkar, S.; Kim, J.-H.; Boons, G.-J. *Org. Lett.* **2007,** *9,* 1959–1962. doi:10.1021/ol070513b
26. Demchenko, A.; Stauch, T.; Boons, G.-J. *Synlett* **1997,** 818–820. doi:10.1055/s-1997-5762
27. Fair, R. J.; Hahm, H. S.; Seeberger, P. H. *Chem. Commun.* **2015,** *51,* 6183–6185. doi:10.1039/C5CC01368B

License and Terms

BEILSTEIN JOURNAL OF ORGANIC CHEMISTRY

Synthesis of multivalent carbohydrate mimetics with aminopolyol end groups and their evaluation as L-selectin inhibitors

Joana Salta[1], Jens Dernedde[2] and Hans-Ulrich Reissig[*1]

Full Research Paper

Open Access

Address:
[1]Freie Universität Berlin, Institut für Chemie und Biochemie, Takustrasse 3, D-14195 Berlin, Germany and [2]Charité Universitätsmedizin Berlin, Institut für Laboratoriumsmedizin, Klinische Chemie und Pathobiochemie, Campus Virchow Klinikum, Augustenburger Platz 1, D-13353 Berlin, Germany

Email:
Hans-Ulrich Reissig[*] - hreissig@chemie.fu-berlin.de

* Corresponding author

Keywords:
aminopolyols; carbohydrate mimetics; carboxylic acid amides; inhibition; multivalency; selectins; sulfation

Beilstein J. Org. Chem. **2015,** *11,* 638–646.
doi:10.3762/bjoc.11.72

Received: 26 February 2015
Accepted: 21 April 2015
Published: 05 May 2015

This article is part of the Thematic Series "Multivalency as a chemical organization and action principle".

Guest Editor: R. Haag

Abstract

In this article a series of divalent and trivalent carbohydrate mimetics on the basis of an enantiopure aminopyran and of serinol is described. These aminopolyols are connected by amide bonds to carboxylic acid derived spacer units either by Schotten–Baumann acylation or by coupling employing HATU as reagent. The *O*-sulfation employing the SO_3·DMF complex was optimized. It was crucial to follow this process by 700 MHz ^{1}H NMR spectroscopy to ensure full conversion and to use a refined neutralization and purification protocol. Many of the compounds could not be tested as L-selectin inhibitor by SPR due to their insolubility in water, nevertheless, a divalent and a trivalent amide showed surprisingly good activities with IC_{50} values in the low micromolar range.

Introduction

In a series of publications [1-6] our group reported on the syntheses of carbohydrate mimetics [7-11] that are based on aminopyrans, aminooxepanes or other aminopolyols. These compounds and their conjugates were prepared to be examined as selectin inhibitors. There we have found that sulfated aminopyrans connected by amide bonds to gold nanoparticles are highly potent inhibitors of L- and P-selectin with IC_{50} values in the subnanomolar range [12,13]. These lectins are crucial in the inflammatory process [14-18] and hence compounds inhibiting their activity are of interest as potential therapeutics [19-23]. In a previous report [24] we described the synthesis of divalent carbohydrate mimetics connecting aminopyran **1** or its simplified analog serinol (**2**) (Scheme 1) to different linker units by reductive amination of aldehydes. We now enclose our results on the preparation of related di- and trivalent carbohydrate mimetics in which compounds **1** or **2** are connected to carboxylic acid cores by amide bonds. A series of compounds with spacer units of different length and rigidity were prepared in order to find smaller inhibitors than the above mentioned nanoparticles and also to examine multivalency

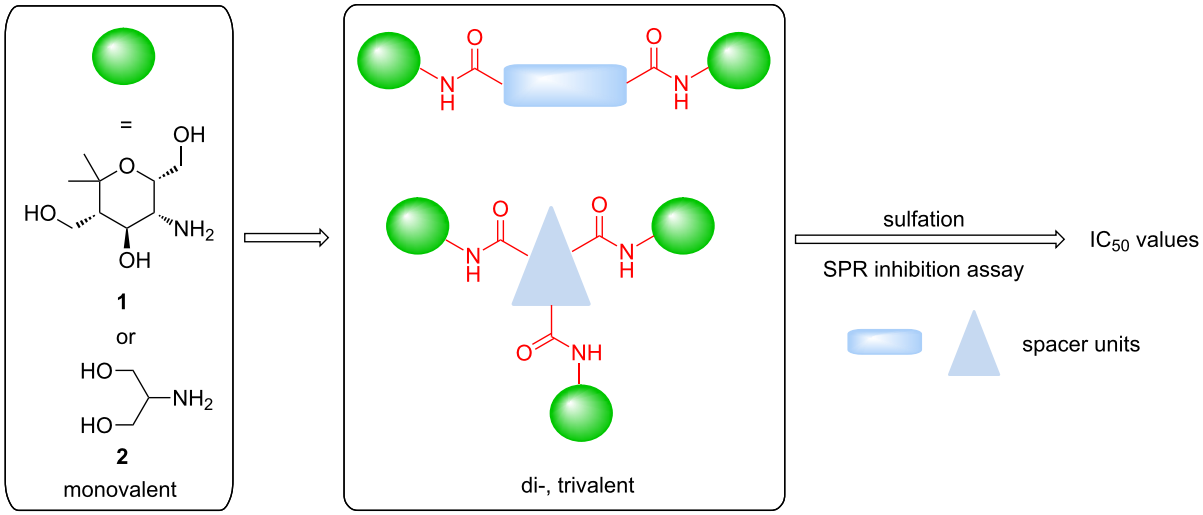

Scheme 1: General approach to divalent or trivalent carbohydrate mimetics on the basis of aminopyran **1** or serinol (**2**) and their evaluation as selectin inhibitors.

effects [25,26]. Several of these compounds could successfully be sulfated and tested as L-selectin inhibitors.

Results and Discussion

Aminopyran **1** was easily available following the previously reported synthetic route [24,27,28], whereas serinol (**2**) is commercially available. As a first approach to construct amide derivatives we envisioned the Schotten–Baumann acylation using acid chlorides. For this purpose a protection of the hydroxy groups of aminopyran **1** with the *tert*-butyldimethylsilyl (TBS) group was chosen. Reaction of **1** with *tert*-butyldimethylsilyl triflate (TBSOTf) and a tertiary amine as base under standard conditions furnished compound **3** (Scheme 2). This transformation required remarkably long reaction times when applied to compound **1** and only after 5 days a yield of 97% could be obtained. As a first model reaction protected aminopyran **3** was treated with commercially available hexanoyl chloride affording the desired amide **4** in excellent yield. After cleavage of the TBS protecting groups, the fully deprotected monovalent aminopyran derivative **5** was isolated in quantitative yield.

After the successful synthesis of the monovalent compound **5**, the same conditions were examined for the synthesis of related divalent systems. When these reaction conditions were applied to protected aminopyran **3** with succinic acid dichloride, the desired divalent product **6** was not formed (Scheme 3). After several attempts changing reaction time and equivalents of protected aminopyran **3** and succinic acid dichloride, neither the desired product **6** nor the corresponding pyrrolidine-2,5-dione resulting from an intramolecular reaction were formed.

It was quite unexpected that we could not achieve this transformation since in the literature similar conditions were found for

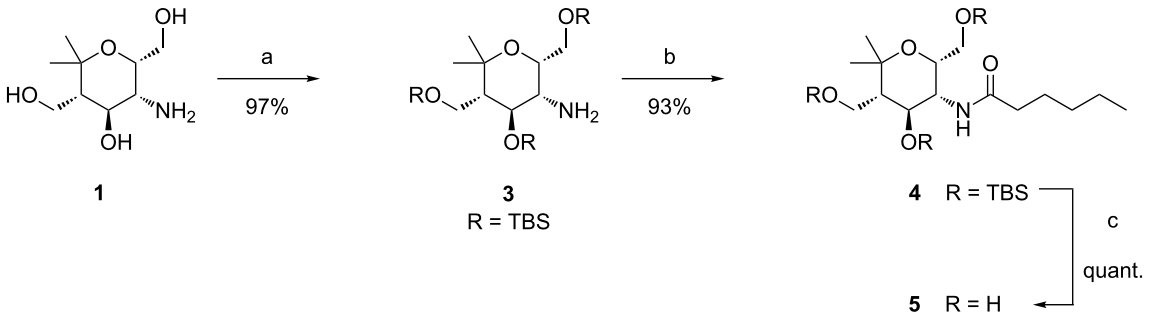

Scheme 2: Hydroxy group protection of aminopyran **1** to give compound **3**, synthesis of amide **4** and subsequent deprotection. Conditions: a) TBSOTf, Et_3N, DMAP, DMF, 5 d, 0 °C to rt; b) hexanoyl chloride, Et_3N, CH_2Cl_2, 18 h, rt; c) HF·pyridine, 24 h, 0 °C to rt.

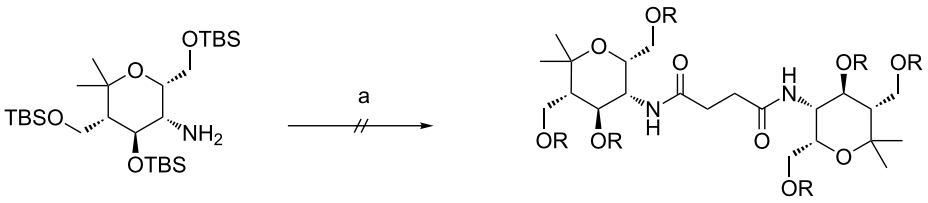

Scheme 3: Attempt to synthesize protected divalent compound **6**. Conditions: a) succinic acid dichloride, Et_3N, CH_2Cl_2, 24 h, rt.

the synthesis of multivalent acetyl-protected carbohydrates [29]. As possible explanation we assume that the formation of product **6** is sterically too hindered due to the bulkiness of the TBS-protecting groups of **3** and the short distance between the two aminopyran units. For this reason, other dicarboxylic acid derivatives with longer chains and different flexibility were tested and gratifyingly the desired products could be prepared (Table 1). The reaction with the aromatic linker terephthaloyl dichloride (**7**, Table 1, entry 1) afforded the desired protected divalent compound **10** in excellent yield. Using the aliphatic sebacoyl dichloride (**8**) as linker (Table 1, entry 2), the expected product **11** could be isolated in 58% yield. The interesting *trans*-azobenzene derivative **9** [30] was also employed as precursor and the divalent compound **12** was obtained in excel-

Table 1: Synthesis of amides **10–12** and subsequent deprotection to give divalent compounds **13–15**.

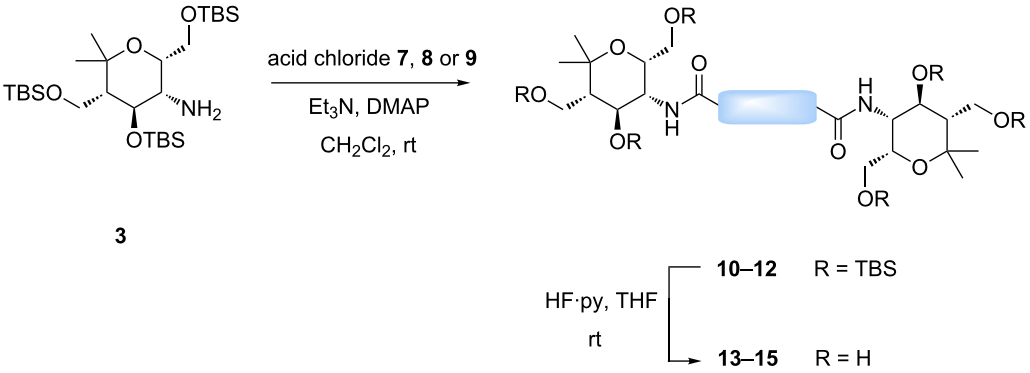

Entry	Acid dichloride	Time 1[a] [h]	Product	Yield [%]	Time 2[b] [h]	Product	Yield [%]
1	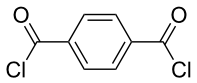 **7**	20	**10**	quant.	22	**13**	quant.
2	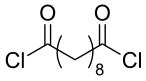 **8**	20	**11**	58	24	**14**	80
3	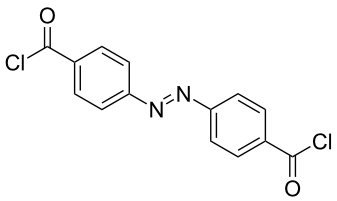 **9**	24	**12**	quant.	24	**15**	quant.

[a]First step; [b]second step.

lent yield (Table 1, entry 3). This product is particular intriguing since it offers the possibility to generate a light-switchable divalent carbohydrate mimetic. Deprotection using HF·pyridine complex proved to be an adequate method and all fully deprotected amides **13**–**15** were isolated in excellent yields.

As previously mentioned, an additional goal of this study was the investigation of multivalent compounds starting from the simple aminopolyol **2**. Analogously to aminopyran **1**, the hydroxy groups of **2** were first protected with TBS groups under standard conditions to furnish compound **16**. To be able to compare aminopyran **1** with aminopolyol **2** two divalent amides were synthesized from compound **16** using the same carboxylic acid dichlorides **7** and **8** as linkers affording the desired compounds **18** and **19** in excellent yields (Table 2, entries 1 and 2). Moreover, another divalent amide **20** with a longer spacer unit was synthesized using adipic acid dichloride (**17**) as precursor (Table 2, entry 3). Although TBS deprotection with the HF·pyridine complex proved to be a fairly efficient method (see Table 1), other options were searched in order to find milder conditions, cheaper reagents and a simpler work-up protocol for the very hydrophilic products. Acid-promoted solvolysis in the absence of water [31] was considered as good alternative that should have the advantage of generating side products that can easily be removed in vacuo, making further purification unnecessary. First attempts with acetyl chloride (0.6 equivalents) as source of dry hydrochloric acid and methanol as protic solvent gave only poor conversions, probably due to the low solubility of the starting material **18** in this alcohol. On the other hand, excellent results could be achieved with 2-propanol as solvent. Under these conditions the fully deprotected divalent amides **21**–**23** were isolated in an operationally very simple manner and in excellent yields (Table 2).

In order to directly obtain the unprotected multivalent carbohydrate mimetics we looked for alternative methods not requiring the protection of the hydroxy groups of **1** or **2**. The most common method in modern synthetic chemistry to generate amide bonds is the use of coupling reagents that first activate the carboxylic acid which subsequently reacts with an amine, also in the presence of unprotected hydroxy groups. From the many known coupling reagents [32,33] we selected HATU (1-[bis(dimethylamino)methylene]-1*H*-1,2,3-triazolo[4,5-*b*]pyridinium-3-oxide hexafluorophosphate), a coupling reagent frequently used in peptide synthesis [34]. We applied standard conditions for the preparation of one divalent and two trivalent amides (Scheme 4). To our pleasure divalent compound **25**, from reaction of unprotected aminopyran **1** and succinic acid

Table 2: Synthesis of amides **18**–**20** from protected serinol **16** and subsequent deprotection to give divalent compounds **21**–**23**.

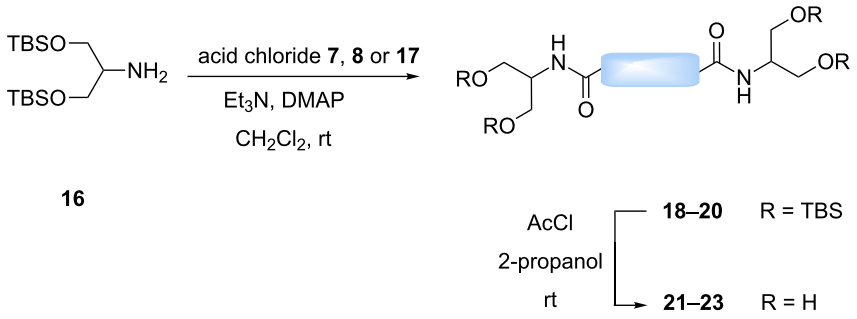

16

Entry	Acid dichloride	Time 1[a] [h]	Product	Yield [%]	Time 2[b] [h]	Product	Yield [%]
1	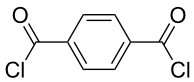 **7**	17	**18**	83	1.5	**21**	90
2	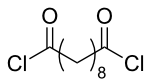 **8**	18	**19**	75	2.5	**22**	quant.
3	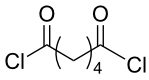 **17**	17	**20**	62	1.5	**23**	97

[a]First step; [b]second step.

(**24**), was isolated in good yield. This successful transformation is evidence that the TBS protected aminopyran **3** is probably sterically too hindered to react with succinic acid dichloride (see above, Scheme 3). Using this procedure, trivalent carbohydrate mimetics **27** and **29** were synthesized in very good yields. Once again it was noticed that the reaction proceeds efficiently even without a large excess of the corresponding aminopyran **1**. For the synthesis of each of the trivalent compounds **27** and **29**, respectively, only 1.3 equivalents of amine per carboxylic acid unit were used. With the aromatic tricarboxylic acid **26** as rigid linker unit, the polarity of the final product is only moderate and the reaction and purification proceeded perfectly. Starting from the aminopyran **1** the desired trivalent compound **27** was received in very good yield. On the other hand, unprotected compound **1** and tricarboxylic acid **28** did not furnish the expected product, most probably due to the high polarity of the coupling product which is then lost during the attempted purification by column chromatography. To overcome these difficulties, TBS-protected aminopyran **3** was used and coupled with **28** efficiently affording the protected trivalent compound **29**.

For our planned examination of the multivalent compounds as selectin inhibitors, the *O*-sulfated derivatives were also required. Since the introduction of sulfate groups drastically changes the physical and chemical properties of the molecules, isolation of pure fully *O*-sulfated compounds continues to be a

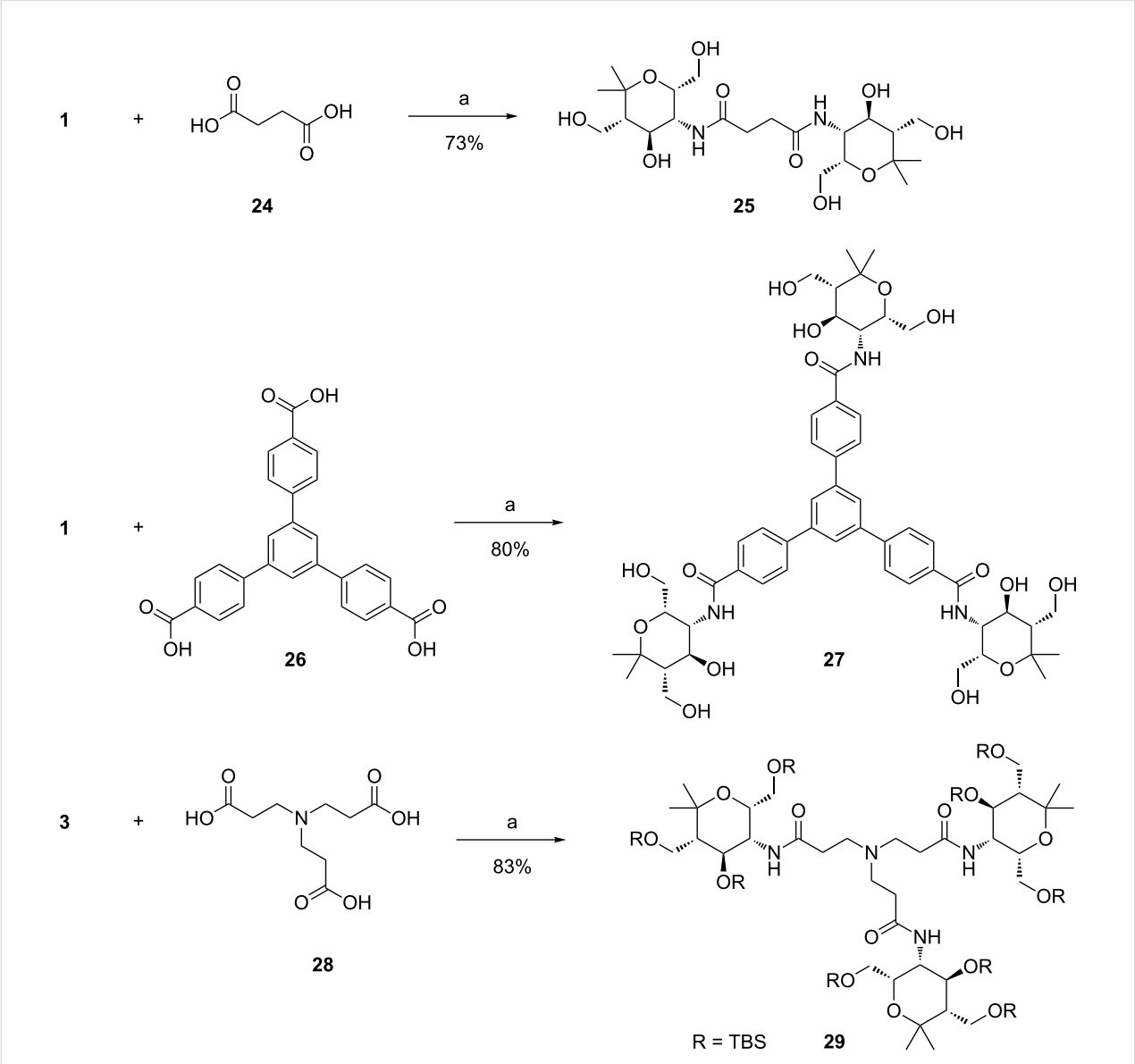

Scheme 4: HATU-mediated synthesis of divalent amide **25** and trivalent amides **27** and **29**. Conditions: a) HATU, Et_3N, DMF, 24 h, rt.

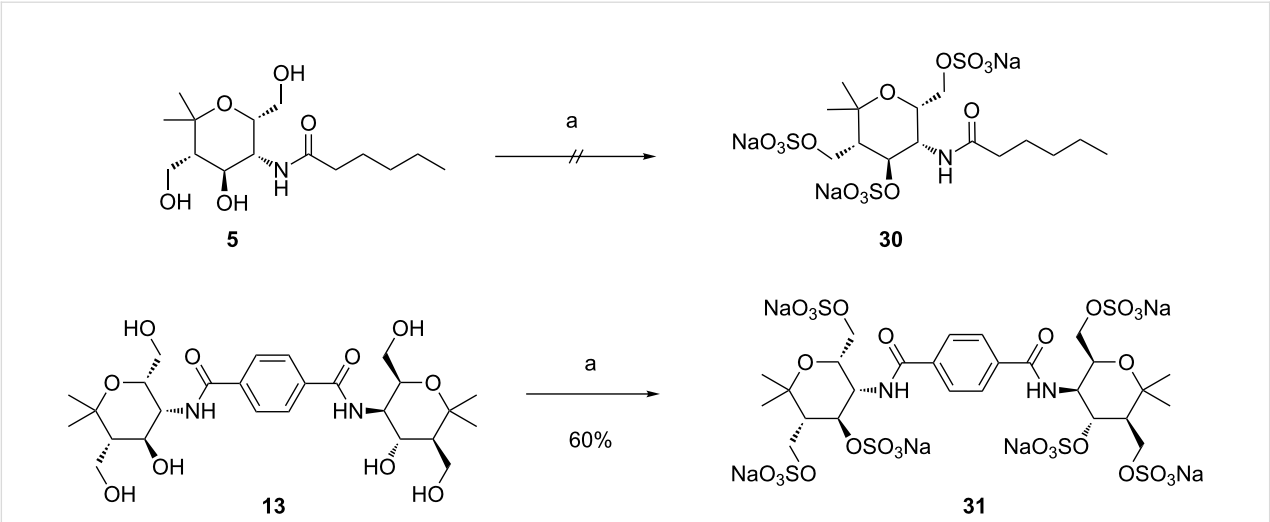

Scheme 5: Polysulfations of amides **5** and **13**. Conditions: a) 1) SO_3·DMF, DMF-d_7, 1 d, rt; 2) 1 M NaOH, 0 °C; 3) dialysis, H_2O.

great challenge. The polysulfation of the presented carbohydrate mimetics proved to be the most demanding step of the synthesis requiring many attempts and optimizations to find a suitable and reasonably reproducible procedure. Since other sulfation methods such as SO_3·pyridine [35] provided unsatisfactory results an excess of SO_3·DMF [13,36] was used as sulfating agent and the resulting sulfuric acid monoesters (in a mixture with an excess of the sulfating reagent) were directly converted into the corresponding sodium salts using a 1 M solution of sodium hydroxide. Subsequent purification by dialysis against water should afford the desired pure polysulfated compounds. We performed the sulfation reactions in deuterated DMF as solvent in order to allow the direct reaction control by ^{1}H NMR spectroscopy. When by ^{1}H NMR control a mixture of products was observed, additional equivalents of the sulfating agent were added and stirring was continued for another day; this procedure was repeated until full conversion of the compound was observed. Unfortunately, with this protocol the *O*-sulfation and purification of the monovalent model compound **5** did not lead to a homogenous product (Scheme 5). In this case, we tried to follow the reaction progress by ^{1}H NMR spectroscopy at 400 MHz which is apparently not sufficiently sensitive. Hence product **31** was contaminated by other compounds. Gratifyingly, the polysulfation of divalent amide **13** afforded the hexasulfated product **31** in 60% yield (full conversion already after one day as observed by ^{1}H NMR spectroscopy at 700 MHz).

A polysulfation reaction was also performed with amides derived from serinol (Scheme 6). The sulfation of compound **21**

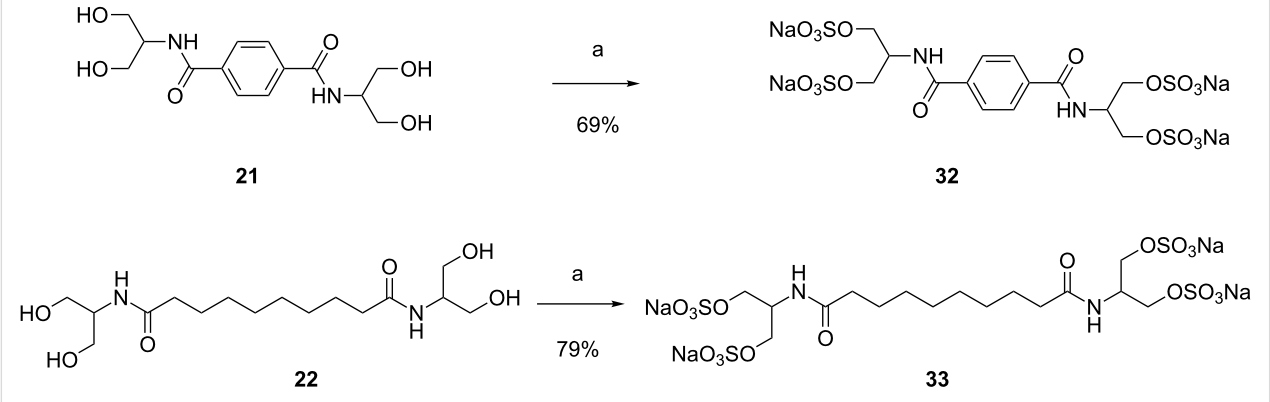

Scheme 6: Polysulfation of divalent amides **21** and **22** leading to tetrasulfated amides **32** and **33**. Conditions: a) 1) SO_3·DMF, DMF-d_7, 5 d (for **32**), 1 d (for **33**), rt; 2) 1 M NaOH, 0 °C; 3) dialysis, H_2O.

was carried out using 3 equivalents of sulfating agent per hydroxy group for five days. The desired polysulfated compound **32** could be isolated with a good yield. When the sulfation reaction was performed using diamide **22**, the reaction was much faster and after one day a homogeneous product was shown by 1H NMR spectroscopy. In this case no additional equivalents of the sulfating agent were added to the mixture and after dialysis the desired product **33** was isolated in very good yield.

The examples depicted in Scheme 5 and Scheme 6 were selected from quite a number of experiments. Often these transformations were not well reproducible due to purification problems. Although the reason for this irreproducibility was not clear, it was noted that during neutralization even addition of small amounts of 1 M sodium hydroxide solution to the reaction mixture did not allow accurate pH control. The resulting highly basic conditions could lead to decomposition or regeneration of the hydroxy groups leading to inhomogeneous mixtures. A better pH control could be achieved using 0.5 M sodium hydroxide solution and hence the pH could be stopped close to neutrality. Additionally, the obtained mixture was filtrated through an ion exchange DOWEX® Na^+ (50WX8-200) column to assure that all sulfuric acid monoesters as well as the excess of the sulfating agent were converted into the corresponding sodium salts. After this filtration a dialysis of the mixture generally afforded pure products. The modified procedure was applied to the *O*-sulfation of amide **27** and the reaction was complete after 3 days. Sodium hydroxide solution (0.5 M) was added until pH 9 was reached and the mixture was filtrated through a DOWEX® Na^+ column. After purification, the desired sodium salt **34** was successfully obtained in excellent yield (Scheme 7).

For the evaluation of the synthesized carbohydrate mimetics as potential selectin inhibitors, surface plasmon resonance (SPR) spectroscopy [37] was applied. Following the same competitive binding assay previously established for the test of such compounds [38,39], only a few of the presented unsulfated or sulfated compounds could be screened as potential inhibitors. The unsulfated amides **14**, **21** and **22** were not soluble in water and therefore not applicable for testing. The soluble divalent compound **23** (Table 2) did not show any inhibition even at the tested maximum concentration of 1 mM. These negative results are similar to those with the related unsulfated amine derivatives previously reported [24]. We expected that all polysulfated amides are water soluble at concentrations suitable for the SPR assay, but disappointingly amides **31** and **33** (Scheme 5 and Scheme 6) were not sufficiently soluble and therefore no tests could be performed with these compounds. At least divalent amide **32** and trivalent amide **34** showed inhibitory activity as L-selectin ligands in the 1 μmolar range (Figure 1). In a qualitative test compound **34** also inhibited P-selectin, a result to be confirmed in quantitative studies. Quite surprisingly, the flexible divalent serinol derivative **32** showed a good inhibitory potential with an IC_{50} value of 1 μM. The rigid trivalent compound **34** has a slightly inferior activity with an IC_{50} value of 2 μM, but is still a fairly good inhibitor.

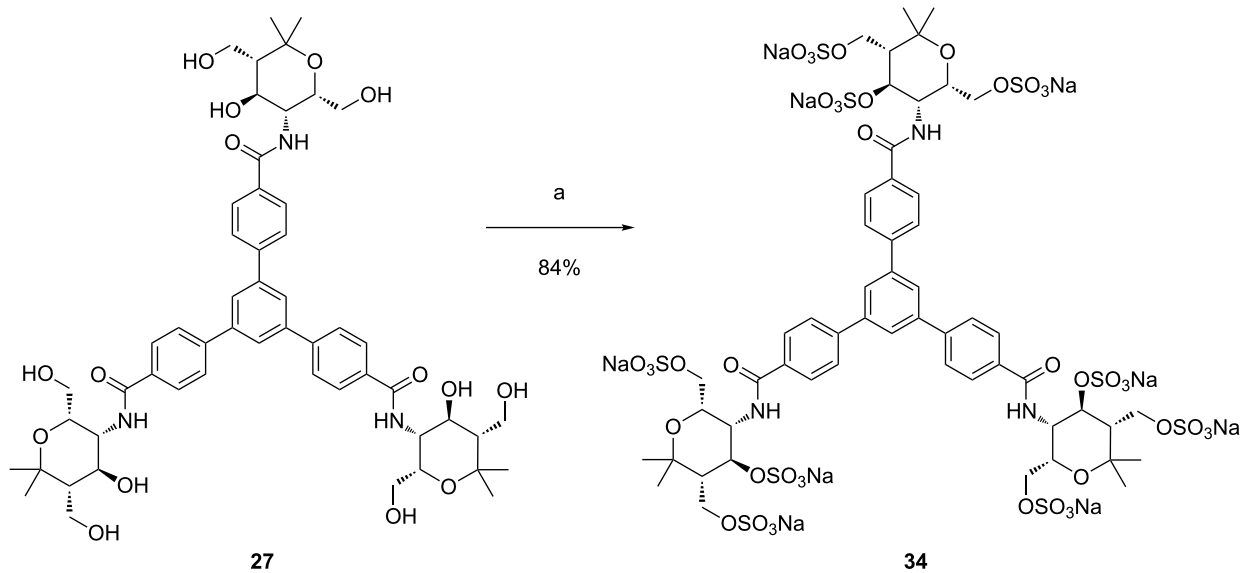

Scheme 7: Conversion of trivalent compound **27** into nonasulfated carbohydrate mimetic **34**. Conditions: a) 1) SO_3·DMF, DMF-d_7, 3 d, rt; 2) 0.5 M NaOH, 0 °C, DOWEX® Na^+; 3) dialysis, H_2O.

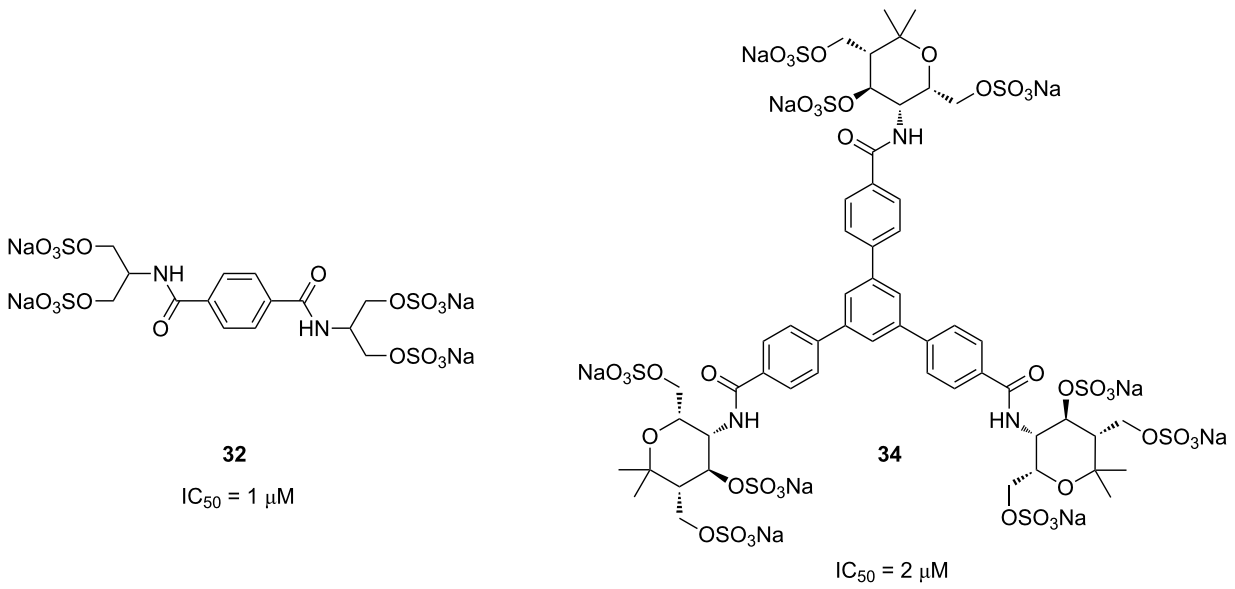

Figure 1: Structures of *O*-sulfated divalent amide **32** and trivalent amide **34** and their respective IC_{50} values for L-selectin as determined by SPR.

When comparing the two *O*-sulfated amides **32** and **34** a multivalency effect is not evident and a sound structure–activity discussion is not feasible as the two compounds have different end groups and different flexibilities. A series of related compounds is required to have a better understanding of structure–property relationships and the influence of multivalency. Unfortunately, only a few of our prepared compounds were sufficiently soluble in water to be suitable for the SPR test. However, a series of other multivalent conjugates was synthesized by using click chemistry with the azide derived from aminopyran **1** and results will be published in due time [40].

Conclusion

In this article we disclose the preparation of divalent and trivalent carbohydrate mimetics with end groups derived from aminopyran **1** and serinol (**2**). The units were connected by amide bonds that were either formed by Schotten–Baumann reaction using the corresponding acid chlorides or by a coupling of the amines to carboxylic acids using HATU as reagent. The subsequent *O*-sulfation of the obtained compounds with SO_3·DMF was optimized with the help of ^{1}H NMR spectroscopic control (700 MHz). A crucial detail is also the neutralization step which works reliable only with 0.5 M sodium hydroxide solution. By these methods a few oligovalent *O*-sulfated carbohydrate mimetics could be prepared and tested as L-selectin inhibitors by SPR. The divalent amide **32** and trivalent amide **34** showed surprisingly good activities with IC_{50} values in the micromolar range. Further studies are required to reveal a multivalency effect and to understand structure–property relationships of compounds of this type.

Supporting Information

Supporting Information File 1

General information, experimental procedures and analytical data as well as copies of NMR spectra of all compounds.
[http://www.beilstein-journals.org/bjoc/content/supplementary/1860-5397-11-72-S1.pdf]

Acknowledgements

This work was generously supported by the Deutsche Forschungsgemeinschaft (SFB 765) and by Bayer HealthCare. We acknowledge Dr. T. Ngo for providing the azo compound **9**, C. Kühne for valuable discussions and Dr. R. Zimmer and Dr. M. Kandziora for their help during preparation of the manuscript.

References

1. Bouché, L.; Reissig, H.-U. *Pure Appl. Chem.* **2012,** *84,* 23–36. doi:10.1351/PAC-CON-11-09-20
2. Bouché, L.; Kandziora, M.; Reissig, H.-U. *Beilstein J. Org. Chem.* **2014,** *10,* 213–223. doi:10.3762/bjoc.10.17
3. Bouché, L.; Reissig, H.-U. *Eur. J. Org. Chem.* **2014,** 3697–3703. doi:10.1002/ejoc.201402191
4. Kandziora, M.; Reissig, H.-U. *Beilstein J. Org. Chem.* **2014,** *10,* 1749–1758. doi:10.3762/bjoc.10.182
5. Kandziora, M.; Reissig, H.-U. *Eur. J. Org. Chem.* **2015,** 370–377. doi:10.1002/ejoc.201403186
6. Kandziora, M.; Mucha, E.; Zucker, S. P.; Reissig, H.-U. *Synlett* **2015,** *26,* 367–374. doi:10.1055/s-0034-1379503

7. Sears, P.; Wong, C.-H. *Angew. Chem.* **1999,** *111,* 2446–2471. doi:10.1002/(SICI)1521-3757(19990816)111:16<2446::AID-ANGE2446>3.0.CO;2-4
   Angew. Chem., Int. Ed. **1999,** *38,* 2300-2324. doi:10.1002/(SICI)1521-3773(19990816)38:16<2300::AID-ANIE2300>3.0.CO;2-6
8. Gruner, S. A. W.; Locardi, E.; Lohof, E.; Kessler, H. *Chem. Rev.* **2002,** *102,* 491–514. doi:10.1021/cr0004409
9. Werz, D. B.; Ranzinger, R.; Herget, S.; Adibekian, A.; von der Lieth, C.-W.; Seeberger, P. H. *ACS Chem. Biol.* **2007,** *2,* 685–691. doi:10.1021/cb700178s
10. Koester, D. C.; Holkenbrink, A.; Werz, D. B. *Synthesis* **2010,** 3217–3242. doi:10.1055/s-0030-1258228
11. Cipolla, L.; Peri, F. *Mini-Rev. Med. Chem.* **2011,** *11,* 39–54. doi:10.2174/138955711793564060
12. Dernedde, J.; Enders, S.; Reissig, H.-U.; Roskamp, M.; Schlecht, S.; Yekta, S. *Chem. Commun.* **2009,** 932–934. doi:10.1039/b818263a
13. Roskamp, M.; Enders, S.; Pfrengle, F.; Yekta, S.; Dekaris, V.; Dernedde, J.; Reissig, H.-U.; Schlecht, S. *Org. Biomol. Chem.* **2011,** *9,* 7448–7456. doi:10.1039/c1ob05583f
14. McEver, R. P.; Moore, K. L.; Cummings, R. D. *J. Biol. Chem.* **1995,** *270,* 11025–11028. doi:10.1074/jbc.270.19.11025
15. Sears, P.; Wong, C. H. *Proc. Natl. Acad. Sci. U. S. A.* **1996,** *93,* 12086–12093. doi:10.1073/pnas.93.22.12086
16. McEver, R. P.; Cummings, R. D. *J. Clin. Invest.* **1997,** *100,* 485–491. doi:10.1172/JCI119556
17. Cummings, R. D. *Braz. J. Med. Biol. Res.* **1999,** *32,* 519–528. doi:10.1590/S0100-879X1999000500004
18. Ley, K. *Trends Mol. Med.* **2003,** *9,* 263–268. doi:10.1016/S1471-4914(03)00071-6
19. Raffler, N. A.; Rivera-Nieves, J.; Ley, K. *Drug Discovery Today: Ther. Strategies* **2005,** *2,* 213–220. doi:10.1016/j.ddstr.2005.08.012
20. Chang, J.; Patton, J. T.; Sarkar, A.; Ernst, B.; Magnani, J. L.; Frenette, P. S. *Blood* **2010,** *116,* 1779–1786. doi:10.1182/blood-2009-12-260513
21. Hudak, J. E.; Bertozzi, C. R. *Chem. Biol.* **2014,** *21,* 16–37. doi:10.1016/j.chembiol.2013.09.010
22. Kretzschmar, G.; Toepfer, A.; Hüls, C.; Krause, M. *Tetrahedron* **1997,** *53,* 2485–2494. doi:10.1016/S0040-4020(96)01178-7
23. Kretzschmar, G. *Tetrahedron* **1998,** *54,* 3765–3780. doi:10.1016/S0040-4020(98)00105-7
24. Salta, J.; Reissig, H.-U. *Synthesis* **2015**. doi:10.1055/s-0034-1380571
25. Fasting, C.; Schalley, C. A.; Weber, M.; Seitz, O.; Hecht, S.; Koksch, B.; Dernedde, J.; Graf, C.; Knapp, E.-W.; Haag, R. *Angew. Chem.* **2012,** *124,* 10622–10650. doi:10.1002/ange.201201114
   Angew. Chem., Int. Ed. **2012,** *51,* 10472–10498. doi:10.1002/anie.201201114
26. Cecioni, S.; Imberty, A.; Vidal, S. *Chem. Rev.* **2015,** *115,* 525–561. doi:10.1021/cr500303t
27. Al-Harrasi, A.; Reissig, H.-U. *Angew. Chem.* **2005,** *117,* 6383–6387. doi:10.1002/ange.200501127
   Angew. Chem. Int. Ed. **2005**, *44*, 6227-6231. doi:10.1002/anie.200501127
28. Al-Harrasi, A.; Pfrengle, F.; Prisyazhnyuk, V.; Yekta, S.; Koóš, P.; Reissig, H.-U. *Chem. – Eur. J.* **2009,** *15,* 11632–11641. doi:10.1002/chem.200900996
29. Choudhury, A. K.; Kitaoka, M.; Hayashi, K. *Eur. J. Org. Chem.* **2003,** 2462–2470. doi:10.1002/ejoc.200300018
30. Ameerunisha, S.; Zacharias, P. S. *J. Chem. Soc., Perkin Trans. 2* **1995,** 1679–1682. doi:10.1039/P29950001679
31. Khan, A. T.; Mondal, E. *Synlett* **2003,** *5,* 0694–0698. doi:10.1055/s-2003-38360
32. Montalbetti, C. A. G. N.; Falque, V. *Tetrahedron* **2005,** *61,* 10827–10852. doi:10.1016/j.tet.2005.08.031
33. Valeur, E.; Bradley, M. *Chem. Soc. Rev.* **2009,** *38,* 606–631. doi:10.1039/B701677H
34. Carpino, L. A.; Imazumi, H.; El-Faham, A.; Ferrer, F. J.; Zhang, C.; Lee, Y.; Foxman, B. M.; Henklein, P.; Hanay, C.; Mügge, C.; Wenschuh, H.; Klose, J.; Beyermann, M.; Bienert, M. *Angew. Chem.* **2002,** *114,* 457–461. doi:10.1002/1521-3757(20020201)
   Angew. Chem. Int. Ed. **2002**, *41*, 441-445. doi:10.1002/1521-3773(20020201)
35. Dhamale, O. P.; Zhong, C.; Al-Mafraji, K.; Boons, G.-J. *Org. Biomol. Chem.* **2014,** *12,* 2087–2098. doi:10.1039/C3OB42312C
36. Schweiger, R. G. *Carbohydr. Res.* **1972,** *21,* 219–228. doi:10.1016/S0008-6215(00)82148-5
37. Safina, G. *Anal. Chim. Acta* **2012,** *712,* 9–29. doi:10.1016/j.aca.2011.11.016
38. Enders, S.; Bernhard, G.; Zakrzewicz, A.; Tauber, R. *Biochim. Biophys. Acta* **2007,** *1770,* 1441–1449. doi:10.1016/j.bbagen.2007.06.015
39. Schlemmer, C.; Wiebe, C.; Ferenc, D.; Kowalczyk, D.; Wedepohl, S.; Ziegelmüller, P.; Dernedde, J.; Opatz, T. *Chem. – Asian J.* **2014,** *9,* 2119–2125. doi:10.1002/asia.201402118
40. Salta, J.; Eberle, F.; Dernedde, J.; Reissig, H.-U., manuscript in preparation.

License and Terms

BEILSTEIN JOURNAL OF ORGANIC CHEMISTRY

Design, synthesis and photochemical properties of the first examples of iminosugar clusters based on fluorescent cores

Mathieu L. Lepage[1], Antoine Mirloup[2], Manon Ripoll[1], Fabien Stauffert[1], Anne Bodlenner[1], Raymond Ziessel[*2] and Philippe Compain[*1,3]

Full Research Paper

Open Access

Address:
[1]Laboratoire de Synthèse Organique et Molécules Bioactives (SYBIO), Université de Strasbourg/CNRS (UMR 7509), Ecole Européenne de Chimie, Polymères et Matériaux (ECPM), 25 rue Becquerel, 67087 Strasbourg, France, [2]Institut de Chimie et Procédés pour l'Energie, l'Environnement et la Santé (ICPEES), Laboratoire de Chimie Organique et Spectroscopie Avancées (LCOSA), Université de Strasbourg/CNRS (UMR 7515), Ecole Européenne de Chimie, Polymères et Matériaux (ECPM), 25 rue Becquerel, 67087 Strasbourg, France and [3]Institut Universitaire de France, 103 Bd Saint-Michel, 75005 Paris, France

Email:
Raymond Ziessel[*] - ziessel@unistra.fr; Philippe Compain[*] - philippe.compain@unistra.fr

* Corresponding author

Keywords:
BODIPY; fluorescent probes; iminosugars; 4-methylumbelliferone; multivalency; pyrene

Beilstein J. Org. Chem. **2015,** *11,* 659–667.
doi:10.3762/bjoc.11.74

Received: 27 February 2015
Accepted: 17 April 2015
Published: 06 May 2015

This article is part of the Thematic Series "Multivalency as a chemical organization and action principle".

Guest Editor: R. Haag

Abstract

The synthesis and photophysical properties of the first examples of iminosugar clusters based on a BODIPY or a pyrene core are reported. The tri- and tetravalent systems designed as molecular probes and synthesized by way of Cu(I)-catalysed azide–alkyne cycloadditions are fluorescent analogues of potent pharmacological chaperones/correctors recently reported in the field of Gaucher disease and cystic fibrosis, two rare genetic diseases caused by protein misfolding.

Introduction

Since the isolation in the 1970's of 1-deoxynojirimycin (DNJ) from natural sources and the finding of its biological activity as an α-glucosidase inhibitor, thousands of sugar mimetics with a nitrogen atom replacing the endocyclic oxygen have been reported in the literature [1,2]. Iminosugars are mainly known to be inhibitors of a number of carbohydrate-processing enzymes with an emphasis on glycosidases [1,2]. In the early 2000's, iminosugars were, remarkably, found to inhibit metalloproteinases [3], protein kinases [4] and cholinesterases [5], which are enzymes that act on non-sugar substrates. The versatility of iminosugars as inhibitors of enzymes of therapeutic interest has been harnessed to cure a diversity of diseases including diabetes, viral infection, lysosomal storage disorders, tumour metastasis and cystic fibrosis [1]. First therapeutic successes have been obtained as demonstrated by the number of structures involved in clinical trials and two medicines on the

market: Glyset (*N*-hydroxyethyl DNJ) for the treatment of complications associated with type II diabetes and Zavesca (*N*-Bu DNJ, **1**), the first oral treatment for Gaucher and Niemann–Pick diseases (Figure 1) [1,6-8]. Despite their high therapeutic potential, the extensive studies in the field and the myriad of compounds synthesized, very few examples of multivalent iminosugars were reported in the literature until recently [9,10]. From 2010, the field has however experienced a major take-off with the discovery of the first strong multivalent effects in glycosidase inhibition observed with DNJ clusters based on β-cyclodextrin or C_{60} cores showing strong affinity enhancements over the corresponding monomers (up to 610-fold per DNJ unit) [11,12]. In the following years, an impressive ever-growing number of multivalent iminosugars based on various scaffolds, ligands and linkers have been synthesized to further investigate the impact of multivalency on glycosidase inhibition [9-26]. The interest of the inhibitory multivalent effect for drug discovery was demonstrated by targeting glycosidases involved in rare genetic diseases linked to misfolded proteins [24-26]. The first examples of multivalent iminosugars such as **2** and **3** acting as pharmacological chaperones were thus disclosed in the field of Gaucher disease, the most common lysosomal storage disorder (Figure 1) [24,25]. DNJ clusters **2** and **3** are indeed able to increase mutant β-glucocerebrosidase (GCase) residual activity levels as much as 3.3-fold in cells of Gaucher patients at micromolar concentrations. In another rare genetic disease, the rescue by multimeric correctors of the mutant CFTR protein implied in cystic fibrosis led to the first report of a multivalent effect for amending protein folding defects in cells [26]. As judged by EC_{50} (half-maximal effective concentration) values, trivalent DNJ clusters **2** were indeed up to 225-fold more efficient as CFTR correctors than the clinical candidate *N*-Bu DNJ (**1**), a potent inhibitor of trimming ER glucosidases [26]. Taken together, these recent studies provide new therapeutic answers for a number of protein folding disorders [27,28] but also raise many fundamental questions concerning the mechanisms at play. In the present paper, we report the first examples of fluorescently-labeled multivalent iminosugars designed as molecular tools to investigate the mode of action of pharmacological chaperones/correctors in cells and in vivo, and get insights into the multivalent effect observed in CFTR correcting activity. The originality of our approach relies on the fact that, in the structures designed, this is the scaffold itself [29,30], based on a pyrene or a boron-dipyrromethene (F-BODIPY) dye, which has fluorescence activity.

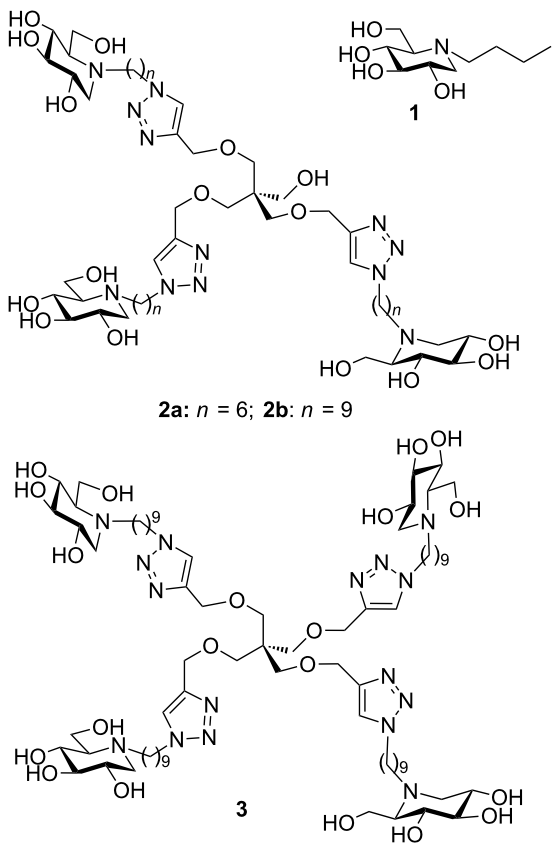

Figure 1: *N*-Bu DNJ (**1**) and examples of potent multivalent pharmacological chaperones and CFTR correctors (**2** and **3**).

Results and Discussion

Synthetic design

The fluorescent probes were designed as analogues of the best multivalent pharmacological chaperones/correctors reported so far that typically display three to four copies of a DNJ ligand linked to a central core via an alkyl chain spacer (Figure 1) [24-26]. The choice of the fluorophore core is naturally primordial for the design of photostable, water-soluble and biocompatible probes with the required photophysical properties. An additional challenge is that, as the central core of a multivalent system, the fluorophore structure defines also its valency, size and shape. Difluoroboradiaza-*s*-indacenes, commonly named boron-dipyrromethene dyes (F-BODIPY), were logically selected for the construction of the probes. These compounds indeed combine high fluorescence quantum yields and high molar extinction coefficients, strong chemical and photochemical stability in solution and in solid state. In addition, they can be easily derivatized [31-37]. If the optical properties of BODIPY are very sensitive to modification of the pyrrole core [38,39], they are less sensitive to the substitution of the central pseudo *meso* position [40,41]. Additionally, the fluorine substitution at the boron has less influence on the spectroscopic properties of the dyes [42]. So far, major endeavors have been dedicated to the preparation of classical F-BODIPY structures and less common E-BODIPY (E for ethynyl) and the examination of their spectroscopic and salient physical properties [43-47]. We have recently argued the case that the fluoro-substitution of

boraindacene was a mean to considerably increase the solubility, the stability and the steric hindrance avoiding the formation of aggregates [48]. In some cases, special sensing properties [49] may be induced by adequate tailoring, including fluorescence amplification [50], and ratiometric pH reporter for imaging protein–dye conjugates in living cells [51], or display physiological binding of D-glucose [52]. The pyrene nucleus was also selected as an alternative fluorophore since it may be easily tetrafunctionalized at the 1, 3, 6 and 8 positions to give a suitable core for the synthesis of tetravalent clusters [53]. In addition, this fluorophore was chosen for its biological/chemical stability and its photophysical properties including high extinction coefficient with reliable fluorescence [54,55]. Another interest of the pyrene scaffold lies in its rigidity, a property that may favourably impact inhibitory multivalent effects [9,11,16,19]. A convergent approach comprising the attachment of azide-armed iminosugars **4** [11,12] on polyalkyne "clickable" scaffolds **5** and **6** via Cu(I)-catalyzed azide–alkyne cycloaddition (CuAAC) was performed for achieving our synthetic goals (Figure 2) [56,57]. With the objective of increasing water solubility and chemical stability in biological medium, triyne **6b**, an analogue of F-BODIPY-based scaffold **6a** was prepared by replacing the fluoro groups on the boron center with ethynyl tetra(ethylene glycol)methyl groups [58,59].

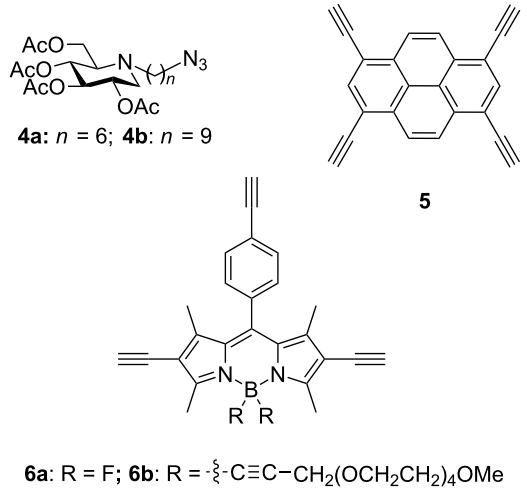

Figure 2: Azide-armed DNJ derivatives **4** and polyalkyne "clickable" scaffolds **5** and **6**.

Synthesis of the BODIPY precursors

The synthesis of the tris-iodo functionalized BODIPY dyes and their acetylenic derivatives is sketched in Scheme 1. The synthesis of derivatives **7** and **8** have previously been reported using a regioselective iodination reaction positions 2 and 6 of the BODIPY [60]. Substitution of both fluoro groups on the boron was realized using the Grignard reagent of 1-[2"'-(2"-{2'-(2-methoxyethoxy)ethoxy}ethoxy)ethoxy]prop-2-yne [61] and the BODIPY derivative **8**. With these precursors in hands it was easy to transform the iodo function to yield the trimethylsilylacetylene derivatives **9** and **11** using standard Sonogashira–Hagihira cross-coupling reactions promoted by low valent palladium precursors [62]. Excellent yields were obtained for the trisubstituted derivatives (88 to 95%). Two diagnostic NMR signals of the poly(ethylene glycol) chains at 4.16 ppm (protons a, integration 4H) and at 3.65 ppm for the methoxy groups (protons b, integration 6H) in addition to the presence of two TMS singlets at 0.20 and 0.28 ppm (respective integration 18 and 9H) confirmed the substitution. Finally, deprotection of the trimethylsilyl group using mild basic conditions provided the target compounds **6a** and **6b** in good yields. Terminal alkynes located in the 2,6 positions were found to resonate at 3.32 ppm and the one in the pseudo meso position 8 resonates at 3.20 ppm.

Fluorescent DNJ cluster synthesis

Following a robust strategy developed in our group [11,12], the last stages of the multivalent probe synthesis involved the attachment of peracetylated azido iminosugars **4** on the scaffolds via CuAAC reaction and afterwards *O*-deacetylation using an anion exchange resin. First attempts to perform CuAAC reactions with triyne substrate **6b** bearing a tetraethylene glycol chain tethered to the boron center via an ethynyl bond proved difficult. The use of copper(I) bromide dimethyl sulfide complex [63] at room temperature led to a complex mixture of products. Better results were obtained with copper(II) sulfate and sodium ascorbate under carefully degassed conditions and the desired protected cluster **12b** could be obtained in 56% yield after purification on silica gel (Scheme 2). The major side-product observed which could not be isolated in pure form may correspond to CuAAC reaction of the azido iminosugar **4a** with the terminal alkyne resulting from the cleavage of the carbon–boron bond in **6b**. The same experimental protocol was applied to functionalized BODIPY **6a**, leading to the desired trivalent cluster **12a** in 83% yield. *O*-Deacetylation of compounds **12** using anion exchange Amberlite IRA-400 (OH^-) resin provided the desired water-soluble clusters **13** in high yields. As judged by ^{11}B NMR, no fluoride displacement occurred at the boron center during the deprotection step.

The synthesis of the 4-valent pyrene-based iminosugars **15** was performed in a similar manner than for BODIPY-based clusters **13** (Scheme 3). The tetrayne **5** synthesized in 3 steps from pyrene [53] was reacted with the azide precursors **4**, and afterwards deprotected to give the desired tetravalent iminosugars **15** in 37 to 72% yields for the two steps. Despite the good water solubility of alkylated DNJ ligands, pyrene-based multivalent iminosugars were only soluble in water/methanol or water/

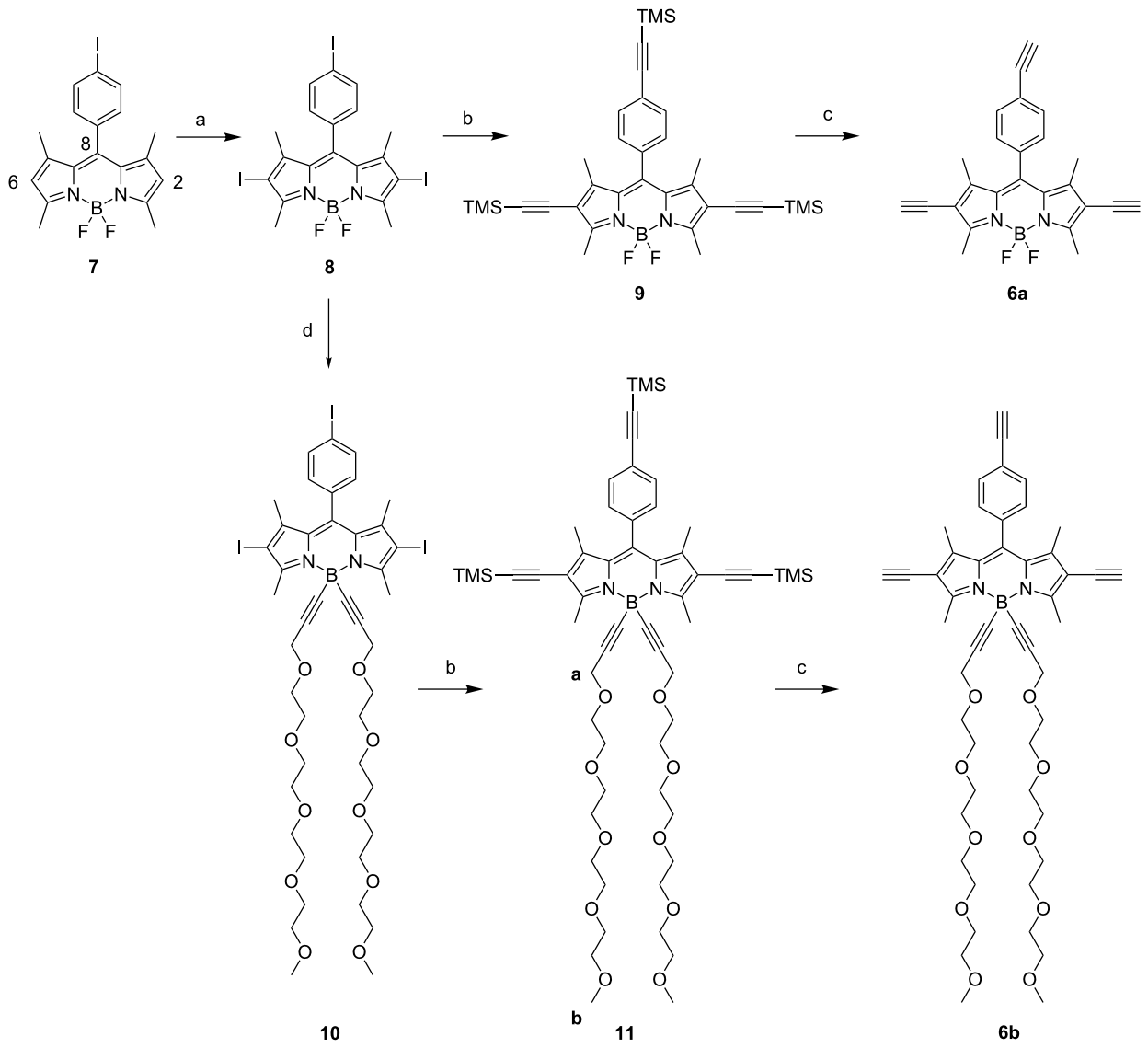

Scheme 1: Synthesis of trisubstituted BODIPY derivatives. (a) ICl, $CHCl_3$/MeOH, rt, 15 min, quantitative; (b) 3-ethynyltrimethylsilane, $[Pd(PPh_3)_2Cl_2]$, CuI, triethylamine, THF, 16 h, 60 °C, 88% (**9**), 95% (**11**); (c) K_2CO_3, DCM/MeOH/water, 50 °C, 16 h, 72% (**6a**), 88% (**6b**); (d) 1-[2"'-(2"-{2'-(2-methoxyethoxy)ethoxy}ethoxy)ethoxy]prop-2-yne, EtMgBr, THF, 60 °C, 16 h, 61%.

DMSO mixtures, those mixtures prevent the agregation of the pyrene core.

Photophysical properties

The absorption and emission features of the BODIPY-based cluster **13a** and the pyrene-based cluster **15a** dyes were investigated in an aqueous buffer solution of glycine (0.1 M) at pH 10.7. This buffer conditions were chosen to be as close as possible to the conditions used for β-glucocerebrosidase activation assays (Gaucher disease) which are based on a fluorescent leaving group (4-methylumbelliferone) allowing fluorescence recording after reaction quenching at pH 10.7 [64].

The BODIPY-based dye **13a** displays an intense absorption at 528 nm (ε = 27,000 $M^{-1}{\cdot}cm^{-1}$) corresponding to the $S_0 \rightarrow S_1$ (π–π* transition). The slight red shift of this absorption compared to unsubstituted BODIPY dyes in the 2,6-substitution positions and measured under similar aqueous conditions, is likely due to the influence of both triazole rings. The second transition at 386 nm is assigned in light of previous studies to the $S_0 \rightarrow S_2$ of the BODIPY subunit [39,65-67]. The triazole rings absorb below 250 nm for the π–π* transition [68]. Excitation at 510 nm affords a relatively intense emission with a quantum yield of 24% (in aqueous glycine buffer at pH 10.7), the profile of the band mirrors the absorption with a maximum

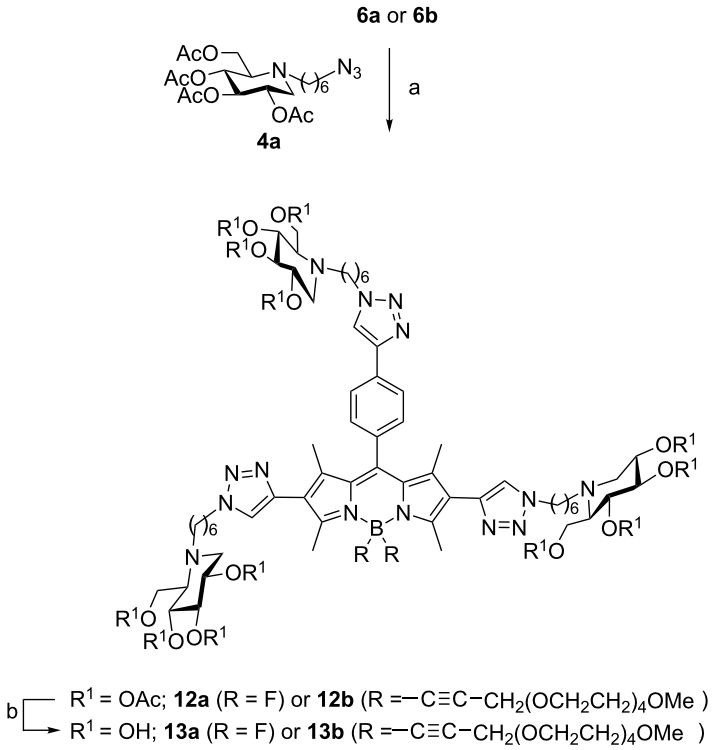

Scheme 2: Synthesis of DNJ clusters **13**: (a) $CuSO_4{\cdot}5H_2O$ cat., sodium ascorbate, THF/H_2O (1:1), 83% (**12a**), 56% (**12b**); (b) Amberlite IRA 400 (OH^-), MeOH/H_2O (1:1), rt, quant. (**13a**), quant. (**13b**).

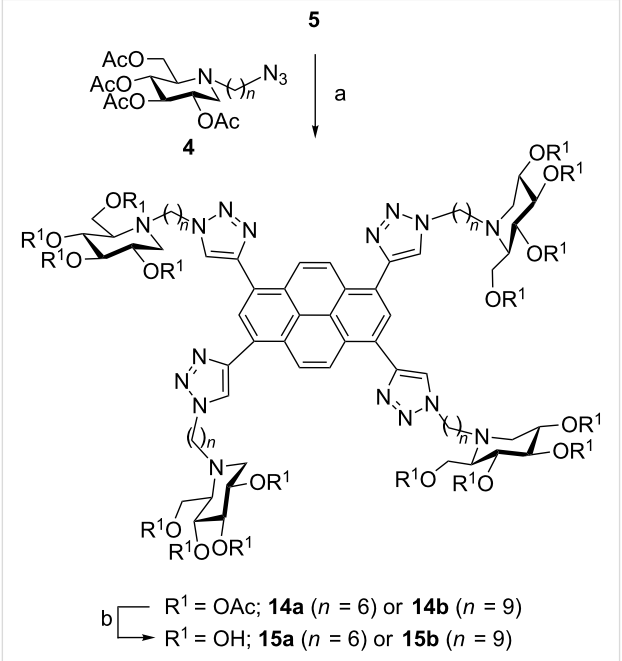

Scheme 3: Synthesis of DNJ clusters **15**: (a) $CuSO_4{\cdot}5H_2O$ cat., sodium ascorbate, DMF/H_2O (6:1), 80 °C (MW) or room temperature, 51% (**14a**), 75% (**14b**); (b) Amberlite IRA 400 (OH^-), MeOH/H_2O (1:1), 40 °C, 73% (**15a**), 96% (**15b**).

at 558 nm which is in keeping with little reorganization in the excited state and characteristic of a singlet emitter. The modest Stokes shift (Δ_{ss} = 1020 cm^{-1}) and the short excited state life time (τ = 3.38 ns) are also in favor of a singlet emitting state. The excitation spectra did display a slight shift compared to the absorption spectra. This may be due to the presence of some aggregates, a problem frequently encountered with aromatic organic dyes in aqueous solutions [69,70]. Addition of 2.5% of a surfactant such as sodium dodecyl sulfate (SDS) improves the spectral overlap with the absorption spectra (Figure 3a), and likely diminishes formation of potent aggregates.

For the pyrene-based cluster **15a** two main absorptions maxima at 391 and 292 nm were observed and safely assigned to the successive pyrene excited states, $S_0 \rightarrow S_1$ at 391 nm and $S_0 \rightarrow S_2$ at 295 nm (Figure 3b) [71]. Emission maximum was recorded at 534 nm from an excitation at 390 nm or 295 nm with a quantum of 43% (in aqueous glycine buffer at pH 10.7). Unlike the BODIPY homologue, the pyrene-based cluster **15a** has a large Stokes shift of 6850 cm^{-1} and a longer excited state life time (τ = 71.7 ns) [72]. Again the excitation spectrum matches the absorption one proving that aggregation is unlikely under the used aqueous conditions.

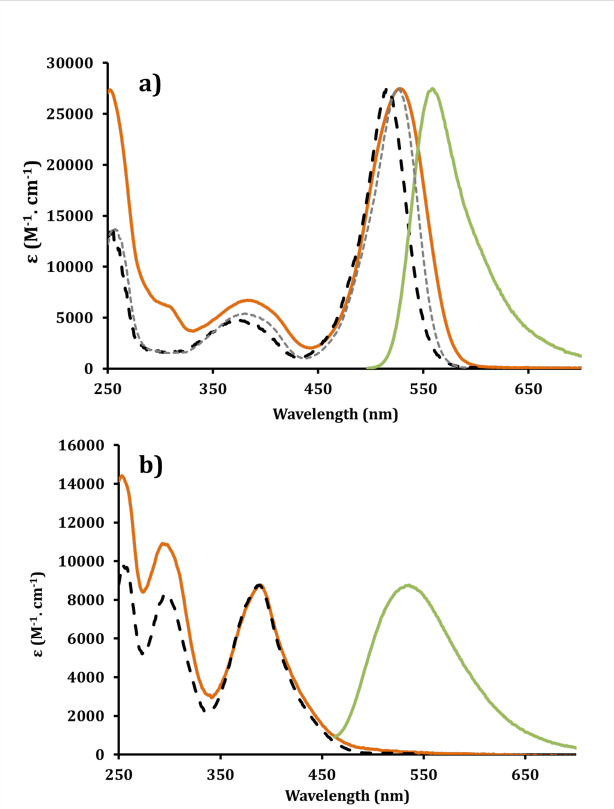

Figure 3: a) Absorption (orange line), corrected emission (green line) (λ_{exc} = 510 nm), excitation (dashed black line) (λ_{em} = 630 nm) and excitation with 2.5% of SDS (small dashed grey line) spectra for **13a**; b) Absorption (orange line), corrected emission (green line) (λ_{exc} = 390 nm) and excitation (dashed black line) (λ_{em} = 550 nm) spectra for **15a**; in glycine buffer at pH 10.7 at rt.

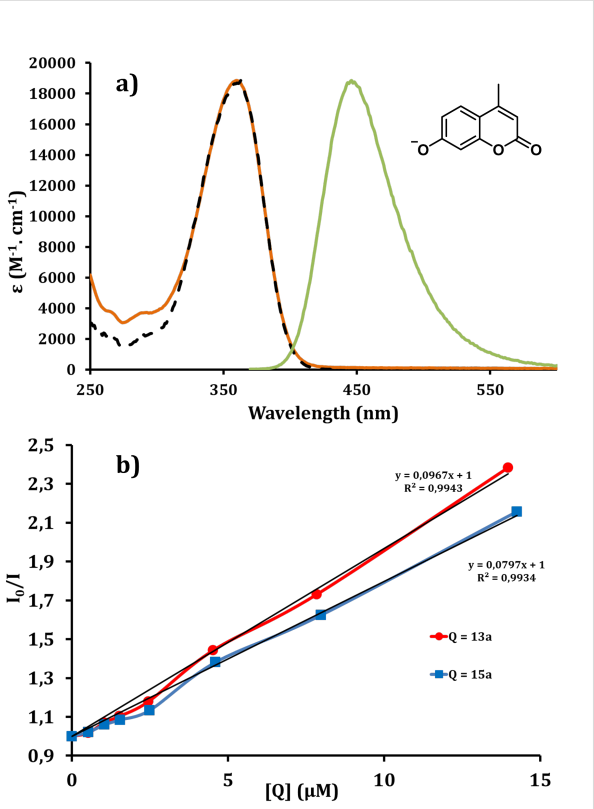

Figure 4: a) Absorption (orange line), corrected emission (green line) (λ_{exc} = 360 nm) and excitation (dashed black line) (λ_{em} = 445 nm) spectra for the anion of 4-methylumbelliferone; b) Stern–Volmer plots concerning the quenching of fluorescence of the anion of 4-methylumbelliferone by **13a** (red line) and **15a** (blue line) and their linear regression.

From a general point of view, fluorescent probes have been used for the detection of diverse analytes and in relevant biosensing and bioimaging applications [73]. One critical aspect for the evaluation of biological activities using fluorescent dyes (e.g., the deprotonated form of 4-methylumbelliferone) [74] is to determine their spectroscopic features in different environments (local pH, local polarity, potential quenchers, hydrophobic environment, …). Here we focus on the UV–visible characteristics of the anion of 4-methylumbelliferone, the dye commonly used for quantifying chaperoning activities (using 4-methylumbelliferyl β-D-glucopyranoside as GCase substrate) [64], to determine whether this assay would be compatible with the evaluation of fluorescent multivalent clusters **13** and **15** as potential pharmacological chaperones.

The same buffer conditions as those used for activation assays (quenched conditions at pH 10.7 in a glycine buffer) were used for this study. The anion of 4-methylumbelliferone displays a strong absorption at 360 nm and a broad emission around 446 nm (Figure 4a).

The fluorescence quantum yield is high (ϕ_{fluo} = 81%) as previously determined under similar conditions [74]. In order to record the efficiency of the fluorescence quenching of the anion of 4-methylumbelliferone by the novel dyes, Stern–Volmer plots were carried out [75]. A titrated solution of the quencher (**13a** or **15a**) was dropwise added to a titrated solution of 4-methylumbelliferone (≈10^{-7} M at pH 10.7) and the fluorescence of the anion was recorded after each addition (Figure 4b). This allows plotting the decrease of fluorescence versus the concentration of quencher. The Stern–Volmer equation $I_0/I = 1 + kq\tau[Q]$ facilitates the calculation of the rates of bimolecular collisional quenching k_q = 1.8 × 10^{13} $M^{-1}{\cdot}s^{-1}$ and 1.5 × 10^{13} $M^{-1}{\cdot}s^{-1}$, respectively for **13a** and **15a** dyes using a lifetime τ = 5.31 ns for the 4-methylumbelliferone anion. The quenching appears efficient in both cases due to suitable spectral overlap between the emission of 4-methylumbelliferone anion and the absorption of the BODIPY **13a** or the pyrene-based cluster **15a**. This dynamic quenching process between these multivalent iminosugars and the 4-methylumbelliferone or other coumarine derivatives has thus to be taken into account

during the quantitative analyses of dedicated biological processes.

Conclusion

We have reported the preparation of multivalent iminosugar clusters based on two fluorescent cores by way of Cu(I)-catalysed azide–alkyne cycloadditions. To our knowledge these are the first examples of the use of BODIPY or pyrene as a scaffold to display multivalent ligands. Although the trivalent BODIPY-derived DNJ clusters are water soluble, a co-solvent is necessary to dissolve the tetravalent pyrene-derived DNJ clusters in water. Photophysical properties of those multivalent dyes in aqueous media (glycine buffer at pH 10.7), are interesting, providing high quantum yields, 24% for **13a** and 43% for **15a**, and well-defined spectroscopic features. Altogether, these results augur well for a new class of molecular tools dedicated to rationalize the mode of action of pharmacological chaperones and CFTR correctors by probing uptake and mapping biodistribution in cells and in vivo.

Supporting Information

Supporting Information File 1

Characterization data and NMR spectra of all new compounds.
[http://www.beilstein-journals.org/bjoc/content/supplementary/1860-5397-11-74-S1.pdf]

Acknowledgements

This work was supported by the Institut Universitaire de France (IUF), the CNRS (UMR 7509), the University of Strasbourg, the Agence Nationale de la Recherche (ANR, grant number 11-BS07-003-02), the International Centre for Frontier Research in Chemistry (icFRC) and doctoral fellowships from the French Department of Research to Mathieu L. Lepage and Fabien Stauffert. Antoine Mirloup thanks the Rhin-Solar EC Network supported by the European Fund for Regional Development (FEDER) in the framework of the Programme INTERREG IV Upper Rhine, Project no. C25 for financial support of this work.

References

1. *Iminosugars: from Synthesis to Therapeutic Applications;* Compain, P.; Martin, O. R., Eds.; Wiley & Sons: Chichester, United Kingdom, 2007. doi:10.1002/9780470517437
2. Stütz, A. E., Ed. *Iminosugars as Glycosidase Inhibitors: Nojirimycin and Beyond;* Wiley-VCH: New York, NY, U.S.A., 1999.
3. Moriyama, H.; Tsukida, T.; Inoue, Y.; Yokota, K.; Yoshino, K.; Kondo, H.; Miura, N.; Nishimura, S.-I. *J. Med. Chem.* **2004,** *47,* 1930–1938. doi:10.1021/jm0304313
4. Orsato, A.; Barbagallo, E.; Costa, B.; Olivieri, S.; De Gioia, L.; Nicotra, F.; La Ferla, B. *Eur. J. Org. Chem.* **2011,** 5012–5019. doi:10.1002/ejoc.201100452
5. Decroocq, C.; Stauffert, F.; Pamlard, O.; Oulaïdi, F.; Gallienne, E.; Martin, O. R.; Guillou, C.; Compain, P. *Bioorg. Med. Chem. Lett.* **2015,** *25,* 830–833. doi:10.1016/j.bmcl.2014.12.071
6. Winchester, B. G. *Tetrahedron: Asymmetry* **2009,** *20,* 645–651. doi:10.1016/j.tetasy.2009.02.048
7. Horne, G.; Wilson, F. X. *Prog. Med. Chem.* **2011,** *50,* 135–176. doi:10.1016/B978-0-12-381290-2.00004-5
8. Nash, R. J.; Kato, A.; Yu, C.-Y.; Fleet, G. W. J. *Future Med. Chem.* **2011,** *3,* 1513–1521. doi:10.4155/fmc.11.117
9. Compain, P.; Bodlenner, A. *ChemBioChem* **2014,** *15,* 1239–1251. doi:10.1002/cbic.201402026
10. Gouin, S. G. *Chem. – Eur. J.* **2014,** *20,* 11616–11628. doi:10.1002/chem.201402537
11. Compain, P.; Decroocq, C.; Iehl, J.; Holler, M.; Hazelard, D.; Mena Barragán, T.; Ortiz Mellet, C.; Nierengarten, J.-F. *Angew. Chem., Int. Ed.* **2010,** *49,* 5753–5756. doi:10.1002/anie.201002802
12. Decroocq, C.; Rodríguez-Lucena, D.; Russo, V.; Mena Barragán, T.; Ortiz Mellet, C.; Compain, P. *Chem. – Eur. J.* **2011,** *17,* 13825–13831. doi:10.1002/chem.201102266
13. Decroocq, C.; Joosten, A.; Sergent, R.; Mena Barragán, T.; Ortiz Mellet, C.; Compain, P. *ChemBioChem* **2013,** *14,* 2038–2049. doi:10.1002/cbic.201300283
14. Joosten, A.; Schneider, J. P.; Lepage, M. L.; Tarnus, C.; Bodlenner, A.; Compain, P. *Eur. J. Org. Chem.* **2014,** 1866–1872. doi:10.1002/ejoc.201301583
15. Bonduelle, C.; Huang, J.; Mena-Barragán, T.; Ortiz Mellet, C.; Decroocq, C.; Etamé, E.; Heise, A.; Compain, P.; Lecommandoux, S. *Chem. Commun.* **2014,** *50,* 3350–3352. doi:10.1039/c3cc48190e
16. Lepage, M. L.; Meli, A.; Bodlenner, A.; Tarnus, C.; De Riccardis, F.; Izzo, I.; Compain, P. *Beilstein J. Org. Chem.* **2014,** *10,* 1406–1412. doi:10.3762/bjoc.10.144
17. Marradi, M.; Cicchi, S.; Sansone, F.; Casnati, A.; Goti, A. *Beilstein J. Org. Chem.* **2012,** *8,* 951–957. doi:10.3762/bjoc.8.107
18. Cardona, F.; Isoldi, G.; Sansone, F.; Casnati, A.; Goti, A. *J. Org. Chem.* **2012,** *77,* 6980–6988. doi:10.1021/jo301155p
19. Brissonet, Y.; Ortiz Mellet, C.; Morandat, S.; Garcia Moreno, M. I.; Deniaud, D.; Matthews, S. E.; Vidal, S.; Šesták, S.; El Kirat, K.; Gouin, S. G. *J. Am. Chem. Soc.* **2013,** *135,* 18427–18435. doi:10.1021/ja406931w
20. Rísquez-Cuadro, R.; García Fernández, J. M.; Nierengarten, J.-F.; Ortiz Mellet, C. *Chem. – Eur. J.* **2013,** *19,* 16791–16803. doi:10.1002/chem.201303158
21. Moreno-Clavijo, E.; Carmona, A. T.; Moreno-Vargas, A. J.; Molina, L.; Wright, D. W.; Davies, G. J.; Robina, I. *Eur. J. Org. Chem.* **2013,** 7328–7336. doi:10.1002/ejoc.201300878
22. D'Adamio, G.; Parmeggiani, C.; Goti, A.; Moreno-Vargas, A. J.; Moreno-Clavijo, E.; Robina, I.; Cardona, F. *Org. Biomol. Chem.* **2014,** *12,* 6250–6266. doi:10.1039/C4OB01117A
23. Marra, A.; Zelli, R.; D'Orazio, G.; La Ferla, B.; Dondoni, A. *Tetrahedron* **2014,** *70,* 9387–9393. doi:10.1016/j.tet.2014.10.035
24. Decroocq, C.; Rodríguez-Lucena, D.; Ikeda, K.; Asano, N.; Compain, P. *ChemBioChem* **2012,** *13,* 661–664. doi:10.1002/cbic.201200005
25. Joosten, A.; Decroocq, C.; de Sousa, J.; Schneider, J. P.; Etamé, E.; Bodlenner, A.; Butters, T. D.; Compain, P. *ChemBioChem* **2014,** *15,* 309–319. doi:10.1002/cbic.201300442

26. Compain, P.; Decroocq, C.; Joosten, A.; de Sousa, J.; Rodríguez-Lucena, D.; Butters, T. D.; Bertrand, J.; Clément, R.; Boinot, C.; Becq, F.; Norez, C. *ChemBioChem* **2013,** *14,* 2050–2058. doi:10.1002/cbic.201300312
27. Gavrin, L. K.; Denny, R. A.; Saiah, E. *J. Med. Chem.* **2012,** *55,* 10823–10843. doi:10.1021/jm301182j
28. Gomes, C. M. *Curr. Top. Med. Chem.* **2012,** *12,* 2460–2469. doi:10.2174/1568026611212220002
29. Ribeiro-Viana, R.; García-Vallejo, J. J.; Collado, D.; Pérez-Inestrosa, E.; Bloem, K.; van Kooyk, Y.; Rojo, J. *Biomacromolecules* **2012,** *13,* 3209–3219. doi:10.1021/bm300998c See for examples of glycoclusters with a BODIPY tag and see ref. [30].
30. Hoogendoorn, S.; van Puijvelde, G. H. M.; Kuiper, J.; van derMarel, G. A.; Overkleeft, H. S. *Angew. Chem., Int. Ed.* **2014,** *53,* 10975–10978. doi:10.1002/anie.201406842
31. Ziessel, R.; Ulrich, G.; Harriman, A. *New J. Chem.* **2007,** *31,* 496–501. doi:10.1039/b617972j
32. Loudet, A.; Burgess, K. *Chem. Rev.* **2007,** *107,* 4891–4932. doi:10.1021/cr078381n
33. Ulrich, G.; Ziessel, R.; Harriman, A. *Angew. Chem., Int. Ed.* **2008,** *47,* 1184–1201. doi:10.1002/anie.200702070
34. Boens, N.; Leen, V.; Dehaen, W. *Chem. Soc. Rev.* **2012,** *41,* 1130–1172. doi:10.1039/C1CS15132K
35. Willems, L. I.; Beenakker, T. J. M.; Murray, B.; Scheij, S.; Kallemeijn, W. W.; Boot, R. G.; Verhoek, M.; Donker-Koopman, W. E.; Ferraz, M. J.; van Rijssel, E. R.; Florea, B. I.; Codée, J. D. C.; van der Marel, G. A.; Aerts, J. M. F. G.; Overkleeft, H. S. *J. Am. Chem. Soc.* **2014,** *136,* 11622–11625.
36. Yadav, A. K.; Shen, D. L.; Shan, X.; He, X.; Kermode, A. R.; Vocadlo, D. J. *J. Am. Chem. Soc.* **2015,** *137,* 1181–1189. doi:10.1021/ja5106738
37. Davison, H. R.; Taylor, S.; Drake, C.; Phuan, P.-W.; Derichs, N.; Yao, C.; Jones, E. F.; Sutcliffe, J.; Verkman, A. S.; Kurth, M. J. *Bioconjugate Chem.* **2011,** *22,* 2593–2599. doi:10.1021/bc2004457
38. Haugland, R. P.; Kang, H. C. U.S. Patent 4,774,339, 1998.
39. Thoresen, L. H.; Kim, H.; Welch, M. B.; Burghart, A.; Burgess, K. *Synlett* **1998,** 1276–1278. doi:10.1055/s-1998-1924
40. Goze, C.; Ulrich, G.; Charbonnière, L.; Ziessel, R. *Chem. – Eur. J.* **2003,** *9,* 3748–3755. doi:10.1002/chem.200305084
41. Qin, W.; Baruah, M.; Van der Auweraer, M.; De Schryver, F. C.; Boens, N. *J. Phys. Chem. A* **2005,** *109,* 7371–7384. doi:10.1021/jp052626n
42. Ulrich, G.; Goze, C.; Guardigli, M.; Roda, A.; Ziessel, R. *Angew. Chem., Int. Ed.* **2005,** *44,* 3694–3698. doi:10.1002/anie.200500808
43. Kim, H.; Burghart, A.; Welch, M. B.; Reibenspies, J.; Burgess, K. *Chem. Commun.* **1999,** 1889–1890. doi:10.1039/a905739k
44. Chen, J.; Reibenspies, J.; Derecskei-Kovacs, A.; Burgess, K. *Chem. Commun.* **1999,** 2501–2502. doi:10.1039/a907559c
45. Rurack, K.; Kollmannsberger, M.; Daub, J. *New J. Chem.* **2001,** *25,* 289–292. doi:10.1039/b007379m
46. Rurack, K.; Kollmannsberger, M.; Daub, J. *Angew. Chem., Int. Ed.* **2001,** *40,* 385–387. doi:10.1002/1521-3773(20010119)40:2<385::AID-ANIE385>3.0.CO;2-F
47. Ziessel, R.; Harriman, A. *Chem. Commun.* **2011,** *47,* 611–631. doi:10.1039/C0CC02687E
48. Ziessel, R.; Ulrich, G.; Haefele, A.; Harriman, A. *J. Am. Chem. Soc.* **2013,** *135,* 11330–11344. doi:10.1021/ja4049306
49. Turfan, B.; Akkaya, E. U. *Org. Lett.* **2002,** *4,* 2857–2859. doi:10.1021/ol026245t
50. Bricks, J. L.; Kovalchuk, A.; Trieflinger, C.; Nofz, M.; Büschel, M.; Tolmachev, A. I.; Daub, J.; Rurack, K. *J. Am. Chem. Soc.* **2005,** *127,* 13522–13529. doi:10.1021/ja050652t
51. Han, J.; Loudet, A.; Barhoumi, R.; Burghardt, R. C.; Burgess, K. *J. Am. Chem. Soc.* **2009,** *131,* 1642–1643. doi:10.1021/ja8073374
52. Hansen, J. S.; Ficker, M.; Petersen, J. F.; Christensen, J. B.; Hoeg-Jensen, T. *Tetrahedron Lett.* **2013,** *54,* 1849–1852. doi:10.1016/j.tetlet.2013.01.101
53. Bernhardt, S.; Kastler, M.; Enkelmann, V.; Baumgarten, M.; Müllen, K. *Chem. – Eur. J.* **2006,** *12,* 6117–6128. doi:10.1002/chem.200500999
54. Somerharju, P. *Chem. Phys. Lipids* **2002,** *116,* 57–74. doi:10.1016/S0009-3084(02)00020-8
55. Pownall, H. J.; Smith, L. C. *Chem. Phys. Lipids* **1989,** *50,* 191–211. doi:10.1016/0009-3084(89)90050-9
56. Leen, V.; Leemans, T.; Boens, N.; Dehaen, W. *Eur. J. Org. Chem.* **2011,** 4386–4396. doi:10.1002/ejoc.201100324
57. Hornillos, V.; Amat-Guerri, F.; Acuña, A. U. *J. Photochem. Photobiol., A: Chem.* **2012,** *243,* 56–60. doi:10.1016/j.jphotochem.2012.06.005
58. Mula, S.; Ulrich, G.; Ziessel, R. *Tetrahedron Lett.* **2009,** *50,* 6383–6388. doi:10.1016/j.tetlet.2009.08.091
59. Bura, T.; Ziessel, R. *Org. Lett.* **2011,** *13,* 3072–3075. doi:10.1021/ol200969r
60. Bonardi, L.; Ulrich, G.; Ziessel, R. *Org. Lett.* **2008,** *10,* 2183–2186. doi:10.1021/ol800560b
61. Jahnke, E.; Weiss, J.; Neuhaus, S.; Hoheisel, T. N.; Frauenrath, H. *Chem. – Eur. J.* **2009,** *15,* 388–404. doi:10.1002/chem.200801668
62. Sonogashira, K.; Tohda, Y.; Hagihara, N. *Tetrahedron Lett.* **1975,** *16,* 4467–4470. doi:10.1016/S0040-4039(00)91094-3
63. Isobe, H.; Fujino, T.; Yamazaki, N.; Guillot-Nieckowski, M.; Nakamura, E. *Org. Lett.* **2008,** *10,* 3729–3732. doi:10.1021/ol801230k
64. Valenzano, K. J.; Khanna, R.; Powe, A. C., Jr.; Boyd, R.; Lee, G.; Flanagan, J. J.; Benjamin, E. R. *Assay Drug Dev. Technol.* **2011,** *9,* 213–235. doi:10.1089/adt.2011.0370
65. Chen, T.; Boyer, J. H.; Trudell, M. L. *Heteroat. Chem.* **1997,** *8,* 51–54. doi:10.1002/(SICI)1098-1071(1997)8:1<51::AID-HC7>3.0.CO;2-5
66. Sathyamoorthi, G.; Wolford, L. T.; Haag, A. M.; Boyer, J. H. *Heteroat. Chem.* **1994,** *5,* 245–249. doi:10.1002/hc.520050309
67. Burghart, A.; Kim, H.; Wech, M. B.; Thoresen, L. H.; Reibenspies, J.; Burgess, K. *J. Org. Chem.* **1999,** *64,* 7813–7819. doi:10.1021/jo990796o
68. Potts, K. T. *Chem. Rev.* **1961,** *61,* 87–127. doi:10.1021/cr60210a001
69. Niu, S.-L.; Ulrich, G.; Retailleau, P.; Harrowfield, J.; Ziessel, R. *Tetrahedron Lett.* **2009,** *50,* 3840–3844. doi:10.1016/j.tetlet.2009.04.017
70. Niu, S. L.; Ulrich, G.; Ziessel, R.; Kiss, A.; Renard, P.-Y.; Romieu, A. *Org. Lett.* **2009,** *11,* 2049–2052. doi:10.1021/ol900302n
71. Berlman, I. B. *Handbook of Fluorescence Spectra of Aromatic Molecules;* Academic Press: New York, NY, USA, 1971.
72. Geiger, M. W.; Turro, N. J. *Photochem. Photobiol.* **1975,** *22,* 273. doi:10.1111/j.1751-1097.1975.tb06749.x
73. Kaur, M.; Choi, D. H. *Chem. Soc. Rev.* **2015,** *44,* 58–77. doi:10.1039/C4CS00248B
74. Chen, R. F. *Anal. Lett.* **1968,** *1,* 423–428. doi:10.1080/00032716808051147
75. Stern, O.; Volmer, M. *Phys. Z.* **1919,** *20,* 183–188.

BEILSTEIN JOURNAL OF ORGANIC CHEMISTRY

Synthesis of carbohydrate-scaffolded thymine glycoconjugates to organize multivalency

Anna K. Ciuk and Thisbe K. Lindhorst*

Full Research Paper

Open Access

Address:
Christiana Albertina University of Kiel, Otto Diels Institute of Organic Chemistry, Otto-Hahn-Platz 3/4, D-24118 Kiel, Germany, Fax: +49 431 8807410

Email:
Thisbe K. Lindhorst* - tklind@oc.uni-kiel.de

* Corresponding author

Keywords:
[2 + 2] photocycloaddition; carbohydrate scaffolds; multivalency; thymine glycoconjugates

Beilstein J. Org. Chem. **2015,** *11,* 668–674.
doi:10.3762/bjoc.11.75

Received: 27 February 2015
Accepted: 24 April 2015
Published: 07 May 2015

This article is part of the Thematic Series "Multivalency as a chemical organization and action principle".

Guest Editor: R. Haag

Abstract

Multivalency effects are essential in carbohydrate recognition processes as occurring on the cell surface. Thus many synthetic multivalent glycoconjugates have been developed as important tools for glycobiological research. We are expanding this collection of molecules by the introduction of carbohydrate-scaffolded divalent glycothymine derivatives that can be intramolecularily dimerized by [2 + 2] photocycloaddition. Thus, thymine functions as a control element that allows to restrict the conformational flexibility of the scaffolded sugar ligands and thus to “organize” multivalency. With this work we add a parameter to multivalency studies additional to valency.

Introduction

Multivalency of molecular interactions is a fundamental principle in carbohydrate recognition. It influences the avidity and specificity of carbohydrate–protein interactions as well as it enables supramolecular changes on the cell surface that are essential for cell–cell communication [1-4]. During the last two decades it has become clear that there is not one mechanism underlying multivalency effects in glycobiology, but that there are a multitude of biological processes involving multivalency in one or the other way. These processes allow to control, regulate and fine-tune the complex life of eukaryotes.

We have recently focused our research dedicated to multivalency effects in carbohydrate recognition on the aspect of conformational control of multivalent assemblies, such as micelles [5] or glycoarrays [6]. This work is based on the idea that changes of ligand orientation as well as changes of their conformational availability are regulating parameters in carbohydrate recognition, in particular on the cell surface. Indeed, we have formerly shown that the molecular dynamics of glycodendrimers influence their recognition by lectins [7]. Recently, we have introduced a photoswitchable glycoazobenzene-covered

surface, in which alteration of ligand orientation allowed to switch cell adhesion without changing the recognition quality or the valency of the ligand itself [6]. It is also well-known that galectin-mediated organization of cell surface glycoconjugates influences glycan dynamics and essential biological processes like signaling [8]. Therefore, in order to advance our understanding of carbohydrate-mediated biological response, we are seeking further molecular architectures that allow us organizing the multivalency of sugar ligands.

We planned for a divalent system to start with, in which the dynamics of two at first flexible branches can be controlled by an intramolecular [2 + 2] cycloaddition reaction (Figure 1A). In order to control the [2 + 2] cycloaddition process, it was planned to install both branches on a carbohydrate scaffold. This would allow to favour the intramolecular [2 + 2] cycloaddition over an intermolecular reaction and moreover, a multifunctional carbohydrate scaffold facilitates further ligation or immobilization, respectively, of the final molecular construct. After appropriate carbohydrate conjugation the same molecular architecture could be applied for organization of a divalent glycoconjugate (Figure 1B).

We selected thymine as a photocontrollable element as it can undergo [2 + 2] photocycloaddition upon irradiation with light of $h\nu \geq 290$ nm [5,9,10]. Furthermore, it is known that the thymine heterocycle can be easily N^3-alkylated with, for example, bromoalkyl glycosides. This reaction can be used to install specific sugar moieties for biological recognition [5]. Hence, thymine was employed as the photosensitive control element, a functionalized mannoside was used as scaffold molecule, and α-D-mannosides as specific carbohydrate ligands for the fabrication of the envisaged divalent glycoconjugate (Figure 1C). In the following, we report the synthesis of the divalent glycoconjugates outlined in Figure 1 and their [2 + 2] photocycloaddition.

Results and Discussion

For the conjugation of two thymine and eventually two glycothymine branches on a glycosidic scaffold, the 2- and 3-hydroxy functions of mannose were chosen. These two functional groups can be easily addressed orthogonally to the rest of the molecule. In addition, the vicinal 2- and 3-hydroxy groups are *cis*-oriented and thus the intramolecular [2 + 2] photocycloaddition of attached thymine moieties should be facilitated. As the anomeric functional group of the chosen mannoside scaffold, a Boc-protected amino group was selected which can be derived from an azide function. Thus, the synthesis of the targeted divalent thymine glycoconjugate started with the known 2-azidoethyl α-D-mannoside (**1**, Scheme 1) [11-13]. The kinetically

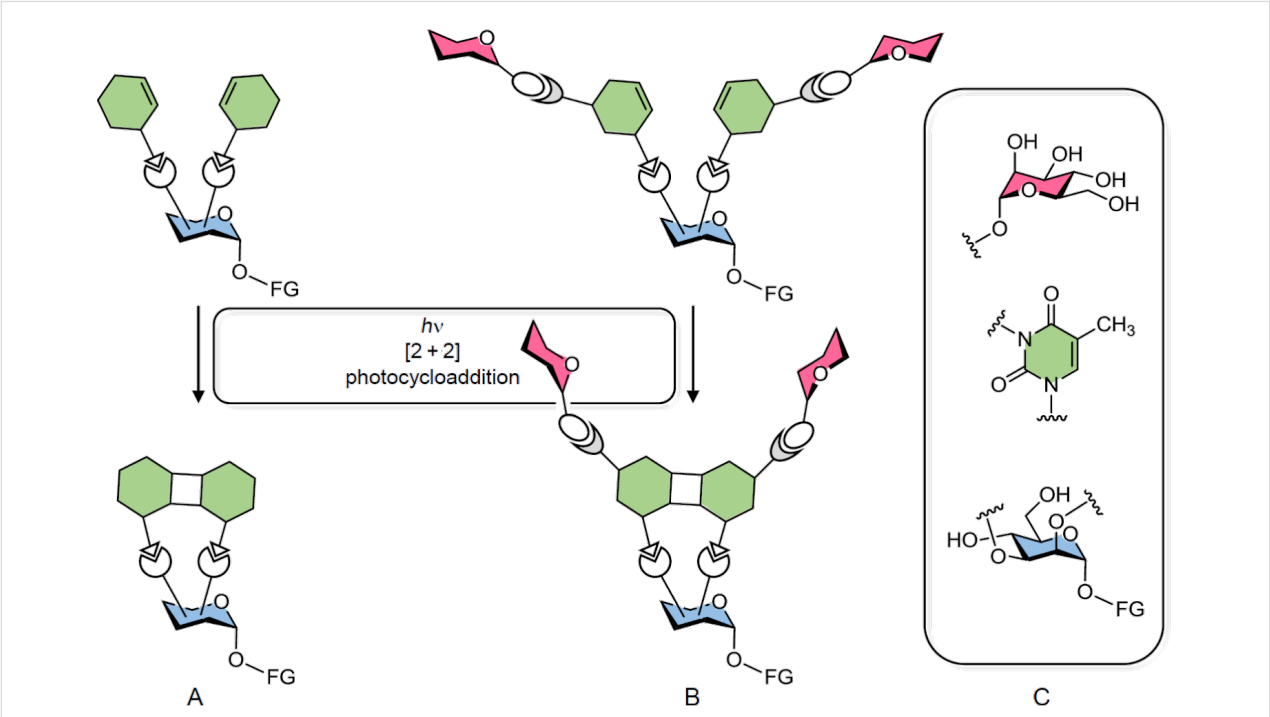

Figure 1: Cartoon of a divalent carbohydrate-scaffolded molecular architecture that allows control of the flexibility of both branches by intramolecular [2 + 2] photocycloaddition (A). To attach the photocontrollable moieties (green) to the carbohydrate scaffold (blue), an appropriate ligation chemistry is required. Additional ligation of sugar ligands (pink) leads to the analogous divalent glycothymine glycoconjugate (B). As building blocks for this molecular architecture a mannoside scaffold (blue), thymine (green), and α-D-mannosyl ligands (pink) were used (C). FG = functional group.

controlled reaction of mannoside **1** with 2-methoxypropene delivers the 4,6-isopropylidene-protected derivative **2** in good yield, leaving the 2- and 3-hydroxy groups free [14,15]. The following Williamson etherification [16] with propargyl bromide yielded the 2,3-di-*O*-propargylmannoside **3** in high yield. Propargylation was selected for this step to allow eventual conjugation with the known azidopropylated thymine derivative **6** [17-20] via copper(I)-catalyzed click reaction [21,22]. Before, the acid-labile isopropylidene protecting group was removed using 10% TFA in dichloromethane leading to mannoside **4**, and then the azide function in **4** was converted in a Staudinger reduction [23] with simultaneous Boc-protection giving rise to mannoside **5** in high overall yield. Boc-protection of the amino group also facilitated the chromatographic purification process in the subsequent steps.

Mannoside **5** is equipped with two propargyl branches projecting from the β-face of the carbohydrate, whereas the Boc-protected aminoethyl aglycone is α-positioned and ready for eventual immobilisation of the final thymine glycoconjugate on a surface or for conjugation to another multivalent compound. For the click reaction of **5** with the thymine derivative **6**, copper sulfate and sodium ascorbate were used. The conjugation product **7** was obtained in 71% yield and showed good water solubility.

Then [2 + 2] photocycloaddition was tested. For irradiation the divalent thymine glycoconjugate **7** was diluted (maximum concentration was 500 µg/1 mL) in a 1:1-mixture of water and acetone in order to favor intramolecular photocycloaddition and avoid the intermolecular reaction. Acetone is required as triplett

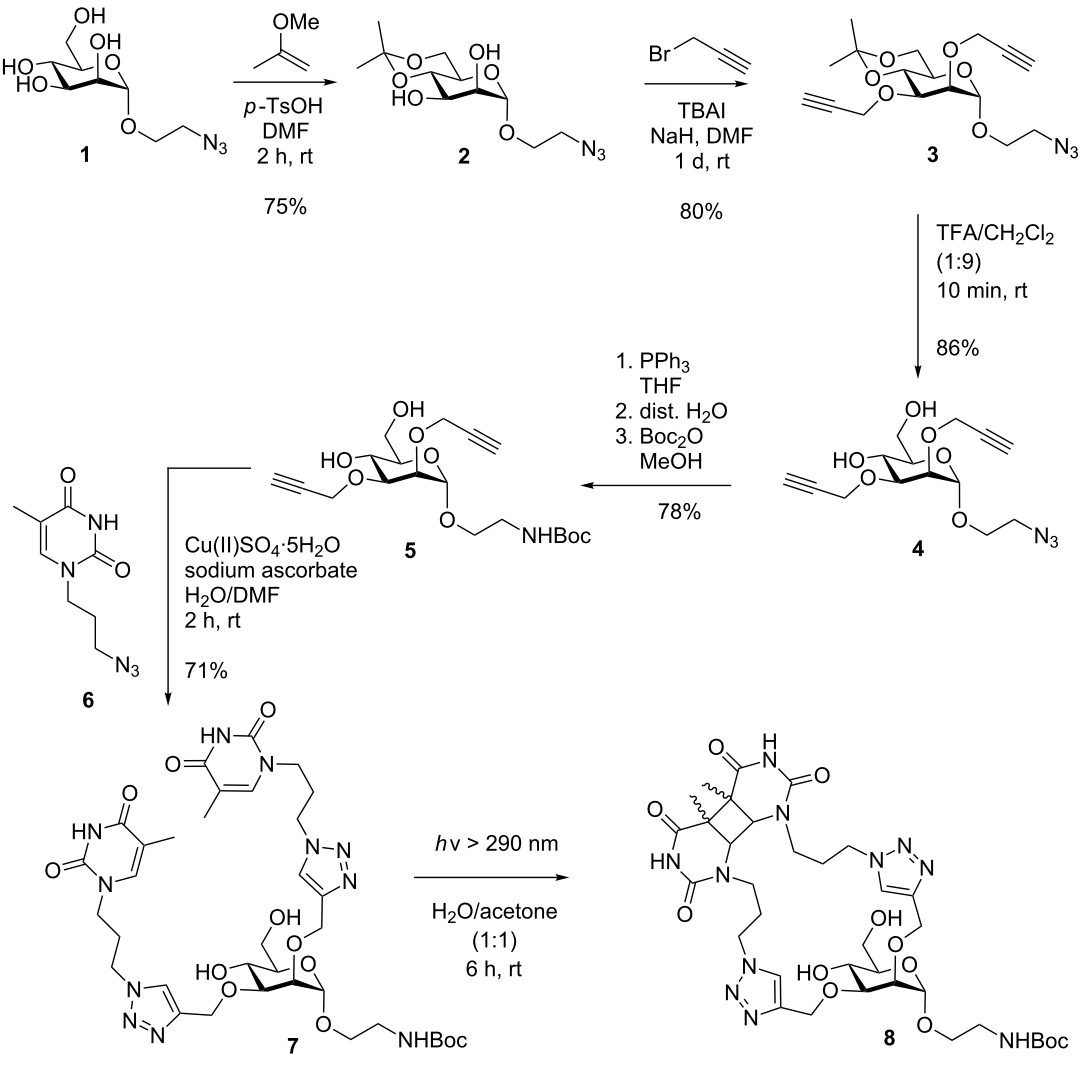

Scheme 1: Synthesis of carbohydrate-scaffolded dimeric thymine **7** and intramolecular photocycloaddition. The irradiation product **8** is a complex isomeric mixture (not shown in detail, cf. Supporting Information File 1).

sensitizer in this process [5]. Irradiation with light of ≥ 290 nm was performed during a period of 3 and 6 hours, respectively. After irradiation, the solvents were removed and the product investigated without any purification or further separation. ^{1}H NMR-spectroscopic analysis shows that the signals for the two thymine H-6 protons in **7** at 7.27 and 7.25 ppm decrease during irradiation and finally almost disappear (they are shifted to ≈3.7 ppm in **8**). In addition, the signals for the two triazole H-11 (7.96 ppm) and for the anomeric scaffold H-1 (H-1$_{core}$) at 4.92 ppm get multiplicated. Interestingly, while the H-1 peak of the starting material is clearly diminished, a total of five, slightly downfield-shifted doublets is seen in the [2 + 2] photocycloaddition product **8** (Figure 2C, 5.0–5.3 ppm). These signals correspond to five different isomeric photocycloaddition products.

The [2 + 2] photocycloaddition of thymine derivatives has been extensively discussed in the literature [9,10,24,25] because it is important in DNA damage (as cycloreversion is in DNA repair) [26,27]. Accordingly, the photodimerisation can occur in an *anti* and a *syn* fashion leading to regioisomeric products (cf. Supporting Information File 1). Both regioisomers can consist of four different stereoisomers, two *cis* and two *trans* isomers according to the relative steric orientation of the thymine methyl groups. It can be assumed that the irradiation of **7** in diluted solution favors the *syn* photocycloaddition leading to two isomeric *cis–syn*- and two *trans–syn*-[2 + 2] photocycloaddition products. In addition, also an *anti* product seems to form as five (not four) H-1 signals are seen in the ^{1}H NMR spectrum.

The photocycloaddition of **7** can also be observed by UV–vis spectroscopy. Upon irradiation, the absorption at 270 nm completely disappears (cf. Supporting Information File 1). Mass-spectrometric analysis allows to exclude intermolecular photocycloaddition as no corresponding mass peaks were detected (cf. Supporting Information File 1).

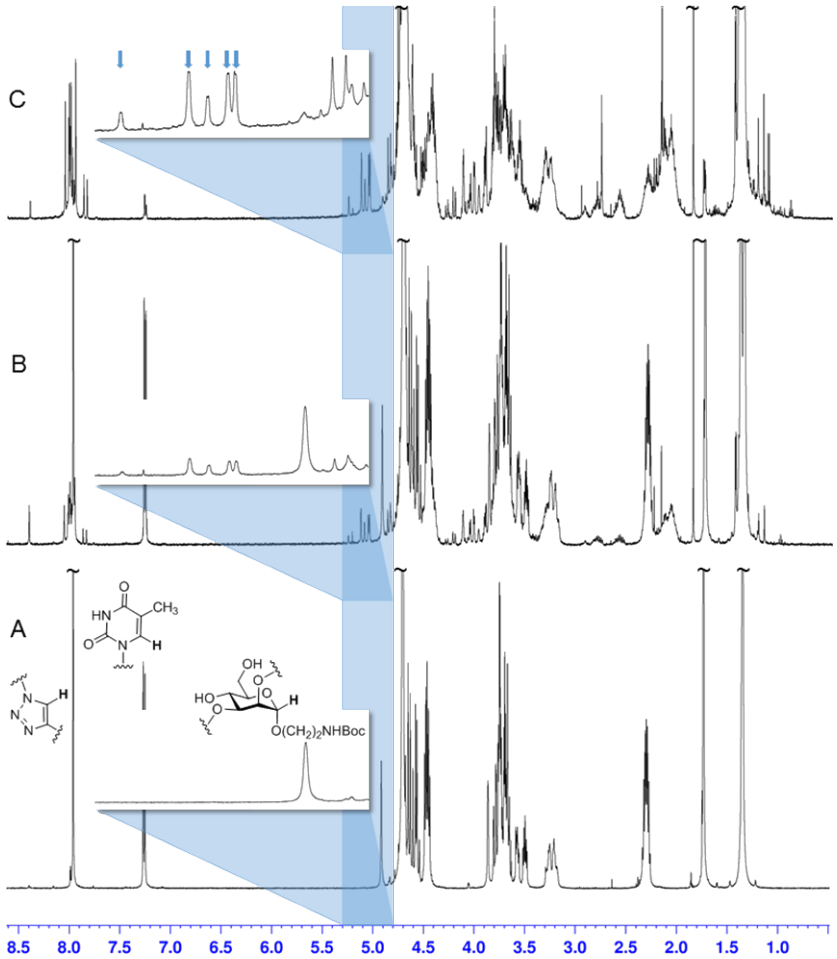

Figure 2: ^{1}H NMR spectra (all in D_2O, 500 MHz) of mannoside **7** (A) and of the irradiation product (**8**) after 3 hours irradiation time (B) and 6 hours irradiation time (C). Progress of photocycloaddition is seen in the changes of the signals for the triazole H-11 and the thymine H-6 protons (left at low field) and the anomeric H-1 of the carbohydrate scaffold (≈4.9 ppm). The anomeric H-1 region is detailed in each case: after 6 hours of irradiation (C) five new signals are seen (blue arrows) corresponding to five different isomers of the photocycloaddition product **8**.

In the next step, glycosylated thymine dimers were targeted (cf. Figure 1B). Based on our earlier work [5], we first planned to employ an appropriate bromoalkyl mannoside for *N*-alkylation of the thymine N^3 [28]. In this step, DBU can be employed as non-nucleophilic base [29] leaving the NHBoc group intact. When sodium hydride is employed instead, NHBoc is deprotonated in addition to thymine and undesired alkylation of NHBoc is occurring. However, also the free hydroxy functions are perturbing the reaction and hence we found no reaction conditions for a clean thymine N^3 functionalization of **7**. Therefore, an OH-protected analogue of **7** was prepared starting from **3** (Scheme 2). Staudinger reduction of the azide group and Boc-protection in the same pot gave **9** and subsequent click reaction with the thymine derivative **6** the isopropylidene-protected

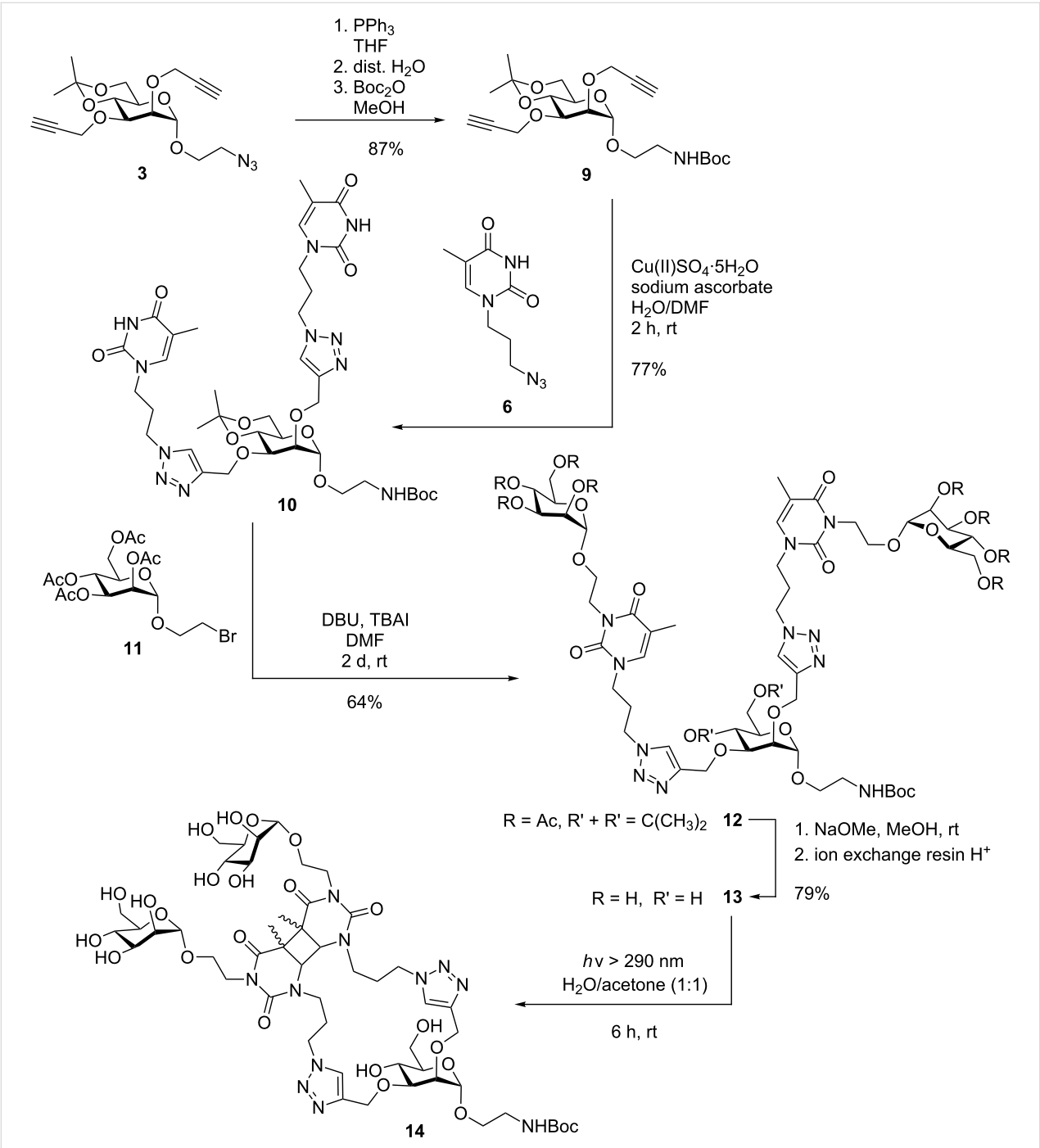

Scheme 2: Synthesis of carbohydrate-scaffolded dimeric glycothymine **13** and intramolecular photocycloaddition. The irradiation product **14** is a complex isomeric mixture (not shown in detail, cf. Supporting Information File 1).

dimeric thymine glycoconjugate **10** in good yield. This could be alkylated employing the bromoethyl mannoside **11** [11] in an optimized procedure employing DBU and TBAI at rt [5] over two days to deliver the protected glycothymine derivative **12** in 64% yield. The acetyl protecting groups were cleaved employing Zemplén's procedure [30]. During work-up with acidic ionic exchange resin, surprisingly cleavage of the isopropylidene protecting group was observed whereas the Boc-protection remained untouched. Thus, the title glycocluster **13** was obtained in a single deprotection step. The new divalent glycoconjugate **13** shows good water solubility and is thus suited for biological testing.

For photodimerization of **13**, it was irradiated for 6 h, again in diluted solution using a 1:1 mixture of water and acetone. As it was observed in the irradiation of **7**, the peaks for the thymine H-6 protons, the triazole H-11, and the anomeric H-1 of the core mannoside underwent a characteristic change in the ^{1}H NMR spectrum (Figure 3). In this case, four, not five (as in **8**), new doublets for H-1$_{core}$ appear in the photodimerized product **14** (Figure 3B). This finding is in line with the formation of two *cis–syn*- and two *trans–syn*-[2 + 2] photocycloaddition products. The formation of *anti*-addition products seems to be hampered in this case because the glycothymine branches in **13** and **14** are sterically more hindered than the thymine branches in **7** and **8**. Again UV–vis spectroscopy further underlines the dimerization success as the absorption maximum at 270 nm disappears and mass spectrometry supports intramolecular photocycloaddition only (cf. Supporting Information File 1).

Conclusion

In line with our former work on the orientational control of carbohydrate ligands assembled on a surface [6], we seeked the synthesis of multivalent glycoconjugates that allow the organization of multivalency. To start this new approach, we have introduced a divalent carbohydrate-scaffolded glycothymine system and showed intramolecular *syn*-[2 + 2] photocycloaddition as planned. This photoreaction changes the conformational availability of the conjugated α-D-mannosyl ligands and thus adds a regulating parameter to multivalency studies. Biological assays employing this type of photocontrollable glycoconjugates will have to follow.

Supporting Information

Supporting Information File 1

Experimental and analytical details and NMR spectra for all new synthetic compounds as well as discussion of [2 + 2] photocycloaddition with **7** and **13**.
[http://www.beilstein-journals.org/bjoc/content/supplementary/1860-5397-11-75-S1.pdf]

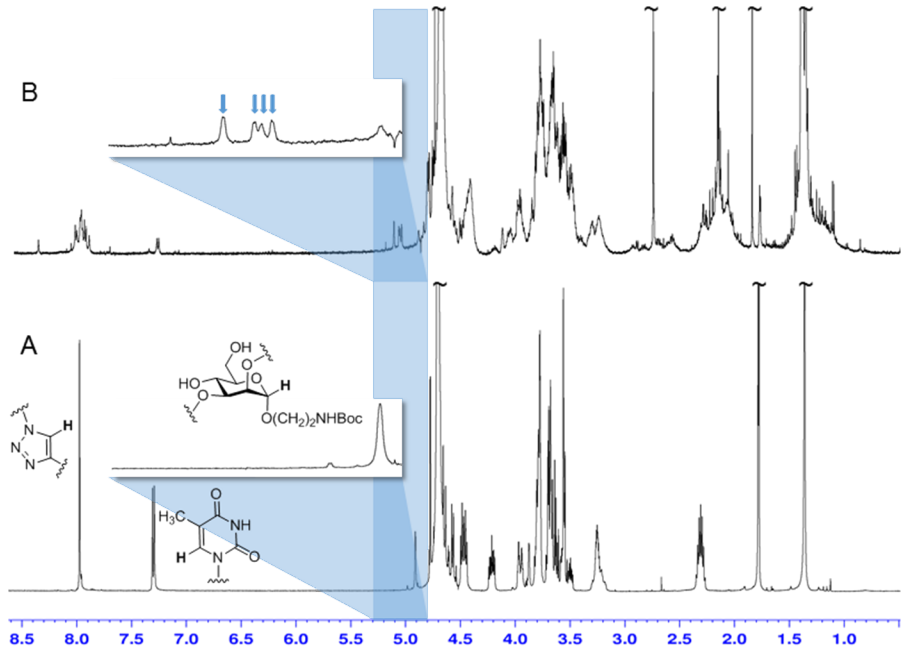

Figure 3: ^{1}H NMR spectra (all in D_2O, 500 MHz) of mannoside **13** (A) and of the irradiation product (**14**) after 6 hours irradiation time (B). Photocycloaddition is indicated by the changes of the signals for the triazole H-11 and the thymine H-6 protons (left at low field) and the anomeric H-1 of the carbohydrate scaffold (≈4.9 ppm). The anomeric H-1 region is detailed in both cases: four new signals are seen in **14** (B) (blue arrows) corresponding to four different isomeric products of the photocycloaddition.

Acknowledgements

Financial support by FCI (Fonds der Chemischen Industrie) is gratefully acknowledged. We thank Dipl.-Chem. Anne Müller for fruitful discussions.

References

1. Mammen, M.; Choi, S.-K.; Whitesides, G. M. *Angew. Chem., Int. Ed.* **1998,** *37,* 2754–2794. doi:10.1002/(SICI)1521-3773(19981102)37:20<2754::AID-ANIE2754>3.0.CO;2-3
   Angew. Chem. **1998**, *110*, 2908–2953. doi:10.1002/(SICI)1521-3757(19981016)110:20<2908::AID-ANGE2908>3.0.CO;2-2
2. Kiessling, L. L.; Gestwicki, J. E.; Strong, L. E. *Angew. Chem., Int. Ed.* **2006,** *45,* 2348–2368. doi:10.1002/anie.200502794
   Angew. Chem. **2006,** *118,* 2408–2429. doi:10.1002/ange.200502794
3. Fasting, C.; Schalley, C. A.; Weber, M.; Seitz, O.; Hecht, S.; Koksch, B.; Dernedde, J.; Graf, C.; Knapp, E.-W.; Haag, R. *Angew. Chem., Int. Ed.* **2012,** *51,* 10472–10498. doi:10.1002/anie.201201114
   Angew. Chem. **2012,** *124,* 10622–10650. doi:10.1002/ange.201201114
4. Christensen, T.; Gooden, D. M.; Kung, J. E.; Toone, E. J. *J. Am. Chem. Soc.* **2003,** *125,* 7357–7366. doi:10.1021/ja021240c
5. Schwekendiek, K.; Kobarg, H.; Daumlechner, L.; Sönnichsen, F. D.; Lindhorst, T. K. *Chem. Commun.* **2011,** *47,* 9399–9401. doi:10.1039/c1cc13246f
6. Weber, T.; Chandrasekaran, V.; Stamer, I.; Thygesen, M. B.; Terfort, A.; Lindhorst, T. K. *Angew. Chem., Int. Ed.* **2014,** *53,* 14583–14586. doi:10.1002/anie.201409808
   Angew. Chem. **2014,** *126,* 14812–14815. doi:10.1002/ange.201409808
7. von der Lieth, C.-W.; Frank, M.; Lindhorst, T. K. *Rev. Mol. Biotechnol.* **2002,** *90,* 311–337. doi:10.1016/S1389-0352(01)00072-1
8. Dennis, J. W.; Nabi, I. R.; Demetriou, M. *Cell* **2009,** *139,* 1229–1241. doi:10.1016/j.cell.2009.12.008
9. Inaki, Y. *CRC Handbook of Organic Photochemistry and Photobiology, 104;* CRC Press: Boca Raton, 2004.
10. Friedel, M. G.; Gierlich, J.; Carell, T. Cyclobutane Pyrimidine Dimers as UV-Induced DNA Lesions. In *The chemistry of cyclobutanes;* Rappoport, Z.; Liebman, J. F., Eds.; Wiley and Sons: Chichester, U.K., 2005; pp 1031–1059. doi:10.1002/0470864028.ch22
11. Dahmén, J.; Freid, T.; Grönberg, G.; Lave, T.; Magnussen, G.; Noori, G. *Carbohydr. Res.* **1983,** *116,* 303–307. doi:10.1016/0008-6215(83)88120-8
12. Chernyak, A. Ya.; Sharma, G. V. M.; Kononov, L. O.; Krishna, P. R.; Levinsky, A. B.; Kochetkov, N. K. *Carbohydr. Res.* **1992,** *223,* 303–309. doi:10.1016/0008-6215(92)80029-Z
13. Kleinert, M.; Röckendorf, N.; Lindhorst, T. K. *Eur. J. Org. Chem.* **2004,** 3931–3940. doi:10.1002/ejoc.200400239
14. Evans, M. E.; Parrish, F. W. *Carbohydr. Res.* **1977,** *54,* 105–114. doi:10.1016/S0008-6215(00)80559-5
15. Jiang, R.; Zong, G.; Liang, X.; Jin, S.; Zhang, J.; Wang, D. *Molecules* **2014,** *19,* 6683–6693. doi:10.3390/molecules19056683
16. Williamson, A. *Justus Liebigs Ann. Chem.* **1851,** *77,* 37–49. doi:10.1002/jlac.18510770104
17. Fenick, D. J.; Falvey, D. E. *J. Org. Chem.* **1994,** *59,* 4791–4799. doi:10.1021/jo00096a021
18. Schall, O. F.; Gokel, G. W. *J. Am. Chem. Soc.* **1994,** *116,* 6089–6100. doi:10.1021/ja00093a005
19. Adams, D. R.; Boyd, A. S. F.; Ferguson, R.; Grieson, D. S.; Monneret, C. *Nucleosides Nucleotides* **1998,** *17,* 1053–1075. doi:10.1080/07328319808004220
20. Nawrot, B.; Michalak, O.; Olejniczak, S.; Wieczorek, M. W.; Lis, T.; Stec, W. J. *Tetrahedron* **2001,** *57,* 3979–3985. doi:10.1016/S0040-4020(01)00277-0
21. Tornøe, C. W.; Christensen, C.; Meldal, M. *J. Org. Chem.* **2002,** *67,* 3057–3064. doi:10.1021/jo011148j
22. Kolb, H. C.; Finn, M. G.; Sharpless, K. B. *Angew. Chem., Int. Ed.* **2001,** *40,* 2004–2021. doi:10.1002/1521-3773(20010601)40:11<2004::AID-ANIE2004>3.0.CO;2-5
    Angew. Chem. **2001,** *113,* 2056–2075. doi:10.1002/1521-3757(20010601)113:11<2056::AID-ANGE2056>3.0.CO;2-W
23. Staudinger, H.; Meyer, J. *Helv. Chim. Acta* **1919,** *2,* 635–646. doi:10.1002/hlca.19190020164
24. Cadet, J.; Voituriez, L.; Hruska, F. E.; Kan, L.-S.; de Leeuw, F. A. A. M.; Altona, C. *Can. J. Chem.* **1985,** *63,* 2861–2868. doi:10.1139/v85-477
25. Law, Y. K.; Azadi, J.; Crespo-Hernández, C. E.; Olmon, E.; Kohler, B. *Biophys. J.* **2008,** *94,* 3590–3600. doi:10.1529/biophysj.107.118612
26. Mees, A.; Klar, T.; Gnau, P.; Hennecke, U.; Eker, A. P. M.; Carell, T.; Essen, L.-O. *Science* **2004,** *306,* 1789–1793. doi:10.1126/science.1101598
27. Heil, K.; Pearson, D.; Carell, T. *Chem. Soc. Rev.* **2011,** *40,* 4271–4278. doi:10.1039/C000407N
28. Wilds, C. J.; Noronha, A. M.; Robidoux, S.; Miller, P. S. *J. Am. Chem. Soc.* **2004,** *126,* 9257–9265. doi:10.1021/ja0498540
29. Suwiński, J.; Walczak, K. *Synthesis* **2001,** *2,* 225–228. doi:10.1055/s-2001-10805
30. Zemplén, G.; Pascu, E. *Ber. Dtsch. Chem. Ges. B* **1929,** *62,* 1613–1614. doi:10.1002/cber.19290620640

BEILSTEIN JOURNAL OF ORGANIC CHEMISTRY

Synthesis of tripodal catecholates and their immobilization on zinc oxide nanoparticles

Franziska Klitsche[1], Julian Ramcke[1], Julia Migenda[2], Andreas Hensel[3], Tobias Vossmeyer[3], Horst Weller[3], Silvia Gross[*2] and Wolfgang Maison[*1]

Full Research Paper

Open Access

Address:
[1]Department of Chemistry, University of Hamburg, Institute of Pharmaceutical and Medicinal Chemistry, Bundesstr. 45, 20146 Hamburg, Germany, [2]IENI-CNR, Department of Chemical Sciences, University of Padova, INSTM, Via Marzolo 1, 35131 Padova, Italy and [3]Department of Chemistry, University of Hamburg, Institute of Physical Chemistry, Grindelallee 117, 20146 Hamburg, Germany

Email:
Silvia Gross[*] - silvia.gross@unipd.it; Wolfgang Maison[*] - maison@chemie.uni-hamburg.de

* Corresponding author

Keywords:
bifunctional anchors; catecholates; multivalency; poly(ethylene glycol); ZnO nanoparticles

Beilstein J. Org. Chem. **2015,** *11,* 678–686.
doi:10.3762/bjoc.11.77

Received: 02 March 2015
Accepted: 27 April 2015
Published: 07 May 2015

This article is part of the Thematic Series "Multivalency as a chemical organization and action principle".

Guest Editor: R. Haag

Abstract

A common approach to generate tailored materials and nanoparticles (NPs) is the formation of molecular monolayers by chemisorption of bifunctional anchor molecules. This approach depends critically on the choice of a suitable anchor group. Recently, bifunctional catecholates, inspired by mussel-adhesive proteins (MAPs) and bacterial siderophores, have received considerable interest as anchor groups for biomedically relevant metal surfaces and nanoparticles. We report here the synthesis of new tripodal catecholates as multivalent anchor molecules for immobilization on metal surfaces and nanoparticles. The tripodal catecholates have been conjugated to various effector molecules such as PEG, a sulfobetaine and an adamantyl group. The potential of these conjugates has been demonstrated with the immobilization of tripodal catecholates on ZnO NPs. The results confirmed a high loading of tripodal PEG-catecholates on the particles and the formation of stable PEG layers in aqueous solution.

Introduction

An elegant approach to generate tailored materials and nanoparticles is the formation of molecular monolayers by chemisorption of bifunctional anchor molecules (Figure 1A) [1]. The effectivity of this approach depends critically on the choice of a suitable anchor molecule. For most applications the anchor needs to be modular and should have functional groups for conjugation of effector molecules via high-yielding and robust chemical transformations. On the other hand, the anchor moiety needs to form a stable (in most cases covalent) connection to the target surface. Various bifunctional anchors have been reported for immobilization on different materials and nanoparticles. Basically, silane derivatives are used for glass surfaces [2,3], thiols for noble metal surfaces [4], carboxylates [5] and phosphates [6] as well as phosphonates [7] for metal and metal

oxide surfaces. In addition, bifunctional catechols like dopamine or DOPA (L-3,4-dihydroxyphenylalanine, Figure 1B), have received considerable interest as anchor groups for important metal surfaces such as titanium oxide, iron oxide and stainless steel [8-11]. Immobilization of catecholates was inspired by mussel-adhesive proteins (MAPs) and bacterial siderophores [12].

However, many applications of catecholate immobilization in physiological media are compromised by continuous leaching of grafted material which is a consequence of reversible binding at neutral and slightly acidic pH. Multivalent catecholates, such as MAPs or oligo-DOPA, overcome this drawback of simple catecholate derivatives and show increased binding affinities to metal surfaces. They are therefore attractive anchors for durable immobilizations on metal surfaces in aqueous media [13]. We have recently reported non-peptidic trimeric catecholates and have demonstrated their potential to form stable molecular monolayers on bulk TiO_2 and stainless steel surfaces in aqueous environment [14,15]. In the present work, we describe the synthesis of effector-conjugates of tripodal catecholates and their immobilization on ZnO NPs.

Results and Discussion

Zinc oxide belongs to the most intensively investigated inorganic compounds, due to its outstanding functional properties combined with manifold morphologies, no toxicity and easy preparation [16]. It is a piezoelectronic semiconductor with a high exciton binding energy (60 meV) and a wide band-gap (3.37 eV) at room temperature [17,18]. ZnO is therefore employed in (bio-)sensors [19], ultraviolet (UV) light-emitting diodes [20], UV laser diodes [21] and in the field of catalysis [22,23]. ZnO exists in several morphologies such as nanowires, nanotubes, nanoparticles, nanoplatelets and nanowhiskers [24]. Colloidal ZnO nanoparticles are especially interesting because of their functional properties. Classical methods of colloid chemistry can be used for the preparation of colloidal suspensions [25] and various paths to obtain ZnO colloids have been reviewed by Spanhel [26]. Suitable methods for the synthesis of pure and doped ZnO NPs involve colloidal, sol–gel or solvo-/hydrothermal methods [27], microemulsion and miniemulsion methods [28] or non-aqueous sol–gel routes [29]. Recently, some of us established an easy and fast procedure to obtain nanocrystalline ZnO nanoparticles, which was applied to prepare the ZnO nanoparticles used in this work [30].

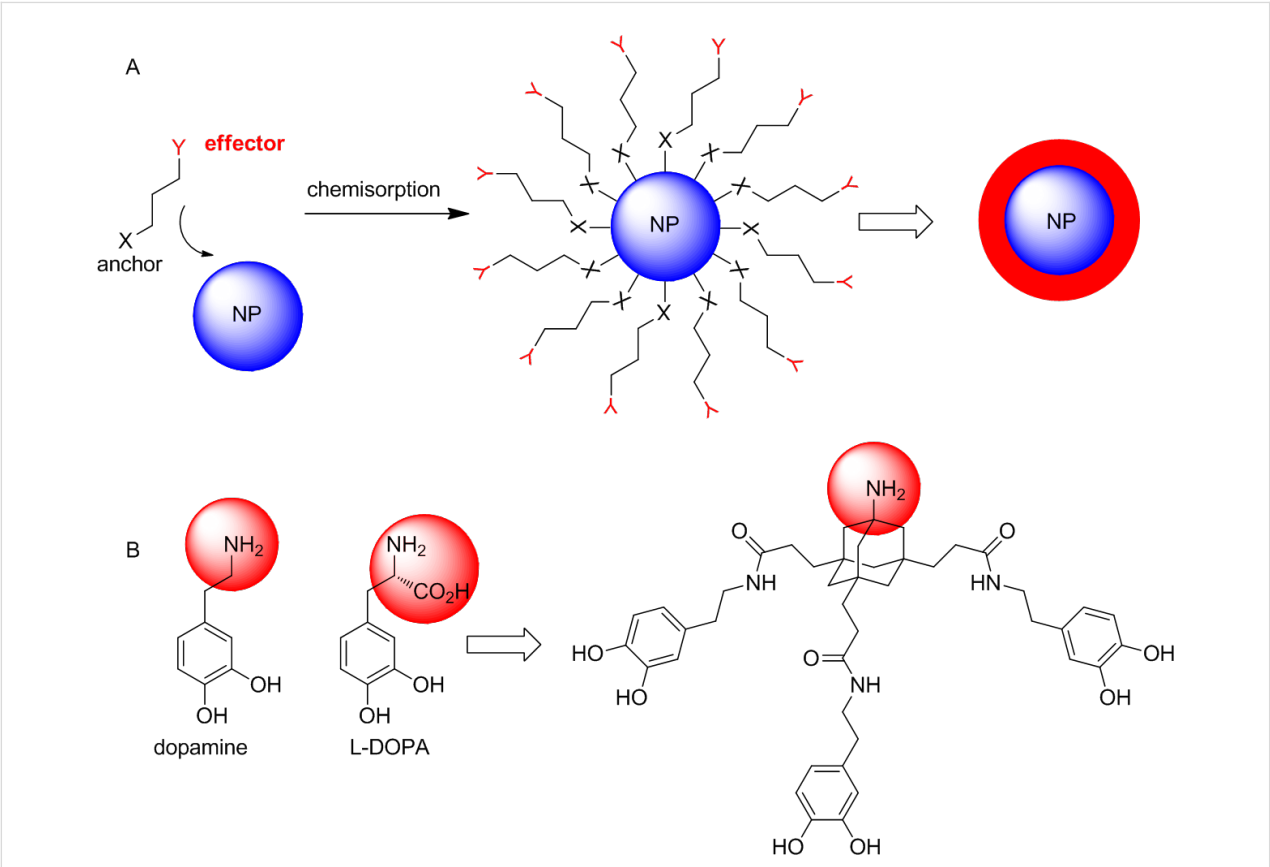

Figure 1: A) Schematic drawing of a bifunctional anchor molecule and its immobilization on a nanoparticle (NP); B) tripodal catechol derivative, derived from the native bifunctional anchors dopamine and L-DOPA.

Immobilization of effector molecules on ZnO NPs has been accomplished with oxygen donors such as carboxylic acids. Bifunctional derivatives bearing an additional effector moiety may be used to generate stable particles with tailored properties, good solubility and biocompatibility. Suitable effectors in this context are PEG [31-33], zwitterions [34,35] or polyglycerols [36,37] which, when immobilized on NPs, may be used to tune their pharmacokinetic properties [38,39]. The resulting particles show a reduced tendency towards plasma protein and tissue binding, both important factors influencing elimination and tissue distribution of biological imaging reagents. Based on our good experiences with the immobilization of tripodal catecholates on TiO_2 and steel, we explored their use for the functionalization of ZnO NPs.

Synthesis of tripodal catecholates

A common synthetic precursor for the synthesis of suitable tripodal catecholates is the AB_3-scaffold **1** [40-42] (Scheme 1)

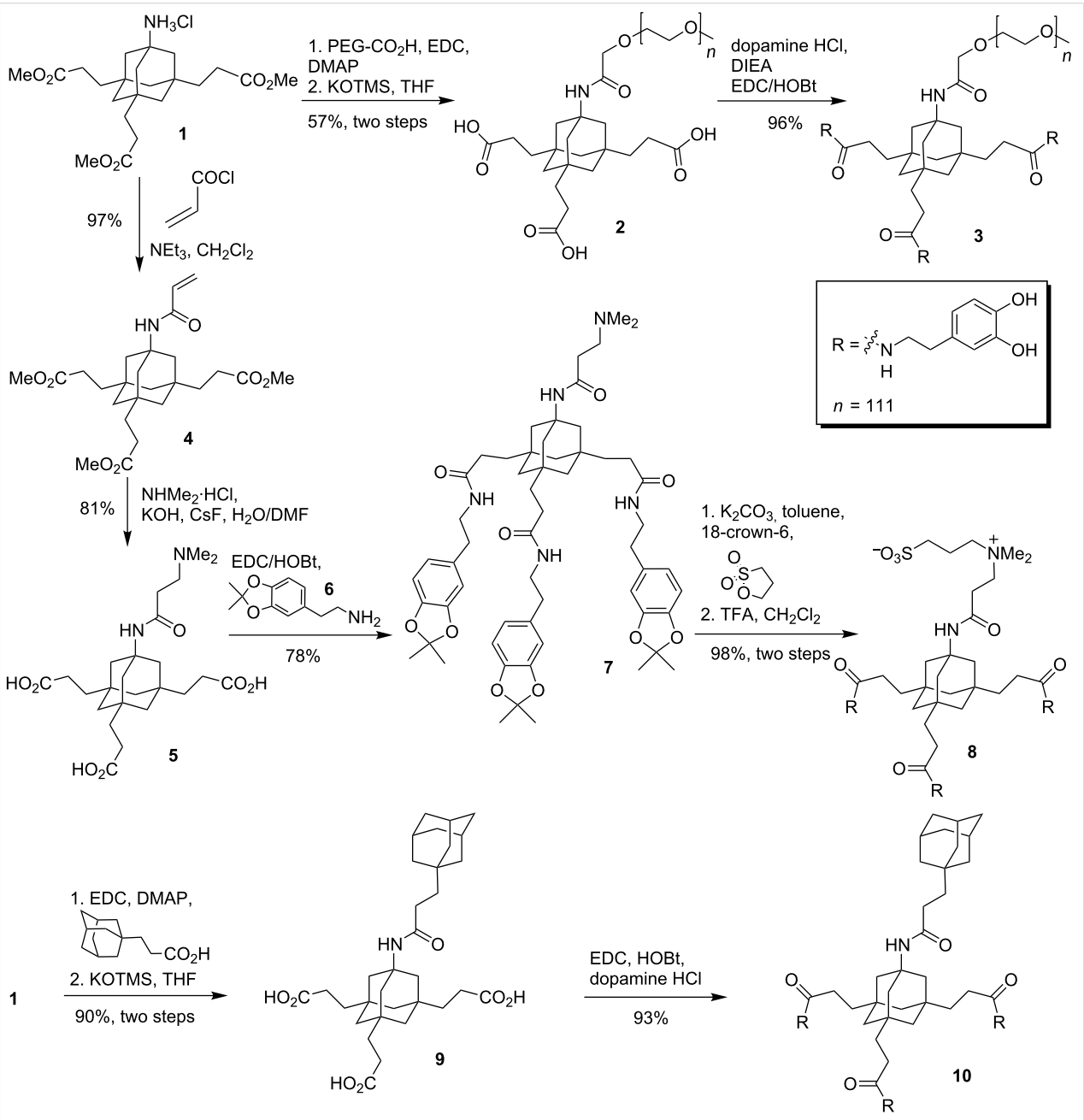

Scheme 1: Synthesis of tripodal catecholates for surface immobilization. PEG-triscatecholate **3** was synthesized from **1** according to literature [31]. Abbreviations: PEG = poly(ethylene glycol) (5 kDa); EDC = 1-ethyl-3-(3-dimethylaminopropyl)carbodiimide; DMAP = 4-(dimethylamino)pyridine; HOBt = hydroxybenzotriazole; TFA = trifluoroacetic acid, KOTMS = potassium trimethylsilanolate, DIEA = *N,N*-diisopropylethylamine.

which is readily available in a few steps from adamantane as a cheap starting material [43]. Amine **1** was coupled to a commercially available PEG-carboxylate (5 kDa) with EDC/DMAP. The resulting PEG-conjugate was treated with KOTMS to remove the methyl esters to give tricarboxylic acid **2** in good 57% yield for the two-step procedure. In a last step, dopamine was coupled to the free carboxylic acids to give PEG-triscatecholate **3** in excellent yield [31]. This PEG-conjugate is ready for the immobilization on NPs and may be used to generate biopassive (stealth) particles for biomedical applications.

As an alternative to PEG as an effector moiety, we tried to conjugate the triscatecholates to a sulfobetaine group. Like PEG, these zwitterionic moieties have been used frequently to confer biopassive properties to metal surfaces but are less prone to oxidative degradation [35]. The synthesis started again from AB_3-scaffold **1** which was acylated with acryloyl chloride to give acrylamide **4**. Treatment of **4** with dimethylamine and excess KOH leads to the nucleophilic addition of the amine and saponification of the methyl esters in one step to give the free acid **5** after acidic work-up. Subsequent coupling of **5** to dopamine acetonide **6** with EDC and HOBt gave the protected triscatecholate **7** in good yield. The sulfobetaine was then generated by treatment of **7** with 1,3-propane sultone and the acetonides were cleaved with TFA to give the free triscatecholate **8**. Following the same synthetic strategy, the hydrophobic derivative **10** bearing an additional adamantyl group as an effector was prepared. This triscatecholate might be useful for the construction of diamandoid hydrophobic coatings [44] or for the reversible attachment of cyclodextrins to NPs by the formation of cyclodextrin/adamantane inclusion complexes [45].

Alternatively, acrylamide **4** and bromide **12** [42] were converted to the corresponding triscatecholates **11** and **13** by coupling to dopamine (Scheme 2). The resulting triscatecholates **11** and **13** may be used as synthetically flexible platforms for functionalizations of surfaces via either nucleophilic addition (to the Michael acceptor in **11**) or radical chemistry after immobilization.

Immobilization on ZnO NPs

Three different catecholates were selected to study the binding properties to ZnO NPs (Figure 2). Monomeric PEG-catecholate **14** [46] and the tripodal homologue **3** were chosen to study the stability of the coatings and the particles in aqueous solution depending on the valency of the catecholate. Bromotriscatecholate **13** was chosen as a hydrophobic analogue to **3**.

ZnO particles were synthesized according to a literature known procedure from $Zn(acac)_2$ [30].

Powders separated by the centrifugation of the precursor suspensions were investigated by X-ray diffraction to confirm the formation of crystalline materials. The XRD pattern confirms the selective formation of pure ZnO wurtzite already at room temperature without the need of any further thermal treatment (Figure 3A). This data is in agreement with TEM micrographs, indicating the presence of spherical particles with an average diameter of 6 nm next to larger crystal aggregates (Figure 3B).

The particles were coated using solutions of monomeric PEG-catecholate **14** and the tripodal catecholates **3** and **13** in a concentrated 3-morpholinopropanesulfonic acid (MOPS) buffer

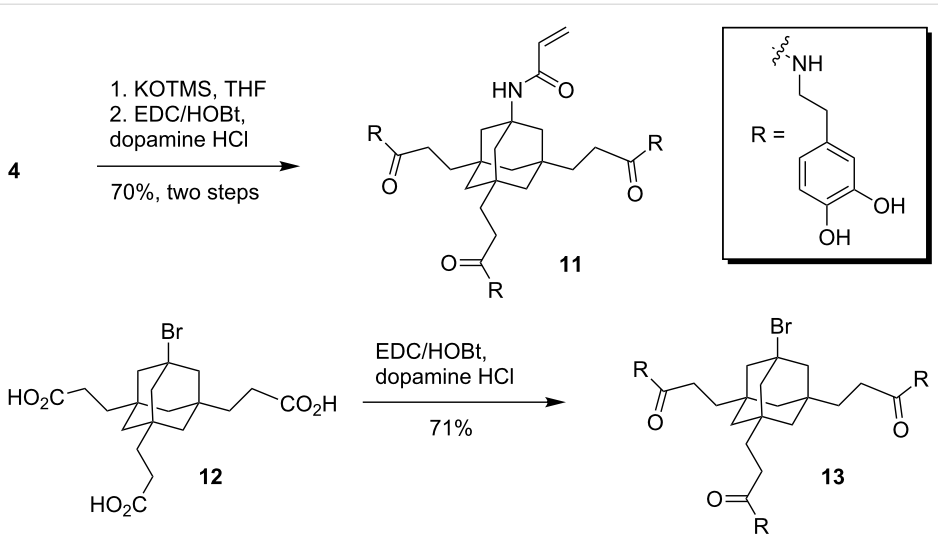

Scheme 2: Synthesis of tripodal catecholate platforms **11** and **13** for surface functionalization.

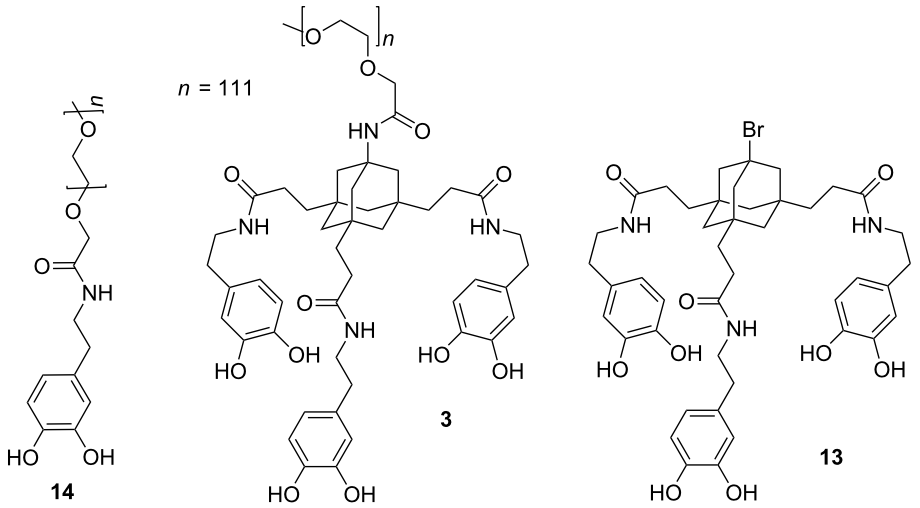

Figure 2: Catecholates for the immobilization on ZnO NPs.

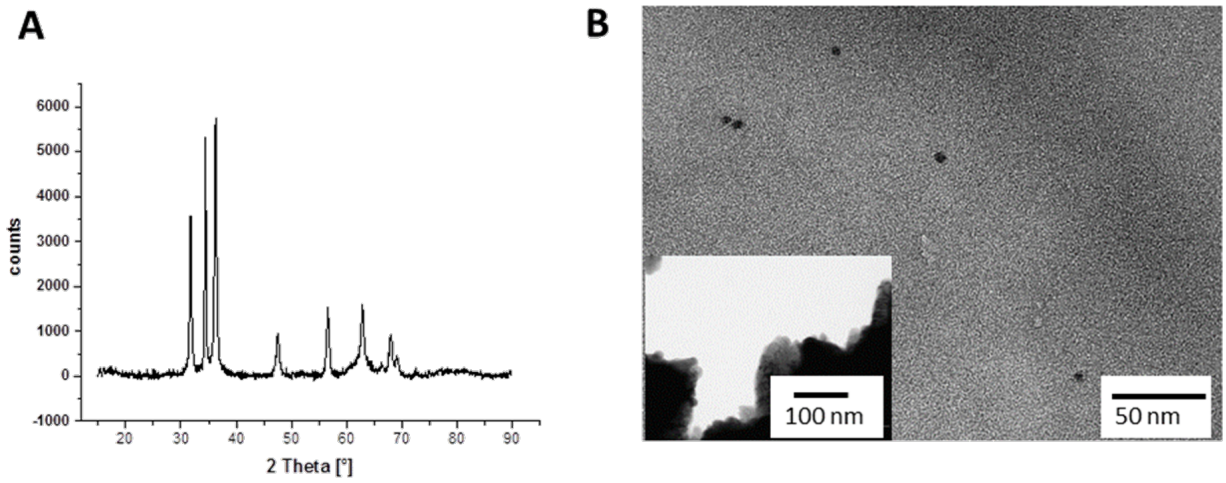

Figure 3: A) XRD pattern of ZnO NPs obtained by the colloidal suspension of $Zn(acac)_2$. B) TEM image of pure ZnO nanoparticles.

at pH 10 [14,31]. Under these conditions, the catechol moieties were reasonably stable and only small amounts (5%) of the corresponding oxidized quinones were detectable by NMR in the solutions after 24 h. The ZnO NPs were treated with the buffered catecholate solutions for 12 h, isolated by centrifugation, washed with a small amount of water (pH 7) and MeOH and freeze-dried before analysis by XRD, IR, HRTEM-EDX and TGA. A reference probe of ZnO NPs was treated the same way, but no catecholate was added to the buffer.

3-Morpholinopropanesulfonate, the ingredient of the MOPS buffer, showed only a weak affinity for ZnO NPs according to the corresponding TGA curve in Figure 4A and EDX (Figure 4C). Sulfonates have been described as ZnO binders before [47,48]. However, the binding affinity of 3-morpholinopropanesulfonate to ZnO NPs is low and most of the ligand is eliminated by washing following the immobilization.

In contrast, TGA indicated a high loading of the particles with both the monomeric PEG-catecholate **14** (48 wt % loading) and the tripodal catecholates **3** (70 wt % loading) and **13** (17 wt % loading). The latter two values are close to the theoretical maximum loading of 63 wt % (for **3**) and 20 wt % (for **13**, note the dramatically lower mass of **13** compared to PEG-conjugates **3** and **14**), which was calculated for an ideal particle of 6 nm diameter and 0.25 nm^2 coverage per catecholate residue [49]. The loading of monomeric PEG-catecholate **14** on ZnO NPs is significantly lower compared to the calculated maximum

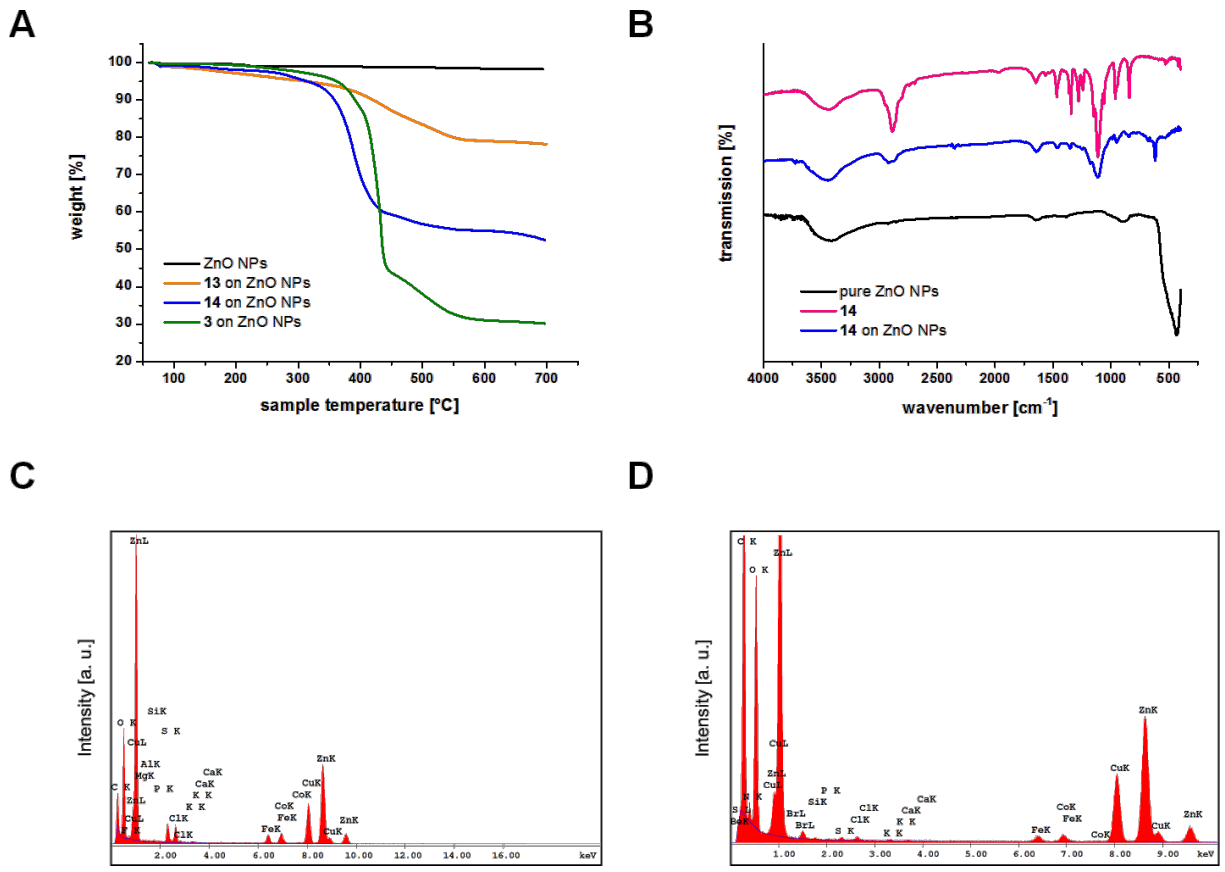

Figure 4: A) TGA data of catecholates **3**, **13** and **14** immobilized on ZnO NPs: pure ZnO NPs treated with MOPS buffer (black line), bromo-triscatecholate **13** on ZnO NPs (after washing with water and MeOH, orange line), monomeric PEG-catecholate **14** on ZnO (after centrifugation, blue line) and tripodal PEG-catecholate **3** on ZnO (after washing with water and MeOH, green line). B) FTIR spectra of pure ZnO NPs (before immobilization, black line), monomeric PEG-catecholate **14** (pink line) and monomeric PEG-catecholate **14** immobilized on ZnO NPs (blue line). C) EDX spectrum of pure ZnO NPs. D) EDX spectrum of bromo-triscatecholate **13** immobilized on ZnO.

loading of 86 wt %. This indicates that a large fraction of **14** is already lost during the first washing procedure, reflecting the reversible binding of monomeric catecholates to metal oxides, as mentioned above. Successful immobilization was also confirmed by IR as showcased for monomeric PEG-catecholate **14** in Figure 4B (for IR spectra of immobilized trimeric catecholates **3** and **13** see Supporting Information File 1).

This effect is increasingly important if the coated particles are handled in aqueous solution. After three successive rounds of washing with water and MeOH, almost all of the monomeric PEG-catecholate **14** is lost from the particles as determined by TGA (Figure 5A) and confirmed qualitatively by comparison of the different intensity of the carbon peaks in the EDX spectra of monomer **14** and trimer **3** on ZnO (Figure 5C and D). In contrast, loading of the tripodal PEG-catecholate **3** is retained at about 70 wt %. The comparably lower loss of catecholate loading confirms the ability of our triscatecholates to form stable layers on ZnO NPs and parallels our previous observations on TiO_2 and stainless steel surfaces [31].

The observed difference in catechol loading has an impact on the stability of the ZnO NPs in water. The TEM images in Figure 6 show the coated particles after three rounds of washing with water and MeOH. Homogenous isolated spherical particles of about 25 nm diameter are observed for tripodal PEG-catecholate **3** (Figure 6C). This compares well to the expected size of 6 nm NPs coated with a 5 kDa PEG [50]. In contrast, the particles initially coated with monomeric PEG-catecholate **14** form larger aggregates (Figure 6A). As expected, particles coated with the hydrophobic tripodal catecholate **13** show the same tendency for aggregation in aqueous solution (Figure 6B).

Conclusion

We report here the synthesis of new tripodal catecholates as valuable multivalent anchor molecules for immobilization on

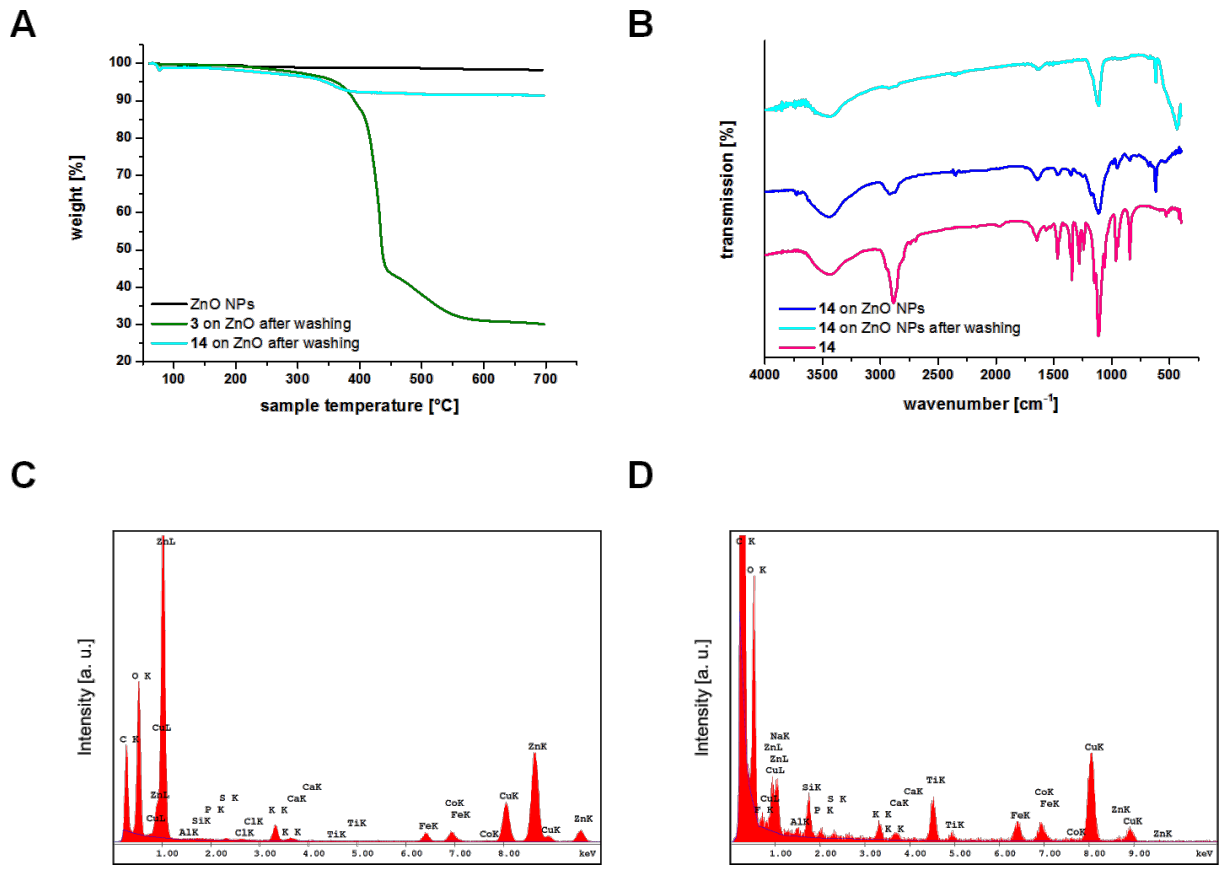

Figure 5: A) TGA data of catecholates **3** and **14** immobilized on ZnO NPs: pure ZnO NPs treated with MOPS buffer (black line), monomeric PEG-catecholate **14** on ZnO after washing with water and MeOH for three times (cyan line) and tripodal PEG-catecholate **3** on ZnO after washing with water and MeOH for three times (green line). B) FTIR spectra of monomeric PEG-catecholate **14** immobilized on ZnO after washing twice with water and MeOH (cyan line), monomeric PEG-catecholate **14** immobilized on ZnO after centrifugation from MOPS buffer (blue line) and monomeric PEG-catecholate **14** (pink line). C) EDX spectrum of monomeric PEG-catecholate immobilized on ZnO NPs after washing with water and MeOH. D) EDX spectrum of tripodal PEG-catecholate immobilized on ZnO NPs after washing with water and MeOH.

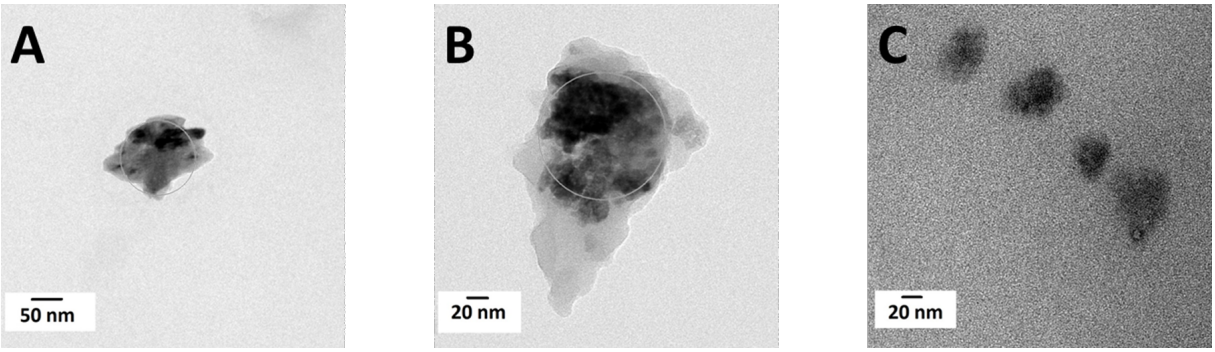

Figure 6: TEM images of ZnO NPs. A) ZnO NPs coated with monomeric PEG-catecholate **14** after washing with water and MeOH for three times. B) ZnO NPs coated with bromo-triscatecholate **13** after washing with water and MeOH for three times. C) ZnO NPs coated with tripodal PEG-catecholate **3** after washing with water and MeOH for three times.

metal surfaces and nanoparticles. These catecholate anchors make use of a biomimetic covalent immobilization concept as found for example in mussel adhesion proteins. Our tripodal catecholate anchors are bifunctional and have been conjugated to various effector molecules such as PEG, a sulfobetaine and an adamantyl group, thus evidencing the feasibility and versatility of the developed approach. The resulting effector-catecholate conjugates are useful for the generation of biopassive

(stealth) surfaces (PEG and sulfobetaine) or switchable hydrophobic/hydrophilic layers (reversible formation of adamantane/cyclodextrin inclusion complexes) on bulk metal surfaces or NPs.

The potential of these conjugates has been demonstrated through the immobilization of the tripodal PEG-catecholate **3** on ZnO NPs and a comparison with the monovalent PEG-catecholate **14**. The results confirmed a high loading of tripodal PEG-catecholate **3** on the particles and the formation of stable catecholate layers in aqueous solution. Immobilization of the monomeric PEG-catecholate **14** was also successful. However, the monomeric catecholate **14** is rapidly eliminated by treatment of the coated particles with water, thus highlighting a much lower stability.

In summary, effector conjugates of tripodal catecholates such as **3** and **13** form stable layers on ZnO NPs even in water. The results reported here confirm our previous studies of tripodal catecholates and their immobilization on TiO_2 and stainless steel.

Experimental

Synthesis

The following compounds were synthesized according to literature procedures: **1** [42], **2** [31], **3** [31], **12** [42] **14** [46].

Thermogravimetric analysis

The TGA data were obtained with a Pyris 1 TGA of Perkin Elmer under Nitrogen gas flow. The samples were heated at 80 °C isothermally for 10 minutes and subsequently heated from 80 °C to 700 °C at a rate of 10 °C per minute. The experiments were carried out at least two times.

Fourier transformation infrared spectroscopy

IR spectra were measured on a Jasco FTIR 4100 device as a disc of anhydrous potassium bromide purchased from Merck.

TEM analysis

For TEM analysis, the functionalized particles were dispersed in MeOH and dropped onto 400-mesh carbon-coated TEM copper grids. The samples were analyzed using a JEOL JEM-1011 microscope, equipped with a LaB6 cathode and operated at 100 kV.

HRTEM and EDX analysis

For high resolution TEM (HRTEM) and energy-dispersive X-ray analysis (EDX), the functionalized particles were dispersed in MeOH and transferred to carbon-coated TEM grids. The samples were analyzed using a Philips CM 300 microscope, operated at 300 kV.

XRD analysis

For XRD analysis, the functionalized particles were dispersed in MeOH, dropped on a standard crystal Si support. Then the solvent was evaporated. The samples were analyzed using a Philips X`Pert PRO MPD diffractometer (Cu Kα radiation, variable entrance slit, Bragg–Brentano geometry, secondary monochromator).

Supporting Information

Supporting Information File 1

Experimental procedures, additional analytical data and NMR spectra.
[http://www.beilstein-journals.org/bjoc/content/supplementary/1860-5397-11-77-S1.pdf]

Acknowledgements

The opportunity to measure TGA at the Pyris 1 TGA of Perkin Elmer in the division of pharmaceutical technology is appreciated. Support by the HMBF and WI-Bank is greatfully acknowledged.

References

1. Pujari, S. P.; Scheres, L.; Marcelis, A. T. M.; Zuilhof, H. *Angew. Chem., Int. Ed.* **2014,** *53,* 6322–6356. doi:10.1002/anie.201306709
2. Sagiv, J. *J. Am. Chem. Soc.* **1980,** *102,* 92–98. doi:10.1021/ja00521a016
3. Flink, S.; van Veggel, F. C. J. M.; Reinhoudt, D. N. *J. Phys. Org. Chem.* **2001,** *14,* 407–415. doi:10.1002/poc.372
4. Love, J. C.; Estroff, L. A.; Kriebel, J. K.; Nuzzo, R. G.; Whitesides, G. M. *Chem. Rev.* **2005,** *105,* 1103–1170. doi:10.1021/cr0300789
5. Tao, Y. T. *J. Am. Chem. Soc.* **1993,** *115,* 4350–4358. doi:10.1021/ja00063a062
6. Hofer, R.; Textor, M.; Spencer, N. D. *Langmuir* **2001,** *17,* 4014–4020. doi:10.1021/la001756e
7. Queffélec, C.; Petit, M.; Janvier, P.; Knight, D. A.; Bujoli, B. *Chem. Rev.* **2012,** *112,* 3777–3807. doi:10.1021/cr2004212
8. Dalsin, J. L.; Hu, B.-H.; Lee, B. P.; Messersmith, P. B. *J. Am. Chem. Soc.* **2003,** *125,* 4253–4258. doi:10.1021/ja0284963
9. Gademann, K.; Kobylinska, J.; Wach, J.-Y.; Woods, T. M. *BioMetals* **2009,** *22,* 595–604. doi:10.1007/s10534-009-9234-3
10. Lee, B. P.; Messersmith, P. B.; Israelachvili, J. N.; Waite, J. H. *Annu. Rev. Mater. Res.* **2011,** *41,* 99–132. doi:10.1146/annurev-matsci-062910-100429
11. Amstad, E.; Gillich, T.; Bilecka, I.; Textor, M.; Reimhult, E. *Nano Lett.* **2009,** *9,* 4042–4048. doi:10.1021/nl902212q
12. Waite, J. H.; Tanzer, M. L. *Science* **1981,** *212,* 1038–1040. doi:10.1126/science.212.4498.1038
13. Gillich, T.; Benetti, E. M.; Rakhmatullina, E.; Konradi, R.; Li, W.; Zhang, A.; Schlüter, A. D.; Textor, M. *J. Am. Chem. Soc.* **2011,** *133,* 10940–10950. doi:10.1021/ja202760x

14. Franzmann, E.; Khalil, F.; Weidmann, C.; Schröder, M.; Rohnke, M.; Janek, J.; Smarsly, B. M.; Maison, W. *Chem. – Eur. J.* **2011,** *17,* 8596–8603. doi:10.1002/chem.201100715
15. Saville, S. L.; Stone, R. C.; Qi, B.; Mefford, O. T. *J. Mater. Chem.* **2012,** *22,* 24909–24917. doi:10.1039/c2jm34902g
16. Morkoç, H.; Özgür, Ü. *Zinc Oxide: Fundamentals, Materials and Device Technology;* Wiley-VCH: Weinheim, 2009.
17. Kumar, S. S.; Venkateswarlu, P.; Rao, V. R.; Rao, G. N. *Int. Nano Lett.* **2013,** *3,* No. 30. doi:10.1186/2228-5326-3-30
18. Özgür, Ü.; Alivov, Ya. I.; Liu, C.; Teke, A.; Reshchikov, M. A.; Doğan, S.; Avrutin, V.; Cho, S.-J.; Morkoç, H. *J. Appl. Phys.* **2005,** *98,* 041301. doi:10.1063/1.1992666
19. Shi, X.; Gu, W.; Li, B.; Chen, N.; Zhao, K.; Xian, Y. *Microchim. Acta* **2014,** *181,* 1–22. doi:10.1007/s00604-013-1069-5
20. de Lacy Costello, B. P. J.; Ewen, R. J.; Ratcliffe, N. M.; Richards, M. *Sens. Actuators, B* **2008,** *134,* 945–952. doi:10.1016/j.snb.2008.06.055
21. Chu, S.; Olmedo, M.; Yang, Z.; Kong, J.; Liu, J. *Appl. Phys. Lett.* **2008,** *93,* 181106. doi:10.1063/1.3012579
22. Shahmoradi, B.; Namratha, K.; Byrappa, K.; Soga, K.; Ananda, S.; Somashekar, R. *Res. Chem. Intermed.* **2011,** *37,* 329–340. doi:10.1007/s11164-011-0255-5
23. Beretta, A.; Sun, Q.; Herman, R. G.; Klier, K. *Ind. Eng. Chem. Res.* **1996,** *35,* 1534–1542. doi:10.1021/ie9505219
24. Wang, Z. L. *Mater. Today* **2004,** *7,* 26–33. doi:10.1016/S1369-7021(04)00286-X
25. Weller, H. *Philos. Trans. R. Soc., A* **2003,** *361,* 229–240. doi:10.1098/rsta.2002.1136
26. Spanhel, L. *J. Sol-Gel Sci. Technol.* **2006,** *39,* 7–24. doi:10.1007/s10971-006-7302-5
27. Ehrentraut, D.; Sato, H.; Kagamitani, Y.; Sato, H.; Yoshikawa, A.; Fukuda, T. *Prog. Cryst. Growth Charact. Mater.* **2006,** *52,* 280–335. doi:10.1016/j.pcrysgrow.2006.09.002
28. Dolcet, P.; Casarin, M.; Maccato, C.; Bovo, L.; Ischia, G.; Gialanella, S.; Mancin, F.; Tondello, E.; Gross, S. *J. Mater. Chem.* **2012,** *22,* 1620–1626. doi:10.1039/C1JM13301B
29. Buha, J.; Djerdj, I.; Niederberger, M. *Cryst. Growth Des.* **2007,** *7,* 113–116. doi:10.1021/cg060623+
30. Famengo, A.; Anantharaman, S.; Ischia, G.; Causin, V.; Natile, M. M.; Maccato, C.; Tondello, E.; Bertagnolli, H.; Gross, S. *Eur. J. Inorg. Chem.* **2009,** 5017–5028. doi:10.1002/ejic.200900506
31. Khalil, F.; Franzmann, E.; Ramcke, J.; Dakischew, O.; Lips, K. S.; Reinhardt, A.; Heisig, P.; Maison, W. *Colloids Surf., B* **2014,** *117,* 185–192. doi:10.1016/j.colsurfb.2014.02.022
32. Jeon, S. I.; Lee, J. H.; Andrade, J. D.; De Gennes, P. G. *J. Colloid Interface Sci.* **1991,** *142,* 149–158. doi:10.1016/0021-9797(91)90043-8
33. Malisova, B.; Tosatti, S.; Textor, M.; Gademann, K.; Zürcher, S. *Langmuir* **2010,** *26,* 4018–4026. doi:10.1021/la903486z
34. Schlenoff, J. B. *Langmuir* **2014,** *30,* 9625–9636. doi:10.1021/la500057j
35. Shao, Q.; Jiang, S. *Adv. Mater.* **2015,** *27,* 15–26. doi:10.1002/adma.201404059
36. Wei, Q.; Krysiak, S.; Achazi, K.; Becherer, T.; Noeske, P.-L. M.; Paulus, F.; Liebe, H.; Grunwald, I.; Dernedde, J.; Hartwig, A.; Hugel, T.; Haag, R. *Colloids Surf., B* **2014,** *122,* 684–692. doi:10.1016/j.colsurfb.2014.08.001
37. Wei, Q.; Becherer, T.; Mutihac, R.-C.; Noeske, P.-L. M.; Paulus, F.; Haag, R.; Grunwald, I. *Biomacromolecules* **2014,** *15,* 3061–3071. doi:10.1021/bm500673u
38. Mrksich, M.; Whitesides, G. M. *Annu. Rev. Biophys. Biomol. Struct.* **1996,** *25,* 55–78. doi:10.1146/annurev.bb.25.060196.000415
39. Wei, Q.; Becherer, T.; Angioletti-Uberti, S.; Dzubiella, J.; Wischke, C.; Neffe, A. T.; Lendlein, A.; Ballauff, M.; Haag, R. *Angew. Chem., Int. Ed.* **2014,** *53,* 8004–8031. doi:10.1002/anie.201400546
40. Pannier, N.; Maison, W. *Eur. J. Org. Chem.* **2008,** 1278–1284. doi:10.1002/ejoc.200701003
41. Nasr, K.; Pannier, N.; Frangioni, J. V.; Maison, W. *J. Org. Chem.* **2008,** *73,* 1056–1060. doi:10.1021/jo702310g
42. Maison, W.; Frangioni, J. V.; Pannier, N. *Org. Lett.* **2004,** *6,* 4567–4569. doi:10.1021/ol048055j
43. Fleck, C.; Franzmann, E.; Claes, D.; Rickert, A.; Maison, W. *Synthesis* **2013,** *45,* 1452–1461. doi:10.1055/s-0033-1338470
44. Yang, W. L.; Fabbri, J. D.; Willey, T. M.; Lee, J. R. I.; Dahl, J. E.; Carlson, R. M. K.; Schreiner, P. R.; Fokin, A. A.; Tkachenko, B. A.; Fokina, N. A.; Meevasana, W.; Mannella, N.; Tanaka, K.; Zhou, X. J.; van Buuren, T.; Kelly, M. A.; Hussain, Z.; Melosh, N. A.; Shen, Z.-X. *Science* **2007,** *316,* 1460–1462. doi:10.1126/science.1141811
45. Dodziuk, H. Molecules with Holes – Cyclodextrins. In *Cyclodextrines and their complexes;* Dodziuk, H., Ed.; Wiley-VCH: Weinheim, 2006; pp 1–30. doi:10.1002/3527608982.ch1
46. Zürcher, S.; Wäckerlin, D.; Bethuel, Y.; Malisova, B.; Textor, M.; Tosatti, S.; Gademann, K. *J. Am. Chem. Soc.* **2006,** *128,* 1064–1065. doi:10.1021/ja056256s
47. Pesika, N. S.; Hu, Z.; Stebe, K. J.; Searson, P. C. *J. Phys. Chem. B* **2002,** *106,* 6985–6990. doi:10.1021/jp0144606
48. Dange, C.; Phan, T. N. T.; André, V.; Rieger, J.; Persello, J.; Foissy, A. *J. Colloid Interface Sci.* **2007,** *315,* 107–115. doi:10.1016/j.jcis.2007.03.068
49. Liu, L.-M.; Li, S.-C.; Cheng, H.; Diebold, U.; Selloni, A. *J. Am. Chem. Soc.* **2011,** *133,* 7816–7823. doi:10.1021/ja200001r
50. Rixman, M. A.; Dean, D.; Ortiz, C. *Langmuir* **2003,** *19,* 9357–9372. doi:10.1021/la034057l

License and Terms

BEILSTEIN JOURNAL OF ORGANIC CHEMISTRY

First principle investigation of the linker length effects on the thermodynamics of divalent pseudorotaxanes

Andreas J. Achazi[1], Doreen Mollenhauer[2] and Beate Paulus[*1]

Full Research Paper

Open Access

Address:
[1]Institut für Chemie und Biochemie, Freie Universität Berlin, Takustr. 3, 14195 Berlin, Germany and [2]Physikalisch-Chemisches Institut, Justus-Liebig-Universität Gießen, Heinrich-Buff-Ring 58, 35392 Gießen, Germany

Email:
Beate Paulus[*] - b.paulus@fu-berlin.de

* Corresponding author

Keywords:
density functional theory (DFT); dispersion correction; Gibbs energy; pseudorotaxanes; solvent effects; COSMO-RS

Beilstein J. Org. Chem. **2015,** *11,* 687–692.
doi:10.3762/bjoc.11.78

Received: 06 March 2015
Accepted: 29 April 2015
Published: 08 May 2015

This article is part of the Thematic Series "Multivalency as a chemical organization and action principle".

Guest Editor: R. Haag

Abstract

The Gibbs energies of association (Gibbs free (binding) energies) for divalent crown-8/ammonium pseudorotaxanes are determined by investigating the influence of different linkers onto the binding. Calculations are performed with density functional theory including dispersion corrections. The translational, rotational and vibrational contributions are taken into account and solvation effects including counter ions are investigated by applying the COSMO-RS method, which is based on a continuum solvation model. The calculated energies agree well with the experimentally determined ones. The shortest investigated linker shows an enhanced binding strength due to electronic effects, namely the dispersion interaction between the linkers from the guest and the host. For the longer linkers this ideal packing is not possible due to steric hindrance.

Introduction

If two or more binding sites of a molecular system are involved in the association process, the interaction energy can be significantly increased compared to the sum of the individual binding energies. This effect is called multivalency [1] and is mainly observed in biochemical systems [2-9]. But the concept of multivalency can be transferred to supramolecular assemblies with suitable building blocks [10-12] including (pseudo)rotaxanes [13-15] as well. One common building block for pseudorotaxanes is the crown/ammonium binding motif. In this motif ammonium can bind on top of small crown ethers, e.g., crown-6, or can pass through larger crown ethers, e.g., crown-8. Jiang et al. [16] have investigated the assembly thermodynamics and kinetics of divalent crown-8/ammonium pseudorotaxanes with different linkers. The shortest linker shows a much larger chelate cooperativity than the longer linkers due to non-innocent linkers that contribute to the binding. To analyze the individual contributions to the binding, we perform first principle calculations of the model system shown in Figure 1, which

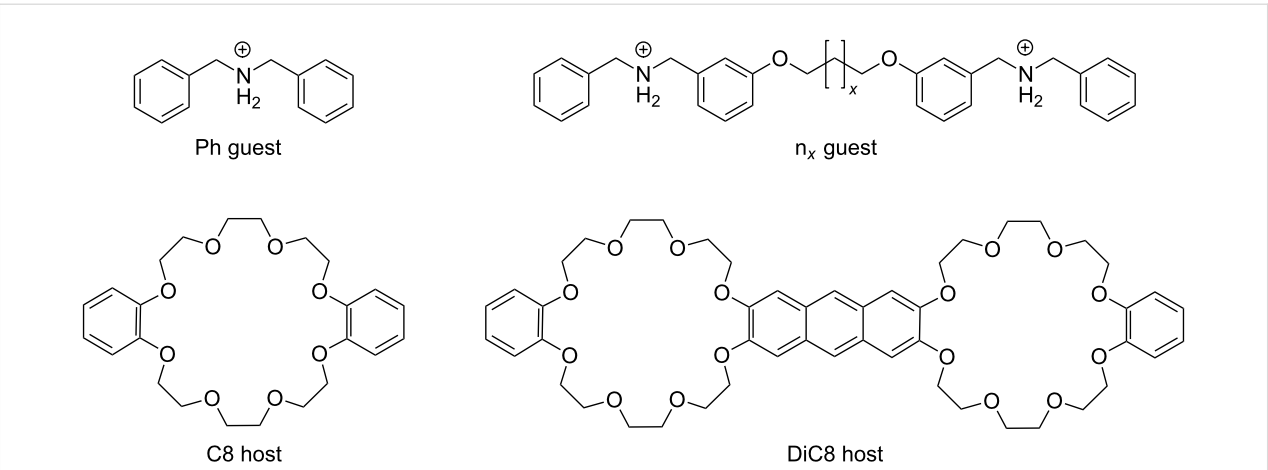

Figure 1: Structures of the mono- and divalent guest and host molecules. The linker in the divalent guest molecule is varied with x = 0, 1 or 2.

is strongly related to the experimentally investigated systems of Jiang et al. [16]. The only difference is that 1,4-diazanaphthalene groups of the host molecule are replaced by phenyl groups and the side chains of the anthracene bridge in the divalent host are neglected. In addition to the electronic contributions, enthalpic and entropic temperature effects as well as solvent effects are included in our simulations in order to compare to experimentally obtained Gibbs energy of association.

Results and Discussion

In order to investigate the cooperativity effects of the binding between divalent host molecules and divalent guest molecules it is important to firstly describe the monovalent binding motif computationally as accurately as possible and to understand the underlying effects that contribute to the binding. Three major terms have to be considered in the evaluation of the Gibbs energy of association ΔG to model the reaction in solution at finite temperature with reasonable accuracy. 1) The electronic association energy ΔE is calculated [17] with the DFT functional TPSS-D3(BJ) [18-20] and the basis set def2-TZVP [21,22]. A comparison with the electronic association energy determined with the DF-LCCSD(T) method [23,24] at the extrapolated basis set limit shows good agreement (see Table 1). Already the DF-LCCSD(T) with the cc-pVTZ basis set deviates only by 5% from the TPSS-D3(BJ) value, whereas the basis set extrapolated value is more or less equivalent to the TPSS-D3(BJ) value (deviation less than 0.3%). This very good agreement is somewhat fortunate, because a basis set extrapolation with DZ and TZ is only accurate to within a few percent. Additionally, the possible errors of the functional and the dispersion correction can also be in the range of 10% for the system under investigation. A more detailed analysis of the accuracy of the TPSS-D3(BJ) functional has been performed for the crown-6/ammonium complex in [25]. Another point to remark is that even for the monovalent system about 36% of the electronic interaction energy is due to the dispersion correction. 2) The finite temperature effects from translation, rotation and vibration are calculated with an approach from Grimme [26], which partially treats the low-lying vibrations as hindered rotations (TPSS-D3(BJ)/def2-SVP [22,27] for vibrations). 3) The influence of the solvent for the association process in solution is derived from the difference of the solvation effects of the product and the reagents, calculated with COSMO-RS [28,29]. For the COSMO-RS (BP_TZVP_C30_1301.ctd parameterization) calculation all structures have been optimized in an ideal conductor [30] and in vacuum with BP86/def-TZVP [31-34]. This procedure yields very good results for the Gibbs energy of association in the case of the crown-6/ammonium complex in comparison with experiment [25]. For the simulations of the crown-8/ammonium systems the same solvent as in the experiment [16] is used, namely a 2.2:1 mixture of chloroform/acetonitrile. The influence of the counter ion PF_6^- onto the Gibbs energy of association is taken into account explicitly.

Table 1: Electronic association energy ΔE for Ph@C8*.[a]

system	method	ΔE (kJ/mol)
Ph@C8*	TPSS/def2-TZVP	−134.9
Ph@C8*	TPSS-D3(BJ)/def2-TZVP	−210.5
Ph@C8*	DF-LCCSD(T)/cbs(DZ-TZ)	−210.0
Ph@C8*	DF-LCCSD(T)/cc-pVDZ	−174.7
Ph@C8*	DF-LCCSD(T)/cc-pVTZ	−199.9

[a]ΔE calculated at TPSS-D3(BJ)/def2-TZVP level of theory is not identical to the one in Table 2, because there another conformer (a slightly more stable one) is used. The Ph@C8* structure has been optimized with TPSS-D3(BJ)/def2-TZVP. For the other methods only single point calculations are done.

The divalent host molecules consist of two crown-8 ethers that are linked by an anthracene bridge. For the divalent guest molecule different flexible linkers, namely $–O(CH_2)_2O–$ (n_0), $–O(CH_2)_3O–$ (n_1) and $–O(CH_2)_4O–$ (n_2) have been investigated both experimentally in [16] and computationally. The results for the electronic association energy ΔE, the Gibbs energy of association ΔG in the gas phase and its enthalpic (ΔH) and entropic ($-T\Delta S$) contributions are given in Table 2. Comparing the electronic association energy for the n_0 guest in the divalent case with the doubled value of the monovalent (Ph@C8) system, an electronic cooperativity effect of 9.7 kJ/mol is discovered. When the linker length is increased, this electronic cooperativity effect is lost, and a lower electronic association energy (by 11.3 kJ/mol) is discovered for the divalent system with the n_1 linker compared to two monovalent systems. For the longer n_2 linker the electronic association energy is even lower by 24.2 kJ/mol for the divalent system compared to two monovalent systems. This is mainly due to the dispersive interaction of the linking unit (two phenyl rings and the linker), which in case of the n_0 guest fits perfectly on top of the anthracene linker of the DiC8 host. The distance between the linker of the host and the linker of the n_0 guest is around 3.7 Å, quite close to an ideal distance for the π–π stacking of two benzene rings. The n_1 and n_2 guest do not perfectly fit with the host (Figure 2). In the n_1-case the linker is folded away from the anthracene bridge, and for the n_2-case one phenyl ring is twisted away due to steric constraints.

Table 2: Electronic association energy ΔE and Gibbs energy of association ΔG in the gas phase at room temperature (T = 298.15 K).[a]

system	ΔE (kJ/mol)	ΔG (kJ/mol)	ΔH (kJ/mol)	$-T\Delta S$ (kJ/mol)
Ph@C8	−215.6	−130.2	−204.8 (+10.9)	+74.6
n_0@DiC8	−440.9	−339.3	−422.6 (+18.3)	+83.3
n_1@DiC8	−419.9	−317.5	−402.6 (+17.3)	+85.2
n_2@DiC8	−407.0	−299.8	−386.8 (+20.2)	+87.0

[a]The enthalpic (ΔH) and entropic ($-T\Delta S$) contribution to ΔG are given. The ΔH contribution resulting from finite temperatures is given in brackets.

The Gibbs energy of association ΔG in the gas phase of the divalent systems (Table 2) result in the same trend as observed for the electronic association energy ΔE, because the enthalpic (ΔH) and entropic ($-T\Delta S$) contributions are similar for n_0@DiC8, n_1@DiC8 and n_2@DiC8.

In Table 3, the Gibbs energies of association in solution with and without counter ion are compared to the calculated electronic association energies, Gibbs energies of association in the gas phase and to the measured experimental values. For the monovalently bound system Ph@C8 the computationally obtained value of ΔG (−12.6 kJ/mol) agrees well with the

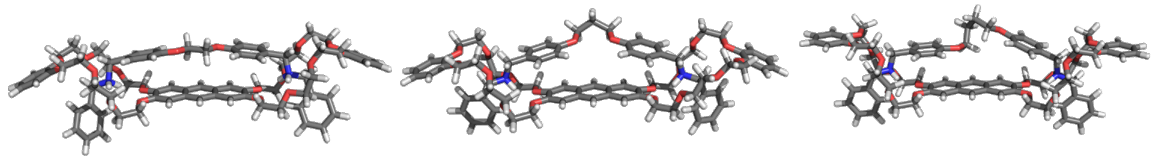

Figure 2: Optimized gas phase structures (TPSS-D3(BJ)/def2-TZVP) of the divalent complexes n_0@DiC8, n_1@DiC8 and n_2@DiC8.

Table 3: Gibbs energy of association ΔG in solution.[a]

system	ΔE (kJ/mol)	ΔG gas phase (kJ/mol)	ΔG solution (kJ/mol)	ΔG counter ion (kJ/mol)	ΔG experiment (kJ/mol)
Ph@C8	−215.6	−130.2	−1.1	−12.6	−15.0
n_0@DiC8	−440.9	−339.3	−42.5	−44.3	−25.1
n_1@DiC8	−419.9	−317.5	−24.2	−28.9	−17.4
n_2@DiC8	−407.0	−299.8	−11.5	−15.3	−16.2

[a]Electronic association energy ΔE, Gibbs energy of association ΔG in gas phase and in solution, in the latter case with and without inclusion of the counter ion PF_6^-, and experimentally determined ΔG for monovalent and divalent pseudorotaxanes in a 2.2:1 solvent mixture of chloroform/acetonitrile at room temperature (T = 298.15 K) are presented.

experimentally determined value (−15.0 kJ/mol). The Gibbs energies of association in gas phase and the Gibbs energies of association in solution show similar differences between n_0@DiC8, n_1@DiC8 and n_2@DiC8 as the electronic association energies. Hence, the dependence on the linker length is of electronic origin and not affected by temperature or solvent effects. Including the counter ion in the determination of ΔG has a much weaker effect in the divalent case compared to the monovalent one, because the guest molecule is larger and the positive charge of the amide group can be distributed better over the molecule. For the divalent pseudorotaxanes the absolute agreement between the calculated and the experimentally determined Gibbs energies is not as good as in the case of monovalent binding, but the same trends are observed in the simulations as in experiment. The divalent pseudorotaxane with the n_0 linker shows a significantly stronger binding than the longer molecules.

Additionally, the full double mutant cycle from [16] has been calculated (Figure 3 and Table 4). The Gibbs energy of association ΔG in case of Ph@DiC8 and n_0@2C8 is in good agreement with the experimental data. For 2Ph@DiC8 and n_0@C8 the deviation is larger just as for the divalent systems in Table 3. This deviation strongly affects the calculated equilibrium constants K, because ΔG is included exponentially in K. Therefore only a qualitatively discussion of the equilibrium constants is possible. With the determined equilibrium constants K, the effective molarity EM can be calculated [16]:

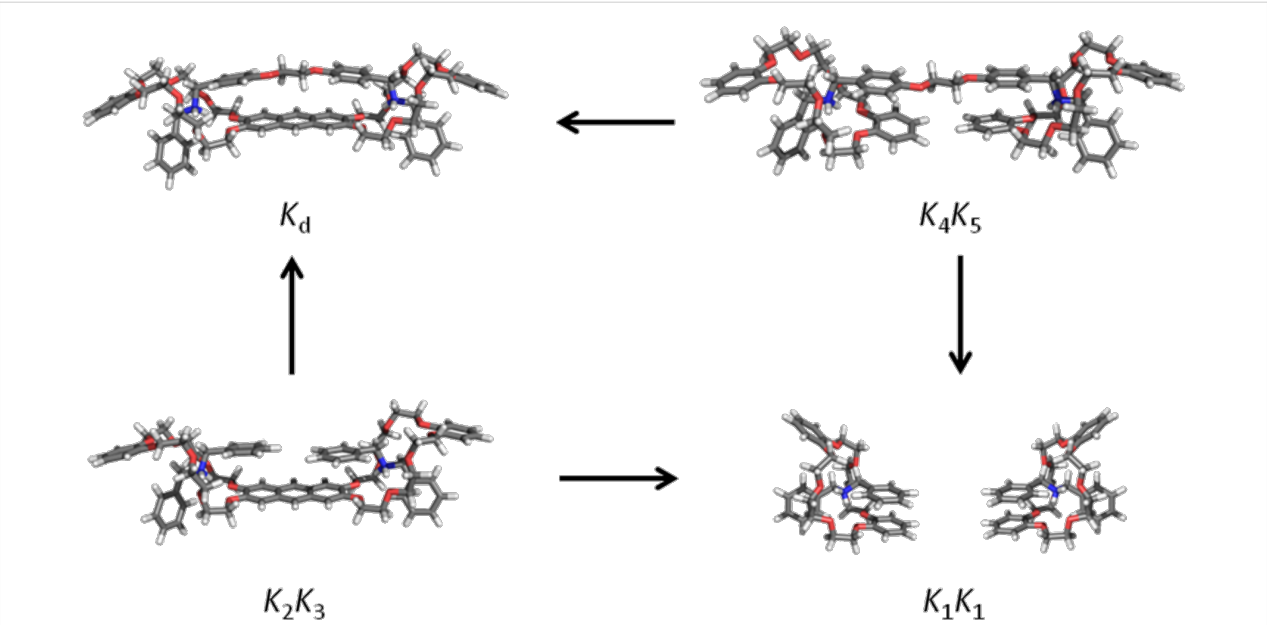

Figure 3: Double mutant cycle for n_0@DiC8. The K variables are declared in Table 4 and are used in Equation 1. Top left: n_0@DiC8, top right: n_0@2C8, bottom left: 2Ph@DiC8 and bottom right: two Ph@C8. The figures show the optimized gas phase structures.

Table 4: Gibbs energy of association ΔG in solution (2.2:1 chloroform/acetonitrile, 298.15 K) and equilibrium constant K for the systems from the double mutant cycle.[a]

system	ΔG counter ion (kJ/mol)	K ($mol^{-1}\cdot L^{-1}$)	#K	ΔG experimental (kJ/mol)	K experimental ($mol^{-1}\cdot L^{-1}$)
Ph@C8	−12.6	161.2	K_1	−15.0	420
Ph@DiC8	−16.2	677.8	K_2	−16.4	735
2Ph@DiC8	−5.11	7.9	K_3	−12.3	145
n_0@C8	+1.4	0.6	K_4	−16.3	714
n_0@2C8	−13.8	261.6	K_5	−13.3	220
n_0@DiC8	−44.3	57679927.3	K_d	−25.1	25000
n_1@DiC8	−28.9	115627.5	K_d	−17.4	1100
n_2@DiC8	−15.3	479.1	K_d	−16.2	700

[a]The effects of the counter ion PF_6^- are included in the calculation. #K declares the equilibrium constant K with regard to Equation 1 and Figure 3.

$$\mathrm{EM} = \frac{K_d K_1^2}{2K_2K_3K_4K_5}, \quad (1)$$

$$K = e^{\frac{-\Delta G}{RT}}. \quad (2)$$

According to Hunter and Anderson [35] EM·K_1 can be used to quantify cooperativity. If EM·$K_1 \approx 1$, the system shows no or small cooperativity, if EM·$K_1 >> 1$ the systems shows positive cooperativity and for EM·$K_1 << 1$ the opposite occurs. The data for the EM·K_1 values are all based on the double mutant cycle of n_0, because the experimental data are also using only the double mutant cycle of n_0 for n_1 and n_2. The experiment shows that n_0@DiC8 (EM·K_1(exp.) = 55.3) has a highly positive cooperativity while n_1@DiC8 (EM·K_1(exp.) = 2.4) and n_2@DiC8 (EM·K_1(exp.) =1.5) have no significant cooperativity. In contrast to the experiment, the calculations show that n_0@DiC8 (EM·K_1(cal.) = $1.6 \cdot 10^8$), n_1@DiC8 (EM·K_1(cal.) = $3.1 \cdot 10^5$) and n_2@DiC8 (EM·K_1(cal.) = $1.3 \cdot 10^3$) have highly positive cooperativity, but all calculated values are much too high compared to experiment due to the deviations of ΔG for 2Ph@DiC8 and n_0@C8. Despite these errors the calculation shows in agreement to experiment, that n_0@DiC8 has a much higher EM·K_1 value than n_1@DiC8 and n_2@DiC8. So the calculations confirm that the linkers contribute to the binding strength in the divalent pseudorotaxanes and can be called non-innocent as in [16].

Regarding the aforementioned deviations from experiment, the difference in the absolute Gibbs energies of association can be explained by the insufficient modeling of solvent effects. The solvent model assumes a uniform distribution of the two different solvents in the mixture. An explicit treatment of at least some solvent molecules would be desirable but is computationally not feasible at the required quantum mechanical level. A combined molecular mechanics/quantum mechanics treatment could be a solution to this problem in the future. Nevertheless, concerning the difference between ΔG in the gas phase and the experimental value, the solvent model that is used in this study yields a significant part of ΔG, but it cannot resolve details of the solvation effects.

At the end of this discussion it is worth mentioning that the most stable structure of the host molecule changes from gas phase to solution. Both the monovalent and the divalent host have a folded ground state structure the in gas phase (Figure 4). The electronic energy ΔE that is needed for unfolding the monovalent host is 29.7 kJ/mol. This value increases up to 72.3 kJ/mol for fully unfolding the divalent host (52.6 kJ/mol for the first step and 19.6 kJ/mol for the second step). In solution (2.2:1 chloroform/acetonitrile, 298.15 K) the monovalent host is more stable in the unfolded form with ΔG being 8.2 kJ/mol lower than that of the folded form. The divalent host stays in the folded structure, and ΔG is 6.5 kJ/mol lower than that of the unfolded form.

Conclusion

The Gibbs energies of association, including enthalpic and entropic temperature effects, solvent effects and the counter ions, have been determined for the divalent crown-8/ammonium pseudorotaxane with different linkers in the guest molecule. Additionally, a full double mutant cycle has been investigated in the same way. Our results agree with the experimental findings that the shortest investigated linker yields a strongly enhanced binding compared to the monovalent case due to the binding of the guest linker to the host linker. Our first principle calculations show clearly that this enhanced binding is due to electronic effects, namely the dispersion interaction of the two

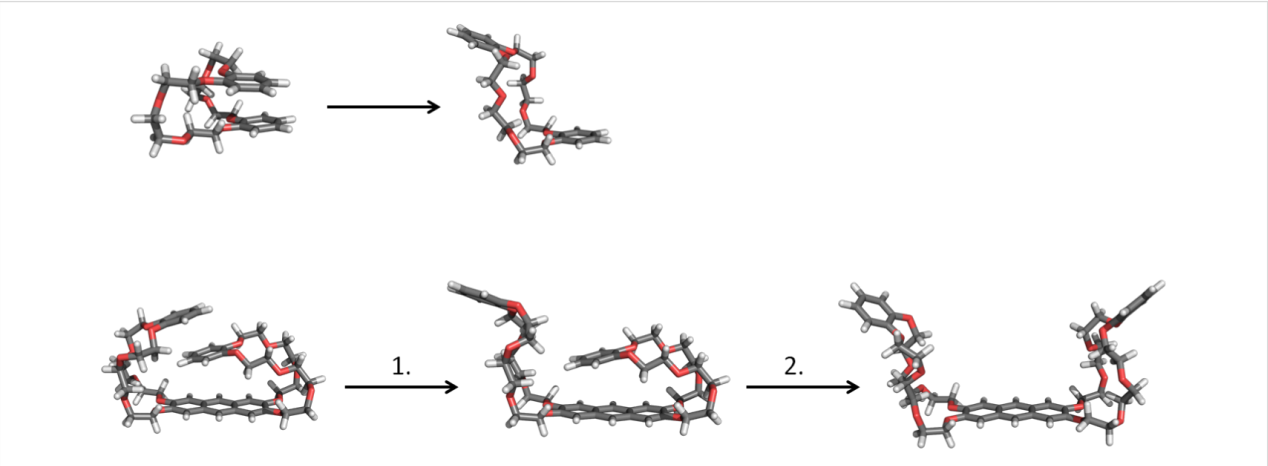

Figure 4: Optimized gas-phase structures for unfolding the monovalent (first row) and divalent (second row) host molecules. For the latter case a two-step process is found.

linkers. For the shortest linker this interaction results in a nearly ideal π–π stacking. For the two longer linkers ideal packing is not possible due to steric hindrance. These investigations proved that besides the primary binding sites in multivalent arrangements the interaction of the linkers can influence the binding process significantly. Therefore the term of non-innocent linkers introduced in [16] is well justified.

Acknowledgements

Support by the German Research Foundation (DFG) through the Collaborative Research Center (CRC) 765 'Multivalency as chemical organization and action principle: new architectures, functions and applications' and the High-Performance Computing facilities of the Freie Universität Berlin (ZEDAT) is acknowledged.

References

1. Fasting, C.; Schalley, C. A.; Weber, M.; Seitz, O.; Hecht, S.; Koksch, B.; Dernedde, J.; Graf, C.; Knapp, E.-W.; Haag, R. *Angew. Chem., Int. Ed.* **2012,** *51,* 10472–10498. doi:10.1002/anie.201201114
2. Mammen, M.; Choi, S. K.; Whitesides, G. M. *Angew. Chem., Int. Ed.* **1998,** *37,* 2754–2794. doi:10.1002/(SICI)1521-3773(19981102)37:20<2754::AID-ANIE2754>3.0.CO;2-3
3. Choi, S.-K. *Synthetic Multivalent Molecules;* Wiley: Hoboken, NJ, USA, 2004. doi:10.1002/0471578908
4. Kitov, P. I.; Sadowska, J. M.; Mulvey, G.; Armstrong, G. D.; Ling, H.; Pannu, N. S.; Read, R. J.; Bundle, D. R. *Nature* **2000,** *403,* 669–672. doi:10.1038/35001095
5. Kitov, P. I.; Bundle, D. R. *J. Am. Chem. Soc.* **2003,** *125,* 16271–16284. doi:10.1021/ja038223n
6. Hartmann, M.; Lindhorst, T. K. *Eur. J. Org. Chem.* **2011,** *2011,* 3583–3609. doi:10.1002/ejoc.201100407
7. Schwefel, D.; Maierhofer, C.; Beck, J. G.; Seeberger, S.; Diederichs, K.; Möller, H. M.; Welte, W.; Wittmann, V. *J. Am. Chem. Soc.* **2010,** *132,* 8704–8719. doi:10.1021/ja101646k
8. Cairo, C. W.; Gestwicki, J. E.; Kanai, M.; Kiessling, L. L. *J. Am. Chem. Soc.* **2002,** *124,* 1615–1619. doi:10.1021/ja016727k
9. Kramer, R. H.; Karpen, J. W. *Nature* **1998,** *395,* 710–713. doi:10.1038/27227
10. Badjić, J. D.; Nelson, A.; Cantrill, S. J.; Turnbull, W. B.; Stoddart, J. F. *Acc. Chem. Res.* **2005,** *38,* 723–732. doi:10.1021/ar040223k
11. Mulder, A.; Huskens, J.; Reinhoudt, D. N. *Org. Biomol. Chem.* **2004,** *2,* 3409–3424. doi:10.1039/b413971b
12. Röckendorf, N.; Lindhorst, T. K. *Top. Curr. Chem.* **2001,** *217,* 201–238. doi:10.1007/3-540-45003-3_6
13. Badjić, J. D.; Balzani, V.; Credi, A.; Lowe, J. N.; Silvi, S.; Stoddart, J. F. *Chem. – Eur. J.* **2004,** *10,* 1926–1935. doi:10.1002/chem.200305687
14. Badjić, J. D.; Balzani, V.; Credi, A.; Silvi, S.; Stoddart, J. F. *Science* **2004,** *303,* 1845–1849. doi:10.1126/science.1094791
15. Badjić, J. D.; Ronconi, C. M.; Stoddart, J. F.; Balzani, V.; Silvi, S.; Credi, A. *J. Am. Chem. Soc.* **2006,** *128,* 1489–1499. doi:10.1021/ja0543954
16. Jiang, W.; Nowosinski, K.; Löw, N. L.; Dzyuba, E. V.; Klautzsch, F.; Schäfer, A.; Huuskonen, J.; Rissanen, K.; Schalley, C. A. *J. Am. Chem. Soc.* **2012,** *134,* 1860–1868. doi:10.1021/ja2107096
17. *TURBOMOLE,* V6.5; TURBOMOLE GmbH: Karlsruhe, Germany, 2013, http://www.turbomole.com.
18. Tao, J.; Perdew, J. P.; Staroverov, V. N.; Scuseria, G. E. *Phys. Rev. Lett.* **2003,** *91,* 146401. doi:10.1103/PhysRevLett.91.146401
19. Grimme, S.; Antony, J.; Ehrlich, S.; Krieg, H. *J. Chem. Phys.* **2010,** *132,* 154104. doi:10.1063/1.3382344
20. Grimme, S.; Ehrlich, S.; Goerigk, L. *J. Comput. Chem.* **2011,** *32,* 1456–1465. doi:10.1002/jcc.21759
21. Weigend, F.; Häser, M.; Patzelt, H.; Ahlrichs, R. *Chem. Phys. Lett.* **1998,** *294,* 143–152. doi:10.1016/S0009-2614(98)00862-8
22. Weigend, F. *Phys. Chem. Chem. Phys.* **2006,** *8,* 1057–1065. doi:10.1039/b515623h
23. Werner, H.-J.; Schütz, M. *J. Chem. Phys.* **2011,** *135,* 144116. doi:10.1063/1.3641642
24. *Molpro,* version 2010.1; 2010, http://www.molpro.net.
25. Achazi, A. J.; v. Krbek, L. K. S.; Schalley, C. A.; Paulus, B. *J. Comput. Chem.* **2015,** in press. doi:10.1002/jcc.23914
26. Grimme, S. *Chem. – Eur. J.* **2012,** *18,* 9955–9964. doi:10.1002/chem.201200497
27. Schäfer, A.; Horn, H.; Ahlrichs, R. *J. Chem. Phys.* **1992,** *97,* 2571–2577. doi:10.1063/1.463096
28. Eckert, F.; Klamt, A. *AIChE J.* **2002,** *48,* 369–385. doi:10.1002/aic.690480220
29. *COSMOtherm,* Version C3.0, Release 13.01; COSMOlogic GmbH & Co. KG: Leverkusen, Germany, 2013.
30. Klamt, A.; Schüürmann, G. D. *J. Chem. Soc., Perkin Trans. 2* **1993,** 799–805. doi:10.1039/P29930000799
31. Becke, A. D. *Phys. Rev. A* **1988,** *38,* 3098–3100. doi:10.1103/PhysRevA.38.3098
32. Perdew, J. P. *Phys. Rev. B* **1986,** *33,* 8822–8824. doi:10.1103/PhysRevB.33.8822
33. Schäfer, A.; Huber, C.; Ahlrichs, R. *J. Chem. Phys.* **1994,** *100,* 5829–5835. doi:10.1063/1.467146
34. Eichkorn, K.; Weigend, F.; Treutler, O.; Ahlrichs, R. *Theor. Chem. Acc.* **1997,** *97,* 119–124. doi:10.1007/s002140050244
35. Hunter, C. A.; Anderson, H. L. *Angew. Chem., Int. Ed.* **2009,** *48,* 7488–7499. doi:10.1002/anie.200902490

License and Terms

BEILSTEIN JOURNAL OF ORGANIC CHEMISTRY

Self-assembly of heteroleptic dinuclear metallosupramolecular kites from multivalent ligands via social self-sorting

Christian Benkhäuser and Arne Lützen*

Full Research Paper

Open Access

Address:
Kekulé-Institute of Organic Chemistry and Biochemistry, University of Bonn, Gerhard-Domagk-Str. 1, D-53121 Bonn, Germany

Email:
Arne Lützen* - arne.luetzen@uni-bonn.de

* Corresponding author

Keywords:
metal complexes; multivalency; self-assembly; self-sorting; supramolecular chemistry; Tröger's base

Beilstein J. Org. Chem. **2015,** *11,* 693–700.
doi:10.3762/bjoc.11.79

Received: 27 February 2015
Accepted: 30 April 2015
Published: 08 May 2015

This article is part of the Thematic Series "Multivalency as a chemical organization and action principle".

Guest Editor: R. Haag

Abstract

A Tröger's base-derived racemic bis(1,10-phenanthroline) ligand (*rac*)-**1** and a bis(2,2'-bipyridine) ligand with a central 1,3-diethynylbenzene unit **2** were synthesized. Each of these ligands acts as a multivalent entity for the binding of two copper(I) ions. Upon coordination to the metal ions these two ligands undergo selective self-assembly into heteroleptic dinuclear metallosupramolecular kites in a high-fidelity social self-sorting manner as evidenced by NMR spectroscopy and mass spectrometry.

Introduction

Self-assembly of defined aggregates from multicomponent mixtures through self-sorting effects has become an important issue in supramolecular chemistry [1-5]. Such self-sorting can either occur in a social self-discriminating or a narcissistic self-recognition manner (Scheme 1). In general, geometrical size and shape complementarity are used to ensure high-fidelity self-sorting.

This strategy has proven to be very successful for the formation of homoleptic complexes through self-recognition [1-4]. However, self-assembly processes of metallosupramolecular aggregates that integrate more than one type of bridging ligand and/or one type of metal ion into an assembly are even more attractive since they allow access to much more complex supramolecular architectures than homoleptic systems do. Unfortunately, the selective formation of heteroleptic complexes from a mixture of different multivalent ligands bridging two or more metal ions is more challenging and there is only a limited number of reliable protocols available yet [6,7]. These comprise (i) topological control pioneered by J. P. Sauvage [8], (ii) steric control as first established by M. Fujita [9] and P. J. Stang [10] using pyridine and lutidine-based ligands or in M. Schmittel's HETPHEN [11], HETTAP [12], and HETPYP concepts [13], (iii) metal coordination specifics as pioneered by J.-M. Lehn with metal centers that prefer five-fold coordination [14], or (iv) charge-separation effects as utilized by P. J. Stang [15].

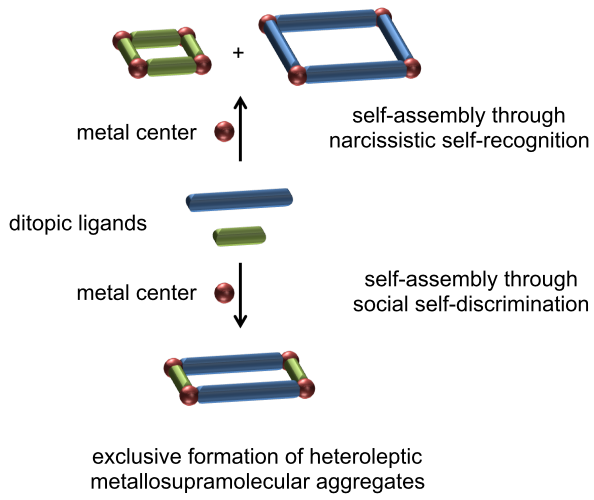

Scheme 1: Schematic representation of self-sorting effects in metallosupramolecular self-assembly processes.

As part of our ongoing efforts to develop general guidelines for the (diastereo)selective self-assembly of metallosupramolecular aggregates from multivalent rigid concave ligand structures through (chiral) self-sorting processes [16-23], we were wondering whether we could yet establish another approach to achieve the formation of heteroleptic metallosupramolecular assemblies in a social self-sorting manner as outlined in Scheme 2.

The basic idea is to design multivalent ligands that do not show a (high) tendency to form discrete oligonuclear homoleptic aggregates but rather form metallosupramolecular polymeric structures when mixed with suitable metal ions. In such a scenario the formation of discrete heteroleptic aggregates might become very favorable when such ligands are used in a multicomponent mixture as the formation of discrete macrocyclic or cage-like aggregates is usually entropically more favorable as long as one works in a medium concentration range because the maximum occupancy rule [24] is obeyed which open-chain oligomeric or polymeric species do not do.

Results and Discussion

Design and synthesis

Our strategy asks for the design of rigid multivalent ligands that present their metal binding sites in a way that the formation of discrete macrocyclic or cage-like homoleptic metal complexes is (almost) prevented when they are mixed with a suitable transition metal ion. As the metal ions we chose copper(I) ions which prefer a tetrahedral coordination sphere by two chelating ligands with N-donor centers such as 2,2'-bipyridines or 1,10-phenanthrolines. Connecting two of these ligands with a concave or V-shaped building block with a rather large bent angle should then prevent the formation of discrete oligonuclear cyclic assemblies due to the fact that the chelating units cannot be arranged in the favorable tetrahedral coordination of the copper ions without putting a considerable amount of steric strain into the aggregate. In the search for ligand structures that fulfill these requirements we came up with ligands **1** and **2** that are depicted in Figure 1.

Ligand **1** has a very rigid twisted V-shaped structure that presents its phenanthroline units in a way that is very unfavorable for the formation of discrete metallomacrocyclic assemblies upon coordination to a metal ion that prefers a tetrahedral coordination by two chelating ligands. The same is true for ligand **2** which adopts a flat conformation to maximize π-conjugation. To form a macrocyclic assembly the bipyridine units in this ligand would have to rotate around the alkynyl linkage by about 90° relative to the central *m*-substituted benzene. This is possible, but not favorable, although the barrier for the rotation around the alkynyl linkage is rather low. In addition the ligand

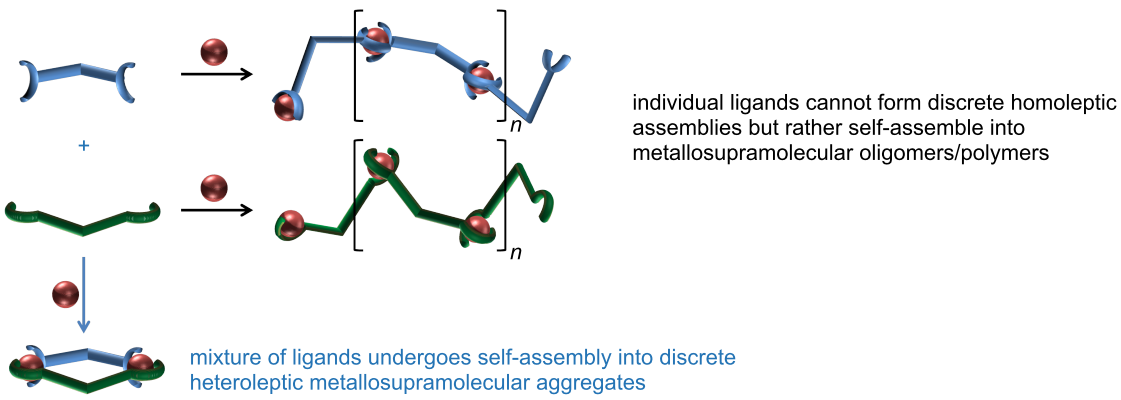

Scheme 2: Schematic representation of our approach to discrete heteroleptic oligonuclear metallosupramolecular aggregates in a social self-sorting manner.

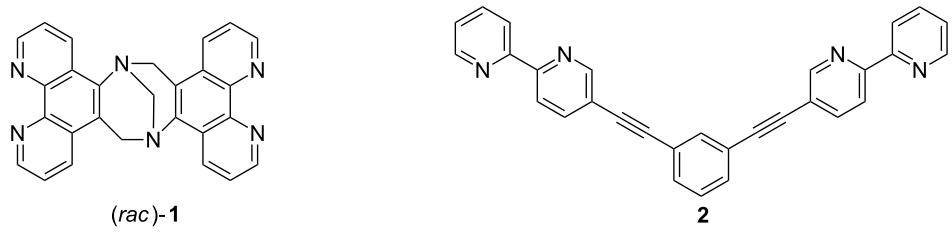

Figure 1: Tröger's base-derived bis(phenanthroline) ligand (*rac*)-**1** and bis(bipyridine) ligand **2**.

would also have to adopt a more strained conformation with considerably bent alkynyl linkages and/or considerably distorted tetrahedral coordination spheres around the metal centers. This makes the two ligands complementary, and hence, prone to the formation of a heteroleptic dinuclear metallosupramolecular assembly with tetrahedral-coordinated metal ions because they are preorganized in a way that they present their metal binding sites in an almost orthogonal fashion and in the right distance.

In fact, (*rac*)-**1** has been synthesized before by E. Yashima from commercially available 5-aminophenanthroline (**3**) [25]. However, when we employed the reaction conditions that K. Wärnmark [26] has developed for the synthesis of other functionalized Tröger's base derivatives we were able to increase the yield of (*rac*)-**1** considerably to 63% (Scheme 3).

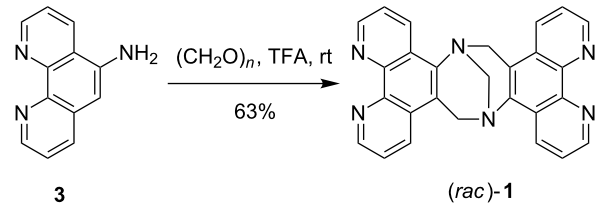

Scheme 3: Synthesis of chiral bis(phenanthroline) ligand (*rac*)-**1** from **3**.

The synthesis of **2** was achieved in six consecutive steps starting from commercially available 2-aminopyridine (**4**) (Scheme 4) following mostly literature-known protocols. The electrophilic iodination of aminopyridine **4** gave iodide **5** in good yield. Compound **5** was then subjected to a Sandmeyer-

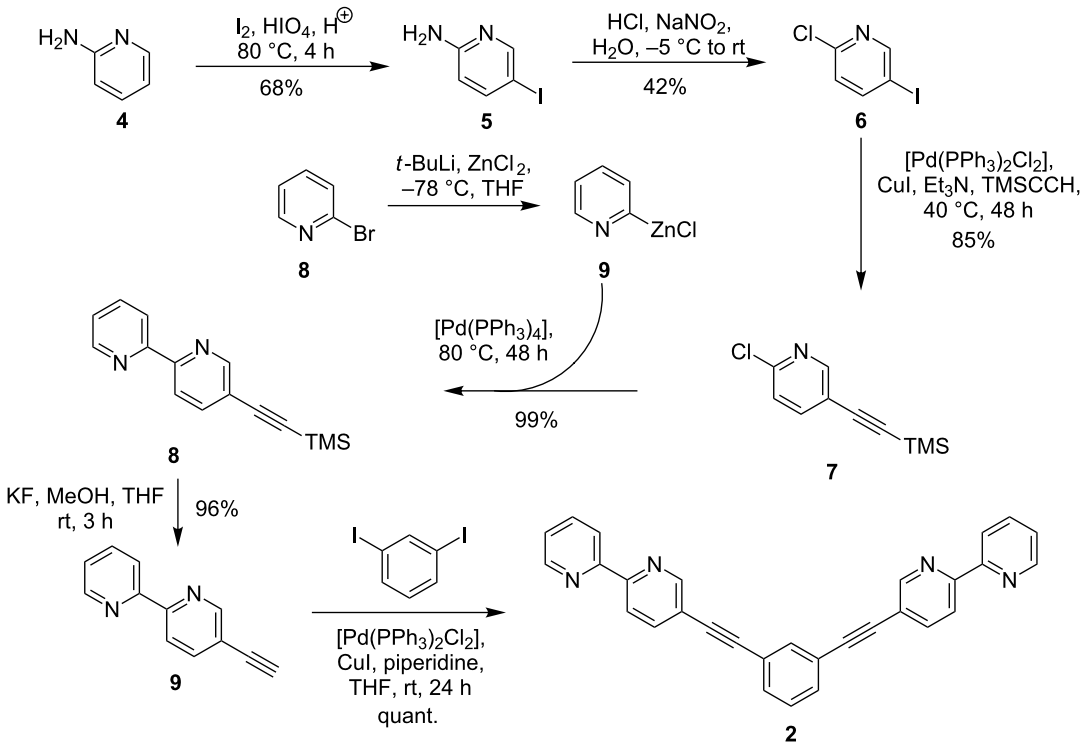

Scheme 4: Synthesis of bis(bipyridine) ligand **2** from 2-aminopyridine (**4**).

like chlorination to **6** which in turn was transformed in a Sonogashira reaction with (trimethylsilyl)acetylene into **7** in a yield of 85% [27]. Alkyne **7** was then subjected to a Negishi reaction with 2-bromopyridine (**8**) derived zinc organyl **9** to give the silyl-protected ethynylated bipyridine **10** in excellent yield of 99% which was subsequently desilylated under standard conditions to give terminal alkyne **11** in 96% yield [28]. Finally, a two-fold Sonogashira reaction with 1,3-diiodobenzene afforded the desired bis(2,2'-bipyridine) ligand **2** in quantitative yield.

Metal coordination

After the successful synthesis we prepared a DMSO solution of copper(I) ions, added it to the ligands (*rac*)-**1** and **2** each in a 1:1 ratio, and compared the resulting spectra to those of the free ligands (Figure 2b and Figure 2d). In both cases the colors of the solutions turned almost immediately to dark red-brown which indicates the formation of copper(I) complexes. As expected, however, NMR spectroscopic (Figure 2a and Figure 2e) and ESI mass spectrometric studies clearly showed that these complexes are oligomeric or polymeric in nature since no discrete smaller aggregates could be detected.

We next mixed the two solutions of the non-defined homoleptic complexes (*rac*)-**1** and **2** and observed a set of sharp and considerably shifted signals in the NMR spectrum. This indicated an almost instantaneous rearrangement of the complexes resulting in the self-assembly of a well-defined discrete heteroleptic dinuclear metallosupramolecular assembly with a kite-like structure in a high-fidelity self-sorting manner (Figure 2c). The composition of the assembly was confirmed by

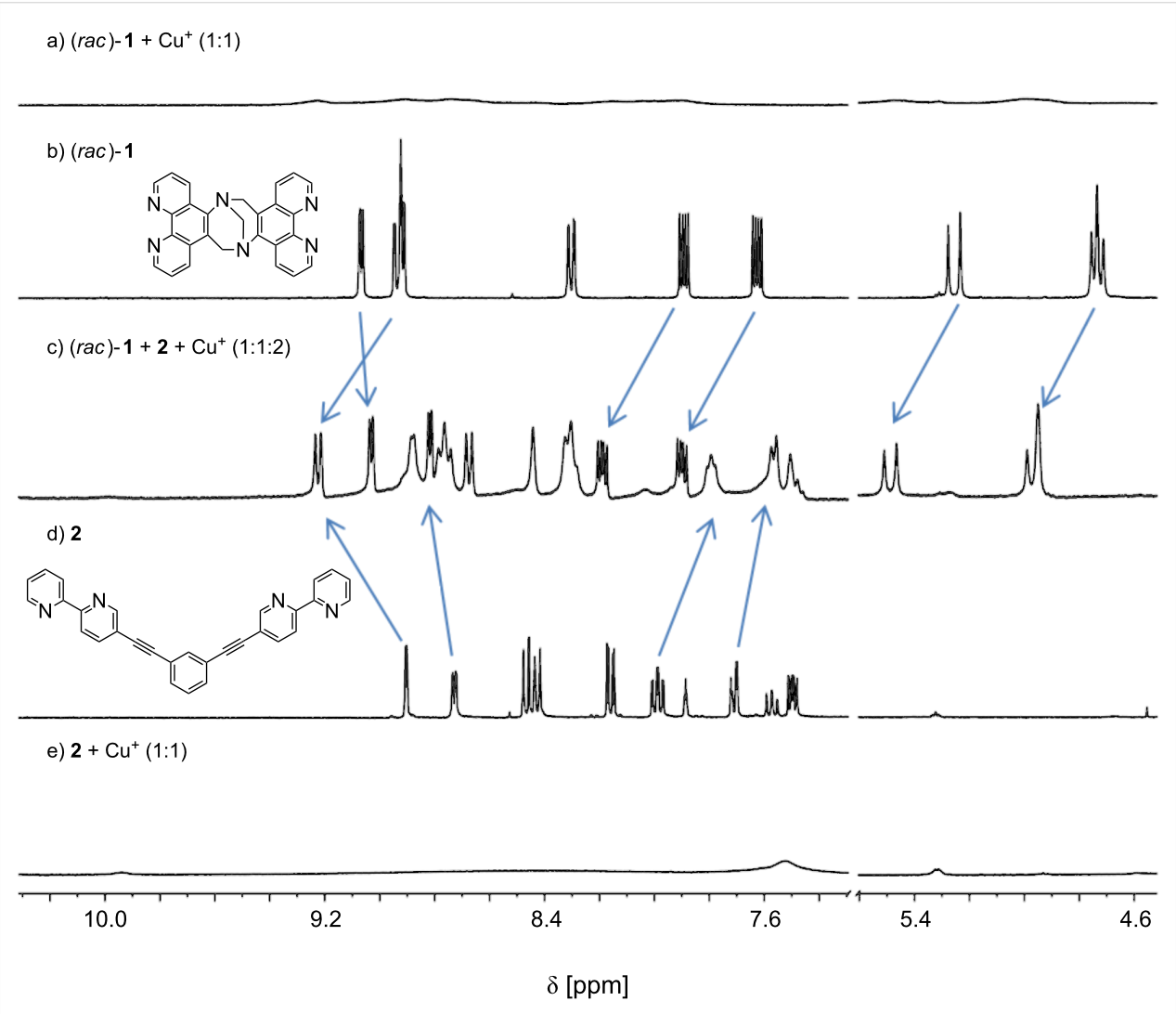

Figure 2: NMR spectra (500.1 MHz in DMSO-d_6 at 295 K) of free ligands b) (*rac*)-**1** and c) **2**; 1:1 mixtures of ligands a) (*rac*)-**1** and e) **2** with Cu^+ salts and c) the resulting NMR of a mixture of these. Arrows indicate the complexation induced shifts of selected signals upon formation of the heteroleptic dinuclear complex.

ESIMS (Figure 3). Of course, the same result was also obtained when two equivalents of the copper(I) salt in DMSO were added to an equimolar mixture of the ligands (*rac*)-**1** and **2**. It should be noted, that the NMR spectrum still shows some broadened signals (e.g., around 9.8, 7.5, and 5.3 ppm) which might indicate that some minor amounts of oligomers/polymers are still existing. However, the intensity of these signals was so low, that we could not assign a diffusion coefficient to them in a 2D-DOSY experiment to corroborate this assumption.

Unfortunately, we were not able to grow suitable single crystals of this complex that could be analyzed by X-ray diffraction. Nevertheless the experimental evidence provided by the NMR and MS investigations clearly indicate the formation of the desired heteroleptic complex $[Cu_2(\mathbf{1})(\mathbf{2})](BF_4)_2$ in racemic form. Scheme 5 summarizes the coordination behavior of the two ligands **1** and **2** and their mixture towards copper(I) ions.

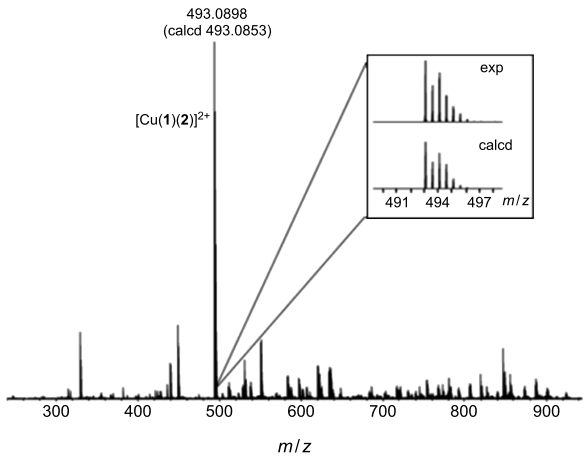

Figure 3: ESI mass spectrum (positive ion mode) of a 1:1:2 mixture of (*rac*)-**1**, **2**, and $CuBF_4$ sprayed from a 10^{-5} mM solution in acetone/DMSO 100:1.

Conclusion

In summary, we have synthesized two concave or V-shaped multivalent ligands − a dissymmetric bis(phenanthroline) ligand (*rac*)-**1** based on the Tröger's base scaffold in its racemic form and a bis(2,2'-bipyridine) ligand **2**. Upon coordination to copper(I) ions none of these ligands alone self-assembles into discrete homoleptic oligonuclear metallosupramolecular aggregates. When mixed in an equimolar ratio, however, these ligands undergo highly selective self-assembly into heteroleptic dinuclear metallosupramolecular $[Cu_2(\mathbf{1})(\mathbf{2})](BF_4)_2$ kites upon

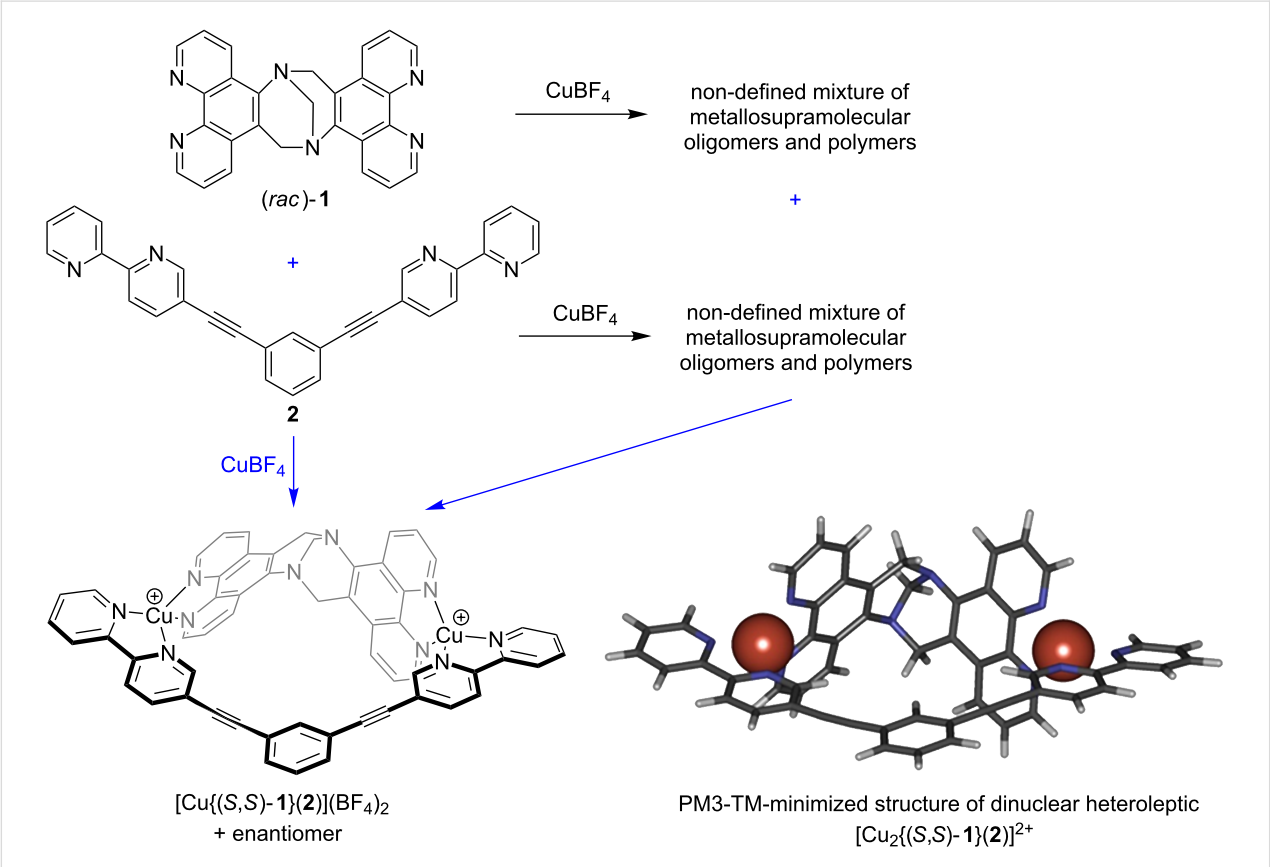

Scheme 5: Summary of the coordination behavior of the two ligands **1** and **2** and their equimolar mixture towards copper(I) ions.

coordination to copper(I) ions in a high-fidelity social self-sorting process. This process is completive according to the classification of M. Schmittel [4] because all of the components of the mixture are used to form the supramolecular aggregates. However, it is not integrative following the classification of self-sorting processes according to C. A. Schalley [5,29,30] because not all of the components present in the mixture form a single type of supramolecular aggregate but they rather form a racemic mixture of chiral aggregates in our case. Hence, the whole process occurs in a social, non-integrative, $2^{4,4}$-fold (3) completive self-discriminating manner according to M. Schmittel's classification [4]. This represents a promising strategy for the rational synthesis of heteroleptic metallosupramolecular aggregates from multivalent ligands that we will explore further in the future.

Experimental

Reactions under inert gas atmosphere were performed under argon using standard Schlenk techniques and oven-dried glassware prior to use. Thin-layer chromatography was performed on aluminum pre-coated TLC plates (silica gel $60F_{254}$) from Merck. Detection was carried out under UV light (254 and 366 nm). Products were purified by column chromatography on silica gel 60 (70–230 mesh) from Merck. The ^{1}H and ^{13}C NMR spectra were recorded on a Bruker Avance 500 spectrometer at 298 K, at 500.1 and 125.8 MHz, or a Bruker AM 400 at 293 K, at 400.1 MHz and 100.6 MHz, respectively. ^{1}H NMR and ^{13}C NMR chemical shifts of the ligands **1** and **2** are reported on the δ scale (ppm) relative to residual non-deuterated solvent (^{1}H) or relative to deuterated solvent (^{13}C), respectively, as the internal standard. Signals were assigned on the basis of ^{1}H, ^{13}C, HMQC, and HMBC NMR experiments. For the numbering of the individual nuclei please see the numbering in the structural formula given for the individual compounds. Unfortunately, we were not able to obtain a sufficiently resolved ^{13}C NMR spectrum of the heteroleptic complex. Mass spectra were recorded with a microOTOF-Q or an Apex IV FT-ICR spectrometer from Bruker. Elemental analyses were carried out with a Heraeus Vario EL. Most solvents were dried, distilled, and stored under argon according to standard procedures. 2-Amino-5-iodopyridine (**5**) [27], 2-chloro-5-iodopyridine (**6**) [27], 2-chloro-5-{(trimethylsilyl)ethynyl}pyridine (**7**) [27], 5-{(trimethylsilyl)ethynyl}-2,2'-bipyridine (**10**) [28], and 5-ethynyl-2,2'-bipyridine (**11**) [28] were prepared according to literature known procedures.

(*rac*)-6*H*,16*H*-5,15-Methanodi-1*N*,10*N*,11*N*,20*N*-phenanthro[5',6'-*b*,5'',6''-*f*][1,5]diazocine ((*rac*)-1): 5-Aminophenanthroline (**3**, 1 g, 5.1 mmol) and paraformaldehyde (323 mg, 10.8 mmol, 2.1 equiv) were mixed in a round-bottomed flask in the dark and cooled with an ice bath. Trifluoroacetic acid (15.2 mL, 133.2 mmol, 26 equiv) was added and the resulting mixture was stirred for 18 h in the dark. After that time the reaction mixture was added drop wise into water (200 mL). After cooling to room temperature the resulting suspension was carefully neutralized with a 6 N aq NaOH solution. The precipitate was collected by filtration, and dried in vacuum. The product was recrystallized from acetone to give the solid product (967 mg, 63%).

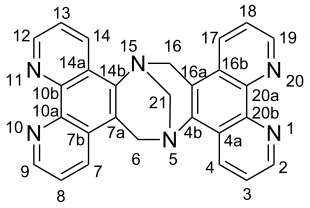

^{1}H NMR (400 MHz, DMSO-d_6) δ 9.07 (dd, $J_{8,9}$ and $J_{18,19}$ = 4.3 Hz, $J_{7,9}$ and $J_{17,19}$ = 1.7 Hz, 2H, H-9, H-19), 8.94 (dd, $J_{7,8}$ and $J_{17,18}$ = 8.3 Hz, $J_{7,9}$ and $J_{17,19}$ = 1.7 Hz, 2H, H-7, H-17), 8.92 (dd, $J_{2,3}$ and $J_{12,13}$ = 4.5 Hz, $J_{2,4}$ and $J_{12,14}$ = 1.6 Hz, 2H, H-2, H-12), 8.30 (dd, $J_{3,4}$ and $J_{13,14}$ = 8.5 Hz, $J_{2,4}$ and $J_{12,14}$ = 1.6 Hz, 2H, H-4, H-14), 7.89 (dd, $J_{7,8}$ and $J_{17,18}$ = 8.3 Hz, $J_{8,9}$ and $J_{18,19}$ = 4.3 Hz, 2H, H-8, H-18), 7.63 (dd, $J_{2,3}$ and $J_{12,13}$ = 4.5 Hz, $J_{3,4}$ and $J_{13,14}$ = 8.5 Hz, 2H, H-3, H-13), 5.26 (d, $J_{6exo,6endo}$ and $J_{16exo,16endo}$ = −17.6 Hz, 2H, H-6_{exo}, H-16_{exo}), 4.74 (s, 2H, H-21), 4.73 (d, $J_{6exo,6endo}$ and $J_{16exo,16endo}$ = −17.6 Hz, 2H, H-6_{endo}, H-16_{endo}) ppm; ^{1}H NMR (400 MHz, $CDCl_3$) δ 9.24 (dd, $J_{8,9}$ and $J_{18,19}$ = 4.4 Hz, $J_{7,9}$ and $J_{17,19}$ = 1.7 Hz, 2H, H-9, H-19), 9.10 (dd, $J_{2,3}$ and $J_{12,13}$ = 4.4 Hz, $J_{2,4}$ and $J_{12,14}$ = 1.7 Hz, 2H, H-2, H-12), 8.94 (dd, $J_{7,8}$ and $J_{17,18}$ = 8.3 Hz, $J_{7,9}$ and $J_{17,19}$ = 1.7 Hz, 2H, H-7, H-17), 8.09 (dd, $J_{3,4}$ and $J_{13,14}$ = 8.5 Hz, $J_{2,4}$ and $J_{12,14}$ = 1.7 Hz, 2H, H-4, H-14), 7.83 (dd, $J_{7,8}$ and $J_{17,18}$ = 8.3 Hz, $J_{8,9}$ and $J_{18,19}$ = 4.3 Hz, 2H, H-8, H-18), 7.58 (dd, $J_{2,3}$ and $J_{12,13}$ = 4.4 Hz, $J_{3,4}$ and $J_{13,14}$ = 8.5 Hz, 2H, H-3, H-13), 5.24 (d, $J_{6exo,6endo}$ and $J_{16exo,16endo}$ = −16.9 Hz, 2H, H-6_{exo}, H-16_{exo}), 4.78 (s, 2H, H-21), 4.73 (d, $J_{6exo,6endo}$ and $J_{16exo,16endo}$ = −16.9 Hz, 2H, H-6_{endo}, H-16_{endo}) ppm; ^{13}C NMR (100 MHz, $CDCl_3$) δ 150.1 (C-9, C-19), 149.1 (C-2, C-12), 146.5, 144.5 (C-10b, C-20b, C-4b, C-14b), 141.3 (C-7, C-17), 131.8 (C-7b, C-16b), 130.1 (C-10a, C-20a), 127.0 (C-7a, C16a), 126.0 (C-3, C-13), 123.6, 123.5 (C-4, C-14, C-8, C-18), 120.0 (C-4a, C-14a), 68.5 (C-21), 53.3 (C-6, C-16); ESIMS (pos.) *m/z*: 449.1 $[M + Na]^+$. These analytical data are in accordance with the literature data [25].

1,3-Bis(2,2'-bipyridin-5-ylethynyl)benzene (2): A two-necked round-bottomed flask was charged with 5-ethynyl-2,2'-bipyridine (**11**, 109 mg, 0.6 mmol, 2 equiv), 1,3-diiodobenzene (100 mg, 0.3 mmol), $[Pd(PPh_3)_2Cl_2]$ (5.32 mg, 2.5 mol %), and copper(I) iodide (1.44 mg, 2.5 mol %) and flushed with argon. Dry THF (15 mL) and dry piperidine (5 mL) were added and

the resulting mixture was stirred at room temperature for 24 h. After that time the precipitate was collected and washed three times with THF to afford the desired solid product in sufficient purity (130 mg, quant).

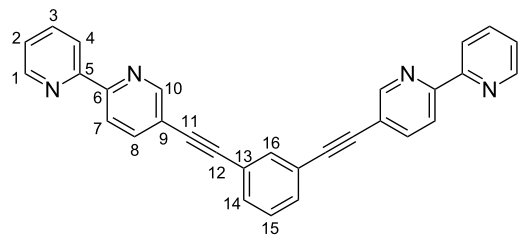

^{1}H NMR (400 MHz, $CDCl_3$) δ 8.83 (dd, $J_{8,10}$ = 2.1 Hz, $J_{7,10}$ = 0.9 Hz, 2H, H-10), 8.70 (ddd, $J_{1,2}$ = 4.8 Hz, $J_{1,3}$ = 1.8 Hz, $J_{1,4}$ = 0.9 Hz, 2H, H-1), 8.48–8.40 (m, 4H, H-4, H-7), 7.95 (dd, $J_{7,8}$ = 8.3 Hz, $J_{8,10}$ = 2.1 Hz, 2H, H-8), 7.84 (ddd, $J_{1,3}$ = 1.8 Hz, $J_{2,3}$ = 7.6 Hz, $J_{3,4}$ = 7.8 Hz, 2H, H-3), 7.80 (dd, $J_{14,16}$ = 1.6 Hz, $J_{15,16}$ = 0.8 Hz, 1H, H-16), 7.57 (dd, $J_{14,15}$ = 7.7 Hz, $J_{14,16}$ = 1.6 Hz, 2H, H-14), 7.40 (dd, $J_{14,15}$ = 7.7 Hz, $J_{15,16}$ = 0.8 Hz, 2H, H-15), 7.33 (ddd, $J_{1,2}$ = 4.8 Hz, $J_{2,3}$ = 7.6 Hz, $J_{2,4}$ = 1.2 Hz, 2H, H-2) ppm; ^{13}C NMR (100 MHz, $CDCl_3$) δ 155.1 (C-6), 154.3 (C-5), 151.9 (C-10), 148.9 (C-1), 139.7 (C-8), 137.8 (C-3), 135.0 (C-16), 132.1 (C-14), 128.9 (C-15), 124.3 (C-2), 123.3 (C-7), 121.8 (C-4), 120.8 (C-13), 120.4 (C-9), 92.8(C-11), 87.3 (C-12); ESIMS (pos.) *m*/*z*: 457.1 $[M + Na]^+$, 435.2 $[M + H]^+$; HRMS–ESI (*m*/*z*): $[M + Na]^+$ calcd for $C_{30}H_{18}N_4Na$, 457.1424; found, 457.1420; Anal. calcd for $C_{30}H_{18}N_4 \cdot H_2O$: C, 79.36; H, 4.46; N, 12.38; found: C, 79.87; H, 4.95; N, 12.48 (%).

Preparation and characterization of the metal complexes: $[Cu(H_3CCN)_4]BF_4$ (6.3 mg, 20 μmol) were dissolved in DMSO-d_6 (1 mL). This solution (500 μL) were added to (*rac*)-**1** (4.26 mg, 10 μmol) and the remaining 500 μL of the solution were added to **2** (4.34 mg, 10 μmol), respectively. The resulting solutions were characterized by NMR. For the ESIMS studies small aliquots of these solutions (10 μL) were taken and diluted with acetone (1 mL). Subsequently the DMSO solutions were mixed and again characterized by NMR. For the ESIMS study a small aliquot of the mixed solution (10 μL) was taken and diluted with acetone (1 mL).

Acknowledgements

We are grateful to the DFG for financial support.

References

1. Gosh, S.; Isaacs, L. Complex self-sorting systems. In *Dynamic Combinatorial Chemistry;* Miller, B. L., Ed.; Wiley-VCH: Weinheim, Germany, 2010; pp 118–154.
2. Osowska, K.; Miljanić, O. Š. *Synlett* **2011,** 1643–1648. doi:10.1055/s-0030-1260815
3. Safont-Sempere, M. M.; Fernández, G.; Würthner, F. *Chem. Rev.* **2011,** *111,* 5784–5814. doi:10.1021/cr100357h
4. Saha, M. L.; Schmittel, M. *Org. Biomol. Chem.* **2012,** *10,* 4651–4684. doi:10.1039/c2ob25098e
5. He, Z.; Jiang, W.; Schalley, C. A. *Chem. Soc. Rev.* **2015,** *44,* 779–789. doi:10.1039/C4CS00305E
6. De, S.; Mahata, K.; Schmittel, M. *Chem. Soc. Rev.* **2010,** *39,* 1555–1575. doi:10.1039/b922293f
7. Saha, M. L.; Neogi, S.; Schmittel, M. *Dalton Trans.* **2014,** *43,* 3815–3834. doi:10.1039/C3DT53570C
8. Dietrich-Buchecker, C. O.; Sauvage, J. P.; Kintzinger, J. P. *Tetrahedron Lett.* **1983,** *24,* 5095–5098. doi:10.1016/S0040-4039(00)94050-4
9. Yoshizawa, M.; Nagao, M.; Kumazawa, K.; Fujita, M. *J. Organomet. Chem.* **2005,** *690,* 5383–5388. doi:10.1016/j.jorganchem.2005.06.022
10. Zhao, L.; Northrop, B. H.; Zheng, Y.-R.; Yang, H.-B.; Lee, H. J.; Lee, Y. M.; Park, J. Y.; Chi, K.-W.; Stang, P. J. *J. Org. Chem.* **2008,** *73,* 6580–6586. doi:10.1021/jo800957r
11. Schmittel, M.; Ganz, A. *Chem. Commun.* **1997,** 999–1000. doi:10.1039/a701509g
12. Schmittel, M.; Kalsani, V.; Kishore, R. S. K.; Cölfen, H.; Bats, J. W. *J. Am. Chem. Soc.* **2005,** *127,* 11544–11545. doi:10.1021/ja0525096
13. Schmittel, M.; He, B.; Fan, J.; Bats, J. W.; Engeser, M.; Schlosser, M.; Deisenroth, H.-J. *Inorg. Chem.* **2009,** *48,* 8192–8200. doi:10.1021/ic900657w
14. Hasenknopf, B.; Lehn, J.-M.; Baum, G.; Fenske, D. *Proc. Natl. Acad. Sci. U. S. A.* **1996,** *93,* 1397–1400. doi:10.1073/pnas.93.4.1397
15. Chi, K.-W.; Addicott, C.; Arif, A. M.; Stang, P. J. *J. Am. Chem. Soc.* **2004,** *126,* 16569–16574. doi:10.1021/ja045542l
16. Rang, A.; Nieger, M.; Engeser, M.; Lützen, A.; Schalley, C. A. *Chem. Commun.* **2008,** 4789–4791. doi:10.1039/b806916f
17. Weilandt, T.; Kiehne, U.; Schnakenburg, G.; Lützen, A. *Chem. Commun.* **2009,** 2320–2322. doi:10.1039/b819335e
18. Dalla Favera, N.; Kiehne, U.; Bunzen, J.; Hytteballe, S.; Lützen, A.; Piguet, C. *Angew. Chem.* **2010,** *122,* 129–132. doi:10.1002/ange.200904614
Angew. Chem., Int. Ed. **2010,** *49,* 125–128. doi:10.1002/anie.200904614
19. Weilandt, T.; Kiehne, U.; Bunzen, J.; Schnakenburg, G.; Lützen, A. *Chem. – Eur. J.* **2010,** *16,* 2418–2426. doi:10.1002/chem.200902993
20. Gütz, C.; Hovorka, R.; Schnakenburg, G.; Lützen, A. *Chem. – Eur. J.* **2013,** *19,* 10890–10894. doi:10.1002/chem.201301499
21. Gütz, C.; Hovorka, R.; Stobe, C.; Struch, N.; Topić, F.; Schnakenburg, G.; Rissanen, K.; Lützen, A. *Eur. J. Org. Chem.* **2014,** 206–216. doi:10.1002/ejoc.201301314
22. Hovorka, R.; Hytteballe, S.; Piehler, T.; Meyer-Eppler, G.; Topić, F.; Rissanen, K.; Engeser, M.; Lützen, A. *Beilstein J. Org. Chem.* **2014,** *10,* 432–441. doi:10.3762/bjoc.10.40
23. Meyer-Eppler, G.; Topić, F.; Schnakenburg, G.; Rissanen, K.; Lützen, A. *Eur. J. Inorg. Chem.* **2014,** 2495–2501. doi:10.1002/ejic.201402057
24. Krämer, R.; Lehn, J.-M.; Marquis-Rigault, A. *Proc. Natl. Acad. Sci. U. S. A.* **1993,** *90,* 5394–5398. doi:10.1073/pnas.90.12.5394
25. Yashima, E.; Akashi, M.; Miyauchi, N. *Chem. Lett.* **1991,** *20,* 1017–1020. doi:10.1246/cl.1991.1017
26. Jensen, J.; Wärnmark, K. *Synthesis* **2001,** 1873–1877. doi:10.1055/s-2001-17525

27. Baxter, P. N. W. *J. Org. Chem.* **2000,** *65,* 1257–1272. doi:10.1021/jo990665n
28. Lützen, A.; Hapke, M. *Eur. J. Org. Chem.* **2002,** 2292–2297. doi:10.1002/1099-0690(200207)2002:14<2292::AID-EJOC2292>3.0.CO;2-D
29. Jiang, W.; Winkler, H. D. F.; Schalley, C. A. *J. Am. Chem. Soc.* **2008,** *130,* 13852–13853. doi:10.1021/ja806009d
30. Jiang, W.; Schalley, C. A. *Proc. Natl. Acad. Sci. U. S. A.* **2009,** *106,* 10425–10429. doi:10.1073/pnas.0809512106

License and Terms

BEILSTEIN JOURNAL OF ORGANIC CHEMISTRY

Exploring monovalent and multivalent peptides for the inhibition of FBP21-tWW

Lisa Maria Henning[‡1], Sumati Bhatia[‡2], Miriam Bertazzon[1], Michaela Marczynke[3], Oliver Seitz[3], Rudolf Volkmer[4,5], Rainer Haag[2] and Christian Freund[*1]

Letter

Open Access

Address:
[1]Institute for Chemistry and Biochemistry, Protein Biochemistry Group, Thielallee 63, Freie Universität Berlin, 14195 Berlin, Germany, [2]Institute for Chemistry and Biochemistry, Freie Universität Berlin, Takustr. 3, 14195 Berlin, Germany, [3]Institute for Chemistry, Humboldt-Universität Berlin, Brook-Taylor-Str. 2, 12489 Berlin, Germany, [4]Leibniz Institut für Molekulare Pharmakologie FMP, Robert-Rössle-Str.10, 13125 Berlin, Germany and [5]Institute of Medical Immunology, Charité-Universitätsmedizin Berlin, Berlin, Germany

Email:
Christian Freund[*] - christian.freund@fu-berlin.de

* Corresponding author ‡ Equal contributors

Keywords:
FBP21-tWW; isothermal titration calorimetry; multivalent polymers; polyglycerol peptide conjugates; proline-rich sequence recognition

Beilstein J. Org. Chem. **2015,** *11,* 701–706.
doi:10.3762/bjoc.11.80

Received: 28 February 2015
Accepted: 29 April 2015
Published: 11 May 2015

This article is part of the Thematic Series "Multivalency as a chemical organization and action principle".

Associate Editor: N. Sewald

Abstract

The coupling of peptides to polyglycerol carriers represents an important route towards the multivalent display of protein ligands. In particular, the inhibition of low affinity intracellular protein–protein interactions can be addressed by this design. We have applied this strategy to develop binding partners for FBP21, a protein which is important for the splicing of pre-mRNA in the nucleus of eukaryotic cells. Firstly, by using phage display the optimized sequence WPPPPRVPR was derived which binds with K_Ds of 80 μM and 150 μM to the individual WW domains and with a K_D of 150 μM to the tandem-WW1–WW2 construct. Secondly, this sequence was coupled to a hyperbranched polyglycerol (hPG) that allowed for the multivalent display on the surface of the dendritic polymer. This novel multifunctional hPG-peptide conjugate displayed a K_D of 17.6 μM which demonstrates that the new carrier provides a venue for the future inhibition of proline-rich sequence recognition by FBP21 during assembly of the spliceosome.

Introduction

Pre-mRNA splicing is an important step in the expression of eukaryotic genes, during which non-coding elements are removed from the pre-mRNA and coding elements are ligated to form a mRNA which can further on be translated into protein. The use of alternative splice sites represents a means to enhance the post-transcriptional diversity of transcripts and ulti-

mately of the proteome of eukaryotic species. Alternative splicing is rare in yeast but a commonality in higher eukaryotes, for which the existence of different splice isoforms is the rule rather than the exception [1]. Aberrant splicing is associated with several diseases [2] and the inhibition of splicing factors has become a recent topic in the field of antitumor drugs [3]. Formin-binding protein 21 (FBP21) has been detected as a component of early spliceosomal complexes and more specifically was shown to interact with proline–arginine-rich peptides in the core splicing protein SmB/B' and the U2-associated protein SF3B4. The interaction of FBP21 with these proteins is conferred by two WW domains that are connected by a short, 8 amino acid long linker sequence. Multivalent recognition of the proline-rich sequences (PRS) by the tandem-WW domains was shown to boost overall affinity, while still keeping the interaction highly dynamic [4,5]. FBP21 was shown to enhance splicing of a reporter construct in living cells [4] while another study suggested that the protein is involved in the alternative splicing of vascular endothelial growth factor (VEGF). In the same study, the natural compound borrelidin was suggested to confer its splicing inhibition function by directly binding to the WW domains of FBP21 [6]. Here, we have taken a different approach to inhibit binding of FBP21-tWW to proline-rich sequences in the spliceosome, where the optimization of a peptide ligand by phage screening and subsequent multivalent display on a dendritic polymer is combined to create higher affinity binders with the potential to be used in cellular studies.

Dendritic polyamines such as polyglycerol amine [7,8], polyethyleneimine [9,10], and polyamidoamine [11] are taken up by the cell and localize to endosomes or endolysosomes, where they lead to proton pumping and concomitant influx due to a proton sponge effect [12], increasing the ionic strength in these organelles. Eventually, this leads to osmotic rupture of the endosome and release of the dendritic polymer into the cytoplasm [13]. These polymeric scaffolds have been explored well for tumor targeting by using polymer-drug conjugates or polyplexes with genes or siRNA [14], but also have the potential to inhibit protein–protein interaction in cells, by displaying multiple ligands for a target protein. The hyperbranched polyglycerol amine (hPG-NH_2) with different degrees of amine functionalization can easily be prepared from hPG-OH with high yields in three steps, as reported in the literature [15]. It can be used for peptide coupling, while it is still maintaining the minimal positive charge on the carrier polymeric backbone which is necessary for cell penetration. The hPG-NH_2 **1** with 70% amine functionalization was chosen to conjugate multiple copies of an optimized targeting peptide, yielding the multivalent hPG-peptide conjugate **2**. The dissociation constant (K_D) of the interaction between hPG-peptide conjugate **2** and FBP21-tWW was measured by isothermal titration calorimetry (ITC) and compared to the K_D of the interaction between the monovalent peptide and FBP21-tWW to analyze if multivalent display in form of the hPG-peptide conjugate **2** increases binding affinity.

Results and Discussion

Phage display

In order to determine an optimal peptide sequence for a FBP21-tWW ligand, we conducted a phage display experiment for each of the two WW domains. Phages used in these experiments carried a randomized X9-peptide fused to phage coat protein VIII [16]. Enrichment factors were calculated after each selection cycle, and reached a plateau after four panning rounds. Phagemids were isolated and sequenced after the third and fourth panning rounds. The sequences for WW1 and WW2 were overlapping to a large extent, showing their similarity in binding preference. This is expected from evolutionary and binding studies carried out earlier [17,18]. The sequences obtained are shown in Figure 1B. In agreement with previous findings for this group of WW domains a polyproline stretch and an arginine residue are present in most sequenced clones. Interestingly, a preference for an aromatic residue N-terminal to the polyproline stretch could also be observed. To define an optimized single monovalent binder, we analyzed the affinities for a selected set of ligands from this panel of sequences with regard to FBP21's WW domains by ITC under the same conditions as were used for the phage display. Four of the six selected peptides showed affinities in the high micromolar range, while the peptide WPPPPRVPR showed higher affinities for both WW domains. K_D values of 155 ± 18 μM and 87.0 ± 3.4 μM were measured for WW1 and WW2, respectively (Figure 1C). The peptide which was found with the highest frequency in the phage display experiment (RPPCGYPLP), did not show any binding to either WW domain in ITC experiments, possibly reflecting the potential of the cysteine residue to form an unspecific complex with glutathione-S-transferase. Similarly, the peptide RPPPPHFPQ could not be confirmed as a binder in the ITC experiments. To further analyze which residues are essential for the interaction, we performed substitution analyses using peptide SPOT arrays (Figure 1D, Supporting Information File 1 Figure S1). The experiment gives some insight into binding specificities. The central role of proline P5 for binding of peptides is evident for both WW domains (Figure 1D, Supporting Information File 1 Figure S1). Proline fulfills two requirements. On the one hand it promotes formation of the PPII helix conformation, on the other hand, it is accommodated well into the hydrophobic groove provided by the individual WW domains [5]. At position P4 proline can be replaced by leucine, a residue well compatible with the PPII helical conformation. Arginine is preferred at position 6 or 9,

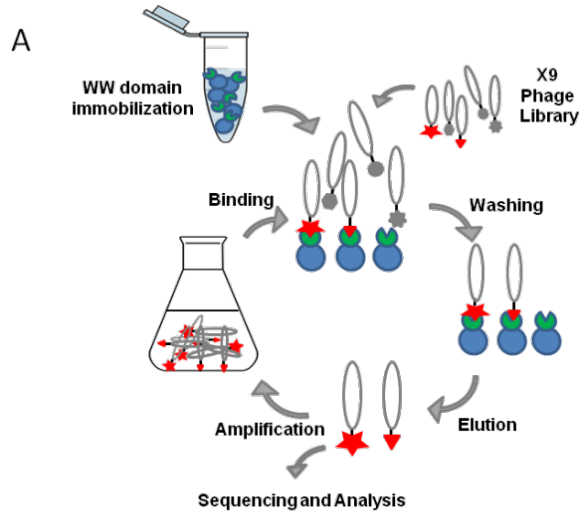

B Obtained sequences:

YPRPAGPRP	5x	RPPCGYPLP	28x
YPRPTNPRP		RPPPLNLHP	3x
WPPPPNTPR	9x	RPPPPRHDP	
YPRPPGPPP	2x	RPPPSTPYP	2x
SPRPPGPPP		WPPPPRVPR	2x
VPPRPPGRP	3x	VMRAPAYPR	
TPRPPLSPR			
RRPPHFPQ	5x		
PPRPLTSHP	2x		
RPPGRPPAL			
RPGPPPGRP			
PRPKTPYPS	4x		
AMRPPLGKP			

C

Peptide	*WW1* K_D (μM)	*WW2* K_D (μM)
YPRPPGPPP	452 ± 45	68.5 ± 6.9
WPPPPRVPR	155 ± 18	87.0 ± 3.4
YPRPTNPRP	490 ± 54	270 ± 24
VMPAYAPR	190 ± 20	334 ± 48

D

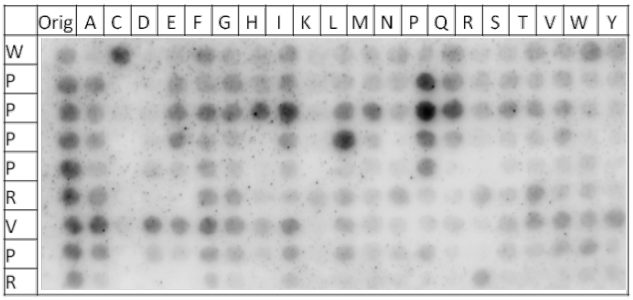

Figure 1: Phage display was used to find an optimized binding partner for FBP21-tWW. A) Schematic representation of the phage display workflow: FBP21-tWW is immobilized and incubated with an X9 phage library. Unbound phages are washed away, then phages expressing a binding peptide are eluted and amplified to create an enriched library, which is then subjected to another round of panning. Phages were sequenced after 3 and 4 rounds of panning. B) Sequences and frequencies of peptides obtained from eluted phages. Shown in red are the peptides which were chosen for further analysis. C) Six peptides representing different groups of binding peptides were synthesized and interactions were analyzed using ITC. Shown are the peptides for which K_D values could be determined. D) A substitution analysis showed that in the binding motif of the peptide WPPPPRVPR, P5 and R9 most strongly contribute to binding of both WW domains. Shown here is the substitution analysis for WW2, the corresponding substitution analysis for WW1 is shown in Figure S1 (Supporting Information File 1).

highlighting the importance of a positive charge in complex formation. Interestingly, WW1 tolerates an exchange for lysine in these positions, while WW2 more strictly requires the arginine. Possibly, the hybrid resonance of the guanidinium group in the arginine is more important in the case of WW2 compared to WW1.

The peptide WPPPPRVPR was further on taken as a basis for exploring the effect of multivalent polymer display. In order not to restrict binding after coupling by shielding of the C-terminal arginine, we decided to attach a small linker to the C-terminus of the derived peptide, yielding the sequence WPPPPRVPRGSG.

Synthesis of hPG-peptide conjugate **2**

hPG-OH (M_n = 9.0 kDa, PDI = 1.86) was prepared according to the published procedure [19] (see Figures S2 and S3 in Supporting Information File 1 for GPC and MALDI–TOF–MS analysis of the hPG-OH core). Seventy percent of all hydroxy groups (≈120 OH groups) on hPG-OH were functionalized with amino groups in a three-step protocol as reported in the literature [19]. The transformation started from the mesylation of the hydroxy groups on the hPG. In the next step, the mesylated polyglycerol was converted to poly(glycerol azide). In the last step, azide functionalities (N_3) were reduced to primary amines ($-NH_2$) via Staudinger reduction to obtain the desired hPG-NH_2 **1** (see Figure S4 in Supporting Information File 1 for GPC analysis of hPG-NH_2 **1**). The appropriate derivative of the targeting peptide, i.e., Ac-WPPPPRVPRGSG-COOH was activated by *N*-hydroxysuccinimidyl ester formation and used for coupling with hPG-NH_2 **1** (M_n = 7.3 kDa, PDI = 1.97) to achieve the hPG-peptide conjugate **2** in good yield as shown in Scheme 1. Only 5.5% of the amine groups on hPG-NH_2 **1** were conjugated with peptide, as determined by ^{1}H NMR analysis,

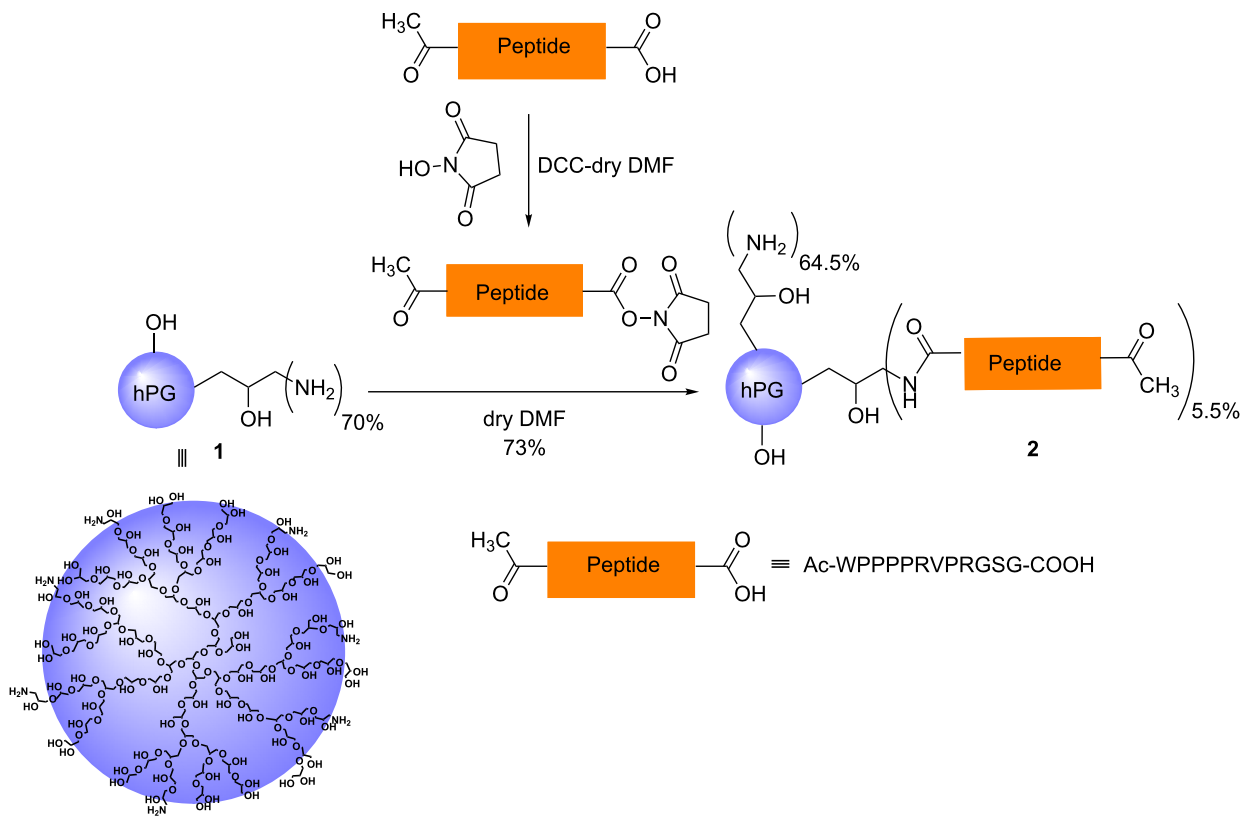

Scheme 1: Schematic representation of the synthesis of hPG-peptide conjugate **2**.

keeping the rest of amine groups free on hPG-peptide conjugate **2** for its cellular penetration properties (see Figures S5 and S6 in Supporting Information File 1 for the ^{1}H NMR spectra of the peptide and hPG-peptide conjugate **2**). The 5.5% peptide conjugation accounts for an average of 7.00 peptide units per polymer.

Analysis of the inhibitory potential of hPG-peptide conjugate 2

ITC measurements were performed to analyze the dissociation constant K_D of the interaction between FBP21-tWW and hPG-peptide conjugate **2** in PBS, pH 7.4 (Figure 2A). To compare the K_D values we also analyzed the binding between FBP21-tWW and the monovalent peptide ligand Ac-WPPP-PRVPRGSG-COOH (Figure 2B). The K_D obtained with the monovalent ligand was 150 ± 6 μM in solution whereas it was 17 ± 0.016 μM for hPG-peptide conjugate **2**, demonstrating an approximately tenfold overall affinity enhancement. However, when considering that ≈7 peptides are bound per nanoparticle, the actual multivalency effect is small.

For both the monovalent ligand and the hPG-conjugate **2**, a stoichiometric factor of approximately one was derived from the fit (1.29 ± 0.0257 for monovalent ligand and tWW, 1.18 ± 0.0221 for tWW and hPG-conjugate 2) suggesting that the observed affinity is mainly conferred by a one-to-one interaction. For the hPG-conjugate this means that most peptides on the hPG particle are not engaged in the interaction with FBP21-tWW. The enthalpy of the interaction is twice as large for the hPG-peptide conjugate as for the monovalent ligand, while the entropy loss upon interaction (−19.5 cal/mol/deg for the interaction with the monovalent ligand and −45.9 cal/mol/deg for the interaction with hPG-peptide conjugate **2**) is significantly lower for the hPG-peptide conjugate, indicating that the hPG scaffold might impose certain geometric constraints on the interaction that are not present in the free peptide.

Conclusion

In summary, we have optimized a peptide ligand for the WW domains of FBP21 and were able to enhance the binding affinity by presenting it on a multivalent dendritic polyglycerol scaffold by a factor of ten in comparison to the monovalent ligand. However, given that on an average seven peptides are presented on the nanoparticle, this overall enhancement is small and should be improved in future by varying the ligand density and size of the hPG-NH_2.

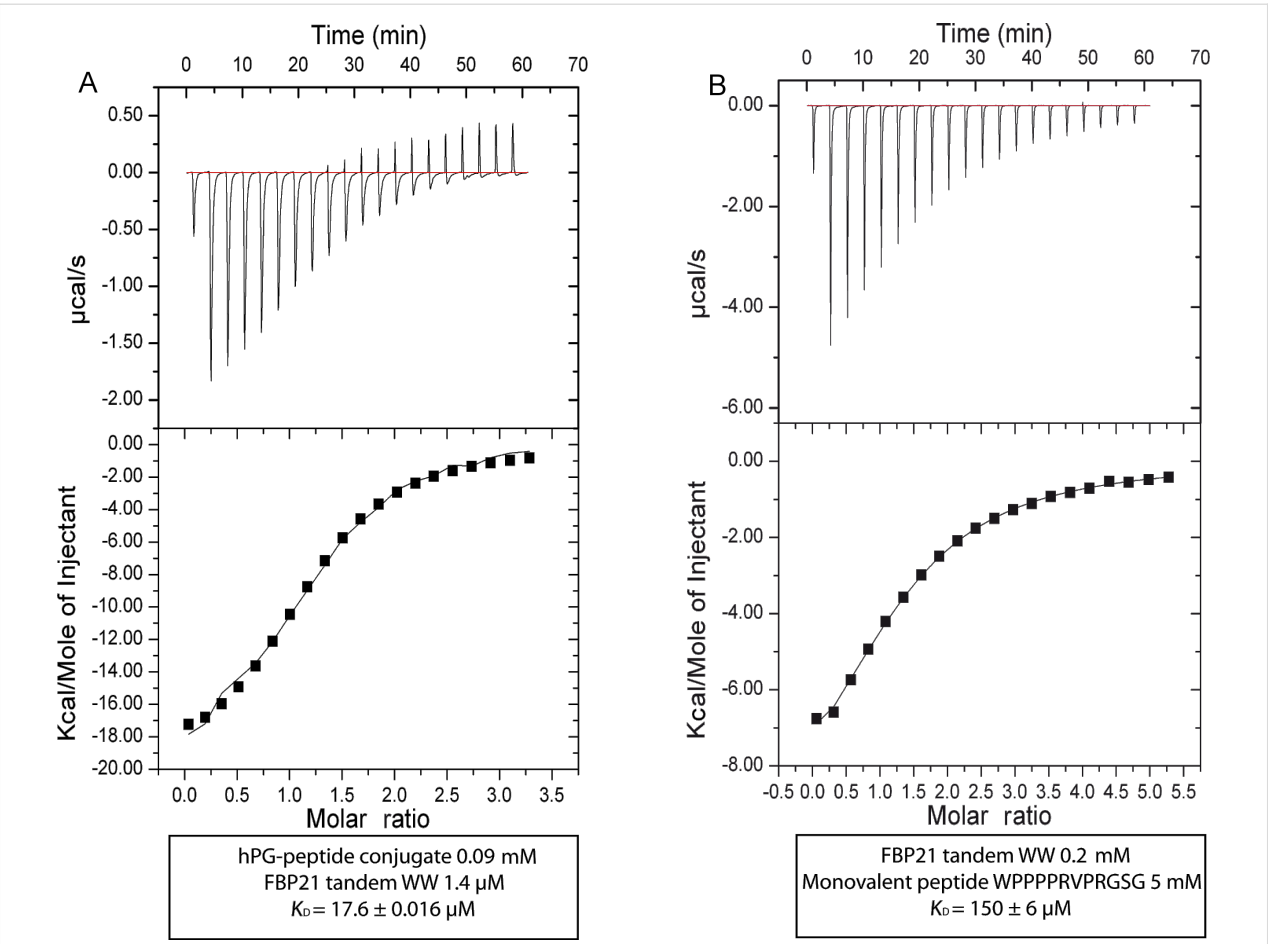

Figure 2: A) ITC measurement with FBP21-tWW and hPG-peptide conjugate **2**, the K_D value is 17.6 ± 0.016 µM. B) ITC measurement with FBP21-tWW and monovalent peptide shows a K_D of 150 ± 6 µM.

Supporting Information

Supporting Information File 1

Details on materials and methods and supplementary figures.
[http://www.beilstein-journals.org/bjoc/content/supplementary/1860-5397-11-80-S1.pdf]

Acknowledgements

Financial support from the German Research Foundation (DFG) through the SFB 765 “Multivalency” and the BMBF is gratefully acknowledged.

References

1. Barbosa-Morais, N. L.; Irimia, M.; Pan, Q.; Xiong, H. Y.; Gueroussov, S.; Lee, L. J.; Slobodeniuc, V.; Kutter, C.; Watt, S.; Çolak, R.; Kim, T.; Misquitta-Ali, C. M.; Wilson, M. D.; Kim, P. M.; Odom, D. T.; Frey, B. J.; Blencowe, B. J. *Science* **2012,** *338,* 1587–1593. doi:10.1126/science.1230612
2. Spitali, P.; Aartsma-Rus, A. *Cell* **2012,** *148,* 1085–1088. doi:10.1016/j.cell.2012.02.014
3. Bonnal, S.; Vigevani, L.; Valcárcel, J. *Nat. Rev. Drug Discovery* **2012,** *11,* 847–859. doi:10.1038/nrd3823
4. Huang, X.; Beullens, M.; Zhang, J.; Zhou, Y.; Nicolaescu, E.; Lesage, B.; Hu, Q.; Wu, J.; Bollen, M.; Shi, Y. *J. Biol. Chem.* **2009,** *284,* 25375–25387. doi:10.1074/jbc.M109.024828
5. Klippel, S.; Wieczorek, M.; Schümann, M.; Krause, E.; Marg, B.; Seidel, T.; Meyer, T.; Knapp, E.-W.; Freund, C. *J. Biol. Chem.* **2011,** *286,* 38478–38487. doi:10.1074/jbc.M111.265710
6. Woolard, J.; Vousden, W.; Moss, S. J.; Krishnakumar, A.; Gammons, M. V. R.; Nowak, D. G.; Dixon, N.; Micklefield, J.; Spannhoff, A.; Bedford, M. T.; Gregory, M. A.; Martin, C. J.; Leadlay, P. F.; Zhang, M. Q.; Harper, S. J.; Bates, D. O.; Wilkinson, B. *Chem. Sci.* **2011,** *2,* 273–278. doi:10.1039/C0SC00297F
7. Haag, R.; Sunder, A.; Stumbé, J.-F. *J. Am. Chem. Soc.* **2000,** *122,* 2954–2955. doi:10.1021/ja994363e
8. Ofek, P.; Fischer, W.; Calderón, M.; Haag, R.; Satchi-Fainaro, R. *FASEB J.* **2010,** *24,* 3122–3134. doi:10.1096/fj.09-149641
9. Akinc, A.; Thomas, M.; Klibanov, A. M.; Langer, R. *J. Gene Med.* **2005,** *7,* 657–663. doi:10.1002/jgm.696

10. Krämer, M.; Stumbé, J.-F.; Grimm, G.; Kaufmann, B.; Krüger, U.; Weber, M.; Haag, R. *ChemBioChem* **2004,** *5,* 1081–1087. doi:10.1002/cbic.200300905
11. Malik, N.; Wiwattanapatapee, R.; Klopsch, R.; Lorenz, K.; Frey, H.; Weener, J. W.; Meijer, E. W.; Paulus, W.; Duncan, R. *J. Controlled Release* **2000,** *65,* 133–148. doi:10.1016/S0168-3659(99)00246-1
12. Mehrabadi, F. S.; Fischer, W.; Haag, R. *Curr. Opin. Solid State Mater. Sci.* **2012,** *16,* 310–322. doi:10.1016/j.cossms.2013.01.003
13. Sonawane, N. D.; Szoka, F. C., Jr.; Verkman, A. S. *J. Biol. Chem.* **2003,** *278,* 44826–44831. doi:10.1074/jbc.M308643200
14. Bhatia, S.; Haag, R. *Dendritic polymers in targeted drug delivery*. In *Targeted Drug Delivery: Concepts and design;* Devarajan, P. V.; Jain, S., Eds.; Springer Verlag: Heidelberg, Germany, 2015; pp 543–569.
15. Roller, S.; Zhou, H.; Haag, R. *Mol. Diversity* **2005,** *9,* 305–316. doi:10.1007/s11030-005-8117-y
16. Felici, F.; Castagnoli, L.; Musacchio, A.; Jappelli, R.; Cesareni, G. *J. Mol. Biol.* **1991,** *222,* 301–310. doi:10.1016/0022-2836(91)90213-P
17. Bedford, M. T.; Reed, R.; Leder, P. *Proc. Natl. Acad. Sci. U. S. A.* **1998,** *95,* 10602–10607. doi:10.1073/pnas.95.18.10602
18. Otte, L.; Wiedemann, U.; Schlegel, B.; Pires, J. R.; Beyermann, M.; Schmieder, P.; Krause, G.; Volkmer-Engert, R.; Schneider-Mergener, J.; Oschkinat, H. *Protein Sci.* **2003,** *12,* 491–500. doi:10.1110/ps.0233203
19. Haag, R.; Tuerk, H.; Mecking, S. Preparation of highly branched polyols based on glycosides useful as an additive in paints and adhesives, additive and crosslinker in polymers, in cosmetics, preparation of nanoparticles and active substance carrier. German patent DE10211664, Oct 2, 2003.

License and Terms

BEILSTEIN JOURNAL OF ORGANIC CHEMISTRY

DNA display of glycoconjugates to emulate oligomeric interactions of glycans

Alexandre Novoa* and Nicolas Winssinger*

Review

Open Access

Address:
Department of Organic Chemistry, NCCR Chemical Biology, University of Geneva 30, quai Ernest Ansermet, 1211 Geneva, Switzerland

Email:
Alexandre Novoa* - alexandre.novoa@unige.ch; Nicolas Winssinger* - nicolas.winssinger@unige.ch

* Corresponding author

Keywords:
glycan; glycoconjugate; DNA display; multivalency; nucleic acid conjugates; oligomeric interaction

Beilstein J. Org. Chem. **2015,** *11,* 707–719.
doi:10.3762/bjoc.11.81

Received: 24 February 2015
Accepted: 06 May 2015
Published: 11 May 2015

This article is part of the Thematic Series "Multivalency as a chemical organization and action principle".

Guest Editor: R. Haag

Abstract

Glycans (carbohydrate portion of glycoproteins and glycolipids) frequently exert their function through oligomeric interactions involving multiple carbohydrate units. In efforts to recapitulate the diverse spatial arrangements of the carbohydrate units, assemblies based on hybridization of nucleic acid conjugates have been used to display simplified ligands with tailored interligand distances and valences. The programmability of the assemblies lends itself to a combinatorial display of multiple ligands. Recent efforts in the synthesis and applications of such conjugates are discussed.

Introduction

Cell surface glycans are important actors in cellular recognition and have been implicated in numerous events such as fertilization, embryonic development, lymphocyte trafficking and cancer metastasis [1-4]. In contrast to many small molecule ligands where a functional output is often the product of a single high-affinity interaction with a target macromolecule, glycans' interactions with glycan-binding proteins (GPB) or lectins are typically low affinity. However high avidity and specificity is achieved through the concerted interactions of multiple ligands with well-defined spatial geometry [5]. The oligomeric nature of these interactions not only provides a mechanism to enhance avidity and specificity but can also trigger a functional output through formation of receptor clusters and membrane deformation [6]. Pathogens frequently use cell surface glycans to gain entry into cells [7]. Accordingly, there is a longstanding interest in tools to manipulate these interactions for structure–function studies and as potential therapeutics [8,9]. The demonstration that the high avidity of oligomeric interactions with cell surface carbohydrates can be outcompeted with a synthetic scaffold that recapitulates the geometry of the oligomeric interactions provided an important precedent [10] and has stimulated intense research in glycomimetics, glycodendrimers, and glycopolymers [11,12]. Over the past decade, there has been a growing interest in using

oligonucleotide hybridization [13-15] to scaffold the assembly of glycans in order to tailor spatial geometry [16]. Attractive features of this hybridization-based supramolecular scaffold are that double strand nucleic acid is fairly rigid with well-defined nucleotide spacing and that the valence and ligand combination can be adjusted through the hybridization instructions (Figure 1). This hybridization can be used to rigidify a nucleic acid strand containing multiple glycans at variable positions, to generate oligomers through half-slide hybridization and to combinatorial pair multiple ligands. The flexibility of the template can be further tuned with single strand stretches that remain flexible. Such assemblies can also be generated in spatially addressable format using DNA microarrays. At the core of this technology is the ability to conjugate biologically relevant glycans or glycomimetics to nucleic acids. Herein, we present an update of the different chemistries used in the glyco-conjugations and the different strategies used to display the glycans with DNA templates.

Review

Glycan–DNA conjugates

An initial solution used in the pioneering work of Kobayashi [17] for nucleic acid–glycan conjugation was the chemoselective reaction of *p*-diazobenzoyl conjugates **1** and **2** with a guanidine nucleotide (G, derivatization at the 8-position) within DNA (Scheme 1) [18]. The conjugation was performed in solution on dsDNA and was used to introduce either lactose or cellobiose moieties (with and without linker). The substitution degree was proportional to the G content of different DNAs and the B-type conformation remained up to a high level of conjugation (25%). Interestingly, the double strand glycosylated DNA showed a higher melting temperature and a stronger enzyme resistance compared to the native DNAs. Most importantly, a superior affinity for the glycan–DNA conjugate (K_A = 10^4–10^5 M^{-1}) compared to glycan alone was observed with RCA_{120} lectin (*Ricinus communis* agglutinin) demonstrating the synergy of interactions amongst the glycan units along the DNA.

As an alternative strategy to gain better control on the composition of DNA–glycan conjugate, the same group reported the synthesis of phosphoramidite derivatized with an acetyl-protected monosaccharide **3** and its incorporation into DNA to access well-defined DNA conjugates **4** (Scheme 2). Cleavage of the acetate groups occurs upon ammonia treatment for DNA cleavage/deprotection [19-21]. Three galactosylated DNA conjugates with different lengths were obtained and mixed with the corresponding half-slide complementary DNA to obtain supramolecular oligomers forming galactoside clusters. The different assemblies were tested for their binding affinity to the RCA_{120} lectin showing a correlation between affinity and the inter-galactose distance thus establishing that DNA display of glycans can be used to tune the optimal spatial arrangement of the ligands in synergic interactions.

This synthetic strategy was further refined by Seeberger and co-workers [22] with the use of commercially available *N*-hydroxysuccinimide (NHS)-carboxy-dT phosphoramidite **5** (Scheme 3). This method allows the sequential introduction of any amine-functionalized glycan during DNA synthesis and was shown to be compatible with more complex glycans such as Lewis X trisaccharide. The capping step in DNA synthesis resulted in acetylation of the glycan thus blocking the glycan's

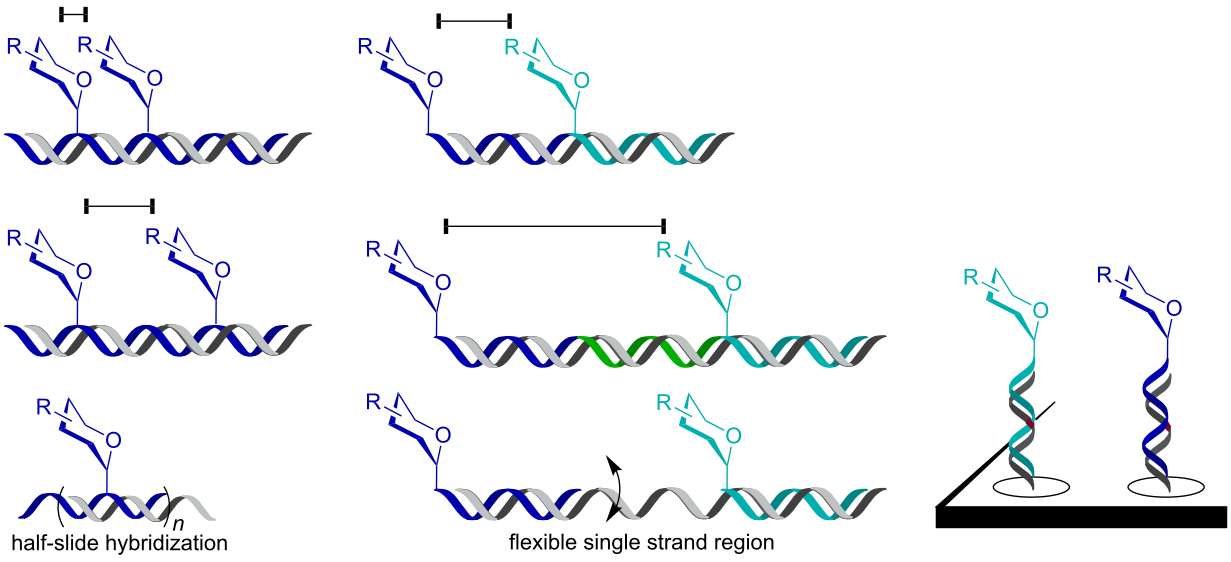

Figure 1: DNA display of glycans.

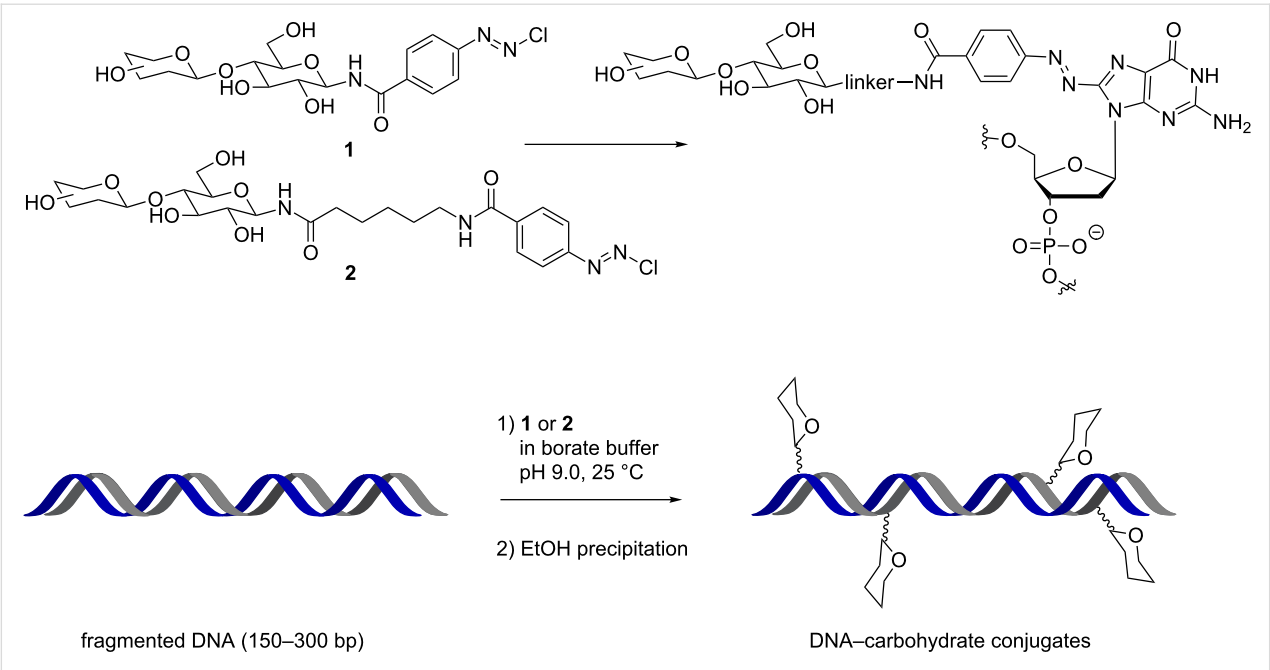

Scheme 1: Synthesis of glycoconjugate DNA by diazo-coupling.

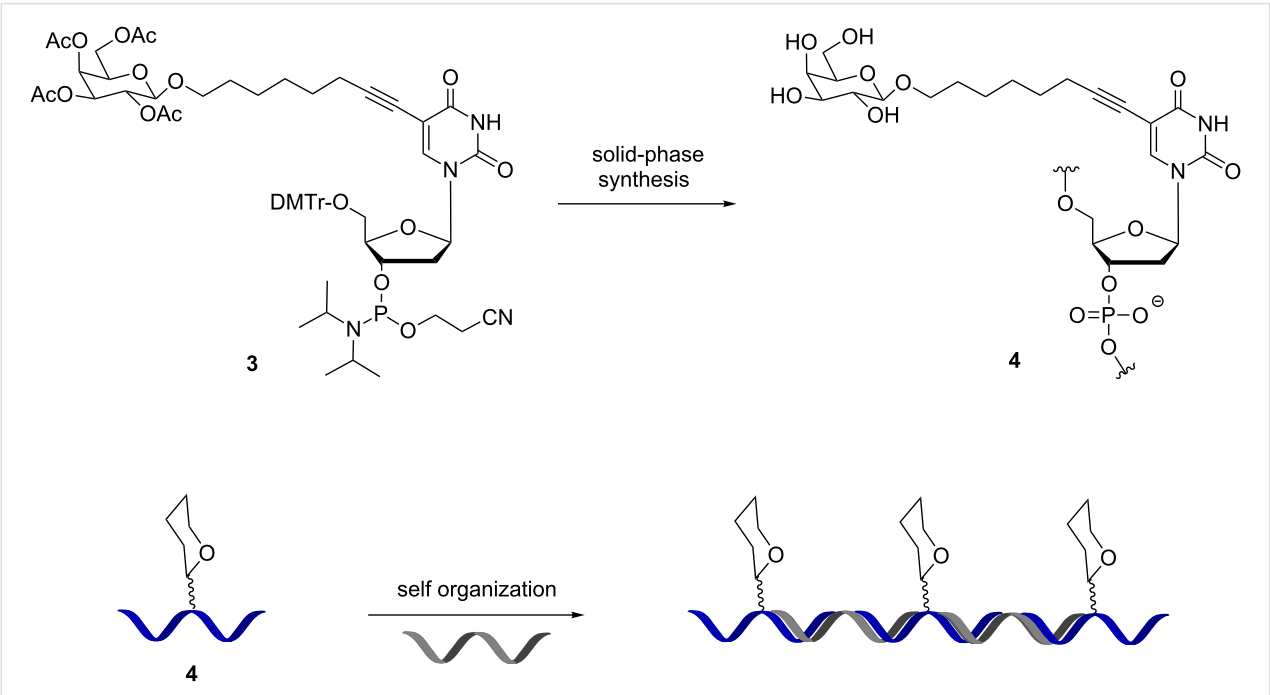

Scheme 2: β-Galactose-modified deoxyuridine phosphoramidite used for solid-phase DNA synthesis and DNA display of glycan.

hydroxy groups. The generality of this method was illustrated with the synthesis of 16 different DNA conjugates containing one or two glycan units. Analysis of glycan-modified duplexes by CD spectroscopy indicated minimal perturbation of the helical structure and thermal stability. Surface plasmon resonance (SPR) affinity measurements with murine C-type lectin receptor (mMGL) showed specific binding only for duplexes containing two or four Lewis-X units.

Alternatively, Ebara and co-workers have shown that glycan–DNA conjugates can be accessed enzymatically using glycan-functionalized desoxyuridine triphosphate as substrate

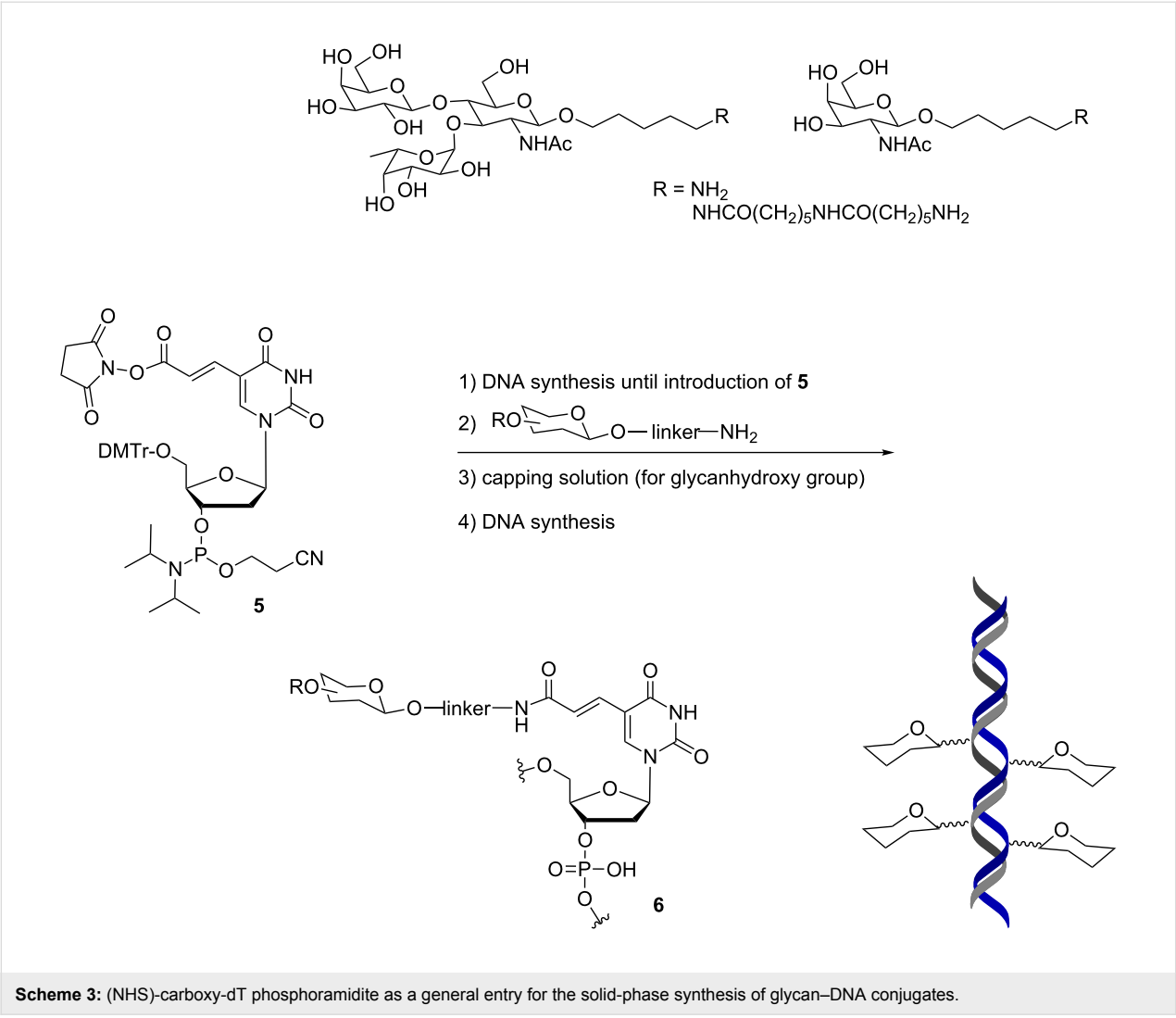

Scheme 3: (NHS)-carboxy-dT phosphoramidite as a general entry for the solid-phase synthesis of glycan–DNA conjugates.

with KOD Dash DNA polymerase [23]. The applicability of the method was illustrated with the incorporation of multiple units of lactose or maltose in different DNA sequences. The same group used this technology to prepare triangular architectures of glycosylated DNA based on a 3-way junction (Figure 2) [24]. The triangular assemblies were built using 1, 2 or 3 glycosylated DNAs, each with 3, 6 or 12 glycan units. As a proof of principle, the assemblies were tested for their affinity to concanavalin A (ConA). This lectin has 4 binding sites for glucosides and mannosides (preferred) spaced by 72 Å. Titration studies showed a clear dependence on the functionalization of each arm in the 3-way junction consistent with a synergistic interaction of each arm with a binding site. However, the number of glycan units (on each arm 3, 6 or 12) had marginal impact on the binding suggesting a saturation of binding site occupancy. For the structure with 6 units of maltose on each arm, a K_D of 1 μM was measured which is 700-fold more potent (40-fold per sugar) than monovalent maltose.

The advent of the copper-catalyzed azide–alkyne cycloaddition (CuAAC) [25,26] has naturally inspired the use of this powerful conjugation method to prepare glycan–DNA conjugates.

Chevolot and co-workers used this method to conjugate glycans at the 3'-end of DNA [27]. The DNA synthesis was initiated with H-phosphonate that was converted to a phosphoramidate alkyne by oxidative amidation using carbon tetrachloride with propargylamine. The microwave-assisted click-conjugation was performed on a solid phase upon completion of the DNA synthesis (Scheme 4).

Lönnberg and co-workers prepared a thymidine modified at the 4'-position with an azidomethyl group to achieve conjugation during solid-phase DNA synthesis or in solution post DNA cleavage [28]. Subsequently, the same group reported a method to introduce two different glycans sequentially on the DNA

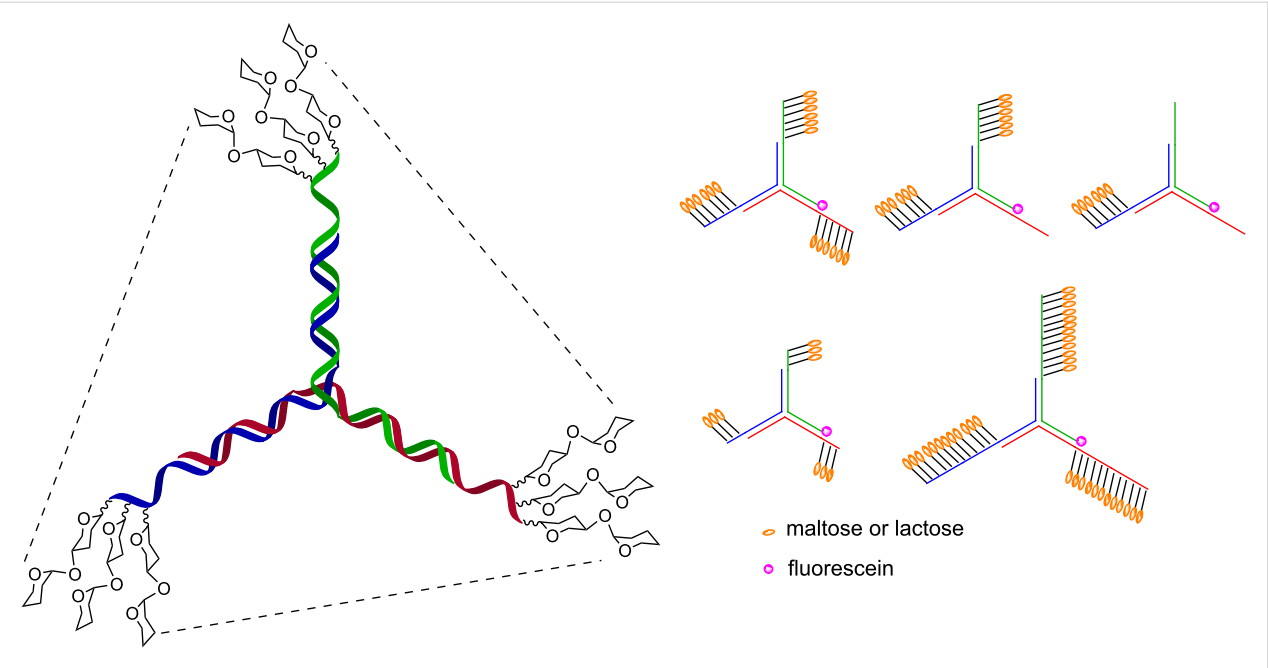

Figure 2: Multivalent triangular glycoDNA assemblies.

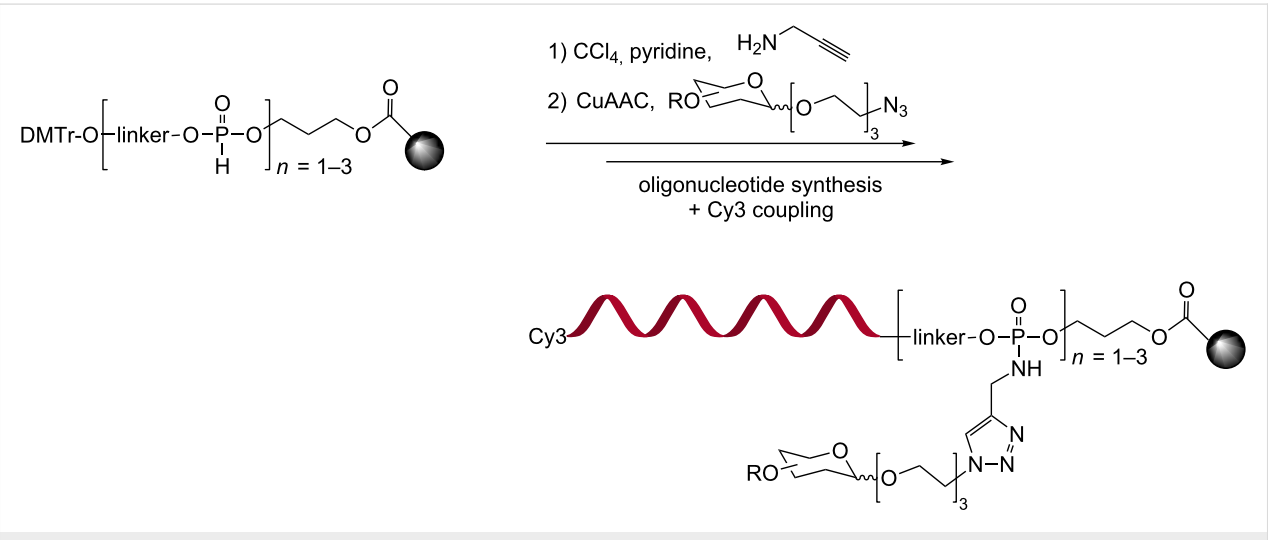

Scheme 4: Preparation of the DNA glycoconjugate by CuAAC.

strand at the 2'-position using an azido and a bromo-modified thymidine **6** and **7** (Scheme 5) [29].

Krauss and co-workers elegantly extended the utility of SELEX [30] to generate aptamers functionalized with glycans through CuAAC [31,32]. Their approach, termed SELMA (selection with modified aptamers), is a multistep procedure that allows screening, selection and amplification of DNA glycoconjugates (Scheme 6). At first, a library of single strand DNA with a hairpin is extended with a polymerase replacing dTTP by an alkyne-modified desoxyuridine triphosphate to give a full hairpin with randomized alkyne groups on one strand. Then, CuAAC is performed with a glycosyl azide and the hairpin is released by strand displacement thus allowing the glycosylated strand to adopt a folded structure. Affinity selection and reiteration of the cycle enables the in vitro evolution of glycan-functionalized aptamers. This technology was used to screen ligands for 2G12, an antibody that neutralizes HIV by binding to the high mannose epitope of gp120. For this purpose, the aptamer library was functionalized with oligomannoses (Man_4-azide or Man_9-azide) leading to the selection of glycan-functionalized aptamers bearing 7–14 glycan units and with a K_D below

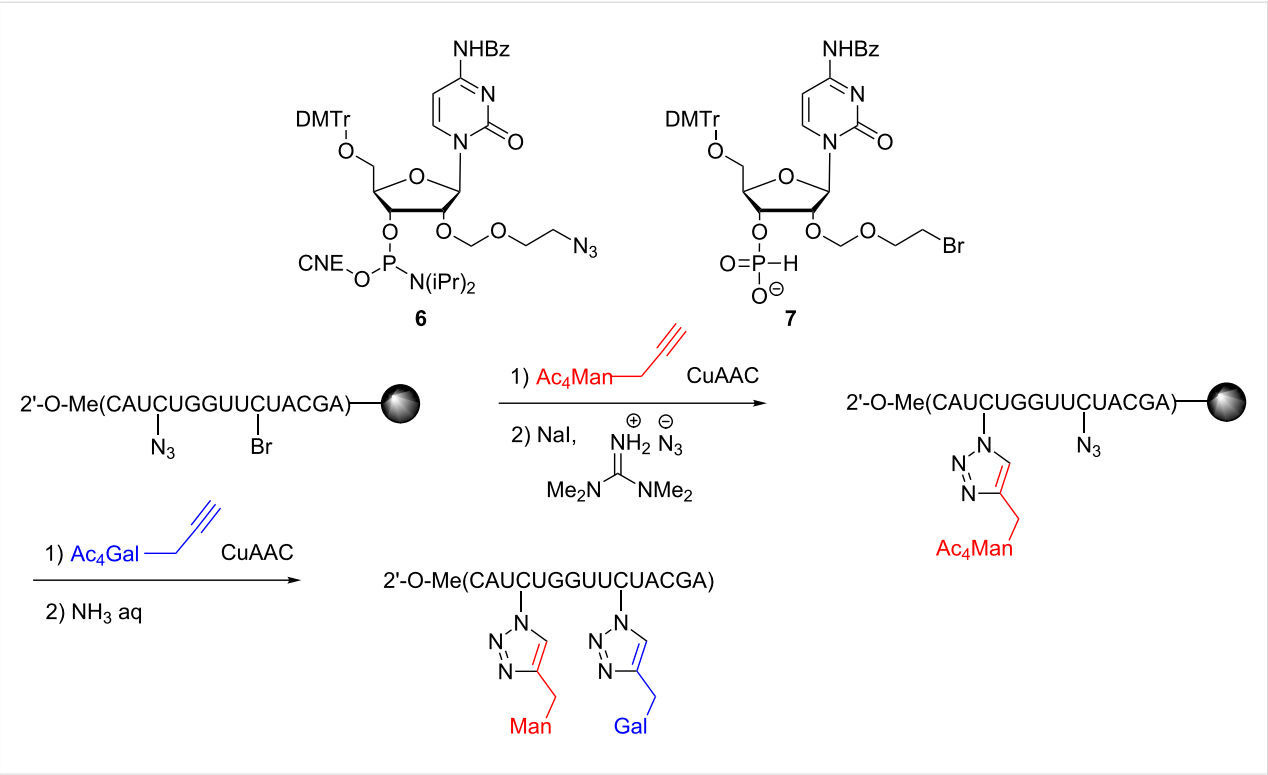

Scheme 5: DNA glycoconjugation by sequential CuAAC.

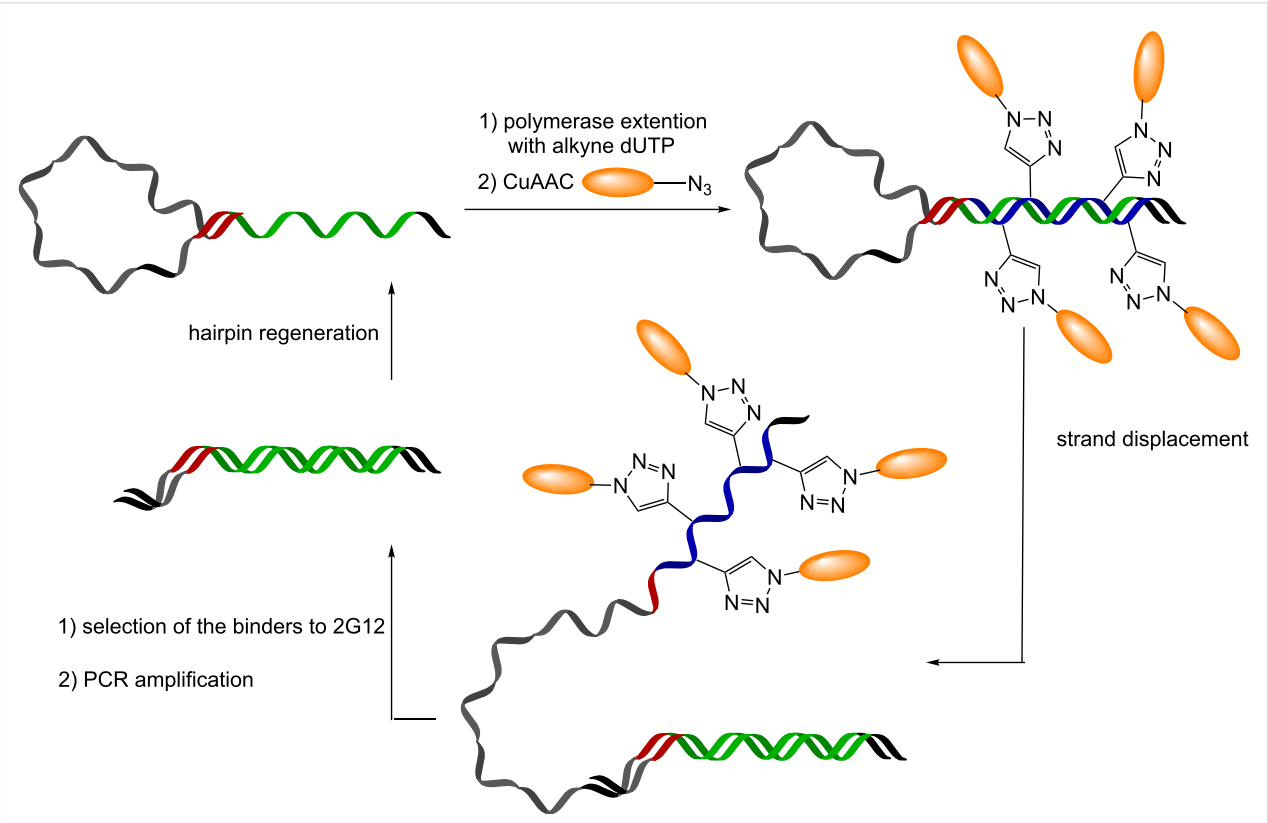

Scheme 6: Selection with modified glycoconjugate aptamers (SELMA).

220 nM. A mutagenesis study showed that the affinity was also sequence dependent and not uniquely due to the high glycosylation of the DNAs. The tertiary structure of the glycan conjugates predisposed the ligands productively thus resulting in a high affinity. A variation of this strategy using mRNA also yielded peptidoglycans with high affinity to 2G12 [33].

DNA–PNA glycosylated hybrids

As an alternative to DNA, peptide nucleic acid (PNA) [34] has also been used to tag glycans and to program their assembly based on the rules of hybridization. From an assembly standpoint, stable PNA–DNA duplexes can be achieved with shorter sequences than the corresponding DNA homoduplex (10–14mer PNA typically provides sufficient duplex stability) [35]. From a chemistry standpoint, the fact that PNA synthesis involves peptide coupling reactions with a broad arsenal of protecting group combinations facilitates the introduction of functionalities for the conjugation of glycans [36]. The first method reported was leveraged on a nucleophilic coupling between readily available glycosyl thiol (obtained in one step by treatment of a native carbohydrate with Lawesson's reagent [37]) and a chloroacetamide-functionalized PNA (Scheme 7) [38,39]. Using this method, we have shown that diverse glycans could be iteratively introduced on amino acid linkers. Inspired by Shoda's activation [40] which provides facile access to complex glycosyl azides from native carbohydrates, we subsequently applied reiterative CuAAC conjugation of glycans on propargyl glycine residues within a peptide [41,42]. Since these methods are compatible with the powerful scheme of mix and split combinatorial chemistry the synthesis of libraries is easily performed wherein each library member is tagged with a unique sequence. Conjugation of glycans at different positions within a PNA oligomer has been achieved by Seitz and co-workers using thiols imbedded in the backbone of the PNA that were chemoselectively conjugated to a maleimide–glycan adduct [43].

Our first efforts in the area of glycan display aimed to demonstrate that a DNA template could be used to program the assembly of discrete PNA-tagged ligands in order to recapitulate the geometry of HIV's gp120 glycan epitope which is composed of multiple copies of a high mannose undecasaccharide [38]. An advantage of displaying ligands through template

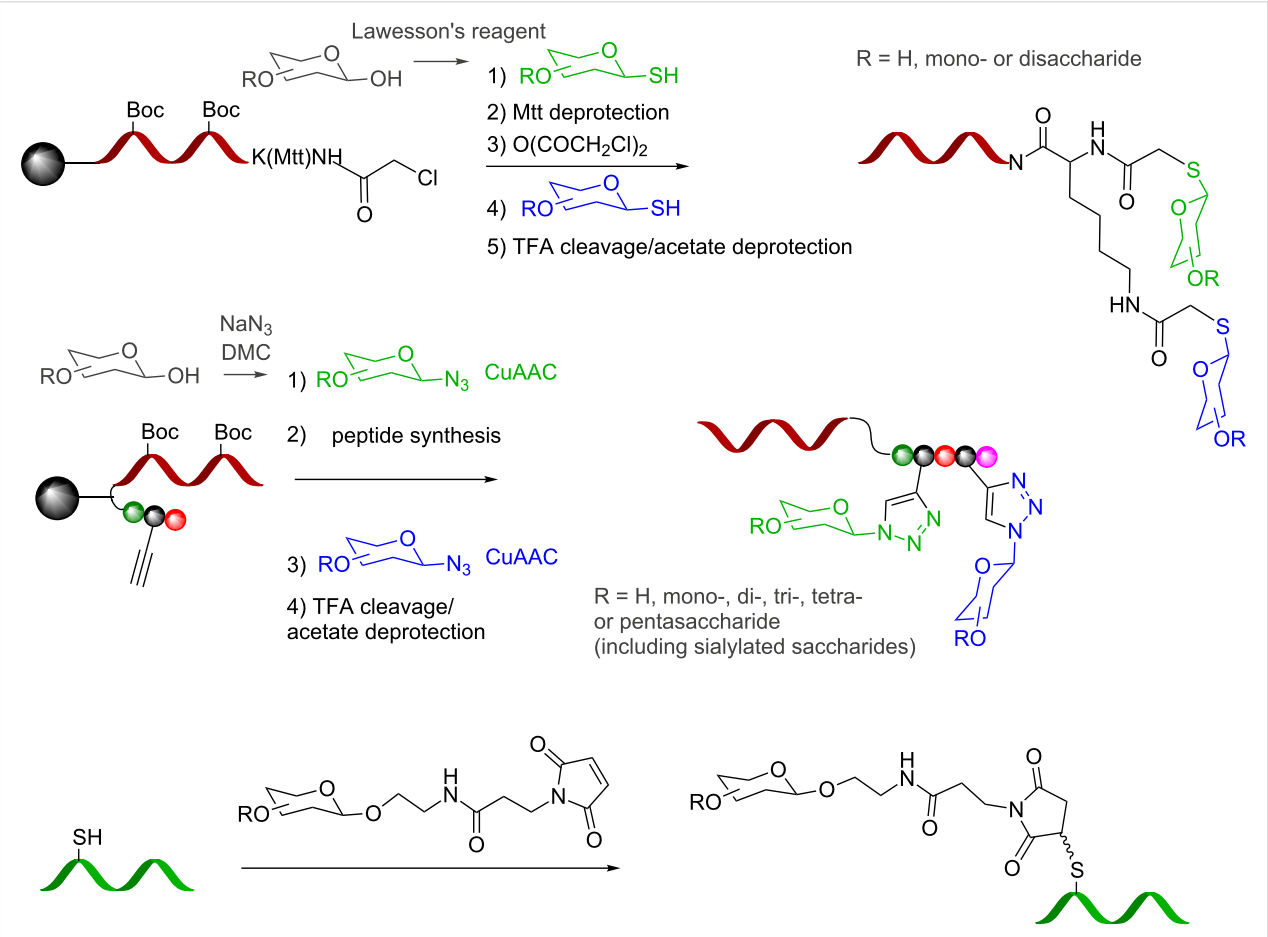

Scheme 7: Synthesis of PNA glycoconjugates (Mtt: 4-methyltrityl; R = H or (oligo)saccharide).

assembly of discrete units is that the pairing and distance can be controlled though the template instructions. To this end a pilot library of fourteen PNA-tagged glycoconjugates that included mannose disaccharides joined by linkers of different lengths were paired through hybridization, varying the ligand combinations and interligand distances. Measuring the affinity of 32 different assemblies against 2G12, an antibody that neutralize HIV through tight binding with the glycan epitope, showed a clear distance–affinity relationship that was consistent with the proposed antibody–epitope interaction. Notably, neither of the PNA-tagged fragments making up the highest affinity assembly had measurable affinity for the antibody thus demonstrating a clear synergy in the interaction of the templated fragments (see Figure 3 for selected examples).

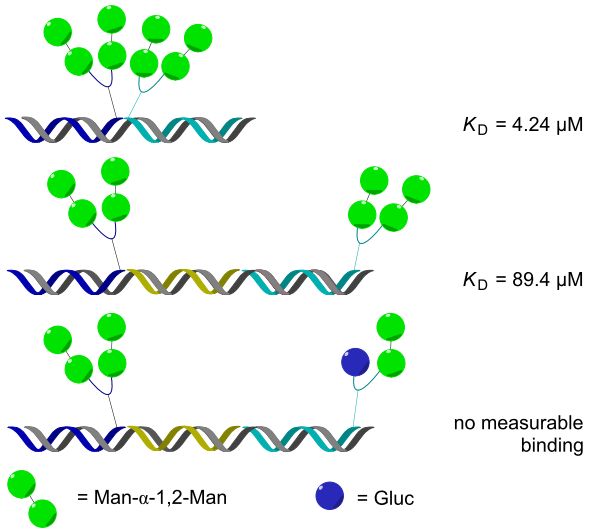

Figure 3: DNA display of PNA-tagged glycans designed to emulate HIV's gp120 epitope.

This approach was subsequently scaled out to optimize the affinity of DC-SIGN ligands using a library of PNA-tagged glycans that included unnatural modifications in the glycans. DC-SIGN is a tetrameric lectin implicated in interactions with a broad array of pathogens including HIV. A library of 37,485 assemblies was prepared by hybridization of two sets of PNA-tagged glycoconjugates onto a library of DNA templates (Figure 4). Screening the library by affinity selection against immobilized DC-SIGN and analysis of the best-fit sample by PCR amplification/sequence analysis of the template led to the discovery of an assembly with a 30-fold enhancement in binding over the unmodified mannose assembly [44]. Importantly, following PCR amplification of the template, the library can be reassembled making the technology compatible with reiterative cycles of selection/amplification.

Seitz and co-workers demonstrated that a DNA display could be used to interrogate topologically more challenging geometries, namely, bridging binding sites on opposing faces of a lectin. Using a set of five different glycan–PNA conjugates and different DNA templates, the optimal spatial arrangement of the

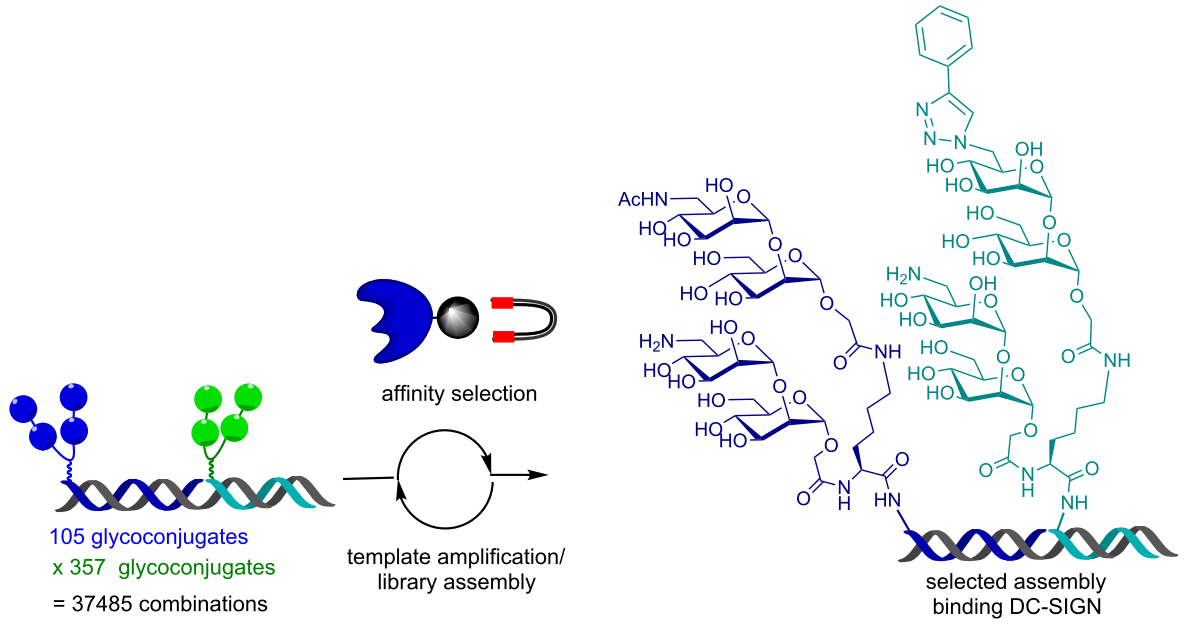

Figure 4: Combinatorial assembly and selection of two PNA glycoconjugate libraries on DNA templates.

ligands was systematically investigated. Additionally, the flexibility of the PNA–DNA duplexes was also modulated by introducing nick-sites and partially unpaired regions in the DNA display (see Figure 5 for selected examples) [43]. Each assembly was tested for its affinity to ECL (*Erythrina cristagalli* lectin) and the results confirmed that the affinity with the lectin is dependent on the distance between the glycan units (as suggested by crystallography) and benefited from the added flexibility of the linker introduced by an unpaired region. The same approach was also used to identify the optimal spatial arrangement for assemblies targeting RCA_{120} and L-selectin with mannose, LacNAc and sialyl Lewis X–PNA conjugates [45]. The highest binding affinity to RCA_{120} was obtained with a bivalent glycan assembly (LacNAc, presented at 140 Å distance) that was 70 times better than the monovalent assembly. Notably, the enhanced binding affinity for the divalent display is consistent with a distance of ca. 130 Å between the binding sites. It was also demonstrated that DNA-templated displays could be harnessed to combine a DNA-based aptamer with a glycan.

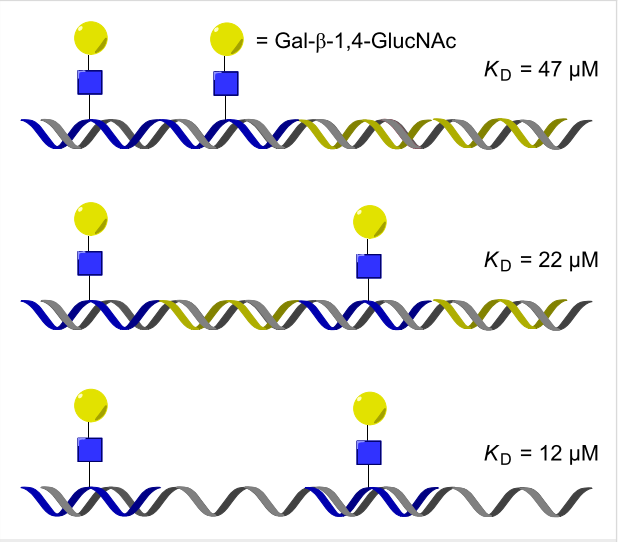

Figure 5: DNA display of ligand bridging opposing binding sites in a lectin (ECL).

Glycan arrays prepared by hybridization to a DNA microarray

Microarray technologies have enjoyed tremendous success based on the miniaturization and the high information content that this format provides. The DNA microarray is now a standard technology and customized arrays with 10^4–10^6 discrete sequences are readily available. Screening for glycan binding in a microarray format has also proven extremely valuable in glycobiology [46,47]. Based on earlier reports that small molecules [48,49] and protein microarrays [50] can be obtained by hybridization of PNA-tagged libraries, Chevolot and co-workers first reported the use of glycan–DNA conjugates to display glycans in a spatially addressable array format [27]. A fluorophore (Cy3) was used to quantify the immobilized conjugate on the array. In a pilot experiment, a galactose binding lectin (RCA_{120}) was applied to confirm the spatial resolution upon hybridization (Figure 6).

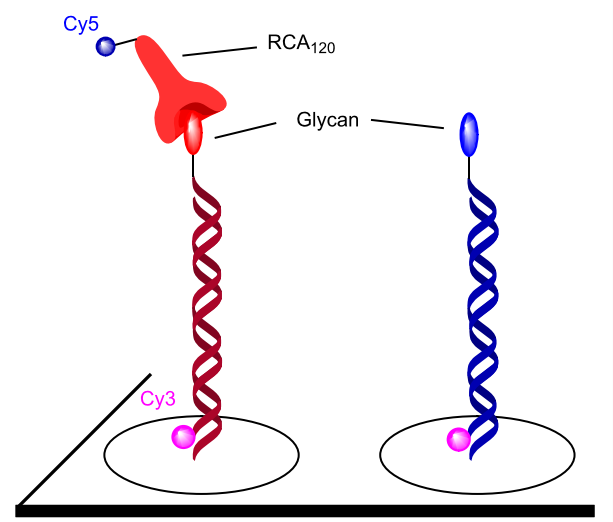

Figure 6: A glycan array prepared by hybridization of glycan–DNA conjugates and screening of RCA_{120}.

The same group extended this concept with conjugates built on a glucose scaffold displaying up to four units of the glycans (Figure 7) to generate homo- or heteroglycan cluster. These conjugates were used for hybridization to DNA arrays and screened against lectins from pathogenic *P. aeruginosa* (PA2L and LecA) [51-53].

Our group used DNA microarrays to combinatorial pair diverse PNA-tagged glycan conjugates displayed at adjacent hybridization sites to produce assemblies emulating the diversity of di-, tri- and tetra-antennary glycans (Figure 8) [39]. Using two sets of 25 PNA conjugates, an array of 625 unique assemblies was produced. Importantly, screening different lectins (ConA or peanut lectin) indicate a synergy between the paired fragments with a composition consistent with the known selectivity of the lectins.

More recently, we reported a combinatorial synthesis of a more diverse library of PNA-encoded glycoconjugates (10,000 members) [41]. The combinatorial synthesis was performed using two sequential CuAAC conjugations with 33 diverse glycosyl azides separated by 3 different peptide spacers and capped by 3 different aryl groups (Figure 9). The fact that the library can be prepared by mix and split synthesis and reformatted in a spatially addressable microarray by simple

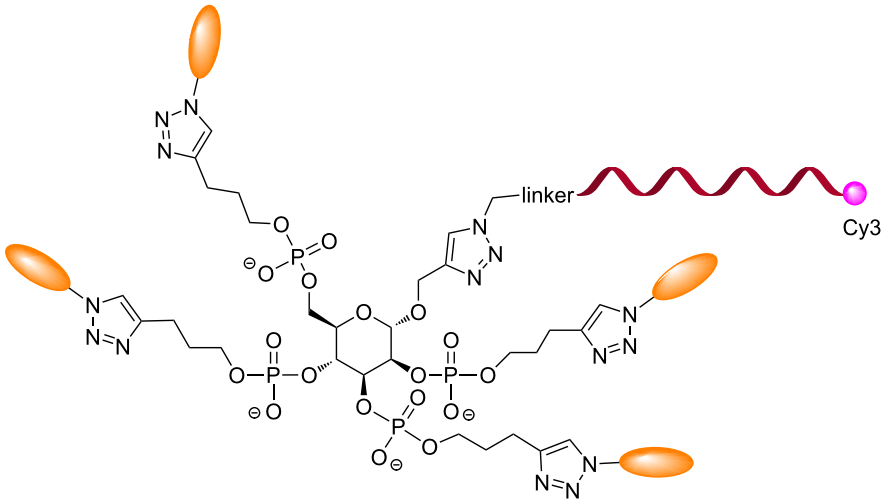

Figure 7: Multivalent sugar-core glycoconjugate DNA.

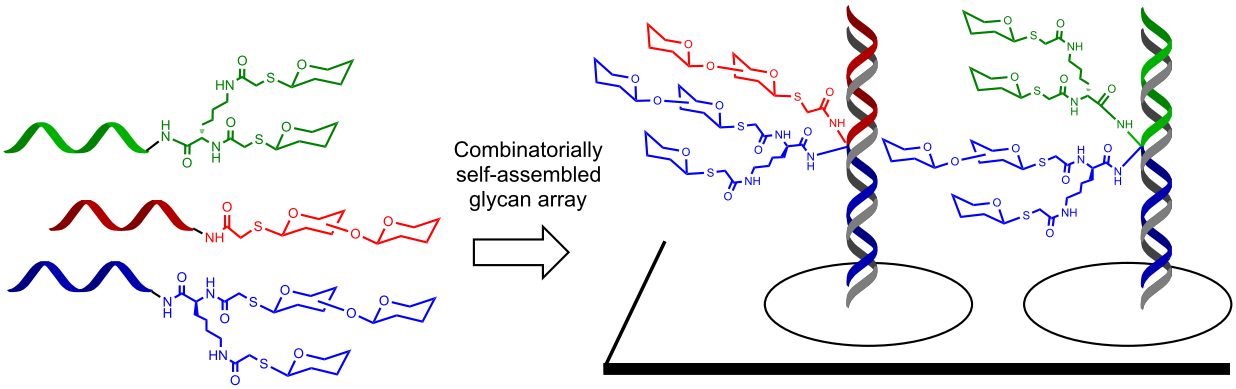

Figure 8: Combinatorial self-assembly of PNA glycoconjugates on a DNA microarray.

hybridization [48] greatly facilitates access to diverse glycoconjugate arrays. Screening the library against a panel of seven different lectins (ConA, Bc2LA, BambL, BSL, LecA , StxB and MAL) showed a distinct binding selectivity in each case for a conjugate of two glycans (relative to control with a single glycan) with a unique linker and capping group combination thus establishing the synergy of interaction between the glycan units and the distinct spatial arrangement conferred by the different linkers. This library represents the largest array of heteroglycan conjugates reported to date. Based on the results obtained with the screen for LecA, a lectin intimately involved in the pathogenicity of *P. aeruginosa*, a focused library displaying two galactose mono- or disaccharides with different linkers was synthesized in order to optimize affinity of a conjugate interacting with one face of the lectin [42]. LecA is a tetrameric protein with two binding sites on each face of the oligomer. An important question in microarray-based affinity screens with proteins involved in oligomeric interactions is whether a high-intensity interaction observed on the array results from a unique high-affinity ligand or from multiple lower affinity ligands due to the high surface density of these in the microarray format (Figure 10). Comparing the binding of a divalent ligand with its monomeric counterpart at decreasing ligand concentration showed a faster decay of binding for the monomeric ligand consistent with the speculation that, at high ligand concentration, the density was sufficiently high for the lectin to interact with multiple ligands across different hybridization sites. Notably, this work led to the discovery of a high-affinity ligand (K_D = 82 nM) that was effective at inhibiting bacterial penetration in epithelial cells.

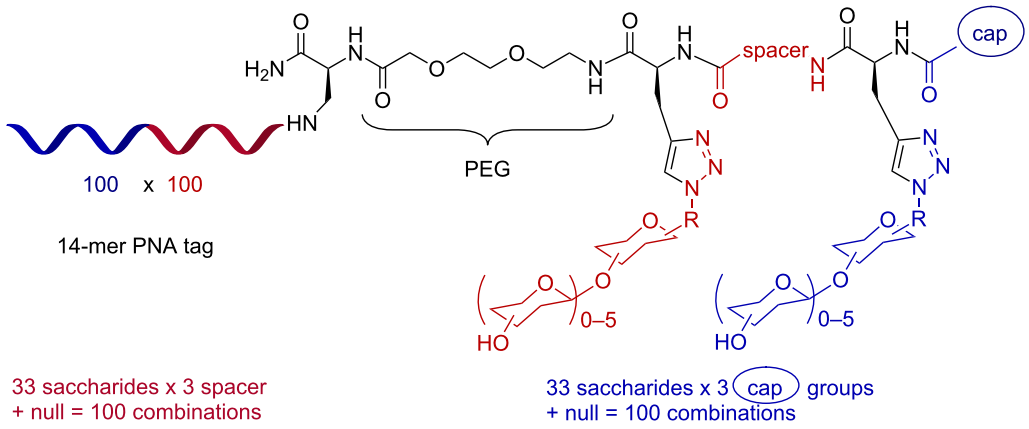

Figure 9: General scheme of the 10,000 member PNA-encoded glycoconjugate library.

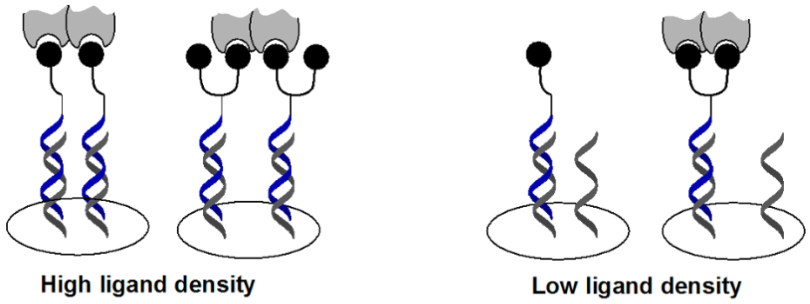

Figure 10: Oligomeric interaction with arrayed mono- and divalent ligands (represented as the black spheres) as a function of surface density.

Conclusion

It is now well-established that nucleic acid-based assemblies can be used to display glycans with a synergy between the interactions of the individual ligands binding with a target. Progress in this area has paralleled similar developments with small molecule conjugates [48,54-63]. Technological developments in conjugation chemistry and solid-phase synthesis have enabled the introduction of complex glycans with modest synthetic investments to obtain the suitably functionalized glycans. Furthermore, methods to access large libraries of peptidoglycan conjugates with nucleic acid tags have been reported opening new horizons in the diversity space that can be screened for this important compound class. The fact that assemblies can be prepared with control over the ligand spacing, combination and valence is empowering. While the geometry of architectures tested has remained fairly simple thus far (linear or 3-way junction), progress in DNA-based nanoassemblies will likely fuel further advances in the area of hybridization-based glycan displays. It can also be anticipated that these assemblies will be used in increasingly more complex systems extending beyond simple affinity measurements, paving the way towards diagnostic or therapeutic applications. We hope that the examples presented in this review will encourage researchers in glycoscience to embrace and further develop the use of glycan display by programmed assemblies.

Acknowledgements

We thank our collaborators in the area of nucleic acid-programmed assemblies and the funding agencies that have contributed to our work (Human Frontier Science Program, Agence Nationale de la Recherche, European Research Council, National Swiss Foundation). This review is not intended to be comprehensive but rather to highlight some recent work; we regret any arbitrary omissions.

References

1. Crocker, P. R.; Paulson, J. C.; Varki, A. *Nat. Rev. Immunol.* **2007,** *7,* 255–266. doi:10.1038/nri2056
2. Borsig, L.; Wong, R.; Hynes, R. O.; Varki, N. M.; Varki, A. *Proc. Natl. Acad. Sci. U. S. A.* **2002,** *99,* 2193–2198. doi:10.1073/pnas.261704098
3. Hudak, J. E.; Canham, S. M.; Bertozzi, C. R. *Nat. Chem. Biol.* **2014,** *10,* 69–75. doi:10.1038/nchembio.1388
4. Varki, A. *Glycobiology* **1993,** *3,* 97–130. doi:10.1093/glycob/3.2.97

5. Fasting, C.; Schalley, C. A.; Weber, M.; Seitz, O.; Hecht, S.; Koksch, B.; Dernedde, J.; Graf, C.; Knapp, E.-W.; Haag, R. *Angew. Chem., Int. Ed.* **2012,** *51,* 10472–10498. doi:10.1002/anie.201201114
6. Römer, W.; Berland, L.; Chambon, V.; Gaus, K.; Windschiegl, B.; Tenza, D.; Aly, M. R. E.; Fraisier, V.; Florent, J.-C.; Perrais, D.; Lamaze, C.; Raposo, G.; Steinem, C.; Sens, P.; Bassereau, P.; Johannes, L. *Nature* **2007,** *450,* 670–675. doi:10.1038/nature05996
7. Imberty, A.; Varrot, A. *Curr. Opin. Struct. Biol.* **2008,** *18,* 567–576. doi:10.1016/j.sbi.2008.08.001
8. Bertozzi, C. R.; Kiessling, L. L. *Science* **2001,** *291,* 2357–2364. doi:10.1126/science.1059820
9. Hudak, J. E.; Bertozzi, C. R. *Chem. Biol.* **2014,** *21,* 16–37. doi:10.1016/j.chembiol.2013.09.010
10. Kitov, P. I.; Sadowska, J. M.; Mulvey, G.; Armstrong, G. D.; Ling, H.; Pannu, N. S.; Read, R. J.; Bundle, D. R. *Nature* **2000,** *403,* 669–672. doi:10.1038/35001095
11. Imberty, A.; Chabre, Y. M.; Roy, R. *Chem. – Eur. J.* **2008,** *14,* 7490–7499. doi:10.1002/chem.200800700
12. Kiessling, L. L.; Gestwicki, J. E.; Strong, L. E. *Angew. Chem., Int. Ed.* **2006,** *45,* 2348–2368. doi:10.1002/anie.200502794
13. Morvan, F.; Vidal, S.; Souteyrand, E.; Chevolot, Y.; Vasseur, J.-J. *RSC Adv.* **2012,** *2,* 12043–12068. doi:10.1039/c2ra21550k
14. Spinelli, N.; Defrancq, E.; Morvan, F. *Chem. Soc. Rev.* **2013,** *42,* 4557–4573. doi:10.1039/C2CS35406C
15. Winssinger, N.; Gorska, K.; Ciobanu, M.; Daguer, J. P.; Barluenga, S. Assembly of PNA-Tagged Small Molecules, Peptides, and Carbohydrates onto DNA Templates: Programming the Combinatorial Pairing and Interligand Distance. In *Peptide Nucleic Acids;* Nielsen, P. E.; Appella, D. H., Eds.; Methods in Molecular Biology, Vol. 1050; Springer, 2014; pp 95–110. doi:10.1007/978-1-62703-553-8_8
16. Wittmann, V.; Pieters, R. J. *Chem. Soc. Rev.* **2013,** *42,* 4492–4503. doi:10.1039/c3cs60089k
17. Matsuura, K.; Akasaka, T.; Hibino, M.; Kobayashi, K. *Bioconjugate Chem.* **2000,** *11,* 202–211. doi:10.1021/bc9901191
18. Rothenberg, J. M.; Wilchek, M. *Nucleic Acids Res.* **1988,** *16,* 7197. doi:10.1093/nar/16.14.7197
19. Matsuura, K.; Hibino, M.; Ikeda, T.; Yamada, Y.; Kobayashi, K. *Chem. – Eur. J.* **2004,** *10,* 352–359. doi:10.1002/chem.200305465
20. Matsuura, K.; Hibino, M.; Yamada, Y.; Kobayashi, K. *J. Am. Chem. Soc.* **2001,** *123,* 357–358. doi:10.1021/ja001945j
21. Yamada, Y.; Matsuura, K.; Kobayashi, K. *Bioorg. Med. Chem.* **2005,** *13,* 1913–1922. doi:10.1016/j.bmc.2005.01.021
22. Schlegel, M. K.; Hütter, J.; Eriksson, M.; Lepenies, B.; Seeberger, P. H. *ChemBioChem* **2011,** *12,* 2791–2800. doi:10.1002/cbic.201100511
23. Matsui, M.; Nishiyama, Y.; Ueji, S.; Ebara, Y. *Bioorg. Med. Chem. Lett.* **2007,** *17,* 456–460. doi:10.1016/j.bmcl.2006.10.020
24. Matsui, M.; Ebara, Y. *Bioorg. Med. Chem. Lett.* **2012,** *22,* 6139–6143. doi:10.1016/j.bmcl.2012.08.028
25. Rostovtsev, V. V.; Green, L. G.; Fokin, V. V.; Sharpless, K. B. *Angew. Chem., Int. Ed.* **2002,** *41,* 2596–2599. doi:10.1002/1521-3773(20020715)41:14<2596::AID-ANIE2596>3.0.CO;2-4
26. Tornøe, C. W.; Christensen, C.; Meldal, M. *J. Org. Chem.* **2002,** *67,* 3057–3064. doi:10.1021/jo011148j
27. Chevolot, Y.; Bouillon, C.; Vidal, S.; Morvan, F.; Meyer, A.; Cloarec, J.-P.; Jochum, A.; Praly, J.-P.; Vasseur, J.-J.; Souteyrand, E. *Angew. Chem., Int. Ed.* **2007,** *46,* 2398–2402. doi:10.1002/anie.200604955
28. Kiviniemi, A.; Virta, P.; Lönnberg, H. *Bioconjugate Chem.* **2008,** *19,* 1726–1734. doi:10.1021/bc800221p
29. Kiviniemi, A.; Virta, P.; Drenichev, M. S.; Mikhailov, S. N.; Lönnberg, H. *Bioconjugate Chem.* **2011,** *22,* 1249–1255. doi:10.1021/bc200097g
30. Wilson, D. S.; Szostak, J. W. *Annu. Rev. Biochem.* **1999,** *68,* 611–647. doi:10.1146/annurev.biochem.68.1.611
31. MacPherson, I. S.; Temme, J. S.; Habeshian, S.; Felczak, K.; Pankiewicz, K.; Hedstrom, L.; Krauss, I. J. *Angew. Chem., Int. Ed.* **2011,** *50,* 11238–11242. doi:10.1002/anie.201105555
32. Temme, J. S.; MacPherson, I. S.; DeCourcey, J. F.; Krauss, I. J. *J. Am. Chem. Soc.* **2014,** *136,* 1726–1729. doi:10.1021/ja411212q
33. Horiya, S.; Bailey, J. K.; Temme, J. S.; Schippe, Y. V. G.; Krauss, I. J. *J. Am. Chem. Soc.* **2014,** *136,* 5407–5415. doi:10.1021/ja500678v
34. Egholm, M.; Buchardt, O.; Christensen, L.; Behrens, C.; Freier, S. M.; Driver, D. A.; Berg, R. H.; Kim, S. K.; Norden, B.; Nielsen, P. E. *Nature* **1993,** *365,* 566–568. doi:10.1038/365566a0
35. Pianowski, Z. L.; Winssinger, N. *Chem. Soc. Rev.* **2008,** *37,* 1330–1336. doi:10.1039/b706610b
36. Zambaldo, C.; Barluenga, S.; Winssinger, N. *Curr. Opin. Chem. Biol.* **2015,** *26,* 8–15. doi:10.1016/j.cbpa.2015.01.005
37. Bernardes, G. J. L.; Gamblin, D. P.; Davis, B. G. *Angew. Chem., Int. Ed.* **2006,** *45,* 4007–4011. doi:10.1002/anie.200600685
38. Gorska, K.; Huang, K. T.; Chaloin, O.; Winssinger, N. *Angew. Chem., Int. Ed.* **2009,** *48,* 7695–7700. doi:10.1002/anie.200903328
39. Huang, K. T.; Gorska, K.; Alvarez, S.; Barluenga, S.; Winssinger, N. *ChemBioChem* **2011,** *12,* 56–60. doi:10.1002/cbic.201000567
40. Tanaka, T.; Nagai, H.; Noguchi, M.; Kobayashi, A.; Shoda, S.-i. *Chem. Commun.* **2009,** 3378–3379. doi:10.1039/b905761g
41. Novoa, A.; Machida, T.; Barluenga, S.; Imberty, A.; Winssinger, N. *ChemBioChem* **2014,** *15,* 2058–2065. doi:10.1002/cbic.201402280
42. Novoa, A.; Eierhoff, T.; Topin, J.; Varrot, A.; Barluenga, S.; Imberty, A.; Römer, W.; Winssinger, N. *Angew. Chem., Int. Ed.* **2014,** *53,* 8885–8889. doi:10.1002/anie.201402831
43. Scheibe, C.; Bujotzek, A.; Dernedde, J.; Weber, M.; Seitz, O. *Chem. Sci.* **2011,** *2,* 770–775. doi:10.1039/c0sc00565g
44. Ciobanu, M.; Huang, K.-T.; Daguer, J.-P.; Barluenga, S.; Chaloin, O.; Schaeffer, E.; Mueller, C. G.; Mitchell, D. A.; Winssinger, N. *Chem. Commun.* **2011,** *47,* 9321–9323. doi:10.1039/c1cc13213j
45. Scheibe, C.; Wedepohl, S.; Riese, S. B.; Dernedde, J.; Seitz, O. *ChemBioChem* **2013,** *14,* 236–250. doi:10.1002/cbic.201200618
46. Rillahan, C. D.; Paulson, J. C. *Annu. Rev. Biochem.* **2011,** *80,* 797–823. doi:10.1146/annurev-biochem-061809-152236
47. Park, S.; Gildersleeve, J. C.; Blixt, O.; Shin, I. *Chem. Soc. Rev.* **2013,** *42,* 4310–4326. doi:10.1039/C2CS35401B
48. Harris, J. L.; Winssinger, N. *Chem. – Eur. J.* **2005,** *11,* 6792–6801. doi:10.1002/chem.200500305
49. Winssinger, N.; Ficarro, S.; Schultz, P. G.; Harris, J. L. *Proc. Natl. Acad. Sci. U. S. A.* **2002,** *99,* 11139–11144. doi:10.1073/pnas.172286899
50. Lovrinovic, M.; Seidel, R.; Wacker, R.; Schroeder, H.; Seitz, O.; Engelhard, M.; Goody, R. S.; Niemeyer, C. M. *Chem. Commun.* **2003,** 822–823. doi:10.1039/b212294d
51. Gerland, B.; Goudot, A.; Ligeour, C.; Pourceau, G.; Meyer, A.; Vidal, S.; Gehin, T.; Vidal, O.; Souteyrand, E.; Vasseur, J.-J.; Chevolot, Y.; Morvan, F. *Bioconjugate Chem.* **2014,** *25,* 379–392. doi:10.1021/bc4005365

52. Gerland, B.; Goudot, A.; Pourceau, G.; Meyer, A.; Vidal, S.; Souteyrand, E.; Vasseur, J.-J.; Chevolot, Y.; Morvan, F. *J. Org. Chem.* **2012,** *77,* 7620–7626. doi:10.1021/jo300826u
53. Gerland, B.; Goudot, A.; Pourceau, G.; Meyer, A.; Dugas, V.; Cecioni, S.; Vidal, S.; Souteyrand, E.; Vasseur, J.-J.; Chevolot, Y.; Morvan, F. *Bioconjugate Chem.* **2012,** *23,* 1534–1547. doi:10.1021/bc2006434
54. Melkko, S.; Scheuermann, J.; Dumelin, C. E.; Neri, D. *Nat. Biotechnol.* **2004,** *22,* 568–574. doi:10.1038/nbt961
55. Daguer, J. P.; Ciobanu, M.; Alvarez, S.; Barluenga, S.; Winssinger, N. *Chem. Sci.* **2011,** *2,* 625–632. doi:10.1039/c0sc00574f
56. Gorska, K.; Beyrath, J.; Fournel, S.; Guichard, G.; Winssinger, N. *Chem. Commun.* **2010,** *46,* 7742–7744. doi:10.1039/c0cc02852e
57. Williams, B. A. R.; Diehnelt, C. W.; Belcher, P.; Greving, M.; Woodbury, N. W.; Johnston, S. A.; Chaput, J. C. *J. Am. Chem. Soc.* **2009,** *131,* 17233–17241. doi:10.1021/ja9051735
58. Abendroth, F.; Bujotzek, A.; Shan, M.; Haag, R.; Weber, M.; Seitz, O. *Angew. Chem., Int. Ed.* **2011,** *50,* 8592–8596. doi:10.1002/anie.201101655
59. Eberhard, H.; Diezmann, F.; Seitz, O. *Angew. Chem., Int. Ed.* **2011,** *50,* 4146–4150. doi:10.1002/anie.201007593
60. Englund, E. A.; Wang, D.; Fujigaki, H.; Sakai, H.; Micklitsch, C. M.; Ghirlando, R.; Martin-Manso, G.; Pendrak, M. L.; Roberts, D. D.; Durell, S. R.; Appella, D. H. *Nat. Commun.* **2012,** *3,* No. 614. doi:10.1038/ncomms1629
61. Dix, A. V.; Moss, S. M.; Phan, K.; Hoppe, T.; Paoletta, S.; Kozma, E.; Gao, Z.-G.; Durell, S. R.; Jacobson, K. A.; Appella, D. H. *J. Am. Chem. Soc.* **2014,** *136,* 12296–12303. doi:10.1021/ja504288s
62. Daguer, J.-P.; Zambaldo, C.; Ciobanu, M.; Morieux, P.; Barluenga, S.; Winssinger, N. *Chem. Sci.* **2015,** *6,* 739–744. doi:10.1039/C4SC01654H
63. Daguer, J.-P.; Zambaldo, C.; Abegg, D.; Barluenga, S.; Tallant, C.; Müller, S.; Adibekian, A.; Winssinger, N. *Angew. Chem., Int. Ed.* **2015,** *54,* 6057–6061. doi:10.1002/anie.201412276

License and Terms

BEILSTEIN JOURNAL OF ORGANIC CHEMISTRY

Probing multivalency in ligand–receptor-mediated adhesion of soft, biomimetic interfaces

Stephan Schmidt[1], Hanqing Wang[2,3], Daniel Pussak[2], Simone Mosca[2] and Laura Hartmann[*2,3,§]

Full Research Paper

Open Access

Address:
[1]Universität Leipzig, Institut für Biochemie, Johannisalle 21–23, D-04103 Leipzig, Germany, [2]Max Planck Institute of Colloids and Interfaces, Research Campus Golm, 14424 Potsdam, Germany and [3]Heinrich-Heine-Universität Düsseldorf, Institut für Organische und Makromolekulare Chemie, Universitätsstr. 1, 40225 Düsseldorf, Germany

Email:
Laura Hartmann[*] - laura.hartmann@hhu.de

* Corresponding author
§ Tel. ++49 211 81-10360, Fax: ++49 211 81-15840

Keywords:
bio-interfaces; cell mimetic; glycocalyx; glycopolymer; molecular recognition; RICM; specific adhesion

Beilstein J. Org. Chem. **2015,** *11,* 720–729.
doi:10.3762/bjoc.11.82

Received: 27 February 2015
Accepted: 28 April 2015
Published: 12 May 2015

This article is part of the Thematic Series "Multivalency as a chemical organization and action principle".

Guest Editor: R. Haag

Abstract

Many biological functions at cell level are mediated by the glycocalyx, a dense carbohydrate-presenting layer. In this layer specific interactions between carbohydrate ligands and protein receptors are formed to control cell–cell recognition, cell adhesion and related processes. The aim of this work is to shed light on the principles of complex formation between surface anchored carbohydrates and receptor surfaces by measuring the specific adhesion between surface bound mannose on a concanavalin A (ConA) layer via poly(ethylene glycol)-(PEG)-based soft colloidal probes (SCPs). Special emphasis is on the dependence of multivalent presentation and density of carbohydrate units on specific adhesion. Consequently, we first present a synthetic strategy that allows for controlled density variation of functional groups on the PEG scaffold using unsaturated carboxylic acids (crotonic acid, acrylic acid, methacrylic acid) as grafting units for mannose conjugation. We showed by a range of analytic techniques (ATR–FTIR, Raman microscopy, zeta potential and titration) that this synthetic strategy allows for straightforward variation in grafting density and grafting length enabling the controlled presentation of mannose units on the PEG network. Finally we determined the specific adhesion of PEG-network-conjugated mannose units on ConA surfaces as a function of density and grafting type. Remarkably, the results indicated the absence of a molecular-level enhancement of mannose/ConA interaction due to chelate- or subsite-binding. The results seem to support the fact that weak carbohydrate interactions at mechanically flexible interfaces hardly undergo multivalent binding but are simply mediated by the high number of ligand–receptor interactions.

Introduction

Vast amounts of biological processes are mediated by interactions between membrane proteins and carbohydrates of the glycocalyx, a glycan coating enveloping prokaryotic or eukaryotic cells. By specific binding to cell receptors, the carbohydrate units of the glycocalyx control important processes such as cell adhesion, communication and inflammatory response [1]. For this reason great effort is set forth to identify the key principles of carbohydrate/protein receptor interaction and to utilize carbohydrate structures as drugs, e.g., in cancer treatment or pathogen-related diseases [2,3]. A well-established key principle of carbohydrate–receptor interactions is multivalency. Natural carbohydrate ligands are typically oligomers consisting of multiple subunits of varying complexity. When binding to receptors this leads to a receptor clustering or so-called glycocluster effect. However, multivalency even goes further: For example when cells form contact layers of surface anchored carbohydrates the glycocalyx interacts also with surface anchored membrane receptors. Thus, the interactions between these surfaces are again multivalent interactions, just on a larger scale between two surfaces. Such carbohydrate based multivalent surface–surface interactions represent a large range of crucial biological events such as initial cell adhesion processes or pathogen invasion in host tissue. Nevertheless, ligand–receptor interactions are typically characterized by studying the binding affinity of freely dissolved ligands without surface anchorage. Typical assays in this context are "chip"-based methods like surface plasmon resonance, quartz crystal microbalance or impedance spectroscopy where the affinity of ligands is measured against only one surface, the biochip surface [4-7]. In addition, other typical affinity assays like microcalorimetry or the agglutination do not take the effect of multivalent surfaces into account. However, merely studying affinity of dissolved ligands does not always capture the biological situation, e.g., when a layer of surface anchored carbohydrates of the glycocalyx interacts with also surface anchored membrane receptors.

In order to directly study the interaction of surface anchored carbohydrate ligands with a receptor surface, we developed a new method using carbohydrate coated hydrogel particles, also called soft colloidal probes (SCPs) that undergo mechanical deformation when coming into contact a with receptor surface [8-11]. The mechanical deformation is a measure of the sum over all specific interactions between the carbohydrate ligand and the protein receptor layer. Detection of the interaction energy is straight forward using the contact area of the SCP with the protein layer via reflection interference contrast microscopy (RICM) (Figure 1). The contact area can be related to the specific adhesion energy W_{adh} of the SCP adhering to a surface using the JKR Model:

$$a^3 = 6\pi \frac{W_{adh}}{E_{eff}} R^2 \tag{1}$$

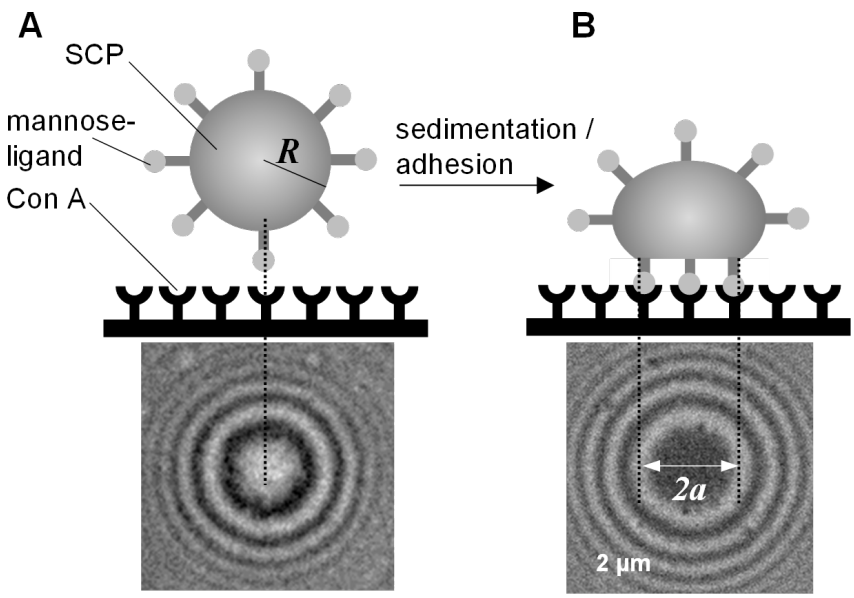

Figure 1: SCP adhesion measurement sketch (top): A mannose-functionalized PEG-SCP sediments onto a Concanavalin A (ConA) receptor surface (left), then mannose units bind to ConA inducing adhesion and mechanical deformation of the SCP (right). The contact area of the SCP can be read out via reflection interference contrast microscopy (RICM) from the central circular interference minimum (bottom).

where a is the radius of contact, R is the radius of the SCP and $E_{eff} = [4E/3(1-\nu^2)]$ its effective elastic modulus, with ν the Poisson ratio and E the Young's modulus of the SCP.

Importantly, the SCP and the receptor surface represent a reduced cell-matrix model system that roughly mimics the biological context and thus allows studying the effect of various parameters affecting the interaction between surface anchored binding partners, e.g., the mechanical flexibility of the interfaces, the surface presentation and density of the binding partners. In this work, we focus on the latter aspects. More specifically, we study the effect of linker type and ligand density on the interaction between sugar-ligands and receptors on a surface. It is well known that multivalency and linker type can drastically affect the interaction on a single molecule level [12]. Since interactions between surfaces are multivalent per se it is important to also study the effect of parameters that may affect this "surface multivalency" and the resulting interaction strength.

In the previous studies, we looked at the interactions between the ConA receptor and its natural sugar ligand mannose. The receptor was immobilized on a glass coverslip and mannose ligands were coupled on the SCPs. Attachment of the sugar ligands on the SCP was achieved by coupling of amine-functionalized mannose to carboxy-functionalized SCPs. Carboxy groups on the SCP were introduced by a radical grafting process where incubation of the PEG microgels with benzophenone and acrylic acid lead to poly(acrylic acid) grafts on the PEG backbone.

Using this model system, we could already show that the mechanical flexibility of the interface presenting the sugar ligands has a pronounced effect on the resulting adhesion energy [8]. This was shown by varying the length of poly(ethylene glycol) chains that establish the soft hydrogel matrix of the SCPs and measuring the interactions between mannose SCPs and ConA surfaces.

In this work, we aim to control the sugar ligand concentration, density and linking chemistry on the SCPs by adopting the radical grafting process for different acrylic monomers. We hypothesize that the use of acrylic acid (AA), methacrylic acid (MA) and crotonic acid (CA), respectively, will lead to different grafting length and grafting density. For example, MA has a much higher reactivity compared to AA and CA. This should lead to long and dense MA grafting to the PEG SCPs. The reactivity of AA is comparatively lower thus increasing the probability for chain transfer reactions and shorter grafts [13]. CA cannot be homopolymerized through free radical polymerization, meaning that only single CA units will be attached to the PEG chains [14]. However, other phenomena may also affect the resulting grafting density such as different tendency of grafting from and grafting to between the different monomers. Thus, in the first part, we study the functionalization degree of the PEG-SCPs for MA, AA and CA grafts via titration and zeta potential measurements. These systems will then be functionalized with mannose ligands to obtain PEG-SCPs with varying ligand density. In the second part, we study the adhesion energy of the functionalized SCPs on ConA receptor-functionalized glass slides. Depending on the type of grafting process and the concentration of functional groups attached to the SCP, the differences in adhesion energy due to surface presentation and density of mannose ligands are discussed.

Results and Discussion

PEG-microgel synthesis and carboxylic acid grafting

We started out synthesizing carboxylic acid-functionalized PEG particles with varying functionalization degree by grafting three types of carboxylic acid monomers to the PEG network: methacrylic acid (MA), acrylic acid (AA) and crotonic acid (CA). Special emphasis is on the precise control of the functionalization degree that ultimately controls the sugar ligand group concentration for adhesion energy measurements. Therefore, the carboxylic acid-functionalized particles were analyzed by titration with toluidine blue O (TBO) and zeta potential measurements. In addition, we explore the effect of the reaction conditions, such as concentration of reagents or UV irradiation time on the functionalization degree of CA-functionalized particles.

Comparison of the functionalization of PEG SCPs with different carboxylic acid monomers

Recently, we introduced micrometer-sized SCPs composed of crosslinked PEG-diacrylamide hydrogels as probes [15]. Here, we used the ability of PEG-diacrylamide to phase separate from an aqueous solution to form microscopic droplets by means of precipitation using sodium sulfate as a kosmotrope. At concentrations of 5 mg/mL PEG-diacrylamide and 1 M sodium sulfate, the polymer–water interactions are less favorable than polymer–polymer and water–water interactions, thus polymer droplets form which are then UV polymerized. Using neutral and inert PEG scaffolds for studying specific adhesion is advantageous because it reduces nonspecific interactions and also complicates the bioconjugation. To deal with this problem, we adjusted a surface chemistry route including radical generation at the PEG backbone by UV irradiation [15]. This enabled the addition of unsaturated carboxylic moieties onto the PEG scaffold (Scheme 1).

It is known that benzophenone can absorb the energy of photons to excite the electron in its carbonyl group from ground state

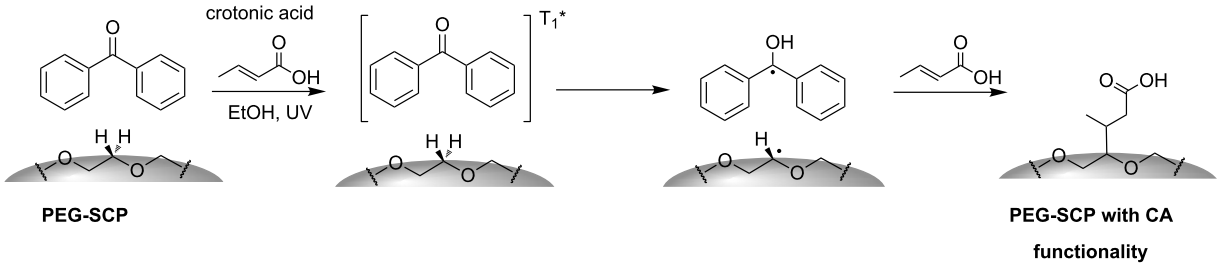

Scheme 1: PEG functionalization is based on radical benzophenone photochemistry and subsequent addition of carboxylic monomers (CA is depicted as an example). In the first step, benzophenone abstracts hydrogen from the polymer surface to generate surface radicals. In the presence of α,β-unsaturated carboxylic acids, the macroradical initiates grafting via the radical-polymerization mechanism.

(S0) to the excited state (S1) or (S2) depending on the wavelength used. Subsequently, the excited electron can go to the triple state (T1) through intersystem crossing (ISC). At the T1 state, the benzophenone molecule has an excited electron which is highly reactive, and can abstract a hydrogen atom from the PEG backbone. The abstracted hydrogen atom generates a radical on the PEG-backbone and a semipinacol radical on the benzophenone carbonyl group [16]. In the presence of α,β-unsaturated carboxylic acids, the PEG-backbone radical attacks the unsaturated carbon bond resulting in the grafting of the carboxylic acid on the PEG-SCPs.

The grafting density of MA, AA and CA on PEG-SCPs was studied under the same reaction conditions for the different carboxylic acids. As a first test, the presence of carboxylic acid groups in the SCPs was evaluated by ATR–FTIR (Figure 2A). An increase of the peak around 1720 cm^{-1} can be observed that corresponds to the signal of the carbonyl group of the carboxylic acid molecule, showing the successful grafting of the acid molecules and that the carbonyl density increases from CA, AA to MA. In order to quantify the carboxylic acid group concentration, a colorimetric titration was carried out using TBO. As expected, the CA grafting resulted in the lowest density, AA grafting intermediate density, and MA grafting in largest density of carboxylic acid groups. The overall ratio for CA, AA and MA was 1:2.4:5.4. (Figure 2B). Zeta potential measurements confirmed this trend (see Supporting Information File 1, S1). It is important to note that not only the surface of the SCPs is functionalized with carboxlic acid groups, but the whole bulk of the particles. This was confirmed via confocal Raman microscopy indicating a homogeneous distribution of functional groups (Supporting Information File 1, S2).

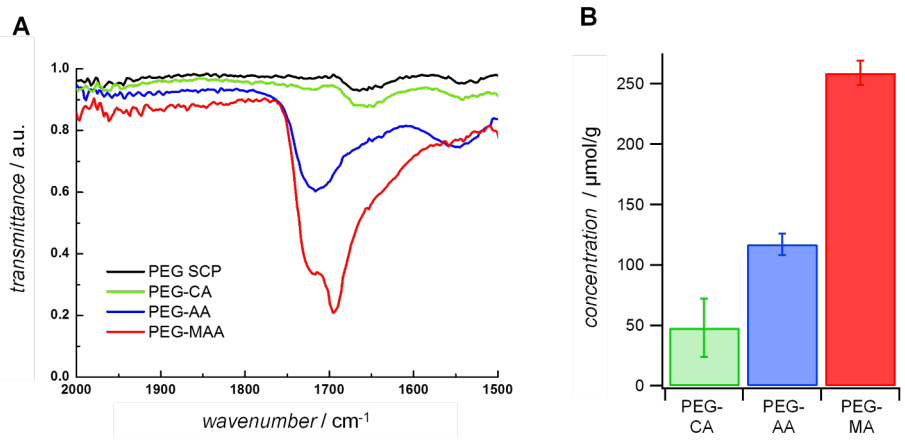

Figure 2: A) ATR–FTIR spectroscopy signifying carbonyl group at around 1720 cm^{-1} and successful grafting; B) Results of the TBO titration of the grafting of carboxylic acid onto PEG SCPs.

The observed increase in grafting density of MA over AA is well established in the literature [13,17,18]. For example, Yang et al. [17] compared the grafting density of MA and AA on low density polyethylene (LDPE) films through measuring the weight increase of the film. With the same reaction conditions and reaction time, the weight increase of methacrylic grafted film was 2 to 5-folds heavier than acrylic acid grafted films, which is in good agreement with our results. The increased grafting reactivity of MA can be explained by the substituent on the double bond. The methyl group of MA may activate the double bond due to hyperconjugation. In addition, the activation energies for polymerization of MA is lower than for AA [19], leading to longer MA grafting units compared to AA. Another interesting fact is that the kinetics of polymerization initiation is slower compared to propagation in case of AA units whereas the opposite is the case for MA. This behavior further increases the length of MA grafts compared to AA. Furthermore, we assume that MA undergoes a strict 'grafting from' mechanism, whereas for AA there is the possibility of a 'grafting onto' mechanism. This is because we observed AA homopolymers in the reaction mixture after particle functionalization as measured via HPLC, whereas no such MA polymers were found (data not shown). It appears that such free poly(acrylic acid) species could attach via a grafting onto mechanism. On the other hand, due to the conformation of the polymer in solution and the steric hindrance, the grafting density should be lower for grafting onto in comparison to the grafting from.

In case of CA it is generally believed that it cannot be homo polymerized via free radical polymerization [14]. CA contains a 1.2-disubstituted ethylene exhibiting high steric hindrance, which might explain the low reactivity compared to the MA and AA. Therefore, radicals at the β-carbon may not be able to further react with other monomer molecules leaving only one CA molecule per graft of the PEG backbone. Since the overall reaction conditions were kept constant for MA, AA and CA grafting, it is clear that CA shows the lowest grafting density due to the expected inability to homo polymerize.

Influence of the reaction conditions for crotonic acid grafting

As CA forms just one carboxy group per radical on the PEG-SCPs, the CA functionalization procedure should give the best control over the actual number of attached functional groups. In order to control the density of CA grafting, several parameters such as, monomer concentration, initiator concentration, irradiation time and reaction conditions, were taken into account. Our intermediate goal was to maximize the CA concentration on the PEG backbone. Therefore, we increased the amount of CA from 1.7 mol/L to 3.5 mol/L (solubility maximum), while the concentration of the other reactants staid constant. As shown by TBO titration, the grafting density on the order of 52 ± 5 μmol/g was invariant to the CA reaction concentration (see Table 1). This suggests that under the applied CA concentration range the grafting density might be limited by the radicals formed on the PEG network. The amount of radicals formed on the PEG chain is not affected by the presence of CA, but rather by the benzophenone concentration which was kept constant so far. Therefore, we varied the benzophenone concentration from 60 mmol/L to 420 mmol/L. From the results shown in Table 1, it can be seen that the benzophenone concentration indeed affected the final functionalization degree. Overall, an increase by 50% was observed when comparing reactions with the lowest and highest amount of benzophenone. Therefore, CA grafting increases with increasing benzophenone concentration, confirming that benzophenone concentration affects the formation of surface radicals, which also suggests a grafting from mechanism for CA.

Table 1: Variation of the crotonic acid and benzophenone concentration and its influence on the grafting. The functionalization degree increases with increasing benzophenone concentration regardless of the crotonic acid concentration.

CA concentration (mol/L)	Benzophenone concentration (mmol/L)	Functionalization degree (μmol/g)
1.7	60	36 ± 2
	140	48 ± 10
	420	57 ± 5
3.5	60	37 ± 2
	140	52 ± 5
	420	60 ± 3

The benzophenone concentration has an effect on the CA functionalization degree but the tunable range is still narrow. Therefore, we varied the irradiation time as this might lead to a more sustained grafting process. We varied the irradiation time (900 s, 2700 s and 3600 s) at concentrations of 140 mM benzophenone and 1.7 M CA and determined the functionalization degree by TBO titration. We found a rather modest increase by 14% with longer irradiation times from 900 s to 3600 s, respectively. From this result we conclude that at an irradiation time of 2700 s, the reaction is completed and further irradiation does not further increase the functionalization degree (Figure 3A). This suggests that at this point benzophenone was completely consumed in form of benzopinacol and no further grafting could occur. To improve the availability of benzophenone in the reaction mixture we replenished the reaction solution with new reactants, i.e., benzophenone and CA at 140 mM and 1.7 M, respectively (Figure 3B). After the PEG-SCPs were

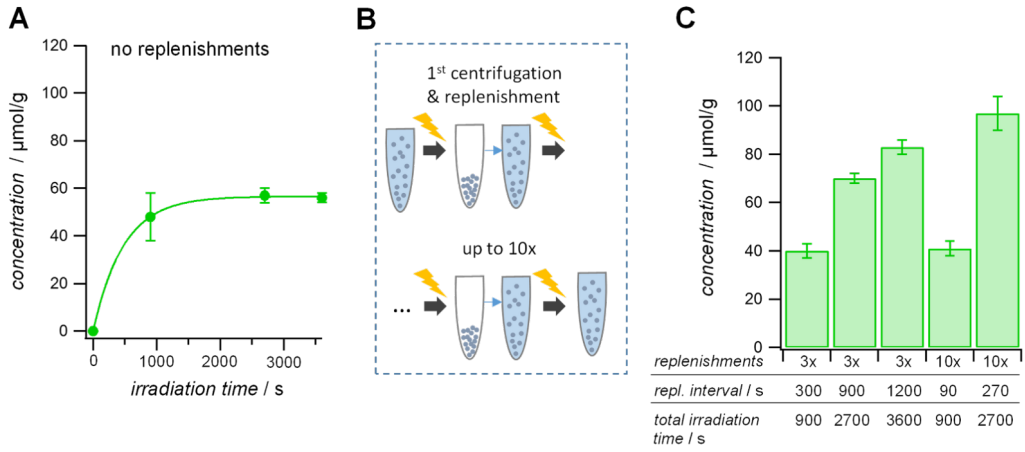

Figure 3: A) CA functionalization degree as a function of the irradiation time. The solid line represents an exponential fit in indicating the effective time constant of CA grafting. B) Graphical scheme of the reactants replenishing procedure. The solution of benzophenone and CA was replaced with a fresh solution after different irradiation intervals up to ten times. C) Results of the solution exchange procedure. By refreshing the solution the functionalization degree increases.

irradiated, the reaction solution was exchanged with fresh reactants via centrifugation, decantation and re-dispersion of the PEG-SCPs before the next irradiation step. Using this approach, we varied the number of replenishing steps as well as irradiation interval between the replenishing step and measured the resulting functionalization degree (Figure 3C).

From the results in Figure 3C, it can be seen that with replenishing the solution, the CA concentration on SCPs was improved significantly. Especially, when the solution was exchanged at intervals of 200–900 s the grafting was rather efficient. For smaller intervals (e.g., 90 s) there is still enough non-reacted benzophenone so that even ten times replenishing did not show a significant increase over non-replenished solution that was irradiated for the same time. The grafting becomes rather inefficient if the replenishing interval is larger than 900 s because then most of the benzophenone has been already consumed before the replenishing step. This can be seen from Figure 3A showing the functionalization degree of PEG particles as a function of time. At around 900 s the exponential fit begins to level off significantly indicating that most of the benzophenone has been consumed already. Therefore replenishing at 1200 s intervals proved to be less efficient as compared to 270 s intervals (Figure 3C). Overall, we found that replenishing at about 200–600 s was the best option in order to increase the CA functionalization degree and to keep both the reaction time and number of replenishing steps in a reasonable range. Using this procedure, we achieved carboxylic acid functionalization degrees similar to AA or MA. This allows for comparative SCP binding studies on the type of grafts introduced to the PEG network.

Adhesion studies with mannose-functionalized PEG-SCPs

Functionalization of carboxylate-functionalized PEG-SCPs with mannose

To study the influence of the degree of functionalization and the grafting type on particle adhesion, we prepared five different SCP systems functionalized with different concentration of carboxylic acid groups: PEG-MA, PEG-AA, PEG-CA_{low}, PEG-CA_{middle}, PEG-CA_{high}. PEG-MA and PEG-AA are SCPs having a polyacid chain on the backbone, whereas the tree different PEG-CA SCPs present single acid moieties attached to the PEG network. As shown in the previous chapter, the functionalization degree of CA was tuned by varying the reaction conditions. The resulting concentrations of carboxylic acids in the PEG network are detailed in Table 2.

Table 2: Results of the functionalization of the carboxylate-functionalized particles with mannose.

PEG-SCP type	Concentration of carboxyl groups (µmol/g)	Concentration of mannose groups (µmol/g)
PEG-CA_{low}	36 ± 2	22 ± 6
PEG-CA_{middle}	57 ± 5	44 ± 8
PEG-CA_{high}	97 ± 7	89 ± 9
PEG-AA	117 ± 9	56 ± 14
PEG-MA	259 ± 24	193 ± 29

In order to study the specific interactions between the mannose ligands and ConA receptors, we used aminoethyl-linked mannose and coupled it via standard coupling chemistry on the

PEG SCPs [8] (Supporting Information File 1, S5). The number of mannose functionalities and therefore the degree of functionalization can be directly measured via UV titration with TBO of the unreacted carboxy groups and compared to the pure carboxylate-functionalized probes (Supporting Information File 1, S3). The coupling of mannose to carboxylic acids was not quantitative, not all carboxylic acid would couple to mannose units. However, controlled variation of the mannose group concentration on SCPs could still be achieved due to the significant decrease of the carboxylic acid groups after coupling revealing the number of attached mannose ligands. The controlled variation of mannose units will be used to further investigate the adhesion behavior in the following section.

Determination of specific adhesion via SCP as function of mannose ligand density

For the SCP adhesion measurements, we used ConA-functionalized glass coverslips. We expect a dense packing of the receptor protein on the glass coverslips using a covalent attachment protocol as described earlier [15]. In a typical binding assay, the SCPs were dispersed in buffer and sediment onto the receptor surface (Figure 1). Upon contact with the ConA receptors, ligands and receptors bind and the SCPs adhere to the receptor surface. Since they are soft, they formed a distinct contact area which can be evaluated using the JRK approach to calculate the adhesion energy W, see Equation 1 (Supporting Information File 1, S6). Qualitatively speaking, the larger the contact area between the mannose presenting SCPs and ConA surface the larger the adhesion energy. When measuring specific adhesion between ligands and receptors, it is essential to carry out control experiments to ensure that the adhesion is indeed due to specific interactions. Therefore, as control an inhibition experiment was performed by adding α-methyl-D-mannose as low molecular weight inhibitor blocking the binding sites of ConA. As a result, all probes detached from the surface and do not adhere anymore indicating that the interaction between SCPs and ConA surface was specific [15].

With regard to the SCP adhesion assay we observed the largest contact in case of PEG-MA SCPs due to the high degree of functionalization, whereas PEG-AA SCPs showed similar adhesion energies to PEG-CA SCPs of similar degree of functionalization (Figure 4A). This could be explained by the fact that PEG-AA and PEG-CA SCPs exhibit a similar density of mannose units. Importantly, when comparing the mannose density on the different SCPs with the resulting adhesion energy we find a simple linear relation (Figure 4B). This suggests that the overall specific interaction of SCP-bound mannose and the ConA layer is simply directly proportional to the density of mannose units per graft. In other words, the affinity of the individual mannose units is the same between AA, CA and MA-SCPs and does not depend on the grafting characteristics, i.e., the length of grafts and the number of attached mannose units. This is an important result, because a potentially multivalent arrangement of mannose on AA and CA grafting units could lead to chelate- or subsite binding at the ConA receptor enhancing the affinity of individual mannose units. In contrast to other work on similar multivalent scaffolds like oligomers, dendrimers or nanoparticles [20-22] where such chelate- and subsite-binding modes were discussed, our SCP-assay did not indicate enhancement of affinity due to multivalent binding modes for any grafting type. This is surprising as for all SCP systems the density of mannoses is large enough to bind to multiple ConA binding sites: For example, in case of the

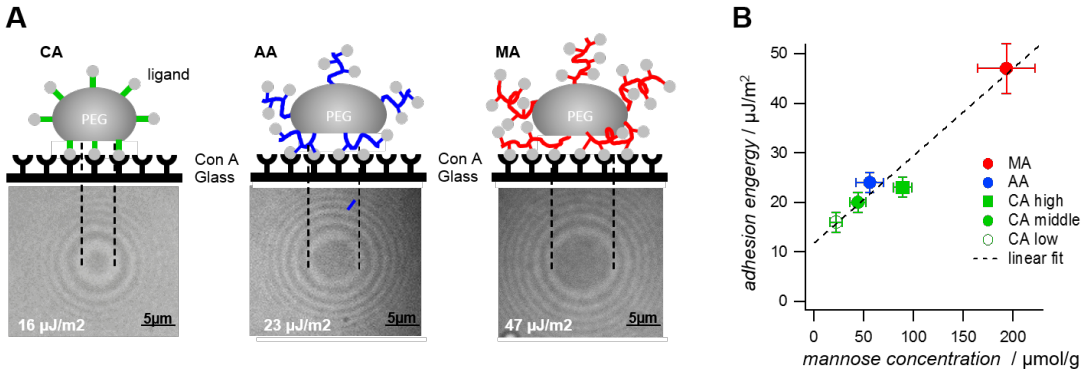

Figure 4: A) Increased mannose densities as schematically shown lead to increased contact areas. For the PEG-CA particles only one mannose unit is attached to the particles per CA graft, whereas for PEG-MA and PEG-AA polyacid chains are present on the surface. B) Plot of the adhesion energy vs mannose concentrations for SCPs with three different grafting types and three different PEG-CA SCPs with varying density of grafting units PEG-CA_{low} PEG-CA_{middle} PEG-CA_{high} (Table 2). The linear fit (R^2 = 0.75) suggests that mannose units have the same affinity regardless of grafting type. Intersection with the y-axis shows indicates the unspecific adhesion energies of unmodified SCPs (data not shown).

PEG-MA the density of mannose was ≈200 μmol/g, which translates to ≈4 grafted mannose units per PEG chain (average MW 8000 kDa). Considering the hydrodynamic radius of a PEG 8000 chains of ≈10 nm [8] this would mean that the spacing of mannose units was on the order of 2 nm and therefore sufficiently high for potential multivalent binding to the binding pockets of ConA (separated by ≈6.5 nm). The absence of a multivalency effect could be explained by the large dissociation rates of mannose–ConA complexes prohibiting chelate or sub-site binding. This is caused by the generally low affinity between sugars and receptors and possibly also by the high flexibility of the polymeric mannose linkers [9]. High molecular flexibility causes a high degree of conformational entropy that negatively affects complex formation between ligands and receptors [23]. Also the design of the binding assay could lead to different conclusions on multivalency effects. In typical inhibition/competition affinity assays steric shielding is the main contributor to the observed multivalency effect [24,25] in particular for large polymeric scaffolds. In direct binding assays, as conducted here, steric shielding is not detected, which could explain the different outcome in terms of binding affinity per mannose unit in comparison to studies using inhibition/competition for binding affinity characterization [20-22].

Conclusion

In this work, we successfully grafted three different carboxylic acid monomers (methacrylic acid, acrylic acid and crotonic acid) on PEG-based SCPs. Methacrylic acid grafts on PEG microparticles result in long poly(methacrylic acid) chains, acrylic acid grafts in shorter oligo(acrylic acid) chains, and crotonic acid grafts in the form of single crotonic acid molecules. Thus, the differently functionalized SCPs vary in both, in their degree of functionalization as well as the multivalent presentation of functional groups (oligo/polymer chains vs single functional groups). Further functionalization of the SCPs with mannose ligands gives a series of sugar-functionalized SCPs with varying degree of functionalization and variation of ligand presentation. The sugar SCPs were then applied in the previously developed SCP-RICM adhesion assay which can be considered as model systems for the interaction of a cell glycocalyx with a protein receptor surface.

The results show that a high mannose concentration generally leads to increased adhesion energies. Although the mannose density was in principle sufficient to form multivalent binding with ConA receptors for all SCP systems, we did not observe an enhancement of binding affinity per mannose unit when increasing the mannose concentration on the particles. This suggests that the surface interactions between mannose and ConA did not lead to multivalent interactions in the sense of a chelate- or subside binding complex. This could be caused by the flexible arrangement of mannose units on the polymer scaffold or insufficient density of the binding partners. In future work we will therefore further increase the density of sugar units, which would ensure closer mimics of the highly dense presentation of ligands within the glycocalyx. Such studies could reveal the optimal ligand surface density and spacing in order to maximize receptor adhesion and selectivity.

Experimental

Materials

Benzophenone was purchased from Acros Organics, benzotriazole-1-yloxytripyrrolidinophosphonium hexafluorophosphate (PyBOP) and 1-hydroxybenzotriazole (HOBt) from IRIS. All other chemicals were purchased from Sigma-Aldrich.

General procedure for the synthesis of carboxylated PEG SCPs

PEG microparticles were synthesized by precipitation polymerization in a similar manner as described in ref. [9]. Briefly, PEG-diacrylamide (M_n = 8000 Da) [26] (50 mg, 6.3 μmol) was dispersed in a 1 M sodium sulfate solution (10 mL). The UV photoinitiator Irgacure 2959 was added at a concentration of (1 mg, 4.5 μmol) to the dispersion and vigorously shaken and photopolymerized with UV light. Water was exchanged by ethanol and benzophenone (250 mg, 1.4 mmol) and an unsaturated carboxylic acid (acrylic acid (1.2 mL, 17.7 mmol), methacrylic acid (1.5 mL, 17.7 mmol) or crotonic acid (1.5 g, 17.7 mmol) were added and the mixture was flushed with argon for 30 s and irradiated with UV light for 900 s. The microparticles were washed with ethanol 3 times and stored in ethanol. The resulting particles were 20–100 μm in diameter [15].

Quantification of carboxylic acid in PEG-SCPs

The carboxylic acids in the PEG-SCPs were quantified by titration with TBO, zeta potential measurements and IR spectroscopy. The TBO measurement was conducted as follows. 1.5 mL of PEG-SCP dispersion were centrifuged and a solution of 0.5 mM TBO solution (pH 10.3) was added to the pellet and incubated for 5 h. After several washing steps with sodium hydroxide solution (pH 10.3) the dispersion was centrifuged/washed in 1:1 acetic acid/water mixture collecting defined volumes of the supernatant. The amount of hydrogel was determined gravimetrically after drying the SCPs and the amount of carboxylic groups was determined photometrically using the released TBO in the supernatant.

For zeta potential measurements 1 mL of carboxylic acid-functionalized PEG-SCPs were injected into a Malvern DTS1060 disposable folded capillary cell. The Zeta-potential was characterized with a Malvern Instruments Nano Series ZS ZEN3500

Zetasizer at 25 °C in Milli-Q water (Type I Water). Each sample was tested 3 times and the averaged value was recorded as the the Zeta-potential of this sample.

General procedure for the synthesis of PEG-Man microparticles

In a similar manner as described in [9] ethanol was exchanged with DMF through several washing steps and the carboxylate-functionalized microparticles (0.03 g) were left in 10 mL of DMF. PyBOP (0.728 g, 1.40 mmol), HOBt (0.097 g, 0.70 mmol) and triethylamine (195 µL, 1.40 mmol) were added to activate the carboxylic groups. This suspension was shaken for 15 min at rt, then aminoethyl-linked acetyl protected mannose [8,8] (0.050 g, 0.12 mmol) was added. The mixture was allowed to react for 3 h at rt. The microparticles were centrifuged and washed 3 times with DMF and 3 times with methanol. Sodium methoxide (0.004 g, 0.08 mmol) were added and reacted for 1 h at rt for deprotection. Then, the microparticles were centrifuged at 5000 rpm for 10 min and washed 3 times with methanol and 3 times with pure water.

Determination of the SCPs elastic modulus

To calculate the adhesion energies of the SCPs, the elastic modulus of the particle is required (see Equation 1). AFM force spectroscopy with a NanoWizard 3 system (JPK instruments AG, Berlin, Germany) was performed to determine the elastic modulus of the microparticles. As AFM probe a glass bead with a diameter of 5.1 µm was glued with an epoxy glue onto a tipless, non-coated cantilever (spring constant 0.32 N/m; CSC12, NanoAndMore GmbH). Several force curves were recorded from different particles and analyzed with an appropriate contact model developed by Glaubitz et al. [27]. The elastic moduli of PEG-SCPs were 32 ± 5 kPa and showed no systematic variation with regard to grafting type or degree of mannose functionalization.

Immobilization of ConA to glass surfaces

ConA was bound to coverslips as previously described [8]. Briefly, coverslips (Ø 24 mm, ≈0.17 mm thickness) were used as glass surface (Thermo scientific, Germany) and cleaned prior to use by washing with isopropanol and piranha solution (96% H_2SO_4 and 30% H_2O_2, 3:1). The coverslips were rinsed with ultra-pure water and dried in a nitrogen stream. Amine surfaces were prepared via chemical vapor deposition of 3-aminopropyltriethoxysilane (APTES) (50 µL) on a freshly cleaned coverslip were placed in a desiccator and vacuum was applied for 1 min. The desiccator was sealed and the coverslips were left for 1 h to react with the vapor. The coverslips were rinsed with Milli-Q water and dried with nitrogen. Then the coverslips were placed in PBS buffer pH 7.4 containing 2.5% glutaraldehyde for 30 min followed by washing with Milli-Q water and drying. ConA (0.2 mg mL^{-1}) in PBS buffer pH 7.4 was placed on the aldehyde-functionalized surfaces for 1 h [19]. and prior to the measurements washed with lectin binding buffer (10 mM HEPES pH 6, 50 mM NaCl, 1 mM $MnCl_2$, 1 mM $CaCl_2$).

Reflection interference contrast microscopy (RICM)

RICM on an inverted microscope (Olympus IX73, Germany) was used to obtain the contact area between the microparticles and a hard glass surface. For illumination an Hg-vapor arc lamp was used with a green monochromator (546 nm). A Zeiss Antiflex 63× NO 1.25 oil-immersion objective, additional polarizers to avoid internal reflections and a Zeiss AxiocamHRm camera were used to image the RICM patterns. To conduct the JKR measurements of the adhesion energies, both the contact radius and the particle radius were measured. Image processing and data analysis were done using the image analysis software ImageJ (public domain NIH) and the mathematical software OriginPro (OriginLab, USA). 1 mL of lectin binding buffer pH 6 was added to the ConA-functionalized surface and PEG-Man SCPs were spread into the solution. The particles were sedimented and the contact radius and the particle radius were measured. Inhibition of the interaction was done by adding of α-methyl-D-mannose (300 µL, 1 mg mL^{-1}) in lectin binding buffer to the suspension and well mixed so that all bound particles were detached from the surface.

Supporting Information

Supporting Information File 1

Additional experimental and analytical data.
[http://www.beilstein-journals.org/bjoc/content/supplementary/1860-5397-11-82-S1.pdf]

Acknowledgements

The authors thank A. Laschewsky and T. Pompe for support and helpful discussions and A. Masic for RAMAN spectroscopy. Financial support was granted by the German Research Foundation (DFG) through the Emmy Noether program HA5950/1-1, through Research Grant SCHM 2748/3-1 as well as the collaborative research center (SFB) 765 at Freie Universität Berlin and Max Planck Society.

References

1. Varki, A. *Essentials of glycobiology;* Cold Spring Harbor Laboratory Press: New York, NY, U.S.A., 2009.
2. Kiessling, L. L.; Grim, J. C. *Chem. Soc. Rev.* **2013,** *42,* 4476–4491. doi:10.1039/c3cs60097a

3. Bernardi, A.; Jiménez-Barbero, J.; Casnati, A.; De Castro, C.; Darbre, T.; Fieschi, F.; Finne, J.; Funken, H.; Jaeger, K.-E.; Lahmann, M.; Lindhorst, T. K.; Marradi, M.; Messner, P.; Molinaro, A.; Murphy, P. V.; Nativi, C.; Oscarson, S.; Penadés, S.; Peri, F.; Pieters, R. J.; Renaudet, O.; Reymond, J.-L.; Richichi, B.; Rojo, J.; Sansone, F.; Schaffer, C.; Turnbull, W. B.; Velasco-Torrijos, T.; Vidal, S.; Vincent, S.; Wennekes, T.; Zuilhof, H.; Imberty, A. *Chem. Soc. Rev.* **2013,** *42,* 4709–4727. doi:10.1039/C2CS35408J
4. Cooper, M. A. *Label-Free Biosensors: Techniques and Applications;* Cambridge University Press: Cambridge, United Kingdom, 2009.
5. Daniels, J. S.; Pourmand, N. *Electroanalysis* **2007,** *19,* 1239–1257. doi:10.1002/elan.200603855
6. Guo, X. *J. Biophotonics* **2012,** *5,* 483–501. doi:10.1002/jbio.201200015
7. Ferreira, G. N. M.; da-Silva, A.-C.; Tomé, B. *Trends Biotechnol.* **2009,** *27,* 689–697. doi:10.1016/j.tibtech.2009.09.003
8. Pussak, D.; Ponader, D.; Mosca, S.; Ruiz, S. V.; Hartmann, L.; Schmidt, S. *Angew. Chem., Int. Ed.* **2013,** *52,* 6084–6087. doi:10.1002/anie.201300469
9. Pussak, D.; Ponader, D.; Mosca, S.; Pompe, T.; Hartmann, L.; Schmidt, S. *Langmuir* **2014,** *30,* 6142–6150. doi:10.1021/la5010006
10. Schmidt, S.; Reinecke, A.; Wojcik, F.; Pussak, D.; Hartmann, L.; Harrington, M. J. *Biomacromolecules* **2014,** *15,* 1644–1652. doi:10.1021/bm500017u
11. Martin, S.; Wang, H.; Hartmann, L.; Pompe, T.; Schmidt, S. *Phys. Chem. Chem. Phys.* **2015,** *17,* 3014–3018. doi:10.1039/C4CP05484A
12. Badjic, J. D.; Nelson, A.; Cantrill, S. J.; Turnbull, W. B.; Stoddart, J. F. *Acc. Chem. Res.* **2005,** *38,* 723–732. doi:10.1021/ar040223k
13. Osada, Y. *J. Polym. Sci., Part A: Polym. Chem.* **1979,** *17,* 3485–3498. doi:10.1002/pol.1979.170171107
14. Miller, M. L.; Skogman, J. *J. Polym. Sci., Part A: Gen. Pap.* **1964,** *2,* 4551–4558. doi:10.1002/pol.1964.100021023
15. Pussak, D.; Behra, M.; Schmidt, S.; Hartmann, L. *Soft Matter* **2012,** *8,* 1664–1672. doi:10.1039/C2SM06911C
16. Schneider, M. H.; Tran, Y.; Tabeling, P. *Langmuir* **2011,** *27,* 1232–1240. doi:10.1021/la103345k
17. Yang, W. T.; Rånby, B. *Macromolecules* **1996,** *29,* 3308–3310. doi:10.1021/ma9515543
18. Li, G.; He, G.; Zheng, Y.; Wang, X.; Wang, H. *J. Appl. Polym. Sci.* **2012,** *123,* 1951–1959. doi:10.1002/app.34683
19. Nho, Y. C.; Jin, J.-H. *J. Appl. Polym. Sci.* **1997,** *63,* 1101–1106. doi:10.1002/(SICI)1097-4628(19970228)63:9<1101::AID-APP1>3.0.CO;2-L
20. Ponader, D.; Wojcik, F.; Beceren-Braun, F.; Dernedde, J.; Hartmann, L. *Biomacromolecules* **2012,** *13,* 1845–1852. doi:10.1021/bm300331z
21. Papp, I.; Dernedde, J.; Enders, S.; Riese, S. B.; Shiao, T. C.; Roy, R.; Haag, R. *ChemBioChem* **2011,** *12,* 1075–1083. doi:10.1002/cbic.201000718
22. Wang, X.; Ramström, O.; Yan, M. *Adv. Mater.* **2010,** *22,* 1946–1953. doi:10.1002/adma.200903908
23. Mammen, M.; Choi, S.-K.; Whitesides, G. M. *Angew. Chem., Int. Ed.* **1998,** *37,* 2754–2794. doi:10.1002/(SICI)1521-3773(19981102)37:20<2754::AID-ANIE2754>3.0.CO;2-3
24. Fasting, C.; Schalley, C. A.; Weber, M.; Seitz, O.; Hecht, S.; Koksch, B.; Dernedde, J.; Graf, C.; Knapp, E.-W.; Haag, R. *Angew. Chem., Int. Ed.* **2012,** *51,* 10472–10498. doi:10.1002/anie.201201114
25. Vonnemann, J.; Liese, S.; Kuehne, C.; Ludwig, K.; Dernedde, J.; Böttcher, C.; Netz, R. R.; Haag, R. *J. Am. Chem. Soc.* **2015,** *137,* 2572–2579. doi:10.1021/ja5114084
26. Hartmann, L.; Watanabe, K.; Zheng, L. L.; Kim, C.-Y.; Beck, S. E.; Huie, P.; Noolandi, J.; Cochran, J. R.; Ta, C. N.; Frank, C. W. *J. Biomed. Mater. Res., Part B* **2011,** *98B,* 8–17. doi:10.1002/jbm.b.31806
27. Glaubitz, M.; Medvedev, N.; Pussak, D.; Hartmann, L.; Schmidt, S.; Helm, C. A.; Delcea, M. *Soft Matter* **2014,** *10,* 6732–6741. doi:10.1039/C4SM00788C

License and Terms

BEILSTEIN JOURNAL OF ORGANIC CHEMISTRY

Multivalent polyglycerol supported imidazolidin-4-one organocatalysts for enantioselective Friedel–Crafts alkylations

Tommaso Pecchioli, Manoj Kumar Muthyala, Rainer Haag* and Mathias Christmann*

Full Research Paper

Open Access

Address:
Institut für Chemie und Biochemie, Freie Universität Berlin, Takustraße 3, 14195 Berlin, Germany

Email:
Rainer Haag* - haag@chemie.fu-berlin.de; Mathias Christmann* - mathias.christmann@fu-berlin.de

* Corresponding author

Keywords:
Friedel–Crafts; homogeneous catalysis; hyperbranched polyglycerol; imidazolidin-4-one; multivalency

Beilstein J. Org. Chem. **2015,** *11,* 730–738.
doi:10.3762/bjoc.11.83

Received: 06 March 2015
Accepted: 29 April 2015
Published: 12 May 2015

This article is part of the Thematic Series "Multivalency as a chemical organization and action principle".

Associate Editor: D. Dixon

Abstract

The first immobilization of a MacMillan's first generation organocatalyst onto dendritic support is described. A modified tyrosine-based imidazolidin-4-one was grafted to a soluble high-loading hyperbranched polyglycerol via a copper-catalyzed alkyne–azide cycloaddition (CuAAC) reaction and readily purified by dialysis. The efficiency of differently functionalized multivalent organocatalysts **4a–c** was tested in the asymmetric Friedel–Crafts alkylation of *N*-methylpyrrole with α,β-unsaturated aldehydes. A variety of substituted enals was investigated to explore the activity of the catalytic system which was also compared with monovalent analogues. The catalyst **4b** showed excellent turnover rates and no loss of activity due to immobilization, albeit moderate enantioselectivities were observed. Moreover, easy recovery by selective precipitation allowed the reuse of the catalyst for three cycles.

Introduction

In nature, multivalent architectures, e.g., enzymes, bacteria or viruses, are responsible for cooperative interactions between different interfaces or molecules [1]. The realization of the concept of multivalency has attracted attention from different fields ranging from medicine and biochemistry [2] to supramolecular chemistry [3,4] and materials sciences [5]. However, applications in catalysis are still limited [6-8]. Recently, the use of polymeric support has stimulated the development of multivalent architectures for catalytic applications [9]. In general, both linear and various families of branched polymers such as dendrimers, dendritic-hybrid and hyperbranched polymers are used as macromolecular support for catalysis [10-12]. Linear polymers such as poly(ethylene glycol) (PEG) [13] or non-cross-linked polystyrene (NCPS) [14] are readily available but suffer from poor loading capacity, while in the case of dendrimers, the highest loading can be achieved due to their

extraordinary branching [15]. These well-defined molecules are soluble in many organic solvents and can combine the advantages of hetero- and homogeneous catalysis [16,17]. However, their tedious and multistep syntheses using either divergent or convergent approaches are arguably the reason for their limited use as support in organic synthesis [18]. To overcome these obstacles, a hybrid dendron-polymer might constitute a valuable alternative for high-loading platforms [19], despite the use of solid support such as polystyrene may lead to the disadvantage of operating in heterogeneous media. In contrast to the stepwise syntheses of dendrimers and dendron hybrids, the hyperbranched polymers can be easily obtained in kilogram scale through one-pot reactions [10], maintaining properties such as high loading capacity combined with the solubility characteristics of the respective dendrimers [20,21]. As a macromolecule, the supported catalyst can be recovered from the reaction media by selective precipitation, dialysis or filtration techniques, depending on its particular physical properties. Hyperbranched polymers like polytriallylsilane or polyglycerol have been used in a wide range of transformations including aldol condensations [22], Suzuki cross-couplings [23] and Diels–Alder reactions [24], to name a few, with metal complexes as catalytically active principle.

The advent of organocatalysis has allowed for selective C–C bond formation by using small organic molecules [25-31]. In contrast to metal complexes, chiral or achiral organocatalysts are easily attached on supports. They do not suffer from metal leaching and they can be reused more readily [32-36]. Moreover, their stability allows to perform reactions under mild and aerobic conditions and in the presence of water, both as co-solvent or the only solvent [37]. In the last years, several reports on water effects in organocatalytic reactions were published [38-42]. The use of supported catalyst has proven beneficial with regard to rate acceleration and increased selectivity due to formation of an aqueous microenvironment favored by the swelling properties of polymeric materials [43]. Particularly, in the case of dendritic proline derivatives [44-46] and *N*-alkylimidazole decorated dendron-hybrids [47], the presence of water was crucial for aldol and Baylis–Hillman reactions, as recently reported by Miller and Portnoy [48].

To the best of our knowledge, the immobilization of chiral organocatalysts on hyperbranched polymeric support has remained unexplored. Therefore, we decided to use hyperbranched polyglycerol (hPG) [49] as a polymeric support. The high local concentration of hydrophilic functionality present on its periphery is especially attractive since it might promote water coordination. These properties prompted us to investigate the effects of high-loading support in asymmetric organocatalysis.

The use of chiral imidazolidinones in organocatalysis has been extensively reported for a wide range of enantioselective reactions involving α,β-unsaturated aldehydes, such as the Diels–Alder reactions [50], 1,3-dipolar cycloadditions [51] and Friedel–Crafts alkylations [52,53]. To date, heterogenizations have been applied mainly in Diels–Alder reactions [54-61]. Nevertheless, Friedel–Crafts alkylations are recently emerging as a compelling field of study as reported by Pericàs [62] and others [58,60]. The simple approach providing an enantioselective entry to new C–C bonds allows for the use of readily available starting materials and can typically be carried out in THF–water mixtures. Our aim was to employ this transformation as a benchmark in order to explore the efficiency of novel multivalent architectures.

Herein, we describe the first immobilization of imidazolidin-4-one onto hyperbranched polyglycerol (hPG) and its application as multivalent organocatalyst.

Results and Discussion

To explore the synthetic utility of hPG in organocatalysis, we here report the synthesis and application of a series of three multivalent dendronized imidazolidin-4-ones PG-95 (**4a**), PG-57 (**4b**) and PG-30 (**4c**) representing different degrees of functionalization: 95% (**4a**), 57% (**4b**) and 30% (**4c**), respectively. An (*S*)-tyrosine-derived imidazolidin-4-one **5** was anchored to the polymeric support through a CuAAC reaction. Following the same strategy, a monovalent analog **8** bearing a G1 glycerol dendron tail was also prepared for comparison with the multivalent systems **4a–c** and evaluation of the possible presence of cooperative effects (Scheme 1).

Polyglycerol **1** (M_n = 9000 g/mol, loading OH = 13.5 mmol/g, PDI = 1.87) was obtained following a previously reported procedure by a one-step ring opening anionic polymerization (ROAP) [49]. The controlled mesylation on hPG **1** yielded **2a–c** (95%, 57% and 30% of functionalization, respectively (for details see Supporting Information File 1)), which were converted to the corresponding azides **3a–c** [63,64]. Azide **6** was prepared according to well-established protocols [65]. Consequently, we adopted the Sharpless–Fokin modification for the Huisgen azide–alkyne cycloaddition [66] to achieve the final immobilization of the modified imidazolidin-4-one onto the hyperbranched polymer and on the G1 dendron [65]. The progress of the reaction was monitored by IR spectroscopy and TLC. Purification of the products **4a–c** was carried out by washing with aqueous saturated EDTA solution followed by dialysis in methanol/chloroform mixture for 24 h, and then in methanol and chloroform, respectively, for additional 12 h each. The catalyst structures were confirmed by ^{1}H and ^{13}C NMR spectroscopy and the functionalization degrees of **4a–c** were

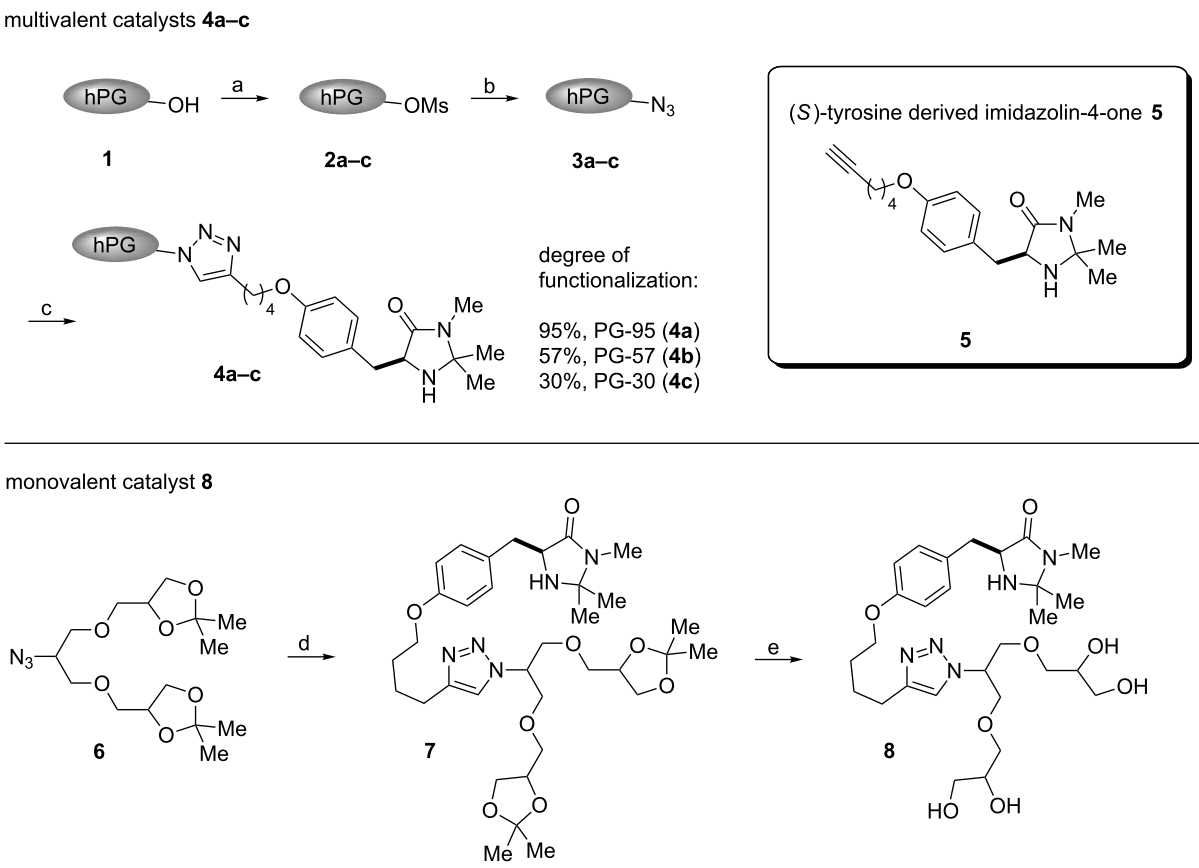

Scheme 1: Synthesis of hyperbranched polyglycerol-supported and G1 dendronized imidazolidin-4-ones **4a–c** and **8** using a CuAAC reaction. Reaction conditions: (a) **1** (1.0 equiv), MsCl (1.2 equiv, with respect to degrees of functionalization), pyridine, 25 °C, 16 h, 76% **2a**, 82% **2b** and 87% **2c**. (b) **2a–c** (1.0 equiv), NaN_3 (3.0 equiv), DMF, 65 °C, 72 h, 72% **3a**, 81% **3b** and 86% **3c**. (c) **3a–c** (1.0 equiv), **5** (2.0 equiv), $CuSO_4{\cdot}5H_2O$ (0.2 equiv), sodium ascorbate (2.0 equiv), THF/H_2O 3:1 (v/v), 25 °C, 48 h, 71% **4a**, 40% **4b** and 35% **4c**. (d) **6** (1.1 equiv), **5** (1.0 equiv), $CuSO_4{\cdot}5H_2O$ (0.1 equiv), sodium ascorbate (0.2 equiv), DIPEA (0.1 equiv), THF/H_2O 3:1 (v/v), 25 °C, 12 h, 70%. (e) **7**, Dowex 50, MeOH, reflux, 12 h, 95%.

determined by correlating the aromatic with the polyglycerol backbone protons (for details see Supporting Information File 1).

The synthesis of modified imidazolidin-4-one **5** started with (*S*)-tyrosine methyl ester hydrochloride (**9**). Following a protocol by Zhang and co-workers [58], **10** was obtained in good yield and subsequent anchoring of the linker was realized through *O*-alkylation on phenol **10**, leading to linkable catalyst **5** in excellent yield (Scheme 2).

The reactivity of the multivalent catalysts **4a–c** was investigated in the Friedel–Crafts alkylation of *N*-methylpyrrole (**11**) with α,β-unsaturated aldehydes reported by MacMillan [53]. To

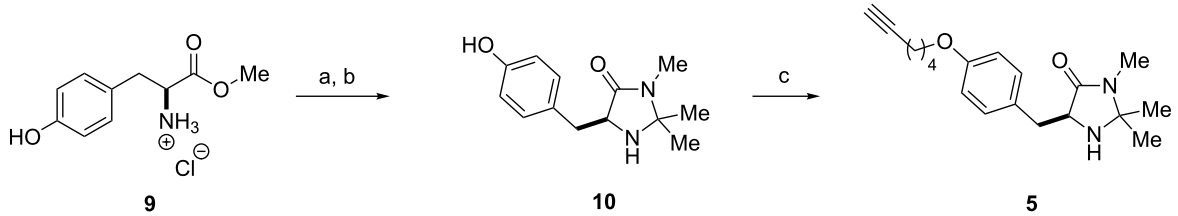

Scheme 2: Synthesis of tyrosine-based imidazolidin-4-one **5**. Reaction conditions: (a) **9** (1.0 equiv), $MeNH_2$ (5.0 equiv), EtOH, 25 °C, 20 h. (b) PTSA (0.01 equiv), acetone, MeOH, reflux, 18 h, 79% (2 steps). (c) **10** (1.0 equiv), NaH (1.1 equiv), 6-chloro-1-hexyne (1.3 equiv), TBAI (0.01 equiv), DMF, 25 °C, 16 h, 88%.

make the results comparable, we normalized the loading of the multivalent catalysts **4a–c** with respect to the number of single anchored imidazolidin-4-ones. Therefore, a constant number of catalytic units for each degree of functionalization was maintained. Initially, we decided to perform the reaction using *trans*-cinnamaldehyde (**12**) as a model substrate and trifluoroacetic acid (TFA) as an additive. In a preliminary survey on the water influence, a catalyst loading of 3.5 mol % in THF was selected to allow **4a** and **4b** to operate under homogeneous conditions, while in the same solvent **4c** proved to be less soluble (Table 1).

Table 1: Initial screening on the Friedel–Crafts alkylation of *N*-methylpyrrole (**11**) with *trans*-cinnamaldehyde (**12**).[a]

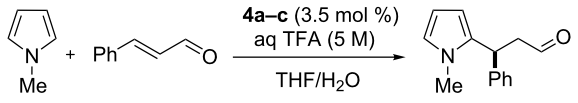

11 **12** **13**

Entry	Catalyst	THF/H_2O (v/v)	Yield (%)[b]	ee (%)[c]
1	PG-95 (**4a**)	100:0	38	66
2	PG-57 (**4b**)	100:0	56	69
3	PG-30 (**4c**)	100:0	26	56
4	PG-95 (**4a**)	95:5	62	68
5	PG-57 (**4b**)	95:5	68	66
6	PG-30 (**4c**)	95:5	32	59
7	PG-95 (**4a**)	90:10	42	59
8	PG-57 (**4b**)	90:10	38	60
9	PG-30 (**4c**)	90:10	45	54
10	PG-95 (**4a**)	0:100	–[d]	–
11	PG-57 (**4b**)	0:100	–[d]	–
12	PG-30 (**4c**)	0:100	–[d]	–

[a]Reaction conditions: *trans*-cinnamaldehyde (**12**, 0.25 mmol, 1.0 equiv), *N*-methylpyrrole (**11**, 1.25 mmol, 5.0 equiv), catalyst **4a–c** (3.5 mol %), aq TFA (5 M; 3.5 mol %), 0.63 M with respect to *trans*-cinnamaldehyde (**12**), 25 °C, 20 h. [b]Isolated yield. [c]Determined by chiral GC. [d]Complex mixture of products.

Moderate conversion of **13** were achieved using only THF as a solvent and in presence of substoichiometric amounts of water (0.4 equiv) [41]. Addition of water as co-solvent proved beneficial for the formation of product **13**. Notably, PG-95 (**4a**) and PG-57 (**4b**) exhibited comparable trends and the best yield and ee were observed when 5 vol % of water was added to the reaction mixture (Table 1, entries 4 and 5). Increasing the water content to 10 vol % resulted in incomplete conversion to **13** and lower ee values of the product (Table 1, entries 7 and 8). In case of the more hydrophilic PG-30 (**4c**) the activity increased with the amount of water in the reaction medium; yields and selectivities remained moderate. Attempts to carry out the reaction in water as the only solvent were unsuccessful (Table 1, entries 10–12). As expected, the outcomes of this reaction were strongly dependent on the solvent/water ratio and the catalysts **4a–c** exhibited different activity with changes on the degrees of functionalization. In general, catalysts **4a** and **4b** were found to be more efficient in comparison to the less functionalized **4c**. Probably, the poor ability of **4c** to catalyze the model transformation might be explained by its low solubility in the reaction medium, most likely due to the large number of free hydroxy groups on the periphery of the multivalent catalyst. Instead, catalysts **4a–c** demonstrated to be completely soluble in chloroform and methanol. Unfortunately, the use of these solvents led to decreased yields and selectivities of **13**. Therefore, we decided to further investigate the superior catalysts PG-95 (**4a**) and PG-57 (**4b**) in THF/H_2O mixture.

As reported in the literature, immobilization of chiral imidazolidin-4-ones on polymeric support might affect the formation of the desired products and lead to decreased enantioselectivities [58]. Indeed, in all the experiments reported in Table 1 the enantiomeric excess of **13** was lower compared to MacMillan's original experiments [53]. In an attempt to improve the enantiomeric ratios, we studied the influence of temperature using the optimized conditions obtained for **4a** and **4b** in Table 1 (for results, see Table 2).

Table 2: Influence of temperature in the Friedel–Crafts alkylation.[a]

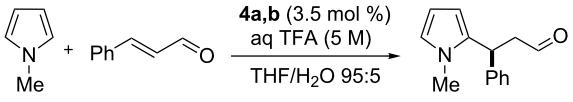

11 **12** **13**

Entry	Catalyst	*T* (°C)	*t* (h)	Yield (%)[b]	ee (%)[c]
1	PG-95 (**4a**)	25	20	62	68
2	PG-57 (**4b**)	25	20	68	66
3	PG-95 (**4a**)	4	35	60	68
4	PG-57 (**4b**)	4	35	64	68
5	PG-95 (**4a**)	–24	48	46	76
6	PG-57 (**4b**)	–24	48	25	78

[a]Reaction conditions: *trans*-cinnamaldehyde (**12**, 0.25 mmol, 1.0 equiv), *N*-methylpyrrole (**11**, 1.25 mmol, 5.0 equiv), catalyst **4a,b** (3.5 mol %), aq TFA (5 M; 3.5 mol %), THF/H_2O 95:5 (v/v), 0.63 M with respect to *trans*-cinnamaldehyde (**12**). [b]Isolated yield. [c]Determined by chiral GC.

To our dismay, running the transformation at lower temperatures did not lead to any significant improvements, although slight changes were observed. Carrying out the reactions at 4 °C gave similar ee values (Table 2, entries 3 and 4), whereas at −24 °C the alkylation led to marginally increased selectivities, at the cost of a drop in the yield (Table 2, entries 5 and 6).

Nevertheless, the observed enantiomeric excess of the product **13** is still low when compared with those (93% ee, at −30 °C) originally reported in the case of the traditional (*S*)-phenylalanine-based imidazolidin-4-one [53].

Using the optimized solvent system (Table 1), we then turned our attention to study the catalyst loading and further prove the efficiency of multivalent **4a** and **4b** (Table 3).

Table 3: Catalyst loading study.[a]

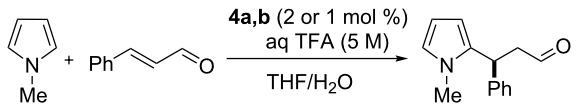

11 **12** **13**

Entry	Catalyst	Load. (mol %)	THF/H_2O (v/v)	Yield (%)[b]	ee (%)[c]
1	PG-95 (**4a**)	2	95:5	43	59
2	PG-57 (**4b**)	2	95:5	62	64
3	PG-95 (**4a**)	2	97:3	66	68
4	PG-57 (**4b**)	2	97:3	65	67
5	PG-95 (**4a**)	1	98.5:1.5	46	67
6	PG-57 (**4b**)	1	98.5:1.5	50	74

[a]Reaction conditions: *trans*-cinnamaldehyde (**12**, 0.50 mmol, 1.0 equiv), *N*-methylpyrrole (**11**, 2.50 mmol, 5.0 equiv), catalyst **4a,b** (2 or 1 mol %), aq TFA (5 M; 2 mol %, entries 1–4 or 1 mol %, entries 5 and 6), 0.63 M with respect to *trans*-cinnamaldehyde (**12**), 25 °C, 48 h. [b]Isolated yield. [c]Determined by chiral GC.

Initial attempts with 2 mol % of the multivalent **4a** and **4b**, using 5 vol % of water in THF led to the isolation of **13** in moderate yield and slightly lower enantioselectivies, a result even more pronounced in the case of PG-95 (**4a**) (Table 3, entries 1 and 2). Next, we questioned if in addition to a catalyst loading reduction also a concomitant reduction of the water amount was necessary to maintain yield and enantiomeric ratio. Consistently, we reduced the water amount from 5 to 3 vol % and observed higher conversion to **13** and improved ee values (Table 3, entries 3 and 4). Therefore, in the following experiments the catalyst/water ratio was kept constant. The excellent efficiency of the catalyst was confirmed with moderate to good yields of **13** even though using 1 mol % of **4a** and **4b**, respectively (Table 3, entries 5 and 6). Considering, for the supported case, a typical catalyst loading for this transformation to be 10 mol % in order to achieve good conversion [62], the loadings reported in Table 3 could be decreased by one order of magnitude.

After solvent and temperature screening, our studies were focused on dilution experiments (Table 4).

Table 4: Dilution experiments.[a]

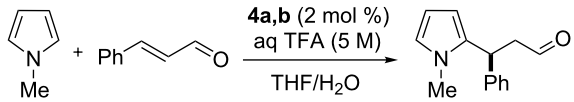

11 **12** **13**

Entry	Catalyst	Conc. (M)[b]	THF/H_2O (v/v)	Yield (%)[c]	ee (%)[d]
1[e]	PG-95 (**4a**)	0.63	97:3	66	68
2[e]	PG-57 (**4b**)	0.63	97/3	65	67
3	PG-95 (**4a**)	0.30	98.5:1.5	70	68
4	PG-57 (**4b**)	0.30	98.5:1.5	87	70
5	PG-95 (**4a**)	0.10	99.5:0.5	<1[f]	n.d.[g]
6	PG-57 (**4b**)	0.10	99.5:0.5	29[f]	n.d.[g]

[a]Reaction conditions: *trans*-cinnamaldehyde (**12**, 0.25 mmol, 1.0 equiv), *N*-methylpyrrole (**11**, 1.25 mmol, 5.0 equiv), catalyst **4a,b** (2 mol %), aq TFA (5 M; 2 mol %), 25 °C, 48 h. [b]With respect to *trans*-cinnamaldehyde (**12**). [c]Isolated yield. [d]Determined by chiral GC. [e]*trans*-Cinnamaldehyde (**12**, 0.50 mmol, 1.0 equiv), *N*-methylpyrrole (**11**, 2.50 mmol, 5.0 equiv). [f]Determined by ^{1}H NMR. [g]n.d. = not determined.

The best yield and enantioselectivity of **13** was obtained using PG-57 (**4b**) and lowering the concentration from 0.63 to 0.30 M (Table 4, entry 4). Contrarily, PG-95 (**4a**) did not lead to any appreciable improvement (Table 4, entry 3). By reducing the concentration to 0.10 M, **4b** gave only poor to moderate yields while the efficiency of **4a** decreased even more sharply and only traces of product **13** were observed (Table 4, entries 5 and 6). On the other hand, the enantioselectivities remained unchanged passing from concentration of 0.63 M to more diluted conditions (0.30 M). This outcome might be attributed to the constant local neighborhood in the polymer periphery where the catalytic centers are located, therefore the concentration may not affect the chiral induction [24].

After the completion of our systematic optimization of the reaction parameters using the model transformation, the most active catalyst **4b** was selected for a screening of different enals in the alkylation reaction of *N*-methylpyrrole (**11**). A study on the substrate scope was further carried out under the established conditions (see Table 4, entry 4). A variety of substituted α,β-unsaturated aldehydes **14a–e** was employed using 2 mol % PG-57 (**4b**) in THF/H_2O 98.5:1.5 (v/v) (Table 5).

Multivalent catalyst **4b** showed good to excellent activities in a range of substrates and moderate to good enantiomeric ratios for the formation of products **15a–e**, as shown in Table 5. Electron-deficient aromatic enals **14d,e** afforded higher yields and selectivities, confirming the strong influence of the substituent (Table 5, entries 4 and 5). Contrarily, aliphatic enals **14a,b** were

Table 5: Substrate scope.[a]

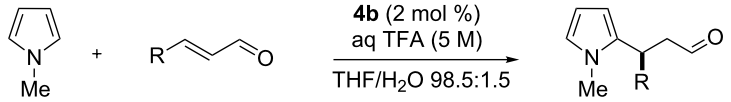

11 **14a–e** **15a–e**

Entry	Substrate		Product		*t* (h)	Yield (%)[b]	ee (%)[c]
1	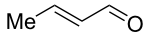	**14a**	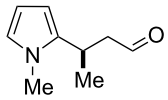	**15a**	24	86	69
2	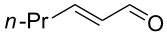	**14b**	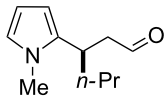	**15b**	24	83	68
3	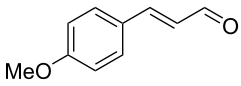	**14c**	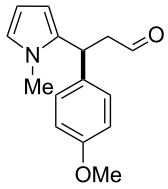	**15c**	48	80	56
4	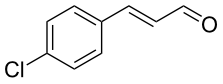	**14d**	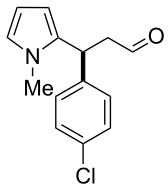	**15d**	48	86	71
5	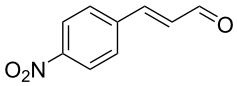	**14e**	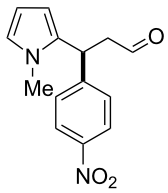	**15e**	48	99	78

[a]Reaction conditions: aldehyde **14a–e** (0.25 mmol, 1.0 equiv), *N*-methylpyrrole (**11**, 1.25 mmol, 5.0 equiv), catalyst **4b** (2 mol %), aq TFA (5 M; 2 mol %), THF/H_2O 98.5:1.5 (v/v), 0.30 M with respect to aldehyde **14a–e**, 25 °C. [b]Isolated yield. [c]Determined by chiral GC.

well-tolerated and the outcomes were not affected significantly (Table 5, entries 1 and 2).

In our studies on the utilization of hPG as a soluble support in organocatalysis, hyperbranched PG-95 (**4a**) and PG-57 (**4b**) were finally compared with the monovalent G1-dendron imidazolidin-4-one **8** previously prepared and the original MacMillan's first generation catalyst **16** using the optimum conditions (Table 6).

As shown in Table 6, multivalent **4b** and monovalent **8** afforded similar results (Table 6, entries 2 and 3), probably due to their comparable high hydrophilicity. This outcome did not indicate additional cooperative effects between the active catalytic sites. Increased activities were observed compared to MacMillan's catalyst **16**, albeit with lower enantioselectivity (Table 6, entries 2, 3 and 4). Catalyst **4a** showed turnover rates comparable with the traditional imidizolidin-4-one **16** (Table 6, entries 1 and 4). In conclusion, high- (PG-95, **4a**) or low- (PG-30, **4c**) loaded support were less active when compared to an intermediate degree of functionalization (PG-57, **4b**). In the case of PG-57 (**4b**) a good compromise between hydrophilicity and solubility was achieved. The results reported in Table 6 point out that catalyst **4b** was not suffering from diminished reactivity as often observed with immobilizations. Additionally the polymeric support was found to be responsible for enhanced reactiv-

Table 6: Comparison of hPG catalysts **4a**,**b** with monovalent analogue **8** and MacMillan's first generation **16**.[a]

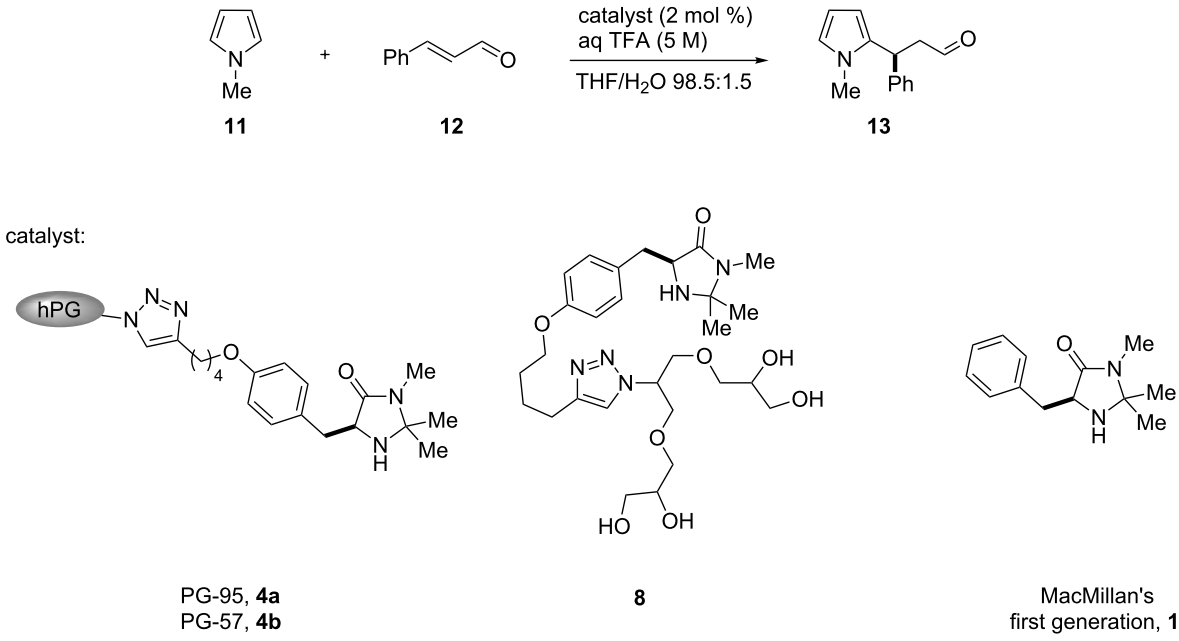

Entry	Catalyst	Yield (%)[b]	ee (%)[c]
1	PG-95 (**4a**)	70	68
2	PG-57 (**4b**)	87	70
3	**8**	83	67
4	**16**	64	77

[a]Reaction conditions: *trans*-cinnamaldehyde (**12**, 0.25 mmol, 1.0 equiv), *N*-methylpyrrole (**11**, 1.25 mmol, 5.0 equiv), cat. (2 mol %), aq TFA (5 M; 2 mol %), THF/H_2O 98.5:1.5 (v/v), 0.30 M with respect to *trans*-cinnamaldehyde (**12**), 25 °C, 48 h. [b]Isolated yield. [c]Determined by chiral GC.

ity with respect to the original imidazolidin-4-one **16**. The presence of anchimeric assistance by hydroxy groups, in the hydrolysis step of the iminium intermediate, might account for the observed improved turnover rates.

To complete our studies on the generality of hPG catalysts, finally, recycling of the polymer was studied. Heterogeneous catalysis allowed for simple separations of the immobilized species from the reaction media. Indeed, working under homogeneous conditions did not enable separation by simple filtration. On the other hand, the multivalent catalysts **4a** and **4b** showed poor solubility in solvents with low polarity, thus allowing for an easy recovery in 60–70% yield after selective precipitation using Et_2O. The utility of our soluble support was examined in the catalytic efficiency of recovered PG-57 (**4b**) (Table 7).

Table 7: Catalyst recycle.[a]

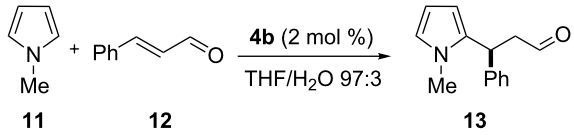

Entry	Cycle	Yield (%)[b]	ee (%)[c]
1[d]	1	65	67
2	2	54	65
3[d]	3	45	65

[a]Reaction conditions: *trans*-cinnamaldehyde (**12**, 1.0 equiv), *N*-methylpyrrole (**11**, 5.0 equiv), catalyst **4b** (2 mol %), THF/H_2O 97:3 (v/v), 0.63 M with respect to *trans*-cinnamaldehyde (**12**), 25 °C, 48 h. [b]Isolated yield. [c]Determined by chiral GLC. [d]Aq TFA (5 M; 2 mol %) was added to the reaction mixture.

Catalyst **4b** was used three times in the asymmetric alkylation reaction. The experiment showed constant enantiomeric ratios although decreased activity and yields were observed. The lower yields exhibited after each cycle might be attributed to the decreased solubility of the recovered polymer. For the same reason, early attempts using the optimized parameters (conc.

0.30 M) were not successful; therefore the same PG-57 (**4b**) was subjected to more concentrated conditions (conc. 0.63 M). Moreover, addition of the acidic co-catalyst was crucial to establish the reactivity of the imidazolidin-4-one in the third cycle. Attempts to elucidate the reason of the decreased reactivity and analysis of the recovered polymer by ^{1}H NMR indicated the leakage of the imidazolidin-4-one moiety. Nevertheless, studies focussing on improved catalyst stability and recycling are in progress.

Conclusion

In summary, we have successfully employed a CuAAC strategy in the first immobilization of a chiral imidazolidin-4-one onto hyperbranched polyglycerol support and examined its efficiency in organocatalysis. Catalyst **4c** proved to be less soluble in the reaction media compared to **4a** and **4b**, and showed poor activity and selectivity. The soluble polymers **4a** and **4b** enabled homogeneous reactions without loss of efficiency due to immobilization. The activity of multivalent catalyst **4a** was comparable with that exhibited by the traditional MacMillan's catalyst, while **4b** was shown to be superior. Nevertheless, erosion in enantioselectivity was observed, probably as a consequence of high local concentration effects on the periphery of the dendritic architecture, where the catalytic sites are located. The novel multivalent system **4b** achieved good conversion to afford product **13**, even with low polymer loading (1 mol %) compared to common loadings of 10 mol % required for the supported imidazolidin-4-ones. Moreover, **4b** was shown to be well-tolerated in a range of α,β-unsaturated aldehydes. The improved efficiency shown by **4b** might derive from an anchimeric assistance in the hydrolysis step of the iminium ion. Interestingly, the presence of such an effect might offer opportunities for further studies. One of the advantages of the multivalent catalyst **4b** was demonstrated to be its easy separability from the reaction media and its reuse for three consecutive times, whereas further investigations will be necessary on recycling of the polymeric support.

Supporting Information

Supporting Information File 1

Experimental procedures, analytical data, copies of NMR spectra and GC reports.
[http://www.beilstein-journals.org/bjoc/content/supplementary/1860-5397-11-83-S1.pdf]

Acknowledgements

We gratefully acknowledge financial support from the Deutsche Forschungsgemeinschaft within the Sonderforschungsbereich 765.

References

1. Fasting, C.; Schalley, C. A.; Weber, M.; Seitz, O.; Hecht, S.; Koksch, B.; Dernedde, J.; Graf, C.; Knapp, E.-W.; Haag, R. *Angew. Chem., Int. Ed.* **2012,** *51,* 10472–10498. doi:10.1002/anie.201201114
2. Mammen, M.; Choi, S.-K.; Whitesides, G. M. *Angew. Chem., Int. Ed.* **1998,** *37,* 2754–2794. doi:10.1002/(SICI)1521-3773(19981102)37:20<2754::AID-ANIE2754>3.0.CO;2-3
3. Mulder, A.; Huskens, J.; Reinhoudt, D. N. *Org. Biomol. Chem.* **2004,** *2,* 3409–3424. doi:10.1039/B413971B
4. Badjić, J. D.; Nelson, A.; Cantrill, S. J.; Turnbull, W. B.; Stoddart, J. F. *Acc. Chem. Res.* **2005,** *38,* 723–732. doi:10.1021/ar040223k
5. Dallas, P.; Sharma, V. K.; Zboril, R. *Adv. Colloid Interface Sci.* **2011,** *166,* 119–135. doi:10.1016/j.cis.2011.05.008
6. Park, J.; Hong, S. *Chem. Soc. Rev.* **2012,** *41,* 6931–6943. doi:10.1039/c2cs35129c
7. Shibasaki, M.; Yoshikawa, N. *Chem. Rev.* **2002,** *102,* 2187–2210. doi:10.1021/cr010297z
8. van den Beuken, E. K.; Feringa, B. L. *Tetrahedron* **1998,** *54,* 12985–13011. doi:10.1016/S0040-4020(98)00319-6
9. Haag, R.; Roller, S. *Top. Curr. Chem.* **2004,** *242,* 1–42.
10. Hajji, C.; Haag, R. *Top. Organomet. Chem.* **2006,** *20,* 149–176. doi:10.1007/3418_035
11. Wang, D.; Astruc, D. *Coord. Chem. Rev.* **2013,** *257,* 2317–2334. doi:10.1016/j.ccr.2013.03.032
12. Bergbreiter, D. E.; Tian, J.; Hongfa, C. *Chem. Rev.* **2009,** *109,* 530–582. doi:10.1021/cr8004235
13. Chinnusamy, T.; Hilgers, P.; Reiser, O. Catalysts Bound to Soluble Polymers. In *Recoverable and Recyclable Catalysts;* Benaglia, M., Ed.; John Wiley & Sons: Chichester, UK, 2009; pp 77–100.
14. Chen, J.; Yang, G.; Zhang, H.; Chen, Z. *React. Funct. Polym.* **2006,** *66,* 1434–1451. doi:10.1016/j.reactfunctpolym.2006.04.008
15. Caminade, A.-M.; Turrin, C.-O.; Laurent, R.; Ouali, A.; Delavaux-Nicot, B., Eds. *Dendrimers: Towards Catalytic, Material and Biomedical Uses;* John Wiley & Sons: Chichester, UK, 2011.
16. Helms, B.; Fréchet, J. M. J. *Adv. Synth. Catal.* **2006,** *348,* 1125–1148. doi:10.1002/adsc.200606095
17. Gade, L. H., Ed. *Dendrimer Catalysis;* Top. Organomet. Chem., Vol. 20; Springer: Berlin, 2006. doi:10.1007/11603788
18. Haag, R.; Roller, S. Dendritic Polymers as High-Loading Supports for Organic Synthesis and Catalysis. In *Polymeric Materials in Organic Synthesis and Catalysis;* Buchmeiser, M. R., Ed.; Wiley-VCH: Weinheim, Germany, 2003; pp 305–344.
19. Carlmark, A.; Hawker, C.; Hult, A.; Malkoch, M. *Chem. Soc. Rev.* **2009,** *38,* 352–362. doi:10.1039/B711745K
20. Gao, C.; Yan, D. *Prog. Polym. Sci.* **2004,** *29,* 183–275. doi:10.1016/j.progpolymsci.2003.12.002
21. Jikei, M.; Kakimoto, M. *Prog. Polym. Sci.* **2001,** *26,* 1233–1285. doi:10.1016/S0079-6700(01)00018-1
22. Schlenk, C.; Kleij, A. W.; Frey, H.; van Koten, G. *Angew. Chem., Int. Ed.* **2000,** *39,* 3445–3447. doi:10.1002/1521-3773(20001002)39:19<3445::AID-ANIE3445>3.0.CO;2-8
23. Hebel, A.; Haag, R. *J. Org. Chem.* **2002,** *67,* 9452–9455. doi:10.1021/jo026076q
24. Hajji, C.; Roller, S.; Beigi, M.; Liese, A.; Haag, R. *Adv. Synth. Catal.* **2006,** *348,* 1760–1771. doi:10.1002/adsc.200606168
25. Seayad, J.; List, B. *Org. Biomol. Chem.* **2005,** *3,* 719–724. doi:10.1039/B415217B

26. Dalko, P. I.; Moisan, L. *Angew. Chem., Int. Ed.* **2001,** *40,* 3726–3748. doi:10.1002/1521-3773(20011015)40:20<3726::AID-ANIE3726>3.0.CO;2-D
27. Dalko, P. I.; Moisan, L. *Angew. Chem., Int. Ed.* **2004,** *43,* 5138–5175. doi:10.1002/anie.200400650
28. Bertelsen, S.; Jørgensen, K. A. *Chem. Soc. Rev.* **2009,** *38,* 2178–2189. doi:10.1039/B903816G
29. Enders, D.; Grondal, C.; Hüttl, M. R. S. *Angew. Chem., Int. Ed.* **2007,** *46,* 1570–1581. doi:10.1002/anie.200603129
30. Scheffler, U.; Mahrwald, R. *Chem. – Eur. J.* **2013,** *19,* 14346–14396. doi:10.1002/chem.201301996
31. Dondoni, A.; Massi, A. *Angew. Chem., Int. Ed.* **2008,** *47,* 4638–4660. doi:10.1002/anie.200704684
32. Kristensen, T. E.; Hansen, T. *Eur. J. Org. Chem.* **2010,** 3179–3204. doi:10.1002/ejoc.201000319
33. Cozzi, F. *Adv. Synth. Catal.* **2006,** *348,* 1367–1390. doi:10.1002/adsc.200606096
34. Benaglia, M.; Puglisi, A.; Cozzi, F. *Chem. Rev.* **2003,** *103,* 3401–3430. doi:10.1021/cr010440o
35. Trindade, A. F.; Gois, P. M. P.; Afonso, C. A. M. *Chem. Rev.* **2009,** *109,* 418–514. doi:10.1021/cr800200t
36. Gruttadauria, M.; Giacalone, F.; Noto, R. *Chem. Soc. Rev.* **2008,** *37,* 1666–1688. doi:10.1039/B800704G
37. Wu, Y.; Zhang, Y.; Yu, M.; Zhao, G.; Wang, S. *Org. Lett.* **2006,** *8,* 4417–4420. doi:10.1021/ol061418q
38. Gruttadauria, M.; Giacalone, F.; Noto, R. *Adv. Synth. Catal.* **2009,** *351,* 33–57. doi:10.1002/adsc.200800731
39. Hernàndez, J. G.; Juaristi, E. *Chem. Commun.* **2012,** *48,* 5396–5409. doi:10.1039/C2CC30951C
40. Mase, N.; Barbas, C. F., III. *Org. Biomol. Chem.* **2010,** *8,* 4043–4050. doi:10.1039/C004970K
41. Hayashi, Y. *Angew. Chem., Int. Ed.* **2006,** *45,* 8103–8104. doi:10.1002/anie.200603378
42. Mlynarski, J.; Paradowska, J. *Chem. Soc. Rev.* **2008,** *37,* 1502–1511. doi:10.1039/B710577K
43. Font, D.; Sayalero, S.; Bastero, A.; Jimeno, C.; Pericàs, M. A. *Org. Lett.* **2008,** *10,* 337–340. doi:10.1021/ol702901z
44. Bellis, E.; Kokotos, G. *J. Mol. Catal. A: Chem.* **2005,** *241,* 166–174. doi:10.1016/j.molcata.2005.05.047
45. Kehat, T.; Portnoy, M. *Chem. Commun.* **2007,** 2823–2825. doi:10.1039/B703016A
46. Mitsui, K.; Hyatt, S. A.; Turner, D. A.; Hadad, C. M.; Parquette, J. R. *Chem. Commun.* **2009,** 3261–3263. doi:10.1039/B902960E
47. Goren, K.; Portnoy, M. *Chem. Commun.* **2010,** *46,* 1965–1967. doi:10.1039/B915577E
48. Goren, K.; Karabline-Kuks, J.; Shiloni, Y.; Barak-Kulbak, E.; Miller, S. J.; Portnoy, M. *Chem. – Eur. J.* **2015,** *21,* 1191–1197. doi:10.1002/chem.201404560
49. Sunder, A.; Mülhaupt, R.; Haag, R.; Frey, H. *Adv. Mater.* **2000,** *12,* 235–239. doi:10.1002/(SICI)1521-4095(200002)12:3<235::AID-ADMA235>3.0.CO;2-Y
50. Ahrendt, K. A.; Borths, C. J.; MacMillan, D. W. C. *J. Am. Chem. Soc.* **2000,** *122,* 4243–4244. doi:10.1021/ja000092s
51. Puglisi, A.; Benaglia, M.; Cinquini, M.; Cozzi, F.; Celentano, G. *Eur. J. Org. Chem.* **2004,** 567–573. doi:10.1002/ejoc.200300571
52. Terrasson, V.; Marcia de Figueiredo, R.; Campagne, J. M. *Eur. J. Org. Chem.* **2010,** 2635–2655. doi:10.1002/ejoc.200901492
53. Paras, N. A.; MacMillan, D. W. C. *J. Am. Chem. Soc.* **2001,** *123,* 4370–4371. doi:10.1021/ja015717g
54. Selkälä, S. A.; Tois, J.; Pihko, P. M.; Koskinen, A. M. P. *Adv. Synth. Catal.* **2002,** *344,* 941–945. doi:10.1002/1615-4169(200210)344:9<941::AID-ADSC941>3.0.CO;2-M
55. Mitsudome, T.; Nose, K.; Mizugaki, T.; Jitsukawa, K.; Kaneda, K. *Tetrahedron Lett.* **2008,** *49,* 5464–5466. doi:10.1016/j.tetlet.2008.07.011
56. Chu, Q.; Zhang, W.; Curran, D. P. *Tetrahedron Lett.* **2006,** *47,* 9287–9290. doi:10.1016/j.tetlet.2006.10.101
57. Park, J. K.; Sreekanth, P.; Kim, B. M. *Adv. Synth. Catal.* **2004,** *346,* 49–52. doi:10.1002/adsc.200303167
58. Zhang, Y.; Zhao, L.; Lee, S. S.; Ying, J. Y. *Adv. Synth. Catal.* **2006,** *348,* 2027–2032. doi:10.1002/adsc.200600240
59. Benaglia, M.; Celentano, G.; Cinquini, M.; Puglisi, A.; Cozzi, F. *Adv. Synth. Catal.* **2002,** *344,* 149–152. doi:10.1002/1615-4169(200202)344:2<149::AID-ADSC149>3.0.CO;2-U
60. Chiroli, V.; Benaglia, M.; Puglisi, A.; Porta, R.; Jumde, R. P.; Mandoli, A. *Green Chem.* **2014,** *16,* 2798–2806. doi:10.1039/C4GC00031E
61. Pecinovsky, C. S.; Nicodemus, G. D.; Gin, D. L. *Chem. Mater.* **2005,** *17,* 4889–4891. doi:10.1021/cm0514995
62. Riente, P.; Yadav, J.; Pericàs, M. A. *Org. Lett.* **2012,** *14,* 3668–3671. doi:10.1021/ol301515d
63. Paez, J. I.; Brunetti, V.; Strumia, M. C.; Becherer, T.; Solomun, T.; Miguel, J.; Hermanns, C. F.; Calderón, M.; Haag, R. *J. Mater. Chem.* **2012,** *22,* 19488–19497. doi:10.1039/c2jm32486e
64. Roller, S.; Zhou, H.; Haag, R. *Mol. Diversity* **2005,** *9,* 305–316. doi:10.1007/s11030-005-8117-y
65. Wyszogrodzka, M.; Haag, R. *Chem. – Eur. J.* **2008,** *14,* 9202–9214. doi:10.1002/chem.200800892
66. Rostovtsev, V. V.; Green, L. G.; Fokin, V. V.; Sharpless, K. B. *Angew. Chem., Int. Ed.* **2002,** *41,* 2596–2599. doi:10.1002/1521-3773(20020715)41:14<2596::AID-ANIE2596>3.0.CO;2-4

License and Terms

BEILSTEIN JOURNAL OF ORGANIC CHEMISTRY

Glycodendrimers: tools to explore multivalent galectin-1 interactions

Jonathan M. Cousin and Mary J. Cloninger*

Full Research Paper

Open Access

Address:
Department of Chemistry and Biochemistry, Montana State University, Bozeman, MT 59717, USA

Email:
Mary J. Cloninger* - mcloninger@chemistry.montana.edu

* Corresponding author

Keywords:
dendrimer; galectin-1; glycodendrimer; multivalent; nanoparticle

Beilstein J. Org. Chem. **2015,** *11,* 739–747.
doi:10.3762/bjoc.11.84

Received: 01 March 2015
Accepted: 04 May 2015
Published: 12 May 2015

This article is part of the Thematic Series "Multivalency as a chemical organization and action principle".

Guest Editor: R. Haag

Abstract

Four generations of lactose-functionalized polyamidoamine (PAMAM) were employed to further the understanding of multivalent galectin-1 mediated interactions. Dynamic light scattering and fluorescence microscopy were used to study the multivalent interaction of galectin-1 with the glycodendrimers in solution, and glycodendrimers were observed to organize galectin-1 into nanoparticles. In the presence of a large excess of galectin-1, glycodendrimers nucleated galectin-1 into nanoparticles that were remarkably homologous in size (400–500 nm). To understand augmentation of oncologic cellular aggregation by galectin-1, glycodendrimers were used in cell-based assays with human prostate carcinoma cells (DU145). The results revealed that glycodendrimers provided competitive binding sites for galectin-1, which diverted galectin-1 from its typical function in cellular aggregation of DU145 cells.

Introduction

Galectin-1 is a multivalent protein that mediates biological activity through multivalent interactions with cell surface glycoconjugates [1-4]. Galectin-1 is a non-covalent homodimer that belongs to a family of β-galactoside binding proteins called galectins [5-7]. The monomeric units are oriented such that the two carbohydrate recognition domains are located on apposing faces of the dimer (Figure 1). Although individual binding interactions with carbohydrates are weak [8], ligands for galectin-1 typically possess an array of carbohydrates to enhance the binding affinity [1,9,10]. Galectin-1 binding to carbohydrates cross-links adjacent glycoconjugates to mediate biological activity [10-16]. Specifically, galectin-1 has been reported to be involved in multivalent mechanisms that cluster cell surface glycoproteins [10,17], cross-link receptors [13,18], and form lattices and larger aggregates [12,19,20]. Synthetic multivalent ligands displaying multiple copies of recognition elements are a logical tool to study mechanisms of galectin-1 mediated biological activities.

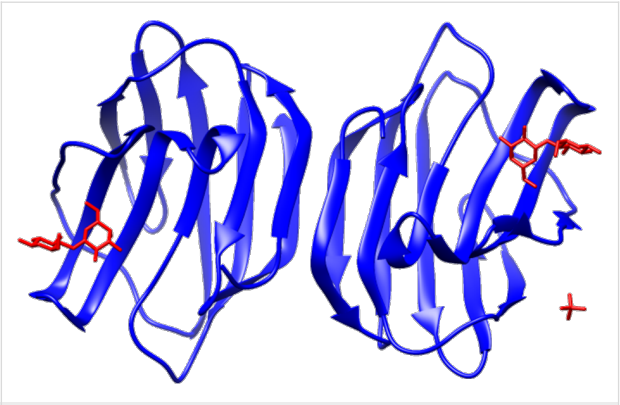

Figure 1: The structure of galectin-1. Reproduced with permission from [21]. Copyright 2004 Elsevier.

Mutivalent frameworks have been used to organize lectins and to mediate biological activity for the advancement of mechanistic understandings [22-25]. Synthetic multivalent ligands have been observed to enhance galectin-1 binding through the glycoside cluster effect by mediating the formation of cross-linked aggregates [26-28]. Tinari et al. observed galectin-1 augmentation of homotypic cellular aggregation in human melanoma cells (A375) through bivalent binding of 90K/Mac-2BP, a cell surface glycoprotein [29]. To further the understanding of structural specificity in binding events, Iurisci et al. designed multivalent oligosaccharide ligands to inhibit galectin-1 induced homotypic cellular aggregation in the A375 cell line [30]. Belitsky et al. designed self-assembled pseudopolyrotaxanes as a flexible and adaptable multivalent neoglycoconjugate for galectin-1 [31]. Using this multivalent supramolcular architecture, galectin-1 was observed to bind to flexible multivalent ligands with higher affinity than could be achieved using less dynamic ligand displays.

To further the mechanistic understanding of multivalent galectin-1 in biological processes such as cellular aggregation/tumor formation, we applied lactose functionalized poly(amidoamine) (PAMAM) dendrimers as a multivalent framework. We hypothesized that multivalent glycodendrimers would organize extracellular galectin-1 into aggregates that would influence the biological activity of galectin-1. To test this hypothesis, lactose functionalized dendrimers were used to nucleate the aggregation of galectin-1 into nanoparticles, and the sizes of the galectin-1/glycodendrimer nanoparticles were characterized using dynamic light scattering (DLS) and fluorescence microscopy (FM) when varying ratios of galectin-1 were added to the glycodendrimers. The galectin-1/glycodendrimer nanoparticle aggregates were then used to inhibit the galectin-1 induced aggregation of DU145 human prostate carcinoma cells. The studies reported here indicate that the pattern of galectin-1 that is presented to the cells influences their behavior, thus advancing the understanding of the mechanism of action of galectin-1 mediated cellular aggregation processes and indicating that multivalent interactions can be very effectively used to organize proteins into biologically active arrays.

Results

Nanoparticle formation

Poly(amidoamine) (PAMAM) dendrimers were used as a multivalent framework to study multivalent protein–carbohydrate interactions. The PAMAM structure is shown in Figure 2a. Second, third, fourth, and sixth generation dendrimers were functionalized with lactoside endgroups using a bis-ethoxy linker for solubility to afford **1**–**4** (G(2), G(3), G(4), and G(6), respectively, Figure 2b) [32].

The sizes of the galectin-1/glycodendrimer nanoparticles that were formed using multivalent lactose-functionalized PAMAM dendrimers **1**–**4** were determined by fluorescence microscopy (FM) and dynamic light scattering (DLS). For fluorescence microscopy, galectin-1 was labeled with AlexaFluor-555, and aggregation was characterized when a large, medium, or slight excess of galectin-1 was used relative to the concentration of the dendrimer (220:1, 9:1, or 3:1 ratio of galectin-1 to dendrimer, respectively). Fluorescent microsphere standards (FluoSpheres Fluorescent Microspheres, Molecular Probes) and image analysis software (Pixcavator 6.0) were used for size quantifications.

The results from the fluorescence microscopy studies using **2**, **3**, and **4** are summarized in Figure 3 (see Supporting Information File 1 for tabulated data), and representative micrographs are shown in Figure 4. (Aggregates formed using **1** were below the detection limits of the technique.) In the presence of a large excess of galectin-1 (220:1), all of the glycodendrimers **2**, **3**, and **4** organized galectin-1 into relatively small, similarly sized nanoparticles (Figure 4a–c). When a 9:1 or a 3:1 ratio of galectin-1 to glycodendrimer was used (Figure 4d–f and 4g–i), the aggregates that formed were generally larger and more polydisperse than when a 220-fold excess of galectin-1 was used. Only fourth generation dendrimer **3** forms comparable aggregates regardless of whether a slight excess of galectin-1 or a large excess of galectin-1 is added.

DLS was used as a complementary technique to characterize galectin-1 nanoparticles formed using **4**. These results, shown in Figure 5, also indicate the formation of small, homogeneous nanoparticles when a large excess of galectin-1 (220:1) was used. In agreement with the results obtained from the fluorescence microscopy studies, the nanoparticle sizes that were determined by DLS were larger when smaller-fold excesses of galectin-1 were used. Fluorescence microscopy proved to be a

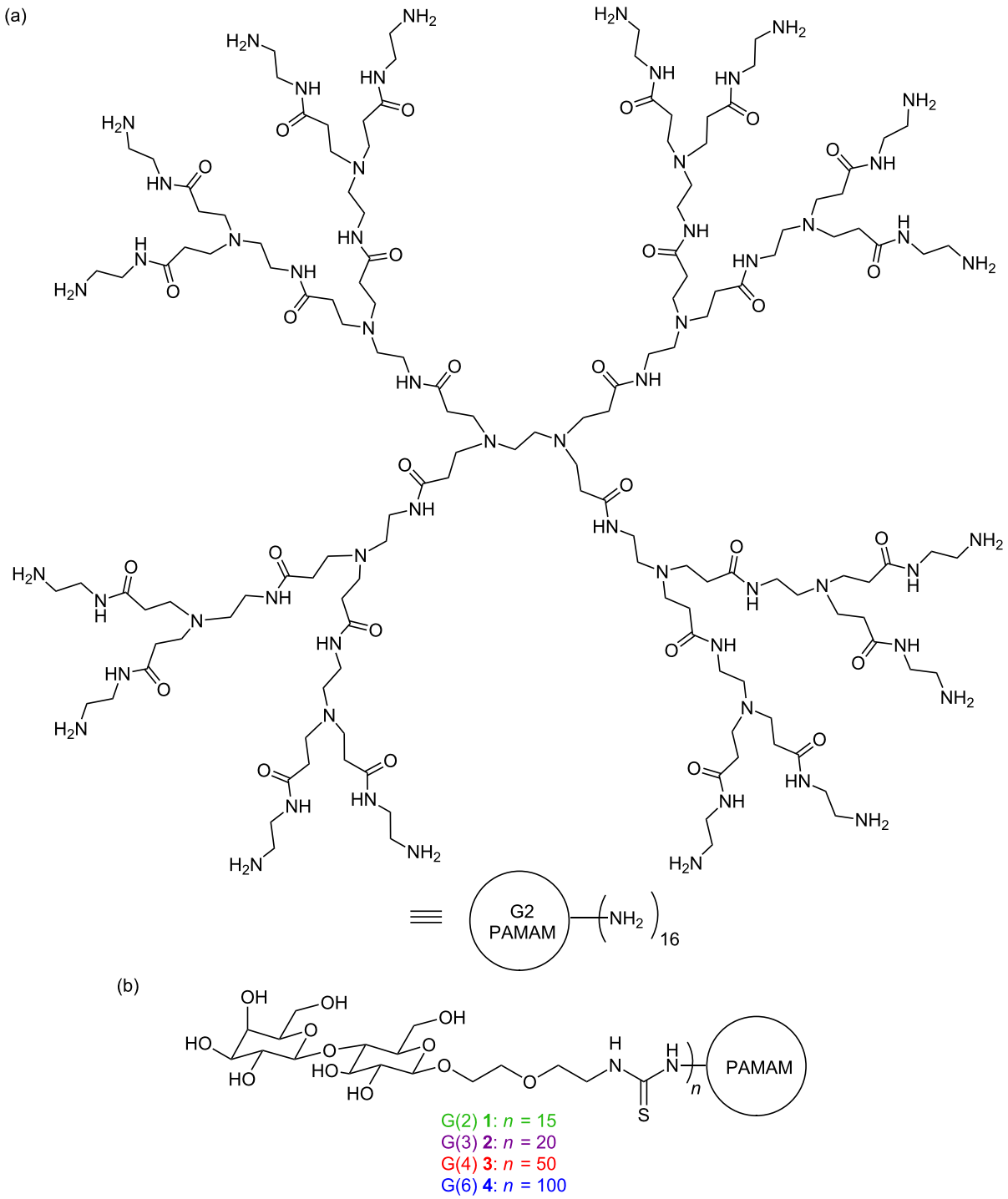

Figure 2: (a) Generation 2 PAMAM dendrimer. (b) Lactose-functionalized dendrimers **1**–**4**. Color-coding corresponds to colors used in the figures throughout this publication to indicate the different glycodendrimer generations.

more robust technique for characterization of galectin-1 nanoparticles; galactin-1 nanoparticles formed using **2** and **3** exceeded the detection limits of DLS.

Using DLS, the specificity of the interaction between galectin-1 and the lactosides on the multivalent glycodendrimers was assessed. Serially diluted solutions of monomeric lactose were

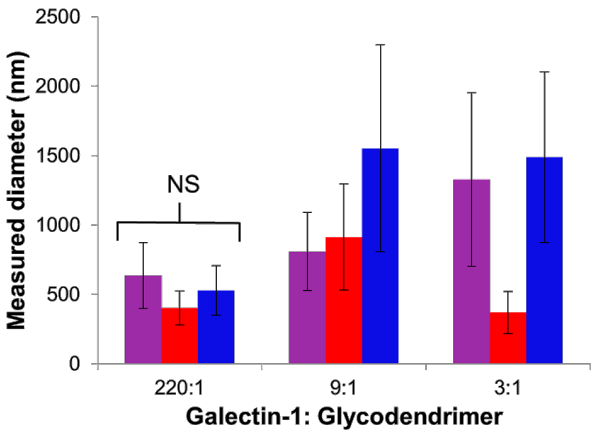

Figure 3: Average diameter (nm) of multivalent galectin-1 nanoparticles formed with multivalent glycodendrimers. For compounds **2** (purple), **3** (red), and **4** (blue), nanoparticle diameter (nm) was measured upon the addition of 0.18 μM glycodendrimer for 220:1, of 4.5 μM glycodendrimer for 9:1, and of 13 μM glycodendrimer for 3:1 to 40 μM galectin-1. NS represents non-significant difference in aggregate size measured for all generations determined by ANOVA.

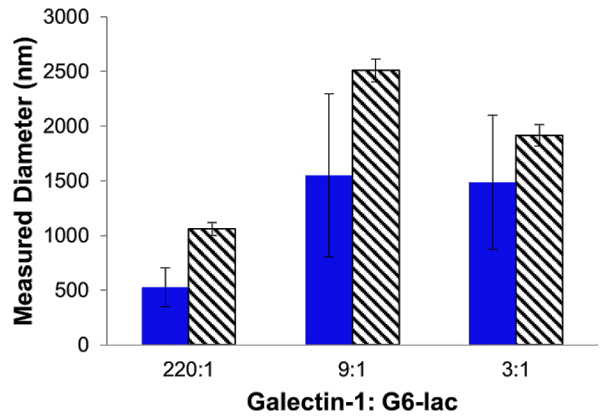

Figure 5: Comparison of average nanoparticle diameter (nm) formed with **4** measured by FM (blue) and DLS (diagonal stripes).

co-incubated with galectin-1 and compound **4**. Complete inhibition of aggregation was achieved by monomeric lactose, with an IC_{50} of 1.9 mM, indicating that a specific interaction between

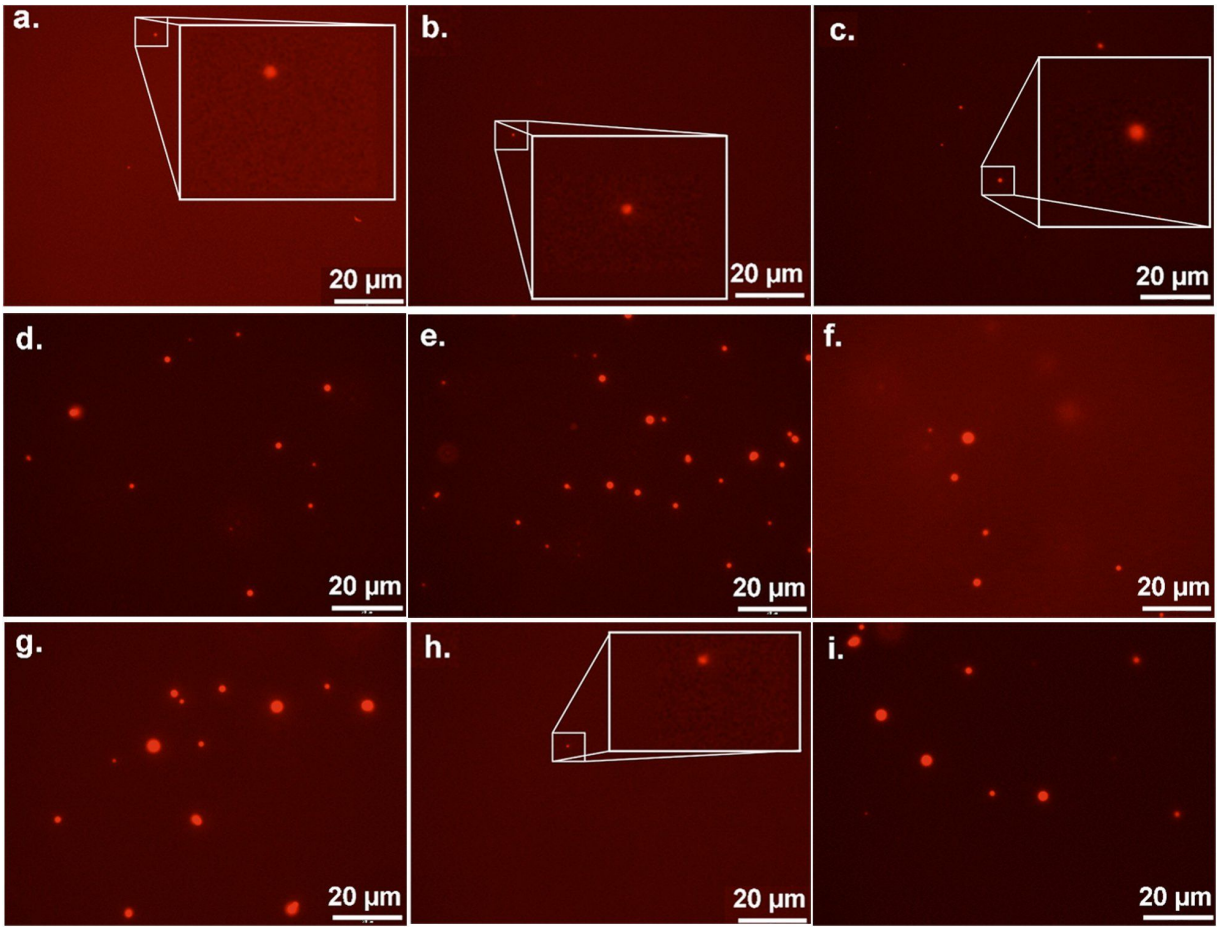

Figure 4: Representative fluorescent micrographs of glycodendrimer mediated galectin-1 nanoparticles. Nanoparticles formed with compounds (a) **2**, (b) **3**, and (c) **4** in a 220 molar excess of galectin-1 are shown in the top row and magnified by 4× for visualization. Nanoparticles formed with compounds (d) **2**, (e) **3**, and (f) **4** in a 9 molar excess of galectin-1 are shown in the middle row. In the bottom row, nanoparticles formed with compounds (g) **2**, (h) **3** (magnified by 4× for visualization), and (i) **4** in a 3 molar excess of galectin-1 are shown.

the lactose endgroups on the dendrimers and the carbohydrate recognition site of galectin-1 occurs when nanoparticles are formed (Figure 6).

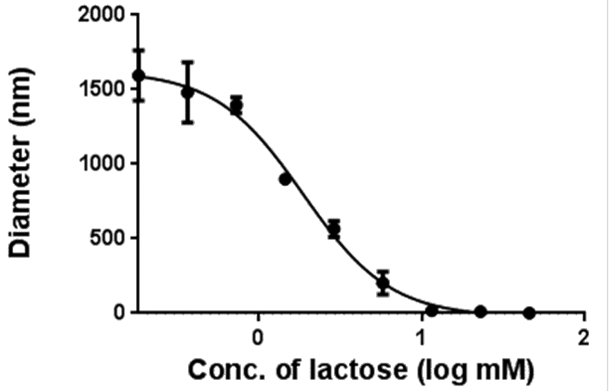

Figure 6: Lactose inhibition of galectin-1 nanoparticle formation with compound **4**.

Control experiments were performed with different functional groups on the multivalent framework. No aggregates were detected upon the addition of a polyhydroxylated sixth generation dendrimer, indicating that binding requires more than merely an array of hydrogen bonds. Small nanoparticles (340 ± 20 nm) were obtained when mannose functionalized G(6)-PAMAMs were combined with galectin-1, and neither monomeric lactose nor monomeric mannose inhibited the formation of these aggregates. This indicates that nanoparticles formed using the mannose-functionalized dendrimer do not rely on interactions in the β-galactoside binding site on galectin-1 and that non-specific glycodendrimer/galectin-1 interactions are responsible for the formation of these small aggregates. Miller et al. observed galectin-1 binding to α-galactomannan derivatives, and NMR was used to determine that the interaction did not occur in the canonical CRD [33].

Cell-based assay

After determining that lactose-functionalized dendrimers **1**–**4** reproducibly nucleate formation of galectin-1 aggregates that are quite homogeneous, we used these nanoparticles in cellular aggregation assays with galectin-1 and DU145 human prostate cancer cells. The DU145 cell line was chosen because it expresses a putative galectin-1 ligand – the Thomsen Friedenreich (TF) antigen on Mucin-1 [34,35].

As shown in Figure 7, untreated DU145 cells were not aggregated (i.e., free cells); upon the addition of exogenous galectin-1, however, extensive aggregation was observed. When lactose functionalized dendrimers **1**–**4** were added to the DU145 cells with galectin-1, cellular aggregation was inhibited. The smallest glycodendrimer, second generation compound **1**, most effectively inhibited cellular aggregation. Even at the lowest concentration of **1** shown in Figure 7, complete inhibition of cellular aggregation was observed (Figure 7a). Incomplete inhibition of aggregation was observed for compounds **3** and **4**. For fourth generation lactose functionalized dendrimer **3**, the percentage of free cells plateaued at 50% (Figure 7c). With sixth generation lactose functionalized dendrimer, **4**, only 30% of the cells remained clustered (Figure 7d). Although glycodendrimer concentrations were normalized so that the same concentration of lactoside residues were present at each stage in the assay irrespective of the scaffold generation number, dose-responsive inhibition of galectin-1 mediated cancer cell adhesion was only observed with lactose functionalized G(3)-dendrimer **2** at these concentrations (Figure 7b, and representative images 7e–h, the dose-responsive curve for lower concentrations of **1** is provided in Supporting Information File 1). Nearly complete inhibition of cellular aggregation was observed with compound **2** at the highest concentration of **2**. The inhibition observed with compounds **1** and **2** indicates that the smaller glycodendrimers are the most effective inhibitors of galectin-1 induced cellular aggregation.

A control experiment was performed to measure the ability of monomeric lactose to inhibit aggregation of DU145 cells in the presence of 3.7 μM exogenous galectin-1. The concentration of monomeric lactose required to inhibit cellular aggregation is 6 mM. On a per lactose basis, this concentration is 15-fold higher than the 66 μM concentration of **1** that was required for complete inhibition of cellular aggregation. Additionally, mannose-functionalized G(6)-PAMAM dendrimers did not inhibit cellular aggregation.

Discussion

The results of the fluorescence microscopy and DLS studies described above reveal that multivalent glycodendrimers organize galectin-1 into nanoparticles. In the presence of a large excess of galectin-1, multivalent glycodendrimers **2**–**4** organize galectin-1 into relatively small and remarkably homologous nanoparticles (Figure 3 and Figure 4a–c). This is likely a result of the multivalent framework being saturated with galectin-1, providing few uncomplexed nucleation sites for incorporation into larger nanoparticles (Figure 8). Therefore, an increase in the concentration of the multivalent framework should correlate to an increase in aggregate size, as was observed for 9:1 and 3:1 ratios of galectin-1 to glycodendrimer (Figure 3 and Figure 8). The exception to this is that small homogeneous nanoparticles were observed for compound **3** when a slight excess of galectin-1 was used (3:1). In this lactoside-rich environment, the presence of a large excess of lactoside residues apparently enabled increased nucleation at the expense of

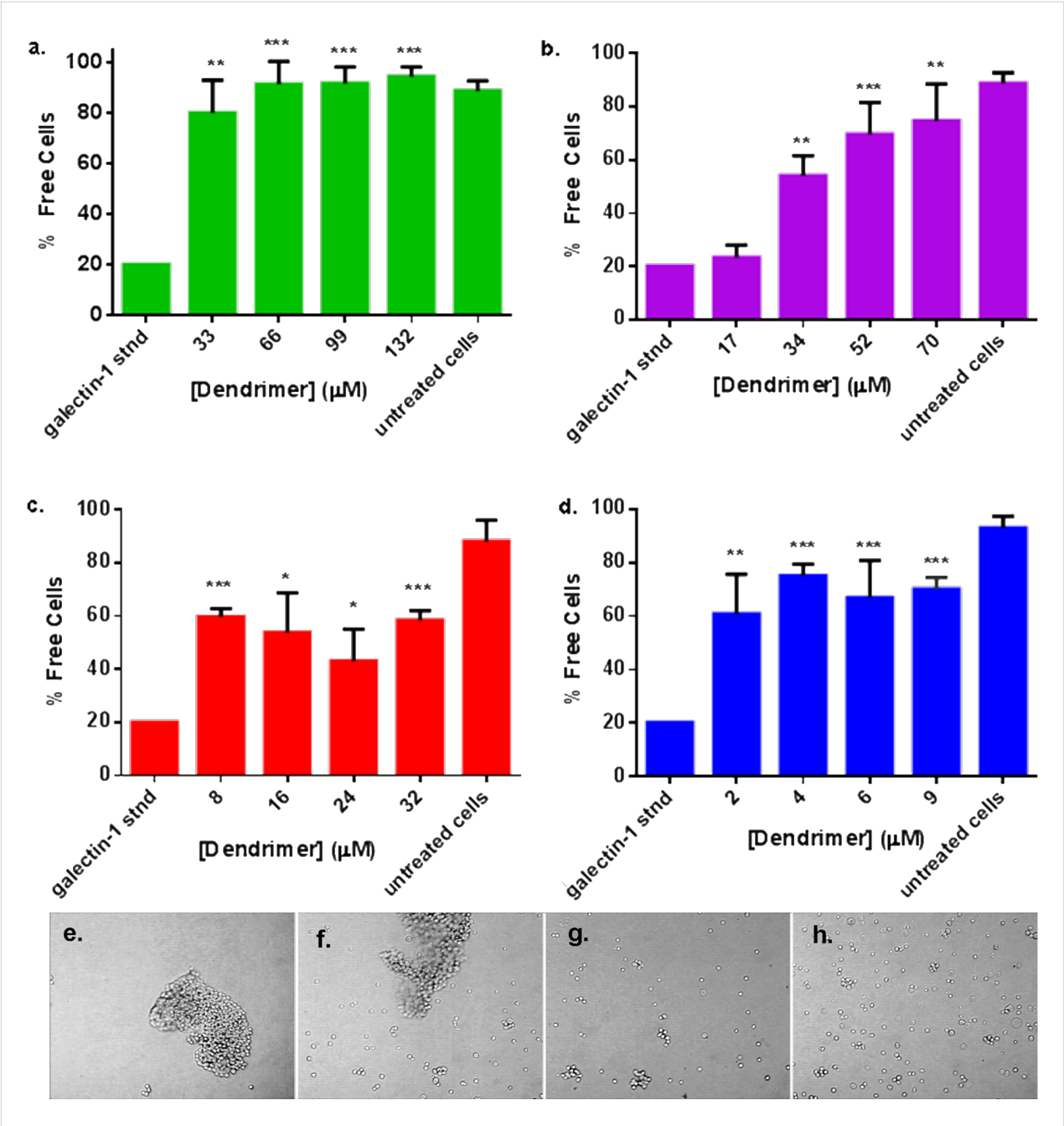

Figure 7: Cellular aggregation assays with DU145 human prostate carcinoma cells. Cancer cell aggregation assays were performed in the presence of 3.7 μM galectin-1 and increasing glycoderdrimer concentrations, with controls for galectin-1 treated cells and untreated cells. Glycodendrimer concentrations were normalized to present the same concentration of lactose residues. The results show inhibition of galectin-1 induced aggregation by (a) **1,** (b) **2**, (c) **3**, and (d) **4**. Data are shown as mean ± S.D. of measurements from at least three experiments. Statistical analysis was performed using an unpaired two-tailed student's T-Test by comparing the % free cells to the galectin-1 standard and * indicates p value < 0.05, ** indicates $p < 0.01$, and *** indicates $p < 0.001$, representative images of cellular aggregation are provided for DU145 with 3.7 μM galectin-1 and: (e) 17 μM **2**; (f) 34 μM **2**; (g) 52 μM **2**; and (h) 70 μM **2**.

aggregation, but it isn't clear why **3** is different from the other dendrimers in this regard. Overall, the results described here agree with mathematical modeling studies that identified scaffold concentration as a key determinant in maximizing scaffold-mediated nucleation [36].

The size of the nanoparticles formed in the presence of a large excess of galectin-1 is fundamentally remarkable. In the presence of enough galectin-1 to saturate the multivalent framework, aggregates approximately 400 nm in diameter were measured (Figure 3). The distance between the galectin-1 CRDs

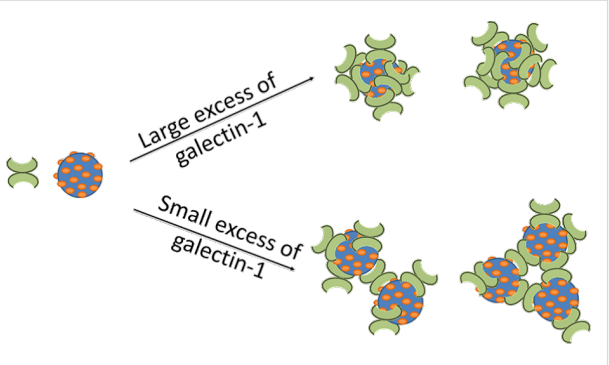

Figure 8: Schematic representation of galectin-1/glycodendrimer aggregates at varying stoichiometries.

is approximately 5 nm [21]. The diameter of the G(3), G(4), and G(6)-PAMAM dendrimers used to synthesize compounds **2**, **3**, and **4**, respectively, range from approximately 4 nm to 7 nm [37]. Therefore, multiple galectin-1 and glycodendrimer particles must interact to form the 400 nm aggregates, and this is favorable even when the scaffold is ostensibly saturated with galectin-1.

The DU145 human prostate carcinoma cell line was chosen to demonstrate that multivalent interactions initiated by a synthetic multivalent system can be used for effectively controlling cellular processes. DU145 cells express elevated levels of both galectin-1 [38] and its putative receptor Mucin-1 [34], which suggests that galectin-1 mediated β-galactoside binding is critical to cellular aggregation/tumor formation in this cell line. In the presence of exogenous galectin-1, extensive cellular aggregation was observed. Inducement of aggregation by exogenous galectin-1 comports with literature reporting pro-adhesive activity with galectin-1 [38-41]. There are two likely mechanism for galectin-1 mediation of cellular aggregation: (i) cross-linking of glycoconjugates (TF antigen Mucin-1) on adjacent cells which directly facilitates aggregation; and (ii) clustering of receptors (TF antigen Mucin-1) which exposes adhesion molecules that interact with adhesion molecules on neighboring cells to cause aggregation.

All four generations of the glycodendrimers inhibited galectin-1 mediated cellular aggregation of the DU145 cells, which indicates that glycodendrimers mediate inhibition of cellular aggregation by competitively binding galectin-1, thereby altering its presentation to cells and preventing cellular cross-linking. Lactose functionalized G(2)-PAMAM **1** was the most potent inhibitor of galectin-1 induced cellular aggregation, exhibiting complete inhibition of cancer cell adhesion at low dosage (Figure 4). Galectin-1/**1** nanoparticles were not detected by DLS or fluorescence microscopy. Because galectin-1 is known to bind these glycodendrimers, it is likely that aggregates formed but were below the detection limit of the fluorescence microscopy technique (which is about 200 nm). The formation of aggregates smaller than 200 nm in diameter, and thus not detectable by fluorescence microscopy, lends further credence to the argument that small galectin-1/glycodendrimer aggregates effectively alter the presentation of galectin-1 to cells, thereby altering the cells' recognition events.

Inhibition by monomeric lactose well illustrates the multivalency avidity enhancement. Monomeric lactose inhibited cell adhesion at a concentration of 6 mM, while inhibition of cellular adhesion by **1** occurred at a lactose concentration of 0.4 mM. This is a 15-fold increase in the concentration of lactose required to disrupt galectin-1 mediated cancer cell adhesion compared to the multivalent counterpart. The pronounced inhibition suggests that multivalent glycodendrimers **1**–**4** have a strong influence on the native cellular adhesion mechanism.

Conclusion

The concept that multivalency can be used to effectively control cellular activities was investigated using lactose functionalized dendrimers. First, the ability of the multivalent framework to organize galectin-1 was assessed with dynamic light scattering and fluorescence microscopy. These studies indicate that multivalent glycodendrimers nucleate the aggregation of galectin-1 into nanoparticles, which were remarkably homogenous when formed in the presence of a large excess galectin-1. Next, glycodendrimers were added to cancer cells to modulate galectin-1 mediated cellular aggregation. The glycodendrimers inhibited cellular aggregation by providing competitive binding sites for the galectin-1 and diverting the galectin-1 from its native role in cellular cross-linking, which leads to cellular aggregation/tumor formation. These studies reveal that mutivalency can be exploited not only to modulate biological activities but also as a platform to advance the understanding of biologically relevant protein/carbohydrate interactions through the ability to organize proteins into biologically active arrays.

Experimental

General information

Galectin-1 was provided by Dr. Linda Baum and Mabel Pang of UCLA. General reagents were purchased from Acros and Sigma-Aldrich Chemical Companies. PAMAM dendrimers were purchased from Dendritech. The lactose-functionalized dendrimers used (**1**–**4**) were synthesized and characterized according to the reported procedure [32].

Fluorescence microscopy

Reagents for fluorescence microscopy were purchased from Molecular Probes. To measure galectin-1 nanoparticles formed using glycodendrimers with fluorescence microscopy, both

species were fluorescently labeled. Galectin-1 was labeled with Alexa Fluor A555 NHS Ester (succinimidyl ester) (Molecular Probes) [42]. Fluorescent images were captured on an Olympus BX-61 motorized microscope with MicroSuite software with a 100× oil immersion objective at an exposure time of 2 ms. Size quantification was achieved using fluorescent microsphere standards (200 nm, 1000 nm, and 10000 nm reported diameter) (FluoSpheres Fluorescent Microspheres, Molecular Probes) and image analysis software (Pixcavator 6.0). At a constant concentration of galectin-1 (40 μM), aggregate size was measured at ratios of galectin-1 to glycodendrimer of 220:1, 9:1, and 3:1.

Dynamic light scattering

Dynamic light scattering was performed using a 90 Plus Particle Size Analyzer (Brookhaven Instruments Corp.) to measure galectin-1/glycodendrimer aggregates at same concentrations and ratios that were used in the fluorescence microscopy assays. Monomeric lactose was co-incubated with galectin-1 and compound **4** for inhibition assays. For controls, mannose-functionalized G(6)-PAMAM dendrimer [43] and a polyhydroxylated G(6)-PAMAM dendrimer (Dendritech) were used. Inhibition experiments using mannose functionalized G(6) were performed using monomeric mannoside and monomeric lactoside, respectively.

Cell-based assay

Human prostate carcinoma cells (DU145, ATCC HTB-81) were purchased from ATCC, and maintained in Dulbecco's modified Eagle's medium (DMEM, Gibco) supplemented with 10% fetal bovine serum (FBS, Gibco). 2 mg/mL stock solutions of glycodendrimers were prepared in PBS buffer. Increasing glycodendrimer concentrations were added to a constant concentration of galectin-1 (3.7 μM) and cancer cells (≈240,000/eppendorf). Glycodendrimer concentrations were calculated to present approximately equal concentrations of lactosides residues at the same stage in the assays irrespective of PAMAM generation. Control assays for untreated cells (untreated standard) and the galectin-1 treated cells (galectin-1 standard) were performed. Control assays with the glycodendrimers and without galectin-1 were previously performed [44]. Assays were incubated at 37 °C and gently rotated for 1 hour. Images were captured on a Jenco microscope with 10× objective, and quantification was achieved using image analysis software (Pixcavator 6.0). Particles of fewer than five cells were defined as free cells and particles greater than five cells were defined as aggregated. Statistical analyses were performed using unpaired two-tailed student's T-Test by comparison to the galectin-1 standard. Statistically significant data is represented as * if $p < 0.05$, ** if $p < 0.01$, and *** if $p < 0.001$. The interaction between the galectin-1 and the DU145 cells generated large aggregates that exceeded the detection limit of the technique. Visual inspection of galectin-1 treated cells confirmed nearly complete aggregation of all cells; therefore, the percentage of free cells for the galectin-1 treated DU145 cells without glycodendrimer (galectin-1 stnd) was conservatively set at 20%.

Supporting Information

Supporting Information File 1

Experimental procedures, fluorescent micrographs of fluorescent standards and calibration curve, and statistical analysis of fluorescent microscopy results.
[http://www.beilstein-journals.org/bjoc/content/supplementary/1860-5397-11-84-S1.pdf]

Acknowledgements

We would like to acknowledge Dr. Linda Baum and Mabel Pang for providing the galectin-1, the Imaging and Chemical Analysis Laboratory at MSU for guidance with the fluorescent microscope, Dr. Candace Goodman for assistance with DLS and fluorescence microscopy, and Dr. Anna Michel for assistance with the cell-based assays. This research was supported by NIH GM62444 and NSF 121434.

References

1. Astorgues-Xerri, L.; Riveiro, M. E.; Tijeras-Raballand, A.; Serova, M.; Neuzillet, C.; Albert, S.; Raymond, E.; Faivre, S. *Cancer Treat. Rev.* **2014,** *40,* 307–319. doi:10.1016/j.ctrv.2013.07.007
2. Camby, I.; Le Mercier, M.; Lefranc, F.; Kiss, R. *Glycobiology* **2006,** *16,* 137R–157R. doi:10.1093/glycob/cwl025
3. Liu, F.-T.; Rabinovich, G. A. *Nat. Rev. Cancer* **2005,** *5,* 29–41. doi:10.1038/nrc1527
4. Rabinovich, G. A. *Br. J. Cancer* **2005,** *92,* 1188–1192. doi:10.1038/sj.bjc.6602493
5. Barondes, S. H.; Castronovo, V.; Cooper, D. N. W.; Cummings, R. D.; Drickamer, K.; Feizi, T.; Gitt, M. A.; Hirabayashi, J.; Hughes, C.; Kasai, K.; Leffler, H.; Liu, F.-T.; Lotan, R.; Mercurio, A. M.; Monsigny, M.; Pillai, S.; Poirer, F.; Raz, A.; Rigby, P. W. J.; Rini, J. M.; Wang, J. L. *Cell* **1994,** *76,* 597–598. doi:10.1016/0092-8674(94)90498-7
6. Barondes, S. H.; Cooper, D. N. W.; Gitt, M. A.; Leffler, H. *J. Biol. Chem.* **1994,** *269,* 20807–20810.
7. Klyosov, A. A.; Witczak, Z. J.; Platt, D. *Galectins;* Wiley: Hoboken, 2008. doi:10.1002/9780470378076
8. Brewer, C. F. *Glycoconjugate J.* **2002,** *19,* 459–465. doi:10.1023/B:GLYC.0000014075.62724.d0
9. Suzuki, O.; Abe, M. *Int. J. Oncol.* **2014,** *44,* 1433–1442. doi:10.3892/ijo.2014.2319
10. D'Haene, N.; Sauvage, S.; Maris, C.; Adanja, I.; Le Mercier, M.; Decaestecker, C.; Baum, L.; Salmon, I. *PLoS One* **2013,** *8,* e67029. doi:10.1371/journal.pone.0067029
11. Brewer, C. F. *Biochim. Biophys. Acta, Gen. Subj.* **2002,** *1572,* 255–262. doi:10.1016/S0304-4165(02)00312-4

12. Belardi, B.; O'Donoghue, G. P.; Smith, A. W.; Groves, J. T.; Bertozzi, C. R. *J. Am. Chem. Soc.* **2012,** *134,* 9549–9552. doi:10.1021/ja301694s
13. Hernandez, J. D.; Nguyen, J. T.; He, J.; Wang, W.; Ardman, B.; Green, J. M.; Fukuda, M.; Baum, L. G. *J. Immunol.* **2006,** *177,* 5328–5336. doi:10.4049/jimmunol.177.8.5328
14. Wang, J.; Lu, Z.-H.; Gabius, H.-J.; Rohowsky-Kochan, C.; Ledeen, R. W.; Wu, G. *J. Immunol.* **2009,** *182,* 4036–4045. doi:10.4049/jimmunol.0802981
15. Mancini, S. J. C.; Elantak, L.; Boned, A.; Espeli, M.; Guerlesquin, F.; Schiff, C. Examination of Galectin-Induced Lattice Formation on Early B-Cell Development. *Galectins: Methods and Protocols;* Springer Science & Business Media: New York, 2015; Vol. 1207, pp 169–184. doi:10.1007/978-1-4939-1396-1_11
16. Bojić-Trbojević, Z.; Krivokuća, M. J.; Kolundžić, N.; Petronijević, M.; Vrzic-Petronijević, S.; Golubović, S.; Vićovac, L. *Histochem. Cell Biol.* **2014,** *142,* 541–553. doi:10.1007/s00418-014-1229-7
17. Huang, Y.-J.; Shiau, A.-L.; Chen, S.-Y.; Chen, Y.-L.; Wang, C.-R.; Tsai, C.-Y.; Chang, M.-Y.; Li, Y.-T.; Leu, C.-H.; Wu, C.-L. *Eur. Cells Mater.* **2012,** *23,* 170–181.
18. Sacchettini, J. C.; Baum, L. G.; Brewer, C. F. *Biochemistry* **2001,** *40,* 3009–3015. doi:10.1021/bi002544j
19. Brewer, C. F.; Miceli, M. C.; Baum, L. G. *Curr. Opin. Struct. Biol.* **2002,** *12,* 616–623. doi:10.1016/S0959-440X(02)00364-0
20. Garner, O. B.; Baum, L. G. *Biochem. Soc. Trans.* **2008,** *36,* 1472–1477. doi:10.1042/BST0361472
21. López-Lucendo, M. F.; Solis, D.; André, S.; Hirabayashi, J.; Kasai, K.; Kaltner, H.; Gabius, H.-J.; Romero, A. *J. Mol. Biol.* **2004,** *343,* 957–970. doi:10.1016/j.jmb.2004.08.078
22. Mammen, M.; Choi, S.-K.; Whitesides, G. M. *Angew. Chem., Int. Ed.* **1998,** *37,* 2754–2794. doi:10.1002/(SICI)1521-3773(19981102)37:20<2754::AID-ANIE2754>3.0.CO;2-3
23. Gestwicki, J. E.; Strong, L. E.; Cairo, C. W.; Boehm, F. J.; Kiessling, L. L. *Chem. Biol.* **2002,** *9,* 163–169. doi:10.1016/S1074-5521(02)00102-3
24. Kiessling, L. L.; Gestwicki, J. E.; Strong, L. E. *Curr. Opin. Chem. Biol.* **2000,** *4,* 696–703. doi:10.1016/S1367-5931(00)00153-8
25. Kiessling, L. L.; Gestwicki, J. E.; Strong, L. E. *Angew. Chem., Int. Ed.* **2006,** *45,* 2348–2368. doi:10.1002/anie.200502794
26. Lee, Y. C.; Lee, R. T. *Acc. Chem. Res.* **1995,** *28,* 321–327. doi:10.1021/ar00056a001
27. Tejler, J.; Tullberg, E.; Frejd, T.; Leffler, H.; Nilsson, U. J. *Carbohydr. Res.* **2006,** *341,* 1353–1362. doi:10.1016/j.carres.2006.04.028
28. André, S.; Ortega, P. J. C.; Perez, M. A.; Roy, R.; Gabius, H.-J. *Glycobiology* **1999,** *9,* 1253–1261. doi:10.1093/glycob/9.11.1253
29. Tinari, N.; Kuwabara, I.; Huflejt, M. E.; Shen, P. F.; Iacobelli, S.; Liu, F.-T. *Int. J. Cancer* **2001,** *91,* 167–172. doi:10.1002/1097-0215(200002)9999:9999<::AID-IJC1022>3.3.CO;2-Q
30. Iurisci, I.; Cumashi, A.; Sherman, A. A.; Tsvetkov, Y. E.; Tinari, N.; Piccolo, E.; D'Egidio, M.; Adamo, V.; Natoli, C.; Rabinovich, G. A.; Iacobelli, S.; Nifantiev, N. E.; Behalf, C. I. *Anticancer Res.* **2009,** *29,* 403–410.
31. Belitsky, J. M.; Nelson, A.; Hernandez, J. D.; Baum, L. G.; Stoddart, J. F. *Chem. Biol.* **2007,** *14,* 1140–1151. doi:10.1016/j.chembiol.2007.09.007
32. Goodman, C. K.; Wolfenden, M. L.; Nangia-Makker, P.; Michel, A. K.; Raz, A.; Cloninger, M. J. *Beilstein J. Org. Chem.* **2014,** *10,* 1570–1577. doi:10.3762/bjoc.10.162
33. Miller, M. C.; Klyosov, A. A.; Mayo, K. H. *Glycobiology* **2012,** *22,* 543–551. doi:10.1093/glycob/cwr173
34. Joshi, M. D.; Ahmad, R.; Yin, L.; Raina, D.; Rajabi, H.; Bubley, G.; Kharbanda, S.; Kufe, D. *Mol. Cancer Ther.* **2009,** *8,* 3056–3065. doi:10.1158/1535-7163.MCT-09-0646
35. Jeschke, U.; Karsten, U.; Wiest, I.; Schulze, S.; Kuhn, C.; Friese, K.; Walzel, H. *Histochem. Cell Biol.* **2006,** *126,* 437–444. doi:10.1007/s00418-006-0178-1
36. Yang, J.; Hlavacek, W. S. *Math. Biosci.* **2011,** *232,* 164–173. doi:10.1016/j.mbs.2011.06.003
37. Esfand, R.; Tomalia, D. A. *Drug Discovery Today* **2001,** *6,* 427–436. doi:10.1016/S1359-6446(01)01757-3
38. Clausse, N.; van den Brule, F.; Waltregny, D.; Garnier, F.; Castronovo, V. *Angiogenesis* **1999,** *3,* 317–325. doi:10.1023/A:1026584523789
39. van den Brule, F. A.; Waltregny, D.; Castronovo, V. *J. Pathol.* **2001,** *193,* 80–87. doi:10.1002/1096-9896(2000)9999:9999<::AID-PATH730>3.0.CO;2-2
40. Hughes, R. C. *Biochimie* **2001,** *83,* 667–676. doi:10.1016/S0300-9084(01)01289-5
41. Ito, K.; Stannard, K.; Gabutero, E.; Clark, A. M.; Neo, S.-Y.; Onturk, S.; Blanchard, H.; Ralph, S. J. *Cancer Metastasis Rev.* **2012,** *31,* 763–778. doi:10.1007/s10555-012-9388-2
42. Ahmad, N.; Gabius, H.-J.; Sabesan, S.; Oscarson, S.; Brewer, C. F. *Glycobiology* **2004,** *14,* 817–825. doi:10.1093/glycob/cwh095
43. Woller, E. K.; Walter, E. D.; Morgan, J. R.; Singel, D. J.; Cloninger, M. J. *J. Am. Chem. Soc.* **2003,** *125,* 8820–8826. doi:10.1021/ja0352496
44. Michel, A. K.; Nangia-Makker, P.; Raz, A.; Cloninger, M. J. *ChemBioChem* **2014,** *15,* 2106–2112. doi:10.1002/cbic.201402134

License and Terms

BEILSTEIN JOURNAL OF ORGANIC CHEMISTRY

Discrete multiporphyrin pseudorotaxane assemblies from di- and tetravalent porphyrin building blocks

Mirko Lohse[1], Larissa K. S. von Krbek[2], Sebastian Radunz[1], Suresh Moorthy[2], Christoph A. Schalley[*2] and Stefan Hecht[*1]

Full Research Paper

Open Access

Address:
[1]Department of Chemistry, Humboldt-Universität zu Berlin, Brook-Taylor-Str. 2, 12489 Berlin, Germany. Fax: +49 (0)30 2093-6940; Tel: +49 (0)30 2093-7308 and [2]Institut für Chemie und Biochemie, Freie Universität Berlin, Takustraße 3, 14195 Berlin, Germany. Fax: +49(0)308385-5366; Tel: +49(0)308385-2639

Email:
Christoph A. Schalley[*] - christoph@schalley-lab.de; Stefan Hecht[*] - sh@chemie.hu-berlin.de

* Corresponding author

Keywords:
crown ethers; multicomponent assembly; multivalency; porphyrins; pseudorotaxanes

Beilstein J. Org. Chem. **2015,** *11,* 748–762.
doi:10.3762/bjoc.11.85

Received: 28 February 2015
Accepted: 29 April 2015
Published: 12 May 2015

This article is part of the Thematic Series "Multivalency as a chemical organization and action principle".

Guest Editor: R. Haag

Abstract

Two pairs of divalent and tetravalent porphyrin building blocks carrying the complementary supramolecular crown ether/secondary ammonium ion binding motif have been synthesized and their derived pseudorotaxanes have been studied by a combination of NMR spectroscopy in solution and ESI mass spectrometry in the gas phase. By simple mixing of the components the formation of discrete dimeric and trimeric (metallo)porphyrin complexes predominates, in accordance to binding stoichiometry, while the amount of alternative structures can be neglected. Our results illustrate the power of multivalency to program the multicomponent self-assembly of specific entities into discrete functional nanostructures.

Introduction

Supramolecular chemistry [1], the chemistry “beyond the molecule“ [2], has immensely reshaped the concepts of chemistry by putting the intermolecular interaction into the focus. Different fields of chemistry, from materials [3-6] and analytical sciences [7-12] to life science [13-17] have benefited from the development of the basic concepts of molecular recognition, templation [18], self-assembly [19], or self-sorting [20,21], just to name a few. More recently, multivalent binding [22-24] and cooperativity [25,26] have attracted significant attention mediated in particular by the desire to understand biological phenomena, such as virus docking to cells [27], toxin inhibition [28], or leucocyte recruitment in inflammation processes of the endothelium [29]. Multivalency has also inspired synthetic supramolecular architecture as it not only contributes to binding enhancement, but also helps to exert control over complex formation. For example, “molecular elevators” have been

constructed by Stoddart et al. [30,31] and giant porphyrin wheels were prepared by Anderson and co-workers [32,33], both using a multivalent template strategy.

The crown ether/secondary ammonium ion binding motif [34] is a powerful tool to create well-defined pseudorotaxane structures [35-39], which have also served as precursors in rotaxane syntheses [40-42] thus providing access to interlocked, mechanically bound molecules. Based on these structures, functional supramolecular architectures such as molecular switches and motors [43-45] as well as artificial muscles [46-50], have been synthesized.

Due to their four-fold symmetry, porphyrins are excellent candidates to extend these concepts to tetravalent supramolecules. Beyond being a mere spacer and scaffold connecting the binding sites, porphyrins also offer interesting physical and optical properties [51,52]. Therefore, they have played a pivotal role in supramolecular chemistry [53-66], for example as potential candidates for artificial light-harvesting systems [67-73].

Here, we report the synthesis of two new porphyrin-based di- and tetravalent ammonium guest molecules **A2** and **A4** and their complementary porphyrin-based di- and tetravalent crown ether hosts **C2** and **C4** (Figure 1). The selection of these building blocks is based on force-field calculations, which suggest a good geometric fit between the crown ether hosts and the ammonium ion guests. The two monovalent building blocks **A1** and **C1** serve as control compounds. Based on this

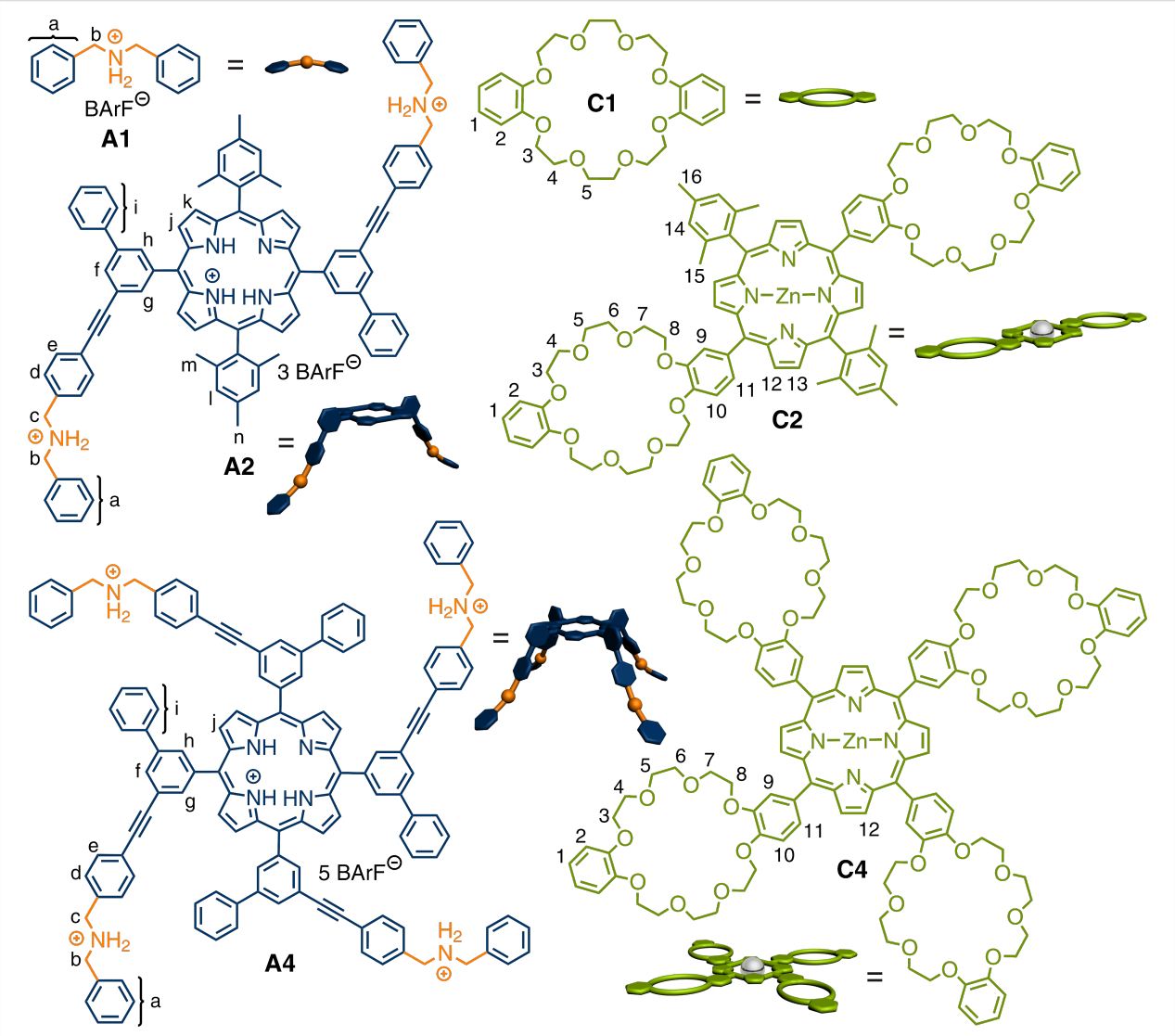

Figure 1: Mono-, di-, and tetravalent axles **A1**, **A2** and **A4** and mono-, di-, and tetravalent hosts **C1**, **C2** and **C4**. Numbers and letters are assigned to specific H atoms as discussed later in the main text.

"toolbox", which can be expanded in the future with other functional building blocks, the formation of specific multiply threaded pseudorotaxanes was achieved, thereby demonstrating the ability to program complex multicomponent self-assembly [74,75].

Results and Discussion

Synthesis

The synthesis of the two ammonium-substituted porphyrins **A2** and **A4** was performed convergent by first preparing two different (zinc)porphyrin cores **1** and **2** (Scheme 1), which are

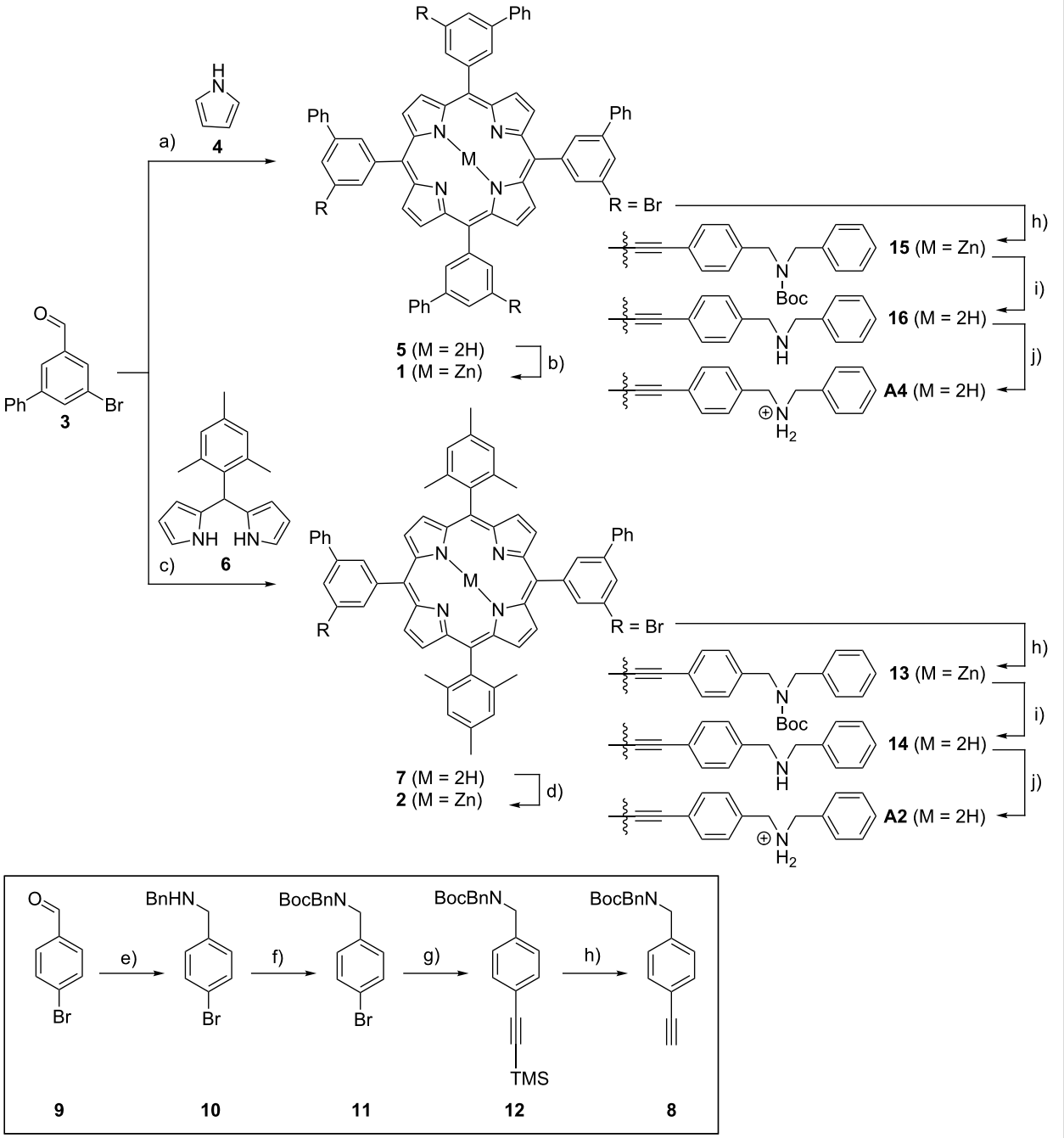

Scheme 1: Overview of the synthesis of the guests **A2** and **A4**. a) Pyrrole (**4**), $BF_3{\cdot}Et_2O$, DDQ, $CHCl_3$, rt; b) $Zn(OAc)_2$, $CHCl_3$/MeOH, rt; c) dipyrromethane **6**, $BF_3{\cdot}Et_2O$, DDQ, $CHCl_3$, rt; d) $Zn(OAc)_2$, $CHCl_3$/MeOH, rt; e) 1. benzylamine, trimethyl orthoformate, rt, 2. $NaBH_4$, THF/MeOH, rt; f) Boc_2O, triethylamine, CH_2Cl_2, rt; g) 1. ethynyltrimethylsilane, CuI, PPh_3, $Pd(PPh_3)_4$, TEA, toluene, 80 °C, 2. KOH, THF, rt; h) precursor **8**, CuI, PPh_3, $Pd(PPh_3)_4$, TEA, toluene, 80 °C; i) TFA, CH_2Cl_2, rt; j) 1. HCl, MeOH/$CHCl_3$, rt, 2. NaBArF, MeOH.

equipped with two and four bromine atoms in the *m*-position of the *meso*-phenyl substituents, respectively, for further functionalization. Zinc porphyrins **1** and **2** have been synthesized following standard protocols for symmetrical [76] A_4 and *trans*-disubstituted [77] A_2B_2 *meso*-functionalized porphyrins. The tetrabrominated core **1** was synthesized from aldehyde **3** and pyrrole (**4**) to form the free base porphyrin **5**, which is subsequently converted into its zinc complex **1**. On the other hand the difunctional core **2** was obtained through the condensation of aldehyde **3** with mesityldipyrromethane (**6**) followed by metalation of the intermediately formed free base porphyrin **7** to give its respective zinc complex **2**. In the next step, axle precursor **8** was synthesized by reductive amination of 4-bromobenzaldehyde (**9**) and benzylamine yielding amine **10**, which was subsequently Boc-protected, then reacted with trimethylsilylacetylene in a Sonogashira cross-coupling followed by desilylation. Finally, the porphyrin cores **1** and **2** were combined with axle precursor **8** in another two and four-fold Sonogashira cross-coupling reaction. After deprotection of the termini of the attached axles with trifluoroacetic acid (TFA), protonation of the free amines with HCl, and anion exchange with sodium tetrakis(3,5-bis(trifluoromethyl)phenyl)borate (NaBArF), the target compounds **A2** and **A4** were obtained. The weakly coordinating BArF counter-ion has been used to overcome solubility problems in organic solvents. It should be noted that the porphyrin is demetalated to yield the free base porphyrin during the deprotection of the Boc group. Furthermore, NMR integration of signals corresponding to the BArF protons relative to those corresponding to the macrocycle indicates that the porphyrin core is protonated (three BArF anions per divalent guest **A2**; five BArF anions per tetravalent guest **A4**). Based on the assumption that protonation of the porphyrin core, which is rather remote to the primary binding sites, does not influence the association strongly, no selective deprotonation of the porphyrin core has been attempted.

The preparation of the corresponding crown ether hosts (Scheme 2) involved an initial Williamson ether synthesis in which catechol (**17**) was first extended with 2-[2-(2-chloroethoxy)ethoxy]ethanol to diol **18**, which was then converted in dibromide **19** by an Appel reaction. Macrocyclization of **19** with 3,4-dihydroxybenzaldehyde under "pseudo high-

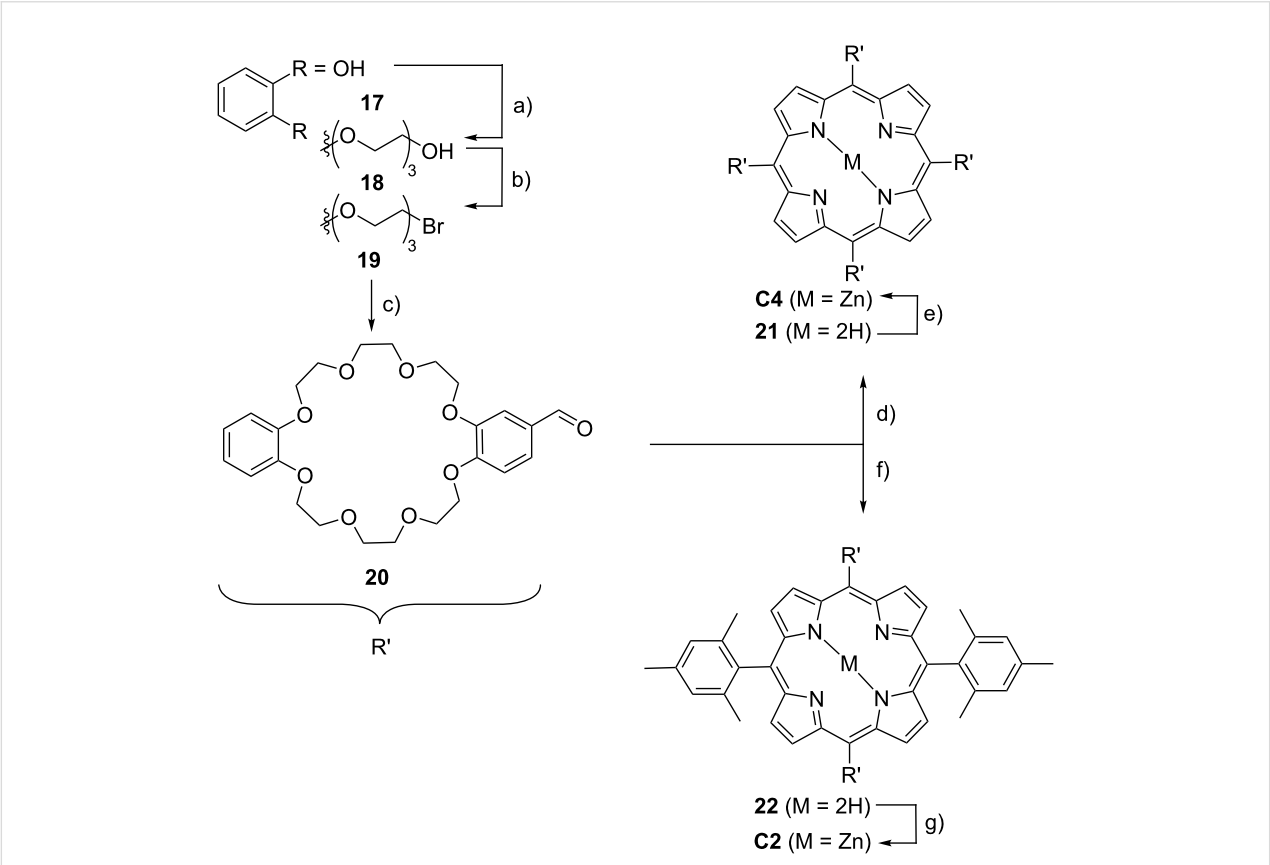

Scheme 2: Synthesis of crown ether hosts **C4** and **C2**: a) K_2CO_3, LiBr, **17**, 2-[2-(2-chloroethoxy)ethoxy]ethanol, DMF, 100 °C; b) CBr_4, PPh_3, CH_2Cl_2, rt; c) Cs_2CO_3, 3,4-dihydroxybenzaldehyde, DMF, 85 °C; d) 1. pyrrole (**4**), propionic acid, 140 °C, 2. $Zn(OAc)_2$, MeOH/$CHCl_3$, rt; e) 1. dipyrromethane (**6**), $BF_3{\cdot}Et_2O$, DDQ, $CHCl_3$, rt, 2. $Zn(OAC)_2$, MeOH/$CHCl_3$, rt.

dilution" conditions, i.e., slow addition of the two reactants into a solution of Cs_2CO_3 in DMF at 100 °C provides the corresponding crown ether aldehyde **20**. Porphyrin synthesis using **20** and pyrrole (**4**) following the Lindsey protocol [77] for A_4 porphyrins gives the desired tetravalent porphyrin host as the free base **21**, which is subsequently converted into the desired product **C4** by metalation using zinc(II) acetate. Host **C2** was synthesized according to the above-mentioned standard procedure [76] for *trans*-A_2B_2-porphyrins from **20** and mesityldipyrromethane **6** to form the divalent free base porphyrin **22**. Final zinc insertion provides the desired host **C2**.

For further detailed synthetic procedures and characterization data the reader is referred to Supporting Information File 1.

Formation and characterization of complexes

NMR spectroscopy of simple pseudorotaxanes prepared from crown ether wheels and secondary ammonium axles provides complexation-induced shift data, which can be easily interpreted and yield insight into complexation. Earlier experiences with divalent crown/ammonium pseudorotaxanes however also demonstrated that the NMR spectroscopic approach is often rather limited for more complex structures [78], as very complicated spectra are obtained with typically overlapping signals that prevent further (straightforward) analysis. Another complication, which makes the NMR analysis difficult, is the fact that the di- and tetravalent crown ethers **C2** and **C4** are achiral themselves, but become chiral, when complexed to axle components **A2** and **A4**. Consequently, the signals for all methylene protons of the crown ethers split into two diastereotopic ones not only producing another set of signals, but also more complicated splitting patterns. Furthermore, the crown ethers are connected to the porphyrin core by single bonds, around which they can easily rotate in the non-complexed state. This rotation is, however, fixed upon complexation and two possible orientations of each of the crown ethers on its corresponding axle are possible. One can therefore expect a mixture of stereoisomers to form. In the simplest case, **A2@C2**, two enantiomers and one *meso*-form are expected to exist, which should result in two overlapping sets of signals. For the other three complexes, the situation is even more complicated. Therefore, a straightforward and easy analysis of the NMR spectra will likely be impossible.

In our earlier studies [37,78,79], however, electrospray ionization (ESI) mass spectrometry (MS) turned out to be a perfectly suited method to characterize the complexes present in solution. The formation of unspecific complexes as well as fragmentation upon ionization have been found to be quite limited so that the picture obtained from the mass spectra can be expected to provide realistic insights into the composition of the complexes present in solution. As all stereoisomers have the same elemental composition, their presence as a mixture does not obscure the mass spectrometric results. For these reasons, we describe our NMR spectroscopic data, but focus on ESI–MS of the complexes under study starting with the four possible combinations of **A2** and **A4** with monovalent dibenzo[24]crown-8 **C1** as well as of **C2** and **C4** with monovalent dibenzylammonium **A1** (Figure 2, top), followed by the results obtained for the multivalent 1:1 and 2:1 complexes **A2@C2**, **A2$_2$@C4**, **A4@C2$_2$** and **A4@C4** (Figure 2, bottom).

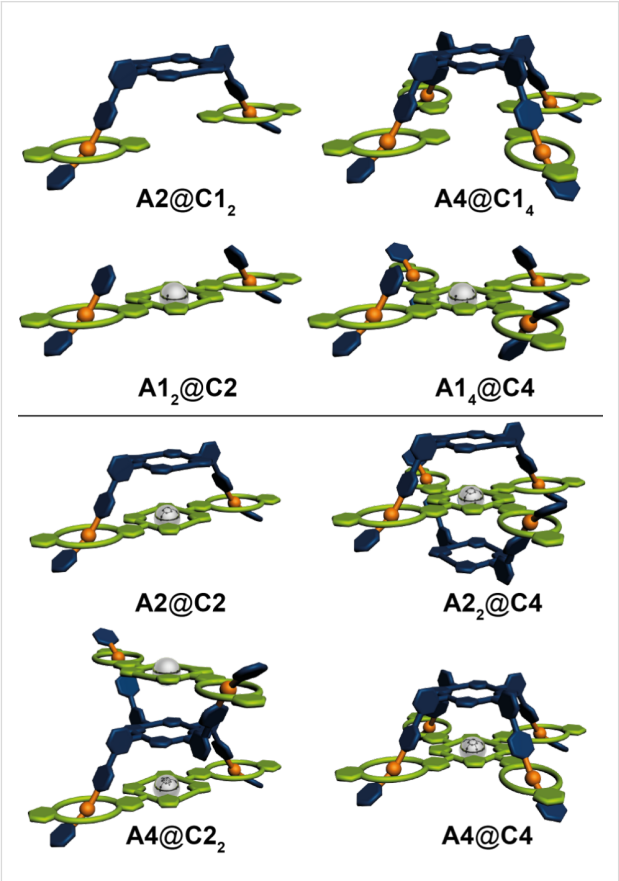

Figure 2: Schematic representation of the host–guests complexes. Top: complexes **A2@C1$_2$**, **A4@C1$_4$**, **A1$_2$@C2** and **A1$_4$@C4**, which are built from one multi- and several monovalent building blocks. Bottom: complexes **A2@C2, A2$_2$@C4, A4@C2$_2$** and **A4@C4**, which are built from di- or tetravalent building blocks.

[3]- and [5]pseudorotaxanes from monovalent building blocks

First the association of **A2** and **A4** with monovalent **C1** as well as **C2** and **C4** with monovalent **A1** was investigated and it can be seen that in all four cases successful complexation with the expected stoichiometry was achieved. For instance, upon addition of **C1** to a 3 mM solution of **A2** (Figure 3a) a continuous complexation, indicated by the appearance of a new set of signals due to slow exchange rates on the NMR-time scale,

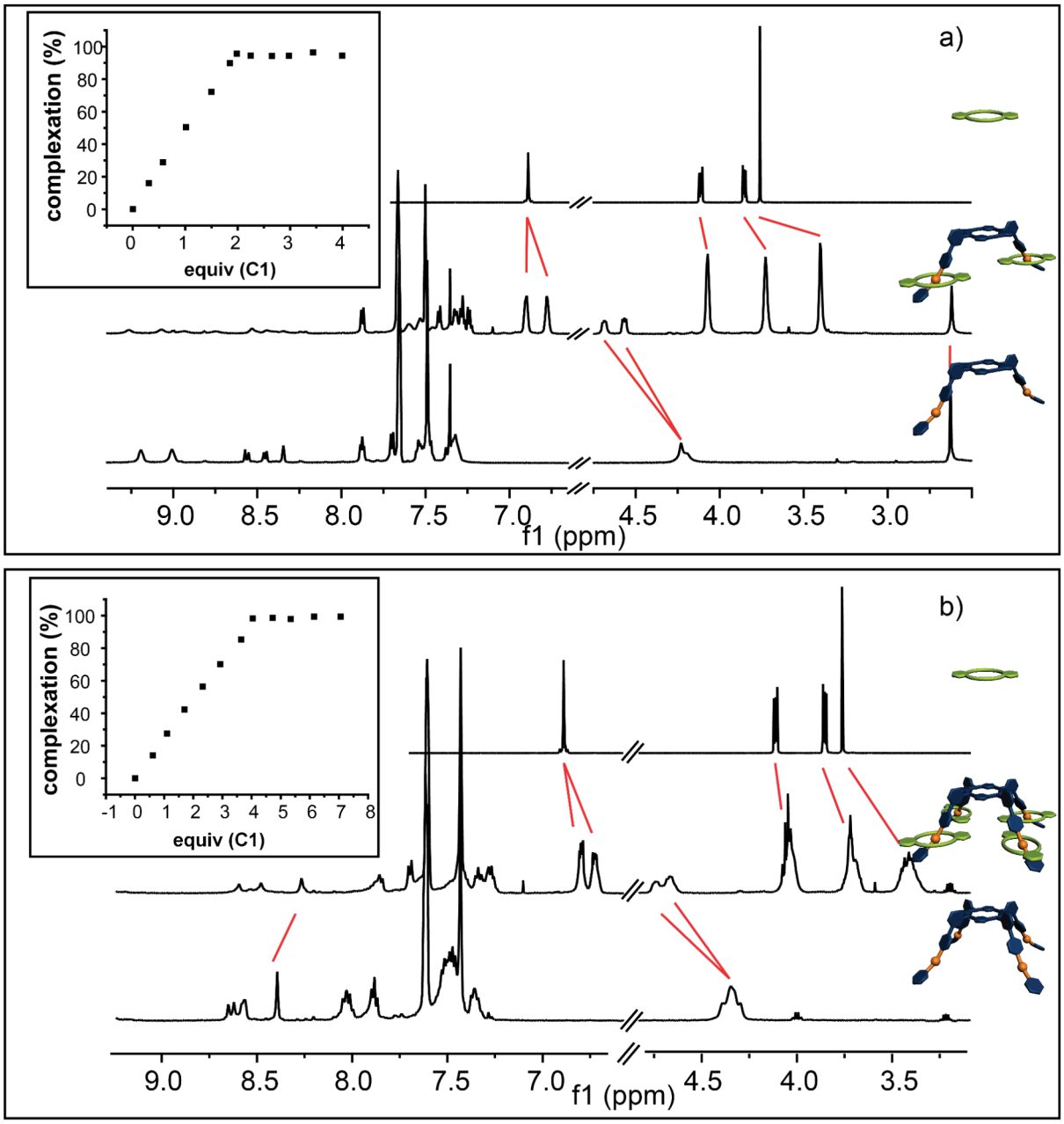

Figure 3: ^{1}H NMR (500 MHz, 298 K, CD_2Cl_2, 3 mM) of a) **C1** (top), **A2@C1$_2$** (middle) and **A2** (bottom); b) **C1** (top), **A4@C1$_4$** (middle) and **A4** (bottom) showing clear evidence of the complexation. The red lines indicate the shift of the proton signals upon addition. The inserts show the titration curve of each complexation with the expected ratio of the complex formed.

could be observed. Upon association the benzyl signals $H^{b/c}$ shift downfield by approximately +0.3 ppm and split into two separate pair of signals, which is typical for a complexation of **C1** with a dibenzylammonium moiety [36]. The aromatic signals of **C1** $H^{1/2}$ shift slightly upfield by −0.1 ppm and split as well. The signals of the crown ether region shift upfield by −0.05, −0.14, and −0.38 ppm due to complexation. An overstoichiometric addition of **C1** results in no further association (see Figure 3a, inset), clearly proving the desired host–guest ratio in the supramolecular structure. Similar results are obtained for the other [3]- and [5]pseudorotaxanes (Figure 3b and Figure 4a,b). However, it should be noted that despite extensive titration experiments (see Supporting Information File 1 for details) a detailed analysis of the binding constants of these systems cannot be obtained as the binding constants are too high for a NMR-based method.

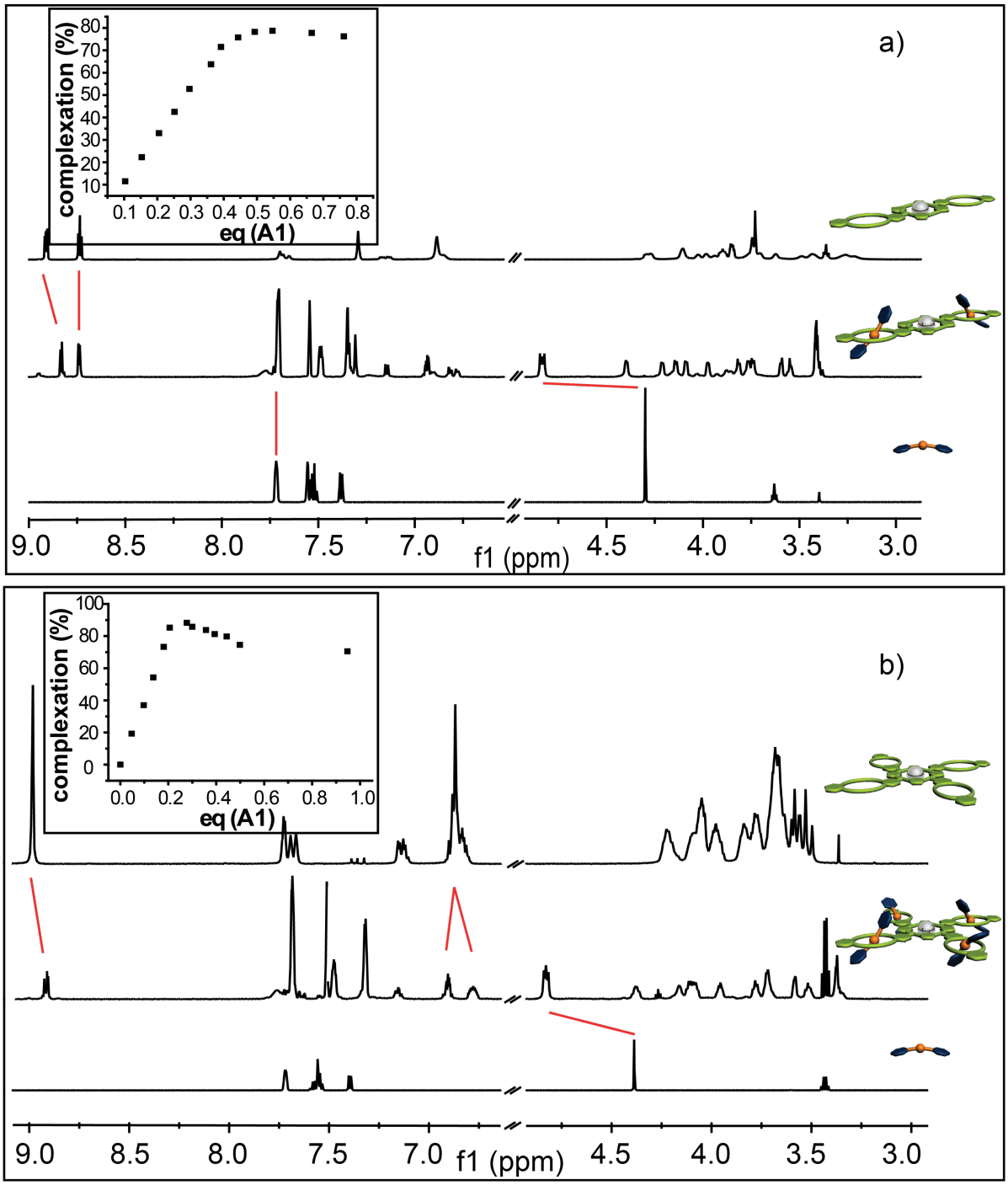

Figure 4: ^{1}H NMR (500 MHz, 298 K, CD_2Cl_2, 3 mM) of a) **C2** (top), **A1$_2$@C2** (middle) and **A1** (bottom) and b) **C4** (top), **A1$_4$@C4** (middle) and **A1** (bottom) showing clear evidence of the complexation. The red lines indicate the shift of the proton signals upon addition. The inserts show the titration curve of each complexation with the expected ratio of the complex formed.

Guests **A2** and **A4** as well as the hosts **C2** and **C4** show typical absorption behavior for porphyrin-based molecules. All four have pronounced absorption maxima at around 420 nm (Soret band) and less intense absorption bands between 500 and 600 nm (Q-bands). However, **A4** shows rather strong aggregation even in the µM concentration regime likely caused by elec-

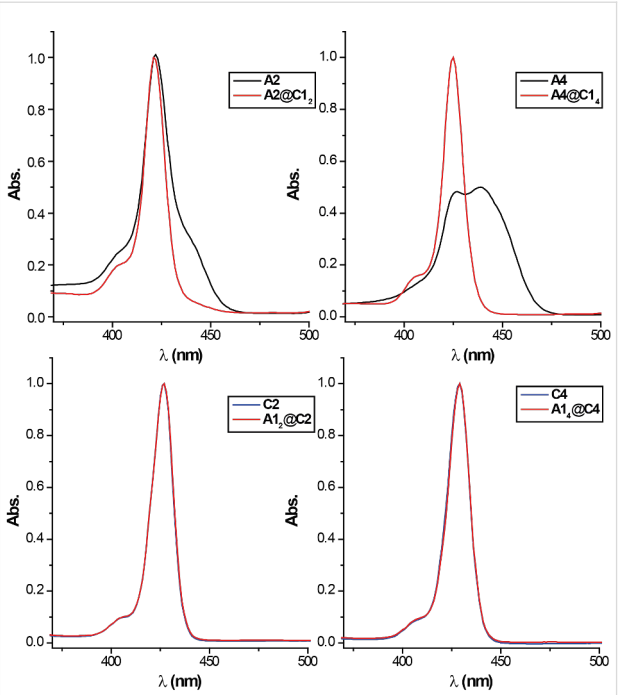

Figure 5: Normalized UV–vis absorption spectra (CH_2Cl_2, 3 μM) of **A2**, **A4**, **C2** and **C4** and their complexes formed with the monovalent building blocks **A1** and **C1** showing no significant batho- or hypsochromic shift. Absorption spectrum of **A4** was normalized to 0.5 because of the strong self-aggregation and the resulting broad Soret band.

trostatic interactions mediated by the closely associated BArF counter-ions that are expected to be significant as rather non-polar solvents are being used. This aggregation results in a broad red-shifted absorption band. Upon complexation this aggregate is broken, resulting in the recovery of a typical sharp Soret band at 420 nm. Note that UV–vis titration shows no significant batho- or hypsochromic shift upon association (Figure 5) of neither di- and tetravalent guests **A2** and **A4** with monovalent host **C1** nor of monovalent guest **A1** to the di- and tetravalent hosts **C2** and **C4**. The lack of such optical signature of the complexation event in the characteristic porphyrin absorption can be explained by the fact that the binding sites are electronically decoupled from the porphyrin core.

The [3]- and [5]pseudorotaxanes with the monovalent building blocks were further investigated by ESI-Q-TOF mass spectrometry. Separate solutions of hosts and guests were prepared (**A1**/**C1**: 4 mM, **A2**/**C2**: 2 mM, **A4**/**C4**: 1 mM all in CH_2Cl_2), and the same aliquots of the individual solutions were combined to obtain equal concentrations of ammonium ion functions and crown ether moieties in each solution. The solutions of the pseudorotaxanes were allowed to equilibrate for 24 hours at room temperature and diluted to 0.2 μM prior to analysis. The respective [3]- or [5]pseudorotaxanes could be detected for all mixtures (Figure 6). In the cases of the 1:2 and 1:4 mixtures of **A2** and **A4** with **C1**, respectively, the respective pseudorotaxanes **A2**@**C1**$_2$ and **A4**@**C1**$_4$ give rise to the second and third most abundant species (Figure 6a,b). One signal represents the desired doubly, respectively quadruply charged pseudorotaxane ([**A2**@**C1**$_2$]$^{2+}$ at m/z 1094 and [**A4**@**C1**$_4$]$^{4+}$ at m/z = 898). In addition, a second set of signals for the triply, respectively five-fold charged species ([**A2**@**C1**$_2$ + H]$^{3+}$ at m/z = 729 and [**A4**@**C1**$_4$ + H]$^{5+}$ at m/z = 719) could be observed. The most abundant species – most probably due to its high ESI response factor – is the one sodium ion containing molecular ion of **C1** ([Na@**C1**]$^{+}$ at m/z 471, see Supporting Information File 1). The spectra of the di- and tetravalent hosts **C2** and **C4** and the monovalent guest **A1** show a more complex signal pattern (Figure 6c,d). In the mixture of divalent crown ether **C2** with **A1** three different species in a statistical distribution of 1:2:1 were detected: the host with two axles [**A1**$_2$@**C2**]$^{2+}$ (m/z = 948), the host with one axle and one sodium ion [Na**A1**@**C2**]$^{2+}$ (m/z = 861) and the host loaded with two sodium ions ([Na$_2$@**C2**]$^{2+}$ m/z = 773). This can be easily explained with the nature of the ESI spray process, which is known to cause the dissociation in multiply charged non-covalently bound complexes. The results of the NMR titrations, however, clearly indicate the doubly bound pseudorotaxane **A1**$_2$@**C2** to be the most prominent species in solution (Figure 4a). The fact that the desired pseudorotaxane **A1**$_2$@**C2** can be detected by mass spectrometry despite the likely dissociation of the multiply charged complex in the ion source shows that this technique gives reasonable results for determining the species present in solution. The 4:1 mixture of **A1** and **C4** gives rise to an even more complex signal pattern (Figure 6d). Due to the four binding sites of **C4**, there are numerous possibilities of **A1** and sodium cations to bind. There are species with three or four guest ions detected with an approximately statistic distribution: [Na$_{(4-x)}$**A1**$_x$@**C4**]$^{4+}$ (x = 1, 2, 3, 4) and [Na$_{(3-y)}$**A1**$_y$@**C4**]$^{3+}$ (y = 1, 2, 3). The desired [5]pseudorotaxane is not very stable at the ionization conditions, but is nevertheless detected ([**A1**$_4$@**C4**]$^{4+}$ at m/z = 737). As explained above, this shows that mass spectrometry gives a reasonable image of the species present in solution, because we already know from NMR titration studies that the [5]pseudorotaxane **A1**$_4$@**C4** is the predominant species in solution (Figure 4b).

To summarize, all four desired [3]- or [5]pseudorotaxanes could be detected by mass spectrometry despite the likeliness of **A1**$_2$@**C2** and **A1**$_4$@**C4** to dissociate upon electrospray ionization. These results show that mass spectrometry should be a well suited method for the investigation of the multivalent pseudorotaxanes under study. These usually show much higher binding constants than the monovalent analogue and should therefore very likely survive the ionization process.

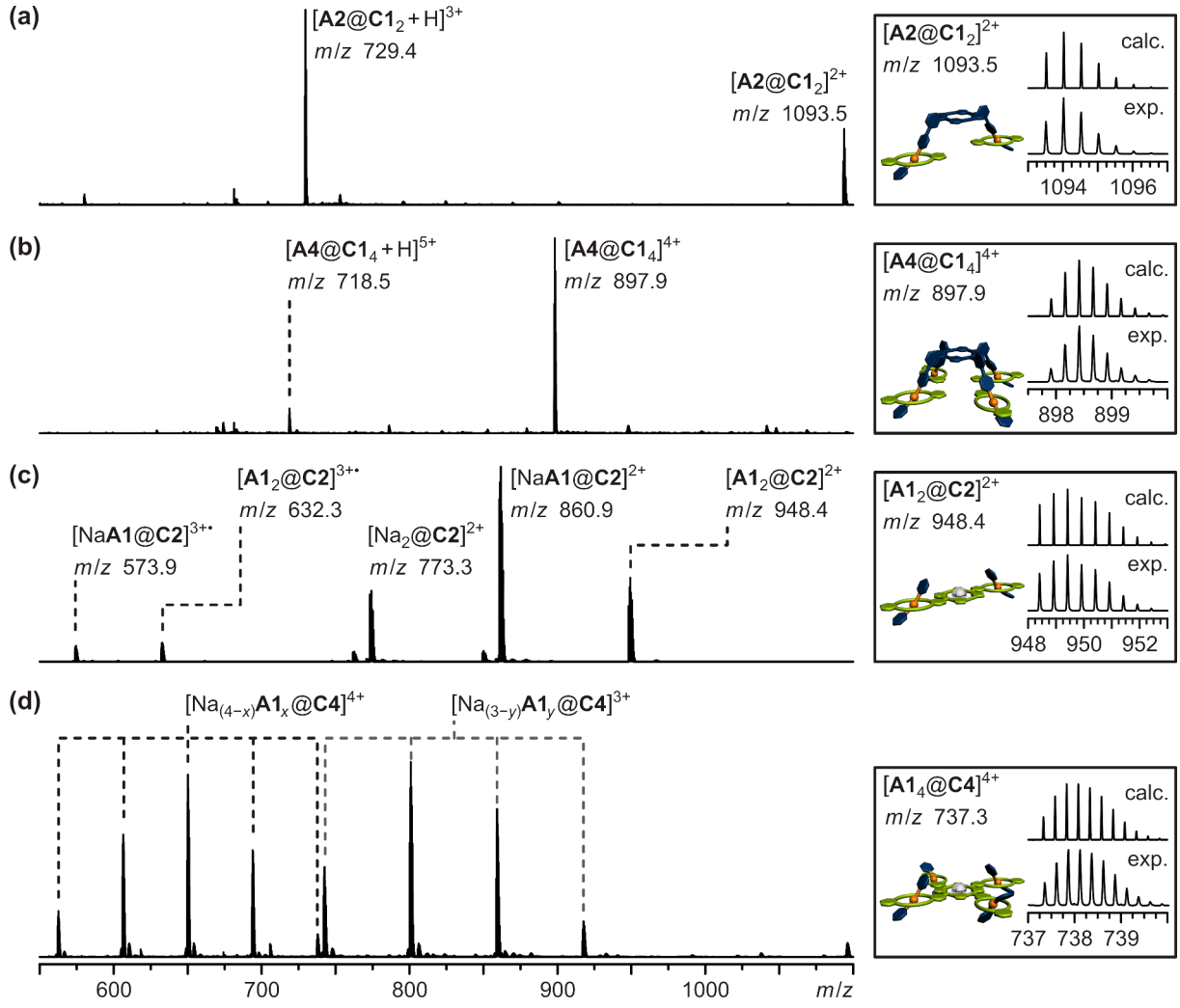

Figure 6: ESI-Q-TOF-MS spectra (CH_2Cl_2, 0.2 μM; left hand side) and respective experimental and calculated isotopic patterns of the desired [3]- or [5]pseudorotaxanes (right hand side): a) 1:2 mixture of **A2** and **C1**, b) 1:4 mixture of **A4** and **C1**, c) 2:1 mixture of **A1** and **C2**, d) 4:1 mixture of **A1** and **C4**. For reasons of clarity not all of the peaks are assigned (see Supporting Information File 1 for details).

[2]- and [3]pseudorotaxanes from di- and tetravalent building blocks

Subsequently, we investigated the di- and tetravalent pseudorotaxanes formed between **A2**, **A4**, **C2**, and **C4**. As already mentioned above, NMR spectroscopy is limited for the given systems because of the numerous isomers that can be formed. However, some general conclusion can be made. In all four cases one can observe a shift of the benzylic protons $H^{b/c}$ down field by approximately 0.5 ppm, which is typical for the threading in a crown ether/secondary ammonium ion binding motif. Furthermore, the signals for the crown ether region broaden significantly, which is in agreement with the assumption that upon complexation the number of signals increases because the methylene protons become diasterotopic and different supramolecular stereoisomers can form. However, based on the present NMR spectroscopy data (Figure 7 and Figure 8) one cannot exclude the formation of polymeric aggregates or only partially threaded structures. For this reason the formed complexes were analyzed in detail using mass spectrometry.

Comparing the absorption of the complexes (Figure 9), one can see that the tetravalent **A4@C4** complex shows the strongest blue shift while the divalent **A4@C2$_2$** shows almost no change in the spectrum (except breaking the **A4** aggregate). The hypsochromic shift indicates a parallel alignment of the porphyrin moieties, which is in good agreement with the hypothesized structure. However, since the observed shifts are rather small the interactions, i.e., exciton coupling, between the two porphyrin chromophores seems to be rather weak.

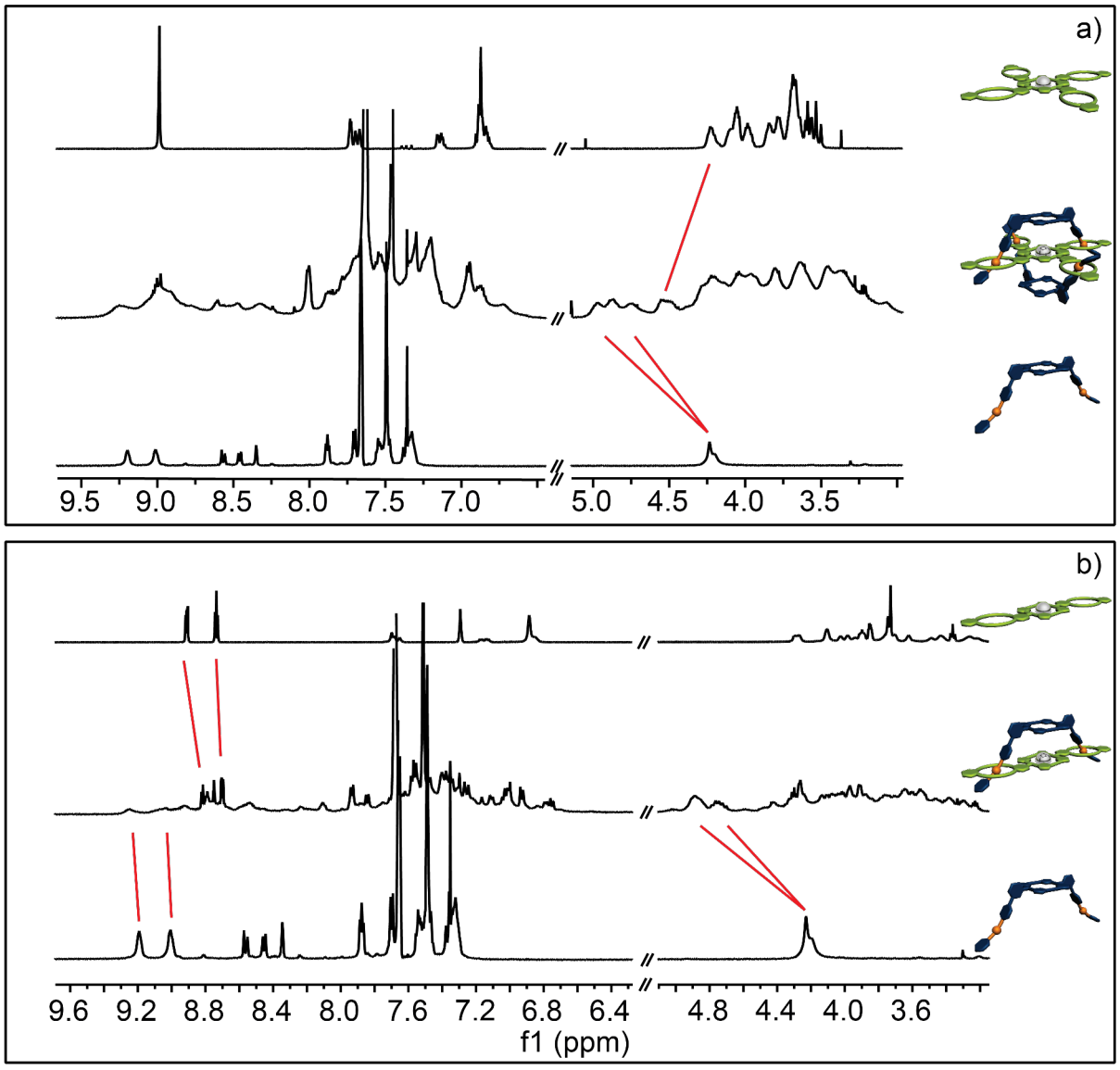

Figure 7: ^{1}H NMR (500 MHz, 298 K, CD_2Cl_2, 1 mM) of a) **C4** (top), **A2$_2$@C4** (middle) and **A2** (bottom); b) **C2** (top), **A2@C2** (middle) and **A2** (bottom). Disappearance and shift of the signals (red lines) suggest complexation. Due to the presence of a complex stereoisomeric mixture only qualitative information of the complexation is possible.

For mass spectrometric analysis (ESI-Q-TOF MS) of the desired pseudorotaxanes separate solutions of hosts and guests were prepared (CH_2Cl_2, **A2**/**C2**: 0.6 mM, **A4**/**C4**: 0.3 mM). They were mixed in the respective 1:1, 1:2, and 2:1 molar ratios and allowed to equilibrate for 14 hours at 6 °C, after which no further changes in the mass spectra were observed and thus equilibrium was reached. The pseudorotaxane solutions were diluted to 0.2 µM prior to analysis. The respective mass spectra are shown in Figure 10. Guest **A2** was combined with host **C2** as well as **C4** in 1:1 and 2:1 ratios, respectively. The expected pseudorotaxanes $[\mathbf{A2@C2}]^{2+}$ (m/z = 1396) and $[\mathbf{A2_2@C4}]^{4+}$ (m/z = 1185) are detected as the major species (Figure 10a,b). A species with only one guest **A2** in host **C4** $[Na_2\mathbf{A2@C4}]^{4+}$ (m/z = 873) could also be detected but with very low intensity. This partly bound species **A2@C4** could in principle allow formation of small oligomers, if present in solution. The fact that no oligomers could be detected and the very small abundance of the signal of the partly bound state $[Na_2\mathbf{A2@C4}]^{4+}$ (m/z = 873) leads to the conclusion, that this partly bound pseudorotaxane is most probably a product of the electrospray ionization process.

In cases of the 1:1 mixture of **A4** and **C4** and the 1:2 mixture of **A4** and **C2** the desired pseudorotaxanes $[\mathbf{A4@C4}]^{4+}$

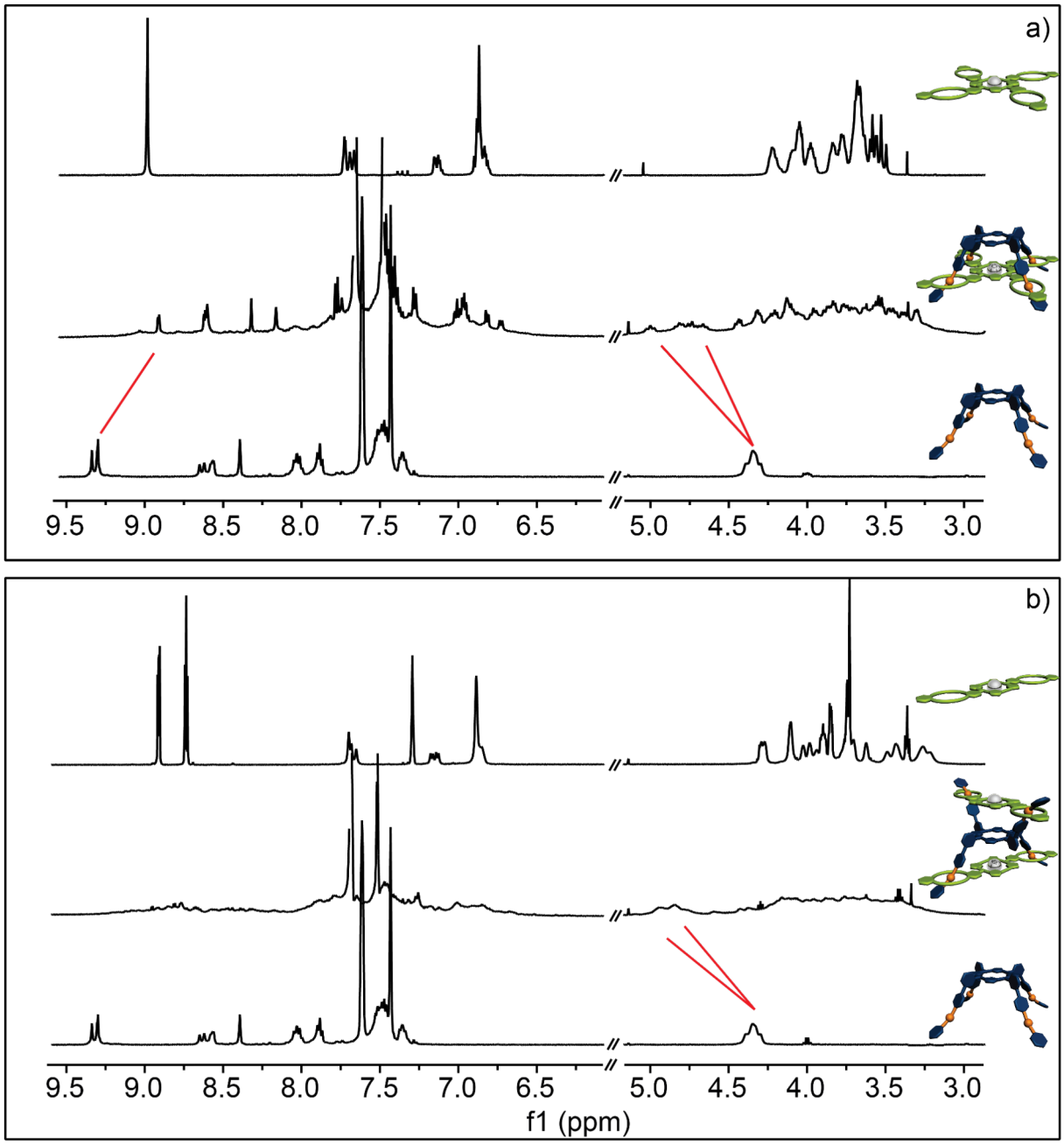

Figure 8: ^{1}H NMR (500 MHz, 298 K, CD_2Cl_2, 1 mM) of a) **C4** (top), **A4@C4** (middle) and **A4** (bottom) and b) **C2** (top), **A4@C2$_2$** (middle) and **A4** (bottom). Disappearance and shift of the signals (red lines) suggest complexation. Due to the presence of a complex stereoisomeric mixture only qualitative information of the complexation is possible.

(m/z = 989) and [**A4@C2**$_2$]$^{4+}$ (m/z = 1200) are the most abundant species and there are again only traces of the possible 1:1 pseudorotaxane [**A4@C2**]$^{4+}$ (m/z = 825) detected (Figure 10c,d). As mentioned above, this is most probably a product of the ionization process. The free hosts **C4** and **C2** are detected in only small amounts or traces. Again, in both cases no oligomers are observed.

In summary, the formation of all desired multivalent pseudorotaxanes of building blocks **A2**, **A4**, **C2**, and **C4** could be verified by mass spectrometry. The defined stoichiometry for the observed pseudorotaxanes in the gas phase ([**A2@C2**]$^{2+}$, [**A2**$_2$**@C4**]$^{4+}$, [**A4@C4**]$^{4+}$, [**A4@C2**$_2$]$^{4+}$), the only slight abundance of partly bound pseudorotaxanes ([Na$_2$**A2@C4**]$^{4+}$, [**A4@C2**]$^{4+}$) and the absence of any oligomeric species gives

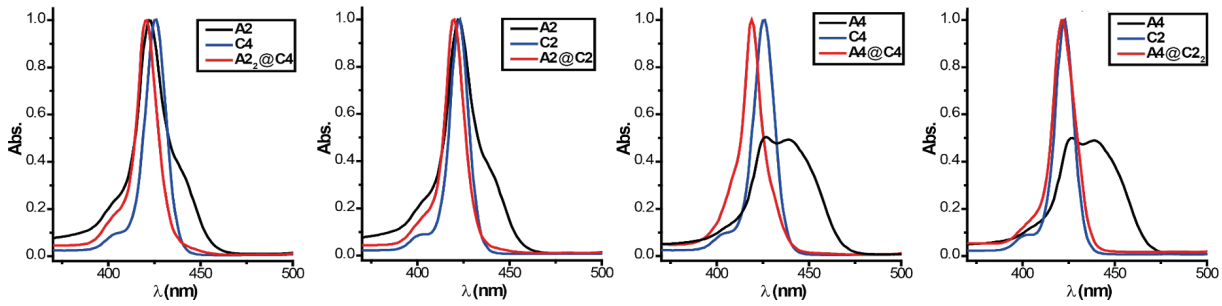

Figure 9: Normalized UV–vis absorption spectra (CH_2Cl_2, 2 μM) of the guests **A2** and **A4** (black), the hosts **C2** and **C4** (blue) and of the mixtures (red), showing a slight hypsochromic shift of the absorption maxima upon complexation.

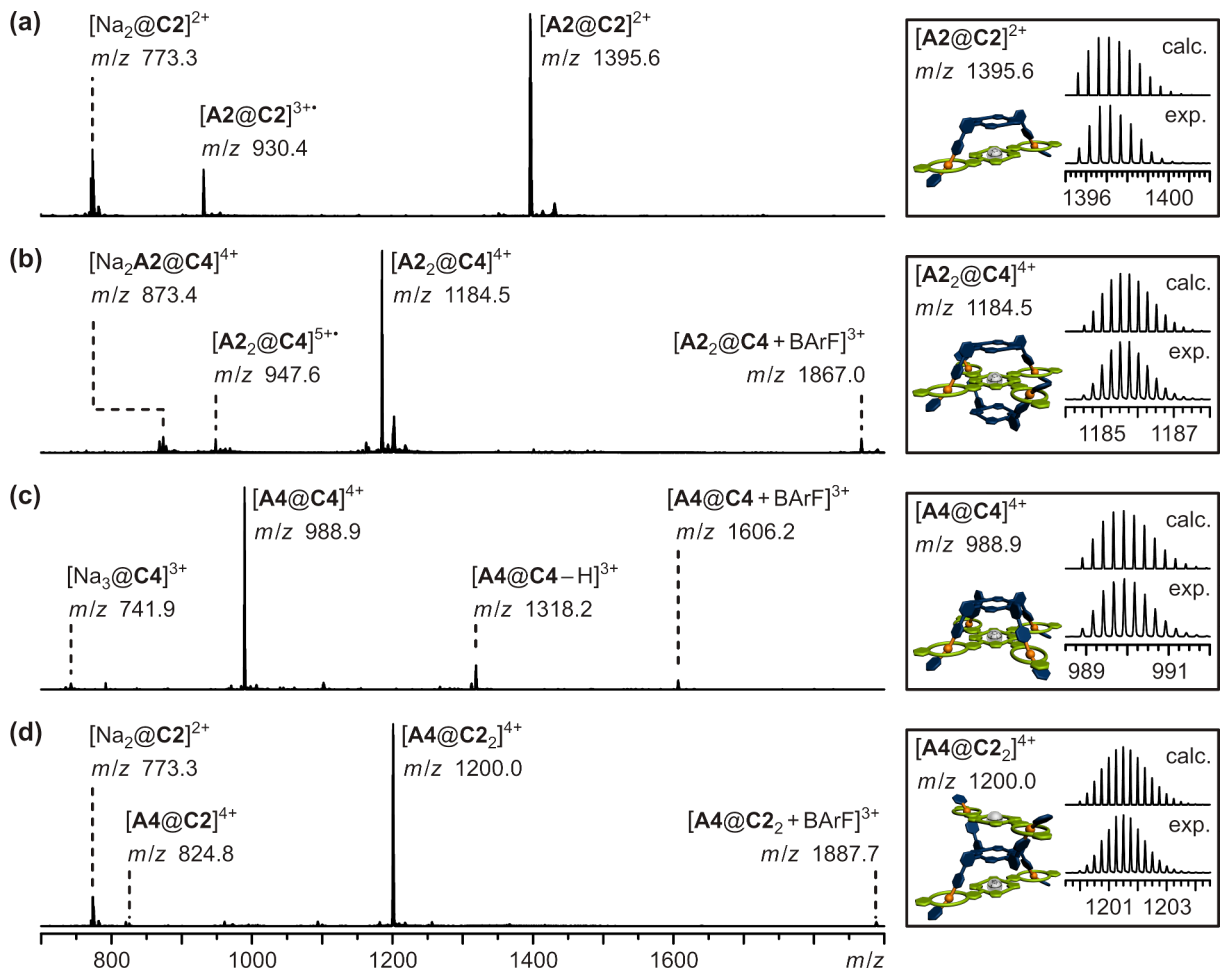

Figure 10: ESI-Q-TOF-MS spectra (CH_2Cl_2, 0.2 μM; left hand side) and respective experimental and calculated isotopic patterns of the desired [2]- or [3]pseudorotaxanes (right hand side): a) 1:1 mixture of **A2** and **C2**, b) 2:1 mixture of **A2** and **C4**, c) 1:1 mixture of **A4** and **C4**, d) 1:2 mixture of **A4** and **C2**.

clear evidence, that this specific binding situation is also present in solution.

Conclusion

The successful synthesis of di- and tetravalent porphyrin-based guests **A2** and **A4** as well as their complementary di- and tetravalent hosts **C2** and **C4** could be achieved. All four molecules show strong binding even to simple monovalent building blocks **A1** and **C1**, respectively, which could be shown by NMR-titration experiments as well as mass spectrometry. Furthermore, the formation of the di- and tetravalent pseudorotaxanes **A2@C2**, $\mathbf{A2_2@C4}$, $\mathbf{A4@C2_2}$, and **A4@C4** could be demonstrated qualitatively by NMR spectroscopy and was investigated in detail by mass spectrometry. Since the association constants in the monovalent cases are already too high to be determined by NMR-titration experiments, currently ongoing work is dealing with the daunting task to quantify the binding constants for the di- and tetravalent multiporphyrin complexes for example using isothermal calorimetry (ITC), in order to analyze the thermodynamics and kinetics of multivalent binding in these architectures in detail. In the future, we will continue to exploit the concept of complementary multivalent binding to program the increasingly complex self-assembly of multiple different chromophore components into functional supramolecular architectures.

Supporting Information

Supporting Information File 1

Detailed synthetic procedures.
[http://www.beilstein-journals.org/bjoc/content/supplementary/1860-5397-11-85-S1.pdf]

Acknowledgements

The authors thank the Deutsche Forschungsgemeinschaft for generous financial support (SFB 765). L.v.K. is grateful to the Studienstiftung des Deutschen Volkes for a Ph.D. fellowship. S.M. acknowledges the Alexander-von-Humboldt foundation for a postdoctoral fellowship.

References

1. Steed, J. W.; Atwood, J. L. *Supramolecular Chemistry;* Wiley: Chichester, UK, 2007.
2. Lehn, J.-M. *Angew. Chem., Int. Ed.* **1988,** *27,* 89–112. doi:10.1002/anie.198800891
3. Desiraju, G. R. *Angew. Chem., Int. Ed.* **2007,** *46,* 8342–8356. doi:10.1002/anie.200700534
4. Hirst, A. R.; Escuder, B.; Miravet, J. F.; Smith, D. K. *Angew. Chem., Int. Ed.* **2008,** *47,* 8002–8018. doi:10.1002/anie.200800022
5. Bhosale, R.; Mišek, J.; Sakai, N.; Matile, S. *Chem. Soc. Rev.* **2010,** *39,* 138–149. doi:10.1039/B906115K
6. Zhao, Y.; Sakai, F.; Su, L.; Liu, Y.; Wei, K.; Chen, G.; Jiang, M. *Adv. Mater.* **2013,** *25,* 5215–5256. doi:10.1002/adma.201302215
7. Cametti, M.; Crousse, B.; Metrangolo, P.; Milani, R.; Resnati, G. *Chem. Soc. Rev.* **2012,** *41,* 31–42. doi:10.1039/C1CS15084G
8. Valeur, B.; Leray, I. *Coord. Chem. Rev.* **2000,** *205,* 3–40. doi:10.1016/S0010-8545(00)00246-0
9. Flink, S.; van Veggel, F. C. J. M.; Reinhoudt, D. N. *J. Phys. Chem. B* **1999,** *103,* 6515–6520. doi:10.1021/jp990014v
10. Beer, P. D.; Gale, P. A. *Angew. Chem., Int. Ed.* **2001,** *40,* 486–516. doi:10.1002/1521-3773(20010202)40:3<486::AID-ANIE486>3.0.CO;2-P
11. Martínez-Máñez, R.; Sancenón, F. *Chem. Rev.* **2003,** *103,* 4419–4476. doi:10.1021/cr010421e
12. Llinares, J. M.; Powell, D.; Bowman-James, K. *Coord. Chem. Rev.* **2003,** *240,* 57–75. doi:10.1016/S0010-8545(03)00019-5
13. Chen, Y.; Liu, Y. *Chem. Soc. Rev.* **2010,** *39,* 495–505. doi:10.1039/B816354P
14. Feiters, M. C.; Rowan, A. E.; Nolte, R. J. M. *Chem. Soc. Rev.* **2000,** *29,* 375–384. doi:10.1039/a804252g
15. Wang, L.; Li, L.-L.; Ma, H. L.; Wang, H. *Chin. Chem. Lett.* **2013,** *24,* 351–358. doi:10.1016/j.cclet.2013.03.018
16. Huskens, J. *Curr. Opin. Chem. Biol.* **2006,** *10,* 537–543. doi:10.1016/j.cbpa.2006.09.007
17. Vigneron, J.-P. *Molecules* **1999,** *4,* 180–203. doi:10.3390/40700180
18. Diederich, F.; Stang, P. J. *Templated Organic Synthesis;* Wiley-VCH: Weinheim, Germany, 2000.
19. Whitesides, G. M.; Mathias, J. P.; Seto, C. T. *Science* **1991,** *254,* 1312–1319. doi:10.1126/science.1962191
20. Safont-Sempere, M. M.; Fernández, G.; Würthner, F. *Chem. Rev.* **2011,** *111,* 5784–5814. doi:10.1021/cr100357h
21. He, Z.; Jiang, W.; Schalley, C. A. *Chem. Soc. Rev.* **2015,** *44,* 779–789. doi:10.1039/C4CS00305E
22. Mammen, M.; Choi, S.-K.; Whitesides, G. M. *Angew. Chem., Int. Ed.* **1998,** *37,* 2754–2794. doi:10.1002/(SICI)1521-3773(19981102)37:20<2754::AID-ANIE2754>3.0.CO;2-3
23. Mulder, A.; Huskens, J.; Reinhoudt, D. N. *Org. Biomol. Chem.* **2004,** *2,* 3409–3424. doi:10.1039/b413971b
24. Fasting, C.; Schalley, C. A.; Weber, M.; Seitz, O.; Hecht, S.; Koksch, B.; Dernedde, J.; Graf, C.; Knapp, E.-W.; Haag, R. *Angew. Chem., Int. Ed.* **2012,** *51,* 10472–10498. doi:10.1002/anie.201201114
25. Hunter, C. A.; Anderson, H. L. *Angew. Chem., Int. Ed.* **2009,** *48,* 7488–7499. doi:10.1002/anie.200902490
26. Ercolani, G.; Schiaffino, L. *Angew. Chem., Int. Ed.* **2011,** *50,* 1762–1768. doi:10.1002/anie.201004201
27. Papp, I.; Sieben, C.; Sisson, A. L.; Kostka, J.; Böttcher, C.; Ludwig, K.; Herrmann, A.; Haag, R. *ChemBioChem* **2011,** *12,* 887–895. doi:10.1002/cbic.201000776
28. Kitov, P. I.; Sadowska, J. M.; Mulvey, G.; Armstrong, G. D.; Ling, H.; Pannu, N. S.; Read, R. J.; Bundle, D. R. *Nature* **2000,** *403,* 669–672. doi:10.1038/35001095
29. Simanek, E. E.; McGarvey, G. J.; Jablonowski, J. A.; Wong, C.-H. *Chem. Rev.* **1998,** *98,* 833–862. doi:10.1021/cr940226i
30. Badjić, J. D.; Balzani, V.; Credi, A.; Lowe, J. N.; Silvi, S.; Stoddart, J. F. *Chem. – Eur. J.* **2004,** *10,* 1926–1935. doi:10.1002/chem.200305687

31. Balzani, V.; Clemente-León, M.; Credi, A.; Lowe, J. N.; Badjić, J. D.; Stoddart, J. F.; Williams, D. J. *Chem. – Eur. J.* **2003,** *9,* 5348–5360. doi:10.1002/chem.200304979
32. O'Sullivan, M. C.; Sprafke, J. K.; Kondratuk, D. V.; Rinfray, C.; Claridge, T. D. W.; Saywell, A.; Blunt, M. O.; O'Shea, J. N.; Beton, P. H.; Malfois, M.; Anderson, H. L. *Nature* **2011,** *469,* 72–75. doi:10.1038/nature09683
33. Kondratuk, D. V.; Perdigao, L. M. A.; O'Sullivan, M. C.; Svatek, S.; Smith, G.; O'Shea, J. N.; Beton, P. H.; Anderson, H. L. *Angew. Chem., Int. Ed.* **2012,** *51,* 6696–6699. doi:10.1002/anie.201202870
34. Timko, J. M.; Moore, S. S.; Walba, D. M.; Hiberty, P. C.; Cram, D. J. *J. Am. Chem. Soc.* **1977,** *99,* 4207–4219. doi:10.1021/ja00455a001
35. Ashton, P. R.; Campbell, P. J.; Glink, P. T.; Philp, D.; Spencer, N.; Stoddart, J. F.; Chrystal, E. J. T.; Menzer, S.; Williams, D. J.; Tasker, P. A. *Angew. Chem., Int. Ed. Engl.* **1995,** *34,* 1865–1869. doi:10.1002/anie.199518651
36. Ashton, P. R.; Chrystal, E. J. T.; Glink, P. T.; Menzer, S.; Schiavo, C.; Spencer, N.; Stoddart, J. F.; Tasker, P. A.; White, A. J. P.; Williams, D. J. *Chem. – Eur. J.* **1996,** *2,* 709–728. doi:10.1002/chem.19960020616
37. Jiang, W.; Schalley, C. A. *Proc. Natl. Acad. Sci. U. S. A.* **2009,** *106,* 10425–10429. doi:10.1073/pnas.0809512106
38. Clifford, T.; Abushamleh, A.; Busch, D. H. *Proc. Natl. Acad. Sci. U. S. A.* **2002,** *99,* 4830–4836. doi:10.1073/pnas.062639799
39. Dong, S.; Zheng, B.; Wang, F.; Huang, F. *Acc. Chem. Res.* **2014,** *47,* 1982–1994. doi:10.1021/ar5000456
40. Amabilino, D. B.; Stoddart, J. F. *Chem. Rev.* **1995,** *95,* 2725–2828. doi:10.1021/cr00040a005
41. Yamaguchi, N.; Gibson, W. H. *Chem. Commun.* **1999,** 789–790. doi:10.1039/a901044k
42. Jiang, W.; Sattler, D.; Rissanen, K.; Schalley, C. A. *Org. Lett.* **2011,** *13,* 4502–4505. doi:10.1021/ol201618f
43. Balzani, V.; Credi, A.; Raymo, F. M.; Stoddart, J. F. *Angew. Chem., Int. Ed.* **2000,** *39,* 3348–3391. doi:10.1002/1521-3773(20001002)39:19<3348::AID-ANIE3348>3.0.CO;2-X
44. Kay, E. R.; Leigh, D. A.; Zerbetto, F. *Angew. Chem., Int. Ed.* **2007,** *46,* 72–191. doi:10.1002/anie.200504313
45. Vukotic, V. N.; Loeb, S. J. *Chem. Soc. Rev.* **2012,** *41,* 5896–5906. doi:10.1039/c2cs35141b
46. Liu, Y.; Flood, A. H.; Bonvallet, P. A.; Vignon, S. A.; Northrop, B. H.; Tseng, H.-R.; Jeppesen, J. O.; Huang, T. J.; Brough, B.; Baller, M.; Magonov, S.; Solares, S. D.; Goddard, W. A.; Ho, C.-M.; Stoddart, J. F. *J. Am. Chem. Soc.* **2005,** *127,* 9745–9759. doi:10.1021/ja051088p
47. Coskun, A.; Banaszak, M.; Astumian, R. D.; Stoddart, J. F.; Grzybowski, B. A. *Chem. Soc. Rev.* **2012,** *41,* 19–30. doi:10.1039/C1CS15262A
48. Bruns, C. J.; Stoddart, J. F. *Acc. Chem. Res.* **2014,** *47,* 2186–2199. doi:10.1021/ar500138u
49. Romuald, C.; Busseron, E.; Coutrot, F. *J. Org. Chem.* **2010,** *75,* 6516–6531. doi:10.1021/jo101234u
50. Clark, P. G.; Day, M. W.; Grubbs, R. H. *J. Am. Chem. Soc.* **2009,** *131,* 13631–13633. doi:10.1021/ja905924u
51. Milgrom, L. R. *The Colours of Life: An Introduction to the Chemistry of Porphyrins and Related Compounds;* Oxford University Press: Oxford, UK, 2001.
52. Ishii, K.; Kobayashi, N. In *The Porphyrin Handbook;* Kadish, K.; Guilard, R.; Smith, K. M., Eds.; Academic Press: Amsterdam, 2003; pp 1–42. doi:10.1016/B978-0-08-092390-1.50007-2
53. Durot, S.; Taesch, J.; Heitz, V. *Chem. Rev.* **2014,** *114,* 8542–8578. doi:10.1021/cr400673y
54. Mandal, S.; Rahaman, M.; Sadhu, S.; Nayak, S. K.; Patra, A. *J. Phys. Chem. C* **2013,** *117,* 3069–3077. doi:10.1021/jp3100188
55. Liu, Y.; Huang, Z.; Liu, K.; Kelgtermans, H.; Dehaen, W.; Wang, Z.; Zhang, X. *Polym. Chem.* **2014,** *5,* 53–56. doi:10.1039/C3PY01036H
56. Fathalla, M.; Strutt, N. L.; Barnes, J. C.; Stern, C. L.; Ke, C.; Stoddart, J. F. *Eur. J. Org. Chem.* **2014,** 2873–2877. doi:10.1002/ejoc.201402018
57. Watanabe, K.; Kitagishi, H.; Kano, K. *Angew. Chem., Int. Ed.* **2013,** *52,* 6894–6897. doi:10.1002/anie.201302470
58. Puglisi, A.; Purrello, R.; Rizzarelli, E.; Sortino, S.; Vecchio, G. *New J. Chem.* **2007,** *31,* 1499–1506. doi:10.1039/b703680a
59. Králová, J.; Kejik, Z.; Bříza, T.; Poučková, P.; Král, A.; Martásek, P.; Král, V. *J. Med. Chem.* **2010,** *53,* 128–138. doi:10.1021/jm9007278
60. Kiba, T.; Suzuki, H.; Hosokawa, K.; Kobayashi, H.; Baba, S.; Kakuchi, T.; Sato, S.-I. *J. Phys. Chem. B* **2009,** *113,* 11560–11563. doi:10.1021/jp905904h
61. Kano, K.; Kitagishi, H.; Dagallier, C.; Kodera, M.; Matsuo, T.; Hayashi, T.; Hisaeda, Y.; Hirota, S. *Inorg. Chem.* **2006,** *45,* 4448–4460. doi:10.1021/ic060137b
62. Kim, Y.-H.; Hong, J.-I. *Chem. Commun.* **2002,** 512–513. doi:10.1039/b109596j
63. D'Souza, F.; Chitta, R.; Gadde, S.; Zandler, M. E.; Sandanayaka, A. S. D.; Araki, Y.; Ito, O. *Chem. Commun.* **2005,** 1279–1281. doi:10.1039/b416736h
64. Even, P.; Boitrel, B. *Coord. Chem. Rev.* **2006,** *250,* 519–541. doi:10.1016/j.ccr.2005.09.003
65. Zhang, H.; Liu, Q.; Li, J.; Qu, D.-H. *Org. Lett.* **2013,** *15,* 338–341. doi:10.1021/ol3032686
66. Jahan, M.; Safari, N.; Khosravi, H.; Moghimi, A.; Notash, B. *Polyhedron* **2005,** *24,* 1682–1688. doi:10.1016/j.poly.2005.04.033
67. Imahori, H.; Fukuzumi, S. *Adv. Funct. Mater.* **2004,** *14,* 525–536. doi:10.1002/adfm.200305172
68. Imahori, H.; Sakata, Y. *Eur. J. Org. Chem.* **1999,** 2445–2457. doi:10.1002/(SICI)1099-0690(199910)1999:10<2445::AID-EJOC2445>3.0.CO;2-G
69. Yong, C.-K.; Parkinson, P.; Kondratuk, D. V.; Chen, W.-H.; Stannard, A.; Summerfield, A.; Sprafke, J. K.; O'Sullivan, M. C.; Beton, P. H.; Anderson, H. L.; Herz, L. M. *Chem. Sci.* **2015,** *6,* 181–189. doi:10.1039/C4SC02424A
70. Parkinson, P.; Knappke, C. E. I.; Kamonsutthipaijit, N.; Sirithip, K.; Matichak, J. D.; Anderson, H. L.; Herz, L. M. *J. Am. Chem. Soc.* **2014,** *136,* 8217–8220. doi:10.1021/ja504730j
71. Liu, J.-Y.; Huang, Y.; Menting, R.; Röder, B.; Ermilov, E. A.; Ng, D. K. P. *Chem. Commun.* **2013,** *49,* 2998–3000. doi:10.1039/c3cc00262d
72. Menting, R.; Lau, J. T. F.; Xu, H.; Ng, D. K. P.; Röder, B.; Ermilov, E. A. *Chem. Commun.* **2012,** *48,* 4597–4599. doi:10.1039/c2cc30286a
73. Burrell, A. K.; Officer, D. L.; Plieger, P. G.; Reid, D. C. W. *Chem. Rev.* **2001,** *101,* 2751–2796. doi:10.1021/cr0000426
74. Yamada, Y.; Okamoto, M.; Furukawa, K.; Kato, T.; Tanaka, K. *Angew. Chem., Int. Ed.* **2012,** *51,* 709–713. doi:10.1002/anie.201107104
75. van Nostrum, C. F.; Picken, S. J.; Schouten, A.-J.; Nolte, R. J. M. *J. Am. Chem. Soc.* **1995,** *117,* 9957–9965. doi:10.1021/ja00145a004

76. Lindsey, J. S.; Schreiman, I. C.; Hsu, H. C.; Kearney, P. C.; Marguerettaz, A. M. *J. Org. Chem.* **1987,** *52,* 827–836. doi:10.1021/jo00381a022
77. Geier, G. R., III; Lindsey, J. S. *Tetrahedron* **2004,** *60,* 11435–11444. doi:10.1016/j.tet.2004.09.081
78. Jiang, W.; Schäfer, A.; Mohr, P. C.; Schalley, C. A. *J. Am. Chem. Soc.* **2010,** *132,* 2309–2320. doi:10.1021/ja9101369
79. Jiang, W.; Schalley, C. A. *J. Mass Spectrom.* **2010,** *45,* 788–798. doi:10.1002/jms.1769

License and Terms

BEILSTEIN JOURNAL OF ORGANIC CHEMISTRY

Multivalent dendritic polyglycerolamine with arginine and histidine end groups for efficient siRNA transfection

Fatemeh Sheikhi Mehrabadi[1], Hanxiang Zeng[2], Mark Johnson[2], Cathleen Schlesener[1], Zhibin Guan[*2] and Rainer Haag[*1]

Full Research Paper

Open Access

Address:
[1]Institut für Chemie und Biochemie, Freie Universität Berlin, Takustrasse 3, 14195 Berlin, Germany and [2]Department of Chemistry, University of California, 1102 Natural Sciences 2, Irvine, California 92697-2025, USA

Email:
Zhibin Guan[*] - zguan@uci.edu; Rainer Haag[*] - haag@chemie.fu-berlin.de

* Corresponding author

Keywords:
arginine; dendritic polyglycerolamine; histidine; multivalent vector; siRNA delivery

Beilstein J. Org. Chem. **2015,** *11,* 763–772.
doi:10.3762/bjoc.11.86

Received: 24 February 2015
Accepted: 28 April 2015
Published: 13 May 2015

This article is part of the Thematic Series "Multivalency as a chemical organization and action principle".

Associate Editor: H. Ritter

Abstract

The success of siRNA-based therapeutics highly depends on a safe and efficient delivery of siRNA into the cytosol. In this study, we post-modified the primary amines on dendritic polyglycerolamine (dPG-NH_2) with different ratios of two relevant amino acids, namely, arginine (Arg) and histidine (His). To investigate the effects from introducing Arg and His to dPG, the resulting polyplexes of amino acid functionalized dPG-NH_2s (AAdPGs)/siRNA were evaluated regarding cytotoxicity, transfection efficiency, and cellular uptake. Among AAdPGs, an optimal vector with (1:3) Arg to His ratio, showed efficient siRNA transfection with minimal cytotoxicity (cell viability ≥ 90%) in NIH 3T3 cells line. We also demonstrated that the cytotoxicity of dPG-NH_2 decreased as a result of amino acid functionalization. While the incorporation of both cationic (Arg) and pH-responsive residues (His) are important for safe and efficient siRNA transfection, this study indicates that AAdPGs containing higher degrees of His display lower cytotoxicity and more efficient endosomal escape.

Introduction

Since the discovery of RNA interference (RNAi) and awareness of its role in posttranscriptional gene silencing, tremendous efforts and capital have been devoted to the development of therapeutics based on this pathway [1]. So far, there are at least 22 RNAi-based drugs in clinical trials and many more are being developed [1]. Although a direct delivery of "naked" siRNA or chemically modified oligonucleotides [2] has been studied, delivery vectors are typically required for efficient siRNA delivery in vivo due to unmodified siRNA's low stability towards endogenous enzymes, poor cellular uptake, and its immunogenic potential [3].

Among the different polymeric vectors, polycationic dendrimers and related structures have found wide application

in gene/siRNA delivery [4]. This is because the synthesis of dendrimers and dendritic polymers under controlled conditions results in defined structures with low dispersity. Moreover, the tree-like structure of such polymers provides multivalent positions for functionalization and interaction with DNA/siRNA.

Dendritic polyglycerol (dPG) can be synthesized on a kilogram scale by a one-step, ring-opening polymerization of glycidol with controllable sizes and degrees of branching [5]. Additionally, dPG has multiple groups for further functionalization, high chemical stability, and good biocompatibility in vitro and in vivo [6-8]. All these characteristics make dPG an ideal scaffold for a broad range of applications from anti fouling [9] to biomedical purposes [6] such as anti-inflammatory [10] and anticancer therapy [11,12].

Previously a number of cationic polymers like chitosan [13-15], PEI [16], and PAMAM [17] have been post-modified with histidine (His) or arginine (Arg) groups. The introduction of histidine groups has been beneficial for improving the endosomal release properties [18], and conjugation of arginine groups has enhanced the transfection efficiency of cationic carriers [19,20]. Since the incorporation of either amino acid alone can improve siRNA transfection, we hypothesized that functionalization with both Arg and His may have a synergistic effect on siRNA transfection. Moreover, the biocompatible nature of the amino acids can possibly decrease the cytotoxicity of the resulting vectors. Furthermore, Arg and His groups interact in histones, as natural DNA binding proteins, via their positive residues with the negative phosphates groups of the DNA [21]. Here, we chose dendritic polyglycerolamine (dPG-NH_2) with moderate amine loading (50% of all hydroxy groups on a 10 kDa dPG core) and introduced both amino acids via amide coupling to mimic DNA histones interactions.

In a recent study, our group demonstrated the potential of dPG-NH_2 with high amine loading (≥90%) for siRNA delivery in vivo [22]. Moreover, it has been shown that dPG-NH_2 90% is able to efficiently downregulate the formation of several proteins in vitro [23]. In spite of its high efficiency, the therapeutic window of dPG-NH_2 90% is small and the cytotoxicity increases at higher concentrations which limits its further application. Here, we compare the potential of multivalent amino acid functionalized dPGs (AAdPGs), for siRNA transfection with dPG-NH_2 90%. The initial in vitro results indicated that AAdPGs were capable of mediating efficient siRNA delivery to NIH 3T3 cells and induced comparable gene silencing to both dPG-NH_2 90% and lipofectamine RNAiMAX. In comparison with dPG-NH_2 90%, the new vectors showed reduced cytotoxicity and enhanced siRNA binding.

Results and Discussion

Functionalization of dPG-NH_2 with arginine and histidine

Amino acids have been implemented for the improvement of gene/siRNA transfection using various strategies. Beside peptide dendrimers [24,25], another strategy is to functionalize the periphery groups on cationic vectors such as PLL [26], PEI [16], and PAMAM [19]. In the current study, ≈50% of all hydroxy groups on dPG (M_n = 8.4 kDa, PDI = 1.7) were converted to amino groups according to an earlier published procedure (Scheme S1, Supporting Information File 1) [27]. The high density of amines on dPG facilitates the introduction of groups like amino acids by feasible strategies like amide coupling. Here, we coupled both Arg and His groups in different ratios to dPG-NH_2 via the latter strategy (Scheme 1). By introducing Arg on the dendritic scaffold, this group can serve as a complexing agent and the surplus guanidium groups with high affinity to phosphate groups can interact with the cell membrane and improve the cellular uptake [28]. Additionally, the histidine groups can facilitate tackling the endosomal release problem by improving the polyplexes's buffering capacity [18]. Moreover, arginine and histidine groups can form intermolecular hydrogen bonds with cell surface phosphate groups. These interactions can induce cellular uptake of AAdPG polyplexes. Therefore, four cationic vectors were prepared by Arg and His functionalization of the dPG scaffold. The list of all synthesized samples is presented in Table 1. The samples were named based on their degree of Arg and/or His functionalization on the polymeric backbone (dPG). The functionalization degree for each polymer was determined by comparing the peak integral of either the methylene groups of arginine in high field or the imidazole ring of histidine in the aromatic area (7.2–8.7 ppm) with the assignable dPG backbone signal (Supporting Information File 1).

Variable composition of arginine and histidine on dPG-NH_2 50%

To investigate the effect from introducing both His and Arg to dPG backbone on transfection efficiency, cytotoxicity, and cellular uptake, two vectors were synthesized with equal (dPG-13Arg13His) and different (dPG-8Arg30His) composition ratios of both amino acids. Moreover, two further vectors with either Arg (dPG-13Arg) or His (dPG-13His) were prepared to examine the effect of each amino acid alone. The summary of all dPG-based vectors is shown in Table 1.

siRNA Binding

The ability of AAdPGs to form complexes with siRNA was examined by agarose gel electrophoresis retardation assay. The electrophoretic mobility of the siRNA should have been reduced or completely eliminated as a result of complexation

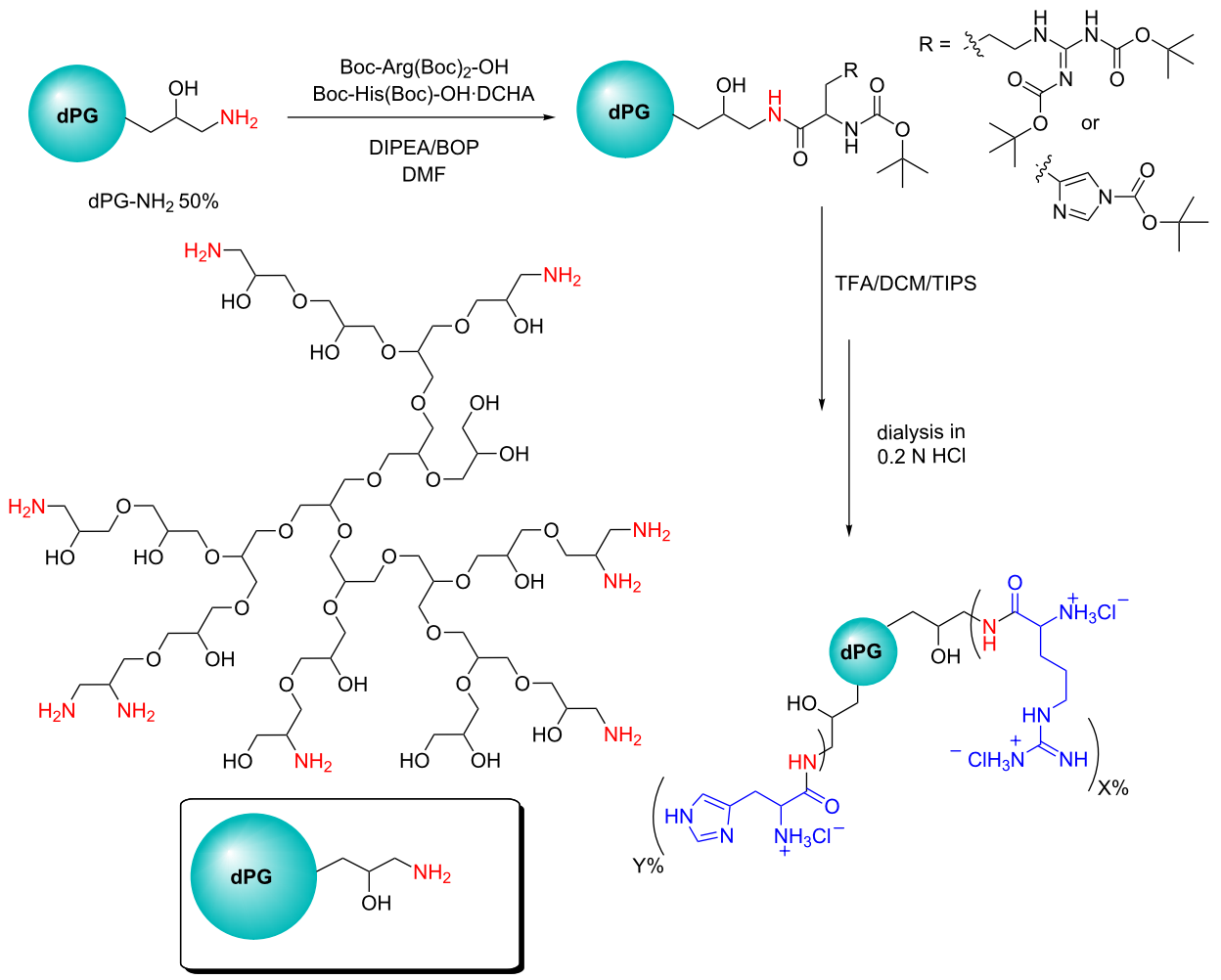

Scheme 1: Synthesis of multivalent arginine and histidine functionalized dPG-NH_2 50%. The depicted dPG-NH_2 represents only a small idealized fragment of a 10 kDa molecule.

Table 1: Summary of AAdPG vectors and their corresponding polyplex characterization.

Compound	Zeta potential (mV)[a]	diameter (nm)[b]	PDI[c]	(Arg) %[d]	(His) %[d]	Arg:His
dPG-NH_2 50%	10.0 ± 0.2	124.1 ± 0.7	0.07	–	–	–
dPG-13Arg13His	10.9 ± 0.8	97.17 ± 0.87	0.13	13	13	1:1
dPG-13Arg	10.6 ± 0.9	60.04 ± 1.2	0.18	13	–	–
dPG-13His	10.3 ± 0.3	70.23 ± 0.8	0.17	–	13	–
dPG-8Arg30His	11.0 ± 0.9	104.9 ± 0.45	0.18	8	30	~1:3

[a]ζ were measured at pH 7.4; [b]intensity distributions are reported; [c]PDI of polyplexes were determined by DLS; [d]degree of functionalization on dPG which were determined by ^{1}H NMR spectroscopy.

with AAdPGs. As shown in Figure 1, all AAdPGs were able to neutralize the negative charge of the siRNA and effectively retard it at N/P ratios between 2 to 4. The binding capacity of all vectors was slightly different from each other. The results of this assay clearly display that all synthesized vectors were able to form polyplexes with siRNA at low N/P ratios. Moreover, the complex formation ability of the new vectors is comparable with dPG-NH_2 50% and 90%.

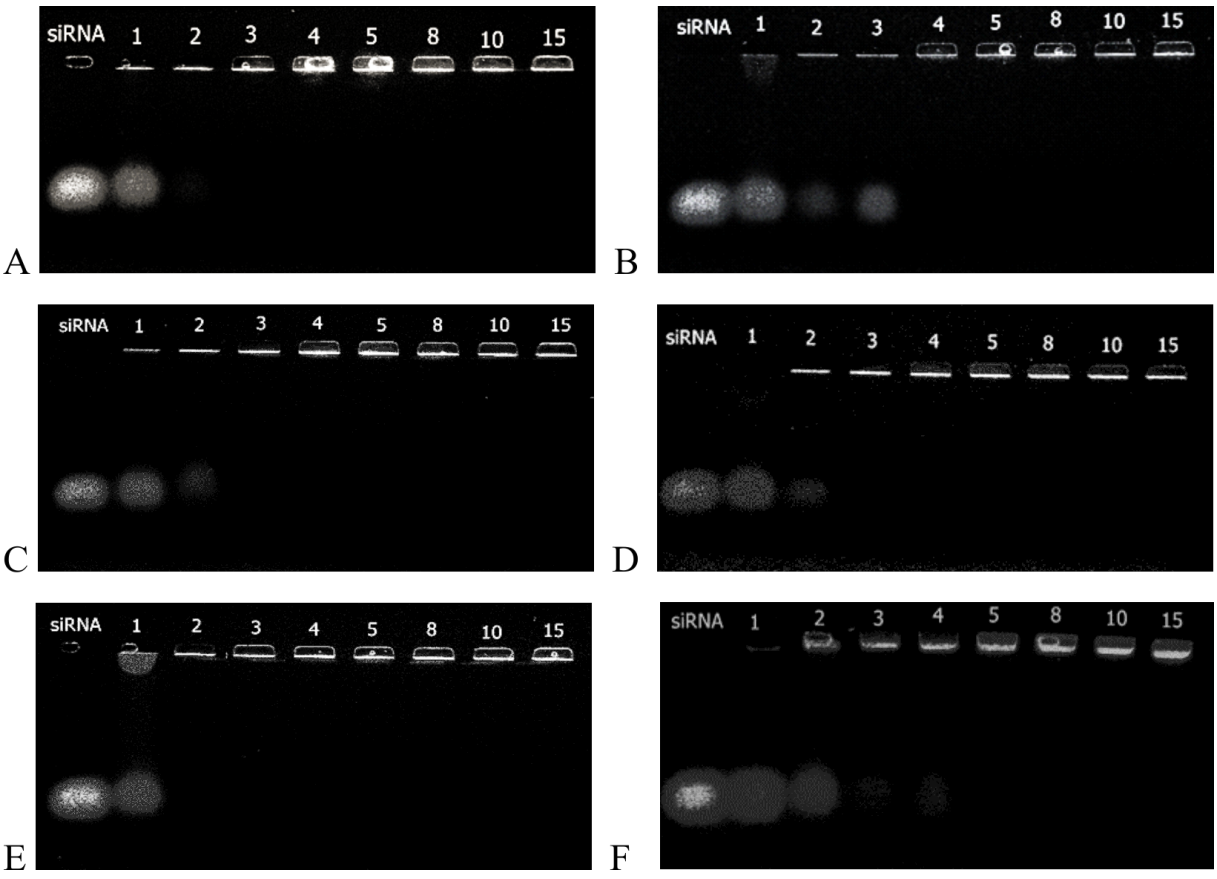

Figure 1: Agarose gel electrophoresis retardation assay of AAdPGs/siRNA polyplexes. (A) dPG-13Arg13His, (B) dPG-13Arg, (C) dPG-13His, (D) dPG-8Arg30His, (E) dPG-NH_2 50%, and (F) dPG-NH_2 90%. Naked siRNA always appears in the first lane. The numbers on the top of each lane correspond to the different N/P ratios.

Average particle size and surface charges of AAdPG/siRNA polyplexes

The appropriate particle size and surface charge are critical characteristics of nanoplexes for efficient transfection [29]. Physicochemical characterization of AAdPG/siRNA polyplexes was conducted using dynamic light scattering (DLS). Figure 2 shows the size distribution of dPG polyplexes (at N/P ratio 10). The average size of all nanoparticles ranges from 60–100 nm. In general, the AAdPG/siRNA polyplexes were smaller than the corresponding dPG-NH_2 50%/siRNA polyplexes. Moreover, AAdPG complexes have a broader distribution of the final nanoparticles. The size of dPG-13Arg and dPG-13His complexes was slightly smaller than the other dPG-based vectors. The surface charge of the final nanoparticles was comparable to the corresponding complexes of siRNA and dPG-NH_2 50% with terminal primary amines and about 10 mV. The positive charge of the polyplexes is a further indication of efficient siRNA complexation by AAdPGs. The results for the size and zeta potential measurements of all vectors are summarized in Table 1.

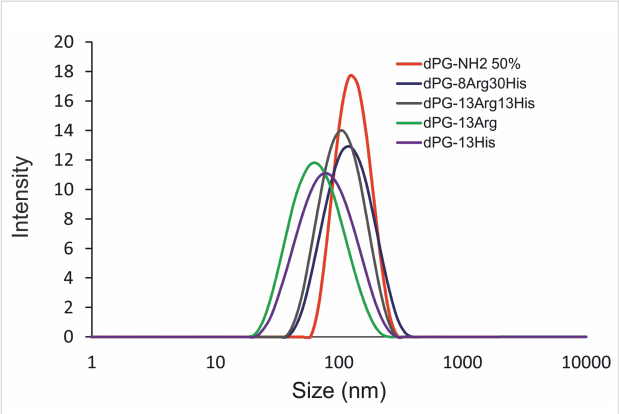

Figure 2: Size measurements of dPG-NH_2 50% and AAdPGs/siRNA complexes. Intensity distributions of all polyplexes are depicted.

Cell viability assay

The cytotoxicity of cationic polymers is mainly attributed to the interactions of these polymers with the cell membrane and depends on multiple factors such as molecular weight, the

nature of the polymer surface, and its charge density [30]. The results of the in vitro MTT assays on the NIH 3T3 cell line for cytotoxicity evaluation of AAdPG polyplexes are shown in Figure 3. These results were compared with dPG-NH_2 50% as a backbone and dPG-NH_2 90%. Generally, these data indicates that cytotoxicity of the final polyplexes is reduced by functionalization of dPG-NH_2 50% with Arg and His. Moreover, decreasing the percentage of arginine on a dendritic scaffold improved the cytotoxicity of the nanoplexes. Replacing the primary amines on dPG-NH_2 with histidine groups would possibly decrease the density of positive charge on dPG and increase cell viability. The best cytotoxicity profile was observed for dPG-8Arg30His with no considerable cytotoxicity (cell viability ≥ 90%) up to N/P ratio 40 (Figure 3). We further compared the cytotoxicity of dPG-8Arg30His with dPG-NH_2 90% at N/P ratio 30 where the efficiencies of both vectors were comparable. Overall, these results demonstrated that dPG-8Arg30His is a safer vector compared to dPG-NH_2 90% (Figure 4).

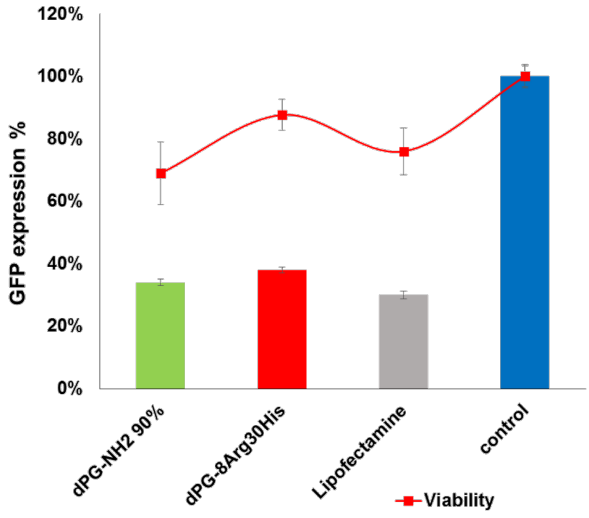

Figure 4: Cell viability versus transfection efficiency of dPG-8Arg30His and dPG-NH_2 90% at N/P ratio 30.

In vitro transfection assay

The transfection efficiency of the AAdPGs was assessed in GFP expressing NIH 3T3 cells (Figure 5). In general, the results indicate that post-modification of the dendritic scaffold with Arg and His improves the efficiency of siRNA transfection. The most efficient vector in the knockdown of GFP (down regulation of GFP expression to 38%) was obtained by converting almost all primary amines on dPG to Arg and His with a 1:3 ratio. Moreover, by comparing the knockdown efficiency of dPG-13Arg (without any histidine functionality) with all the other vectors containing histidine, the critical role of histidine as a buffering agent in enhancing transfection efficiency was determined. Furthermore, we compared the result of our best vector, dPG-8Arg30His, in terms of transfection with dPG-NH_2 90%. These results indicate that dPG-8Arg30His (at N/P ratio 30) is as potent as dPG-NH_2 90% in GFP knockdown while maintaining its low cytotoxicity (Figure 4).

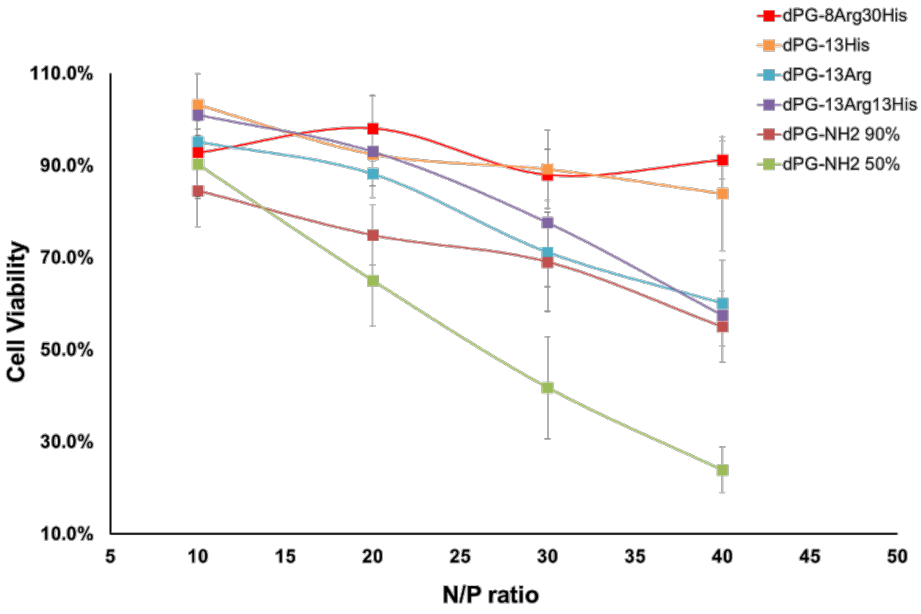

Figure 3: The result of MTT assay on a NIH 3T3 cell line transfected with AAdPG, dPG-NH_2 50%, and 90%/siRNA polyplexes at different N/P ratios with 100 nM siRNA concentration.

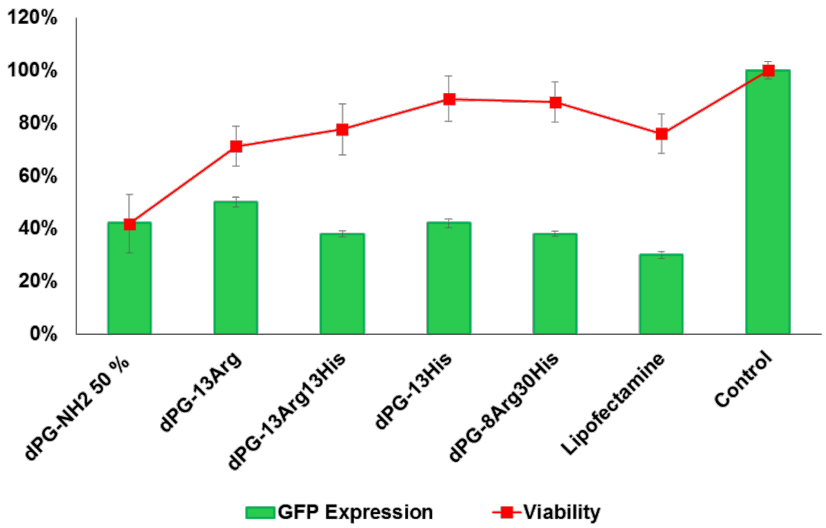

Figure 5: Summary of transfection results versus viability of AAdPGs with various Arg and His composition ratio at N/P ratio 30.

Cellular uptake and confocal microscopy

The cellular uptake and localization of fluorescently labeled siRNA/AAdPG complexes were quantified using flow cytometry and confocal microscopy (Figure 6). By comparing the cellular uptake of dPG-NH_2 functionalized solely with either histidine or arginine, for example, dPG-13Arg, one can clearly see that Arg functionalization improved cellular uptake of both dPG-NH_2s. These results are in agreement with several studies where the transmembrane function of arginine-rich peptides was demonstrated [31,32]. Interestingly, there is a reverse effect with respect to cellular uptake after functionalization of dPG-NH_2 with histidine. Notably, dPG-NH_2s have shown a higher cellular uptake than lipofectamine which is most probably due to their high positive surface charge. These results in combination with transfection efficiency data suggest that the higher transfection efficiency of histidine-functionalized vectors is presumably due to their improved endosomal release.

Conclusion

We successfully post-modified dPG-NH_2 with variable ratios of Arg and His as mimicry of natural histones to afford safe and efficient siRNA transfection. At certain ratios of Arg to His (1:3) a multivalent cationic vector was obtained with comparable transfection efficiency to lipofectamine (down regulation of GFP expression to 37% at N/P ratio 40) and marginal cytotoxicity (cell viability ≥ 90% at N/P ratio 40). The efficiency of this new vector is comparable to our well-studied vector, dPG-NH_2 90%. Post modification of dPG-NH_2 with Arg and His did not dramatically affect the physicochemical properties (particle size and zeta potential) of the resulting vectors and their nanoplexes but notably improved cell viability. This can be attributed to the steric congestion around the amine groups and more biocompatible surface functionalities after amino acid functionalization of dPG-NH_2. Compared to arginine, the introduction of histidine more effectively reduced the cytotoxicity and mediated an efficient endosomal escape. Moreover, by comparing the result of cellular uptake with transfection efficiencies, one can conclude that enhanced cellular uptake does not guarantee by itself efficient siRNA transfection and that incorporation of endosomal releasing groups like histidine seems to play a more crucial role in efficient transfection as compared to arginine.

Experimental

Materials

All chemicals and reagents were used as received from the suppliers without further purification. Protected amino acids and coupling reagents were purchased from abcr GmbH (Karlsruhe, Germany). GelRed™ siRNA stain was purchased from VWR (Radnor, PA). All cell culture media and fetal bovine serum (FBS) was purchased from Invitrogen (Carlsbad, CA). All siRNA used in this study was purchased from Ambion (Carlsbad, CA) with Silencer® Select negative control siRNA and Silencer®Cy™-3 labeled Negative Control siRNA used for control and cellular uptake studies, respectively. Unmodified Silencer® series siRNA was used for GFP silencing experiments with the following sequence: sense 5'-CAAGCUGACCCUGAAGUUCTT-3' and antisense 5'-GAACUUCAGGGUCAGCUUGCC-3'. All water used in the biological experiments was nanopure water obtained from Barnstead Nanopure Diamond (Waltham, MA). Both unmodified and engineered NIH 3T3 cells expressing green fluorescence protein (GFP) were kindly provided by Professor Young Jik Kwon (Department of Chemical Engineering, UC Irvine, CA).

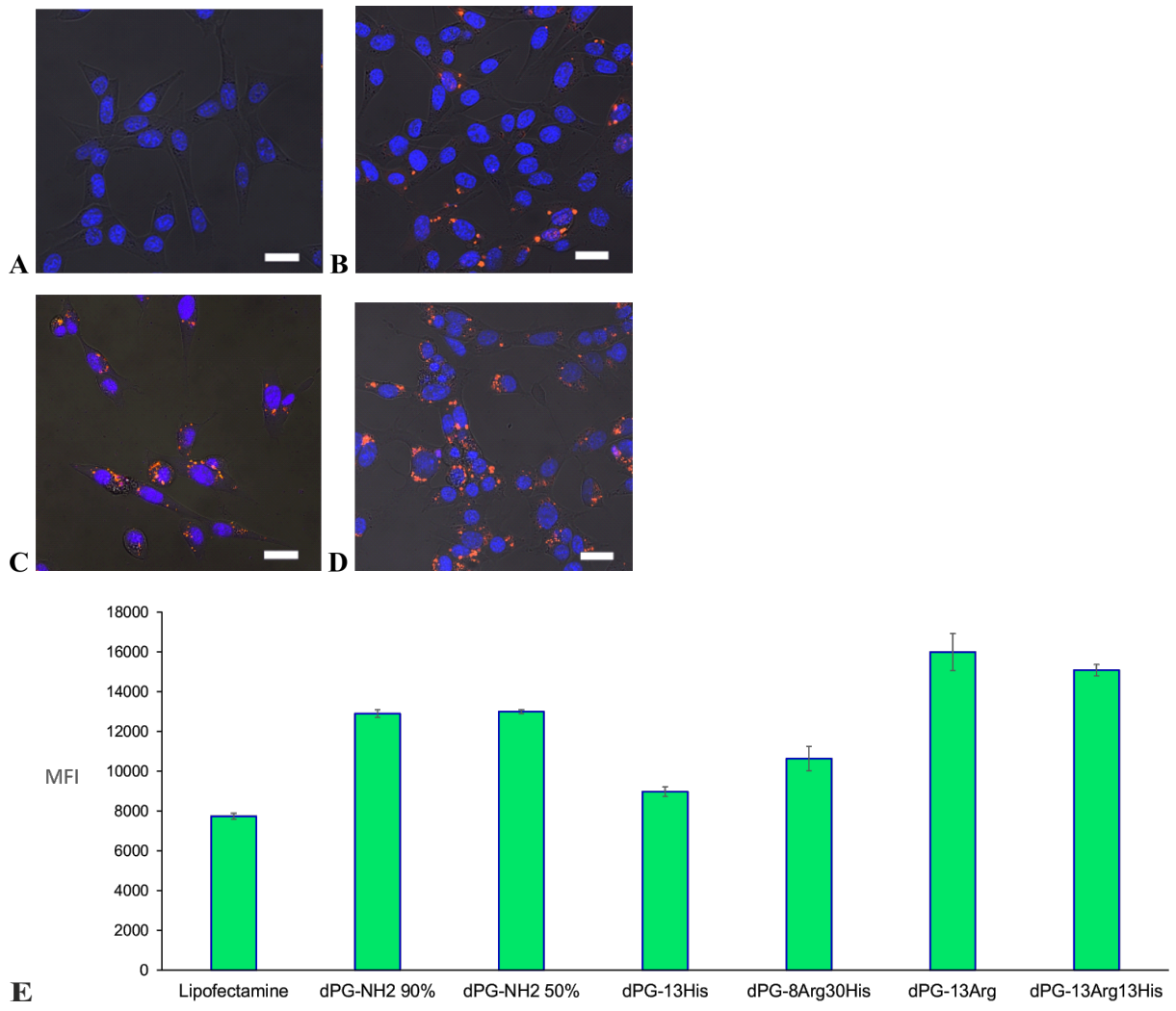

Figure 6: Confocal images of NIH 3T3 cells treated with Cy3-siRNA/vector complexes: (A) naked siRNA, (B) lipofectamine, (C) dPG-13His, (D) dPG-13Arg, and (E) mean Cy-3 fluorescence intensity of 3T3 cells treated with Cy3-siRNA/vector complexes assessed by FACS.

Functionalization of dPG-NH_2 with arginine (Arg) and histidine (His)

dPG (M_n = 8.4 kDa, PDI = 1.7) was prepared according to a published procedure [33]. Fifty percent of all (~110) hydroxy groups on dendritic polyglycerol were functionalized with amino groups in a three-step protocol [27]. Briefly, the transformation was started with the mesylation of the hydroxy groups on dPG. In the next step, the mesylated polyglycerol was converted to polyglycerolazide. In the last step, azide functionalities (N_3) were reduced to primary amines (-NH_2) via Staudinger reduction (Scheme S1 in Supporting Information File 1). For coupling both amino acids Arg and His to the dendritic backbone, a solution of dPG-NH_2, 30 mg (0.20 mmol of amines) in methanol, was dried carefully under high vacuum. The concentrated solution was then diluted in 1.5 mL DMSO. The solution of dPG-NH_2 in DMSO was left under vacuum for 30 min in order to remove methanol residues. Boc-protected histidine and arginine were added to the solution of dPG-NH_2 in specific molar ratios. 1.2 Equivalents of BOP and DIPEA with respect to the amino groups were added to the reaction subsequently. The reaction mixture was stirred at room temperature overnight. This mixture was then transferred directly into a dialysis tube of 1000 MWCO and dialyzed in methanol for 2 days. After removing methanol on a rotary evaporator completely, the reaction mixture was treated with a mixture of TFA/DCM/TIPS. The reaction was left running overnight to complete the deprotection. After the deprotection step, dialysis in 0.2 N solution of HCl for two days resulted in the formation of products as chloride salt which were obtained as pale yellow to brown solids by lyophilization. Noteworthy that each dPG unit (10 kDa) has is about 100 hydroxy groups and therefore the functionalization percentages always corresponds approxi-

mately to the same number of functional groups per dPG. For example, dPG-NH_2 50% has about 50 NH_2 groups per polymer unit. The amino acid functionalization percentage of each polymer was defined using ^{1}H NMR analysis. ^{1}H NMR (400 MHz, D_2O) dPG-13Arg13His: δ = 1.6 (s, $NHCH_2CH_2CH_2CH$, 2H), 1.9 (s, $NHCH_2CH_2CH_2CH$, 2H), 3–4.5 (m, dPG backbone, $NHCH_2CH_2CH_2CH$ and $NHCH_2CH_2CH_2CHNH_2CO$ of arginine groups, $NH_2COCHCH_2C$ and $NH_2COCHCH_2C$ of histidine groups), 7.4 (s, C*H*NHCHN, 1H of imidazole groups) and 8.7 (s, CHNHC*H*N, 1H of imidazole groups) ppm. dPG-13Arg: δ = 1.6 (s, $NHCH_2CH_2CH_2CH$, 2H), 1.9 (s, $NHCH_2CH_2CH_2CH$, 2H), 3–4.5 (m, dPG backbone, $NHCH_2CH_2CH_2CH$ and $NHCH_2CH_2CH_2CHNH_2CO$ of arginine groups) ppm. dPG-13His: δ = 3–4.5 (m, dPG backbone, $NH_2COCHCH_2C$ and $NH_2COCHCH_2C$ of histidine groups), 7.4 (s, C*H*NHCHN, 1H of imidazole groups) and 8.7 (s, CHNHC*H*N, 1H of imidazole groups) ppm. dPG-8Arg30His: δ = 1.6 (s, $NHCH_2CH_2CH_2CH$, 2H), 1.9 (s, $NHCH_2CH_2CH_2CH$, 2H), 3–4.5 (m, dPG backbone, $NHCH_2CH_2CH_2CH$ and $NHCH_2CH_2CH_2CHNH_2CO$ of arginine groups, $NH_2COCHCH_2C$ and $NH_2COCHCH_2C$ of histidine groups), 7.4 (s, C*H*NHCHN, 1H of imidazole groups) and 8.7 (s, CHNHC*H*N, 1H of imidazole groups) ppm.

Gel electrophoresis

The binding of AAdPGs to siRNA was evaluated by agarose gel electrophoresis retardation assay. Stock solutions of siRNA and AAdPGs were prepared in phosphate buffer (10 mM, pH 7.4). To a 2 μL solution of siRNA (4 μM), different amounts of AAdPG compounds were added to achieve different N/P ratios (the molar ratio between amine groups of dPGs to siRNA phosphate groups). The final volume of the mixture was adjusted to 12.5 μL by the same buffer solution. siRNA and AAdPGs were incubated at room temperature for 30 min. After incubation, 2.5 μL of 6X orange gel loading dye was added to each sample. 10 μL of the final mixture was then loaded on a 1% agarose gel with 1X GelRed™. After filling the gel packets with polyplexes, electrophoresis was run in TAE buffer for 45 min at 60 V. The results were visualized under UV illumination.

DLS/Zeta

The size and zeta potential (ζ) of AAdPG/siRNA polyplexes were measured by a Zetasizer Nano ZS analyzer™ with integrated 4 mW He-Ne laser, λ = 633 nm (Malvern Instruments™ Ltd, U.K.). Stock solutions of dPG samples and siRNA (50 μM) in nanopure water were prepared. An appropriate amount of each dPG sample was mixed with 2.85 μL siRNA (6 nmol phosphate) solution. The mixtures were diluted to 100 μL and after short vortexing were incubated for 30 min at rt. Subsequently, DLS measurements were recorded. The same mixture from DLS measurements was taken and diluted with 0.8 μL phosphate buffer (10 mM, pH 7.4). These samples were then subjected to zeta potential measurements. The measurements were repeated at least three times for each sample and the mean values were reported.

MTT assay

Unmodified NIH 3T3 cells were seeded at a density of 5,000 cells per well in 96-well plates 24 h in advance. The culture media was changed from 100 μL DMEM with 10% fetal bovine serum (FBS) to 80 μL plain DMEM immediately before exposure to the complexes. The dPG/siRNA complexes were prepared by first diluting the siRNA to 1.5 μM with PBS (10 mM phosphate, 10 mM NaCl, pH 7.4) and then adding the proper amount of vector solution (5 mg/mL in ddH_2O) to give the desired N/P ratio and concentration. After 30 minutes incubation at rt, 20 μL of the complex solutions were added to each well to give a final volume of 100 μL per well. After 4 h incubation, the media was replaced with 10% FBS/DMEM and the cells cultured for another 48 h. To assess the viability, the media was replaced with 50 μL DMEM solution containing 0.5 mg/mL MTT, followed by 4 h incubation at 37 °C. 100 μL of DMSO was added to each well to dissolve the formazan and the plate was incubated at 37 °C for 30 min with agitation. The absorbance at 540 nm was measured using a plate reader and the viability determined by comparison with untreated controls.

Transfection

NIH 3T3 fibroblast cells expressing GFP were seeded at a density of 10,000 cells/well in 48-well plates 24 h in advance and the culture media replaced with 200 μL plain DMEM immediately prior to transfection. AAdPG/siRNA complexes were prepared as described previously with either anti-GFP siRNA or negative control siRNA. 50 μL of the complex solutions were added to each well to give a final volume of 250 μL per well. After 4 h incubation, the media was replaced with 10% FBS/DMEM and the cells cultured for another 48 h. Before the analysis, cells were released from each well with trypsin and harvested by centrifugation (5 min, 500G). GFP fluorescence of transfected cells was measured on a Becton-Dickinson LSR II flow cytometer with argon ion excitation laser. For each sample, data representing 10,000 objects were collected as a list-mode file and analyzed using FACSDivaTM software (Becton Dickinson, version 6.1.3) and the percent knockdown was calculated by comparing the mean fluorescence intensity of cells treated with vector/anti-GFP siRNA to that of cells treated with complexes formed with the control siRNA.

Cellular uptake study

For quantitative assessment of cellular uptake, negative control siRNA labeled with Cy3 (siRNA-Cy3) was complexed with the

vectors in PBS as described previously. Unmodified NIH 3T3 cells were seeded in 48-well plates and transfected with the siRNA-Cy3/vector complexes following the same transfection protocol used for GFP silencing experiments. Immediately after the 4 h exposure to the transfection media, the cells were trypsinized and collected via centrifugation. The transfected cells were analyzed by FACS to determine the mean Cy3-fluoroscence of each sample.

Confocal microscopy

Unmodified NIH 3T3 fibroblast cells were seeded at a density of 10,000 cells/well on an 8-well chamber slide (Lab-Tek, Rochester, NY) 24 h before transfection. Cy3-labeled siRNA was complexed with the vectors and the cells transfected with the complexes following the previously described protocol. After 4 h exposure to the transfection media, the media was changed back to DMEM supplemented with 10% fetal bovine serum. Confocal fluorescence spectroscopy was performed at different time points after the transfection. The nuclei were stained with Hoechst 33342 following the standard protocol. The images were acquired using a Zeiss LSM 510 inverted laser-scanning confocal microscope with a 40× numerical aperture oil immersion planapochromat objective. A 559 nm helium–neon laser, a SMD640 dichroic mirror, and a 575–620 nm band-pass barrier filter were used to obtain the images of Cy3-labeled siRNA. Images of the stained nuclei were acquired using a 780 nm two-photon excitation light, a 635 nm dichroic mirror, and a 655–755 nm band-pass barrier filter. The two fluorescent images were scanned separately and overlaid together with the differential interference contrast image (DIC). The cells were scanned as a z-stack of two-dimensional images (1024 × 1024 pixels) and an image cutting approximately through the middle of the cellular height was selected to present the intracellular siRNA localization.

Statistical analysis

All transfection studies were performed in triplicates; data were expressed as mean ± SEM.

Supporting Information

Supporting Information File 1

Synthetic procedure of dPG-NH_2 and NMR spectra.
[http://www.beilstein-journals.org/bjoc/content/supplementary/1860-5397-11-86-S1.pdf]

Acknowledgements

FSM would like to thank SFB 765 and BMBF (Bundesministerium für Bildung und Forschung) for financial support. We would like to thank Dr. Pamela Winchester for proofreading of the manuscript. ZG would like to acknowledge the financial support of the US National Institute of Health (DK098446).

References

1. Kanasty, R.; Dorkin, J. R.; Vegas, A.; Anderson, D. *Nat. Mater.* **2013,** *12,* 967–977. doi:10.1038/nmat3765
2. DiFiglia, M.; Sena-Esteves, M.; Chase, K.; Sapp, E.; Pfister, E.; Sass, M.; Yoder, J.; Reeves, P.; Pandey, R. K.; Rajeev, K. G.; Manoharan, M.; Sah, D. W. Y.; Zamore, P. D.; Aronin, N. *Proc. Natl. Acad. Sci. U. S. A.* **2007,** *104,* 17204–17209. doi:10.1073/pnas.0708285104
3. Whitehead, K. A.; Langer, R.; Anderson, D. G. *Nat. Rev. Drug Discovery* **2009,** *8,* 129–138. doi:10.1038/nrd2742
4. Mehrabadi, F. S.; Fischer, W.; Haag, R. *Curr. Opin. Solid State Mater. Sci.* **2012,** *16,* 310–322. doi:10.1016/j.cossms.2013.01.003
5. Sunder, A.; Hanselmann, R.; Frey, H.; Mülhaupt, R. *Macromolecules* **1999,** *32,* 4240–4246. doi:10.1021/ma990090w
6. Calderón, M.; Quadir, M. A.; Sharma, S. K.; Haag, R. *Adv. Mater.* **2010,** *22,* 190–218. doi:10.1002/adma.200902144
7. Kainthan, R. K.; Janzen, J.; Levin, E.; Devine, D. V.; Brooks, D. E. *Biomacromolecules* **2006,** *7,* 703–709. doi:10.1021/bm0504882
8. Kainthan, R. K.; Brooks, D. E. *Biomaterials* **2007,** *28,* 4779–4787. doi:10.1016/j.biomaterials.2007.07.046
9. Wei, Q.; Krysiak, S.; Achazi, K.; Becherer, T.; Noeske, P.-L. M.; Paulus, F.; Liebe, H.; Grunwald, I.; Dernedde, J.; Hartwig, A.; Hugel, T.; Haag, R. *Colloids Surf., B* **2014,** *122,* 684–692. doi:10.1016/j.colsurfb.2014.08.001
10. Gröger, D.; Paulus, F.; Licha, K.; Welker, P.; Weinhart, M.; Holzhausen, C.; Mundhenk, L.; Gruber, A. D.; Abram, U.; Haag, R. *Bioconjugate Chem.* **2013,** *24,* 1507–1514. doi:10.1021/bc400047f
11. Calderón, M.; Welker, P.; Licha, K.; Fichtner, I.; Graeser, R.; Haag, R.; Kratz, F. *J. Controlled Release* **2011,** *151,* 295–301. doi:10.1016/j.jconrel.2011.01.017
12. Hussain, A. F.; Krüger, H. R.; Kampmeier, F.; Weissbach, T.; Licha, K.; Kratz, F.; Haag, R.; Calderón, M.; Barth, S. *Biomacromolecules* **2013,** *14,* 2510–2520. doi:10.1021/bm400410e
13. Kim, T. H.; Ihm, J. E.; Choi, Y. J.; Nah, J. W.; Cho, C. S. *J. Controlled Release* **2003,** *93,* 389–402. doi:10.1016/j.jconrel.2003.08.017
14. Park, S.; Lee, S. K.; Lee, K. Y. *J. Controlled Release* **2011,** *152,* e165–e166. doi:10.1016/j.jconrel.2011.08.065
15. Noh, S. M.; Park, M. O.; Shim, G.; Han, S. E.; Lee, H. Y.; Huh, J. H.; Kim, M. S.; Choi, J. J.; Kim, K.; Kwon, I. C.; Kim, J.-S.; Baek, K.-H.; Oh, Y.-K. *J. Controlled Release* **2010,** *145,* 159–164. doi:10.1016/j.jconrel.2010.04.005
16. Swami, A.; Aggarwal, A.; Pathak, A.; Patnaik, S.; Kumar, P.; Singh, Y.; Gupta, K. C. *Int. J. Pharm.* **2007,** *335,* 180–192. doi:10.1016/j.ijpharm.2006.11.033
17. Kim, T.-i.; Baek, J.-u.; Yoon, J. K.; Choi, J. S.; Kim, K.; Park, J.-s. *Bioconjugate Chem.* **2007,** *18,* 309–317. doi:10.1021/bc0601525
18. Midoux, P.; Pichon, C.; Yaouanc, J. J.; Jaffres, P.-A. *Br. J. Pharmacol.* **2009,** *157,* 166–178. doi:10.1111/j.1476-5381.2009.00288.x
19. Choi, J. S.; Nam, K.; Park, J.-y.; Kim, J.-B.; Lee, J.-K.; Park, J.-s. *J. Controlled Release* **2004,** *99,* 445–456. doi:10.1016/j.jconrel.2004.07.027
20. Kim, T.-i.; Baek, J.-u.; Bai, C. Z.; Park, J.-s. *Biomaterials* **2007,** *28,* 2061–2067. doi:10.1016/j.biomaterials.2006.12.013

21. Luger, K.; Mäder, A. W.; Richmond, R. K.; Sargent, D. F.; Richmond, T. J. *Nature* **1997,** *389,* 251–260. doi:10.1038/38444
22. Ofek, P.; Fischer, W.; Calderón, M.; Haag, R.; Satchi-Fainaro, R. *FASEB J.* **2010,** *24,* 3122–3134. doi:10.1096/fj.09-149641
23. Fischer, W.; Calderón, M.; Schulz, A.; Andreou, I.; Weber, M.; Haag, R. *Bioconjugate Chem.* **2010,** *21,* 1744–1752. doi:10.1021/bc900459n
24. Luo, K.; Li, C.; Li, L.; She, W.; Wang, G.; Gu, Z. *Biomaterials* **2012,** *33,* 4917–4927. doi:10.1016/j.biomaterials.2012.03.030
25. Zeng, H.; Little, H. C.; Tiambeng, T. N.; Williams, G. A.; Guan, Z. *J. Am. Chem. Soc.* **2013,** *135,* 4962–4965. doi:10.1021/ja400986u
26. Kasai, S.; Nagasawa, H.; Shimamura, M.; Uto, Y.; Hori, H. *Bioorg. Med. Chem. Lett.* **2002,** *12,* 951–954. doi:10.1016/S0960-894X(02)00066-5
27. Roller, S.; Zhou, H.; Haag, R. *Mol. Diversity* **2005,** *9,* 305–316. doi:10.1007/s11030-005-8117-y
28. Mitchell, D. J.; Steinman, L.; Kim, D. T.; Fathman, C. G.; Rothbard, J. B. *J. Pept. Res.* **2000,** *56,* 318–325. doi:10.1034/j.1399-3011.2000.00723.x
29. Ramezani, M.; Malaekeh-Nikouei, B.; Malekzadeh, S.; Baghayeripour, M. R.; Malaekeh-Nikouei, M. *Curr. Nanosci.* **2012,** *8,* 680–684. doi:10.2174/157341312802884535
30. Fischer, D.; Li, Y.; Ahlemeyer, B.; Krieglstein, J.; Kissel, T. *Biomaterials* **2003,** *24,* 1121–1131. doi:10.1016/S0142-9612(02)00445-3
31. Fischer, P. M.; Krausz, E.; Lane, D. P. *Bioconjugate Chem.* **2001,** *12,* 825–841. doi:10.1021/bc0155115
32. Schwartz, J. J.; Zhang, S. G. *Curr. Opin. Mol. Ther.* **2000,** *2,* 162–167.
33. Haag, R.; Tuerk, H.; Mecking, S. Verfahren zur Herstellung Hochverzweigter Polymere. Ger. Pat. Appl. DE 10211664 A1, Oct 2, 2003.

License and Terms

BEILSTEIN JOURNAL OF ORGANIC CHEMISTRY

Regulation of integrin and growth factor signaling in biomaterials for osteodifferentiation

Qiang Wei[1,2], Theresa L. M. Pohl[1,2], Anja Seckinger[3], Joachim P. Spatz[*1,2] and Elisabetta A. Cavalcanti-Adam[*1,2]

Review

Open Access

Address:
[1]Department of Biophysical Chemistry, Institute for Physical Chemistry, University of Heidelberg, INF 253, 69120 Heidelberg, Germany, [2]Department of New Materials and Biosystems, Max-Planck Institute for Intelligent Systems, Stuttgart, Germany and [3]Department of Internal Medicine V, Oncology, Hematology, and Rheumatology, Heidelberg University Hospital, 69120 Heidelberg, Germany

Email:
Joachim P. Spatz[*] - spatz@is.mpg.de;
Elisabetta A. Cavalcanti-Adam[*] - ada.cavalcanti-adam@urz.uni-heidelberg.de

* Corresponding author

Keywords:
biomaterials; growth factor; integrin; osteodifferentiation; stem cells

Beilstein J. Org. Chem. **2015,** *11,* 773–783.
doi:10.3762/bjoc.11.87

Received: 26 March 2015
Accepted: 07 May 2015
Published: 13 May 2015

This article is part of the Thematic Series "Multivalency as a chemical organization and action principle".

Guest Editor: R. Haag

Abstract

Stem cells respond to the microenvironment (niche) they are located in. Under natural conditions, the extracellular matrix (ECM) is the essential component the in stem cell niche, in which both integrin ligands and growth factors are important regulators to directly or indirectly modulate the cell behavior. In this review, we summarize the current knowledge about the potential of integrin ligands and growth factors to induce osteogenic differentiation of stem cells, and discuss the signaling pathways that are initiated by both individual and cooperative parameters. The joint effect of integrin ligands and growth factors is highlighted as the multivalent interactions for bone therapy.

Review

Introduction

Current bone grafting therapeutics do not provide satisfying solutions to the problems of non-healing bone defects. The gold-standard therapy is the grafting of autologous bone; however, it is limited by low availability as well as donor site pain and morbidity on the one hand. On the other hand, the allografts are suffering risk from possible infections and immune response [1]. More recently, stem cell therapy has been extensively studied and gained much focus for bone regeneration to achieve a suitable alternative to current grafting solutions in modern medicine [2].

Stem cells can differentiate into specialized cells and have self-renewal ability to further generate more stem cells. For example, mesenchymal stem cells (MSCs) derived from bone

marrow, can differentiate into a variety of lineages, including osteoblasts, chondrocytes, adipocytes, and reticular cells (Figure 1) [3]. Osteogenic differentiation is especially valuable in regenerative medicine approaches [4]. It has been proven that stem cell fate can be regulated from the specific microenvironment known as stem cell niche. The extracellular matrix (ECM), which virtually all cells in the body are exposed to and stem cells reside in, is an essential component in the stem cell niche [3]. The ECM is not an inert scaffold; instead, it is a dynamic network of molecules secreted by cells. Moreover, its biochemical, biophysical, and mechanical properties have emerged as important regulators for the direct or indirect modulation of cell behavior [4]. Cells interact with the ECM via several kinds of transmembrane receptors, in which the major class involved is integrin's [5]. Integrin ligands in the ECM include fibronectin, vitronectin, collagen, and laminin, which contain integrin-binding motifs [6]. These integrin-ECM interactions allow cells to sense matrix properties, such as topography and forces, from the ECM and respond in an appropriate manner [4]. Therefore, the use of integrin ligands to regulate stem cell fate becomes a hot spot of research. Both natural and synthetic integrin ligands were developed to control the interaction between biomaterials and stem cells. The effect of the topography and the distribution of the ligands on cell adhesion, proliferation, and differentiation were intensively studied as well [7].

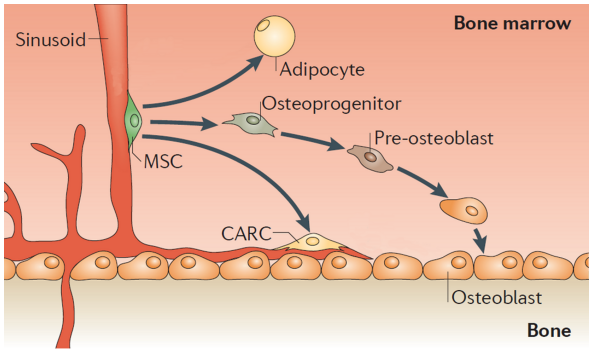

Figure 1: Differentiation potential of mesenchymal stem cells (MSCs) in bone marrow. MSCs can differentiate into a variety of lineages, including osteoblasts, chondrocytes, adipocytes, and reticular cells. Osteogenic differentiation is especially valuable in regenerative medicine approaches. Reprinted with permission from [3]. Copyright 2011 Nature Publishing Group.

Besides integrin ligands, growth factors, which can stimulate cell growth and differentiation, have also been employed for bone treatment [8,9]. Growth factors are water soluble proteins embedded in the ECM network mainly via non-covalent interactions with glycosaminoglycanes (GAG) [10]. Therefore, the ECM serves as a reservoir by establishing stable gradients of growth factors to regulate their bioavailability [11]. This matrix-immobilization of the factors might result in long-term binding to cell surface receptors, since the binding affinity of ECM-factors is relatively weak compared to growth factor receptor interactions [8]. Moreover, the factors can be released upon matrix turnover and degradation.

It has been proven that a large number of growth factors can induce bone healing [9], for example, bone morphogenetic proteins (BMPs) [12], transforming growth factor beta (TGF-β) [13], fibroblast growth factors (FGFs) [14], vascular endothelial growth factor (VEGF) [15], etc. Among them, BMPs are believed to be the most effective growth factors to induce bone growth [9]. However, when the BMP doses used clinically are much higher than the physiological concentrations, e.g., in the case of a systemic stimulation way, they lead to high costs of treatment and side-effects like pathologic changes or ectopic ossification [1]. To solve this problem, local delivery concepts that use implantable devices have been widely investigated [8,9].

Integrin ligands and growth factors are not independent systems for modulating osteogenic differentiation. It has been shown that integrins exert an extensive crosstalk with many growth factor receptors [16]. Integrin ligands actively participate in the regulation of growth factor-mediated signaling. Ligand–integrin interactions can induce ligand-independent partial activation of growth factor receptors and result in optimal cell survival and migration signals. Growth factor-mediated activation of the receptors leads to clustering of integrins and activation of integrin signaling [8,17]. In a word, the crosstalk between integrins and growth factor receptors is bidirectional that integrins may affect receptor signaling, and receptors may regulate integrin expression and activation [16].

In the first part of the review, we summarize how integrin ligands control cell adhesions and provide insight on how these interactions can regulate stem cell fate. In the second part, we report the current knowledge about growth factors and their ability to induce osteogenic differentiation of stem cells and we outline the delivery of these factors in vivo and in vitro. Furthermore, the studies on the cooperation of integrin ligands and growth factors for bone therapy are reviewed, and the coordinated signaling of integrins and growth factor receptors are discussed.

Integrin ligands for cell adhesion and stem cell fate

In order to enhance the effectiveness of cell-based bone therapy, it is important to understand the signals from integrin–ligand interactions. New technologies have been employed to provide

insights into how cells sense the information from ligands and how they respond at the molecular level, which ultimately regulate the differentiation of stem cells.

Integrin and integrin ligands

Integrins, which are non-covalently linked heterodimeric transmembrane receptors, contain an α and a β subunit. Both subunits exhibit mostly short cytoplasmic domains and large extracellular domains (Figure 2a). The cytoplasmic domains coordinate the assembly of cytoskeletal proteins and signaling complexes, while the extracellular domains engage either ECM components or counter receptors of the adjacent cells [18]. Therefore, the integrins serve to link the two compartments, namely the ECM and the intracellular actin filamentous

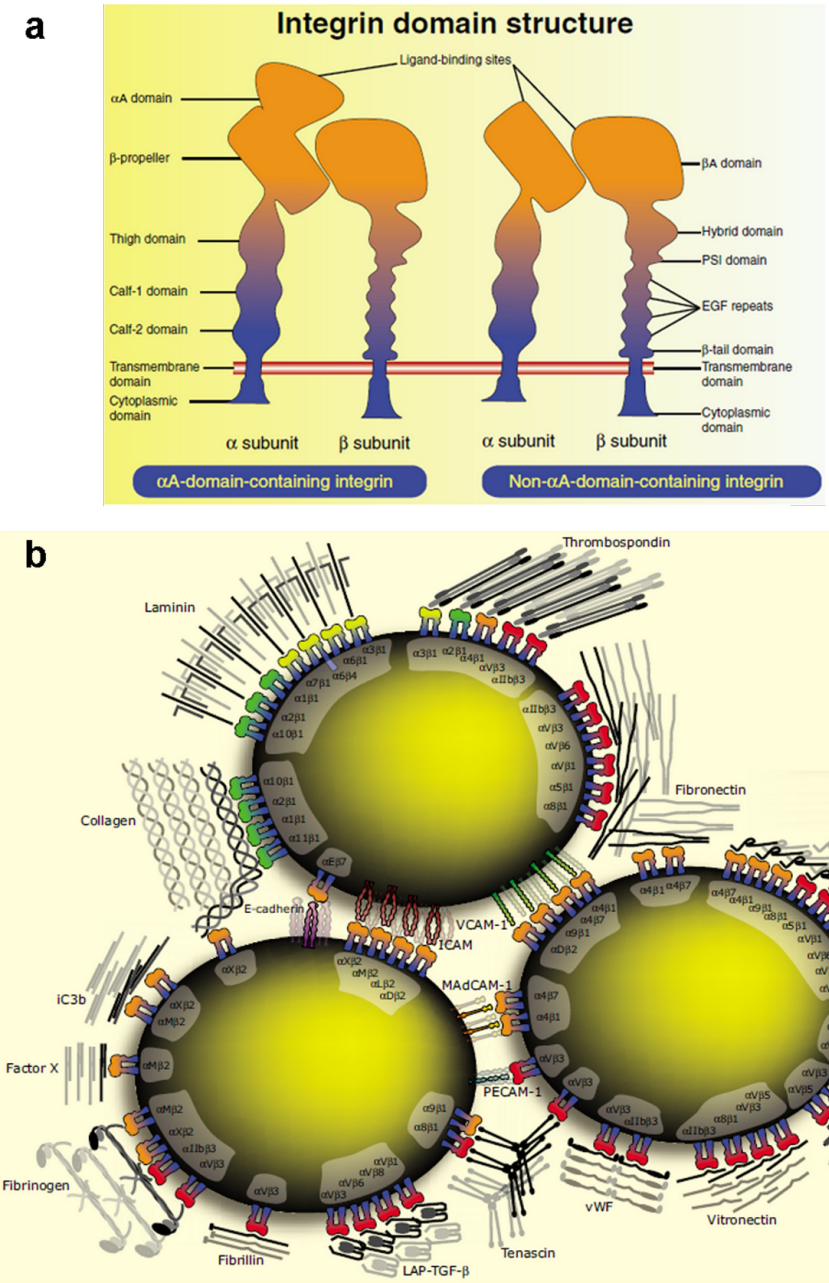

Figure 2: (a) The structure of the integrin heterodimeric receptors with α and β subunits. (b) The major integrin–ligand combinations on the cell surfaces. Abbreviations: BSP, bone sialoprotein; Del-1, developmental endothelial locus-1; EGF, epidermal growth factor; ICAM, intercellular cell adhesion molecule; iC3b, inactivated complement component C3b; LAP-TGF-β, latency associated peptide transforming growth factor β; MAdCAM-1, mucosal addressin cell adhesion molecule 1; MFG-E8, milk fat globule EGF factor 8; PECAM-1, platelet endothelial cell adhesion molecule 1 (CD31); PSI, plexin/semaphorin/integrin homology; VCAM-1, vascular cell adhesion molecule 1; vWF, von Willebrand factor. Reprinted from [18]. Copyright 2006 The Company of Biologists.

cytoskeleton across the plasma membrane. The interactions between integrins and ligands result in two major functions. First, the interactions physically integrate the ECM-bound cells and their cytoskeleton. Second, the signals resulting from these interactions enable cells to sense the chemical and mechanical properties of the microenvironment (niche) and to respond by activating signaling systems for regulating the cell fate [19]. Conversely, the contraction of the attached cytoskeleton pulls integrins together into larger adhesive clusters [7].

The type of the integrin–ligand interactions and the integrin–ligand pairs have been well described in previous reviews [18,20]. Most integrin receptors can bind a wide variety of ligands. Many ECM ligands and cell surface adhesion proteins, on the other hand, bind to multiple integrin receptors (Figure 2b) [18]. A set of receptor–ligand combinations with high-affinity interaction has even been identified. The best characterized and most widely used ligand is the arginine-glycine-aspartic acid (RGD) sequence. RGD motifs are present in many ECM glycoproteins, e.g., fibronectin, vitronectin and osteopontin [21], and are recognized by all five α_V, two β1 (α5 and α8), and αIIbβ3 integrins [18]. More particularly, RGD binds in a pocket between the α and β subunits. The arginine residue (R) fits into a cleft in a β-propeller module in the α subunit, in the meanwhile, the aspartic acid residue (D) coordinates a cation bound in the von Willebrand factor A domain of the β subunit [18].

To enhance the selectivity for recognizing distinct integrin subtypes, synthetic specific ligands have been developed [22]. In a recent work, peptidomimetics of the α5β1 antagonist and the αvβ3 antagonist were synthesized, respectively (Figure 3). Both peptidomimetics can selectively mediate cell adhesion by binding with the relative single integrin subtype without losing activity, while avoiding unspecific adhesion and integrin binding. This technology is helpful to understand how cell functions and responses are regulated by a single integrin subtype and is further essential to modulate the osteogenic differentiation of stem cells.

Integrin–ligand interactions to regulate cell adhesion and differentiation

Integrin ligands directly control the cell adhesion and spreading to affect the remolding of the cytoskeleton. The response of the cells activates the signaling pathways to regulate stem cell fate. The affinity of integrin–ligand interactions and the density of the ligands affect cell differentiation. MSCs differentiate towards osteoblasts, when they are cultured on high-affinity cyclic RGD immobilized substrates. When cultured on low-affinity linear RGD functional surface, MSCs express myogenic markers at high ligand density and neural markers at low ligand density [23]. In the other cases, when the ligands are efficient enough to induce cell attachment, the concentration and composition of the ligands do not affect cell differentiation; thus, the distribution of the ligands regulates the shape and spreading of the adherent cells [24]. In the case of single human epidermal stem cells, cells initiates terminal differentiation at higher frequency on a small circular adhesive pattern (20 μm diameter) than on a large circular pattern (50 μm diameter) [25]. The authors further revealed that G-actin level is the key to control the cytoskeletal tension. G-actin inhibits serum response factor (SRF) activity by limiting the availability of its co-factor MAL, when cells spread on large pattern. While cell spreading is restricted on small pattern, the level of G-actin is reduced, SRF activity increases and JunB expression is stimulated. In the case of human mesenchymal stem cells, the differentiation program

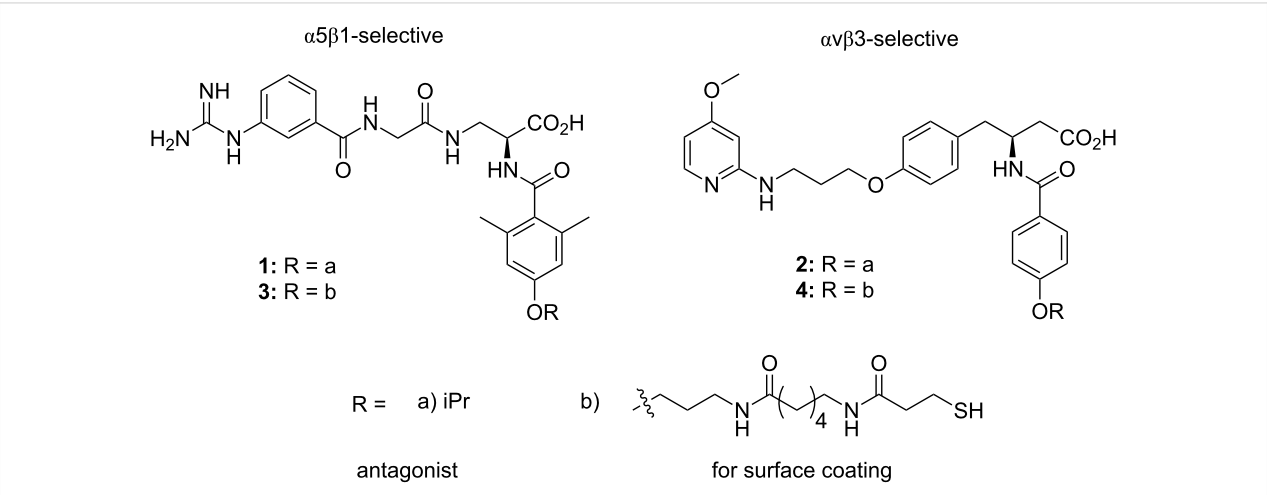

Figure 3: The chemical structure of the α5β1-selective (left) and the αvβ3-selective (right) peptidomimetics. Reprinted with permission from [22]. Copyright 2013 Wiley.

is determined by adhesion and spreading. Spread cells more likely differentiate into osteogenic lineage, and round cells more likely differentiate into adipogenic lineage [26].

To study cell spreading at the molecular level, nanotopography of the ligands available for binding has been modulated. The features of the nanoscale surface have a similar size compared to individual cell receptors, thus it is possible to target receptor-driven pathways and modulate cell responses [7]. Here, the cyclic RGDfK peptides are precisely immobilized on substrates via hexagonally close-packed gold nanodot arrays prepared by block-copolymer micelle nanolithography [27]. The critical distance of the ligands that limited cell spreading is approximately 70 nm (Figure 4). When the distance is larger, the formation of focal adhesions and actin cytoskeletal stress fibers is restricted. As a result, cells are less adhesive on the substrates and turn into quiescent or even apoptotic by anoikis. Contrarily, when the ligands are closer than 70 nm, cells form focal adhesions and contractile actin fibres which enable spreading [27,28].

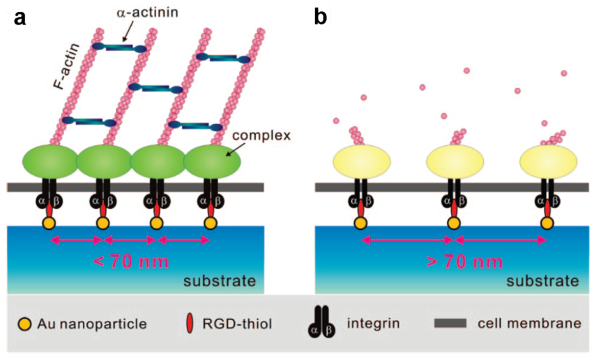

Figure 4: When the distance between two neighboring integrin ligands is <70 nm, the focal adhesions and contractile actin cytoskeletal stress fibres allow cell spreading (a). When the distance is >70 nm, the formation of focal adhesion and actin fibers is hindered (b). Reprinted with permission from [29]. Copyright 2009 American Chemical Society.

Similarly, ligand nanotopography is also important to control the spreading of stem cells for further regulating their differentiation. Osteogenic differentiation of MSCs can be enhanced on helical self-assembling nanoribbons with periodic binding sites in every 63 nm. However, when the distance of the periodic binding sites increases to about 100 nm on twisted nanoribbons, an osteoblast commitment cannot be observed [30].

When the ligand nanoarray with a distance just over 70 nm was disordered, the adhesion and spreading of the cells are enhanced [29]. Although the average center-to-center distance of the ligands is kept constant, some ligands can be arranged more densely and others more loosely. The distance of the ligands on the denser parts shall be smaller than 70 nm, thereby allowing integrin clustering and assembly focal adhesions to induce cell spreading. In a similar concept, a controlled nanodisordered pattern, which is not highly ordered but not random either, induces rapid osteogenesis from skeletal stem cells, due to the enhanced cell spreading [31]. Additionally, the well-designed highly ordered nanopatterns might be used to maintain the phenotype of MSCs. These patterns reduce but do not completely inhibit MSC adhesion. Therefore, the differentiation of MSC to both osteogenesis and adipogenesis is limited. As a result, cells are self-renewed without loss of phenotype [32].

In a recent study, how nanoscale clustering of integrin ligands alters the mechano-regulation of integrins has been revealed with the assistance of molecular tension fluorescence microscopy [33]. In the step of nascent adhesion formation, integrin tension driven by actin polymerization is in an average of 1–3 pN per ligand on the nanoarrays with distance both smaller and larger than 70 nm (approximately 50 and 100 nm, respectively). However, in the step of focal adhesion maturation, the tension on different nanoarrays is significantly different. In the 50 nm case, the average tension increases to about 6–8 pN due to the actomyosin-contractility, while in the 100 nm case, the tension even decreases due to the destabilization of integrin clusters. These results agree with the above cell spreading studies, and are important to understanding the mechanotransduction for regulating stem cell fate.

As a reverse process of cell differentiation, integrin adhesion also influences the reprogramming of differentiated cells to pluripotency. In a recent study, fibroblast adhesion is regulated by parallel microgrooves and aligned nanofibres, which significantly improve cell reprogramming [34]. The regulated cell adhesion can decrease histone deacetylase activity and upregulate the expression of WD repeat domain 5 (WDR5). As a result, the mechanomodulation of the epigenetic state of cells can be controlled. Cell reprogramming allows the patients who have a limited number of harvestable stem cells to find new source for bone healing.

Signaling mechanisms of integrin–ligand interactions to regulate stem cell fate

The signaling pathways that are implicated in triggering cell differentiation in response to the integrin–ligand interactions have been mapped [7,35]. Generally, integrin–ligand interactions elicit the activation of focal adhesion kinase (FAK) and its downstream target-effectors [36]. FAK is a tyrosine kinase and embedded in focal adhesions, the distribution of which is responsive to cell adhesion and spreading. The integrin–ligand interactions also activate a series of other biochemical signals, such as the Ras-ERK cascade, and PI3-K and Rho family

proteins [37]. Another tyrosine kinase Src also appears to be important for the regulation of focal adhesion organization [38]. Both FAK and Src play an important role to regulate G-proteins involved in filopodia, lamellipodia, and contraction [7]. Moreover, FAK can directly serve to gene regulation. It can transfer from focal adhesions to the nucleus to target ubiquitination of the cell-cycle mediator p53 and act as a transcription co-regulator with the GATA4 zinc-finger transcription factor [7,39,40]. Additionally, Rho A kinase (ROCK) can mediate intracellular tension through Rho-driven myosin activation to control the contraction of stress fibres [26,41]. Rho and ROCK have been shown to regulate MSC response to osteogenic niche [42]. The inhibition of ROCK may inhibit MSC growth and differentiation [43].

Integrin–ligand interactions that directly affect the cytoskeletal tension can further alter the shape of the nucleus, chromosomal arrangement and gene transcription. Therefore, the interactions may directly affect cell phenotype [7]. A cell can be described as a mechanical unit rather than biochemical unit in the theory of mechanotransduction. In this theory, integrin–ligand interactions cause cytoskeleton reorganization, which further affects the nuclear morphology, since the nucleus connects to the other side of the cytoskeleton. The change of the nuclear morphology subsequently propagates to the interphase chromosomes which are linked to the nuclear lamins at matrix-attachment regions [44]. Therefore, the genome and gene expression may be influenced. Based on this theory, the MSC differentiation can be modulated by the lamin-A level. Low lamin-A levels result in a more adipogenic differentiation, while the osteogenic differentiation is enhanced by increasing lamin-A levels [45].

Growth factors for modulating osteogenic differentiation

Growth factors, which can be found in all tissues, are important parameters to regulate a variety of cellular functions. They are able to stimulate or inhibit cell proliferation, migration, differentiation, or even gene expression [46,47]. The very same growth factors might trigger different functions in different cell types, because of their pleiotropic characters [48]. The same factors can even act in opposing manner, depending on the local concentration, to up- or down-regulate the synthesis of receptors. Some growth factors need to bind to ECM components, e.g., collagen or heparin to be stabilized or even to be activated [47,49]. Together with cytokines, growth factors, like bone morphogenetic proteins 2 (BMP-2), are involved in processes like wound healing and the bone regeneration [50,51]. BMP-2, which is locally secreted by skeletal and extraskeletal tissues, is part of the complex bone tissue consisting of different cell types and mineralized ECM. The interplay of these bone-matrix-derived growth factors with other molecules, such as hormones, regulates the differentiation of MSCs into osteogenic lineage [48,52], which results in an extraordinary potential for growth, regeneration and remodeling [50].

Bone morphogenetic proteins

BMPs belong to the superfamily of transforming growth factors-beta (TGF-β). Currently there are 14 known BMPs, which form a subfamily together with the growth differentiation factors (GDF) [53]. BMPs were originally known for their ability to induce the formation of de novo bone. However, nowadays they have been identified to affect numerous tissues during development and in the adult, besides influence bone formation and healing [54]. BMPs are involved in versatile non-osteogenic development processes, such as cell proliferation, differentiation, apoptosis, cell fate determination, and morphogenesis of many organs and tissues, gonads and the nervous system [55]. With a few exceptions, the physiological functions of BMP family members are mostly related to bone and cartilage formation as summarized in Table 1. Among those BMP-2, BMP-4, BMP-6, BMP-7, and BMP-9 are known to induce complete bone morphogenesis.

Table 1: Overview of the bone morphogenetic protein family. BMP members in humans and their main biological functions [53,56].

BMP	Alternative name	Main physiological function
BMP-2	BMP-2a	Cartilage and bone morphogenesis, heart formation
BMP-3	BMP-3a, Osteogenin	Negative regulator of bone morphogenesis
BMP-3b	GDF-10	Negative regulator of bone morphogenesis
BMP-4	BMP-2b	Cartilage and bone morphogenesis, kidney formation
BMP-5	–	Limb development, bone morphogenesis
BMP-6	Vgr-1, Dvr-6	Hypertrophy of cartilage and bone morphogenesis, oestrogen mediation
BMP-7	OP-1	Cartilage and bone morphogenesis, kidney formation
BMP-8	OP-2	Bone morphogenesis, spermatogenesis
BMP-9	GDF-2	Bone morphogenesis, development of cholinergic neurons, glucose metabolism
BMP-11	GDF-11	Axial skeleton patterning, eye development, pancreas development, kidney formation

BMPs are transcribed as large precursor proteins composed of a signal peptide, a prodomain and a mature domain. The proproteins dimerize after the signal peptide has been removed and are enzymatically cleaved to yield the biologically active dimeric mature protein [57]. The amino acid sequence of BMPs and their "cystine knot" motif, which is composed of seven cysteine units, is highly conserved [50]. Six of the seven cysteine residues Cys14/Cys79, Cys47/Cys113, and Cys43/Cys111 form intramolecular disulfide bonds to stabilize the monomer, whereas the seventh cysteine (Cys78) contributes to the formation of an intermolecular bond between the two monomers for dimerization. (Figure 5a) [58,59].

This cystine knot, which is highly resistant to heat, denaturants, and extreme acidic pH, defines the three dimensional structure of the protein and thus determines the unique properties of BMPs [47,61,62]. Although homodimers are considered to be the standard form, heterodimers are naturally formed [63]. The heterodimers can be engineered by the co-expression of two different recombinant BMPs. The affinity of the monomers to form dimers for maintaining the cystine knot motif leads to heterodimer formation. This is especially interesting, as BMP-2/BMP-7 for example, shows higher bioactivity compared to their corresponding homodimers [57].

BMP receptors (BMPRs) belong to the group of serine/threonine kinase transmembrane receptors and are subdivided into type I and II receptors [64,65]. There are three type I receptors, namely BMPR-IA (also known as ALK-3, activin receptor-like kinase), BMPR-IB (ALK-6), and the activin receptor ActR-IA (ALK-2); as well as three type II receptors, BMPR-II, ActR-II, and ActR-IIB. The binding of the ligands to these receptors results in heterooligomeric complexes, and thus leads to the activation of signal transduction [57,66-70]. In fact, the binding of BMP can induce different signaling cascades. Either the ligand binds to a preformed complex (PFC) consisting of a type I and II receptor, or the ligand mediates homodimerization of BMPR-I, followed by recruitment of BMPR-II (Figure 5b). The latter oligomerization mode, which is referred to as BMP-induced signaling complex (BISC), leads to internalization via caveolae and induces Smad-independent signaling cascades, resulting in alkaline phosphatase induction through p38 (mitogen-activated protein kinase (MAPK)) signaling cascade. Binding to PFCs triggers clathrin-dependent internalization and initiates a Smad-dependent pathway by phosphorylation of the receptor-regulated Smads (R-Smads, Smad1, 5, or 8) [60,71,72]. After phosphorylation, R-Smads are released from the BMP receptor and form a complex with the common mediator Smad (Co-Smad, Smad 4). This Smad complex translocates into the nucleus and activates the transcription of specific target genes such as the inhibitor of differentiation (Id) (Figure 5b) [70].

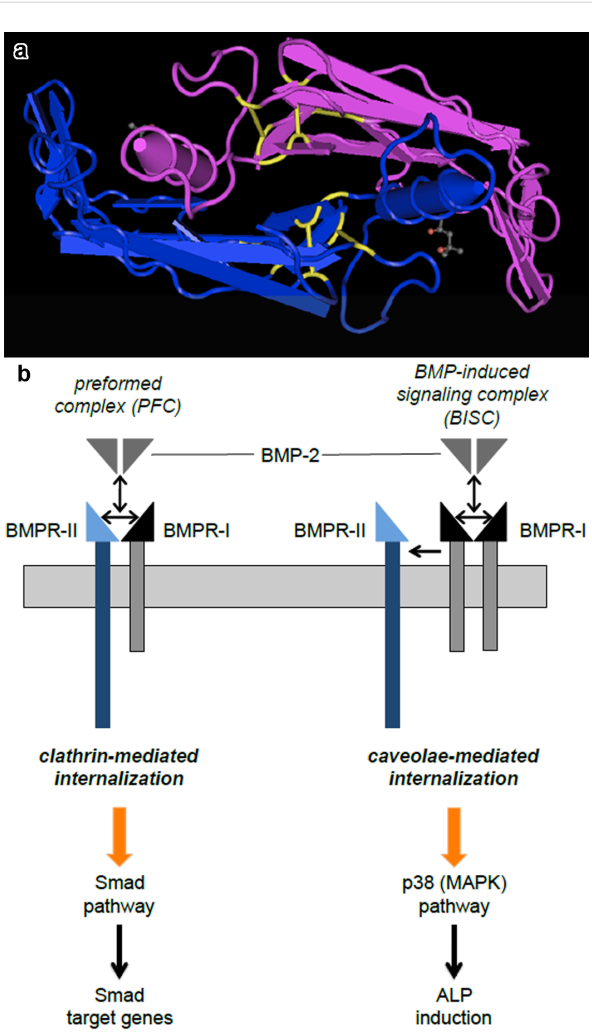

Figure 5: (a) BMP-2 homodimer. 3D-Structure of a BMP-2 homodimer (blue and pink) with cysteine residues, highlighted in yellow to show the intra- and intermolecular disulfide bonds, which determine the three dimensional structure of the protein [59]. (b) Smad dependent and independent BMP signaling pathways. Smad-dependent signaling cascades are induced upon binding of the ligand to a preformed complex (PFC) of BMPR-I and BMPR-II and subsequent internalization via clathrin-mediated internalization. In contrast to that, binding of the ligand to BMPR-I and subsequent recruitment of BMPR-II (BISC) results in caveolae-mediated internalization and triggers Smad independent signaling via p38 (mitogen-activated protein kinase (MAPK)) signaling, resulting in ALP induction. Adapted from [60].

Growth factors for bone therapy

The demographic challenge of an aging population leads to a clinical as well as a socioeconomic need for repair and regeneration of traumatized or lost tissue. Engineering delivery systems to create cartilage and bone for orthopedic application is therefore a pivotal need [48]. Conventional methods for bone therapy with autologous bone grafts are accompanied by many side effects, e.g., blood loss, risk of infection, and postoperative pain at the autograft site, as well as extended operation times. To solve these problems, local stimulation with growth factors are

provided as promising alternatives for bone tissue engineering [73].

Principally, there are two strategies to engineer bone tissue via direct growth factor delivery. Growth factors can be either locally implanted on carrier matrices or systemically distributed. Compared to former case of local delivery, the main advantage of the latter case, systemic stimulation, is that the employed injectable therapeutics is less invasive. However, the disadvantages are apparent as well. Growth factors in service conditions have a markedly shortened half-life and must be administered over long stimulation periods of several days. Moreover, excessive dosage causes side-effects like pathologic changes or ectopic ossification. Therefore, fewer studies have been devoted toward this systemic growth factor delivery [74]. Instead, local delivery concepts that are performed by implantable devices have been widely investigated over the last decades. The well-developed delivery systems for addressing confined bone regeneration include both absorbable and non-absorbable scaffolds, as well as both natural and synthetic materials. Depending on the application site, excipients of different geometries and stiffness were investigated and have shown to affect bone healing [75,76].

Actually, some confined growth factor delivery systems have already been clinically approved, when stimulation is only temporarily necessary until the regeneration occurred [77,78]. However, since bone regeneration is a complex cascade that is regulated by three major components, namely, cells, ECM, and morphogenetic signals, efficient tissue engineering of bone and cartilage must be subjected to each of these parameters [76,79]. A delivery system should therefore ideally fulfill certain requirements. It should be biological and immunological inert; promote specific cell adhesion, proliferation, and angiogenesis; provide growth factors; be rigid to withstand deforming forces (depending on application); be timed biodegradable; neither cause acute nor chronic inflammation; be easily stored and handled (sterilized); and the last be cost-effective [75,80].

The present delivery systems and methods have been systematically reviewed in recent literature [8,9,81]. In brief, growth factors in living systems exist in both soluble and matrix-bound forms [82]. Therefore, growth factor delivery can be designed by both encapsulation and surface immobilization approaches (Figure 6). The proteins should be slowly released from the delivery systems in the former case. The latter immobilization systems have the advantage of controlled and sustained influence on cell behavior [82,83], however, the orientation of many growth factors in single molecule level is not well controllable, which decreases the activity of the immobilized factors. In addition, immobilizing osteoinductive proteins on preferably osteoconductive matrices enables not only to control but even to prolong regenerative stimulation, thus minimizing side effects, while augmenting healing.

Moreover, some growth factors, e.g., FGF family members, play an important role in cell reprogramming. FGF2 can promote fibroblast cells to reprogramme to induce pluripotent

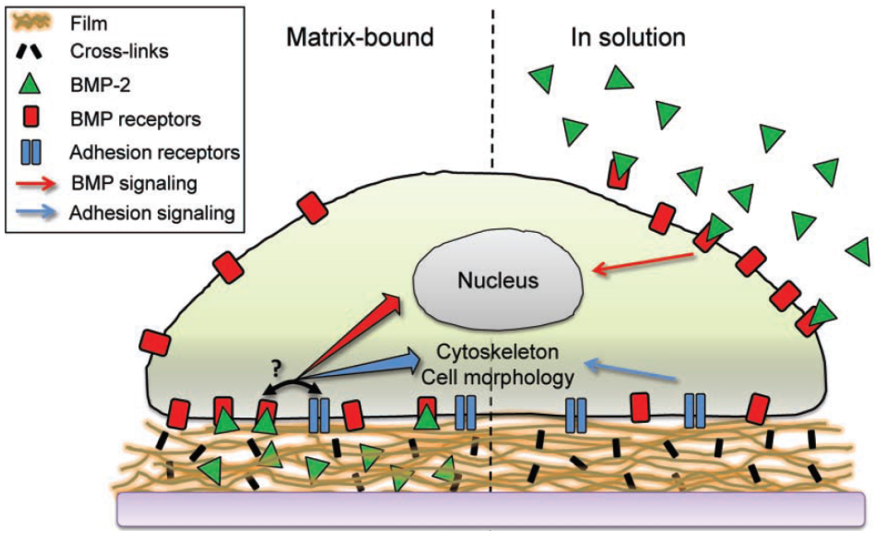

Figure 6: Growth factors, e.g., BMP-2, can be immobilized on the substrates to mimic the matrix-bound form (left), as well as be encapsulated to mimic the soluble form in natural conditions. The different delivery approaches may influence the crosstalk between the growth factors and integrin ligands (discuss below). Reprinted with permission from [85]. Copyright 2011 Wiley.

stem cells (iPSCs) [84]. The reason is that FGF2 sustains extracellular-signal-regulated kinase (ERK) phosphorylation and the expression of pluripotency marker genes, e.g., NANOG. As mentioned in the section about integrin–ligand interactions to regulate cell adhesion and differentiation, cell reprogramming increases the source for bone therapy.

Joint effects of integrin ligands and growth factors

Since both, integrin ligands and growth factors play an important role in regulating osteogenic differentiation of stem cells as discussed above, these two parameters have been employed together for developing new biomaterials to enhance bone regeneration. For example, the microspheres with immobilized RGD peptide and adsorbed BMP-2 exhibits high potential for cell adhesion and differentiation of MSCs [86]. In another case, the pro-osteogenic α2β1 integrin-specific GFOGER peptide ligands and BMP-2s are integrated in matrix metalloproteinase (MMP)-degradable PEG-maleimide hydrogels. The peptide ligands successfully host stem cells in vivo, and the sustained release of low doses of BMP-2 direct endogenous stem cell differentiation and promote bone healing [87].

Furthermore, the signal integration between integrins and growth factor receptors has been detected [35], which is in accordance with the positive experimental results on the combined effect of ligands and factors as shown above. Several distinct classes of signal coordination, including concomitant activation, collaborative activation, and direct activation signaling pathways, have been described [88].

First, the integrins and growth factors can activate independent signals to trigger the same signaling molecules as concomitant activation. It has been reported that the Ras-MAPK (mitogen-activated protein kinase) pathway, phosphoinositide 3-kinase (PI3K)-Akt pathway, and regulation of Rho family GTPases can be activated by this concomitant signaling way [35,88,89]. Second, integrin activation assists in growth-factor-dependent receptor signaling, as collaborative activation. Integrins may gather some signaling proteins to create an environment to help some growth factor receptors for their interaction with downstream signaling molecules [90]. These receptors include the epidermal growth factor receptor (EGFR), Met, platelet-derived growth factor receptor (PDGFR), insulin receptor, and vascular endothelial growth factor receptor (VEGFR) [35,88]. The collaboration is important for adhesion-dependent cell survival. Integrin-mediated cell adhesion responds to growth factors. When this response is impaired by cell detachment, it can result in cell growth arrest and even anoikis [91,92]. Third, integrins can also directly activate growth factor receptors by a growth-factor-independent receptor signaling pathway as direct activation. For example, EGFR phosphorylation can be induced by integrins in the absence of EGF [93]. Integrin-induced effects on receptor activation are distinct from the effects that are stimulated by the growth factor alone [88].

The growth factor receptor can activate the integrin gene expression to increase the amount of expressed integrins, which further activate the signaling pathways as mentioned above to amplify the signal [88]. Furthermore, integrins in some conditions can negatively regulate the growth factor receptor signaling. Ligand–integrin interactions have the ability to trigger phosphatase activation and recruitment to inhibit the signaling of growth factor receptors [88].

Conclusion

It may be insufficient to directly implant cells into human body, which may die or differentiate to the unexpected directions. Therefore, the appropriate extracellular environment must be carefully considered in biomaterial science to employ stem cells for cell therapies. Integrin ligands and growth factors are two of the most important parameters in the stem cell niche to determine the cell fate. In this review we highlighted the effect of integrin ligands and growth factors on the regulation of osteogenic differentiation of stem cells for bone regeneration. These two parameters can be either individually or cooperatively employed to induce cell differentiation. The relationship between these two parameters was also underlined. Although many signaling pathways that initiated by these two have been described, a deeper understanding of the efficiency of each parameter, especially in the case of cooperation, is still required to guide the integration of the two parameters in artificial medical systems. For example, the immobilization or encapsulation methods, the concentration and ratio, and the distribution, i.e., spatial relationship should be optimized in biomaterials and cell therapeutics. Overall, engineering the local delivery of integrin ligands and growth factors provides powerful and effective methods to regulate the stem cell fate.

Acknowledgements

The authors are grateful for the support from the Deutsche Forschungsgemeinschaft (DFG SFB TRR79 TPM9) and also acknowledge the support from the Max Planck Society.

References

1. De Long, W. G., Jr.; Einhorn, T. A.; Koval, K.; McKee, M.; Smith, W.; Sanders, R.; Watson, T. *J. Bone Joint Surg. Am.* **2007,** *89,* 649–658. doi:10.2106/JBJS.F.00465
2. Kimelman, N.; Pelled, G.; Helm, G. A.; Huard, J.; Schwarz, E. M.; Gazit, D. *Tissue Eng.* **2007,** *13,* 1135–1150. doi:10.1089/ten.2007.0096
3. Nombela-Arrieta, C.; Ritz, J.; Silberstein, L. E. *Nat. Rev. Mol. Cell Biol.* **2011,** *12,* 126–131. doi:10.1038/nrm3049

4. Marie, P. J. *Nat. Rev. Endocrinol.* **2013,** *9,* 288–295. doi:10.1038/nrendo.2013.4
5. Hynes, R. O. *Cell* **2002,** *110,* 673–687. doi:10.1016/S0092-8674(02)00971-6
6. Jalali, S.; del Pozo, M. A.; Chen, K.-D.; Miao, H.; Li, Y.-S.; Schwartz, M. A.; Shyy, J. Y.-J.; Chien, S. *Proc. Natl. Acad. Sci. U. S. A.* **2001,** *98,* 1042–1046. doi:10.1073/pnas.98.3.1042
7. Dalby, M. J.; Gadegaard, N.; Oreffo, R. O. C. *Nat. Mater.* **2014,** *13,* 558–569. doi:10.1038/nmat3980
8. Lienemann, P. S.; Lutolf, M. P.; Ehrbar, M. *Adv. Drug Delivery Rev.* **2012,** *64,* 1078–1089. doi:10.1016/j.addr.2012.03.010
9. King, W. J.; Krebsbach, P. H. *Adv. Drug Delivery Rev.* **2012,** *64,* 1239–1256. doi:10.1016/j.addr.2012.03.004
10. Bishop, J. R.; Schuksz, M.; Esko, J. D. *Nature* **2007,** *446,* 1030–1037. doi:10.1038/nature05817
11. Hynes, R. O. *Science* **2009,** *326,* 1216–1219. doi:10.1126/science.1176009
12. Wozney, J. M.; Rosen, V.; Celeste, A. J.; Mitsock, L. M.; Whitters, M. J.; Kriz, R. W.; Hewick, R. M.; Wang, E. A. *Science* **1988,** *242,* 1528–1534. doi:10.1126/science.3201241
13. Ripamonti, U.; Ferretti, C.; Teare, J.; Blann, L. *J. Craniofac. Surg.* **2009,** *20,* 1544–1555. doi:10.1097/SCS.0b013e3181b09ca6
14. Park, M. S.; Kim, S.-S.; Cho, S.-W.; Choi, C. Y.; Kim, B.-S. *J. Biomed. Mater. Res., Part B* **2006,** *79,* 353–359. doi:10.1002/jbm.b.30549
15. Street, J.; Bao, M.; deGuzman, L.; Bunting, S.; Peale, F. V., Jr.; Ferrara, N.; Steinmetz, H.; Hoeffel, J.; Cleland, J. L.; Daugherty, A.; van Bruggen, N.; Redmond, H. P.; Carano, R. A. D.; Filvaroff, E. H. *Proc. Natl. Acad. Sci. U. S. A.* **2002,** *99,* 9656–9661. doi:10.1073/pnas.152324099
16. Brizzi, M. F.; Tarone, G.; Defilippi, P. *Curr. Opin. Cell Biol.* **2012,** *24,* 645–651. doi:10.1016/j.ceb.2012.07.001
17. Streuli, C. H.; Akhtar, N. *Biochem. J.* **2009,** *418,* 491–506. doi:10.1042/BJ20081948
18. Humphries, J. D.; Byron, A.; Humphries, M. J. *J. Cell Sci.* **2006,** *119,* 3901–3903. doi:10.1242/jcs.03098
19. Winograd-Katz, S. E.; Fässler, R.; Geiger, B.; Legate, K. R. *Nat. Rev. Mol. Cell Biol.* **2014,** *15,* 273–288. doi:10.1038/nrm3769
20. Plow, E. F.; Haas, T. K.; Zhang, L.; Loftus, J.; Smith, J. W. *J. Biol. Chem.* **2000,** *275,* 21785–21788. doi:10.1074/jbc.R000003200
21. Schwab, E. H.; Halbig, M.; Glenske, K.; Wagner, A.-S.; Wenisch, S.; Cavalcanti-Adam, E. A. *Int. J. Med. Sci.* **2013,** *10,* 1846–1859. doi:10.7150/ijms.6908
22. Rechenmacher, F.; Neubauer, S.; Polleux, J.; Mas-Moruno, C.; De Simone, M.; Cavalcanti-Adam, E. A.; Spatz, J. P.; Fassler, R.; Kessler, H. *Angew. Chem., Int. Ed.* **2013,** *52,* 1572–1575. doi:10.1002/anie.201206370
23. Kilian, K. A.; Mrksich, M. *Angew. Chem., Int. Ed.* **2012,** *51,* 4891–4895. doi:10.1002/anie.201108746
24. Watt, F. M.; Huck, W. T. S. *Nat. Rev. Mol. Cell Biol.* **2013,** *14,* 467–473. doi:10.1038/nrm3620
25. Connelly, J. T.; Gautrot, J. E.; Trappmann, B.; Tan, D. W.-M.; Donati, G.; Huck, W. T. S.; Watt, F. M. *Nat. Cell Biol.* **2010,** *12,* 711–718. doi:10.1038/ncb2074
26. McBeath, R.; Pirone, D. M.; Nelson, C. M.; Bhadriraju, K.; Chen, C. S. *Dev. Cell* **2004,** *6,* 483–495. doi:10.1016/S1534-5807(04)00075-9
27. Arnold, M.; Cavalcanti-Adam, E. A.; Glass, R.; Blümmel, J.; Eck, W.; Kantlehner, M.; Kessler, H.; Spatz, J. P. *ChemPhysChem* **2004,** *5,* 383–388. doi:10.1002/cphc.200301014
28. Cavalcanti-Adam, E. A.; Aydin, D.; Hirschfeld-Warneken, V. C.; Spatz, J. P. *HFSP J.* **2008,** *2,* 276–285. doi:10.2976/1.2976662
29. Huang, J.; Gräter, S. V.; Corbellinl, F.; Rinck, S.; Bock, E.; Kemkemer, R.; Kessler, H.; Ding, J.; Spatz, J. P. *Nano Lett.* **2009,** *9,* 1111–1116. doi:10.1021/nl803548b
30. Das, R. K.; Zouani, O. F.; Labrugère, C.; Oda, R.; Durrieu, M.-C. *ACS Nano* **2013,** *7,* 3351–3361. doi:10.1021/nn4001325
31. Dalby, M. J.; Gadegaard, N.; Tare, R.; Andar, A.; Riehle, M. O.; Herzyk, P.; Wilkinson, C. D. W.; Oreffo, R. O. C. *Nat. Mater.* **2007,** *6,* 997–1003. doi:10.1038/nmat2013
32. Tsimbouri, P. M.; McMurray, R. J.; Burgess, K. V.; Alakpa, E. V.; Reynolds, P. M.; Murawski, K.; Kingham, E.; Oreffo, R. O. C.; Gadegaard, N.; Dalby, M. J. *ACS Nano* **2012,** *6,* 10239–10249. doi:10.1021/nn304046m
33. Liu, Y.; Medda, R.; Liu, Z.; Galior, K.; Yehl, K.; Spatz, J. P.; Cavalcanti-Adam, E. A.; Salaita, K. *Nano Lett.* **2014,** *14,* 5539–5546. doi:10.1021/nl501912g
34. Downing, T. L.; Soto, J.; Morez, C.; Houssin, T.; Fritz, A.; Yuan, F. L.; Chu, J.; Patel, S.; Schaffer, D. V.; Li, S. *Nat. Mater.* **2013,** *12,* 1154–1162. doi:10.1038/nmat3777
35. Giancotti, F. G.; Tarone, G. *Annu. Rev. Cell Dev. Biol.* **2003,** *19,* 173–206. doi:10.1146/annurev.cellbio.19.031103.133334
36. Clark, E. A.; Brugge, J. S. *Science* **1995,** *268,* 233–239. doi:10.1126/science.7716514
37. Schlaepfer, D. D.; Hunter, T. *Trends Cell Biol.* **1998,** *8,* 151–157. doi:10.1016/S0962-8924(97)01172-0
38. Cox, E. A.; Bennin, D.; Doan, A. T.; O'Toole, T.; Huttenlocher, A. *Mol. Biol. Cell* **2003,** *14,* 658–669. doi:10.1091/mbc.E02-03-0142
39. Lim, S.-T. *Mol. Cells* **2013,** *36,* 1–6. doi:10.1007/s10059-013-0139-1
40. Lim, S.-T.; Miller, N. L. G.; Nam, J.-O.; Chen, X. L.; Lim, Y.; Schlaepfer, D. D. *J. Biol. Chem.* **2010,** *285,* 1743–1753. doi:10.1074/jbc.M109.064212
41. Trappmann, B.; Gautrot, J. E.; Connelly, J. T.; Strange, D. G. T.; Li, Y.; Oyen, M. L.; Stuart, M. A. C.; Boehm, H.; Li, B.; Vogel, V.; Spatz, J. P.; Watt, F. M.; Huck, W. T. S. *Nat. Mater.* **2012,** *11,* 642–649. doi:10.1038/nmat3339
42. Dalby, M. J.; Andar, A.; Nag, A.; Affrossman, S.; Tare, R.; McFarlane, S.; Oreffo, R. O. C. *J. R. Soc., Interface* **2008,** *5,* 1055–1065. doi:10.1098/rsif.2008.0016
43. McMurray, R. J.; Gadegaard, N.; Tsimbouri, P. M.; Burgess, K. V.; McNamara, L. E.; Tare, R.; Murawski, K.; Kingham, E.; Oreffo, R. O. C.; Dalby, M. J. *Nat. Mater.* **2011,** *10,* 637–644. doi:10.1038/nmat3058
44. Guarda, A.; Bolognese, F.; Bonapace, I. M.; Badaracco, G. *Exp. Cell Res.* **2009,** *315,* 1895–1903. doi:10.1016/j.yexcr.2009.01.019
45. Swift, J.; Ivanovska, I. L.; Buxboim, A.; Harada, T.; Dingal, P. C. D. P.; Pinter, J.; Pajerowski, J. D.; Spinler, K. R.; Shin, J.-W.; Tewari, M.; Rehfeldt, F.; Speicher, D. W.; Discher, D. E. *Science* **2013,** *341,* 6149. doi:10.1126/science.1240104
46. Lind, M. *Acta Orthop. Scand.* **1996,** *67,* 407–417. doi:10.3109/17453679609002342
47. Nimni, M. E. *Biomaterials* **1997,** *18,* 1201–1225. doi:10.1016/S0142-9612(97)00050-1
48. Rose, F. R. A. J.; Hou, Q.; Oreffo, R. O. C. *J. Pharm. Pharmacol.* **2004,** *56,* 415–427. doi:10.1211/0022357023312
49. Masters, K. S. *Macromol. Biosci.* **2011,** *11,* 1149–1163. doi:10.1002/mabi.201000505
50. Rengachary, S. S. *Neurosurg. Focus* **2002,** *13,* e2.

51. Barrientos, S.; Stojadinovic, O.; Golinko, M. S.; Brem, H.; Tomic-Canic, M. *Wound Repair Regen.* **2008,** *16,* 585–601. doi:10.1111/j.1524-475X.2008.00410.x
52. Bianco, P.; Robey, P. G. *Nature* **2001,** *414,* 118–121. doi:10.1038/35102181
53. Schulz, T. J.; Tseng, Y.-H. *Cytokine Growth Factor Rev.* **2009,** *20,* 523–531. doi:10.1016/j.cytogfr.2009.10.019
54. Helm, G.; Anderson, D. G.; Andersson, G. B. J.; Boden, S. D.; Damien, C.; Ebara, S.; Lane, J. M.; McKay, B.; Sandhu, H. S.; Seeherman, H.; Wozney, J. *Spine* **2002,** *27,* S9. doi:10.1097/00007632-200208151-00003
55. Hogan, B. L. *Genes Dev.* **1996,** *10,* 1580–1594. doi:10.1101/gad.10.13.1580
56. Bessa, P. C.; Casal, M.; Reis, R. L. *J. Tissue Eng. Regener. Med.* **2008,** *2,* 1–13. doi:10.1002/term.63
57. Shimasaki, S.; Moore, R. K.; Otsuka, F.; Erickson, G. F. *Endocr. Rev.* **2004,** *25,* 72–101. doi:10.1210/er.2003-0007
58. Schlunegger, M. P.; Grütter, M. G. *Nature* **1992,** *358,* 430–434. doi:10.1038/358430a0
59. Scheufler, C.; Sebald, W.; Hülsmeyer, M. *J. Mol. Biol.* **1999,** *287,* 103–115. doi:10.1006/jmbi.1999.2590
60. Nohe, A.; Hassel, S.; Ehrlich, M.; Neubauer, F.; Sebald, W.; Henis, Y. I.; Knaus, P. *J. Biol. Chem.* **2002,** *277,* 5330–5338. doi:10.1074/jbc.M102750200
61. Wozney, J. M.; Rosen, V. *Clin. Orthop. Relat. Res.* **1998,** 26–37.
62. Rosen, V. *Ann. N. Y. Acad. Sci.* **2006,** *1068,* 19–25. doi:10.1196/annals.1346.005
63. Chen, D.; Zhao, M.; Harris, S. E.; Mi, Z. *Front. Biosci.* **2004,** *9,* 349–358. doi:10.2741/1090
64. Tendijke, P.; Yamashita, H.; Sampath, T. K.; Reddi, A. H.; Estevez, M.; Riddle, D. L.; Ichijo, H.; Heldin, C. H.; Miyazono, K. *J. Biol. Chem.* **1994,** *269,* 16985–16988.
65. Koenig, B. B.; Cook, J. S.; Wolsing, D. H.; Ting, J.; Tiesman, J. P.; Correa, P. E.; Olson, C. A.; Pecquet, A. L.; Ventura, F. S.; Grant, R. A.; Chen, G.-X.; Wrana, J. L.; Massagué, J.; Rosenbaum, J. S. *Mol. Cell. Biol.* **1994,** *14,* 5961–5974. doi:10.1128/MCB.14.9.5961
66. Kirsch, T.; Sebald, W.; Dreyer, M. K. *Nat. Struct. Biol.* **2000,** *7,* 492–496. doi:10.1038/75903
67. Kirsch, T.; Nickel, J.; Sebald, W. *EMBO J.* **2000,** *19,* 3314–3324. doi:10.1093/emboj/19.13.3314
68. Keller, S.; Nickel, J.; Zhang, J.-L.; Sebald, W.; Mueller, T. D. *Nat. Struct. Mol. Biol.* **2004,** *11,* 481–488. doi:10.1038/nsmb756
69. Sebald, W.; Nickel, J.; Zhang, J.-L.; Mueller, T. D. *Biol. Chem.* **2004,** *385,* 697–710. doi:10.1515/BC.2004.086
70. Miyazono, K.; Maeda, S.; Imamura, T. *Cytokine Growth Factor Rev.* **2005,** *16,* 251–263. doi:10.1016/j.cytogfr.2005.01.009
71. Xiao, Y.-T.; Xiang, L.-X.; Shao, J.-Z. *Biochem. Biophys. Res. Commun.* **2007,** *362,* 550–553. doi:10.1016/j.bbrc.2007.08.045
72. Sieber, C.; Kopf, J.; Hiepen, C.; Knaus, P. *Cytokine Growth Factor Rev.* **2009,** *20,* 343–355. doi:10.1016/j.cytogfr.2009.10.007
73. Bishop, G. B.; Einhorn, T. A. *Int. Orthop.* **2007,** *31,* 721–727. doi:10.1007/s00264-007-0424-8
74. Gittens, S. A.; Uludag, H. *J. Drug Targeting* **2001,** *9,* 407–429. doi:10.3109/10611860108998776
75. Burg, K. J. L.; Porter, S.; Kellam, J. F. *Biomaterials* **2000,** *21,* 2347–2359. doi:10.1016/S0142-9612(00)00102-2
76. V, L.; Meinel, L.; Merkle, H. P.; Gander, B. *Eur. J. Pharm. Biopharm.* **2004,** *58,* 197–208.
77. Vasita, R.; Katti, D. S. *Expert Rev. Med. Devices* **2006,** *3,* 29–47. doi:10.1586/17434440.3.1.29
78. McKay, B.; Sandhu, H. S. *Spine* **2002,** *27,* S66–S85. doi:10.1097/00007632-200208151-00014
79. Reddi, A. H. *J. Cell. Biochem.* **1994,** *56,* 192–195. doi:10.1002/jcb.240560213
80. Solheim, E. *Int. Orthop.* **1998,** *22,* 410–416. doi:10.1007/s002640050290
81. Mehta, M.; Schmidt-Bleek, K.; Duda, G. N.; Mooney, D. J. *Adv. Drug Delivery Rev.* **2012,** *64,* 1257–1276. doi:10.1016/j.addr.2012.05.006
82. Pohl, T. L. M.; Boergermann, J. H.; Schwaerzer, G. K.; Knaus, P.; Cavalcanti-Adam, E. A. *Acta Biomater.* **2012,** *8,* 772–780. doi:10.1016/j.actbio.2011.10.019
83. Schwab, E. H.; Pohl, T. L. M.; Haraszti, T.; Schwaerzer, G. K.; Hiepen, C.; Spatz, J. P.; Knaus, P.; Cavalcanti-Adam, E. A. *Nano Lett.* **2015,** *15,* 1526–1534. doi:10.1021/acs.nanolett.5b00315
84. Chen, G.; Gulbranson, D. R.; Yu, P.; Hou, Z.; Thomson, J. A. *Stem Cells* **2012,** *30,* 623–630. doi:10.1002/stem.1021
85. Crouzier, T.; Fourel, L.; Boudou, T.; Albigès-Rizo, C.; Picart, C. *Adv. Mater.* **2011,** *23,* H111–H118. doi:10.1002/adma.201004637
86. Park, J. S.; Yang, H. N.; Jeon, S. Y.; Woo, D. G.; Na, K.; Park, K.-H. *Biomaterials* **2010,** *31,* 6239–6248. doi:10.1016/j.biomaterials.2010.05.002
87. Shekaran, A.; Garcia, J. R.; Clark, A. Y.; Kavanaugh, T. E.; Lin, A. S.; Guldberg, R. E.; Garcia, A. J. *Biomaterials* **2014,** *35,* 5453–5461. doi:10.1016/j.biomaterials.2014.03.055
88. Ivaska, J.; Heino, J. *Annu. Rev. Cell Dev. Biol.* **2011,** *27,* 291–320. doi:10.1146/annurev-cellbio-092910-154017
89. Schwartz, M. A.; Ginsberg, M. H. *Nat. Cell Biol.* **2002,** *4,* E65–E68. doi:10.1038/ncb0402-e65
90. Yamada, K. M.; Even-Ram, S. *Nat. Cell Biol.* **2002,** *4,* E75–E76. doi:10.1038/ncb0402-e75
91. Danen, E. H. J.; Yamada, K. M. *J. Cell. Physiol.* **2001,** *189,* 1–13. doi:10.1002/jcp.1137
92. Schwartz, M. A.; Assoian, R. K. *J. Cell Sci.* **2001,** *114,* 2553–2560.
93. Moro, L.; Venturino, M.; Bozzo, C.; Silengo, L.; Altruda, F.; Beguinot, L.; Tarone, G.; Defilippi, P. *EMBO J.* **1998,** *17,* 6622–6632. doi:10.1093/emboj/17.22.6622

License and Terms

BEILSTEIN JOURNAL OF ORGANIC CHEMISTRY

Orthogonal dual-modification of proteins for the engineering of multivalent protein scaffolds

Michaela Mühlberg[‡1,2], Michael G. Hoesl[‡3], Christian Kuehne[4], Jens Dernedde[4], Nediljko Budisa[*3] and Christian P. R. Hackenberger[*1,5,§]

Full Research Paper

Open Access

Address:
[1]Forschungsinstitut für Molekulare Pharmakologie (FMP), Robert-Roessle-Str. 10, 13125 Berlin, Germany, [2]Freie Universität Berlin, Institut für Chemie und Biochemie, Takustr. 3, 14195 Berlin, Germany, [3]Technische Universität Berlin, AK Biokatalyse, Institut für Chemie, Müller-Breslau-Str. 10, 10623 Berlin, Germany, [4]Charité - Universitätsmedizin Berlin, Institut für Laboratoriumsmedizin, Klinische Chemie und Pathobiochemie, Augustenburger Platz 1, 13353 Berlin, Germany and [5]Humboldt Universität zu Berlin, Institut für Organische und Bioorganische Chemie, Institut für Chemie, Brook-Taylor-Str. 2, 12489 Berlin, Germany

Email:
Nediljko Budisa[*] - nediljko.budisa@tu-berlin.de;
Christian P. R. Hackenberger[*] - hackenbe@fmp-berlin.de

* Corresponding author ‡ Equal contributors
§ Fax: +49 (0)30 94793-188

Keywords:
chemoselectivity; dual protein modification; lectin; multivalency

Beilstein J. Org. Chem. **2015,** *11,* 784–791.
doi:10.3762/bjoc.11.88

Received: 11 February 2015
Accepted: 05 May 2015
Published: 13 May 2015

This article is part of the Thematic Series "Multivalency as a chemical organization and action principle".

Guest Editor: R. Haag

Abstract

To add new tools to the repertoire of protein-based multivalent scaffold design, we have developed a novel dual-labeling strategy for proteins that combines residue-specific incorporation of unnatural amino acids with chemical oxidative aldehyde formation at the *N*-terminus of a protein. Our approach relies on the selective introduction of two different functional moieties in a protein by mutually orthogonal copper-catalyzed azide–alkyne cycloaddition (CuAAC) and oxime ligation. This method was applied to the conjugation of biotin and β-linked galactose residues to yield an enzymatically active thermophilic lipase, which revealed specific binding to *Erythrina cristagalli* lectin by SPR binding studies.

Introduction

The chemical modification of proteins has been developed to a core discipline in chemical biology with diverse applications in all areas of the life sciences, including pharmacology, biophysics, biotechnology and cell biology [1-4]. In addition to the use of chemical labeling methods to study structure and function of proteins in vitro and in vivo, chemoselective conjugation techniques are also used to functionalize artificial protein scaffolds, such as viral capsids [5-7]. Such templates have self-assembled hierarchical structures that allow the generation of nanostructured scaffolds with precisely defined dimensions and

configurations [7-12]. We have recently contributed to this field using globular proteins as multivalent scaffolds for the structurally-defined presentation of ligands. In a proof-of-principle study to engineer multivalent glycoprotein conjugates, we have used the incorporation of non-canonical amino acids (NCAA) [13] by supplementation based incorporation (SPI) [14-17] in auxotroph expression systems followed by the chemoselective Cu-catalyzed azide–alkyne cycloaddition (CuAAC) to attach carbohydrate ligands to the protein barstar [18].

In the current study, we aimed to extend this approach to the dual modification of proteins using a combination of two chemoselective, orthogonal conjugation reactions for the introduction of glycan ligands and biotin to a protein. Our main objective in this paper was the development of a robust synthetic methodology that allows the site-specific attachment of two distinct chemical modifications to a given protein, which can be used to target multivalent interactions. As a protein scaffold we selected the thermophilic lipase from *Thermoanaerobacter thermohydrosulfuricus* (TTL), since this protein is tolerant to high temperatures, a variety of solvents and other additives, and an enzymatic assay is available as a control for retained protein integrity and catalytic function [19].

Dual labeling techniques in protein synthesis are dependent on the availability of unnatural protein expression methods to install orthogonal chemical handles for subsequent biorthogonal modification reactions [20,21]. For instance, the groups of Chin, Liu and Lemke introduced two mutually compatible chemical handles by combining nonsense and/or quadruplet codon suppressions [22-25]. Although recombinant expression strains have been engineered to improve incorporation efficiency [26-28], double labeling approaches by nonsense or quadruplet codon suppression are often coping with low protein yields. The main reasons for these low yields are the competition of NCAA incorporation with translational frame shifting or termination, and low catalytic efficiency of engineered aminoacyl-tRNA synthetases [29].

Certainly, the most straightforward approach to achieve the dual modification of proteins is to combine unnatural protein expression with the site-directed modification of canonical amino acids, particularly cysteine. For example, SPI was used to introduce a NCAA such as azidohomoalanine (Aha) in a methionine-(Met)-auxotroph in combination with the chemical modification of the natural amino acid cysteine [30,31]. These handles were, e.g., addressed by CuAAC and disulfide bond formation, respectively, to introduce two distinct modifications. In addition also amber suppression for the installation of a ketone-containing NCAA (Ac-Phe) was combined with Cys-labeling for a site-specific FRET-labeling of proteins [32]. Despite these advances, the chemical modification of cysteine has some drawbacks including the high tendency for disulfide bond formation or cross reaction with other cysteine residues, reaction reversibility, and occasionally side-reactions with basic side chains, e.g., lysines [33].

Specifically, in the current paper we use in the current paper the oxime ligation [34,35] as the second orthogonal conjugation reaction in addition to CuAAC for the attachment of functional moieties to Aha residues installed by auxotroph expression. In order to install a second unnatural functionality in the protein, in addition to SPI, we utilized the well-established oxidative aldehyde formation at the *N*-terminus with $NaIO_4$ [36-41]. With this approach, we aimed to engineer an artificial lectin-binding protein via chemical installation of several galactose moieties by CuAAC [18]. The second functionalization site at the protein's *N*-terminus was conjugated with biotin using oxime ligation, by which the protein scaffold was immobilized on a streptavidin gold chip to monitor carbohydrate–protein binding studies by surface plasmon resonance (SPR). This immobilization strategy allowed easy handling and reproducible orientation, which are notable improvements over the alternative active ester immobilization. Although not directly demonstrated in the current paper, our approach required considerably lower amounts of the inhibiting glycoconjugate in comparison to the reverse approach, which involves immobilization of lectin and titration of the binder.

Results and Discussion

Protein design

Aha labelled TTL variants were always expressed with the SPI approach. Aha is a Met analogue and incorporation leads to full substitution of all Met residues in TTL by Aha residues. Six of the ten Met positions are solvent accessible (M1,M20, M21, M145, M150, M161) [42]. These positions are well distributed over the protein surface. In addition to the reasons stated in the introduction, the Met surface distribution made TTL an attractive choice for this proof-of-principle study to generate a double-functionalized protein scaffold for multivalent binding studies.

In the beginning of our studies, we expressed TTL recombinantly with an *N*-terminal His-tag and tobacco etch virus protease (TEV) cleavage site, leaving an *N*-terminal Ser after the cleavage. However, we were unable to cleave the tag. This is probably due to structural constraints at the TTL's N-terminus leaving the TEV protease recognition site inaccessible for the protease (for more information on protein design see Supporting Information File 1). Therefore, the construct was altered to contain an unmodified *N*-terminus with Ser at position 2. The *N*-terminal Met is cleaved when followed by small

amino acids like glycine, alanine or serine in the native process of *N*-terminal methionine excision (NME) [43]. This process exposes Ser2 at the *N*-terminus for subsequent *N*-terminal oxime ligation. It has to be noted that the incorporation of Aha, as known [42,44], can hamper NME and therefore delivers in our case an approximate 1:1 mixture of TTL (estimated by MS, see Supporting Information File 1) with an *N*-terminal Ser (Ser-TTL[Aha]) and an *N*-terminal Aha (AhaSer-TTL[Aha]) together with nine additional Aha residues (Scheme 1). However, this *N*-terminal heterogeneity did not hamper our subsequent application, since only biotinylated protein could bind to the chip for SPR studies (see below).

Dual-labeling of TTL

Oxime ligation and CuAAC have been reported previously to be orthogonal to each other in DNA model systems and proteins obtained from amber and ochre suppression [24,45,46]. Since glycol cleavage is needed to generate the *N*-terminal aldehyde [39,40], we initialized our synthetic route with $NaIO_4$ treatment since the galactose units installed by CuAAC would be efficient targets for a glycol cleavage, as shown previously [47]. Based on optimization experiments for the periodate treatment of *N*-terminal Ser peptides (data not shown), TTL was treated with sodium periodate in a phosphate buffer at pH 7 and 15 °C for 1 h and quenched with *N*-acetyl-Met to quantitatively form the aldehyde Ald-TTL[Aha] (Scheme 1, Figure 1A) [48]. For the oxime ligation with the synthesized biotin hydroxylamine derivative **1** (see Supporting Information File 1), several reaction conditions were screened to achieve full conversion based on MALDI–MS analysis for the Ald-TTL[Aha], in which the unreactive AhaSer-TTL[Aha] served as a reference point (Figure 1A), whereby it has to be noted that due to the limited resolution of the MALDI for proteins all detected mass values differ by a few Dalton from the theoretical masses, and the peak intensity for the functionalized biotinylated lipase (**Gal-0**) was usually lower in all MALDI spectra which was addressed to the lower detectability of **Gal-0** due to the attached biotin. Under rather mild reaction conditions at pH 7 with *p*-anisidine as a catalyst only 10% product was formed [49]. Lowering the pH and increasing the amount of hydroxylamine **1** promoted the desired Schiff's base formation (see Supporting Information File 1) and full conversion to **Gal-0** could be achieved in an ammonium acetate buffer (100 mM, pH 3.0) with 20 equiv hydroxylamine **1**. The successful biotinylation could also be shown by SDS PAGE (sodium dodecyl sulfate polyacrylamide gel electrophoresis) and Western Blot analysis (see Figure 1B–C, lane 3).

To probe CuAAC, we first reacted the unmodified protein mixture (Aha)Ser-TTL[Aha] with the previously synthesized β-butynyl galactose **2** (Scheme 1). The conjugation reaction was performed in phosphate buffer (100 mM, 100 mM NaCl, pH 7) with varying amounts of $CuSO_4$. Tris(3-hydroxypropyltriazolylmethyl)amine (THPTA), a good stabilizer for Cu(I) in solution [50], was applied in all coupling reactions and conversions were again checked by MALDI–MS, gel electrophoresis and Western Blot (Figure 1B,C, lane 4). As evidenced by MS-analysis, we could observe that both proteins Ser-TTL[Aha] (nine azides) and AhaSer-TTL[Aha] (ten azides) reacted with galactose alkyne **2** via CuAAC and different

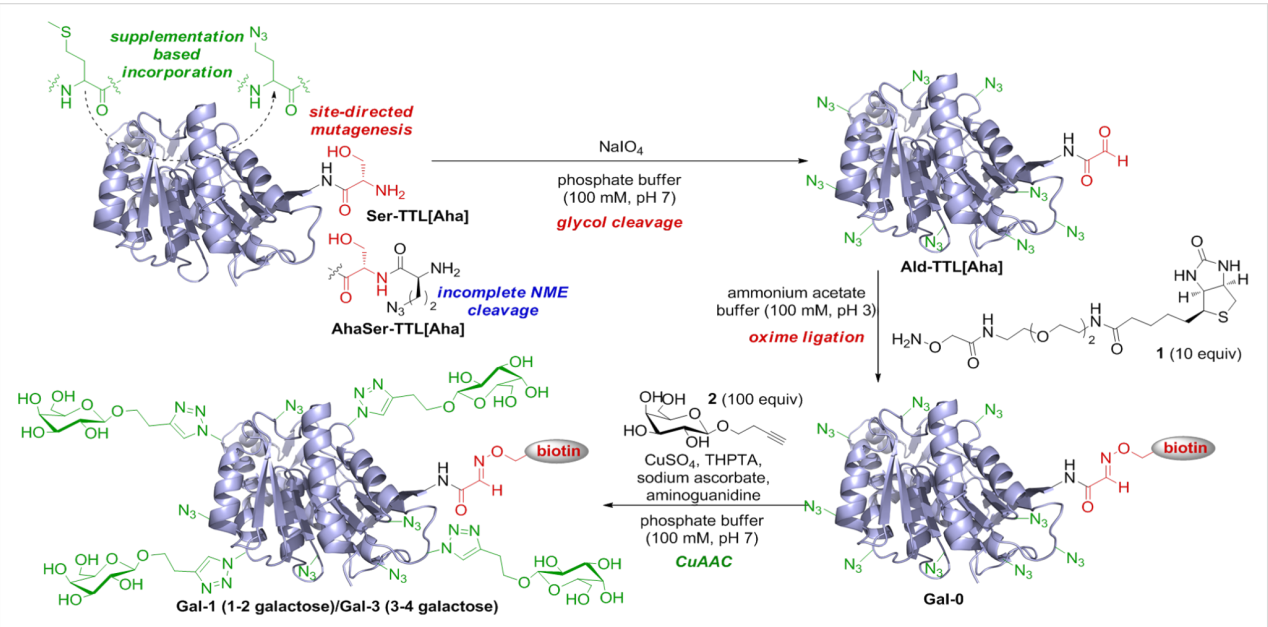

Scheme 1: Protein design and dual-functionalization of TTL: periodate cleavage, oxime ligation and CuAAC.

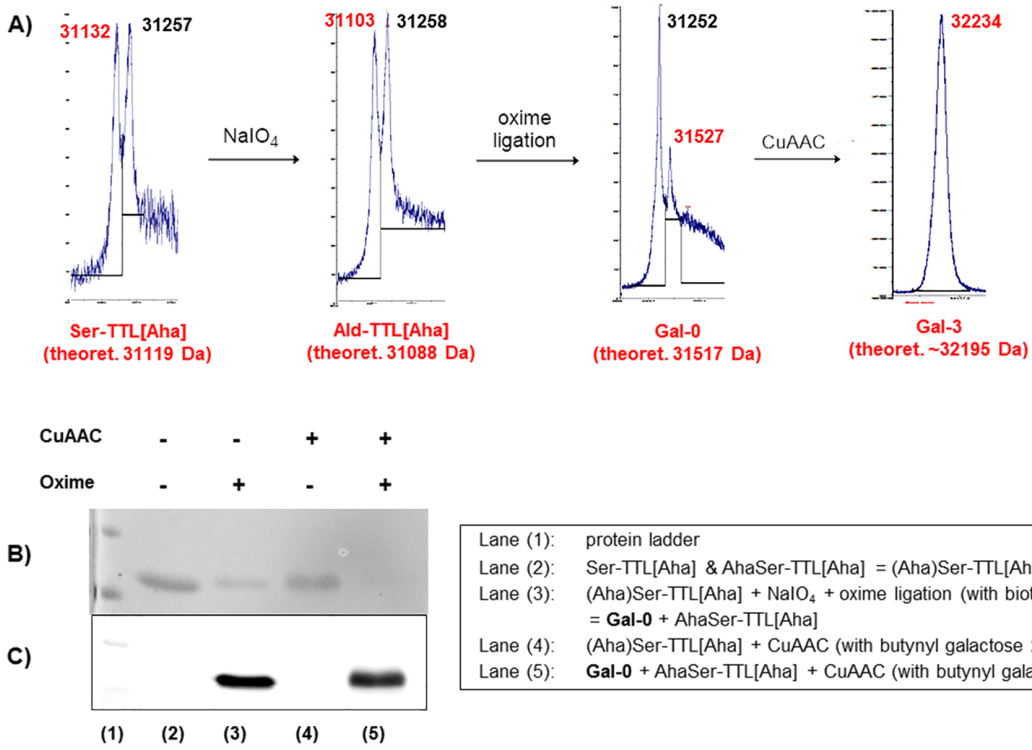

Figure 1: Dual-functionalization of TTL: A) MALDI–MS spectra (red: modified protein (as marked below); black: reference protein AhaSer-TTL[Aha]; *m/z* (calculated): $[M+H]^+$ 31245 Da; for full spectra see Supporting Information File 1) B) SDS PAGE of TTL protein conjugates (Coomassie stain), C) Western Blot (streptavidin-peroxidase antibody).

degrees of glycosylation could be achieved depending of the amount of Cu^{2+} applied in the reaction, though the maximum number of galactose units per protein that could be attached appeared to be five (data not shown). By applying a sequential oxime/CuAAC ligation protocol by applying CuAAC to the biotinylated protein **Gal-0**, we could show successful dual-functionalization of our protein. Again, depending on the Cu^{2+} concentration, different numbers of galactose units per protein could be achieved. Although a protein mixture of two proteins, bearing either nine or ten Aha residues which could potentially react with butynyl galactose **2**, the MALDI spectra of the final protein mixture after CuAAC showed surprisingly sharp peaks with a difference of only 1–2 galactose units, which might indicate that both proteins react to a similar degree with the alkynyl galactose **2** (see Supporting Information File 1). Lower concentrations of $CuSO_4$ led to higher degrees of functionalization with 3–4 (10 mol %, **Gal-3**) galactose units, whereas higher amounts of Cu^{2+} led to lower degrees of functionalization with 1–2 clicked sugars (30 mol %, **Gal-1**). Further evidence for successful glycan attachment was provided by tryptic digest and MS/MS-analysis of **Gal-3**, which showed functionalization of two specific Aha residues (see Table S5 in Supporting Information File 1). It should be noted that higher concentrations of Cu^{2+} also led to precipitation and loss of protein material. Finally, the protein mixture was purified by centrifuge membrane filtration with a 100 mM phosphate buffer (100 mM NaCl, pH 7) to yield approximately 20–35% of the initial protein material (Aha)Ser-TTL[Aha] after dual-functionalization as judged by UV (see Supporting Information File 1).

Stability and lectin binding studies

To ensure the stability of TTL throughout the dual-labeling process, we performed a lipase activity assay to demonstrate that the enzymatic activity could be retained. All protein samples thereby showed similar lipase activity, as determined by the colorimetric *p*-nitrophenol assay (see Supporting Information File 1).

Finally, we also conducted surface plasmon resonance (SPR) studies to show the general applicability of our dual modified protein scaffold for measuring lectin binding constants (Figure 2 and Supporting Information File 1). We first probed the qualitative binding of *Erythrina cristagalli* lectin (ECL) to proteins **Gal-1** and **Gal-3** as well as **Gal-0** as a negative control. The three protein samples were each immobilized on a streptavidin-coated chip. Then, ECL was passed over the chip at

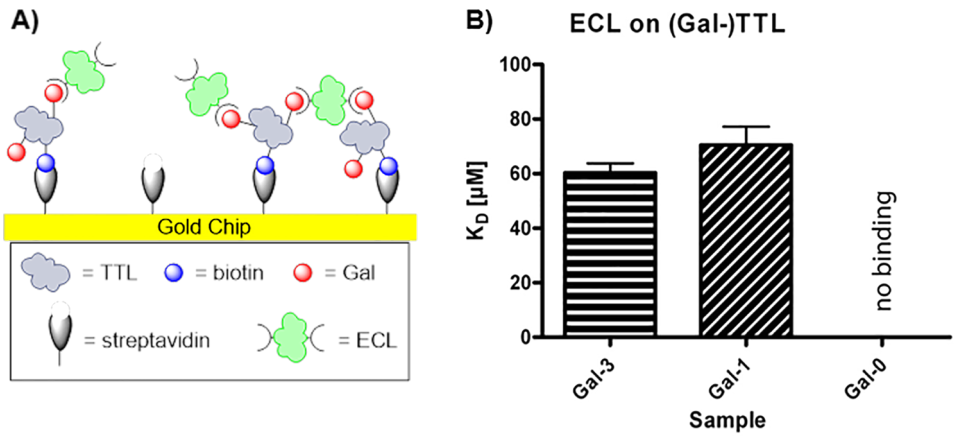

Figure 2: SPR measurements: A) set-up showing different binding events of the double-functionalized TTL to ECL; B) K_D-data obtained for binding of **Gal-0**, **Gal-1** and **Gal-3**.

different concentrations to determine the relative binding affinity for the immobilized glycosyl-TTL coated surface. At a concentration of 10 µM ECL, significant binding of both glycosylated protein samples towards the lectin were obtained (see Supporting Information File 1). The higher valent **Gal-3** revealed enhanced ECL binding, attributed to more frequent rebinding events. Also cross-binding of ECL to adjacent **Gal-3** proteins might occur due to the initial high immobilization level. In contrast, the non-glycosylated lipase exhibited no binding at all. To further characterize the binding efficiency, K_D-values were determined by SPR measurements (for set-up see Supporting Information File 1). Again, for **Gal-0** no binding could be detected. Both glycosylated proteins, **Gal-1** and **Gal-3**, presented very similar and rather low K_D-values (70 and 60 µM, respectively) with a slight tendency for stronger binding for the higher glycosylated protein **Gal-3** (see Supporting Information File 1). However, as the two Gal-binding sites of ECL are localized on opposite sides [51], our rather short butynyl linker might not be able to fully bend around the protein to achieve a multivalent effect [8,52], which might be the reason for the small difference between the two K_D values. In future experiments, different linker lengths should be probed to allow better binding of multiple carbohydrate units of one protein scaffold with multiple binding sites of one lectin molecule.

Conclusion

In conclusion, we succeeded in the incorporation of two unnatural functional groups, namely azides and aldehydes, into a protein by combining a simple supplementation based incorporation and well-known oxidative periodate cleavage. To the best of our knowledge, this is the first successful combination of co-translational NCAA incorporation with post-translational periodate oxidation, which provides a novel tool to obtain a protein with two unnatural functional groups. For the functionalization of these unnatural moieties, we combined CuAAC with oxime ligation for the attachment of two different ligands, galactose and biotin, to the thermostable lipase TTL. The double functionalized TTL scaffold exhibited lectin binding properties while conserving its natural enzymatic activity, thereby demonstrating the principle applicability of this double protein functionalization strategy to the generation of new multivalent binding scaffolds.

Currently, we are further expanding our general dual-labeling strategy to other protein scaffolds as well as NCAAs to provide multiple distinct probes for the generation of individually designed protein binders. An important parameter in the future will be the combination with protein modelling as well as the implementation of different linker lengths between the protein and the binding units, to engineer precise protein models and study a variety of multivalent receptors.

Experimental

General protocol for glycol cleavage and oxime ligation on TTL. A solution of the TTL (12 µM; 100 mM phosphate buffer, 100 mM NaCl, pH 7) was mixed with $NaIO_4$ (3 equiv) and shaken for 1 h at 15 °C. *N*-Acetyl-Met (12 equiv) was added to the mixture and shaken for 1 h at 15 °C. The buffer was exchanged by centrifuge membrane filtration (14000 r/min). For the different buffers and catalysts see Table S1 (Supporting Information File 1). Biotin hydroxylamine **1** was added to the protein solution and the mixture was shaken overnight at 15 °C. For MALDI–MS analysis, the solutions were centrifuge-filtered (14000 r/min) and washed 4× with ammonium acetate solution (100 mM, pH 7) and 4× with ultrapure water. The proteins were analyzed by MALDI–MS measurements (Tables S3 and S4, Supporting Information File 1) and by SDS PAGE (Coomassie stain) and Western Blotting (strepta-

vidin–peroxidase antibody, 1:1000) using a Mini-Protean Tetra cell system (BioRad) (see Figure 1).

For subsequent dual-functionalization, the samples were centrifuge-filtered with Dulbecco's PBS buffer (100 mM, pH 7) after oxime ligation and directly applied in the CuAAC.

General protocol for CuAAC on TTL. A solution of the TTL (10 μM; 100 mM phosphate buffer, 100 mM NaCl, pH 7) was mixed with $CuSO_4$ (1 M in 100 mM phosphate buffer, 100 mM NaCl, pH 7), sodium ascorbate (50 equiv to Cu^{2+}) and 1-*O*-but-3-ynyl-α-galactopyranoside (**2**) (1100 equiv to protein), 80 μL THPTA (5 equiv to Cu^{2+}), and aminoguanidine (8 mM) and shaken overnight at 15 °C. For the different $CuSO_4$ concentrations see Table S2 (Supporting Information File 1). The solutions were centrifuge-filtered (14000 r/min) and washed 3× with buffer/EDTA-solution (100 mM phosphate buffer, 100 mM NaCl, 5 mM EDTA, pH 7) and 4× with ultrapure water. The proteins were analyzed by MALDI–MS measurements (Tables S3 and S4, Supporting Information File 1) and by SDS PAGE (Coomassie stain) and Western blotting (streptavidin–peroxidase antibody, 1:1000) using a Mini-Protean Tetra cell system (BioRad) (see Figure 1). Protein concentrations were checked by UV (λ = 280 nm).

Lipase activity test [53]. Lipase activity was determined by measuring the hydrolysis of *p*-nitrophenyl palmitate (*p*NPP; Sigma). Solution A (10 mM *p*-nitrophenyl palmitate in 10 mL ethanol) and solution B (100 mg gummi arabicum in 90 mL Tris-HCl buffer (50 mM, pH 8)) were mixed 1:9 and dispersed (ultraturrax, 3 min, 20000 min^{-1}) to get solution C. For each measurement, 450 μL of solution C were mixed with 50 μL enzyme solution (0.13 nmol protein). The contribution of autohydrolysis was assessed by including a blank that contained the same volume of 50 mM Tris·HCl pH 8.0 instead of enzyme (background measurement). The samples were shaken at 50 °C for 1 h. Absorbance of released *p*-nitrophenol was measured at λ = 410 nm (Figure S10, Supporting Information File 1).

Surface-plasmon-resonance (SPR). SPR measurements were performed on a BiacoreX (GE Healthcare, Freiburg, Germany). Biotinylated TTL samples were coupled to streptavidin functionalized gold chips (SA-Chips, GE Healthcare, Freiburg, Germany). Before immobilization, the sensor chip was conditioned with three consecutive 1 min injections of 1 M NaCl and 50 mM NaOH.

For initial binding experiments, flow cell 2 (Fc2) of each chip was fully loaded (≈400 RU) with our protein. Flow cell 1 (Fc1) remained untreated and served as a reference. After immobilization, a sample volume of 100 μL of different concentrations of ECL solutions (1 or 10 μM) in HEPES buffered saline with calcium (HBS-Ca), 20 mM HEPES (4-(2-hydroxyethyl)-1-piperazineethanesulfonic acid), pH 7.4, 150 mM NaCl, 1 mM $CaCl_2$ were injected over both lanes at a flow rate of 30 μL/min. The final binding signals were obtained by subtracting the resulting response units (RU) of the free reference lane from the data obtained for the sample lane (Fc2-Fc1, Figure S11, Supporting Information File 1). The association phase was followed by a 180 s dissociation phase. Washing and regenerating of both lanes was done by injecting 4 M $MgCl_2$.

For K_D determination, chips were loaded to one third with the respective TTL and 50 μL ECL were injected in each run with a "wash after injection" step of 180 s for the dissociation phase, recording the response difference between ligand flow cell and reference flow cell. Washing and regeneration was done again by injecting 4 M $MgCl_2$. Kinetic measurements consisted of at least five different concentrations ECL (1, 2, 10, 20 and 100 μL), while one of them was determined twice; additionally one blank was included. For every protein sample (**Gal-1** and **Gal-3**), K_Ds were determined twice. For the TTL without galactose units (**Gal-0**), binding was measured once at the highest possible lectin concentration (100 μM). Data were aligned and after additional subtraction of the blank measurement from each sensorgram (Figures S12–S14, Supporting Information File 1), analyzed on equilibrium binding by nonlinear curve fitting of the Langmuir binding isotherm (Figures S15 and S16, Supporting Information File 1).

Supporting Information

Details on materials, protein design, construction of the expression plasmids, protein expression and purification, mass spectrometry data for the expressed proteins, general methods, synthetic protocols and analytical data (including ^{1}H, ^{13}C and ^{19}F NMR spectra) for compounds **1** and **2**, reaction conditions for the ligation strategies, SDS PAGE and Western Blot lanes are provided as Supporting Information.

Supporting Information File 1

Additional data.
[http://www.beilstein-journals.org/bjoc/content/supplementary/1860-5397-11-88-S1.pdf]

Acknowledgements

The authors acknowledge support from the DFG (SFB 765 and SPP 1623), the BMBF (Biokatalyse 2021), the Fonds der Chemischen Industrie (FCI), the Einstein Foundation, the Boehringer-Ingelheim Foundation (Plus 3 award) and the Studi-

enstiftung des deutschen Volkes. We thank Lukas Artner, Robert Vallée and Chris Weise for experimental contributions and helpful discussions. Nina Bach and Katja Bäuml from the chair of Organic Chemistry II of the TU München are highly acknowledged for conducting ESI–MS measurements. We greatly thank Traudl Wenger for assistance in protein expression and purification.

References

1. Schumacher, D.; Hackenberger, C. P. R. *Curr. Opin. Chem. Biol.* **2014,** *22,* 62–69. doi:10.1016/j.cbpa.2014.09.018
2. Hackenberger, C. P. R.; Schwarzer, D. *Angew. Chem.* **2008,** *120,* 10182–10228. doi:10.1002/ange.200801313
   Angew. Chem., Int. Ed. **2008,** *47,* 10030–10074. doi:10.1002/anie.200801313
3. Sletten, E. M.; Bertozzi, C. R. *Angew. Chem.* **2009,** *123,* 7108–7133. doi:10.1002/ange.200900942
   Angew. Chem., Int. Ed. **2009,** *48,* 6974–6998. doi:10.1002/anie.200900942
4. Takaoka, Y.; Ojida, A.; Hamachi, I. *Angew. Chem.* **2013,** *125,* 4182–4200. doi:10.1002/ange.201207089
   Angew. Chem., Int. Ed. **2013,** *52,* 4088–4106. doi:10.1002/anie.201207089
5. Tong, G. J.; Hsiao, S. C.; Carrico, Z. M.; Francis, M. B. *J. Am. Chem. Soc.* **2009,** *131,* 11174–11178. doi:10.1021/ja903857f
6. Flenniken, M. L.; Willits, D. A.; Harmsen, A. L.; Liepold, L. O.; Harmsen, A. G.; Young, M. J.; Douglas, T. *Chem. Biol.* **2006,** *13,* 161–170. doi:10.1016/j.chembiol.2005.11.007
   See for a review.
7. Udit, A. K.; Hackenberger, C. P. R.; O'Reilly, M. K. *ChemBioChem* **2010,** *11,* 481–484. doi:10.1002/cbic.201000001
8. Fasting, C.; Schalley, C. A.; Weber, M.; Seitz, O.; Hecht, S.; Koksch, B.; Dernedde, J.; Graf, C.; Knapp, E.-W.; Haag, R. *Angew. Chem.* **2012,** *124,* 10622–10650. doi:10.1002/ange.201201114
   Angew. Chem.,Int. Ed. **2012,** *51,* 10472–10498. doi:10.1002/anie.201201114
9. Cecioni, S.; Imberty, A.; Vidal, S. *Chem. Rev.* **2015,** *115,* 525–561. doi:10.1021/cr500303t
10. Kuan, S. L.; Wu, Y.; Weil, T. *Macromol. Rapid Commun.* **2013,** *34,* 380–392. doi:10.1002/marc.201200662
11. Kostiainen, M. A.; Szilvay, G. R.; Lehtinen, J.; Smith, D. K.; Lindner, M. B.; Urtti, A.; Ikkala, O. *ACS Nano* **2007,** *1,* 103–113. doi:10.1021/nn700053y
12. Solomon, D.; Kitov, P. I.; Paszkiewicz, E.; Grant, G. A.; Sadowska, J. M.; Bundle, D. R. *Org. Lett.* **2005,** *7,* 4369–4372. doi:10.1021/ol051529+
13. Hoesl, M. G.; Budisa, N. *Angew. Chem.* **2011,** *123,* 2948–2955. doi:10.1002/ange.201005680
    Angew. Chem., Int. Ed. **2011,** *50,* 2896–2902. doi:10.1002/anie.201005680 See for a recent review.
14. Budisa, N. *Angew. Chem.* **2004,** *116,* 6586–6624. doi:10.1002/ange.200300646
    Angew. Chem., Int. Ed. **2004,** *43,* 6426–6463. doi:10.1002/anie.200300646
15. Minks, C.; Alefelder, S.; Moroder, L.; Huber, R.; Budisa, N. *Tetrahedron* **2000,** *56,* 9431–9442. doi:10.1016/S0040-4020(00)00827-9
16. Budisa, N.; Steipe, B.; Demange, P.; Eckerskorn, C.; Kellermann, J.; Huber, R. *Eur. J. Biochem.* **1995,** *230,* 788–796.
17. Yoshikawa, E.; Fournier, M. J.; Mason, T. L.; Tirrell, D. A. *Macromolecules* **1994,** *27,* 5471–5475. doi:10.1021/ma00097a029
18. Artner, L. M.; Merkel, L.; Bohlke, N.; Beceren-Braun, F.; Weise, C.; Dernedde, J.; Budisa, N.; Hackenberger, C. P. R. *Chem. Commun.* **2012,** *48,* 522–524. doi:10.1039/C1CC16039G
19. Royter, M.; Schmidt, M.; Elend, C.; Höbenreich, H.; Schäfer, T.; Bornscheuer, U. T.; Antranikian, G. *Extremophiles* **2009,** *13,* 769–783. doi:10.1007/s00792-009-0265-z
20. Chalker, J. M.; Bernardes, G. J. L.; Davis, B. G. *Acc. Chem. Res.* **2011,** *44,* 730–741. doi:10.1021/ar200056q
21. Wang, L.; Schultz, P. G. *Angew. Chem.* **2005,** *117,* 34–68. doi:10.1002/ange.200460627
    Angew. Chem., Int. Ed. **2005,** *44,* 34–66. doi:10.1002/anie.200460627
22. Neumann, H.; Wang, K.; Davis, L.; Garcia-Alai, M.; Chin, J. W. *Nature* **2010,** *464,* 441–444. doi:10.1038/nature08817
23. Wan, W.; Huang, Y.; Wang, Z.; Russell, W. K.; Pai, P.-J.; Russell, D. H.; Liu, W. R. *Angew. Chem.* **2010,** *122,* 3279–3282. doi:10.1002/ange.201000465
    Angew. Chem., Int. Ed. **2010,** *49,* 3211–3214. doi:10.1002/anie.201000465
24. Wu, B.; Wang, Z.; Huang, Y.; Liu, W. R. *ChemBioChem* **2012,** *13,* 1405–1408. doi:10.1002/cbic.201200281
25. Nikić, I.; Plass, T.; Schraidt, O.; Szymański, J.; Briggs, J. A. G.; Schultz, C.; Lemke, E. A. *Angew. Chem.* **2014,** *126,* 2278–2282. doi:10.1002/ange.201309847
    Angew. Chem., Int. Ed. **2014,** *53,* 2245–2249. doi:10.1002/anie.201309847
26. Mukai, T.; Hayashi, A.; Iraha, F.; Sato, A.; Ohtake, K.; Yokoyama, S.; Sakamoto, K. *Nucleic Acids Res.* **2010,** *38,* 8188–8195. doi:10.1093/nar/gkq707
27. Johnson, D. B. F.; Xu, J.; Shen, Z.; Takimoto, J. K.; Schultz, M. D.; Schmitz, R. J.; Xiang, Z.; Ecker, J. R.; Briggs, S. P.; Wang, J. *Nat. Chem. Biol.* **2011,** *7,* 779–786. doi:10.1038/nchembio.657
28. Lajoie, M. J.; Rovner, A. J.; Goodman, D. B.; Aerni, H.-R.; Haimovich, A. D.; Kuznetsov, G.; Mercer, J. A.; Wang, H. H.; Carr, P. A.; Mosberg, J. A.; Rohland, N.; Schultz, P. G.; Jacobson, J. M.; Rinehart, J.; Church, G. M.; Isaacs, F. J. *Science* **2013,** *342,* 357–360. doi:10.1126/science.1241459
29. Nehring, S.; Budisa, N.; Wiltschi, B. *PLoS One* **2012,** *7,* e31992. doi:10.1371/journal.pone.0031992
30. van Kasteren, S. I.; Kramer, H. B.; Jensen, H. H.; Campbell, S. J.; Kirkpatrick, J.; Oldham, N. J.; Anthony, D. C.; Davis, B. G. *Nature* **2007,** *446,* 1105–1109. doi:10.1038/nature05757
31. Simon, M.; Zangemeister-Wittke, U.; Plückthun, A. *Bioconjugate Chem.* **2012,** *23,* 279–286. doi:10.1021/bc200591x
32. Brustad, E. M.; Lemke, E. A.; Schultz, P. G.; Deniz, A. A. *J. Am. Chem. Soc.* **2008,** *130,* 17664–17665. doi:10.1021/ja807430h
33. Hughes, A. B. *Amino Acids, Peptides and Proteins in Organic Chemistry;* Wiley-VCH: Weinheim, 2009; Vol. 1, pp 445 ff.
34. Cornish, V. W.; Hahn, K. M.; Schultz, P. G. *J. Am. Chem. Soc.* **1996,** *118,* 8150–8151. doi:10.1021/ja961216x
35. Chen, Y.-X.; Triola, G.; Waldmann, H. *Acc. Chem. Res.* **2011,** *44,* 762–773. doi:10.1021/ar200046h
    See for a recent review on oxime ligation.
36. Dierks, T.; Dickmanns, A.; Preusser-Kunze, A.; Schmidt, B.; Mariappan, M.; von Figura, K.; Ficner, R.; Rudolph, M. G. *Cell* **2005,** *121,* 541–552. doi:10.1016/j.cell.2005.03.001
37. Wu, P.; Shui, W.; Carlson, B. L.; Hu, N.; Rabuka, D.; Lee, J.; Bertozzi, C. R. *Proc. Natl. Acad. Sci. U. S. A.* **2009,** *106,* 3000–3005. doi:10.1073/pnas.0807820106

38. Gilmore, J. M.; Scheck, R. A.; Esser-Kahn, A. P.; Joshi, N. S.; Francis, M. B. *Angew. Chem.* **2006,** *118,* 5433–5437. doi:10.1002/ange.200600368
Angew. Chem., Int. Ed. **2006,** *118,* 5307–5311. doi:10.1002/anie.200600368
39. Geoghegan, K. F.; Stroh, J. G. *Bioconjugate Chem.* **1992,** *3,* 138–146. doi:10.1021/bc00014a008
40. Dixon, H. B. F.; Weitkamp, L. R. *Biochem. J.* **1962,** *84,* 462–468.
41. Kitov, P. I.; Vinals, D. F.; Ng, S.; Tjhung, K. F.; Derda, R. *J. Am. Chem. Soc.* **2014,** *136,* 8149–8152. doi:10.1021/ja5023909
42. Hoesl, M. G.; Acevedo-Rocha, C. G.; Nehring, S.; Royter, M.; Wolschner, C.; Wiltschi, B.; Budisa, N.; Antranikian, G. *ChemCatChem* **2011,** *3,* 213–221. doi:10.1002/cctc.201000253
43. Wiltschi, B.; Merkel, L.; Budisa, N. *ChemBioChem* **2009,** *10,* 217–220. doi:10.1002/cbic.200800605
44. Acevedo-Rocha, C. G.; Hoesl, M. G.; Nehring, S.; Royter, M.; Wolschner, C.; Wiltschi, B.; Antranikian, G.; Budisa, N. *Catal. Sci. Technol.* **2013,** *3,* 1198–1201. doi:10.1039/c3cy20712a
45. Wong, C.-H.; Zimmermann, S. C. *Chem. Commun.* **2013,** *49,* 1679–1695. doi:10.1039/c2cc37316e
46. Clavé, G.; Volland, H.; Flaender, M.; Gasparutto, D.; Romieu, A.; Renard, P.-Y. *Org. Biomol. Chem.* **2010,** *8,* 4329–4345. doi:10.1039/c0ob00133c
47. Zhang, L.; Tam, J. P. *Anal. Biochem.* **1996,** *233,* 87–93. doi:10.1006/abio.1996.0011
48. Merkel, L.; Cheburkin, Y.; Wiltschi, B.; Budisa, N. *ChemBioChem* **2007,** *8,* 2227–2232. doi:10.1002/cbic.200700540
49. Dirksen, A.; Hackeng, T. M.; Dawson, P. E. *Angew. Chem.* **2006,** *118,* 7743–7746. doi:10.1002/ange.200602877
Angew. Chem., Int. Ed. **2006,** *45,* 7581–7584. doi:10.1002/anie.200602877
50. Presolski, S. I.; Hong, V.; Cho, S.-H.; Finn, M. G. *J. Am. Chem. Soc.* **2010,** *132,* 14570–14576. doi:10.1021/ja105743g
51. Turton, K.; Natesh, R.; Thiyagarajan, N.; Chaddock, J. A.; Acharya, K. R. *Glycobiology* **2004,** *14,* 923–929. doi:10.1093/glycob/cwh114
52. Kiessling, L. L.; Gestwicki, J. E.; Strong, L. E. *Angew. Chem.* **2006,** *118,* 2408–2429. doi:10.1002/ange.200502794
Angew. Chem., Int. Ed. **2006,** *45,* 2348–2368. doi:10.1002/anie.200502794
53. Winkler, U. K.; Stuckmann, M. *J. Bacteriol.* **1979,** *138,* 663–670.

License and Terms

BEILSTEIN JOURNAL OF ORGANIC CHEMISTRY

Impact of multivalent charge presentation on peptide–nanoparticle aggregation

Daniel Schöne[1], Boris Schade[2], Christoph Böttcher[2] and Beate Koksch[*1]

Full Research Paper

Open Access

Address:
[1]Institute of Chemistry and Biochemistry - Organic Chemistry, Freie Universität Berlin, Takustr. 3, 14195 Berlin, Germany and [2]Electron Microscopy, Freie Universität Berlin, Fabeckstr. 36a, 14195 Berlin, Germany

Email:
Beate Koksch[*] - beate.koksch@fu-berlin.de

* Corresponding author

Keywords:
coiled-coil peptides; α-helical fibrils; controlled aggregation; gold nanoparticles; multivalency

Beilstein J. Org. Chem. **2015,** *11,* 792–803.
doi:10.3762/bjoc.11.89

Received: 27 February 2015
Accepted: 29 April 2015
Published: 15 May 2015

This article is part of the Thematic Series "Multivalency as a chemical organization and action principle".

Guest Editor: R. Haag

Abstract

Strategies to achieve controlled nanoparticle aggregation have gained much interest, due to the versatility of such systems and their applications in materials science and medicine. In this article we demonstrate that coiled-coil peptide-induced aggregation based on electrostatic interactions is highly sensitive to the length of the peptide as well as the number of presented charges. The quaternary structure of the peptide was found to play an important role in aggregation kinetics. Furthermore, we show that the presence of peptide fibers leads to well-defined nanoparticle assembly on the surface of these macrostructures.

Introduction

In the past few decades metal and semiconductor nanoparticles, including gold nanoparticles, have gained much interest due to their desirable optical, magnetic, and electronic properties [1]. In particular, the distinct colour of gold nanoparticles is a result of the localised surface plasmon resonance (LSPR) band caused by collective electron oscillations. The LSPR induces a certain excitation band at visible wavelengths in the absorption spectrum, the position and width of which is highly dependent upon nanoparticle size. However, nanoparticle aggregation induces a spectral red-shift and broadening of the band in the absorption spectrum which depends on the distance between nanoparticles, the density of the assembly and the size of the particles [2,3]. Thus the controlled assembly of nanoparticles by means of biomolecules is crucial for biological and medical applications such as sensing [4], bioimaging [5], and medical diagnostics [6]. Although nanoparticles are also applied as targeted biomarkers and drug-delivery agents to tumor cells [7], only very little is known about the effects of nanoparticles on whole organisms [8].

Furthermore, there is great interest in using biomolecules as components to build up self-assembled supramolecular organic–inorganic hybrid materials for engineering novel functional materials and molecular devices [9,10]. In spite of the

increasing demand for smaller, more complex, but even cheaper materials, the commonly used "top-down" methods are not available. Thus, new strategies like the "bottom-up" approach have been developed to achieve materials in the nanometer range [11,12]. This technique is based on the self-assembly of small building blocks to construct functional materials by means of biomolecules. Recent studies have made use of DNA, lipids, peptides, and proteins to build up organic–inorganic hybrid materials [9]. Due to their versatile and unique functionalities, which can be used for catalytic [13], optics [14], and switching [15] applications, a variety of specific and site selective binding properties are available [16]. In particular, the specificity of Watson–Crick base pairing of DNA nucleotides can be used for the directed and predictable self-assembly of nanoparticles [17]. The DNA mediated assembly of nanoparticles is realized in two different ways. In the first regime, two sets of nanoparticles are functionalized with complementary single-stranded DNA sequences which then anneal to one another [18]; in an alternative setup, adding a complementary linker to nanoparticles functionalised with single-stranded DNA can drive the assembly to form extended networks [19].

Although the relationship between the primary and quaternary structures of peptides and proteins are less clear than for DNA, protein-based recognition systems containing antigen–antibody [20], biotin–streptavidin [21], and peptide–peptide [22] interactions have been explored. In particular, peptide-based assemblies afford numerous advantages such as the modification of nanostructures by mutations of the primary sequence of peptides which may lead to the formation of various hierarchical morphologies [23-25]. The strategies for the assembly of nanoparticles are very similar to those for DNA. Either one part of the recognition system is directly bound to the surface of the nanoparticle by a disulfide bond and the addition of a linker induces assembly, or both linker and acceptor are immobilised on the surface of different nanoparticles and induce assembly [9]. Peptide-based nanoparticle aggregation was demonstrated first by Woolfson and coworkers by means of coiled-coil peptides that were immobilized on the nanoparticle surface [26].

Reversibility of the assembly formation, a key feature of a switchable system, has thus far been explored only for a few nanoparticle systems by means of temperature [19]; most of the assemblies are irreversibly formed [9], or reversibility is only achieved by adding, for example, oxidizing reagents [27]. Continuous switch behaviour between aggregated and non-aggregated nanoparticles is not obtained as the formation of assemblies is most likely achieved by hydrogen bonds or other common receptor–binding interactions [28]. Although it is known that nanoparticles can be organised by binding to membranes by means of electrostatic interactions between the charged head group of the lipid and the oppositely charged nanoparticle [29], only limited effort has been put forth to use peptides or proteins to organize nanoparticles by electrostatic interactions [30,31]. As the overall net charge of a peptide is pH dependent, this can be a powerful tool for the controlled and reversible assembly of nanoparticles.

Recently we published the use of coiled-coil model peptide VW05 for the reversible assembly of mercaptoundecanoic acid functionalized gold nanoparticles using electrostatic interactions [32,33]. We showed that the interaction can be repeatedly switched by adjusting the pH value. We further demonstrated that the ability of the peptide to interact with nanoparticles is directly related to its helical structure and the resulting local charge at the solvent-exposed face of the coiled-coil: a control peptide with the same amino acid composition, which did not follow the regular heptad repeat, was not able to organize nanoparticles in networks. Thus, the electrostatic interaction is not only determined by the overall net charge of the peptide but requires defined spatial ordering and regularity.

Here we report the use of modified peptide variants of the previously studied VW05 for the controlled assembly of gold nanoparticles. As the assembly of charged gold nanoparticles depends on the local charge of the coiled-coil in a multivalent fashion, we wanted to study different aspects of nanoparticle–peptide interactions such as the aggregation tendency of the peptide and the morphology of the obtained peptide–nanoparticle assemblies.

Results

Design of the model peptides

The α-helical coiled-coil folding motif combines the chemical diversity of peptides with the molecular recognition properties and structural stability of DNA, and provides a valuable and variable system for the organisation of functionalized nanoparticles [34-36].

The coiled-coil folding motif consists of two to seven α-helices that are wrapped around each other to form a left-handed supercoil. The primary sequence consists of a regular pattern of seven amino acids denoted with a, b, c, d, e, f, and g, which is referred to as the heptad repeat. Positions a and d are commonly occupied by nonpolar amino acids such as leucine or valine to form the hydrophobic core which represents one recognition domain. Amino acids in e and g positions, which flank the hydrophobic core, are often charged and form a second recognition domain due to complementary interhelical electrostatic interactions between the helices. Both recognition domains drive the formation of the coiled-coil, thus they are responsible

for the thermodynamic stability of this quaternary structure. Positions b, c, and f, on the other hand, are solvent-exposed and exert only a minor influence on the coiled-coil structure and stability. They are mainly occupied by hydrophilic amino acids and therefore play an important role in interactions with other molecules in the surrounding environment.

In a previous study we showed that the coiled-coil model peptide VW05 induces controlled aggregation of charged gold nanoparticles. The overall primary sequence of VW05 was designed to provide a pH-responsive aggregation of nanoparticles based on electrostatic interactions. Accordingly, a scrambled version of VW05 with the same amino acid composition and net charge did not show any evidence for electrostatic interactions with the nanoparticles and did not trigger nanoparticle aggregation. Thus, it was concluded that the observed nanoparticle–peptide aggregate formation results from the well-defined presentation of four arginine residues in f-positions of the coiled-coil motif [32].

In the current study we investigate in detail the effect of the number of presented charges on the aggregation of VW05-based peptides with gold nanoparticles. Therefore, the modified variants R1A3 and R2A2 of the parent peptide, as well as the extended versions R2A3, R2A4, and R2A5, were synthesized and characterized. In the first two cases either three or two arginine residues were substituted with alanine, respectively; alanine is not only neutral, but is also known for its high α-helix propensity. Due to the need of an overall positive net charge of R1A3 and R2A2 to form electrostatic interactions with the nanoparticles, pH 9 is suitable for this study as the calculated overall net charge is positive at this pH value. Taking into account that the assembly of gold nanoparticles may also depend on the length of the peptide and/or on the ratio of presented charges per residue, peptides of greater length are also included in this study by adding one, two, or three heptad repeats containing alanine in their f-positions (R2A3, R2A4 and R2A5); these were based on the sequence of R2A2 (Figure 1).

Secondary and quaternary structure of the model peptides

Circular dichroism (CD) spectroscopy and analytical ultracentrifugation of VW05 at pH 9 reveals an α-helical coiled-coil structure that consists of three monomers. Since the modifica-

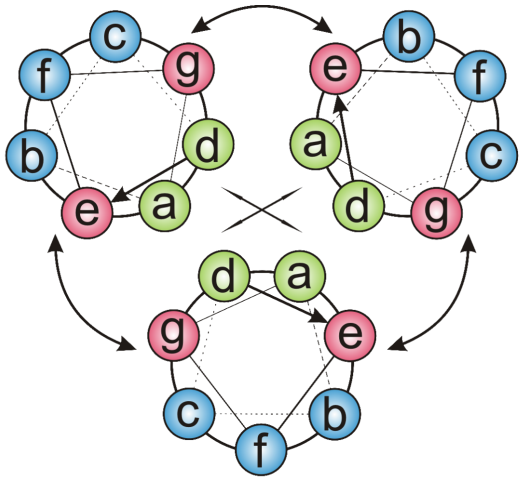

a b c d e f g

VW05:
H_2N-Abz-LE**R**KLKELE**R**KLKELE**R**KLKELE**R**KL-COOH
R1A3:
H_2N-Abz-LE**A**KLKELE**R**KLKELE**A**KLKELE**A**KL-COOH
R2A2:
H_2N-Abz-LE**A**KLKELE**R**KLKELE**A**KLKELE**R**KL-COOH
R2A3:
H_2N-Abz-LE**A**KLKELE**R**KLKELE**A**KLKELE**R**KLKELE**A**KL-COOH
R2A4:
H_2N-Abz-LE**A**KLKELE**A**KLKELE**R**KLKELE**A**KLKELE**R**KLKELE**A**KL-COOH
R2A5:
H_2N-Abz-LE**A**KLKELE**A**KLKELE**A**KLKELE**R**KLKELE**A**KLKELE**R**KLKELE-**A**KL-COOH

Figure 1: Helical wheel representation and sequences of the peptides used in this study.

tions of the parent sequence occurred in the solvent-exposed f position only, we expected no differences in the secondary or quaternary structures of peptides R1A3, R2A2, R2A3, R2A4 and R2A5. CD measurements were carried out at pH 9 and pH 11 at a final peptide concentration of 30 µM (Figure 2A/B). The spectra confirmed that all peptides fold into α-helices as indicated by the two characteristic minima at 208 nm and 222 nm and the maximum at 195 nm. Whereas there are no significant differences in the CD spectra at pH 9 of R2A2, R2A3, R2A4, and R2A5, the signal intensity of R1A3 is dramatically decreased. Furthermore, the minimum at 222 nm is increased and this may point to the formation of assemblies containing α-helical fibrils. This is probably a consequence of the formation of peptide fiber bundles which tend to precipitate and thus decrease the concentration. In addition, the fiber bundles may decrease the amount of peptide that is available to generate the CD signal. Increasing the peptide concentration up to 100 µM or incubating samples for periods up to three days do not result in any changes in the CD spectra, indicating that there is no concentration-dependent change in the secondary structure of the peptides. At pH 11 the CD spectra of all peptides are virtually identical and indicate the presence of α-helical coiled-coil structures.

Dynamic light scattering (DLS) was applied to study the oligomerization state of the peptide variants, as analytical ultracentrifugation can not be used for further characterization of peptide fibers due to extreme sample heterogeneity. Since the oligomerization state of VW05 has been studied before [30], the DLS spectrum of VW05 was used as a reference for all other peptides. All measurements were performed at a sample concentration of 15 µM at pH 9 and pH 11 because the net charge of the peptides switches from positive to negative within this pH range. The trimeric coiled-coil VW05 has an average hydrodynamic diameter of approximately 3 nm (Figure 2C). As expected from CD spectroscopy, R1A3 forms α-helical assemblies at pH 9 with an average size of approximately 1 µm but appears to adopt a soluble coiled-coil structure at pH 11 because the particle size decreases to 3 nm. Surprisingly, all other VW05 variants form α-helical assemblies at pH 9 with average sizes of 790 nm (R2A2), 230 nm (R2A3), 180 nm (R2A4), and 160 nm (R2A5). It seems that with increasing sequence length the size of the peptide fibers decreases. This observation is in agreement with a report of Ryadnov and coworkers [37]. Moreover, a second, larger species appears with a size of 1 µm. The occurrence of two fiber species may be the result of competing interactions between arginine residues in f-position and gluta-

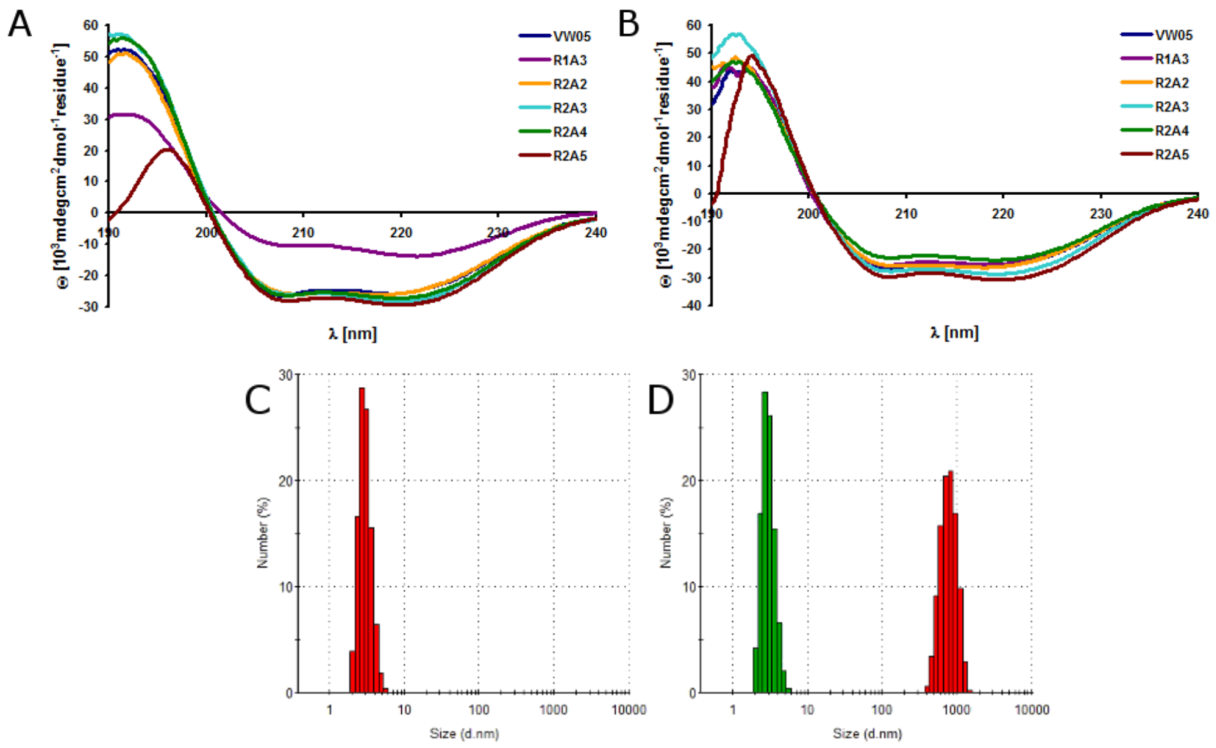

Figure 2: CD spectra of 30 µM peptide VW05, R1A3, R2A2, R2A3, R2A4 and R2A5 at (A) pH 9 and (B) pH 11 in 10 mM Tris/HCl buffer. Dynamic light scattering of (C) VW05 and (D) R2A2 both at 15 µM at (red) pH 9 and (green) pH 11. All measurements were carried out in 10 mM Tris/HCl buffer.

mates. This can either stabilize or diminish peptide aggregation. Increasing the pH to 11 leads to a disruption of α-helical peptide fibers that produces coiled-coil monomers. This effect was observed in all cases (Figure 2D).

To resolve the morphology of the quaternary structures, TEM and/or Cryo TEM were applied to all peptides at pH 9 except for VW05; a representative image for R2A2 is shown in Figure 3. Negative staining TEM of 100 µM R2A2 at pH 9 demonstrates the formation of α-helical fibers. Moreover, these fibers appear to form bundles that consist of many long and parallel single fibers; single peptide fibers alone have not been detected. The formed fiber bundles appear to be very rigid in their structure as they appear only as straight and long fibers with a length ranging from several 100 nm up to more than 1 µm. The average diameter of one single fiber is 2.5–3 nm. One single helix has a diameter of 0.5–1 nm, thus one fiber presumably consists of multiple coiled-coil trimers. On the other hand, even single peptide fibers were observed using Cryo TEM; however, they seem to be much shorter in length. However, resolving the microstructure of one fiber bundle using Cryo TEM was not possible. Surprisingly, fiber bundles could not be observed for peptides R2A4 and R2A5 whose sequences were extended by either two or three heptad repeats. It must be concluded that sample drying and the addition of a staining reagent has an effect on the final fiber structure.

Peptide-induced nanoparticle assembly

The absorption maximum of the LSPR band is a size-dependent property of a gold nanoparticle: the greater the size of the gold nanoparticle, the more red-shifted its absorption maximum. When numerous smaller gold nanoparticles get into close proximity due to aggregation they behave as one larger gold nanoparticle the electronic properties of which can be monitored by the red-shift and broadening of the absorption maximum of the LSPR band. UV–vis absorption spectroscopy was applied to monitor the LSPR band of mercaptoundecanoic acid-functionalized gold nanoparticles (Au/MUA) in the presence of the VW05 variants. Peptides at concentrations ranging from 5 to 30 µM, at pH 9, were added to a nanoparticle solution and UV–vis absorption measurements were carried out. To determine the time-dependence of the assembly process, all measurements were repeated at a three hour time point and a three day time point.

The nanoparticles used in this project were synthesised according to the literature and subsequently refunctionalized in a ligand exchange reaction with mercaptoundecanoic acid [38,39]. The obtained Au/MUA nanoparticles have an average diameter of 5.5 nm, as determined by TEM, and are monodisperse, as confirmed by DLS. An absorption maximum of 525 nm is observed for the Au/MUA nanoparticles in the absence of peptide, even over an incubation time of three days. After addition of the peptide R1A3, only a negligible red-shift of 0.5 nm of the absorption maximum is detected (Figure 4E). Neither an extended incubation time of three days nor an increase in the concentration of the applied peptide to 30 µM leads to a significant increase in the red-shift. This result sharply contrasts with that of the VW05 parent peptide, indicating that the absence of a red-shift and thus a lack of nanoparticle aggregation is very likely a consequence of the reduced number of presented arginine residues in the f-positions of R1A3 compared to VW05. Thus this observation implies that either R1A3 does not interact with Au/MUA nanoparticles or that its interactions are not strong enough to bring the nanoparticles into close proximity to induce a red-shift. Probably the

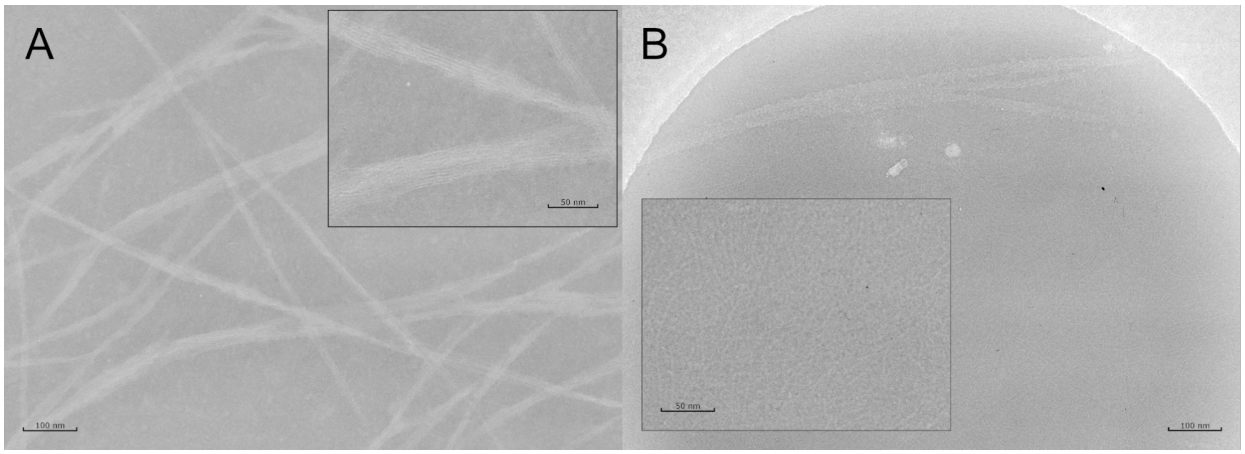

Figure 3: (A) TEM of 100 µM R2A2 in 10 mM Tris/HCl buffer, pH 9. Sample was negative stained with 2% PTA; defocus −0.5 µm. (B) Cryo TEM of 100 µm R2A2 in 10 mM Tris/HCl buffer, pH 9; defocus −1.8 µm.

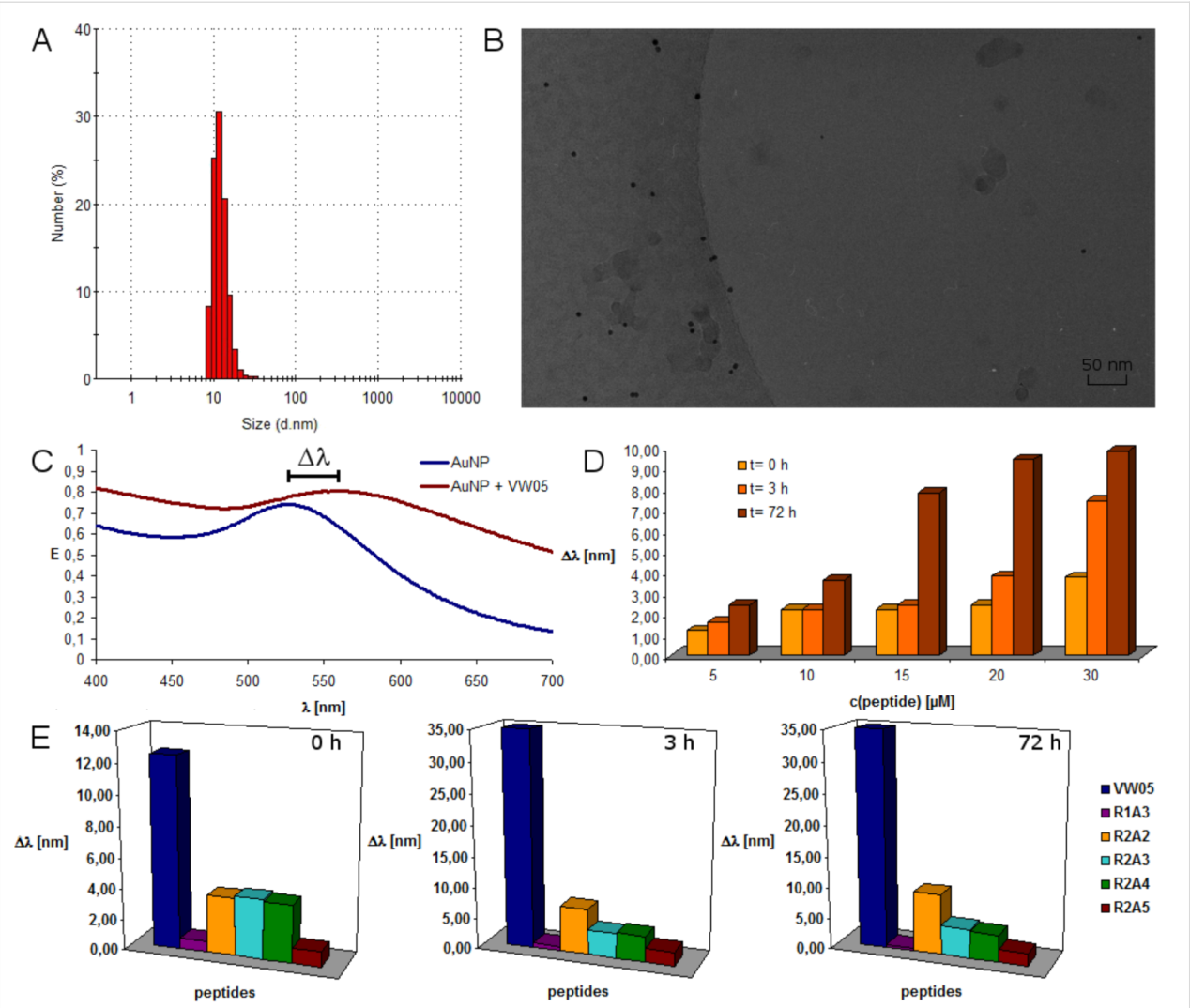

Figure 4: (A) Dynamic light scattering of 0.05 μM Au/MUA nanoparticles at pH 9. (B) Cryo TEM image of 0.05 μM Au/MUA nanoparticles at pH 9. (C) UV–vis spectra of 0.05 μM Au/MUA nanoparticles at pH 9 and in the presence of 30 μM VW05. (D) Time and concentration dependent shift in the absorption maximum of 0.05 μM Au/MUA nanoparticles in the presence of different amounts of R2A2. (E) Time-dependent shift in the absorption maximum at a fixed peptide concentration of 30 μM.

distance between two arginine residues is insufficient for an interaction, which was later on proven by the lack of changes in the secondary structure of peptide R1A3. Accordingly, an increase in the number of arginine residues at f-positions to two in case of R2A2 leads to a significant shift of the LSPR band of 1.20 to 3.75 nm (Figure 4D). As shown in Figure 4D, these red-shifts increase with the peptide concentration as well as with the incubation time; for example, at a concentration of 30 μM of R2A2 the absorption maximum changes by 3.75 nm to 9.80 nm over three days. Although the observed red-shift is minor compared to the parent peptide VW05 at an equal peptide concentration, it can be assumed that incubation with R2A2 leads to an aggregation of Au/MUA nanoparticles. A stepwise increase in the sequence length by adding one heptad repeat without changing the amount of arginine residues (R2A3) leads to a comparable effect (Figure 4E). In contrast, increasing the incubation time to three days does not change the red-shift significantly (Figure 4E); for example, the measured red-shift is 3.75 nm after adding the peptide and 4.70 nm after three days. Adding yet another heptad repeat to the sequence to yield R2A4 affects nanoparticle assembly only marginally, since there is no significant change in the LSPR band compared to R2A3. Even after an incubation time of three days the difference in the red-shift is less than 0.5 nm. Nevertheless, a peptide-induced assembly can be discussed for both peptides. On the other hand, a further increase in the peptide length (R2A5) has a significant effect on the observed LSPR band and thus on nanoparticle aggregation. The determined red-shift of 1 nm is very similar to the observed shift of 0.5 nm for R1A3 measured immediately after adding the peptide. With increasing incuba-

tion time the absorption maximum is slightly shifted but even after three days the value is only half of those measured for R2A3 and R2A4.

It is known that gold nanoparticles may affect the secondary structure of a peptide or protein [33]. To investigate the effect of Au/MUA nanoparticles on the secondary structure of the peptides included in this study, CD spectroscopy was applied with a peptide concentration of 15 µM and 0.05 µM Au/MUA nanoparticle concentration. The obtained CD spectra of VW05 show a strong decrease in signal intensity immediately after the addition of Au/MUA nanoparticles (Figure 5A). This can be explained by the almost complete immobilization of the peptide on the nanoparticle surface in multiple layers. Thus, the concentration of dissolved peptide is dramatically decreased and a CD signal can not be detected anymore. A similar effect could be described by Calzolai and coworkers using silver nanoparticles [40]. Furthermore, the minimum at 222 nm increases compared to the minimum at 208 nm which can be attributed to the formation of α-helical fibers. Extending the incubation time to three hours leads to an almost complete loss in the signal intensity of peptide VW05. Peptides R2A2, R2A3, and R2A4 show a somewhat similar effect after incubation with Au/MUA nanoparticles. A decrease in signal intensity as well as an increase in the minimum at 222 nm is observed, although the loss of intensity is not as strong as that observed for VW05. This observation can be attributed to the accumulation of VW05 on the surface of the nanoparticles, whereas the variants form fibrils and do not accumulate in the same way. However, the CD spectra remain stable and no further decrease in the signal intensity is observed during a longer incubation time. CD measurements of R1A3, which induced no red-shift of Au/MUA nanoparticles, reveal no significant structural changes due to nanoparticle addition.

Agarose gel electrophoresis was used to evaluate whether a peptide–nanoparticle interaction takes place. Au/MUA nanoparticles show a band of relatively high electrophoretic mobility at pH 9, and the addition of only 5 µM VW05 leads to a complete loss in mobility of Au/MUA nanoparticles (Figure 6). On the other hand, the mobility of the Au/MUA nanoparticle band only slightly decreases when R1A3 is present; even a very high concentration of peptide R1A3 (200 µm) does not change this finding. All other peptides cause a stepwise decrease in Au/MUA nanoparticle mobility in a concentration-dependent manner. A peptide concentration of 100 µM is necessary to completely abolish electrophoretic mobility. To monitor the position of the peptide band next to Au/MUA nanoparticles and the presence of unbound peptide, the agarose gel was visualised by UV light at a wavelength of 254 nm. While an electrophoretic mobility of VW05 could be detected only for a high peptide concentration of 100 µM, the peptide band of R1A3 did not show any mobility. This effect could be explained by the formation of α-helical fibrils (vide infra) that are not able to enter the pores of the gel. The absence of a peptide band at 5 µM R1A3 is presumably due to the limited sensitivity of this technique. In contrast, R2A2 and all analogues with extended peptide length (see Supporting Information File 1) show a well-defined peptide band at a concentration of 10 µM with intensities increasing with peptide concentration.

Isothermal titration calorimetry (ITC) was used to determine the thermodynamic parameters as well as the binding constant for the assembly of Au/MUA nanoparticles (Table 1). By fitting with a one set of binding site mode the binding stoichiometry N, the binding constant K_B, and the enthalpy ΔH can be directly obtained from the measured data whereas the entropy ΔS is calculated.

Due to very weak or absent interactions of R1A3 or R2A5 with Au/MUA nanoparticles it was not possible to determine thermodynamic parameters. Surprisingly, the obtained binding constants are not in accordance with the observations made based on the UV–vis measurements. The shift in the absorption maximum obtained from UV–vis measurements for R2A2 is much smaller than that of VW05, but its binding constant of

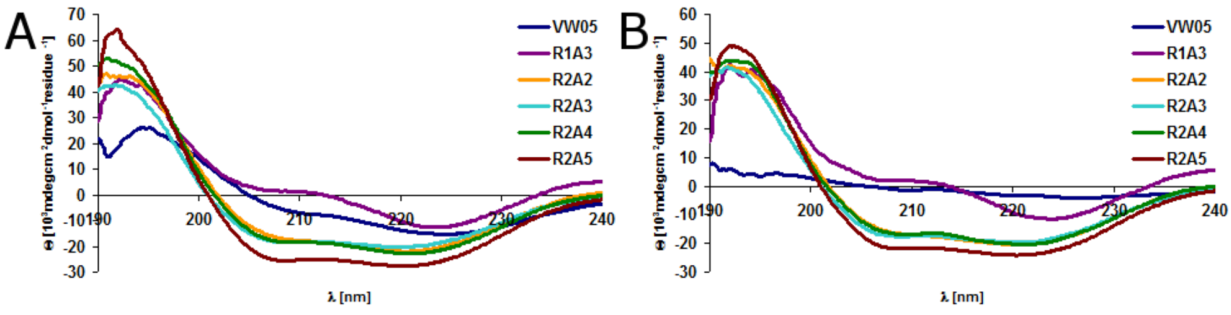

Figure 5: CD spectra of 15 µM peptide in the presence 0.05 µM Au/MUA nanoparticles at pH 9 after (A) 0 hours and (B) three hours.

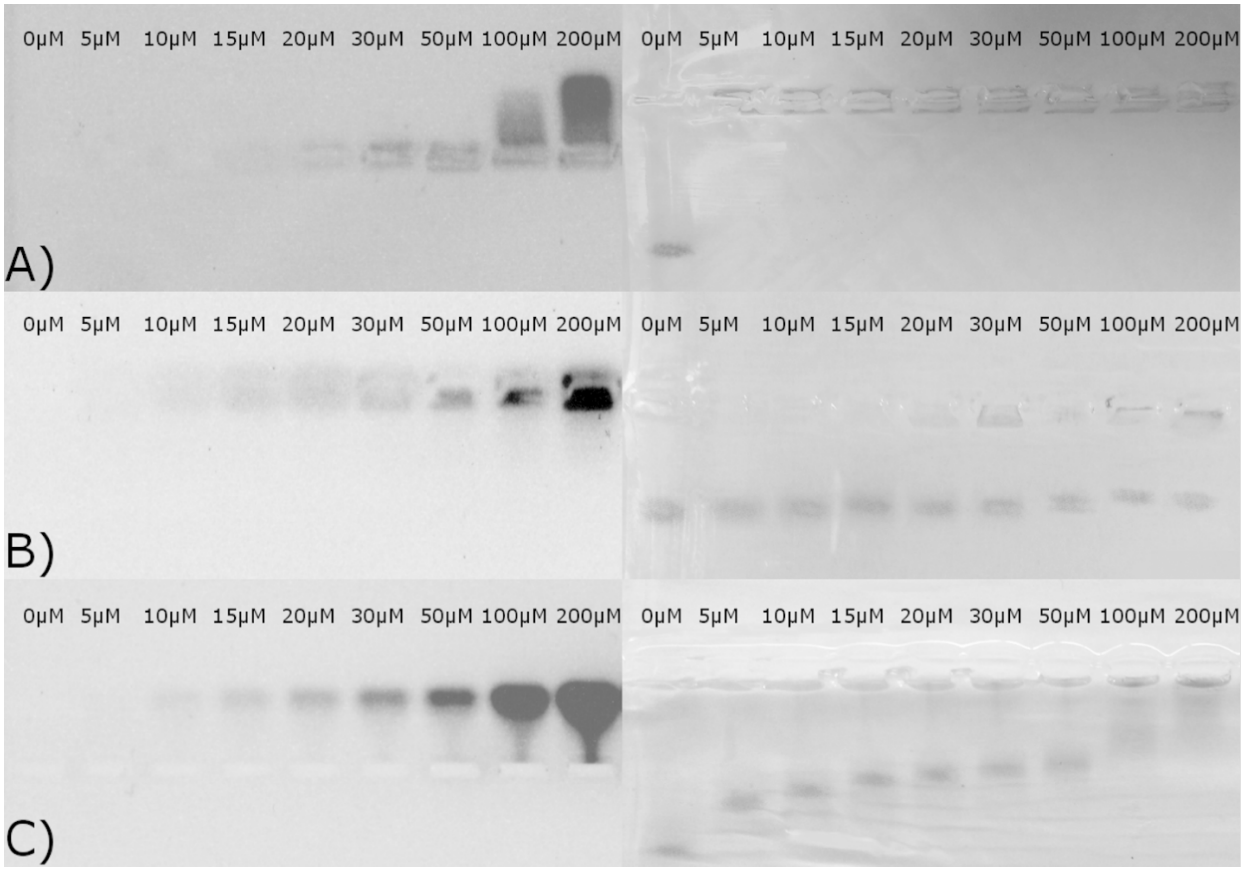

Figure 6: Agarose gel of (A) VW05, (B) R1A3, and (C) R2A2 in the presence of 0.05 μM Au/MUA nanoparticles at pH 9 visualised by UV light (left) and visible light (right).

Table 1: Thermodynamic parameters for the aggregation of Au/MUA nanoparticles with peptides VW05, R2A2, R2A3, and R2A4 obtained by ITC.

	N	K_B [10^5 M^{-1}]	ΔH [kcal mol^{-1}]	ΔS [cal deg mol^{-1}]
VW05	20.2 ± 1.6	5.3 ± 1.7	3.5 ± 0.4	38
R2A2	17.9 ± 0.4	18.2 ± 5.9	−7.3 ± 0.2	5.8
R2A3	18.8 ± 1.4	6.3 ± 1.8	−4.9 ± 0.5	9.7
R2A4	17.3 ± 1.8	2.5 ± 0.8	−3.9 ± 0.5	11.5

$18.2 \cdot 10^5$ M^{-1} is about 3.5-fold higher than that of VW05, although the amount of presented charges is reduced in R2A2. The stepwise increase in peptide length induced a dramatic decrease of the K_B value. However, the K_B of R2A3 is slightly higher compared to VW05. Only a further increase in peptide length lead to a significant decrease in the binding constant compared to VW05. Although gel electrophoresis revealed a remarkable difference in the binding stoichiometry of VW05 versus R2A2 and its longer analogues, the binding stoichiometry is similar in all cases. The greatest N value is observed for the parent peptide VW05. Furthermore, major differences were observed with regard to the molar binding energy ΔH. First of all a positive molar binding energy for VW05 was determined while this was found to be negative for R2A2, R2A3, and R2A4. This can be explained by the different quaternary structure of peptides R2A2, R2A3, and R2A4 compared to VW05. The latter forms coiled-coil trimers that are refolded into α-helical fibers in the presence of Au/MUA nanoparticles, whereas R2A2 and its analogues are already present as fibers before interacting with nanoparticles, which results in a negative molar binding energy. The molar binding energy of these peptides can be directly correlated with their binding constants, as, for example, R2A2 shows the highest binding affinity, produces the greatest release of energy and has the smallest binding energy. With increasing peptide length, the binding affinity decreases, as does the release of energy, which is indi-

cated by the increase in molar binding energy. Nevertheless, all peptide–nanoparticle interactions are entropically favored processes as entropy increases with along with binding energy.

Morphological studies of peptide-induced nanoparticle assemblies

Cryo TEM was used to gain insight into the morphology of the peptide–nanoparticle aggregates. The concentration of peptide in all samples was 100 µM. It was already known that VW05 induces the aggregation of Au/MUA nanoparticles in a very disordered fashion. In the case of the modified analogues of VW05, the Au/MUA nanoparticles assemble in a completely different way. As can be seen in Figure 7A the nanoparticles are almost exclusively organized at the surface of the peptide fiber bundles. A similar effect was reported by Cherny and coworkers [41]. Since the nanoparticle concentration was 0.05 µM, an excess of peptide was present in solution. Thus it was expected that Au/MUA nanoparticles would be equally distributed on the surface of the peptide fibers. However, the nanoparticles were found to accumulate on the surface of larger fiber bundles, whereas some fiber bundles and especially single-peptide fibers remain unbound (Figure 7b). Upon increasing the nanoparticle concentration to 0.4 µM, unbound peptide could not be detected anymore whereas single and unbound nanoparticles are observed (Figure 7c). The obtained assemblies show a highly ordered adsorption of nanoparticles on the surface of the fiber in a three dimensional manner, which was supported by stereo Cryo TEM. Nevertheless, the decoration of peptides fibers with gold nanoparticles could only be observed for peptides that form fiber bundles. Peptides R2A4 and R2A5, which did not show bundle formation, led to a unordered nanoparticle aggregation comparable to those of VW05. Obviously, the single peptide fibers are more flexible and can surround the nanoparticles.

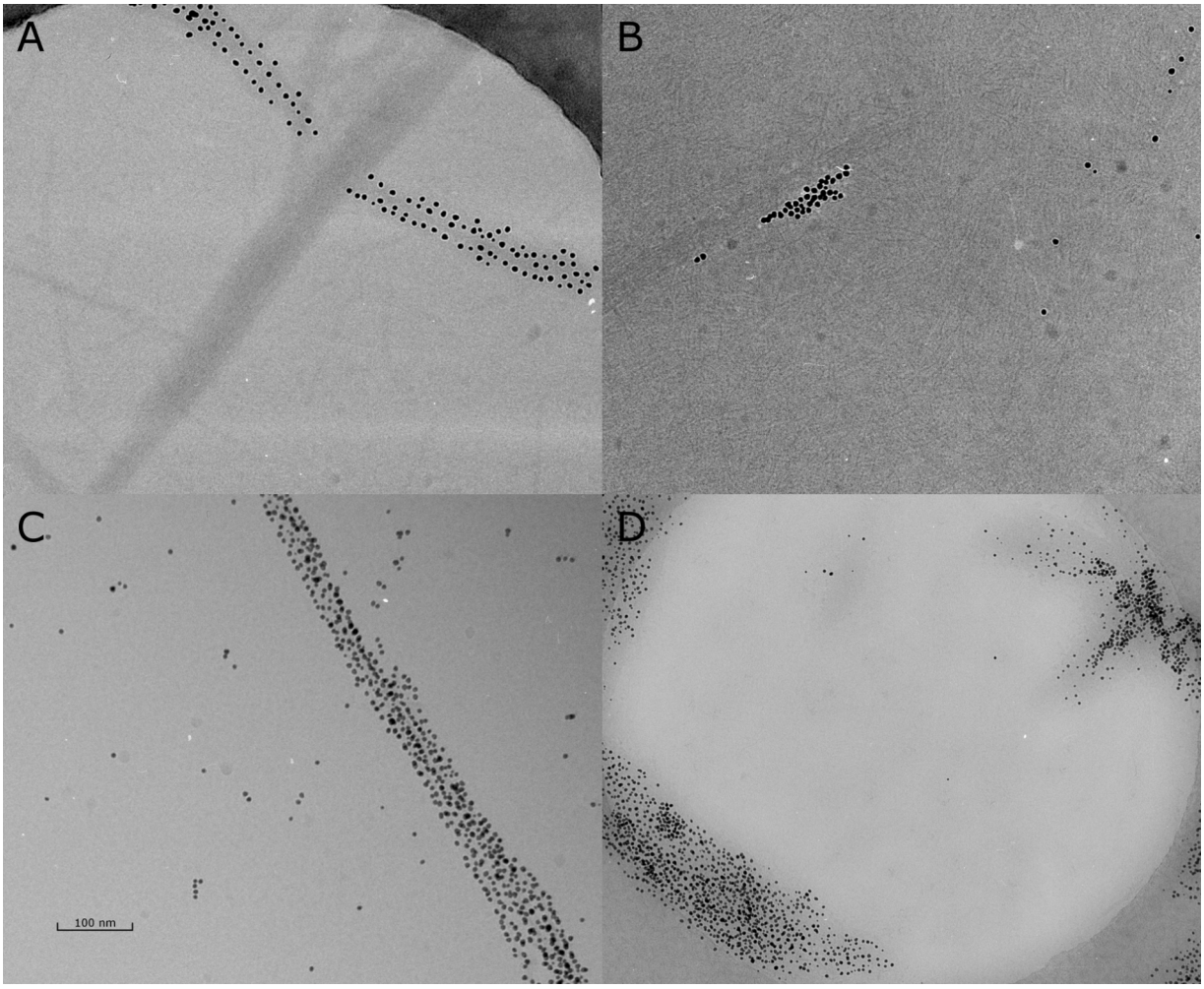

Figure 7: Cryo TEM images of 100 µM R2A2 and 0.05 µM Au/MUA nanoparticles at pH 9 at a defocus of (A) −1.2 µm, (B) −1.8 µm and (D) after pH switch from 11 to 9 at a defocus of −1.8 µm. (C) Cryo TEM images of 100 µM R2A2 and 0.4 µM Au/MUA nanoparticles at pH 9 at a defocus of −1.8 µM.

To evaluate whether the observed morphology is a result of the presence of peptide fibers even before the addition of nanoparticle, the pH of the peptide nanoparticle mixture was increased to pH 11 (Figure 7d). As previously reported for VW05 the change in pH results in disruption of the fibers and coiled-coil peptides are formed again. A subsequent decrease of the pH to 9 led to a dramatic change in the morphology of the peptide–nanoparticle assemblies. Whereas long and relatively thin nanoparticle-decorated fibers were observed prior to the change in pH, shorter and significantly brighter assemblies were obtained afterwards. However, even these assemblies do not exhibit the high level of organisation of nanoparticles on the fiber surface that had been previously observed. Moreover, a fully disordered nanoparticle accumulation was detected. These aggregates may be formed due to coiled-coil structures of the peptides since they appear to be very similar to those observed for VW05.

Discussion

We have studied the effect of peptide length and net charge of coiled-coil-based sequences on their interaction with Au/MUA nanoparticles. Five analogues of the previously reported peptide VW05 were generated (Table 2) to study peptide-induced nanoparticle aggregation caused by electrostatic interactions. Due to the different number of presented arginine residues and length of the peptides the aggregation tendency and morphology of nanoparticles was modified. Peptide R1A3 presents one arginine residue in an f-position per 26-mer and was not efficient in interacting with nanoparticles. Peptides R2A2, R2A3, R2A4 and R2A5 efficiently interact with nanoparticles, although increasing the peptide length leads to a decrease in peptide–nanoparticle interactions as observed in lower binding affinities and reduced red-shifts of the absorption maximum. Obviously, a ratio of peptide length to presented charges not higher than 23.5 is required for specific interactions between coiled-coil peptides and nanoparticles.

Furthermore, the quaternary structure of the initial peptide plays an important role in nanoparticle assembly and the final morphology of nanoparticle–peptide aggregates. Whereas coiled-coil-forming peptides cause a more disordered nanoparticle assembly, fiber-forming peptides induce a well defined accumulation of the nanoparticles on their surface. Surprisingly, nanoparticles aggregate on the surface of larger fiber bundles but do not do so on single fibers. This may be the case because the amount of arginine residues in a single peptide fiber is insufficient to interact with nanoparticles. In addition, peptide fiber bundles were observed that do not have any nanoparticles attached to their surface. Apparently there is an unequal assembly of nanoparticles on the surface of the peptides.

The presence of preassembled peptide fibers has important consequences for the binding stoichiometry, the binding constant, and the molar binding energy of peptide–nanoparticle aggregation. Gel electrophoresis reveals a significant population of unbound peptide for R2A2, R2A3, and R2A4 at a peptide concentration of 10 μM, whereas a concentration of 100 μM of VW05 is required to observe unbound peptide. Nevertheless, peptide VW05 and its analogues have almost the same binding stoichiometry determined by ITC. This can be explained by considering the following points. Due to the fibril formation of R2A2, R2A3, and R2A4 Au/MUA nanoparticles interact with distinct positions on the surface of the peptide fiber. Cryo TEM images reveal, that an excess of peptide remains unbound in solution. In contrast, a coiled-coil peptide directly covers the nanoparticle surface and causes the assembly of two or more nanoparticles. Moreover the nanoparticles are covered with multiple peptide layers which is an ongoing process. In addition, the high local peptide concentration leads to α-helical fibril formation. As gel electrophoresis was carried out after an incubation time of 30 min, an excess of peptide could either bind to the nanoparticle surface or form fibrils. Thus, a higher binding stoichiometry is obtained by gel electrophoresis.

The differences in the quaternary structures of the peptides also lead to an unexpected observation in the binding constant data. Due to the greater number of arginine residues in VW05 it was expected that VW05 would have the highest binding constant. In fact the binding constant is 3.5-fold smaller compared to R2A2 and even the binding constant of R2A3 is slightly higher. Therefore it can be assumed that the fiber formation increases

Table 2: List of amino acid to arginine ratios for the sequences investigated here.

	amino acid residues	arginine residues	amino acids/arginine ratio
VW05	26	4	6.5
R1A3	26	1	26
R2A2	26	2	13
R2A3	33	2	16.5
R2A4	40	2	20
R2A5	47	2	23.5

the binding constant significantly (Table 1). Compared to coiled-coil oligomers the α-helical peptide fiber has a highly ordered structure and the charge density is well localized on the surface of the fiber. Thus, the peptide nanoparticle interactions are more efficient due to direct interactions of nanoparticles with the surface of the fibers without any changes in the peptide structure. On the other hand, the peptide VW05 covers the surface of the nanoparticle, which results in an aggregation of the nanoparticles as well as a α-helical fiber formation of VW05. The latter one is a result of the high local peptide concentration on the surface of nanoparticles. However, peptide refolding reduces the binding constant K_B. Thus, a well-defined peptide structure is crucial for increasing the binding constant. On the other hand, a larger number of arginine residues is not a prerequisite for increasing the binding constant.

Furthermore, the molar binding energies of the fiber forming peptides R2A2, R2A3, and R2A4 are different compared to the coiled-coil peptide VW05. In principle it can be assumed that the electrostatic interaction of peptide and nanoparticle is a reaction that releases heat which is indicated by a negative binding energy. Thus, the interaction between nanoparticle and fiber-forming peptide results in a negative binding energy which decreases along with the binding constant. During the VW05-induced aggregation of nanoparticles two reactions take place: 1) peptide-induced nanoparticle assembly, and 2) refolding of the coiled-coil peptide into α-helical fibers. But whereas the former is an exothermic reaction, the latter is an endothermic reaction: due to the fiber formation the coiled-coil structure has to be dissolved into single random-coil peptides. This is an energetically disfavoured process. Apparently the energy that is needed for dissolving the coiled-coil is higher than the energy that is delivered due to nanoparticle assembly and refolding into α-helical fibers. Thus, the whole reaction is endothermic.

Moreover, a pH switch has a dramatic effect on the observed nanoparticle assembly for the peptide–nanoparticle aggregates of R2A2, R2A3, and R2A4. Increasing the pH value to 11 causes a refolding of the peptide fibers into a coiled-coil structure. A subsequent decrease to pH 9 results in two concomitant reactions: the formation of peptide fibers and the nanoparticle aggregation. Cryo TEM reveals that both reactions occur approximately with the same reaction rates: on the one hand short and bright nanoparticle assemblies are detected that are presumably formed due to peptide fibers. On the other hand nanoparticle assemblies are observed that are very similar to those obtained for VW05 [32]. Apparently the nanoparticle decoration on the surface of the peptides is an intrinsic property of the fiber.

Conclusion

The results presented herein demonstrate that the aggregation of Au/MUA nanoparticles depends not only on the number of presented arginine residues but also on the sequence length. The peptides studied here require a ratio not higher than 23.5 to specifically interact with oppositely charged nanoparticles. Thus the size of the peptide and finally the charge density plays an important role for its aggregation efficiency.

Furthermore, we could show that the quaternary structure of the peptide has important consequences for the formed nanoparticle assemblies, as well as for the thermodynamics of aggregation. First of all a peptide fiber leads to a well-defined nanoparticle aggregation on the surface, whereas soluble coiled-coil or random-coil peptides induce either an unstructured aggregation, or, in the case of random-coil peptides, no aggregation at all. Secondly, the peptide fiber with its well-defined presentation of charges causes an increase in the binding constant as well as in the binding energy. Thus, even a peptide with a lower number of charges can induce more rapid aggregation of nanoparticles if the peptide forms fibers. In contrast, nanoparticle aggregation induced by coiled-coil peptides even with a higher number of charges occurs more slowly.

Supporting Information

Supporting Information File 1

Experimental procedures.
[http://www.beilstein-journals.org/bjoc/content/supplementary/1860-5397-11-89-S1.pdf]

Supporting Information File 2

TEM images.
[http://www.beilstein-journals.org/bjoc/content/supplementary/1860-5397-11-89-S2.pdf]

Acknowledgements

The authors gratefully thank Dr. Allison Berger for proofreading of the manuscript. This work was supported by the Deutsche Forschungsgemeinschaft (SFB 765; TP A5).

References

1. Katz, E.; Willner, I. *Angew. Chem., Int. Ed.* **2004,** *43,* 6042–6108. doi:10.1002/anie.200400651
2. Storhoff, J. J.; Lazarides, A.; Mucic, R.; Mirkin, C. A.; Letsinger, R. L.; Schatz, G. C. *J. Am. Chem. Soc.* **2000,** *122,* 4640–4650. doi:10.1021/ja993825l
3. Park, S. Y.; Lee, J.-S.; Georganopoulou, D.; Mirkin, C. A.; Schatz, G. C. *J. Phys. Chem. B* **2006,** *110,* 12673–12681. doi:10.1021/jp062212+

4. Stoeva, S. I.; Lee, J.-S.; Smith, J. E.; Rosen, S. T.; Mirkin, C. A. *J. Am. Chem. Soc.* **2006,** *128,* 8378–8379. doi:10.1021/ja0613106
5. Lee, D.-E.; Koo, H.; Sun, I.-C.; Ryu, J. H.; Kim, K.; Kwon, I. C. *Chem. Soc. Rev.* **2012,** *41,* 2656–2672. doi:10.1039/C2CS15261D
6. Huang, X.; Jain, P. K.; El-Sayed, I. H.; El-Sayed, M. A. *Nanomedicine* **2007,** *2,* 681–693. doi:10.2217/17435889.2.5.681
7. Brigger, I.; Dubernet, C.; Couvreur, P. *Adv. Drug Delivery Rev.* **2002,** *54,* 631–651. doi:10.1016/S0169-409X(02)00044-3
8. Marquis, B. J.; Love, S. A.; Braun, K. L.; Haynes, C. L. *Analyst* **2009,** *134,* 425–439. doi:10.1039/b818082b
9. Niemeyer, C. M. *Angew. Chem., Int. Ed.* **2001,** *40,* 4128–4158. doi:10.1002/1521-3773(20011119)40:22<4128::AID-ANIE4128>3.0.CO;2-S
10. Niemeyer, C. M. *Science* **2002,** *297,* 62–63. doi:10.1126/science.1073843
11. Moore, G. E. *Electronics* **1965,** *38,* 114–116.
12. Whitesides, G. M.; Mathias, J. P.; Seto, C. T. *Science* **1991,** *254,* 1312–1319. doi:10.1126/science.1962191
13. Gole, A.; Dash, C.; Soman, C.; Sainkar, S. R.; Rao, M.; Sastry, M. *Bioconjugate Chem.* **2001,** *12,* 684–690. doi:10.1021/bc0001241
14. Hazarika, P.; Kukolka, F.; Niemeyer, C. M. *Angew. Chem., Int. Ed.* **2006,** *45,* 6827–6830. doi:10.1002/anie.200602049
15. Liu, D.; Bruckbauer, A.; Abell, C.; Balasubramanian, S.; Kang, D.-J.; Klenerman, D.; Zhou, D. *J. Am. Chem. Soc.* **2006,** *128,* 2067–2071. doi:10.1021/ja0568300
16. Mo, X.; An, Y.; Yun, C.-S.; Yu, S. M. *Angew. Chem., Int. Ed.* **2006,** *45,* 2267–2270. doi:10.1002/anie.200504529
17. Seeman, N. C. *Nano Lett.* **2001,** *1,* 22–26. doi:10.1021/nl000182v
18. Yao, H.; Yi, C.; Tzang, C.-H.; Zhu, J.; Yang, M. *Nanotechnology* **2007,** *18,* 015102. doi:10.1088/0957-4484/18/1/015102
19. Mirkin, C. A.; Letsinger, R. L.; Mucic, R. C.; Storhoff, J. J. *Nature* **1996,** *382,* 607–609. doi:10.1038/382607a0
20. Shenton, W.; Davies, S. A.; Mann, S. *Adv. Mater.* **1999,** *11,* 449–452. doi:10.1002/(SICI)1521-4095(199904)11:6<449::AID-ADMA449>3.0.CO;2-A
21. Niemeyer, C. M.; Ceyhan, B. *Angew. Chem., Int. Ed.* **2001,** *40,* 3685–3688. doi:10.1002/1521-3773(20011001)40:19<3685::AID-ANIE3685>3.0.CO;2-E
22. Aili, D.; Gryko, P.; Sepulveda, B.; Dick, J. A. G.; Kirby, N.; Heenan, R.; Baltzer, L.; Liedberg, B.; Ryan, M. P.; Stevens, M. M. *Nano Lett.* **2011,** *11,* 5564–5573. doi:10.1021/nl203559s
23. Aggeli, A.; Nyrkova, I. A.; Bell, M.; Harding, R.; Carrick, L.; McLeish, T. C. B.; Semenov, A. N.; Boden, N. *Proc. Natl. Acad. Sci. U. S. A.* **2001,** *98,* 11857–11862. doi:10.1073/pnas.191250198
24. Lamm, M. S.; Rajagopal, K.; Schneider, J. P.; Pochan, D. J. *J. Am. Chem. Soc.* **2005,** *127,* 16692–16700. doi:10.1021/ja054721f
25. Woolfson, D. N.; Ryadnov, M. G. *Curr. Opin. Chem. Biol.* **2006,** *10,* 559–567. doi:10.1016/j.cbpa.2006.09.019
26. Ryadnov, M. G.; Ceyhan, B.; Niemeyer, C. M.; Woolfson, D. N. *J. Am. Chem. Soc.* **2003,** *125,* 9388–9394. doi:10.1021/ja0352045
27. de laRica, R.; Fratila, R. M.; Szarpak, A.; Huskens, J.; Velders, A. H. *Angew. Chem., Int. Ed.* **2011,** *50,* 5704–5707. doi:10.1002/anie.201008189
28. Taylor, R. W.; Lee, T.-C.; Scherman, O. A.; Esteban, R.; Aizpurua, J.; Huang, F. M.; Baumberg, J. J.; Mahajan, S. *ACS Nano* **2011,** *5,* 3878–3887. doi:10.1021/nn200250v
29. Verma, A.; Stellacci, R. *Small* **2010,** *6,* 12–21. doi:10.1002/smll.200901158
30. Sharma, N.; Top, A.; Kück, K. L.; Pochan, D. J. *Angew. Chem., Int. Ed.* **2009,** *48,* 7078–7082. doi:10.1002/anie.200901621
31. Stevens, M. M.; Flynn, N. T.; Wang, C.; Tirrell, D. A.; Langer, R. *Adv. Mater.* **2004,** *16,* 915–918. doi:10.1002/adma.200306430
32. Wagner, S. C.; Roskamp, M.; Cölfen, H.; Böttcher, C.; Schlecht, S.; Koksch, B. *Org. Biomol. Chem.* **2009,** *7,* 46–51. doi:10.1039/B813429D
33. Wagner, S. C.; Roskamp, M.; Pallerla, M.; Araghi, R. R.; Schlecht, S.; Koksch, B. *Small* **2010,** *6,* 1321–1328. doi:10.1002/smll.200902067
34. Fillon, Y.; Verma, A.; Gosh, P.; Ernenwein, D.; Rotello, V. M.; Chmielewski, J. *J. Am. Chem. Soc.* **2007,** *129,* 6676–6677. doi:10.1021/ja070301+
35. Lundqvist, M.; Nygren, P.; Jonsson, B.-H.; Broo, K. *Angew. Chem., Int. Ed.* **2006,** *45,* 8169–8173. doi:10.1002/anie.200600965
36. Aili, D.; Enander, K.; Rydberg, J.; Lundström, I.; Baltzer, L.; Liedberg, B. *J. Am. Chem. Soc.* **2006,** *128,* 2194–2195. doi:10.1021/ja057056j
37. De Santis, E.; Faruqui, N.; Noble, J. E.; Ryadnov, M. G. *Nanoscale* **2014,** *6,* 11425–11430. doi:10.1039/C4NR03328K
38. Zheng, N.; Fan, J.; Stucky, G. D. *J. Am. Chem. Soc.* **2006,** *128,* 6550–6551. doi:10.1021/ja0604717
39. Simard, J.; Briggs, C.; Boal, A. K.; Rotello, V. M. *Chem. Commun.* **2000,** 1943–1944. doi:10.1039/b004162i
40. Laera, S.; Ceccone, G.; Rossi, F.; Gilliland, D.; Hussain, R.; Siligardi, G.; Calzolai, L. *Nano Lett.* **2011,** *11,* 4480–4484. doi:10.1021/nl202909s
41. Ryadnov, M. G.; Cherny, D. I. *Macromol. Biosci.* **2012,** *12,* 195–201. doi:10.1002/mabi.201100295

License and Terms

BEILSTEIN JOURNAL OF ORGANIC CHEMISTRY

Influence of length and flexibility of spacers on the binding affinity of divalent ligands

Susanne Liese and Roland R. Netz*

Full Research Paper

Open Access

Address:
Fachbereich für Physik, Freie Universität Berlin, 14195 Berlin, Germany

Email:
Roland R. Netz* - rnetz@physik.fu-berlin.de

* Corresponding author

Keywords:
binding affinity; divalent ligand; effective concentration; multivalency

Beilstein J. Org. Chem. **2015,** *11,* 804–816.
doi:10.3762/bjoc.11.90

Received: 03 March 2015
Accepted: 29 April 2015
Published: 15 May 2015

This article is part of the Thematic Series "Multivalency as a chemical organization and action principle".

Guest Editor: R. Haag

Abstract

We present a quantitative model for the binding of divalent ligand–receptor systems. We study the influence of length and flexibility of the spacers on the overall binding affinity and derive general rules for the optimal ligand design. To this end, we first compare different polymeric models and determine the probability to simultaneously bind to two neighboring receptor binding pockets. In a second step the binding affinity of divalent ligands in terms of the IC_{50} value is derived. We find that a divalent ligand has the potential to bind more efficiently than its monovalent counterpart only, if the monovalent dissociation constant is lower than a critical value. This critical monovalent dissociation constant depends on the ligand-spacer length and flexibility as well as on the size of the receptor. Regarding the optimal ligand-spacer length and flexibility, we find that the average spacer length should be equal or slightly smaller than the distance between the receptor binding pockets and that the end-to-end spacer length fluctuations should be in the same range as the size of a receptor binding pocket.

Introduction

Multivalency is a common design principle in biological systems. The simultaneous binding of several, relatively weakly binding partners is a widely used strategy to strengthen the overall binding affinity [1-3]. Multivalency is believed to play an important role in evolutionary processes, since the collective interaction of several rather simple ligands makes the development of more complex binding partners with a higher binding affinity unnecessary [2]. Also in drug design, the synthesis of artificial multivalent ligands is a promising route to increase the binding affinity or to reduce the amount of substance required for treatment [4-7].

The term multivalency is used for systems that consist of several identical binding partners. Thereby, the larger binding partner, for example a protein, is commonly denoted as receptor, whereas the smaller binding partner, for instance an

enzyme or a single molecule, is denoted as ligand. The binding strength of a multivalent structure significantly depends on details of the presentation of ligands and receptors [1]. Each multivalent ligand consists of several monovalent ligands that are connected via a scaffold. The binding affinity of such a multivalent ligand is determined by the interplay between gain in binding energy and loss of entropy associated with conformational degrees of freedom. The more flexible the scaffold is, the better it can adapt to the geometry of the receptor, but the more pronounced on the other hand is the entropy penalty. This simple, qualitative argument shows that the careful choice of the ligand scaffold is essential, in order to benefit from multivalent enhancement. It is therefore desirable to derive a model that allows one to predict the binding affinity of a given ligand-scaffold construct. Several theoretical studies have been dedicated to study the interaction between multi- and polyvalent ligands with receptors arranged on planar surfaces [8-13]. The overwhelming variety of multivalent ligand architectures that range from small divalent ligands to densely packed nanoparticles, led to different approaches to describe multivalency, depending on the size and valency of the system. Several studies aimed to treat ligand–receptor systems with different structures and valencies in the framework of a generalized theory [14,15].

The smallest multivalent system consists of a divalent ligand that interacts with a divalent receptor. Despite its seeming simplicity, the rational design of divalent ligands is still challenging [16-19]. In this paper we examine a general model for a divalent receptor–ligand system in order to estimate the binding affinity from the dissociation constant of the monovalent ligand and the length and flexibility of the ligand spacer.

Figure 1a schematically depicts a divalent ligand–receptor system. The receptor possesses two binding pockets at a distance d from each other. A binding range of σ characterizes each binding pocket. The divalent ligand consists of two ligand units that are connected via a spacer. The contour length of the spacer is denoted as L. There are three different modes in which a divalent ligand can bind to a divalent receptor. Each of these binding modes has a different number of realization possibilities as summarized in Figure 1b: (1) One binding pocket is occupied by one ligand. (2) Two binding pockets are occupied by two ligands. (3) Two binding pockets are occupied by one ligand. The binding affinity in the latter case is strongly influenced by the conformational linker properties, which can be conveniently discussed in terms of the effective concentration. The effective concentration describes the local concentration of one ligand unit close to one binding pocket, if the other ligand unit is assumed to be bound to the other binding pocket. The effective concentration thus corresponds to the probability that the spacer extends to an end-to-end distance that is equal to d, if spacer–receptor interactions are neglected [20]. In the first section different models for the effective concentration are discussed, with particular focus on the influence of the spacer stiffness and the binding range σ.

For each binding mode depicted in Figure 1b the following dissociation constants are derived: (1) The dissociation constant is equal to the dissociation constant of the monovalent ligand, K_{mono}, multiplied by a factor of $1/\alpha$, which accounts for the reduced degrees of freedom of the spacer, since it cannot penetrate the receptor. The parameter α can adopt value between 0 and 1. In the limiting case, in which the spacer sterically inhibits the ligand unit from binding to the receptor, α becomes 0. In the hypothetical case, in which the conformational degrees of freedom of the spacer do not reduce at all when binding to a receptor, the parameter α becomes 1. (2) Each ligand contributes with a factor of K_{mono}/α to the dissociation constant. (3) The dissociation constant consists of the monovalent dissociation constant for each ligand times the probability that the spacer bridges the two binding pockets. A detailed derivation of the dissociation constants is presented in Supporting Information File 1. Furthermore, Figure 1b summarizes the combinatorial factors for each binding mode that count the number of equivalent permutations. We regard the divalent ligands as distinguishable, we note in passing that this could reflect poly-

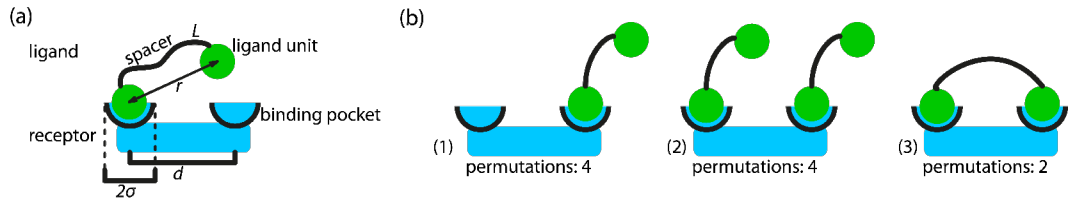

Figure 1: (a) Schematic of a divalent ligand–receptor system: The receptor has two binding pockets with a distance *d* from each other and a binding range σ. The ligand consists of two identical ligand units, connected via a spacer of contour length *L*. The end-to-end distance of the ligand is denoted as *r*. (b) Binding modes of a divalent ligand: (1) One ligand occupies one binding pocket. (2) Two ligands occupy two binding pockets. (3) One ligand occupies both binding pockets.

meric spacers that exhibit chemical asymmetry. Our final results do not depend on whether we assume indistinguishable ligand units or not.

Results and Discussion

Effective concentration – wormlike-chain model

Samuel and Sinha [21] developed an exact method to describe the conformational statistics of wormlike chains for the whole range from short to long polymers. Their model is applied here to determine the effective concentration C_{eff}, which is equivalent to the end-to-end distance probability distribution, with the normalization $4\pi\int_0^\infty dr\, r^2 C_{\text{eff}}(r) = 1$. An example is shown in Figure 2. The length of the fully extended spacer L is set to 5 nm. The effective concentration, i.e., the probability that a spacer of given length and stiffness extends to a certain end-to-end-distance d, is shown for different persistence lengths l_p. The flexible spacer (l_p = 1 nm) exhibits a maximum at d = 0. Furthermore, the distribution is very broad, indicating that a flexible spacer can easily bridge two binding pockets, even if the spacer length does not exactly match the inter binding pocket distance d. For a slightly stiffer spacer (l_p = 1.3 nm), C_{eff} is even broader, but the maximum of C_{eff} is reduced by a factor of about one half and the distribution shows a plateau between d = 0 nm and d = 3 nm. For stiff spacers (l_p = 5 nm and l_p = 10 nm), C_{eff} exhibits a narrow peak close to the fully extended state. In the bound state, the ligand units explore the range σ of a receptor binding pocket. Hence, it is useful to consider the effective concentration averaged over the range of both binding pockets. We denote the averaged effective concentration as $\tilde{C}_{\text{eff}}$ with

$$\tilde{C}_{\text{eff}}(d) = \frac{\int_{V_{\text{bp}}} d\boldsymbol{r}_1 \int_{V_{\text{bp}}} d\boldsymbol{r}_2 C_{\text{eff}}(|\boldsymbol{r}_2 - \boldsymbol{r}_1|)}{\int_{V_{\text{bp}}} d\boldsymbol{r}_1 \int_{V_{\text{bp}}} d\boldsymbol{r}_2}, \quad (1)$$

with V_{bp} the volume of one binding pocket, $\mathbf{r}_1$ and $\mathbf{r}_2$ the positions within the first and second binding pocket. We introduce the connecting vector $\mathbf{r} = |\mathbf{r}_1 - \mathbf{r}_2|$ and express $\mathbf{r}$ in spherical coordinates:

$$\tilde{C}_{\text{eff}}(d) = \frac{\int_{V_{\text{bp}}} d\boldsymbol{r}_1 \int_0^{2\pi} d\varphi \int_{d-2\sigma}^{d+2\sigma} dr r^2 \int_0^{\theta(r)} d\theta' \sin(\theta') C_{\text{eff}}(\boldsymbol{r})}{\int_{V_{\text{bp}}} d\boldsymbol{r}_1 \int_0^{2\pi} d\varphi \int_{d-2\sigma}^{d+2\sigma} dr r^2 \int_0^{\theta(r)} d\theta' \sin(\theta')}, \quad (2)$$

with r the distance between the two ligand units, θ the angle between $\boldsymbol{r}$ and the connecting vector of the binding pocket midpoints and φ an angle that describes the rotation around the connecting vector of the binding pocket midpoints. Since the range of the binding pocket σ is assumed to be much smaller than the distance between the binding pockets d, we conclude that the integrals in Equation 2 approximately factorize. Furthermore, the size of the binding pocket limits the range over which the angle θ can vary. In the range, where r varies between $d - \sigma$ and $d + \sigma$, the angle θ can adopt a maximum value of arctan(σ/r). The upper limit for the integration over θ then reads

$$\frac{\int_0^{\arctan\left(\frac{\sigma}{r}\right)} d\theta' \sin(\theta') \approx \left(\frac{\sigma}{r}\right)^2}{2}, \text{valid for } \sigma \ll r.$$

The integration over $\boldsymbol{r}$ can now be described by variations of r in the range from $d - \sigma$ and $d + \sigma$. With these approximations, Equation 2 can be written as an effective average over one dimension:

$$\tilde{C}_{\text{eff}}(d) = \frac{\int_{d-\sigma}^{d+\sigma} dr C_{\text{eff}}(r)}{2\sigma}. \quad (3)$$

In Figure 2, the averaged effective concentration is shown as green, dashed lines, with σ = 0.25 nm. A flexible spacer can easily extend to all positions within the binding pockets. Hence, one cannot observe any significant difference between $\tilde{C}_{\text{eff}}$ and C_{eff}. In contrast, a very stiff spacer cannot explore the whole binding pocket. Therefore, the averaged effective concentration is reduced and slightly broadened around its maximum, as can be seen best in Figure 2 for l_p = 10 nm.

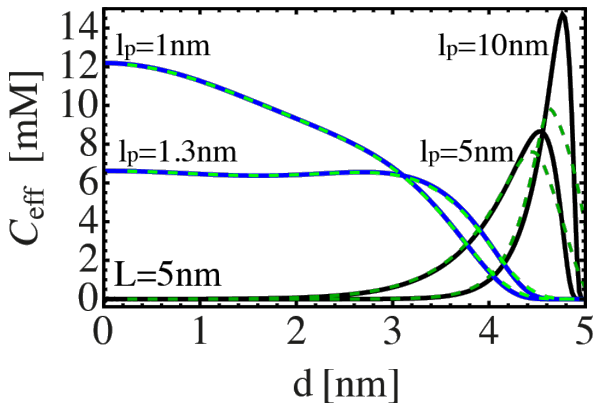

Figure 2: Effective concentration Ceff of spacers with a contour length of L = 5 nm as a function of the distance between the binding pockets. The effective concentration is shown for different spacer stiffness, in terms of different persistence lengths between l_p = 1–10 nm (continuous lines). The effective concentration $\tilde{C}_{\text{eff}}$, averaged over a binding pocket range σ = 0.25 nm, is shown as green, dashed lines.

Figure 3 summarizes the averaged end-to-end distance r_{ete}, the end-to-end distance that corresponds to a maximum in C_{eff}, r_{max}, the variance of the end-to-end distance distribution Δr, the maximum of the effective concentration C_{eff}^{max} and the effective concentration at r_{ete}, $C_{eff}(r_{ete})$, for different persistence lengths. The influence of the binding range σ is neglected here. The average end-to-end distance r_{ete} increases monotonically with increasing persistence length and approaches the contour length L for very stiff spacers. All other quantities reveal a clear-cut difference between the flexible and stiff limits. The classification "flexible" and "stiff" is, of course, to some degree arbitrary. We here apply a definition that is based on the discontinuity in r_{max}, which is the most prominent feature in the chain observables. In the following, spacers with a persistence length smaller than $0.26L$ are called flexible and spacers with a persistence length larger than $0.26L$ are called stiff. The variance Δr exhibits a maximum around $l_p = 0.26L$, for stiffer spacers Δr reduces rapidly. As can be seen in Figure 3, the variance Δr depends on the persistence length as $\Delta r = 0.1L^2/l_p$ (dotted line) for stiff spacers. Mac Kintosh et al. found the same scaling for the fluctuations of semiflexible polymers [22]. The maximum of the effective concentration C_{eff}^{max} (continuous line) as well as the effective concentration at r_{ete}, $C_{eff}(r_{ete})$, (dashed line) are minimal in the same region where Δr is maximal. Since for a stiff spacer r_{max} and r_{ete} are both close to L, C_{eff}^{max} and $C_{eff}(r_{ete})$ exhibit only small deviations from each other. For flexible spacers on the other hand, $C_{eff}(r_{ete})$ can be much smaller than the maximal effective concentration. The results presented here show that neither the persistence length nor the contour length alone are sufficient to describe the behavior of the effective concentration, rather the ratio between persistence length and contour length, l_p/L, characterizes the conformational behavior. Note that for a typical receptor distance of d = 5 nm, DNA molecules with l_p = 53 nm are characterized by a ratio $l_p/L \approx 10$ and thus correspond to the very stiff limit. Polyethylene glycol (PEG) with a persistence length of about l_p = 0.38 nm on the other hand is characterized by a ratio smaller than $l_p/L = 0.08$ and thus correspond to the flexible limit [23].

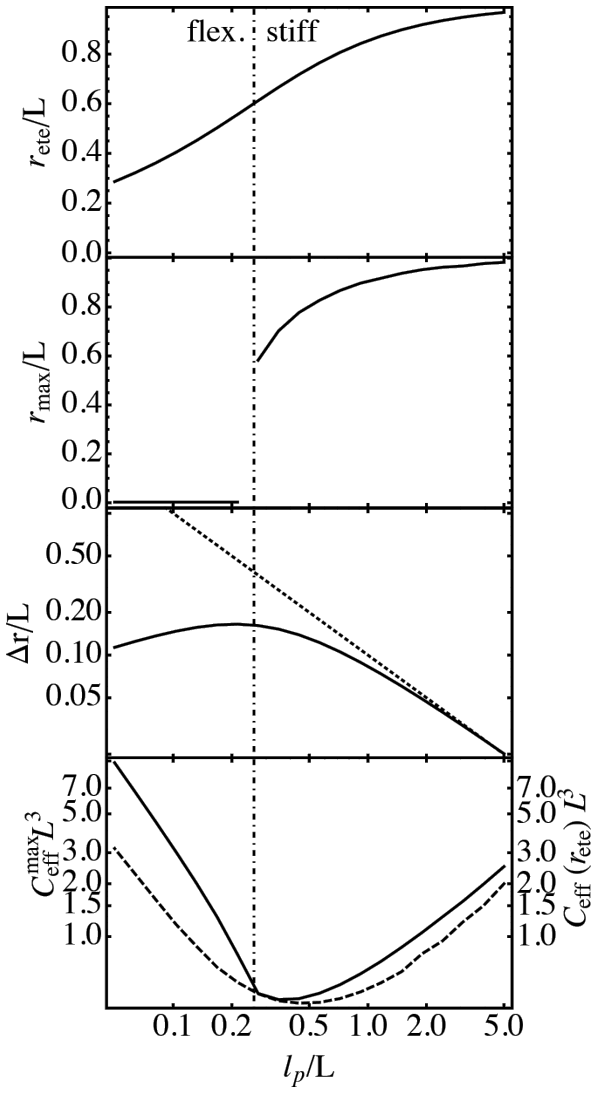

Figure 3: Average end-to-end distance, r_{ete}, end-to-end-distance where the effective concentration C_{eff} exhibits a maximum, r_{max}, variance of the end-to-end distance distribution, Δr, maximum of the effective concentration, C_{eff}^{max} (continuous line), and effective concentration at r_{ete}, $C_{eff}(r_{ete})$ (dashed line), in dependence of the persistence length l_p. All lengths are measured in units of the spacer contour length L. Spacers with a persistence length $l_p < 0.26L$ are called flexible. Spacers with a persistence length $l_p > 0.26L$ are called stiff. For stiff spacers the relation between $\Delta r/L$ and the persistence length is well described by $\Delta r/L = 0.1L/l_p$ (dotted line).

Effective concentration – harmonic spring and Gaussian chain approximation

The wormlike-chain model requires complex numerical analysis for the calculation of conformational chain properties. In a simplified model the spacer statistics can be described as a harmonic spring or a Gaussian chain with suitably chosen parameters. The advantage of this model is that the effective concentration can be derived in closed form. Furthermore, we show that despite its simplified assumptions the model accurately reproduces the effective concentration $C_{eff}(r_{ete})$ for flexible as well as for stiff spacers.

Stiff spacer – harmonic spring approximation

A stiff spacer is on average extended to almost its full length. The fluctuations around its most probable end-to-end distance r_0 are assumed to be much smaller than the contour length L. We approximate the free energy F, similar to a harmonic spring, as

$$F(d) = \frac{k}{2}(d - r_0)^2 , \quad (4)$$

with k the effective spring constant and d the end-to-end distance. The effective concentration $C_{\text{eff}}(d)$, i.e., the normalized probability to extend the spacer to a certain end-to-end distance d, reads

$$\begin{aligned} C_{\text{eff}}(d) &= \frac{e^{-F(d)/k_{\text{B}}T}}{4\pi\int_0^\infty dr\, r^2 e^{-F(r)/k_{\text{B}}T}} \\ &\approx \frac{e^{-F(d)/k_BT}}{4\pi\int_{-\infty}^\infty dr\, r^2 e^{-F(r)/k_{\text{B}}T}} \\ &= \frac{1}{2}\left(\frac{k}{2\pi k_{\text{B}}T}\right)^{3/2} \frac{e^{-F(d)/k_{\text{B}}T}}{1+kr_0^2/k_{\text{B}}T}. \end{aligned} \tag{5}$$

The averaged effective concentration $\tilde{C}_{\text{eff}}$ as defined in Equation 3 then becomes:

$$\begin{aligned} \tilde{C}_{\text{eff}}(d) = &\frac{k/k_{\text{B}}T}{16\pi\sigma\left(1+kr_0^2/k_{\text{B}}T\right)} \\ &\times\left(\operatorname{erf}\left[\sqrt{\frac{k}{2k_{\text{B}}T}}\left(r_0-d+\sigma\right)\right]\right. \\ &\left.-\operatorname{erf}\left[\sqrt{\frac{k}{2k_{\text{B}}T}}\left(r_0-d-\sigma\right)\right]\right). \end{aligned} \tag{6}$$

In order to express the effective concentration in term of the experimentally more relevant average end-to-end distance r_{ete} and the variance Δr, we first have to determine the relation between r_{ete} and Δr on the one side and k and r_0 on the other side.

From the free energy F in Equation 4 the average end-to-end distance r_{ete} and the variance Δr are obtained as:

$$r_{\text{ete}} = \frac{\int_0^\infty dr\, r^3 e^{-F(r)/k_BT}}{\int_0^\infty dr\, r^2 e^{-F(r)/k_BT}} \approx \frac{\int_{-\infty}^\infty dr\, r^3 e^{-F(r)/k_BT}}{\int_{-\infty}^\infty dr\, r^2 e^{-F(r)/k_BT}}. \tag{7}$$

$$\rightarrow r_{\text{ete}} \approx r_0\frac{3+kr_0^2/k_{\text{B}}T}{1+kr_0^2/k_{\text{B}}T} \rightarrow r_{\text{ete}} \approx r_0; \text{if}\ \frac{kr_0^2}{k_{\text{B}}T} \gg 1 \tag{8}$$

$$\left\langle r_{\text{ete}}^2\right\rangle = \frac{\int_0^\infty dr\, r^4 e^{-F(r)/k_BT}}{\int_0^\infty dr\, r^2 e^{-F(r)/k_BT}} \approx \frac{\int_{-\infty}^\infty dr\, r^4 e^{-F(r)/k_BT}}{\int_{-\infty}^\infty dr\, r^2 e^{-F(r)/k_BT}} \tag{9}$$

$$\rightarrow \left\langle r_{\text{ete}}^2\right\rangle \approx r_0^2\frac{3k_{\text{B}}T/kr_0^2+6+kr_0^2/k_{\text{B}}T}{1+kr_0^2/k_{\text{B}}T}. \tag{10}$$

Note that according to our notation, the average end-to-end distance r_{ete} is not equivalent to the root mean squared end-to-end distance $\sqrt{\left\langle r_{\text{ete}}^2\right\rangle}$. The variance Δr hence reads:

$$\Delta r = \sqrt{\left\langle r_{\text{ete}}^2\right\rangle - \left(r_{\text{ete}}\right)^2} \tag{11}$$

$$\begin{aligned} &\rightarrow \Delta r \approx \sqrt{\frac{k_{\text{B}}T}{k}}\sqrt{\frac{3+(kr_0^2/k_{\text{B}}T)^2}{(1+kr_0^2/k_{\text{B}}T)^2}} \\ &\rightarrow \Delta r \approx \sqrt{\frac{k_{\text{B}}T}{k}}; \text{if}\ \frac{kr_0^2}{k_{\text{B}}T} \gg 1. \end{aligned} \tag{12}$$

Using Equation 6 and the results for Δr and r_{ete} in terms of the model parameters k and r_0 in the stiff spacer limit ($kr_0^2/k_{\text{B}}T >> 1$), the averaged effective concentration reads:

$$\tilde{C}_{\text{eff}}(d) = \frac{1}{8\pi\sigma r_{\text{ete}}^2}\left(\operatorname{erf}\left[\frac{r_{\text{ete}}-d+\sigma}{\sqrt{2}\Delta r}\right]-\operatorname{erf}\left[\frac{r_{\text{ete}}-d-\sigma}{\sqrt{2}\Delta r}\right]\right). \tag{13}$$

For a fixed distance d that has to be spanned by the ligand, the effective concentration becomes maximal for $r_{\text{ete}} = d$ and we obtain, for this optimized spacer length, the result:

$$\begin{aligned} &\tilde{C}_{\text{eff}}(d) = \frac{1}{8\pi\sigma d^2}\operatorname{erf}\left[\frac{\sigma}{\sqrt{2}\Delta r}\right], \\ &\text{with}\ \operatorname{erf}[x]-\operatorname{erf}[-x] = 2\operatorname{erf}[x]. \end{aligned} \tag{14}$$

Furthermore, we can differentiate between two cases: 1) the chain fluctuations are smaller than the binding range ($\Delta r << \sigma$) and 2) the chain fluctuations are larger than the binding range ($\Delta r >> \sigma$), leading to

$$\Delta r \ll \sigma \quad \rightarrow \quad \tilde{C}_{\text{eff}}^{\max}(d) \approx \frac{1}{8\pi d^2\sigma} \tag{15}$$

$$\Delta r \gg \sigma \rightarrow \tilde{C}_{\text{eff}}^{\max}(d) \approx \frac{1}{2(2\pi)^{3/2}\, d^2\Delta r}. \tag{16}$$

We see that in both limits, the maximal effective concentration decreases quadratically with the distance d. More importantly, increasing the stiffness of the spacer (decreasing Δr) increases the effective concentration, but only until the variance Δr

becomes of the same order as the binding range σ. For even stiffer spacers the effective concentration stagnates, as can be seen in Equation 15. We conclude that it is not advantageous to increase the spacer stiffness beyond the situation where the end-to-end distance variance Δr becomes smaller than the receptor binding range σ. To compare this model with the wormlike-chain model Equation 16 is rewritten as:

$$\tilde{C}_{\text{eff}}^{\max}(d)\,d^3 \approx \frac{1}{2(2\pi)^{3/2}\,\Delta r/d}. \tag{17}$$

As can be seen in Figure 4a Equation 17 describes the behavior of stiff wormlike chains very well.

Flexible spacer – Gaussian-chain approximation

The effective concentration of flexible polymers is often modeled by a Gaussian chain [11,20,24] with the free energy:

$$F(d) = \frac{3}{2}\frac{d^2}{\langle r_{\text{ete}}^2\rangle}k_{\text{B}}T\,, \tag{18}$$

using the mean squared end-to-end distance $\langle r_{\text{ete}}^2\rangle$. The end-to-end distance r_{ete} and the variance Δr can be expressed in terms of the mean squared end-to-end distance:

$$r_{\text{ete}} = \frac{\int_0^\infty dr\; r^3 e^{-F(r)/k_{\text{B}}T}}{\int_0^\infty dr\; r^2 e^{-F(r)/k_{\text{B}}T}} = \sqrt{\frac{8}{3\pi}\langle r_{\text{ete}}^2\rangle}\,, \tag{19}$$

$$\Delta r = \sqrt{\langle r_{\text{ete}}^2\rangle - (r_{\text{ete}})^2} = \sqrt{\left(1-\frac{8}{3\pi}\right)\langle r_{\text{ete}}^2\rangle}\,. \tag{20}$$

As a consequence the end-to-end distance r_{ete} and the variance Δr are related as

$$\Delta r = r_{\text{ete}}\sqrt{\frac{3\pi}{8}-1}\,. \tag{21}$$

Furthermore, the mean squared end-to-end distance can be written as

$$\langle r_{\text{ete}}^2\rangle = b^2 N\,, \tag{22}$$

with b being the Kuhn length of one chain segment and N the number of segments.

We here present the effective concentration as a function of d and r_{ete}.

$$\begin{aligned} C_{\text{eff}}(d) &= \frac{e^{-F(d)/k_{\text{B}}T}}{4\pi\int_0^\infty dr\, r^2 e^{-F(r)/k_{\text{B}}T}} \\ &= \frac{1}{r_{\text{ete}}^3}\left(\frac{4}{\pi^2}\right)^{3/2}\exp\left[-\frac{4}{\pi}\left(\frac{d}{r_{\text{ete}}}\right)^2\right]. \end{aligned} \tag{23}$$

Using Equations 19–22, r_{ete} can as well be substituted by $\langle r_{\text{ete}}^2\rangle$, Δr or N.

Note that the effective concentration of a flexible spacer with fixed contour length L is maximal at a distance $d = 0$, as shown in Figure 2. In contrast, for a given distance d the effective concentration becomes maximal at $r_{\text{ete}} = \sqrt{8/(3\pi)}\,d$. In other

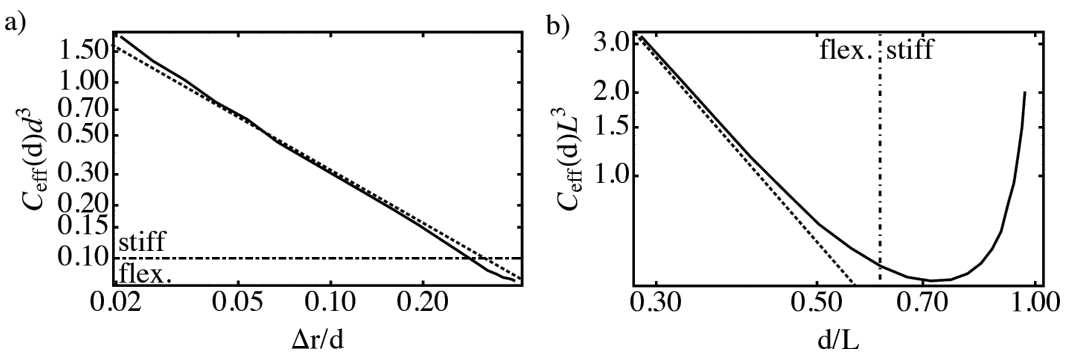

Figure 4: Effective concentration for the optimized average end-to-end distance $r_{\text{ete}}=d$ for the wormlike chain model (continuous line) and the harmonic spring model Equation 17 (dotted line, subfigure a) as well as the Gaussian-chain model Equation 25 (dotted line, subfigure b). In the calculation, we vary the ratio between persistence length and contour length l_{p}/L, which results in different ratios $\Delta r/d$ and d/L, respectively. (a) Stiff spacers are well approximated by Equation 17. (b) Flexible spacers are well approximated by Equation 25.

words, the average end-to-end distance of an optimized flexible spacer is smaller than the distance between the binding pockets by a factor of $\sqrt{8/(3\pi)}$:

$$C_{\text{eff}}^{\max}(d) = \left(\frac{3}{2\pi d^2}\right)^{3/2} e^{-3/2}. \quad (24)$$

Since we consider the fluctuations of a flexible chain much larger than the range of the binding pocket, we neglect the influence of σ on the effective concentration. In order to compare the behavior of a Gaussian chain with the results for a flexible wormlike chain, Equation 24 is rewritten as:

$$C_{\text{eff}}(d) L^3 = \left(\frac{L}{d}\right)^3 \left(\frac{4}{\pi}\right)^{3/2} e^{-4/\pi}. \quad (25)$$

In Figure 4b, Equation 25 is shown together with the numerical results from the wormlike chain model obtained in the previous section. The two models show good agreement in the flexible limit, as expected.

Conformational degrees of freedom of a tethered spacer

If one ligand unit is bound to one of the binding pockets, the conformational degrees of freedom of the spacer are reduced, since it cannot penetrate the receptor surface. We quantify this reduction by the parameter α, which describes the ratio between the partition function of a tethered and a free spacer. The value of α depends on the shape of the receptor and the flexibility of the spacer. To estimate the typical magnitude of α we consider as limiting cases a stiff rod as well as a flexible Gaussian chain tethered to a planar surface.

Stiff spacer

For a stiff rod attached with one end to a planar surface, the parameter α becomes α = 1/2, since the rod can only explore one half space.

Flexible spacer

As a second example we discuss a Gaussian chain. Equivalently to Equation 23 the normalized probability that a Gaussian chain consisting of N segments extends to an end-to-end distance r with b being the length of one segment reads in free space:

$$P(r,N) = \left(\frac{3}{2\pi N b^2}\right)^{3/2} \exp\left[-\frac{3}{2}\frac{r^2}{Nb^2}\right]. \quad (26)$$

We now assume that one end of the chain is attached to the surface. Similar to the considerations made for a stiff rod, we approximate the probability that the first segment does not penetrate the surface by a factor 1/2. The probability distribution for the remaining $N-1$ segments then reads:

$$P'(\rho,z,N) = \frac{1}{2}\left(\frac{3}{2\pi(N-1)b^2}\right)^{3/2} \exp\left[-\frac{3}{2}\frac{\rho^2}{(N-1)b^2}\right] \times\left(\exp\left[-\frac{3}{2}\frac{(z-b)^2}{(N-1)b^2}\right] + \exp\left[-\frac{3}{2}\frac{(z+b)^2}{(N-1)b^2}\right]\right), \quad (27)$$

with ρ the component of the end-to-end vector parallel to the surface and z the height above the surface. The last term in Equation 27 ensures that the chain does not penetrate the surface ($P'(\rho,z=0,N)=0$). To obtain the parameter α, P' has to be integrated over one half space:

$$\alpha(N) = \frac{1}{2}\left(\frac{3}{2\pi(N-1)b^2}\right)^{1/2} \times\int_0^\infty dz\left(\exp\left[-\frac{3}{2}\frac{(z-b)^2}{(N-1)b^2}\right] - \exp\left[-\frac{3}{2}\frac{(z+b)^2}{(N-1)b^2}\right]\right). \quad (28)$$

In the limit of a long chain ($N \gg 1$), Equation 28 can be approximated as:

$$\alpha(N) = \frac{1}{2}\left(\frac{3}{2\pi N b^2}\right)^{\frac{1}{2}} \frac{6}{Nb}\exp\left[-\frac{3}{2N}\right]\int_0^\infty dz\, z\exp\left[-\frac{3}{2}\frac{z^2}{Nb^2}\right] = \sqrt{\frac{3}{2\pi N}}\exp\left[-\frac{3}{2N}\right]. \quad (29)$$

A PEG spacer with b = 0.38 nm requires 30–800 segments to adopt an average end-to-end distance of 2 to 10 nm. In this range α varies between 0.02 and 0.13.

Binding affinity

With the effective concentration and a parameterization for the reduction of the conformational degrees of freedom of the spacer at hand, we now can examine the binding affinity of a divalent ligand. A common way to quantify the binding affinity of a multivalent ligand is the so-called IC_{50} value, the ligand (or inhibitor) concentration at half maximal inhibition. In a first step we want to re-derive the relation between the IC_{50} value and the dissociation constant of a monovalent ligand [25,26].

Monovalent ligand

In the reaction $L + R \rightleftharpoons LR$, the dissociation constant K_{mono} of a monovalent ligand interacting with a monovalent receptor is defined as

$$K_{mono} = \frac{[L][R]}{[RL]}, \tag{30}$$

with [L] and [R] being the concentration of unbound ligands and unbound receptors and [RL] the concentration of bound ligands or equivalently the concentration of bound receptors.

If half of all receptors are occupied, which defines the IC_{50} condition, the other half must be unbound and as a consequence [R] = [RL]. From Equation 30 we see that under IC_{50} conditions the dissociation constant equals the concentration of unbound ligands:

$$K_{mono} = [L]_{50}\,, \tag{31}$$

with the index 50 indicating that the IC_{50} condition is fulfilled. In the monovalent case exactly one ligand binds to one receptor. Thus, the concentration of bound ligands under IC_{50} conditions is given by half the total receptor concentration:

$$[RL]_{50} = \frac{1}{2}[R]_0\,, \tag{32}$$

with $[R]_0 = [R] + [RL]$ the total receptor concentration. Combining Equation 31 and Equation 32 the IC_{50} value is obtained as [25]:

$$IC_{50} \equiv [L]_{0,50} = [L]_{50} + [RL]_{50} = K_{mono} + \frac{1}{2}[R]_0\,. \tag{33}$$

In the limit of dilute receptor conditions ($[R]_0 << K_{mono}$) the IC_{50} value is a good approximation for the dissociation constant, and we find:

$$IC_{50} \approx K_{mono}, \text{if } [R]_0 \ll K_{mono}\,. \tag{34}$$

Divalent ligand

In analogy to the monovalent case, we now derive an expression for the IC_{50} value of a divalent ligand. There are different ways of defining half maximal inhibition for divalent receptors. We first adopt a heuristic definition where half of all receptor binding pockets are occupied by a ligand unit. This definition is most relevant for competitive binding assays, for instance surface plasmon resonance measurements [27], since the measured signal in a competitive binding assay is related to the number of occupied binding pockets. Later, we also define a situation in which at least one ligand unit is bound to half of all receptors as IC_{50} condition, which mimics non-competitive binding assays, as for instance hemagglutination assays [28]. In non-competitive binding assays the number of bound ligands rather than the number of occupied binding pockets is measured. In general the concentration of occupied binding pockets $[bp]_{occ}$ of divalent receptors reads:

$$\begin{aligned}[bp]_{occ} &= 1\cdot[RL_1] + 2\cdot[RL_2] + 2\cdot[RL_3] \\ &= 1\cdot 4\cdot\alpha\frac{[L][R]}{K_{mono}} \\ &\quad +2\cdot 4\cdot\alpha^2\frac{[L]^2[R]}{K_{mono}^2} \\ &\quad +2\cdot 2\cdot\frac{\tilde{C}_{eff}[L][R]}{K_{mono}^2},\end{aligned} \tag{35}$$

with $[RL_n]$ being the concentration of bound ligand–receptor pairs, with n referring to the three binding modes summarized in Figure 1b. Each term on the right hand side of Equation 35 has two prefactors. The first prefactor counts the number of occupied binding pockets per receptor and the second prefactor counts the permutations due to the distinguishability of the ligand units and the receptor binding pockets (see Figure 1b). Note that the number of permutations presented in Figure 1b and Equation 35, are obtained for distinguishable ligand units. For indistinguishable ligand units the number of permutations in each binding mode is reduced. At the same time the dissociation constant of a ligand with indistinguishable ligand units is reduced by the same factor. Hence, the overall concentration of bound ligands does not change. A detailed derivation of the dissociation constants for each binding mode is presented in Supporting Information File 1.

In the same way the total concentration of binding pockets, $[bp]_0$, can be obtained as

$$\begin{aligned}[bp]_0 &= 2\cdot\left([R] + [RL_1] + [RL_2] + [RL_3]\right) \\ &= 2\cdot\Bigg([R] + 4\cdot\alpha\frac{[L][R]}{K_{mono}} \\ &\quad +4\cdot\alpha^2\frac{[L]^2[R]}{K_{mono}^2} \\ &\quad +2\cdot\frac{\tilde{C}_{eff}[L][R]}{K_{mono}^2}\Bigg).\end{aligned} \tag{36}$$

In order to discuss also the IC_{50} condition for non-competitive binding assays we derive the concentration of receptors with at least one binding pocket occupied, $[R]_{1bp}$, and the total receptor concentration, $[R]_0$, as

$$[R]_{1bp} = [RL_1] + [RL_2] + [RL_3] = \left(4\cdot\alpha\frac{[L]}{K_{mono}} + 4\cdot\alpha^2\frac{[L]^2}{K_{mono}^2} + 2\cdot\frac{\tilde{C}_{eff}[L]}{K_{mono}^2}\right)[R], \quad (37)$$

$$[R]_0 = [R] + [RL_1] + [RL_2] + [RL_3] = \left(1 + 4\cdot\alpha\frac{[L]}{K_{mono}} + 4\cdot\alpha^2\frac{[L]^2}{K_{mono}^2} + 2\cdot\frac{\tilde{C}_{eff}[L]}{K_{mono}^2}\right)[R]. \quad (38)$$

With Equations 35–38 the IC_{50} condition for competitive and non-competitive binding is expressed as given in Equation 39 and Equation 40.

In analogy to the monovalent case we define the multivalent dissociation constant K_{multi} as the concentration of free ligand under IC_{50} conditions, as defined in Equation 39 and Equation 40.

Equation 41 and Equation 42 show the multivalent dissociation constant K_{multi} in case of competitive binding and non-competitive binding, respectively.

$$K_{multi} \equiv [L]_{50} = K_{mono}\frac{1}{4\alpha^2}\left(\sqrt{\left(\frac{\tilde{C}_{eff}}{K_{mono}}\right)^2 + 4\alpha^2} - \frac{\tilde{C}_{eff}}{K_{mono}}\right) \approx \begin{cases} \frac{1}{2\alpha}K_{mono}\ ;\text{if}\ \frac{\tilde{C}_{eff}}{K_{mono}} \ll 1 \\ \frac{K_{mono}^2}{2\tilde{C}_{eff}}\ ;\text{if}\ \frac{\tilde{C}_{eff}}{K_{mono}} \gg 1 \end{cases}. \quad (41)$$

Competitive and non-competitive binding exhibit the same qualitative behavior for large effective concentrations. We therefore limit the further discussion to competitive binding, as given in Equation 41.

As one would intuitively expect, the multivalent dissociation constant K_{multi} becomes proportional to the monovalent dissociation constant, if the effective concentration is low, i.e., if $\tilde{C}_{eff} \ll K_{mono}$. In contrast, the multivalent dissociation constant

$$\text{competitive binding: } \frac{1}{2} = \frac{[bp]_{occ}}{[bp]_0} = \frac{1\cdot 4\cdot\alpha\frac{[L]}{K_{mono}} + 2\cdot 4\cdot\alpha^2\frac{[L]^2}{K_{mono}^2} + 2\cdot 2\cdot\frac{\tilde{C}_{eff}[L]}{K_{mono}^2}}{2\cdot\left(1 + 4\cdot\alpha\frac{[L]}{K_{mono}} + 4\cdot\alpha^2\frac{[L]^2}{K_{mono}^2} + 2\cdot\frac{\tilde{C}_{eff}[L]}{K_{mono}^2}\right)} \quad (39)$$

$$\text{non-competitive binding: } \frac{1}{2} = \frac{[R]_{1bp}}{[R]_0} = \frac{4\cdot\alpha\frac{[L]}{K_{mono}} + 4\cdot\alpha^2\frac{[L]^2}{K_{mono}^2} + 2\cdot\frac{\tilde{C}_{eff}[L]}{K_{mono}^2}}{1 + 4\cdot\alpha\frac{[L]}{K_{mono}} + 4\cdot\alpha^2\frac{[L]^2}{K_{mono}^2} + 2\cdot\frac{\tilde{C}_{eff}[L]}{K_{mono}^2}} \quad (40)$$

$$K_{multi} \equiv [L]_{50} = K_{mono}\frac{1}{4\alpha^2}\left(\sqrt{\left(\frac{\tilde{C}_{eff}}{K_{mono}} + 2\alpha\right)^2 + 4\alpha^2} - \left(\frac{\tilde{C}_{eff}}{K_{mono}} + 2\alpha\right)\right) \approx \begin{cases} \left(\sqrt{2}-1\right)\frac{1}{2\alpha}K_{mono}\ ;\text{if}\ \frac{\tilde{C}_{eff}}{K_{mono}} \ll 1 \\ \frac{K_{mono}^2}{2\tilde{C}_{eff}}\ ;\text{if}\ \frac{\tilde{C}_{eff}}{K_{mono}} \gg 1 \end{cases}. \quad (42)$$

decreases, if the dissociation constant of the monovalent ligand is small and if the effective concentration, i.e., the probability to connect two binding pockets, is large.

To determine the total ligand concentration we first have to derive the concentration of bound ligand $[L]_{bound}$ as shown in Equation 43.

Using Equation 38 and 43, a relation between the concentration of bound ligands and the total receptor concentration under IC_{50} conditions is obtained as

$$[L]_{bound,50} = \psi [R]_0, \text{ with}$$

$$\psi = \frac{\left(\sqrt{\left(\frac{\tilde{C}_{eff}}{2\alpha K_{mono}}\right)^2 + 1} - \frac{\tilde{C}_{eff}}{2\alpha K_{mono}}\right)\left(1 - \frac{\tilde{C}_{eff}}{2\alpha K_{mono}}\right) + \frac{3}{2}}{\sqrt{\left(\frac{\tilde{C}_{eff}}{2\alpha K_{mono}}\right)^2 + 1} - \frac{\tilde{C}_{eff}}{2\alpha K_{mono}} + 1}, \quad (44)$$

$$IC_{50} = [L]_{50} + [L]_{bound,50} = K_{multi} + \psi [R]_0 , \quad (45)$$

where we note that that ψ is a coefficient that varies between 1 and 5/4. Similar to the results for monovalent receptor–ligand systems in Equation 34, the IC_{50} value becomes equivalent to the multivalent dissociation constant, in the limit of low receptor concentrations, i.e., for $[R]_0 << K_{multi}$:

$$IC_{50} \approx K_{multi} \; ; \text{if } [R]_0 \ll K_{multi} . \quad (46)$$

To compare monovalent and multivalent ligands we use the relative binding affinity (*RBA*), which we define as

$$RBA = \frac{K_{mono}}{2K_{multi}} . \quad (47)$$

Here, the factor 2 accounts for the valency of the ligand and ensures that the concentration of ligand units are compared. The larger the *RBA* the better is the divalent ligand. For *RBA* = 1 the same concentration of mono- and divalent ligand units, taking into account that a divalent ligand consist of two ligand units, is required to occupy half of the receptor binding pockets. For *RBA* < 1 the monovalent ligand binds better than the divalent ligand. In this case the loss in entropy of the spacer is larger than the gain in binding energy due to the multiple binding of ligand units. Inserting the effective concentration from Equation 13 and Equation 23 into Equation 41 and Equation 47, the *RBA* can be calculated for any given divalent ligand–receptor pair. As an example the *RBA* is depicted for different spacers and different values of K_{mono} in Figure 5. We here assume that the receptor is well described by a large, planar surface. Hence, the parameter α is approximated by 1/2 for stiff spacer and by Equation 29 for flexible spacers. In all cases we consider a divalent receptor with a distance d = 5 nm between the binding pockets. Each binding pocket has a binding range σ = 0.1 nm. In all three subfigures we see that if K_{mono} is too large, i.e., if the monovalent binder is too weak, the *RBA*-

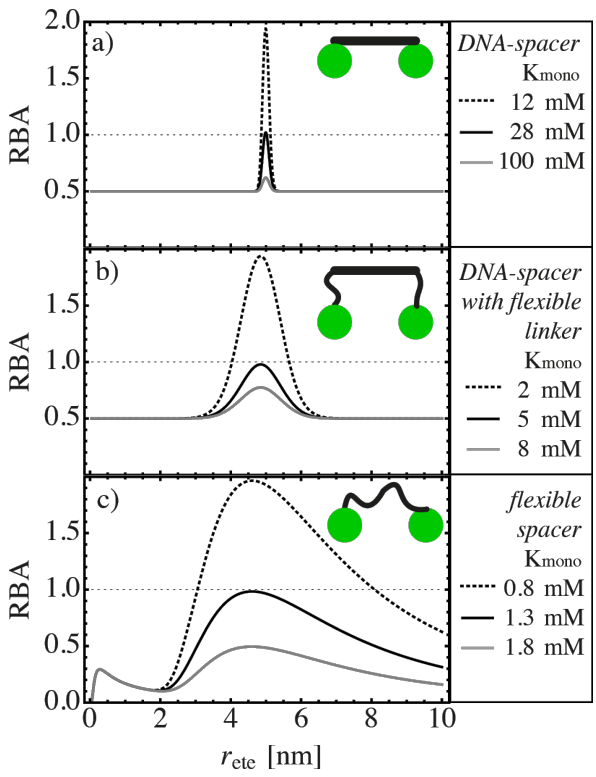

Figure 5: Relative binding affinity (*RBA*) of a divalent ligand in dependence of the end-to-end distance of the spacer r_{ete} from Equation 47. The three different ligand–spacer constructs are schematically depicted in the insets. The binding pockets are separated by d = 5 nm. Each binding pocket has a binding range of σ = 0.1 nm. (a) The ligand units are directly attached to a stiff DNA spacer, characterized by a persistence length l_p = 53 nm. (b) The ligand units are attached to a stiff DNA spacer with flexible linker chain, leading to an end-to-end distance fluctuation of Δr = 0.5 nm. (c) The ligand units are connected via a flexible spacer.

$$[L]_{bound} = 1\cdot[RL_1] + 2\cdot[RL_2] + 1\cdot[RL_3] = \left(1\cdot 4\cdot\alpha\frac{[L]}{K_{mono}} + 2\cdot 4\cdot\alpha^2\frac{[L]^2}{K_{mono}^2} + 1\cdot 2\cdot\frac{\tilde{C}_{eff}[L]}{K_{mono}^2}\right)[R]. \quad (43)$$

value never reaches 1. In such a situation, using the *RBA*-value as a quantifier, the monovalent ligand binds always better than the divalent ligand. Furthermore, at a certain K_{mono}, which we will further on denote as K^*_{mono}, there is exactly one spacer length, parameterized by r_{ete}, for which monovalent and divalent ligands bind equally well. If K_{mono} is lower than K^*_{mono}, there is a broader range of spacer lengths for which the divalent ligand binds better than the monovalent ligand (*RBA* > 1). In Figure 5a the behavior of a stiff spacer with persistence length l_p = 53 nm is depicted, which mimics a DNA spacer to which the ligand units are directly attached. A DNA spacer with a contour length of 5 nm exhibits fluctuations in the range $\Delta r \approx$ 0.05 nm, which is considerably smaller than the binding range σ. As is discussed in the previous section, the maximum and width of the effective concentration and therefore also the maximum and width of the *RBA* are in this case determined by the binding range σ. In Figure 5b we assume a DNA spacer that is decorated with flexible PEG linkers at both ends. The PEG linkers consist of four monomers each. Assuming Gaussian-chain behavior with a segment length of b = 0.38 nm [29], the fluctuations of the PEG linkers and hence the fluctuations of the whole ligand sum up to Δr = 0.5 nm. The shape of the *RBA* now is much broader, showing that the ligand is less affected by a mismatch between spacer length and distance between the binding pockets. Additionally, we obtain K^*_{mono} = 5 mM in Figure 5b which is considerably smaller than K^*_{mono} = 28 mM for the pure DNA spacer in Figure 5a. The same trend is continued in Figure 5c. The more flexible the spacer, the smaller is K^*_{mono}, indicating that flexible spacers are less suitable to improve the binding affinity of weak monovalent binders, even though they are more tolerant with respect to a mismatch between linker length and receptor distance.

To investigate the transition from *RBA* < 1 to *RBA* > 1 further, we determine the critical dissociation constant K^*_{mono} for which the *RBA* is equal to one for the optimized chain length, i.e., for the chain length that maximizes the *RBA* value. Using Equation 41 and Equation 47 it can easily be seen that K^*_{mono} relates to the effective concentration $\tilde{C}_{\text{eff}}(d)$ as

$$K^*_{\text{mono}} = \frac{1}{1-\alpha^2}\tilde{C}_{\text{eff}}(d). \tag{48}$$

In Figure 6, K^*_{mono} is shown for stiff as well as flexible ligands. The stiff ligand is considered to consist of a DNA spacer to which the ligand units are attached via two PEG linkers. Linker length and binding range are set to be identical to the example presented in Figure 5b. The average end-to-end distance of the DNA spacer is either chosen to be equal to d (black, continuous line), or is chosen to be too short by 0.7 nm, which mimics the length of two base pairs (red, continuous line). Even though the mismatch between spacer length and binding pocket distance is small, the ligand becomes significantly less efficient.

The flexible ligand is chosen to resemble a PEG spacer. Again, we assume Gaussian-chain behavior with a segment length of b = 0.38 nm. A ligand with optimized spacer length (black, dashed line) does not exhibit a significant difference to a ligand with a spacer that is shortened by two segments (red, dashed line). This shows again that a flexible chain is more tolerant with respect to a distance mismatch between inter-binding pocket distance d and chain length.

If the monovalent dissociation constant is larger than K^*_{mono}, a monovalent ligand always binds better than a divalent ligand. On the other hand, if the monovalent dissociation constant is smaller than K^*_{mono}, a divalent ligand of optimally (or slightly suboptimal) chosen size binds better than a monovalent ligand.

As can be seen in Figure 6, K^*_{mono} depends on the distance between the binding pockets as well as the spacer length and flexibility. In order to approximate an upper limit for K^*_{mono}, the maximum effective concentration (Equation 24 for a flexible spacer and Equation 15 and Equation 16 for a stiff spacer) is substituted into Equation 48:

$$\text{flexible spacer:}\quad K^*_{\text{mono}} \le \frac{1}{1-\alpha^2}\left(\frac{3}{2\pi d^2}\right)^{3/2} e^{-3/2}, \tag{49}$$

$$\text{stiff spacer:}\quad K^*_{\text{mono}} \le \begin{cases} \dfrac{1}{1-\alpha^2}\dfrac{1}{8\pi^2 d^2 \sigma} & ;\Delta r \ll \sigma \\ \dfrac{1}{1-\alpha^2}\dfrac{1}{2(2\pi)^{3/2} d^2 \Delta r} & ;\Delta r \gg \sigma \end{cases} \tag{50}$$

As an example that is relevant for medical applications we want to briefly discuss the interaction between hemagglutinin (HA), a receptor protein on the surface of influenza viruses, and its ligand sialic acid (SA). The dissociation constant between monomeric SA and trimeric HA is known to be 2.5 mM [1]. Furthermore, the crystal structure of HA [30] indicates a distance between neighboring binding pockets in the range of d = 5 nm. Note that HA is a trivalent receptor, which means that additional binding modes as well as different numbers of permutations (see Figure 1b) have to be considered. Nevertheless, since the efficiency of a divalent ligand is mainly influenced by the effective concentration $\tilde{C}_{\text{eff}}$ and the monovalent dissociation constant K_{mono}, rather than by the number of binding modes, we can compare the values for the SA–HA pair

with the results presented in Figure 6. We see that a divalent ligand consisting of two SA units connected via a PEG spacer is expected to bind less efficient than the monovalent SA. In contrast, a stiff DNA spacer can increase the binding affinity of the divalent ligand compared to the monovalent ligand, if its length is optimized.

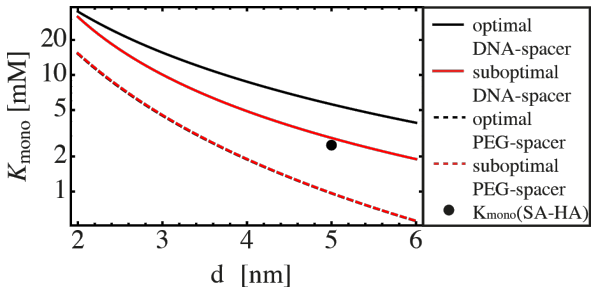

Figure 6: Efficiency diagram: K^*_{mono} is shown for different ligand–spacer constructs. If the monovalent dissociation constant is larger than K^*_{mono}, a monovalent ligand always binds better than a divalent ligand. If, on the other hand, the monovalent dissociation constant is smaller than K^*_{mono}, a divalent ligand of suitably chosen length binds better than its monovalent counterpart. We present K^*_{mono} in dependence of the distance between the binding pockets for a DNA spacer with flexible PEG linkers (Δr = 0.5 nm). In the optimal case, the spacer length is chosen equal to the distance d (black, continuous line). In the slightly suboptimal case, the spacer length is chosen to be 0.7 nm (two base pairs) shorter than the distance d (red, continuous line). In both cases the binding range is set to σ = 0.1 nm. We also show K^*_{mono} for a flexible PEG spacer with optimized spacer length (black, dashed line) and a spacer that is two monomers shorter (≈0.76 nm) (red, dashed line). The monovalent dissociation constant K^*_{mono} as well as the distance between neighboring binding pockets for a SA–HA pair is indicated by a black point.

Conclusion

In the present work we first examine different polymeric models for the effective concentration. We find that a worm-like-chain model can be well reproduced by a simple harmonic spring model and a Gaussian-chain model with suitable chosen parameters, in the stiff and flexible limits, respectively. We next study the binding between divalent ligand–receptor pairs. We find that multivalency increases the overall binding affinity only, if the monovalent ligand–receptor pair binds strongly enough, i.e.; if the monovalent dissociation constant is smaller than a critical value K^*_{mono}. Approximations for K^*_{mono} for both flexible and stiff ligands are derived in dependence of the distance between the binding pockets and the spacer length and flexibility. For the optimal ligand design, we find that for stiff ligands the average end-to-end distance should be equal to the distance between the binding pockets and the average fluctuations should be of the order, but not smaller, than the binding range. The average end-to-end distance of a flexible ligand on the other side should be smaller by a factor of $\sqrt{8/(3\pi)}$ than the binding pocket distance d.

Supporting Information

Supporting Information File 1

Detailed derivation of the dissociation constants for three different binding modes of a divalent ligand.
[http://www.beilstein-journals.org/bjoc/content/supplementary/1860-5397-11-90-S1.pdf]

Acknowledgements

This contribution was generously supported by the Deutsche Forschungsgemeinschaft DFG via grant SFB 765.

References

1. Mammen, M.; Choi, S.-K.; Whitesides, G. M. *Angew. Chem., Int. Ed.* **1998,** *37,* 2754–2794. doi:10.1002/(SICI)1521-3773(19981102)37:20<2754::AID-ANIE2754>3.0.CO;2-3
2. Kiessling, L. L.; Young, T.; Mortell, K. H. Multivalency in Protein–Carbohydrate Recognition. In *Glycoscience – Chemistry and Chemical Biology;* Fraser-Reid, B. O.; Tatsuka, K.; Thiem, J., Eds.; Springer: Berlin, Germany, 2001; pp 1817–1861. doi:10.1007/978-3-642-56874-9_42
3. Pieters, R. J. *Org. Biomol. Chem.* **2009,** *7,* 2013–2025. doi:10.1039/b901828j
4. Disney, M. D.; Zheng, J.; Swager, T. M.; Seeberger, P. H. *J. Am. Chem. Soc.* **2004,** *126,* 13343–13346. doi:10.1021/ja047936i
5. Wang, J.; Tian, S.; Petros, R. A.; Napier, M. E.; DeSimone, J. M. *J. Am. Chem. Soc.* **2010,** *132,* 11306–11313. doi:10.1021/ja1043177
6. Schaschke, N.; Matschiner, G.; Zettl, F.; Marquardt, U.; Bergner, A.; Bode, W.; Sommerhoff, C. P.; Moroder, L. *Chem. Biol.* **2001,** *8,* 313–327. doi:10.1016/S1074-5521(01)00011-4
7. Vance, D.; Shah, M.; Joshi, A.; Kane, R. S. *Biotechnol. Bioeng.* **2008,** *101,* 429–434. doi:10.1002/bit.22056
8. Martinez-Veracoechea, F. J.; Frenkel, D. *Proc. Natl. Acad. Sci. U. S. A.* **2011,** *108,* 10963–10968. doi:10.1073/pnas.1105351108
9. Hu, J.; Lipowsky, R.; Weikl, T. R. *Proc. Natl. Acad. Sci. U. S. A.* **2013,** *110,* 15283–15288. doi:10.1073/pnas.1305766110
10. Wang, S.; Dormidontova, E. E. *Phys. Rev. Lett.* **2012,** *109,* 238102. doi:10.1103/PhysRevLett.109.238102
11. Diestler, D. J.; Knapp, E. W. *J. Phys. Chem. A* **2010,** *114,* 5287–5304. doi:10.1021/jp100077n
12. Weber, M.; Bujotzek, A.; Haag, R. *J. Chem. Phys.* **2012,** *137,* 054111. doi:10.1063/1.4739501
13. Huskens, J.; Mulder, A.; Auletta, T.; Nijhius, C. A.; Ludden, M. J. W.; Reinhoudt, D. N. *J. Am. Chem. Soc.* **2004,** *126,* 6784–6797. doi:10.1021/ja049085k
14. Varilly, P.; Angioletti-Uberti, S.; Mognetti, B. M.; Frenkel, D. *J. Chem. Phys.* **2012,** *137,* 094108. doi:10.1063/1.4748100
15. Angioletti-Uberti, S.; Varilly, P.; Mognetti, B. M.; Tkachenko, A. V.; Frenkel, D. *J. Chem. Phys.* **2013,** *138,* 021102. doi:10.1063/1.4775806
16. Pertici, F.; de Mol, N. J.; Kemmink, J. M.; Pieters, R. J. *Chem. – Eur. J.* **2013,** *19,* 16923–16927. doi:10.1002/chem.201303463
17. Mack, E. T.; Snyder, P. W.; Perez-Castillejos, R.; Bilgiçer, B.; Moustakes, D. T.; Butte, M. J.; Whitesides, G. M. *J. Am. Chem. Soc.* **2012,** *134,* 333–345. doi:10.1021/ja2073033

18. Shan, M.; Bujotzek, A.; Abendroth, F.; Wellner, A.; Gust, R.; Seitz, O.; Weber, M.; Haag, R. *ChemBioChem* **2011,** *12,* 2587–2598. doi:10.1002/cbic.201100529
19. Scheibe, C.; Bujotzek, A.; Dernedde, J.; Weber, M.; Seitz, O. *Chem. Sci.* **2011,** *2,* 770–775. doi:10.1039/c0sc00565g
20. Krishnamurthy, V. M.; Estroff, L. A.; Whitesides, G. M. Multivalency in Ligand Design. In *Fragment-based Approaches in Drug Design;* Jahnke, W.; Erlanson, D. A., Eds.; Wiley-VCH: Weinheim, Germany, 2006; pp 11–53. doi:10.1002/3527608761.ch2
21. Samuel, J.; Sinha, S. *Phys. Rev. E* **2002,** *66,* 050801. doi:10.1103/PhysRevE.66.050801
22. MacKintosh, F. C.; Käs, J.; Janmey, P. A. *Phys. Rev. Lett.* **1995,** *75,* 4425–4428. doi:10.1103/PhysRevLett.75.4425
23. Kienberger, F.; Pastushenko, V. P.; Kada, G.; Gruber, H. J.; Riener, C.; Schindler, H.; Hinterdorfer, P. *Single Mol.* **2000,** *1,* 123–128. doi:10.1002/1438-5171(200006)1:2<123::AID-SIMO123>3.0.CO;2-3
24. Gargano, J. M.; Ngo, T.; Kim, J. Y.; Acheson, D. W. K.; Lees, W. J. *J. Am. Chem. Soc.* **2001,** *123,* 12909–12910. doi:10.1021/ja016305a
25. Shoichet, B. K. *J. Med. Chem.* **2006,** *49,* 7274. doi:10.1021/jm061103g
26. Hulme, E. C. *Receptor–Ligand Interactions A Practical Approach;* Oxford University Press: Oxford, United Kingdom, 1992.
27. Zeng, S.; Baillargeat, D.; Ho, H.-P.; Yong, K.-T. *Chem. Soc. Rev.* **2014,** *43,* 3426–3452. doi:10.1039/c3cs60479a
28. Hirst, G. K. *J. Exp. Med.* **1942,** *75,* 49–64. doi:10.1084/jem.75.1.49
29. Oesterhelt, F.; Rief, M.; Gaub, H. E. *New J. Phys.* **1999,** *1,* 6. doi:10.1088/1367-2630/1/1/006
30. Sauter, N. K.; Hanson, J. E.; Glick, G. D.; Brown, J. H.; Crowther, R. L.; Park, S. J.; Skehel, J. J.; Wiley, D. C. *Biochemistry* **1992,** *31,* 9609–9621. doi:10.1021/bi00155a013

License and Terms

BEILSTEIN JOURNAL OF ORGANIC CHEMISTRY

Mechanical stability of bivalent transition metal complexes analyzed by single-molecule force spectroscopy

Manuel Gensler[1], Christian Eidamshaus[2], Maurice Taszarek[2], Hans-Ulrich Reissig[2] and Jürgen P. Rabe[*1]

Full Research Paper

Open Access

Address:
[1]Department of Physics & IRIS Adlershof, Humboldt-Universität zu Berlin, Newtonstr. 15, D-12489 Berlin, Germany and [2]Institut für Chemie und Biochemie, Freie Universität Berlin, Takustr. 3, D-14195 Berlin, Germany

Email:
Jürgen P. Rabe[*] - rabe@physik.hu-berlin.de

* Corresponding author

Keywords:
molecular rupture mechanism; multivalency; malleability; pyridine coordination compounds; scanning force microscopy

Beilstein J. Org. Chem. **2015,** *11,* 817–827.
doi:10.3762/bjoc.11.91

Received: 15 March 2015
Accepted: 06 May 2015
Published: 15 May 2015

This article is part of the Thematic Series "Multivalency as a chemical organization and action principle".

Guest Editor: R. Haag

Abstract

Multivalent biomolecular interactions allow for a balanced interplay of mechanical stability and malleability, and nature makes widely use of it. For instance, systems of similar thermal stability may have very different rupture forces. Thus it is of paramount interest to study and understand the mechanical properties of multivalent systems through well-characterized model systems. We analyzed the rupture behavior of three different bivalent pyridine coordination complexes with Cu^{2+} in aqueous environment by single-molecule force spectroscopy. Those complexes share the same supramolecular interaction leading to similar thermal off-rates in the range of 0.09 and 0.36 s^{-1}, compared to 1.7 s^{-1} for the monovalent complex. On the other hand, the backbones exhibit different flexibility, and we determined a broad range of rupture lengths between 0.3 and 1.1 nm, with higher most-probable rupture forces for the stiffer backbones. Interestingly, the medium-flexible connection has the highest rupture forces, whereas the ligands with highest and lowest rigidity seem to be prone to consecutive bond rupture. The presented approach allows separating bond and backbone effects in multivalent model systems.

Introduction

In a multivalent molecular system, two partners interact with each other through two or more non-covalent equivalent interaction centers. This principle is important in biochemistry [1] and supramolecular chemistry [2], but still not fully understood on the level of individual non-covalent interactions [3]. Synthetic supramolecular systems are ideal for a quantitative analysis of multivalency on the level of single molecules, because specific ligand design can be used to study selected parameters [4,5].

The mechanical stability of a molecular system is characterized by its rupture forces under a given loading rate. Malleability

describes the ability of a protein complex or bond to deform without being disrupted and is characterized by the rupture length r_b [6]. In natural environments, hydrodynamic effects may cause forces competing with biomolecular interactions, such as the leukocyte adhesion to endothelial cells [7] or the *Escherichia coli* adhesion to uroepithelium cells [8]. The latter has been well analyzed by single-molecule force spectroscopy [9], showing unfolding of a very malleable, helical PapA-domain in p-pili, which plays an important role for the adhesion. This process consumes a large amount of energy, whilst adhesion forces are kept at a low force of 27 pN, in order not to break the adhesive glycolipid–ligand interaction. In contrast, cellulosome–adhesion complexes tighten under load, leading to rupture forces of 600–750 pN, one of the strongest biomolecular interactions discovered until now [10]. Another fascinating biological example is the von Willebrand factor, where nature utilizes shear forces on an ultra large protein as self-regulative mechanism. This protein is activated by hydrodynamic forces occurring in injured blood vessels to promote hemostasis [11]. Mechanical stabilities are also of growing interest for the design of biomaterials mimicking the muscle protein titin [12,13] and smart polymers including latent catalysts for self-healing, mechanochroism or mechanoluminescence [14].

The thermal stability of a molecular system is inversely proportional to the thermal off-rate. However, this alone gives an incomplete image of bond rupture under physiological conditions. For example, depending on the direction of applied forces, the green fluorescent protein shows most-probable rupture forces between 100 pN and 550 pN at pulling speeds of 2 μm/s, but only one thermal pathway of denaturation [15]. Also the mechanical stability of the titin-telethonin complex is highly directed [16]. Instead molecular interactions in biological systems are characterized by a balanced interplay between mechanical stability and malleability. Already in 1999 Rief et al. compared the mechanical stability of the α-helical domain spectrin with refolding forces from domain I27 of the muscle protein titin in β-sheet conformation. While rupture lengths increased from 0.3 nm for titin to 1.5 nm for spectrin, the corresponding rupture forces decreased by the same ratio [17]. In 2007 it was still not clear, whether this interplay follows a linear or non-linear power law [18]. Only recently more experimental data became accessible and in 2013 Hoffmann et al. found an inverse proportional power law [6]. The rupture lengths of proteins range from 0.14 to 2 nm, while proteins with low malleability exhibit higher mechanical stability and vice versa. Then different domains of malleability were successfully attributed to mechanical clamp motifs, as suggested by Sikora et al. [19]. For example, zipper-type unfolding requires less force than shear-type denaturation. However due to the high complexity of biological multivalent interactions less is known about the influence from individual non-covalent interactions. Here, well defined model systems with known valency are valuable tools to be studied by single-molecule force spectroscopy (SMFS).

In SMFS experiments a modified probe – an optical tweezers bead or an SFM cantilever – is used to measure interaction forces with modified synthetic or biological surfaces. The distribution of interaction forces is a measure for mechanical stability. Polymeric spacers are used to detect non-specific interactions and simultaneous bond rupture. In dynamic force spectroscopy (DFS) most-probable rupture forces are measured for various pulling speeds and analyzed according to the Kramers–Bell–Evans (KBE) model, finally giving the rupture length r_b and the thermal off-rate k_{off} (a measure of the inverse thermal stability) [20-22]. This method is especially useful in the case of interactions with low affinity of low yield that are inaccessible for ensemble measurements. For example in 2009 Wollschläger et al. successfully detected a different binding of DNA to the corresponding domain in the transcription factor PhoB from *Escherichia coli* for the wild-type and slightly modified mutants [23]. Utilizing the sequential unzipping of transmembrane proteins, a full mechanical mapping was possible for the β_2-adrenergic receptor [24] and rhodopsin [25]. On the field of supramolecular model systems DFS revealed the mechanical stability of coordination bonds [26-28], host–guest systems [29-32], and rotaxanes [33].

In 2008 Guzman et al. analyzed hydrogen bonds of 4H, 6H and 8H chains in toluene as model for β-sheet force clamps. They suggested that the force is transferred evenly to each hydrogen bond, giving 15 pN at a pulling speed of 200 nm/s [34]. In contrast equilibrium constants of tetravalent hydrogen bonds in chloroform are strongly dependent on arrays of donor (D) and acceptor (A) sites due to cooperative effects. Thus DAD-ADA pairs are thermally weaker than DDD-AAA complexes [35]. In 2011 Embrechts et al. showed that such cooperative effects also influences the mechanical stability of tetravalent interactions [36]. They performed DFS on UAT dimers (DADA–ADAD pairs) with UPy dimers (DDAA–AADD pairs) in hexadecane. The UPy dimers exhibit shorter rupture lengths of 0.20 nm compared to 0.29 nm, resulting in much higher rupture forces from 150 to 250 pN compared to 50–100 pN for UAT dimers. Another model system probing π–π-interactions associated with van-der-Waals forces and possible hydrophobic interactions was published in 2009 by Zhang et al. [37]. They compared the monovalent interaction of a porphyrin ligand to a C_{60} fullerene with the bivalent interaction of two ligands to one C_{60} (pincer complex) in aqueous environment. Thereby the rupture length decreased from 0.31 nm to 0.20 nm, leading to an increase in rupture forces. In contrast we recently found a model system

with the opposite effect [27]. The bivalent interaction of a pyridine nanorod **2a** with Cu^{2+} showed a much longer rupture length of 0.51 nm compared to 0.33 nm for the monovalent interaction **1** in aqueous solutions of $CuSO_4$ (Figure 1). As a result, rupture forces of both valencies were similar. Combining DFS with ab-initio calculations we suggested a stepwise bond-rupture including a hydrogen-bound intermediate. Thus in our system the bivalent effect did not increase the mechanical stability, but the malleability of the interaction.

In the present work we address the question, if it is possible to tune the balanced interplay between most-probable rupture forces and rupture lengths by changing the backbone connection of the pyridine model system into more flexible analogues. By performing DFS according to the KBE model we show that the rupture length may be similar to the monovalent rupture length for the system with medium flexibility **2b** (2 sp^3 carbons in the backbone, r_b = 0.30 nm) and even larger for the system with high flexibility **2c** (3 sp^3 carbons + 2 ether groups in the backbone, r_b = 1.12 nm). Consequently, the interaction of **2b** exhibits higher mechanical stability, but the interaction of **2c** exhibits even less mechanical stability than the monovalent interaction for the whole accessible range of pulling speeds. We will discuss possible mechanisms of simultaneous and successive bond rupture.

Results and Discussion

Regarding the synthesis, pyridine nanorod **3**, which was also precursor for the synthesis of complex **2a** [27], was hydrogenated to receive intermediate **4** (Scheme 1). Subsequent coupling with bifunctional poly(ethylene glycol) (PEG) and purification by dialysis gave compound **5** – the ligand of coordination complex **2b**. The synthesis of compound **10** – the ligand of coordination complex **2c** – started by nucleophilic aromatic substitution of fluorinated pyridine **7** with compound **6** to receive a mixture of products **8** and **9** (Scheme 2). Purified com-

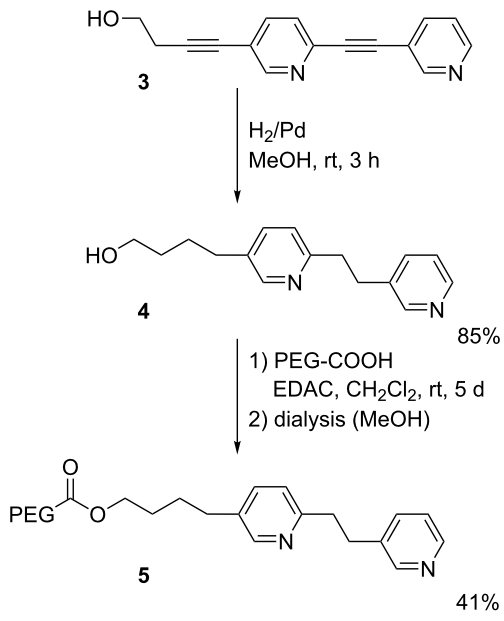

Scheme 1: Synthesis of pyridine-PEG conjugate **5**.

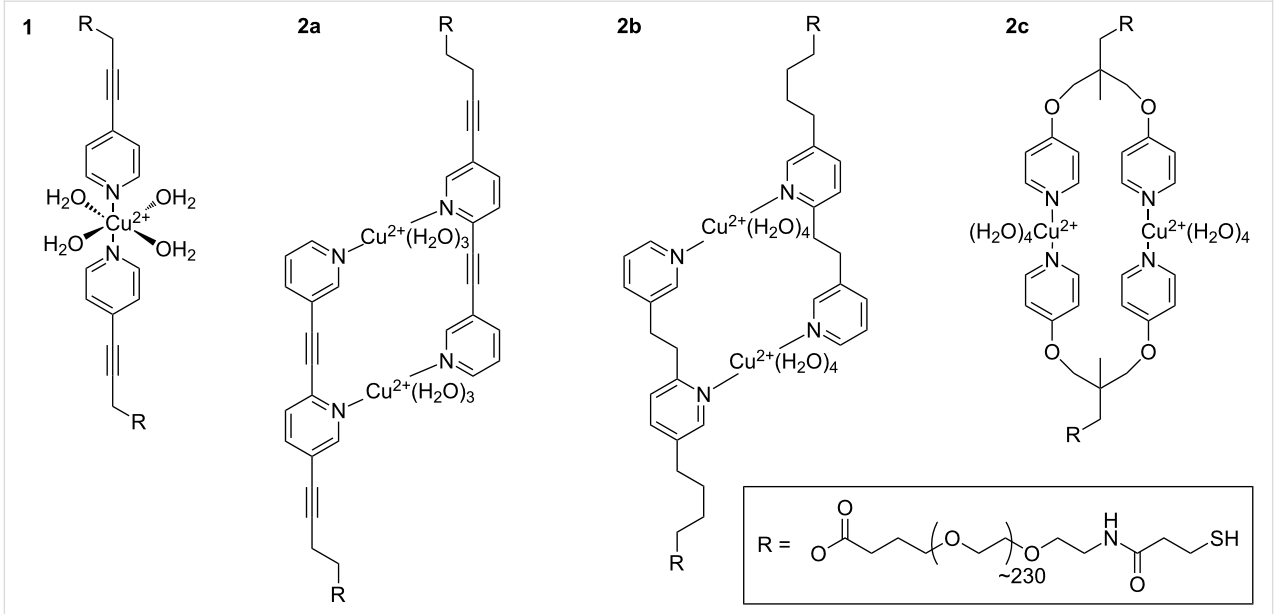

Figure 1: Expected coordination complexes of monovalent and bivalent structures (**1** and **2a–c**, respectively) with copper ions in aqueous solution. The octahedral conformation of **1** with additional water ligands was suggested by ab-initio calculations [27]. For **2a** a quasi-octahedral configuration was calculated with only three water ligands per Cu^{2+} due to steric reasons [27]. Schemes for **2b** and **2c** are suggested accordingly.

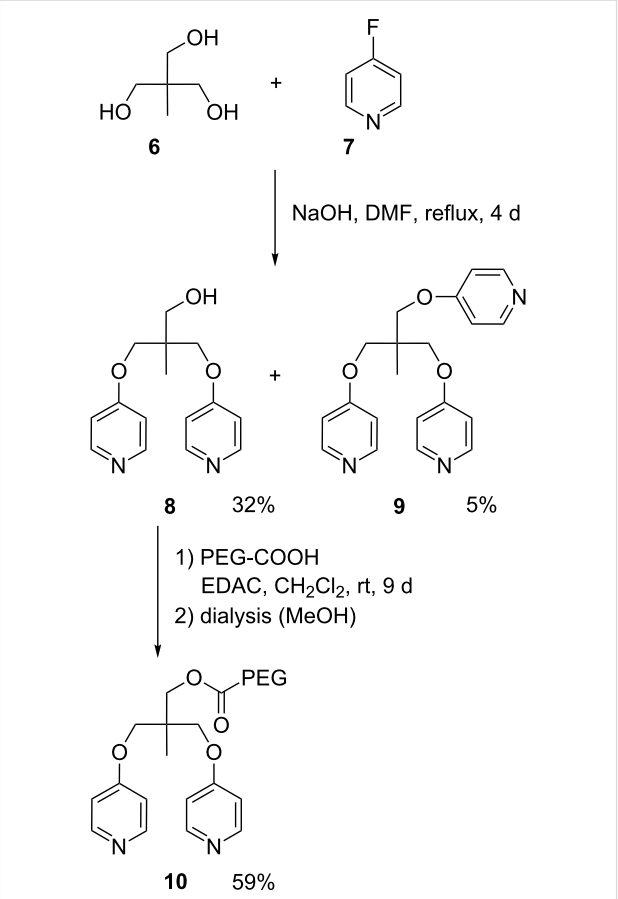

Scheme 2: Synthesis of pyridine-PEG conjugate **10**.

pound **8** was then coupled with bifunctional PEG as written above.

Figure 1 shows the expected coordination complexes of our mono- and bivalent model systems with Cu^{2+} in aqueous solution. In the present work, we analyzed the bivalent systems **2b** and **2c** by DFS, similarly as for the recently published reference case of **2a** [27]. We modified gold coated SFM cantilever probes and surfaces using thiol chemistry (for details see Experimental section below). The interaction between gold and SH-groups is known to withstand rupture forces in the range of 1 to 2 nN [38], followed by the formation of a monoatomic gold nanowire that finally leads to a breakage of gold–gold bonds [39]. The rupture forces of our systems were one order of magnitude smaller, enabling repeated measurements of typically 1000 times per data point without tearing molecules off the SFM cantilever probe. The experimental setup is sketched in Figure 2a, where a bivalent complex of **2b** has already formed during a variable contact time between cantilever and sample. By retracting the sample from the cantilever, the same force is applied to the transition metal complex and the calibrated cantilever spring. Due to the finite size of a scanning force microscope (SFM) cantilever tip, there is also a certain possibility of simultaneous bond formation as shown in Figure 2b, or non-specific interactions directly between tip and surface. For a proper detection of single-molecular events, we utilized PEG chains with a well characterized force-extension behavior [40,41], resulting in a saw tooth signal at sufficiently high tip-sample-separation (Figure 2c, top). Of each force-distance experiment, only the last peak was selected, if it showed the characteristics of a PEG chain and a starting value lower than 6 times the root-mean-square (rms) thermal background noise (dashed line). The latter is important to ensure a proper application of the KBE model. For DFS, measurements have to be performed over a broad range of pulling speeds, resulting in various loading rates (dF/dt) as illustrated in the bottom of Figure 2c.

A simultaneous bond rupture of the system as sketched in Figure 2b would be that of a bivalent system as well. However in contrast to bipyridines **2a**–**2c**, the entropic elasticity of the spring would instantaneously pull away the first bond that is broken, making rebinding effects impossible [42]. Thus rupture forces in such cases are additive [43].

In this study we aimed at detailed information on the rupture behavior of the model systems described above. We utilized the frequently employed KBE model [20-22] to calculate rupture length r_b (a measure of malleability) and k_{off} (a measure of the inverse thermal stability). The model makes some assumptions to a hypothetical potential energy diagram (PED) along the rupture coordinate z (Figure 3). Starting from a bound state 0, a certain activation energy E_A is needed to escape over transition state I. Under an applied force, f, the whole PED is tilted by $\Delta E = -f\,\Delta z$, where Δz is the distance from state 0. As a consequence the potential wall of the transition state I is lowered by $\Delta E = -f\,r_{b,I}$ and the probability of bond rupture is increased. In a SMFS experiment, the force is increased by a certain loading rate, proportional to the pulling speed, and faster loading rates lead to higher average rupture forces. Systems with successive bond rupture have a second transition state II with higher rupture length $r_{b,II}$. If II is of higher energy than I, it is the dominant transition state and rupture is much more sensitive to forces.

Under the assumption of a constant loading rate, the KBE model can be solved analytically resulting in Equation 1, where k_B is the Boltzmann constant and T the absolute temperature. A good derivation of Equation 1 and comparison with non-constant loading rate can be found in [44]. Note that the value of k_{off} describes the thermal off-rate along the mechanical reaction coordinate. Especially in complex systems, other dissociation paths with different thermal off-rate are possible.

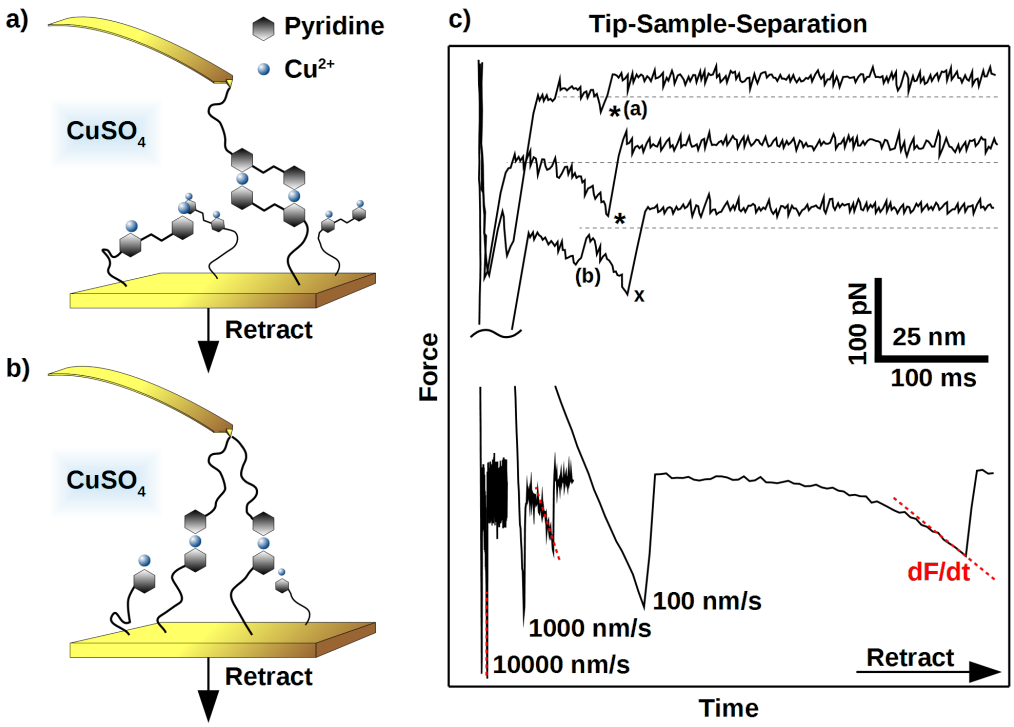

Figure 2: Principle of the SMFS experiment. During retraction of the sample, possible interactions are probed by bending of the calibrated SFM cantilever. a) In a single-molecule rupture event, only one mono- or bivalent ligand is responsible for the last rupture event. b) Possible simultaneous bonds, leading to multiple peaks in force–distance plots. c) Examples of force–retract behavior, plotted against tip–sample-separation (top) or experimental time frame (bottom). Signals marked with x are attributed to simultaneous bond rupture and were discarded. Dashed red lines show the loading rate dF/dt, strongly increasing from slow to fast pulling speeds (100 to 10000 nm/s). Plots are shifted for clarity.

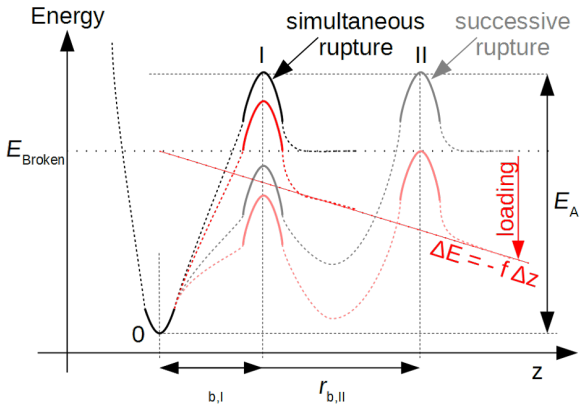

Figure 3: Potential energy diagrams according to the KBE model for simultaneous and successive bond rupture are only characterized by a bound state 0, and one dominant sharp transition state I or II. Loading of a bond deforms the potential energy along the rupture coordinate z according to ΔE, thereby reducing activation energy E_A and increasing force-driven rupture $k_{off}(f)$.

$$f^*\left(\frac{dF}{dt}\right)=\left(\frac{k_BT}{r_b}\right)\ln\left(\frac{dF}{dt}\right)+\left(\frac{k_BT}{r_b}\right)\ln\left(\frac{r_b}{k_{off}k_BT}\right) \quad (1)$$

If experimental results of a DFS experiment show a linear behavior of most probable rupture forces f^* with $\ln(dF/dt)$ (Figure 4), the KBE model may be applied. Then the slope is a measure of the inverse rupture length r_b and the x-intercept a measure of k_{off}. Two linear regimes denote a change in two dominant transition states [45], a non-linear behavior may be due to a more complex PED [46]. A drawback of this method is the reduction of all measured rupture forces to one most-probable force value. Some groups expanded the KBE model to directly fit the whole data set, taking bond heterogeneity [47] or a temperature dependent Arrhenius prefactor into account [48,49]. We thoroughly applied the first mentioned model to our results as well, but did not obtain consistent results. This may be partially due to the fact that the π–π-stacking of pyridines [50] was a competing interaction. The most probable rupture force, used in the KBE model, was due to the coordination complexes. Methods using the whole data set are strongly influenced by the stacking interaction and would have needed heavily time consuming adaption for a proper fit of our data. This was beyond the scope of this work.

Both bivalent systems analyzed in this study could be described by the linear KBE model fit (Figure 4, Table 1). System **2b**

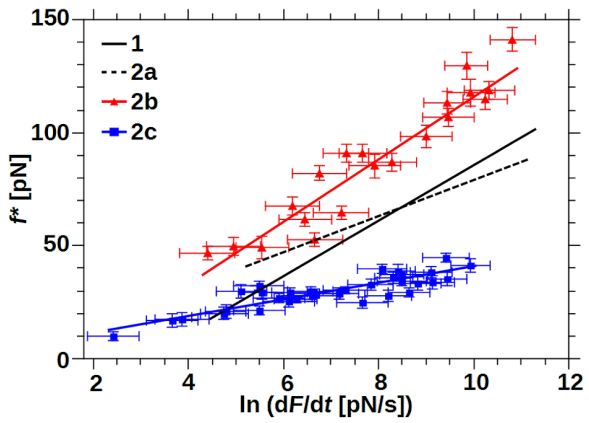

Figure 4: Most probable rupture forces plotted over their corresponding loading rate. Each point denotes for one series of measurements at a certain pulling speed. Error bars: f^* – standard error of rupture force histogram, ln(dF/dt) – average loading rate error of all rupture events in the range of f^*. KBE fits are shown according to Equation 1, black lines according to [27].

exhibited the highest rupture forces over the whole range of measured loading rates. The slope was similar to the monovalent interaction of **1**, resulting in similar rupture lengths. In contrast, rupture forces of system **2c** were smaller than the values for **2a** and **2b** and even lower compared to the monovalent interaction of **1** at loading rates larger than ln(dF/dt) = 5. The flat slope of system **2c** resulted in the largest rupture length of all systems analyzed. System **2a** analyzed previously had a medium-slope and crossed the x-axis at a similar loading rate to system **2c**, giving similar thermal off-rates.

Table 1: KBE model fit results for systems **2b** and **2c**, analyzed in this work, compared with values for **1** and **2a** from [27].

	r_b [nm]	k_{off} [s^{-1}]
1 [27]	0.33 ± 0.01	1.7 ± 0.2
2a [27]	0.51 ± 0.03	0.14 ± 0.06
2b	0.30 ± 0.01	0.36 ± 0.07
2c	1.12 ± 0.07	0.09 ± 0.04

The rupture lengths of systems **1** and **2a** are surprisingly high for interactions on the single-molecular level. For example, a Pd^{2+} pincer complex with two different pyridine ligands shows rupture lengths around 0.2 nm in DMSO [28]. Using ab-initio calculations we could show that a hydrogen-bound intermediate state stabilizes the interaction over a longer distance [27]. In this case, a water molecule from the solvent jumps into the pyridine–Cu^{2+} interaction. Thus we assume a similar dissociation process for **2b** and **2c**. In DMSO such an effect is not possible and the single transition state around 0.2 nm is rate determining. Unfortunately $CuSO_4$ is insoluble in DMSO, preventing corresponding experiments on our systems.

The medium-flexible bipyridine **2b** interacts with a similar rupture length as the monovalent system, but the thermal off-rate is significantly smaller and comparable to system **2a**. Therefore a different supramolecular complex with higher mechanical stability and lower thermal off-rate has been formed. We propose a bivalent interaction similar to the known complex **2a** as shown in Figure 1. From a PED point of view, this behavior is described either by a simultaneous bond rupture as shown in Figure 3, I, or by a successive rupture process (Figure 3, II) where the first transition state is rate dominating. However the KBE model fit for the stepwise process would only extrapolate to the thermal off-rate of the first transition state, gaining the value for a monovalent interaction. Thus in the following discussions we will suggest a simultaneous rupture.

The lower thermal off-rate of the flexible pyridine **2c** compared to **1** also indicates a bivalent interaction. In contrast to **2b**, the rupture length is much larger and we suggest a stepwise bond rupture such as PED II in Figure 3. Still the rupture length of 1.12 nm is too large to be described by the known hydrogen-bound intermediate alone. A possible explanation is the release of geometrical folding after breakage of the first bond. A purely geometrical molecular mechanics estimation of a possible ortho-complex of both Cu^{2+} metal centers results in a 0.61 nm length increase after rupture of the first bond due to the applied strain (Figure 5). The maximum velocity in the DFS experiment is very slow on the atomic length scale, thus the remaining complex could also switch to para-configuration. After additional 0.33 nm rupture length for a monovalent interaction, an overall rupture length around 0.94 nm would be gained by the KBE model. This value is already close to the experimentally observed length.

The mechanical stability, namely the most probable rupture force f^*, of a system that follows the KBE model strongly depends on the applied loading rate. Two interactions with different rupture length may have a crossing of their force-loading-rate behavior. If the intersection is outside the experimental accessible area, a ranking of mechanical stability can still lead to a deeper understanding of the rupture behavior and will be discussed in the following [6,18]. We have chosen a medium loading rate of ln(dF/dt) = 8.5 that is just at the crossing of **1** and **2a**, emphasizing their similar forces over the whole range of experimental loading rates. Also **2b** has the largest and **2c** the smallest rupture forces of all results at this loading rate, reflecting their overall behavior. Figure 6 shows the most probable rupture forces at this loading rate in relation-

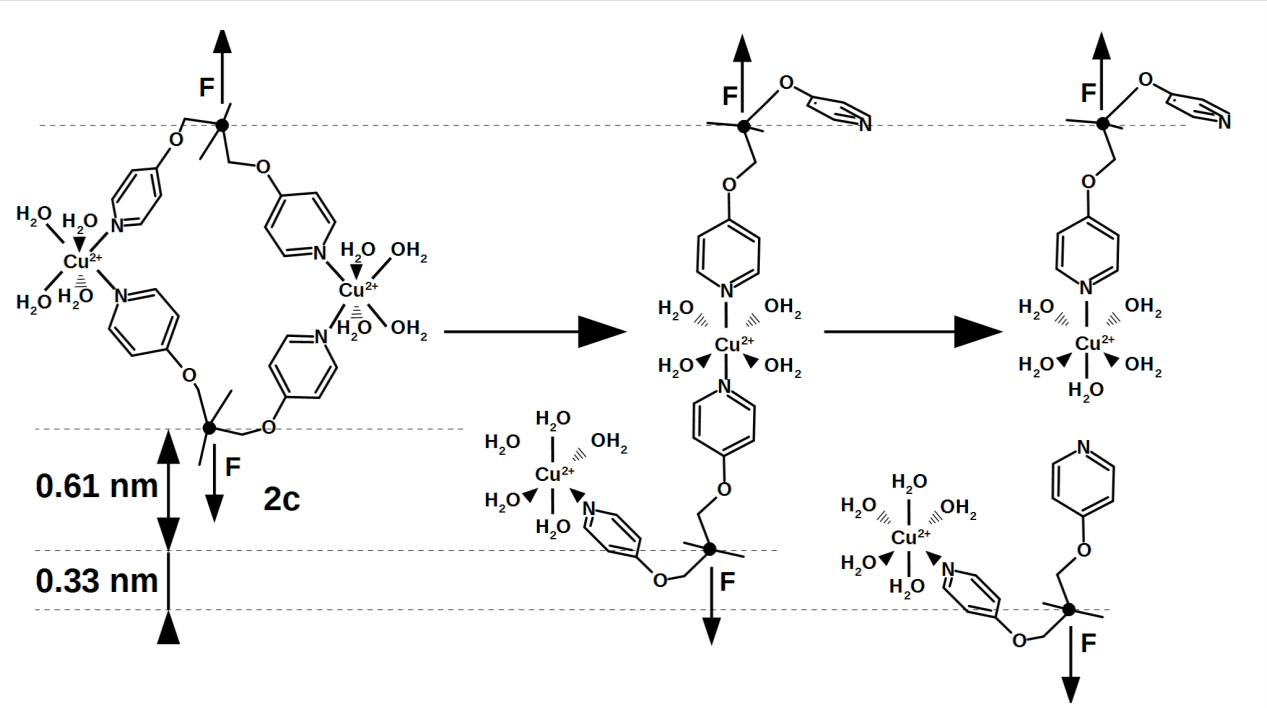

Figure 5: Possible rupture mechanism describing the extraordinary long rupture length of system **2c**. Starting from an ortho-configuration, the first bond rupture leads to an increased distance between both force-points (emphasized by force vector arrows). The second jump is attributed to a hydrogen-bound intermediate found in the monovalent rupture process. Structures were calculated using the molecular mechanics tool based on CHARMM force fields included in ChemSketch (v 14.01, ACD/Labs, Toronto, Canada).

ship to their rupture length r_b. The plot also includes the expected balance between r_b (malleability) and f^* (mechanical stability) over five orders of magnitude in thermal off-rate, according to the KBE model Equation 1. Especially in the high-force and high malleable regimes those "isoenergetic" lines are close by, due to their logarithmic influence. Thus an interaction would need a very small thermal off-rate to combine, for example, malleability and mechanical stability. On the other hand a mechanically very stable system with average thermal off-rate may be gained by a reduction of the rupture length. Such an example was recently published for the cellulosome-adhesion complex, where the force-shielding subdomain XMod drops the rupture length from 0.19 nm to 0.13 nm and decreases the thermal off-rate by three orders of magnitude to finally raise the rupture forces from 280 pN to 610 pN at $\ln(dF/dt) = 8.5$ [10]. On the single-molecular level, the interaction between Zn-porphyrine and C_{60} fullerenes shows a similar trend comparing their monovalent and bivalent interaction [37]. The latter has a shorter rupture length, lower thermal off-rate and consequently higher most probable rupture forces. In contrast our measurements on three bivalent model systems with similar coordination complexes and thus similar thermal off-rates showed a new possible trend for system **2c**. Here, the rupture length increase overcompensated the gain in mechanical stability, leading to even lower rupture forces for loading rates down to $\ln(dF/dt) = 5$ (see also Figure 4). System **2b** with medium flexibility showed the trend, already known for other systems [30].

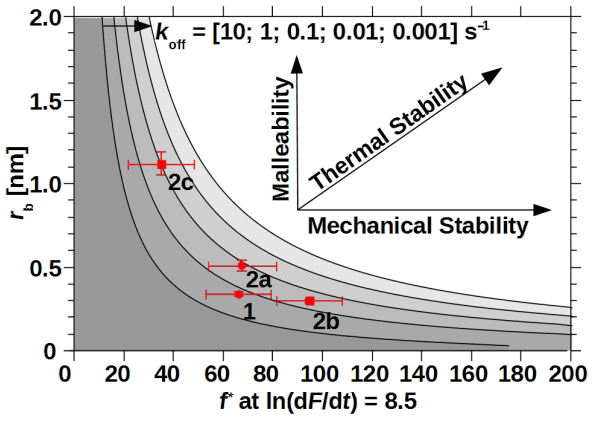

Figure 6: Most probable rupture forces at a logarithmic loading rate of 8.5 in relation to the corresponding rupture lengths of monovalent and all three bivalent interactions. Continuous lines denote for numerically calculated rupture lengths, according to the KBE model (Equation 1) for exponentially decreasing thermal off-rates. Circles: data from [27]; squares: this work; x-error bars: average standard error of measurements around the given loading rate, y-error bars: uncertainty according to KBE fit.

Conclusion

The rupture behavior of three bivalent molecular model systems was varied over a broad range of rupture lengths and most probable rupture forces, employing backbones with different geometries and flexibilities. While the interactions lead to similar thermal off-rates, the rupture mechanisms are different. The system with medium backbone flexibility shows a simultaneous bond rupture, leading to a high mechanical stability. On the other hand, a stepwise rupture processes, possibly combined with an additional release of geometrical folding, results in a very malleable system that is able to deform without breaking. Thus knowledge about backbone properties of bivalent and probably also multivalent interactions is crucial for the specific design of ligands. Future studies will address specific backbone properties and higher valencies on the way to a deeper understanding of their influence on multivalency.

Experimental

Reactions were generally performed under argon in dried flasks. Solvents and reagents were added by syringes. Solvents were dried using standard procedures. Dichloromethane was dried with activated alumina using an MBraun solvent system model MB SPS-800. Other reagents were purchased and used as received without further purification unless otherwise stated. Reactions were monitored by thin-layer chromatography (TLC). Products were purified by flash chromatography on silica gel (32–63 μm, Macherey & Nagel). Yields refer to chromatographically and spectroscopically (^{1}H NMR) homogeneous materials, unless otherwise stated. NMR spectra were recorded on Bruker (AM 250, AC500, AVIII 700) and JEOL (ECX 400, Eclipse 500) instruments. Integrals are in accordance with assignments, and coupling constants are given in Hz. Chemical shifts are reported relative to TMS (^{1}H: δ = 0.00 ppm) and $CDCl_3$ (^{13}C: δ = 77.0 ppm). All ^{13}C NMR spectra are proton decoupled. For detailed peak-assignment 2D spectra were measured (COSY, HMQC, HMBC). Multiplicity is indicated as follows: s (singlet), d (doublet), t (triplet), m (multiplet), m_c (centered multiplet), dd (doublet of doublet), br s (broad singlet). IR spectra were measured with a Nexus FTIR spectrometer equipped with a Nicolet Smart DuraSampleIR ATR. MS and HRMS analyses were performed with Varian Ionspec QFT-7 (ESI–FT ICRMS) instrument. Elemental analyses were carried out with a Vario EL III analyser. Melting points were measured with a Reichert Thermovar apparatus and are uncorrected.

Synthesis of 4-{6-[2-(pyridin-3-yl)ethyl]pyridin-3-yl}butan-1-ol (4): A suspension of 4-{[2-(pyridin-3-yl)ethynyl]pyridin-5-yl}but-3-yn-1-ol (**3**) [27] (45 mg, 0.18 mmol) and Pd/C (45 mg, 100 wt %) in MeOH (3 mL) was stirred under an atmosphere of hydrogen (balloon) for 3 h until complete consumption of the starting material (by TLC). The mixture was filtered through a short plug of silica gel (MeOH) and evaporated to afford 39 mg (85%) of product **4** as a colorless oil. ^{1}H NMR (400 MHz, $CDCl_3$) δ 1.16–1.55, 1.66–1.73 (2 m, 2H each, 2-H/3-H), 2.62 (t, J = 7.5 Hz, 2H, 4-H), 3.05 (s, 4H, 1'-H/2'-H), 3.64 (t, J = 6.4 Hz, 2H, 1-H), 6.94 (d, J = 7.9 Hz, 1H, pyr), 7.19 (dd, J = 4.8 Hz, 7.9 Hz, 1H, pyr), 7.38 (dd, J = 2.3, 7.9 Hz, 1H, pyr), 7.46–7.61 (m, 1 H, pyr), 8.31 (br s, 1 H, pyr), 8.37–8.41 (m, 2 H, pyr) ppm; ^{13}C NMR (101 MHz, $CDCl_3$) δ 27.3, 32.1, 32.3, 33.0 (4 t, C-2/C-3/C-1'/C-2'), 39.0, 62.2 (2 t, C-4/C-1), 122.7, 123.3 (2 s, pyr), 135.2, 136.0, 136.3, 136.8, 147.2, 149.3, 149.7 (7 d, pyr), 157.6 (s, pyr) ppm; IR (ATR) ν: 3305 (OH), 3030–2860 (=C-H, -C-H), 1600–1570 (C=C) cm^{-1}; HRMS (ESI–TOF): *m/z* $[M + H]^+$ calcd for $C_{16}H_{21}N_2O$, 257.1648, found, 257.1634.

Synthesis of pyridine-PEG conjugate 5, ligand of 2b: To a solution of the bifunctional poly(ethylene glycol) (R in Figure 1, H-terminated, 81.0 mg, 0.0081 mmol) and **4** (29.0 mg, 0.113 mmol) in anhydrous CH_2Cl_2 (0.6 mL) was added EDAC (6.5 mg, 0.034 mmol) and the resulting mixture was stirred at room temperature under an atmosphere of argon for 5 days. The solvent was evaporated and the residue was purified by dialysis (MW cut-off: 1000 g/mol) against MeOH to provide the pyridine-PEG conjugate **5** (33 mg, 41%) as a colorless solid. Mp 127 °C; ^{1}H NMR (700 MHz, $CDCl_3$) δ 1.54–1.62, 1.64–1.72 (2 m, 2H each, C-2/C-3), 2.62 (m, 2H, 4-H), 3.06 (s, 4H, 1'-H/2'-H), 3.64 (s, OCH_2CH_2O), 6.94 (t, J = 8.0 Hz, 1H, pyr), 7.19 (dd, J = 5.3, 7.5 Hz, 1 H, pyr), 7.34–7.41 (m, 1 H, pyr), 7.50 (d, J = 7.7 Hz, 1 H, pyr), 8.30 (br s, 1 H, pyr), 8.38–8.44 (m, 2 H, pyr) ppm.

Synthesis of 2-methyl-3-(pyridin-4-yloxy)-2-[(pyridin-4-yloxy)methyl]propan-1-ol (8) and 1,1,1-tris[pyridine-4-yloxy)methyl]ethane (9): To a solution of 2-(hydroxymethyl)-2-methylpropane-1,3-diol (313 mg, 2.33 mmol) in dry DMF (25 mL) was added NaOH (600 mg, 15.0 mmol). After 15 min stirring at room temperature, 4-fluoropyridine (777 mg, 8.00 mmol) was added. The mixture was heated to reflux for 4 days and after cooling to room temperature diluted with CH_2Cl_2/water. The organic phase was washed several times with water and then dried (Na_2SO_4). Column chromatography on aluminum oxide (CH_2Cl_2/MeOH 94:6) afforded 338 mg of a yellowish solid (mixture of **8** and **9**) and 21 mg (3%) of compound **8** as colorless solid. By further purification steps (second chromatography on silica gel followed by HPLC) additional **8** (188 mg, 29%) and **9** (44 mg, 5%) were isolated.

Data of compound 8: Mp 161–162 °C; ^{1}H NMR (400 MHz, CD_3OD) δ 1.19 (s, 3H, Me), 3.68 (s, 2H, 1´-H), 4.09 (m_c, 4H, OCH_2), 7.00 (d, J = 4.5 Hz, 4H, 3-H, 5-H), 8.33 (m_c, 4H, 2-H,

6-H) ppm; ^{13}C NMR (101 MHz, CD_3OD) δ 17.1 (q, Me), 42.0 (s, C-2′), 64.7 (t, OCH_2), 71.0 (t, OCH_2), 111.9 (d, C-3, C-5), 155.7 (d, C-2, C-6), 159.7 (s, C-4) ppm; IR (ATR) ν: 3135 (OH), 3100–3025 (=C-H), 2960–2865 (C-H), 1590–1460 (C=C, C=N), 1055–1025 (C-O) cm^{-1}; HRMS (pos. ESI-TOF) *m/z*: $[M + H]^+$ calcd for $C_{15}H_{19}N_2O_3$, 275.1396; found, 275.1403; anal. calcd for $C_{15}H_{18}N_2O_3$: C, 65.68; H, 6.61; N, 10.21; found: C, 65.17; H, 6.45; N, 10.13.

Data of compound 9: Mp 143–144 °C; ^{1}H NMR (250 MHz, $CDCl_3$) δ 1.33 (s, 3H, Me), 4.10 (s, 6H, OCH_2), 6.80 (m_c, 6H, 3-H, 5-H), 8.41 (m_c, 6H, 2-H, 6-H) ppm; ^{13}C NMR (63 MHz, $CDCl_3$) δ 17.3 (q, Me), 40.2 (s, C-1′), 69.4 (t, OCH_2), 110.3 (d, C-3, C-5), 151.3 (d, C-2, C-6), 164.6 (s, C-4) ppm; IR (ATR) ν: 3050–3035 (=C-H), 2950–2870 (C-H), 1685–1455 (C=C, C=N), 1110 (C-O) cm^{-1}; HRMS (pos. ESI–TOF) *m/z*: $[M + H]^+$ calcd for $C_{20}H_{22}N_3O_3$, 352.1656; found, 352.1659; anal. calcd for $C_{20}H_{21}N_3O_3$: C, 68.36; H, 6.02; N, 11.96; found: C, 68.02; H, 6.00; N, 11.93.

Synthesis of pyridine-PEG conjugate 10, ligand of 2c: To a solution of the bifunctional poly(ethylene glycol) (R in Figure 1, H-terminated, 117 mg, 0.0117 mmol) and compound **8** (32.0 mg, 0.116 mmol) in anhydrous CH_2Cl_2 (0.6 mL) was added EDAC (7 mg, 0.035 mmol) and the resulting mixture was stirred at room temperature under an atmosphere of argon for 9 days. The solvent was evaporated and the residue was purified by dialysis (MW cut-off: 1000 g/mol) against MeOH to provide the pyridine-PEG conjugate **10** (69 mg, 59%) as a colorless solid (mp. 55–58 °C). ^{1}H NMR ($CDCl_3$, 700 MHz) δ 6.81 (dd, J = 4.8, 1.5 Hz, 4H, 3-H, 5-H), 8.43 (dd, J = 4.8, 1.5 Hz, 4H, 2-H, 6-H) ppm.

Surface films of the polymers were prepared in a similar manner as described before [27]. A droplet of a 1 mM aqueous polymer solution was applied to freshly template-stripped gold supports [51] (JPK Instruments, Berlin, Germany) for 12−24 h at room temperature in an enclosed chamber with water reservoir. Immediately before measurements the surfaces were thoroughly rinsed with water [52]. For blank experiments, surfaces were stripped and used without further treatment. Gold-coated Si_3N_4 cantilevers (Olympus Biolever, 60 µm short cantilever: k = 0.03 N/M, 100 µm long cantilever: k = 0.006 N/m, Olympus Corp., Tokyo, Japan) were cleaned by UV/O_3 treatment [53] (Penray low-pressure mercury discharge tube, UVP, Upland, CA) and treated as gold supports above.

SMF measurements were performed as in [27], i.e., on a ForceRobot 200 [54] (JPK Instruments, Berlin, Germany) at room temperature in an enclosed fluid cell filled with 3 mM $CuSO_4$ (**2b**), 30 mM $CuSO_4$ (**3c**) or DI water (blank). SFM cantilevers were calibrated using the thermal noise method [55]. In DFS, experiments were performed at constant velocities between 100 nm/s and 10 µm/s using a grid of different spots on the surface.

Force–distance curves were processed as described in [27]. In short, signals were fitted according to the wormlike-chain model using Hooke, a Python-based force spectroscopy data analysis program [56]. Most probable rupture forces were determined by histogram analysis. Loading rates at the rupture point of each curve were calculated based on the fit function and pulling velocity. Measurements in aqueous solutions without $CuSO_4$ (blank) showed a different force-loading rate behavior, proving specific interactions with the Cu^{2+} ligand. In 3 mM $CuSO_4$, ligand **2c** showed the same behavior as the monovalent system **1**, but a different in 30 mM $CuSO_4$. The latter was used for the analysis presented here.

Acknowledgements

We gratefully acknowledge the German Research Foundation (DFG) for support of this work through the collaborative research center SFB 765. We also thank Dr. R. Zimmer for help during the preparation of this manuscript.

References

1. Kiessling, L. L.; Gestwicki, J. E.; Strong, L. E. *Angew. Chem., Int. Ed.* **2006,** *45,* 2348–2368. doi:10.1002/anie.200502794
2. Badjić, J. D.; Nelson, A.; Cantrill, S. J.; Turnbull, W. B.; Stoddart, J. F. *Acc. Chem. Res.* **2005,** *38,* 723–732. doi:10.1021/ar040223k
3. Fasting, C.; Schalley, C. A.; Weber, M.; Seitz, O.; Hecht, S.; Koksch, B.; Dernedde, J.; Graf, C.; Knapp, E.-W.; Haag, R. *Angew. Chem., Int. Ed.* **2012,** *51,* 10472–10498. doi:10.1002/anie.201201114
4. Mulder, A.; Huskens, J.; Reinhoudt, D. N. *Org. Biomol. Chem.* **2004,** *2,* 3409–3424. doi:10.1039/b413971b
5. Diestler, D. J.; Knapp, E. W. *J. Phys. Chem. C* **2010,** *114,* 5287–5304. doi:10.1021/jp904258c
6. Hoffmann, T.; Tych, K. M.; Hughes, M. L.; Brockwell, D. J.; Dougan, L. *Phys. Chem. Chem. Phys.* **2013,** *15,* 15767–15780. doi:10.1039/c3cp52142g
7. Woelke, A. L.; Kuehne, C.; Meyer, T.; Galstyan, G.; Dernedde, J.; Knapp, E.-W. *J. Phys. Chem. B* **2013,** *117,* 16443–16454. doi:10.1021/jp4099123
8. Mu, X.-Q.; Jiang, Z. G.; Bullitt, E. *J. Mol. Biol.* **2005,** *346,* 13–20. doi:10.1016/j.jmb.2004.11.037
9. Lugmaier, R. A.; Schedin, S.; Kühner, F.; Benoit, M. *Eur. Biophys. J.* **2008,** *37,* 111–120. doi:10.1007/s00249-007-0183-x
10. Schoeler, C.; Malinowska, K. H.; Bernardi, R. C.; Milles, L. F.; Jobst, M. A.; Durner, E.; Ott, W.; Fried, D. B.; Bayer, E. A.; Schulten, K.; Gaub, H. E.; Nash, M. A. *Nat. Commun.* **2014,** *5,* No. 5635. doi:10.1038/ncomms6635
11. Zhang, X.; Halvorsen, K.; Zhang, C.-Z.; Wong, W. P.; Springer, T. A. *Science* **2009,** *324,* 1330–1334. doi:10.1126/science.1170905

12. Li, H.; Linke, W. A.; Oberhauser, A. F.; Carrion-Vazquez, M.; Kerkvliet, J. G.; Lu, H.; Marszalek, P. E.; Fernandez, J. M. *Nature* **2002,** *418,* 998–1002. doi:10.1038/nature00938
13. Lv, S.; Dudek, D. M.; Cao, Y.; Balamurali, M. M.; Gosline, J.; Li, H. *Nature* **2010,** *465,* 69–73. doi:10.1038/nature09024
14. Groote, R.; Jakobs, R. T. M.; Sijbesma, R. P. *Polym. Chem.* **2013,** *4,* 4846–4859. doi:10.1039/c3py00071k
15. Dietz, H.; Berkemeier, F.; Bertz, M.; Rief, M. *Proc. Natl. Acad. Sci. U. S. A.* **2006,** *103,* 12724–12728. doi:10.1073/pnas.0602995103
16. Bertz, M.; Wilmanns, M.; Rief, M. *Proc. Natl. Acad. Sci. U. S. A.* **2009,** *106,* 13307–133310. doi:10.1073/pnas.0902312106
17. Rief, M.; Pascual, J.; Saraste, M.; Gaub, H. E. *J. Mol. Biol.* **1999,** *286,* 553–561. doi:10.1006/jmbi.1998.2466
18. Li, M. S. *Biophys. J.* **2007,** *93,* 2644–2654. doi:10.1529/biophysj.107.106138
19. Sikora, M.; Sulkowska, J. I.; Witkowski, B. S.; Cieplak, M. *Nucleic Acids Res.* **2011,** *39* (Suppl. 1), D443–D450. doi:10.1093/nar/gkq851
20. Kramers, H. A. *Physica* **1940,** *7,* 284–304. doi:10.1016/S0031-8914(40)90098-2
21. Bell, G. I. *Science* **1978,** *200,* 618–627. doi:10.1126/science.347575
22. Evans, E. *Annu. Rev. Biophys. Biomol. Struct.* **2001,** *30,* 105–128. doi:10.1146/annurev.biophys.30.1.105
23. Wollschläger, K.; Gaus, K.; Körnig, A.; Eckel, R.; Wilking, S.-D.; McIntosh, M.; Majer, Z.; Becker, A.; Ros, R.; Anselmetti, D.; Sewald, N. *Small* **2009,** *5,* 484–495. doi:10.1002/smll.200800945
24. Zocher, M.; Zhang, C.; Rasmussen, S. G. F.; Kobilka, B. K.; Müller, D. J. *Proc. Natl. Acad. Sci. U. S. A.* **2012,** *109,* E3463–E3472. doi:10.1073/pnas.1210373109
25. Kawamura, S.; Colozo, A. T.; Ge, L.; Müller, D. J.; Park, P. S.-H. *J. Biol. Chem.* **2012,** *287,* 21826–21835. doi:10.1074/jbc.M112.340182
26. Kudera, M.; Eschbaumer, C.; Gaub, H. E.; Schubert, U. S. *Adv. Funct. Mater.* **2003,** *13,* 615–620. doi:10.1002/adfm.200304359
27. Gensler, M.; Eidamshaus, C.; Galstyan, A.; Knapp, E.-W.; Reissig, H.-U.; Rabe, J. P. *J. Phys. Chem. C* **2015,** *119,* 4333–4343. doi:10.1021/jp511104m
28. Kersey, F. R.; Yount, W. C.; Craig, S. L. *J. Am. Chem. Soc.* **2006,** *128,* 3886–3887. doi:10.1021/ja058516b
29. Schönherr, H.; Beulen, M. W. J.; Bügler, J.; Huskens, J.; van Veggel, F. C. J. M.; Reinhoudt, D. N.; Vancso, G. J. *J. Am. Chem. Soc.* **2000,** *122,* 4963–4967. doi:10.1021/ja994040i
30. Eckel, R.; Ros, R.; Decker, B.; Mattay, J.; Anselmetti, D. *Angew. Chem., Int. Ed.* **2005,** *44,* 484–488. doi:10.1002/anie.200461382
31. Schröder, T.; Geisler, T.; Walhorn, V.; Schnatwinkel, B.; Anselmetti, D.; Mattay, J. *Phys. Chem. Chem. Phys.* **2010,** *12,* 10981–10987. doi:10.1039/c0cp00227e
32. Walhorn, V.; Schäfer, C.; Schröder, T.; Mattay, J.; Anselmetti, D. *Nanoscale* **2011,** *3,* 4859–4865. doi:10.1039/c1nr10912j
33. Lussis, P.; Svaldo-Lanero, T.; Bertocco, A.; Fustin, C.-A.; Leigh, D. A.; Duwez, A.-S. *Nat. Nanotechnol.* **2011,** *6,* 553–557. doi:10.1038/NNANO.2011.132
34. Guzmán, D. L.; Roland, J. T.; Keer, H.; Kong, Y. P.; Ritz, T.; Yee, A.; Guan, Z. *Polymer* **2008,** *49,* 3892–3901. doi:10.1016/j.polymer.2008.06.047
35. Beijer, F. H.; Kooijman, H.; Spek, A. L.; Sijbesma, R. P.; Meijer, E. W. *Angew. Chem., Int. Ed.* **1998,** *37,* 75–78. doi:10.1002/(SICI)1521-3773(19980202)37:1/2<75::AID-ANIE75>3.0.CO;2-R
36. Embrechts, A.; Velders, A. H.; Schönherr, H.; Vancso, G. J. *Langmuir* **2011,** *27,* 14272–14278. doi:10.1021/la203433z
37. Zhang, Y.; Yu, Y.; Jiang, Z.; Xu, H.; Wang, Z.; Zhang, X.; Oda, M.; Ishizuka, T.; Jiang, D.; Chi, L.; Fuchs, H. *Langmuir* **2009,** *25,* 6627–6632. doi:10.1021/la901360c
38. Grandbois, M.; Beyer, M.; Rief, M.; Clausen-Schaumann, H.; Gaub, H. E. *Science* **1999,** *283,* 1727–1730. doi:10.1126/science.283.5408.1727
39. Krüger, D.; Fuchs, H.; Rousseau, R.; Marx, D.; Parrinello, M. *Phys. Rev. Lett.* **2002,** *89,* 186402. doi:10.1103/PhysRevLett.89.186402
40. Heymann, B.; Grubmüller, H. *Chem. Phys. Lett.* **1999,** *307,* 425–432. doi:10.1016/S0009-2614(99)00531-X
41. Oesterhelt, F.; Rief, M.; Gaub, H. E. *New J. Phys.* **1999,** *1,* No. 6. doi:10.1088/1367-2630/1/1/006
42. Noy, A. *Curr. Opin. Chem. Biol.* **2011,** *15,* 710–718. doi:10.1016/j.cbpa.2011.07.020
43. Ray, C.; Brown, J. R.; Kirkpatrick, A.; Akhremitchev, B. B. *J. Am. Chem. Soc.* **2008,** *130,* 10008–10018. doi:10.1021/ja801568y
44. Friedsam, C.; Wehle, A. K.; Kühner, F.; Gaub, H. E. *J. Phys.: Condens. Matter* **2003,** *15,* S1709–S1723. doi:10.1088/0953-8984/15/18/305
45. Merkel, R.; Nassoy, P.; Leung, A.; Ritchie, K.; Evans, E. *Nature* **1999,** *397,* 50–53. doi:10.1038/16219
46. Dudko, O.; Hummer, G.; Szabo, A. *Phys. Rev. Lett.* **2006,** *96,* 108101. doi:10.1103/PhysRevLett.96.108101
47. Raible, M.; Evstigneev, M.; Bartels, F. W.; Eckel, R.; Nguyen-Duong, M.; Merkel, R.; Ros, R.; Anselmetti, D.; Reimann, P. *Biophys. J.* **2006,** *90,* 3851–3864. doi:10.1529/biophysj.105.077099
48. Schmidt, S. W.; Pill, M. F.; Kersch, A.; Clausen-Schaumann, H.; Beyer, M. K. *Faraday Discuss.* **2014,** *170,* 357–367. doi:10.1039/c3fd00119a
49. Schmidt, S. W.; Kersch, A.; Beyer, M. K.; Clausen-Schaumann, H. *Phys. Chem. Chem. Phys.* **2011,** *13,* 5994–5999. doi:10.1039/c0cp02827d
50. Hohenstein, E. G.; Sherrill, C. D. *J. Phys. Chem. A* **2009,** *113,* 878–886. doi:10.1021/jp809062x
51. Hegner, M.; Wagner, P.; Semenza, G. *Surf. Sci.* **1993,** *291,* 39–46. doi:10.1016/0039-6028(93)91474-4
52. Wagner, P.; Hegner, M.; Guentherodt, H.-J.; Semenza, G. *Langmuir* **1995,** *11,* 3867–3875. doi:10.1021/la00010a043
53. Vig, J. R. *J. Vac. Sci. Technol., A* **1985,** *3,* 1027. doi:10.1116/1.573115
54. Struckmeier, J.; Wahl, R.; Leuschner, M.; Nunes, J.; Janovjak, H.; Geisler, U.; Hofmann, G.; Jähnke, T.; Müller, D. J. *Nanotechnology* **2008,** *19,* 384020. doi:10.1088/0957-4484/19/38/384020
55. Hutter, J. L.; Bechhoefer, J. *Rev. Sci. Instrum.* **1993,** *64,* 1868. doi:10.1063/1.1143970
56. Sandal, M.; Benedetti, F.; Brucale, M.; Gomez-Casado, A.; Samorì, B. *Bioinformatics* **2009,** *25,* 1428–1430. doi:10.1093/bioinformatics/btp180

License and Terms

BEILSTEIN JOURNAL OF ORGANIC CHEMISTRY

Adsorption mechanism and valency of catechol-functionalized hyperbranched polyglycerols

Stefanie Krysiak[1], Qiang Wei[2], Klaus Rischka[3], Andreas Hartwig[3], Rainer Haag[2] and Thorsten Hugel[*4]

Full Research Paper

Open Access

Address:
[1]Physik Department and IMETUM, Technische Universität München, 85748 Garching, Germany, [2]Department of Chemistry and Biochemistry, Freie Universität Berlin, 14195 Berlin, Germany, [3]Fraunhofer Institute for Manufacturing Technology and Advanced Materials (FhG IFAM), 28359 Bremen, Germany and [4]Institute of Physical Chemistry, University of Freiburg, Albertstraße 23a, 79104 Freiburg, Germany

Email:
Thorsten Hugel[*] - Thorsten.Hugel@physchem.uni-freiburg.de

* Corresponding author

Keywords:
adhesion; atomic force microscopy; catechol; hyperbranched polyglycerols; valency

Beilstein J. Org. Chem. **2015,** *11,* 828–836.
doi:10.3762/bjoc.11.92

Received: 24 February 2015
Accepted: 29 April 2015
Published: 18 May 2015

This article is part of the Thematic Series "Multivalency as a chemical organization and action principle".

Guest Editor: R. Haag

Abstract

Nature often serves as a model system for developing new adhesives. In aqueous environments, mussel-inspired adhesives are promising candidates. Understanding the mechanism of the extraordinarily strong adhesive bonds of the catechol group will likely aid in the development of adhesives. With this aim, we study the adhesion of catechol-based adhesives to metal oxides on the molecular level using atomic force microscopy (AFM). The comparison of single catechols (dopamine) with multiple catechols on hyperbranched polyglycerols (hPG) at various pH and dwell times allowed us to further increase our understanding. In particular, we were able to elucidate how to achieve strong bonds of different valency. It was concluded that hyperbranched polyglycerols with added catechol end groups are promising candidates for durable surface coatings.

Introduction

While underwater glues are still a challenge for industrial adhesive development, mussels, barnacles and numerous other animals and plants have found a way for strong, long-term adhesion to wet surfaces [1]. Wet hydrophilic surfaces are difficult to be wetted by glues since the adhesive competes with the surface water layer [2]. Mussels can easily adhere to hydrophilic metal oxides (e.g. ship hulls) or mineral surfaces such as rocks, even against large tidal forces. Studying the mechanism of how mussels adhere gives us the opportunity to adapt these principles for the development of industrial coatings and biomedical adhesives.

Mussels adhere to surfaces via their byssus, a bundle of filaments with adhesive plaque on the end [3,4]. They are made of

proteins and contain no living cells. To understand their adhesive properties the proteins in the byssus were studied extensively by numerous groups. The *Mytilus edulis* byssus contains about 25–30 different proteins; however, the part that adheres to external surfaces, the byssal plaque, contains only 7–8. Of these, 5 are unique to the plaque [5,6], namely the *Mytilus edulis* foot proteins (Mefp) 2, 3, 4, 5 and 6. Directly at the contact area, mainly Mefp 3, 5 and 6 are found. Mefp 3 and 5 are rich in 3,4-dihydroxyphenylalanine (DOPA, 15–30 mol %) [7,8]. DOPA is formed by posttranslational modification of tyrosine. Mefp 6 is rich in cystein (11 mol %) [6]. It has been found that the DOPA in Mefp 3 and 5 adheres to the surfaces, while the cystein-rich Mefp 6 controls the redox balance and can keep interfacial DOPA in a reduced state [5,9]. The byssal plaque also shows strong cohesion through crosslinks. The cysteins can crosslink with DOPA and the oxidized DOPA (semiquinones) can crosslink via radical addition. Furthermore, crosslinking by iron chelate complexes of DOPA improves cohesion [10].

The adhesion of a single DOPA to metal oxides was studied with AFM force spectroscopy [11-13] and rupture forces of up to 1000 pN were measured. This is on the same order of magnitude compared to forces of around 1400 pN that have been measured for the rupture of covalent bonds [14-16]. Besides the strength of the bond, the most interesting feature is that DOPA-based bonds were found to be reversible: once broken they can form again [11,17,18]. This flexibility and action seem to be a general principle for the formation of strong and durable interphases in natural as well as artificial systems [19].

Finally, not only is DOPA itself a key to understanding the adhesive properties of blue mussels, but also to understanding the primary structure of the respective protein or peptides containing the DOPA [20]. This primary structure should promote strong bond formation and self-healing. Here we use a hyperbranched polyglycerol as a hydrophilic core with numerous DOPA (catechol) groups attached. A similar system has already proven to be advantageous for an antifouling coating on titanium oxide surfaces [21,22]. An added benefit of this system is that the oxidation of catechol to quinones makes crosslinking possible and allows for good cohesion between the layers of this material. Here we investigated the molecular details, valency and dynamics on how molecules with multiple DOPA groups adhere to surfaces.

Results and Discussion

The publication by Lee et al. [11] sparked considerable interest and since then several research groups have published results of single molecule atomic force measurements of DOPA or DOPA-containing molecules on metal oxide surfaces. The published work shows large variations between <100 pN up to almost 1000 pN [11-13,23]. The reasons for this large variation in the results are unclear, which underscores how little is known about the nature of the interaction between the catechol group of DOPA and metal oxide surfaces.

To determine the force of a single catechol group on titanium dioxide, we performed AFM single molecule force spectroscopy measurements with tips functionalized with dopamine. Dopamine is derived from L-DOPA by removing the carboxyl group. This leaves an amine group that was used to covalently couple the probe molecule to the tip through a PEG linker using NHS-ester chemistry, as illustrated in the inset of Figure 1B. A sample force–distance trace showing the retraction of the tip from the TiO_2 surface is shown.

The experiments were performed at room temperature with a constant pulling velocity of 1 µm/s and a surface dwell time of 1 s. Different buffers were used for the measurements. McIlvaines buffer solutions (a mix of 100 mM citric acid and 200 mM Na_2HPO_4) at pH 3 were used as well as phosphate-buffered saline (PBS) and ultrapure water. The maximum peak force as well as the detach force were extrapolated from the data.

Figure 1A shows the maximum detachment force (max force) of a dopamine-functionalized tip in ultrapure water, PBS and in citric acid/phosphate buffer at pH 3. The measurement in ultrapure water shows a very broad distribution of detachment forces with no distinct peak. There are small peaks at approximately 40, 140 and 320 pN as well as occasional high force events of up to 750 pN. The measurement of the same tip in PBS at pH 7.4 shows a clear bimodal force distribution with peaks at 290 pN and 410 pN and a shoulder at approximately 650 pN. For the same tip at pH 3, a high force peak at 500 pN with a shoulder at about 700 pN was measured.

Although the original measurement by Lee et al. [11] giving an average maximum detachment force of 805 pN was performed in water, our measurement in water showed no high force peak. Due to the lack of buffering capacity of ultrapure water, contamination could change the pH in unpredictable ways. This and the strong pH dependence of the high force interaction made it difficult to reproduce the measurement in ultrapure water. The measurement in PBS showed a bimodal distribution similar to the bimodal distribution measured in buffer of pH 8.3 in the publication by Lee et al. They attributed the high force peak (760 ± 90 pN) to unoxidized DOPA and the lower force peak (210 ± 70 pN) to oxidized DOPA–quinone. Similar to the measurement of Lee et al., the higher forces in our measurement occurred at the beginning of the measurement and the

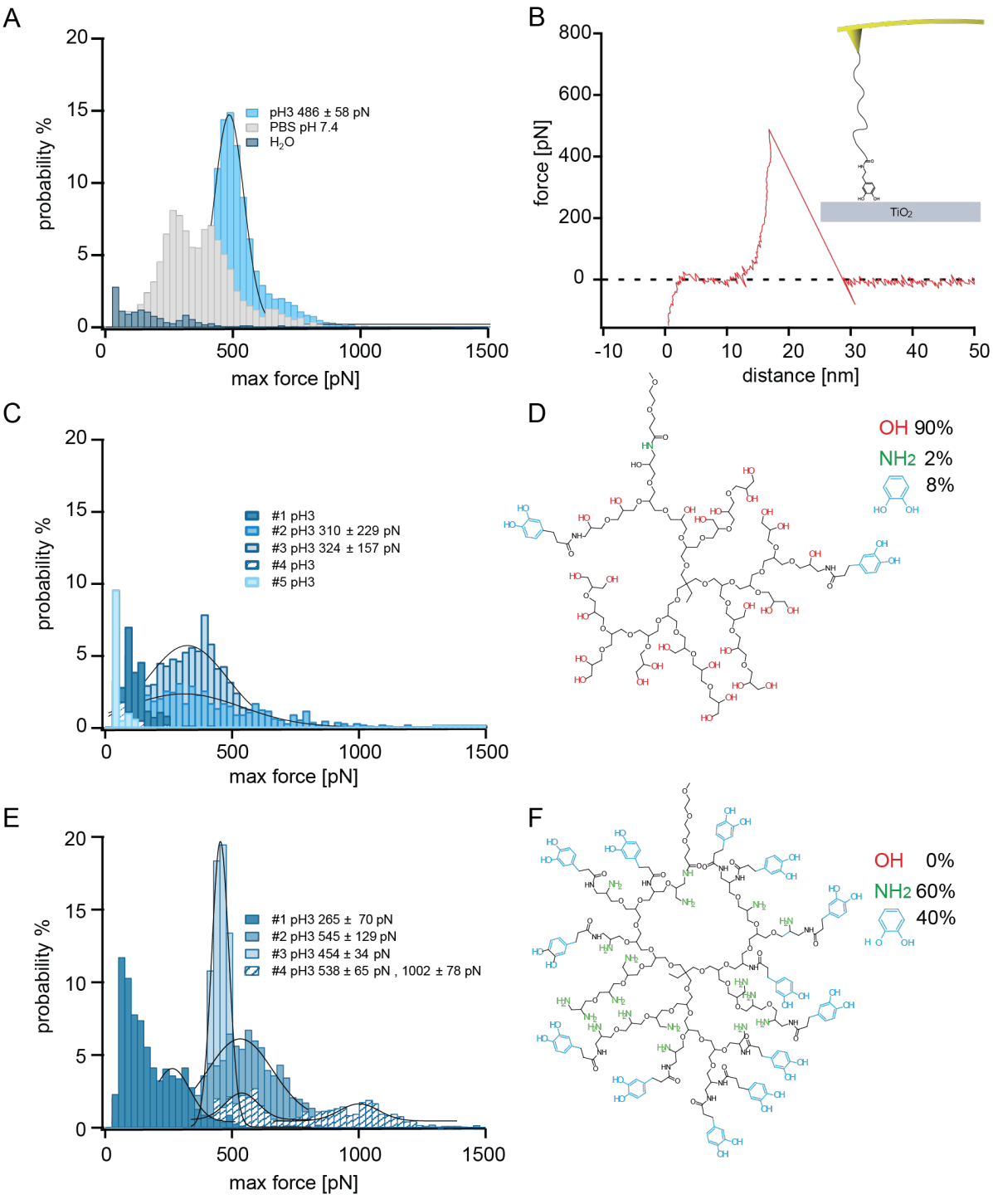

Figure 1: A) A maximum rupture force (max force) histogram for a dopamine-functionalized tip is given for the three measurement buffers: ultrapure water (dark blue), PBS (grey) and citric acid/phosphate buffer pH 3 (light blue). B) A typical retraction force–distance trace of the desorption of dopamine from TiO_2. The inset shows a schematic of the dopamine desorption experiment. The dopamine is covalently coupled to the tip with a PEG linker using NHS ester chemistry and desorbed in buffer from TiO_2. C) The max force histograms of 5 measurements of hPG with 8% catecholic end groups at pH 3 are depicted. D) The structure of the applied molecule. E) Max force histograms of 4 measurements at pH 3 of the hPG with 40% catechol end groups. F) The structure of the molecule utilized in (E), where possible peaks in the max force histograms were fitted and the peak value as well as the standard deviation are given in the insets.

lower forces at the end. This is consistent with longer term oxidation as in the measurements by Wilke et al. [13]. An increasing pH shifted the equilibrium between DOPA and DOPA–quinone towards the oxidized quinone. While the lower force peak values were roughly comparable (290 pN vs 210 pN), our high force peak was considerably smaller than that of Lee et al. (410 pN vs 760 pN). The reasons for this could be differences in experimental parameters like the force loading rate or the surface dwell time or, even more likely, due to their valency, as discussed below. The measurements at low pH 3 showed a clear high force peak and a high probability of a desorption event. At this pH, one can be reasonably sure that the DOPA is not oxidized [24]. We attribute the 500 pN peak to the catechol/titanium dioxide interaction and the shoulder at 700 pN to the interaction of multiple catechols.

In a next step, the hyperbranched polyglycerols (hPGs) with different amounts of catechol end groups were desorbed from TiO_2. The measurements were again performed with a pulling speed of 1 μm/s and a dwell time of 1 s in McIlvaines buffer at pH 3. The molecule with 8% catechol end groups is depicted in Figure 1D. Besides the 8% catechol end groups, most end groups (90%) are hydroxy groups. Of the five measurements depicted in Figure 1C, three showed mostly small maximum forces (below 200 pN) and occasional events at 200–300 pN. Two of the five measurements showed broad high force peaks (310 ± 230 pN, 320 ± 160 pN) containing events in the force range of the high force catechol–TiO_2 interaction as well as events in the lower force range. The events in the lower force range could be due to the hydrogen bonds of the hydroxy end groups, which show forces below 200 pN (data not shown). One of the measurements showed occasional force events in the range of 700 pN to 1.2 nN, indicating that several catechols participated in the interaction. These could be either two catechol groups of one molecule or two molecules with catechol groups. The fact that only two of the five measurements showed high force peak interactions could be explained by geometrical constraints. The molecule was covalently attached to the tip by a PEG tether, which limits the ability of the molecule to rotate. With only 8% catechol, the possibility of interaction of the catechol groups with the surface depends on the position of the catechols relative to the tether. Figure 1D shows an example where it is unlikely for the catechol to interact with the surface. Since the position of the tether (coupled to an amino-functionalized site) and the catechols on the hPG is random, it will be possible to observe catechol–TiO_2 interactions in some measurements and in others not.

The last molecule had a catecholic functionalization for 40% of its end groups and all other end groups were amino groups, as depicted in Figure 1F. The maximum force histograms are shown in Figure 1E. Three of the four measurements showed clear high force peaks at approximately 550, 450 and 540 pN. One showed a lower force peak at 270 pN that could indicate oxidation. Two measurements showed occasional events at even higher forces above 700 pN and another had a second high force peak at 1 nN. This is due to the interaction of two catechol groups, either multivalent by two catechols on one molecule or polyvalent by two molecules each with one catechol, as discussed below.

The measurement showed that adding more catechol end groups increases the likelihood of catechol–titanium dioxide interaction. Measurements of the molecule with 8% catechol showed high desorption forces for two of the five measurements, while for the molecule with 40% catechol, three of the four measurements showed high forces. Multiple catechol–titanium dioxide interactions were occasionally observed in one of the five measurements with 8% catechol and in two of four measurements with 40% catechol. Additionally, one of the four measurements of 40% catechol showed a clear second high force peak with forces corresponding to roughly twice the catechol–titanium dioxide desorption force. An increased adhesion caused by the additional amines would not lead to the observed narrow high force peak, but rather to a broad force peak with a tail towards lower forces.

The measurements discussed thus far have been performed with a surface dwell time of 1 s. In the following the effect of the surface contact time on the probability and force of desorption is tested for hPG functionalized with 40% catechol. When considering surface contact time, not only must the dwell time at the trigger force value be considered, but also the time that is needed to reach the trigger force. Dwell times of 0, 1, 4 and 10 s were measured. In addition, at 0 s to the normal trigger force, a smaller trigger force was used as well. For the small trigger force, the tip needed 30 ms from the first surface contact to reach the trigger force and retract again until contact with the surface was lost. For the larger trigger force, this value was 160 ms. Thus the total surface contact time was 30 ms, 160 ms, 1.16 s, 4.16 s and 10.16 s. Each dwell time measurement was repeated in a different order to ensure that no time effect would obscure the result. Figure 2 summarizes the results of the measurement. In Figure 2A, the maximum force histograms associated with the different dwell times are plotted in different colors. The number of events is normalized to the number of measured force curves. The 0 s (red), 1 s (light blue), and 4 s (dark blue) dwell time measurements showed two clear peaks, each corresponding to interactions of one and two catechol groups with the titanium dioxide surface. The longest 10 s dwell time measurement had even three clear peaks. Two interesting conclusions can be drawn from the data. Multiple catechol

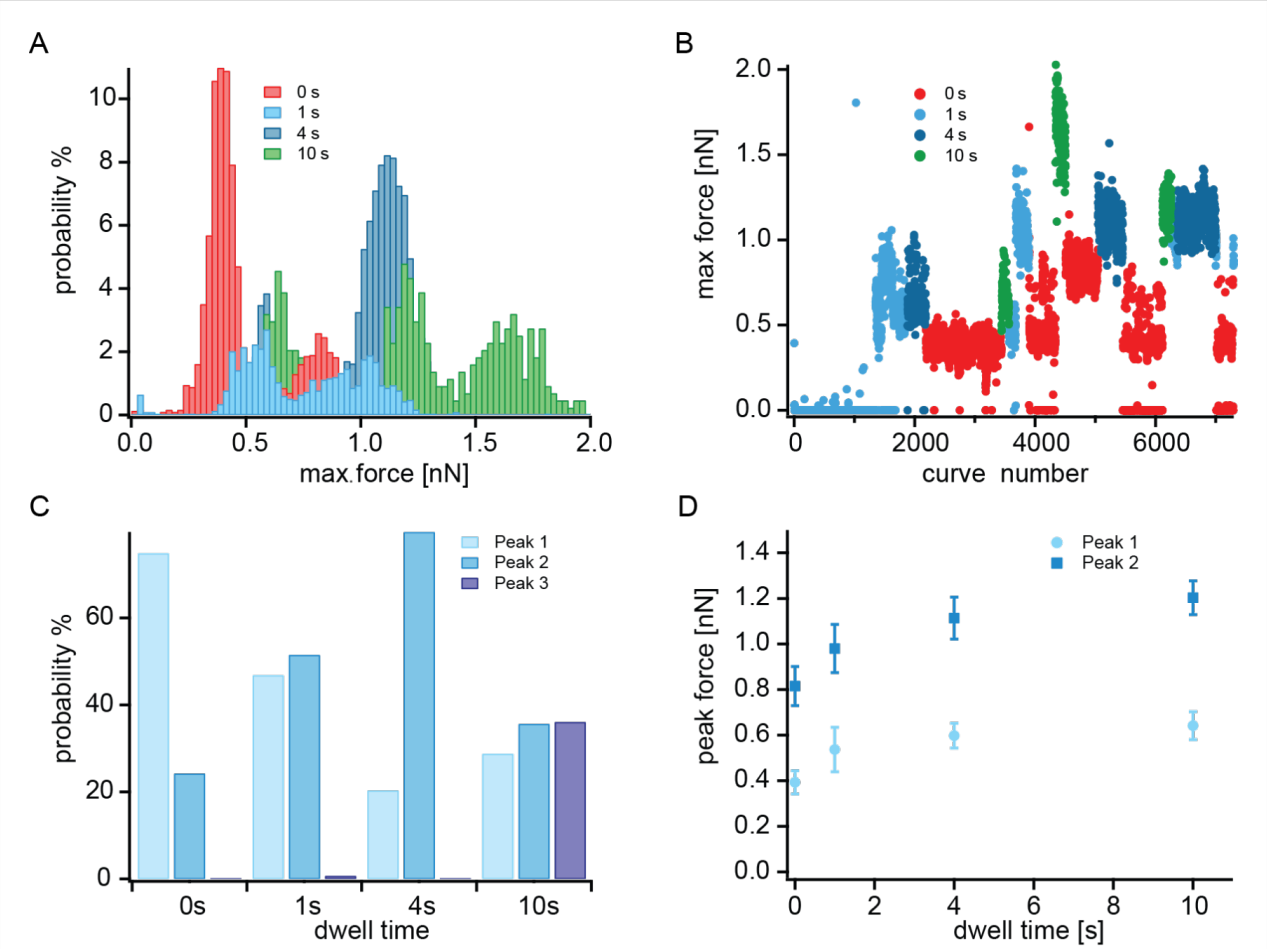

Figure 2: A) Maximum force histograms for the different dwell times indicated in the inset normalized to the number of measured force curves. B) Maximum force vs curve number is plotted to exclude bias due to the order of the measurement. C) Fraction of the number of force peaks belonging to poly- and/or multivalent interactions for the different surface contact times (see main text for details). D) Peak values of the maximum force histograms for the first and second peak are plotted against the dwell time. The standard deviation of the Gaussian fit is given as the error.

events become more likely with increased dwell time, and interestingly, the single catechol interaction force increased with increasing surface contact time. Figure 2B shows the maximum force of each curve plotted against the curve number, where the data points are again color coded. This figure illustrates that the force does not change over time. The probability of observing an event was low for the first 1500 force curves (measured with a 1 s dwell time) and then very high until the end of the measurement. This might be due to conformational changes or the interaction of a different catechol unit. At the beginning of the measurement, the lowest average probability was 42% for the 1 s dwell measurement, because of the low overall probability of events. However, the 61% probability with the smaller trigger force and 30 ms contact time was not caused by the effect of time. This is a markedly lower probability compared to the 99.6% for the higher trigger force and 160 ms contact time. For the 4 s and 10 s dwell times, 99.8% and 100% of the curves showed events.

At the lower surface contact time, the first peak indicating a single catechol interaction is more prominent than the second peak. This behavior changes with increasing dwell time, as illustrated in Figure 2C. The probability of a single, double or triple interaction in relation to the total number of events is plotted for the different surface contact times. For 0 s dwell time, a single interaction was more probable. At 1 s dwell time, single and double events had a similar probability, and at 4 s the double catechol interaction was more likely. For the 10 s measurement, the interaction of one, two or three catechol groups with the surface were all of approximately equal probability. Besides the shift to multiple interactions with increased dwell time, it seems that the force of a single catechol–titanium oxide interaction increases with increasing dwell time. The maximum force peaks in Figure 2A are fitted with a Gaussian function and the peak values as well as the standard variation were extracted. These values are plotted in Figure 2D against the dwell time. The forces of the single peak as well as the

double peak increased with increasing dwell time. The increase was largest between zero dwell time and 1 s dwell time but there was still some measurable increase in force between 4 s and 10 s dwell time, indicating a slow adhesion process of hPG-catechol on titanium dioxide. This is probably due to the required molecular rearrangement of the hPG in order to properly position the catechol groups for the interaction with the surface.

The double peaks in the measurement could be multivalent, as illustrated in Figure 3A, or polyvalent, as in Figure 3B. In a multivalent interaction, more than one catechol group of the same hPG molecule interacts with the surface. For this to be possible, the orientation of the catechol end groups on the surface must be correct for more than one catechol group. With 40% catechol end groups, this should be possible. The other possibility is that more than one functionalized hPG is covalently attached to the tip and that two hPG molecules can simultaneously interact with the surface.

In a number of force–distance curves it was apparent that more than one hPG molecule is part of the interaction. In Figure 4A,B a cluster of measurement points (indicated by a red arrow) related to the rupture of the linker is shown. This cluster of points indicates that there is a second hPG on a different linker and the second hPG catechol bond can hold the force for a short

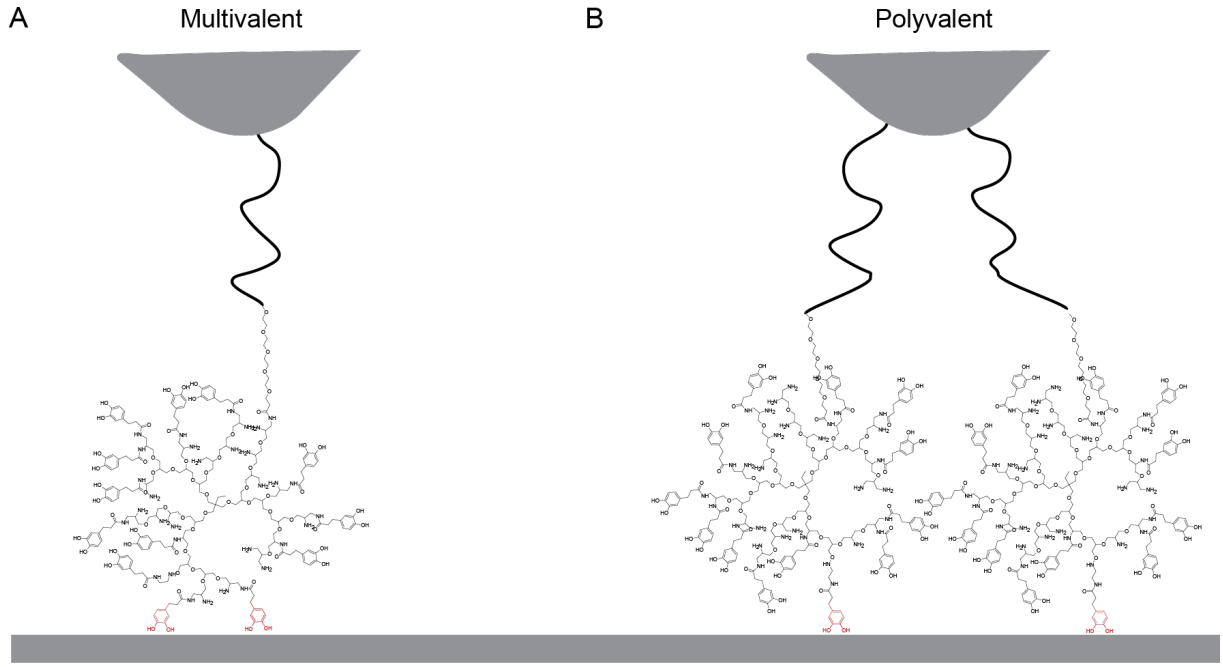

Figure 3: Schematics of the different possibilities for attachment via multiple catechols. A) Multivalent attachment: one hPG molecule is attached to the surface via two catecholic surface anchors. B) Polyvalent attachment: two hPG molecules are attached to the surface with one catechol each and they are attached to the tip via two different PEG linkers.

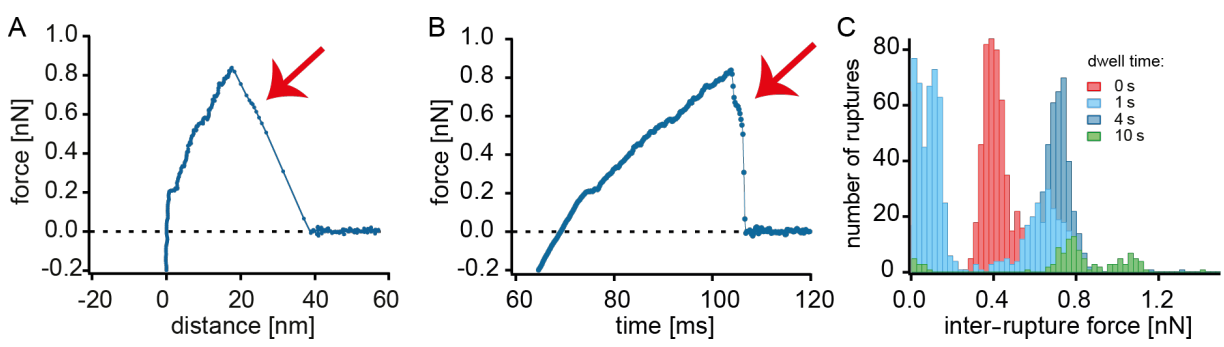

Figure 4: A) Force–distance curves where the rupture is not smooth but rather interrupted by a cluster of measurement points. This inter-rupture force is indicated by a red arrow. B) Same curve as in A) depicted as force vs time. C) Histograms of inter-rupture forces for the different dwell times.

time before rupture. The cluster of measurement points is called an inter-rupture force. In Figure 4C the values of the inter-rupture forces were collected in histograms. Here we ensured that the given inter-rupture force value is the last interaction before the force drops to zero. It is interesting to have a closer look at the inter-rupture forces. They followed the same trend of increasing force with surface contact time but are about 100 pN higher than the maximum forces. The reason for the slightly higher forces is that the force load was shared with another hPG molecule and the full force was only experienced for a short time after the rupture of the first hPG. For the 10 s dwell time measurement, a second peak of inter-rupture force greater than 1 nN was observed. This indicates the presence of one hPG molecule with two catecholic interactions and means that in the case of the triple maximum force peak, two hPG molecules were involved: one with a single catechol anchor and the second with two catecholic anchors. Note that in the last case, two catechols with two PEG linkers were involved that shared the applied force. Therefore, the triple maximum force peak with forces of up to 2 nN could be measured despite rupture forces of 1.4 nN for the Si–O bond between the AFM tip and a single PEG linker.

In summary, a prolonged surface dwell time increased the probability of catecholic interactions. In many of the curves, two different catecholic hPGs interacted simultaneously with the surface in a polyvalent manner as can be seen by the inter-rupture forces. Multivalent binding of two catechols in a single hPG also occurred, but more rarely. In the case of the 10 s dwell measurements there was even a triple interaction involving both poly- and multivalent anchoring. In addition, increasing the surface contact time leads to higher interaction forces for a single catechol on hPG.

Conclusion

The desorption of different catechol-functionalized hyperbranched polyglycerol molecules from a titanium dioxide surface can lead to very high forces and a reversible bond formation. We described several parameters necessary to obtain reliable, high monovalent desorption forces. In addition, we quantified the poly/multivalency of bonds and showed first steps towards controlling this valency. Notably, a very high percentage (40%) of catechol groups on hPGs must be introduced to obtain di- or trivalent interactions. The data also show that the dwell time of catechols in contact with surfaces is crucial. Dwell times on the timescale of seconds increase not only the probability for higher valency, but also the force per single catechol bond. This underlines that catechols need some time to reach the optimum conformation for interface formation [19], possibly by a “standing up/lying down” mechanism [25] or even more likely via “rolling” into minima of the free energy [26]. We anticipate that these results will help improve catecholic hPGs as stable surface coatings in aqueous buffer [22].

Experimental

hPGs

Hyperbranched polyglycerol (hPG) with M_n ≈5000 g/mol and M_w ≈7500 g/mol, was polymerized by a one-step, ring-opening, anionic polymerization, as described in the literature [27,28]. Trimethylolpropane (TMP) was used as the initiator. Amine-functionalized hPG was prepared according to previously published procedures [29]. 3,4-Dihydroxyhydrocinnamic acid and acrylic acid molecules were grafted onto the amine groups by amide coupling to introduce catechol groups [22]. Different molecules with different numbers of amine and catechol end groups were prepared, including hPG with 2% amine groups and 8% catechol groups and hPG with 60% amine groups and 40% catechol groups [18].

hPG with 2% amine groups and 8% catechol groups: ^{1}H NMR (700 MHz, MeOD) δ 6.70–6.54 (m, 27.44H, $CH_{arom.}$), 3.90–3.17 (m, 541.61H, PG-backbone), 2.77 (m, 18.44H, $COCH_2CH_2C$), 2.45 (m, 18.51H, $COCH_2CH_2C$), 1.41–1.39 (m, 2H, CCH_2CH_3 of starter), 0.90 (t, 3H, CCH_2CH_3, of starter) ppm; ^{13}C NMR (175 MHz, MeOD) δ 175.95 (C=O), 175.69 (C=O), 146.34–116.45 ($C_{arom.}$), 81.70–43.60 (PG backbone), 39.50 ($COCH_2CH_2C$), 37.75 ($COCH_2CH_2C$), 32.64 ($COCH_2CH_2C$), 31.95 ($COCH_2CH_2C$), 22.14 (CCH_2CH_3 of starter), 7.09 (CCH_2CH_3 of starter) ppm.

hPG with 60% amine groups and 40% catechol groups: ^{1}H NMR (700 MHz, MeOD) δ 6.72–6.52 (m, 129.12H, $CH_{arom.}$), 4.03–2.97 (m, 541.61H, PG-backbone), 2.75 (m, 85.22H, $COCH_2CH_2C$), 2.48 (m, 87.09H, $COCH_2CH_2C$), 1.49–1.39 (m, 2H, CCH_2CH_3 of starter), 0.90 (t, 3H, CCH_2CH_3, of starter) ppm; ^{13}C NMR (175 MHz, MeOD) δ 176.86 (C=O), 176.29 (C=O), 146.31–111.87 ($C_{arom.}$), 81.18–52.87 (PG backbone), 39.13 ($COCH_2CH_2C$), 37.57 ($COCH_2CH_2C$), 32.31 ($COCH_2CH_2C$), 31.30 ($COCH_2CH_2C$), 24.46 (CCH_2CH_3 of starter), 7.26 (CCH_2CH_3 of starter) ppm.

TiO_2 surface

TiO_2 slides were prepared by sputtering titanium onto silicon wafers. The sputter process was performed using a commercially available radio frequency magnetron sputter unit (Edwards Auto 306). The purity of the Ti target was 99.995%. The titanium was deposited with a power of 83 W for 4 min. The surface layer was naturally oxidized. Directly before the AFM measurements, the TiO_2 slides were put in an oxygen plasma (100 W, 0.3 mbar, 1 h, Edwards GMBH, Kirchheim, Germany) and afterwards rinsed with ultrapure water.

Tip functionalization

The molecule is functionalized to the tip through covalent bonds in a similar manner as previously described [2]. Silicon nitride cantilevers (MLCT, Bruker SPM probes, Camarillo, USA) were first activated in an oxygen plasma chamber (20 W, 0.3 mbar) for 15 min. The cantilevers were rinsed with dry acetone (VWR, Germany) and then incubated for 10 min in a Vectabond (Axxora, Germany) solution (50 µL Vectabond in 2.5 mL dry acetone) for silanization. Afterwards they were rinsed in dry acetone and dry chloroform (VWR, Germany). PEG–Di–NHS (10 kDa, Rapp Polymere GmBH, Tübingen, Germany) was dissolved in dry chloroform (2.5 mM) and the cantilevers were incubated for 60 min. The cantilevers were then rinsed in dry chloroform, ethanol and in the probe molecule reaction buffer and incubated for 1 h in 1 mg/mL probe molecule solution. Dopamine (Sigma-Aldrich) and the hPG without catechol groups were dissolved in sodium borate buffer (50 mM, pH 8.1). hPGs with catechol end groups were dissolved in dry methanol (VWR, Germany). The strength of the Si–O bond is the weakest link of the functionalization and fails at approximately 1.4 nN [16].

AFM measurements

The AFM force spectroscopy measurements were carried out with an MFP-3D device (Oxford Instruments) equipped with a fluid cell at room temperature. The measurements were performed in double distilled water, PBS and McIlvaines buffer at pH 3. For each measurement the Inverse Optical Lever Sensitivity (InvOLS) of the functionalized cantilever was determined from the indentation slope and the spring constant calibrated with the thermal noise method according to [30]. The tip velocity was 1 µm/s and the standard dwell time was 1 s.

Data analysis

The data handling and analysis was performed in Igor Pro (Wave Metrics). Force curves were automatically analyzed for interaction events and the maximum detachment force (maximum force) extracted. To exclude nonspecific effects from the tip–surface interaction, events closer than 15 nm to the surface were excluded.

Acknowledgements

This work was supported by the German Science Foundation (SFB 863) and the Nanosystems Initiative Munich (NIM).

References

1. von Byern, J.; Grunwald, I. *Biological Adhesive Systems: From Nature to Technical and Medical Application;* Springer: Wien, 2010. doi:10.1007/978-3-7091-0286-2
2. Krysiak, S.; Liese, S.; Netz, R. R.; Hugel, T. *J. Am. Chem. Soc.* **2014,** *136,* 688. doi:10.1021/ja410278r
3. Silverman, H. G.; Roberto, F. F. Byssus Formation in Mytilus. In *Biological Adhesive Systems: From Nature to Technical and Medical Application;* von Byern, J.; Grunwald, I., Eds.; Springer: Wien, 2010; pp 273–284. doi:10.1007/978-3-7091-0286-2_18
4. Grunwald, I.; Rischka, K.; Kast, S. M.; Scheibel, T.; Bargel, H. *Philos. Trans. R. Soc. London, A* **2009,** *367,* 1727. doi:10.1098/rsta.2009.0012
5. Floriolli, R. Y.; von Langen, J.; Waite, J. H. *Mar. Biotechnol.* **2000,** *2,* 352.
6. Zhao, H.; Waite, J. H. *J. Biol. Chem.* **2006,** *281,* 26150. doi:10.1074/jbc.M604357200
7. Waite, J. H.; Qin, X. *Biochemistry* **2001,** *40,* 2887. doi:10.1021/bi002718x
8. Papov, V. V.; Diamond, T. V.; Biemann, K.; Waite, J. H. *J. Biol. Chem.* **1995,** *270,* 20183. doi:10.1074/jbc.270.34.20183
9. Yu, J.; Wei, W.; Danner, E.; Ashley, R. K.; Israelachvili, J. N.; Waite, J. H. *Nat. Chem. Biol.* **2011,** *7,* 588. doi:10.1038/nchembio.630
10. Lee, B. P.; Messersmith, P. B.; Israelachvili, J. N.; Waite, J. H. *Annu. Rev. Mater. Res.* **2011,** *41,* 99. doi:10.1146/annurev-matsci-062910-100429
11. Lee, H.; Scherer, N. F.; Messersmith, P. B. *Proc. Natl. Acad. Sci. U. S. A.* **2006,** *103,* 12999. doi:10.1073/pnas.0605552103
12. Wang, J.; Tahir, M. N.; Kappl, M.; Tremel, W.; Metz, N.; Barz, M.; Theato, P.; Butt, H.-J. *Adv. Mater.* **2008,** *20,* 3872. doi:10.1002/adma.200801140
13. Wilke, P.; Helfricht, N.; Mark, A.; Papastavrou, G.; Faivre, D.; Börner, H. G. *J. Am. Chem. Soc.* **2014,** *136,* 12667. doi:10.1021/ja505413e
14. Grandbois, M.; Beyer, M.; Rief, M.; Clausen-Schaumann, H.; Gaub, H. E. *Science* **1999,** *283,* 1727. doi:10.1126/science.283.5408.1727
15. Schmidt, S. W.; Beyer, M. K.; Clausen-Schaumann, H. *J. Am. Chem. Soc.* **2008,** *130,* 3664. doi:10.1021/ja710642a
16. Schwaderer, P.; Funk, E.; Achenbach, F.; Weis, J.; Bräuchle, C.; Michaelis, J. *Langmuir* **2008,** *24,* 1343. doi:10.1021/la702352x
17. Wei, Q.; Becherer, T.; Mutihac, R.-C.; Noeske, P.-L. M.; Paulus, F.; Haag, R.; Grunwald, I. *Biomacromolecules* **2014,** *15,* 3061. doi:10.1021/bm500673u
18. Wei, Q.; Becherer, T.; Noeske, P.-L. M.; Grunwald, I.; Haag, R. *Adv. Mater.* **2014,** *26,* 2688. doi:10.1002/adma.201304737
19. Hartwig, A.; Meissner, R.; Merten, C.; Schiffels, P.; Wand, P.; Grunwald, I. *J. Adhes.* **2012,** *89,* 77. doi:10.1080/00218464.2013.731363
20. Richter, K.; Diaconu, G.; Rischka, K.; Amkreutz, M.; Müller, F. A.; Hartwig, A. *Bioinspired, Biomimetic Nanobiomater.* **2013,** *2,* 45–53. doi:10.1680/bbn.12.00022
21. Wei, Q.; Achazi, K.; Liebe, H.; Schulz, A.; Noeske, P.-L. M.; Grunwald, I.; Haag, R. *Angew. Chem., Int. Ed.* **2014,** *53,* 11650. doi:10.1002/anie.201407113
22. Wei, Q.; Krysiak, S.; Achazi, K.; Becherer, T.; Noeske, P.-L. M.; Paulus, F.; Liebe, H.; Grunwald, I.; Dernedde, J.; Hartwig, A.; Hugel, T.; Haag, R. *Colloids Surf., B* **2014,** *122,* 684. doi:10.1016/j.colsurfb.2014.08.001
23. Li, Y.; Qin, M.; Li, Y.; Cao, Y.; Wang, W. *Langmuir* **2014,** *30,* 4358. doi:10.1021/la501189n
24. Yu, J.; Wei, W.; Menyo, M. S.; Masic, A.; Waite, J. H.; Israelachvili, J. N. *Biomacromolecules* **2013,** *14,* 1072. doi:10.1021/bm301908y

25. Bahri, S.; Jonsson, C. M.; Jonsson, C. L.; Azzolini, D.; Sverjensky, D. A.; Hazen, R. M. *Environ. Sci. Technol.* **2011,** *45,* 3959. doi:10.1021/es1042832
26. Li, S.-C.; Chu, L.-N.; Gong, X.-Q.; Diebold, U. *Science* **2010,** *328,* 882. doi:10.1126/science.1188328
27. Sunder, A.; Hanselmann, R.; Frey, H.; Mülhaupt, R. *Macromolecules* **1999,** *32,* 4240. doi:10.1021/ma990090w
28. Sunder, A.; Mülhaupt, R.; Haag, R.; Frey, H. *Adv. Mater.* **2000,** *12,* 235. doi:10.1002/(SICI)1521-4095(200002)12:3<235::AID-ADMA235>3.0.CO;2-Y
29. Roller, S.; Zhou, H.; Haag, R. *Mol. Diversity* **2005,** *9,* 305. doi:10.1007/s11030-005-8117-y
30. Pirzer, T.; Hugel, T. *Rev. Sci. Instrum.* **2009,** *80,* 035110. doi:10.1063/1.3100258

License and Terms

BEILSTEIN JOURNAL OF ORGANIC CHEMISTRY

Peptide–polymer ligands for a tandem WW-domain, an adaptive multivalent protein–protein interaction: lessons on the thermodynamic fitness of flexible ligands

Katharina Koschek[1,2,3], Vedat Durmaz[4], Oxana Krylova[2], Marek Wieczorek[1,2], Shilpi Gupta[1], Martin Richter[1,2], Alexander Bujotzek[4], Christina Fischer[1], Rainer Haag[1], Christian Freund[1,2], Marcus Weber[4] and Jörg Rademann[*1,2]

Full Research Paper

Open Access

Address:
[1]Institute of Pharmacy & Institute of Chemistry and Biochemistry, Freie Universität Berlin, Königin-Luise-Str. 2+4, 14195 Berlin, Germany, [2]Department of Medicinal Chemistry, Leibniz Institut für Molekulare Pharmakologie, Robert-Rössle-Str. 10, 13125 Berlin, Germany, [3]Fraunhofer Institute for Manufacturing Technology and Advanced Materials (IFAM), Wiener Str. 12, 28359 Bremen, Germany and [4]Konrad-Zuse-Zentrum für Informationstechnik Berlin, Numerical Analysis and Modelling, Takustr. 7, 14195 Berlin, Germany

Email:
Jörg Rademann[*] - joerg.rademann@fu-berlin.de

* Corresponding author

Keywords:
inhibitors of protein–protein interactions; isothermal titration calorimetry; multivalency; peptide–polymer conjugates; proline-rich peptide sequences

Beilstein J. Org. Chem. **2015,** *11,* 837–847.
doi:10.3762/bjoc.11.93

Received: 28 February 2015
Accepted: 30 April 2015
Published: 18 May 2015

This article is part of the Thematic Series "Multivalency as a chemical organization and action principle".

Guest Editor: R. Haag

Abstract

Three polymers, poly(*N*-(2-hydroxypropyl)methacrylamide) (pHPMA), hyperbranched polyglycerol (hPG), and dextran were investigated as carriers for multivalent ligands targeting the adaptive tandem WW-domain of formin-binding protein (FBP21). Polymer carriers were conjugated with 3–9 copies of the proline-rich decapeptide GPPPRGPPPR-NH_2 (**P1**). Binding of the obtained peptide–polymer conjugates to the tandem WW-domain was investigated employing isothermal titration calorimetry (ITC) to determine the binding affinity, the enthalpic and entropic contributions to free binding energy, and the stoichiometry of binding for all peptide–polymer conjugates. Binding affinities of all multivalent ligands were in the μM range, strongly amplified compared to the monovalent ligand **P1** with a $K_D > 1$ mM. In addition, concise differences were observed, pHPMA and hPG carriers showed moderate affinity and bound 2.3–2.8 peptides per protein binding site resulting in the formation of aggregates. Dextran-based conjugates displayed affinities down to 1.2 μM, forming complexes with low stoichiometry, and no precipitation. Experimental results were compared with parameters obtained from molecular dynamics simulations in order to understand the observed differences between the three carrier materials. In summary, the more rigid and condensed peptide–polymer conjugates based on the dextran scaffold seem to be superior to induce multivalent binding and to increase affinity, while the more flexible and dendritic polymers, pHPMA and hPG are suitable to induce crosslinking upon binding.

Introduction

Multivalency is a general principle in nature for increasing the affinity and specificity of ligand–receptor interactions [1]. Multivalent binding is characterized by the cooperative, over-additive enhancement of binding affinities of ligands and receptors in a defined spatial arrangement. The strongest affinity enhancement can be expected in the case of a perfectly fitting, rigid arrangement of ligands and receptors (Figure 1A). In such cases the affinity of the multivalent ligand can be potentiated by the degree of multivalency. Prominent examples for this perfect fit have been reported reaching an exponential binding increase [2]. Rigid scaffolds can be used to present ligands in defined spatial arrangements and thus can be exploited to investigate the distances between receptor sites as "molecular ruler" [3,4].

Many multivalent receptors in nature, however, are characterized by the flexible arrangement of receptor sites and the resulting relative mobility of binding domains seems to have a significant impact on the proper functioning of these proteins [5]. Flexible arrangements of receptor sites can result from different scenarios. In many proteins flexibility is introduced by regions of inherent structural mobility, e.g., by so-called unstructured regions inserted between the receptor domains of a multireceptor protein. Alternatively, the relative mobility of binding sites is realized by their embedding into membranes giving them a certain degree of freedom to move in the plane of the membrane, or by incorporation into dynamic multiprotein complexes.

Design of potent multivalent ligands for flexible receptor arrangements is a considerable challenge, as the flexibility of multivalent ligands and the flexibility of receptors have to be matched in order to balance enthalpic gain with entropic loss of the system. In such a setting, a rigid multivalent ligand binding to a flexible receptor can be expected to reduce the entropy of the system upon binding, and thus will result in a partial or complete loss of the multivalent affinity enhancement. For example, the targeting of flexible protein receptors with ligands attached to a rigid DNA-backbone has been reported to be unsuccessful and no preferred ligand distance was found for this "molecular ruler" for flexible divalent protein targets [4].

Recently, we have introduced multivalent peptide–polymer conjugates as a chemical tool to inhibit protein–protein interactions in living cells [6]. As demonstrated for the pro-apoptotic BH3-peptides, multivalent presentation of monovalent ligand peptides can potentiate the activity of the peptide at identical

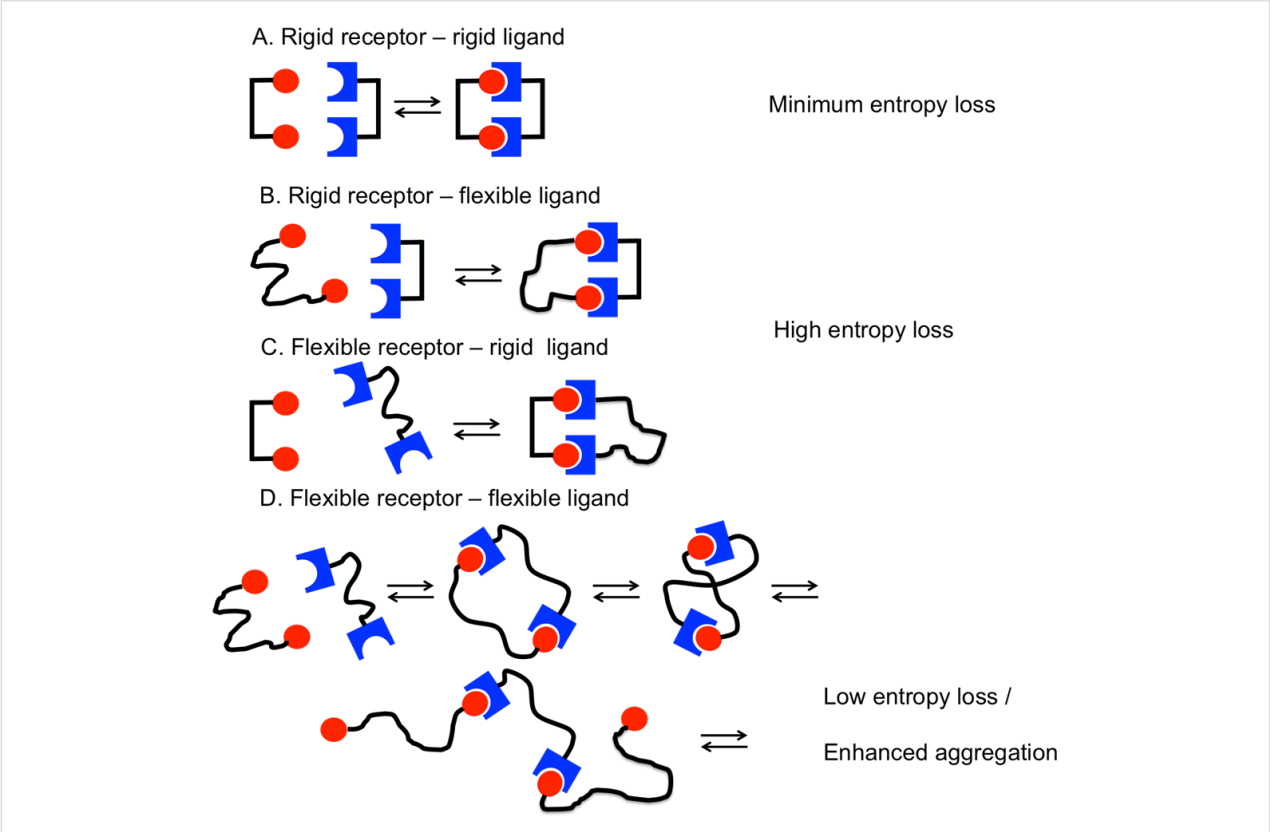

Figure 1: Comparing the entropy loss during ligand–receptor interactions in dependence of the rigidity of the backbone.

overall peptide concentrations. Moreover, attachment of bioactive peptides to polymers strongly enhanced their stability and protected them from proteolysis [7,8]. The construction of peptide-polymer conjugates with additional cell-penetrating peptides attached [9] enabled the smooth intracellular delivery of the conjugated polymer; as a third component fluorescent dyes [10] were coupled to the polymers simultaneously with the bioactive and the cell-penetrating peptides in order to enable the monitoring of cellular uptake and intracellular distribution of the peptide–polymer conjugate.

Until now, various polymer carriers have been used for the construction of peptide–polymer conjugates [11,12], however, a systematic comparison of the different polymeric materials with respect to the structure–activity relationships is missing so far. The goal of this contribution is to synthesize and compare flexible multivalent ligands for an adaptive, divalent receptor as a protein target. As a model protein the tandem-WW-domain of the pre-mRNA splicing factor formin binding protein 21 (FBP21) was selected [13-15]. Considering the importance of FBP21 in the activation of RNA splicing, successful ligands should be valuable tools to interfere with FBP21-dependent splicing events. Several multivalent ligands were synthesized on the basis of various polymer supports differing in their chemical structure, backbone flexibility, morphology, and ligand loading. The obtained materials were then investigated in order to contribute to the understanding of structure–activity relationships of polymeric ligands. For this purpose, the thermodynamics and the stoichiometry of protein binding events were determined experimentally for all multivalent ligands. Finally, atomistic molecular dynamics simulations were conducted in order to rationalize the observed differences on a microscopic level and to derive general principles for the design of optimized multivalent ligands of flexible protein targets.

Results and Discussion

Selection of a bivalent protein receptor as a target

As a representative example for a protein containing a bivalent domain architecture connected with a flexible linker the tandem WW-domains of the protein FBP21 were selected. FBP21 is a protein component of the spliceosome, the multiprotein complex in the nucleus of cells responsible for the processing of primary RNA-transcripts. The two WW domains of FBP21 bind to proline-rich sequences contained in numerous proteins including the core splicing protein SmB/B´and several splicing factors including splicing factor 3B4 (SF3B4) [16,17]. Recently, the enhanced binding affinity of bivalent and tetravalent peptide ligands to this protein was described suggesting that multivalent ligands may play a significant role also in living cells. In addition, several interaction partners of FBP21 have been profiled by SILAC/MS [18]. As monovalent peptide ligands for each of the two WW domains proline-rich sequences (PRS) of the group R_b have been identified, in which the proline residues are flanked by arginine (R in one-letter-code) [16,19]. Multivalent arrangements of these monovalent ligands therefore could serve as potent inhibitors of FBP21-interactions and could be used for the inhibition of FBP21 function. As a monovalent peptide ligand the decapeptide amide GPPPRGPPPR-NH_2 (**P1**) was selected and synthesized on Rink amide polystyrene resin. For attachment to the polymer carriers the N-cysteinylated peptide CGPPPRGPPPR-NH_2 (**P2**) was prepared, containing a free N-terminus in order to enable the attachment to polymers via native chemical ligation or Michael addition to maleimide residues.

Selection of polymer carriers and synthesis of multivalent ligands

Three biocompatible polymers with different chemical structure, backbone flexibility and polymer morphology were selected as multivalent ligand carriers, two linear polymers and one dendritic polymer (Scheme 1). Linear poly(*N*-(2-hydroxypropyl)methacrylamide) (pHPMA) possesses a C2 repeating unit with three fully rotatable bonds, which should convey – compared to the other polymers employed in this study – high backbone flexibility to this carrier. Reactive pHPMA was prepared in a copolymerization of HPMA and the thioester-containing building block *N*-methacryloyl-β-alaninyl-*S*-benzyl thioester under reversible addition–fragmentation chain-transfer (RAFT) conditions yielding a thioester-containing copolymer with 13.3 kDa and polydispersity of 1.2, which we denominated as NCL-polymer [10]. NCL-polymer was converted into multivalent peptide–polymer conjugates pHPMA-**1** and pHPMA-**2** via native chemical ligation with the N-cysteinylated peptide CGPPPRGPPPR-NH_2 (**P2**). In contrast, the second carrier molecule, hyperbranched polyglycerol (hPG) was selected as a dendritic polymer. While the backbone of PG is relatively flexible by itself, the dendritic structure of hPG can be expected to limit the flexibility of attached ligands compared to a linear polymer and might induce a more globular arrangement of the ligands. The hPG polymer carrier was synthesized via an anionic ring-opening polymerization of glycidol [20] and also modified with maleimido groups by reaction with *N*-3-chloropropyl maleimide for ligand attachment.

Finally, dextran, a polysaccharide containing α-1,6-linked D-glucose as repeating unit, was selected as the second linear carrier. The D-glucose units in the polysaccharide are fixed in the $_1C^4$ chair conformation and thus can be expected to rigidify the polymer backbone compared to the other two polymers, leaving only two freely rotatable bonds per building block. Structural studies with dextran suggested a helical structure as

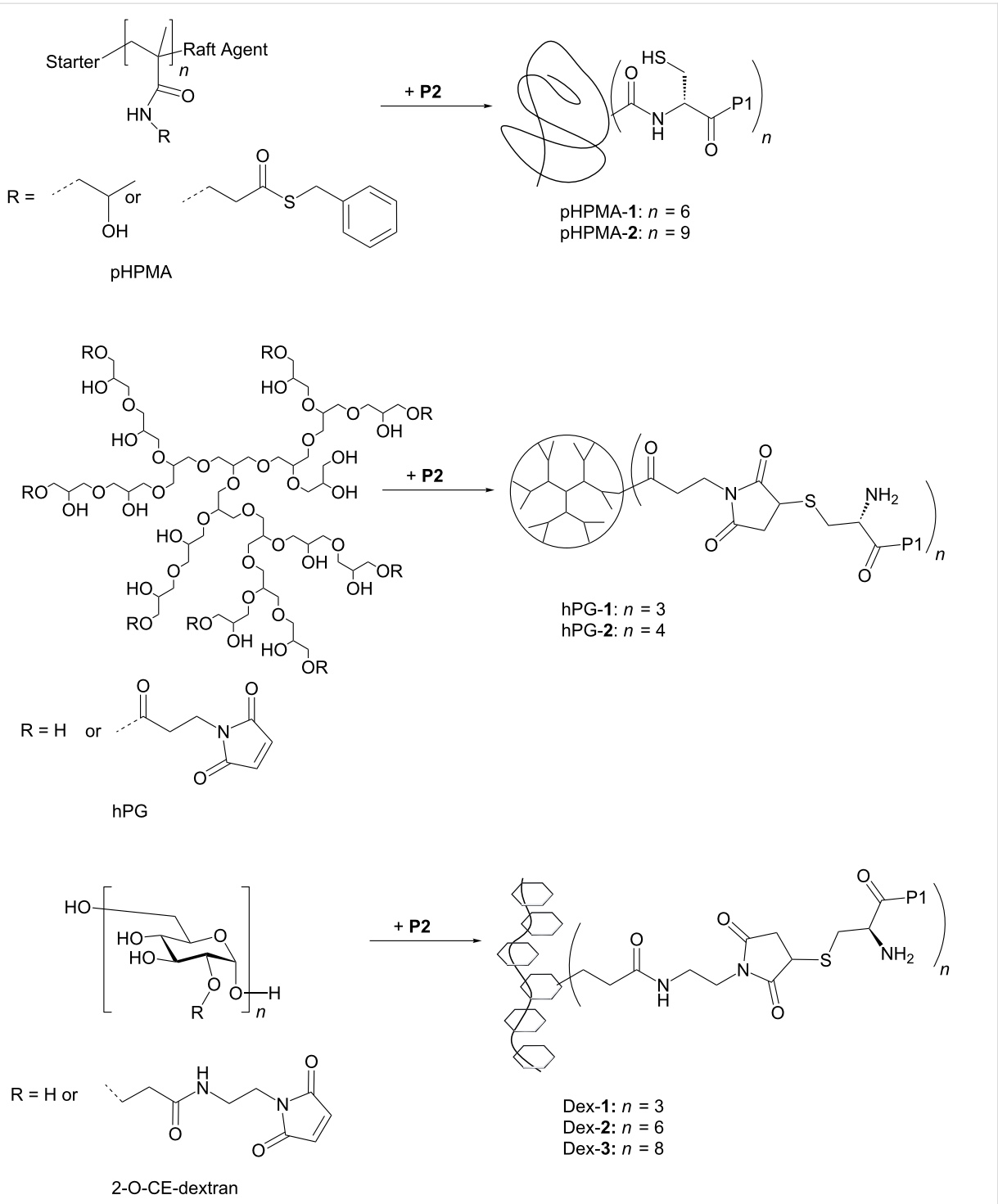

Scheme 1: Selection of three polymer carriers differing with respect to backbone flexibility, and morphology and used for the construction of peptide–polymer conjugates.

the lowest energy conformations of this polymer [21]. Dextran was used as a linear polymer with an average M_W of either 10 kDa (for Dex-**1** and Dex-**2**) or 50 kDa (for Dex-**3**), both with a polydispersity index of 1.5. Under basic conditions the linear polysaccharide was alkylated with acrylamide selectively in the 2-positions of the sugars. The resulting 2-O-carboxyethyl dextran (2-O-CE-dextran) was further converted by condensation with 2-*N*-maleimido-ethylamine and *N*-ethyl-*N*′-dimethylaminopropylcarbodiimide (EDC) [6]. The monovalent ligand peptide **2** was attached to the dextran carriers by nucleo-

philic addition of the thiols to the maleimide double bond furnishing peptide–polymer conjugates Dex-**1**, Dex-**2**, and Dex-**3**.

Peptide loadings of all obtained peptide–polymer conjugates were determined by quantitative amino acid analysis and ranged from 3 to 9 peptides per polymer corresponding to peptide loading densities (percentage of ligand-carrying monomers) between 3 and 10%.

Binding of multivalent peptide–polymer conjugate to the tandem WW domain

Binding studies with peptide–polymer conjugates were conducted employing isothermal titration calorimetry (ITC). This method enables the determination of the binding affinity of the multivalent ligands and elucidates the composition of the free energy of binding from the enthalpic and entropic contributions. In addition, the method can be used to determine the stoichiometry of the formed protein–ligand complex indicating the ratio of peptide ligand molecules relative to each protein binding site thereby giving valuable insights into the multivalency of binding and/or the degree of crosslinking. Thus, the method enables the identification of polymer–protein aggregates containing several polymers and proteins in a complex. No precipitation of the multicomponent aggregates that interfered with ITC measurements was observed during the experiments.

ITC-analysis (Figure 2) of the binding of multivalent peptide–polymer conjugates yielded K_D values either corresponding to the polymer concentration or relative to the overall peptide concentration (N*K_D). A comparison of the binding affinity of the monovalent peptide ligand **P1** and its N-acetylated derivative Ac-**P1** with seven multivalent peptide ligands to the tandem WW-domain revealed a strong enhancement of the binding through multivalency (Table 1, Figure 3). While the peptide alone bound with a dissociation constant (K_D) of larger than 1 mM [16], all multivalent peptide-polymer conjugates possessed K_D values below 10 µM. Though all K_D values of multivalent ligands were in the same concentration range (i.e., between 1.2 and 7 µM), concise differences were revealed for the thermodynamic composition of K_D values (Figure 2). While

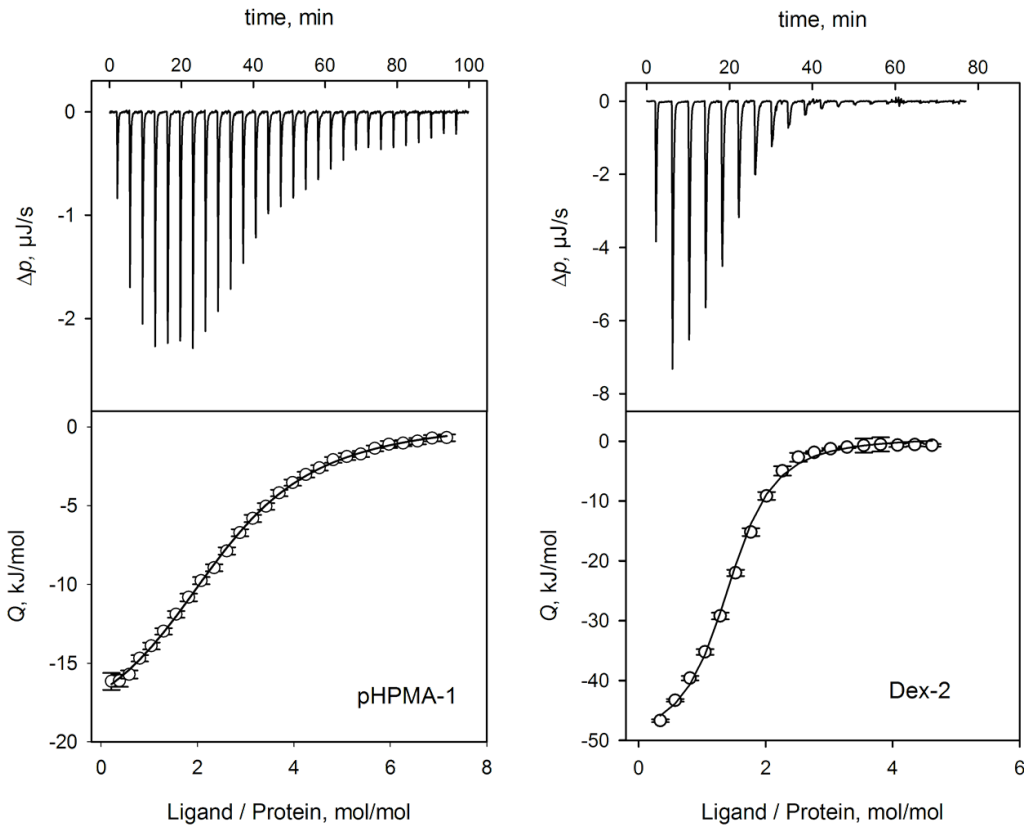

Figure 2: Representative ITC-measurements conducted at 8 °C with the peptide–polymer conjugates A) pHPMA-**1** and B) Dex-**2** showing an increase in affinity for the interaction of Dex-**2** with the FBP21 tandem WW domains. The upper part shows differential heating power (Δ*p*) changes upon injection of peptide–polymer conjugates into the protein; bottom part shows integrated and normalized heat of reaction plotted against peptide/protein molar ratio; binding isotherms are fitted with a 1:1 binding model.

Table 1: ITC measurements of peptide–polymer conjugates with tandem WW domain of FBP21.

Conjugates[a]	N Ligands (rep. units)[b]	Loading density [%]	K_D [μM][c]	Rel. K_D = N*K_D [μM][d]	Binding stoichiometry	Aggregates
P1	–	100	> 1000	> 1000	–	–
Ac-**P1**	–	100	>1000	>1000	–	–
pHPMA-**1**	6 (92)	6.5	5.0 ± 0.8	30 ± 5	2.6	X
pHPMA-**2**	9 (108)	8	3.3 ± 0.6	30 ± 5	2.8	X
hPG-**1**	3 (97)	3	6.3 ± 1.7	19 ± 5	2.3	X
hPG-**2**	4 (97)	4	5.0 ± 1.3	20 ± 5	2.4	X
Dex-**1**	3 (62)	5	7.0 ± 1.2	21 ± 4	1.8	–
Dex-**2**	6 (62)	10	1.2 ± 0.7	7 ± 4	1.4	–
Dex-**3**	8 (248)	3	1.6 ± 0.4	13 ± 3	1.3	–

[a]Dextran, hyperbranched PG and poly(HPMA) coupled with the N-cysteinylated peptide CGPPPRGPPPR (**P2**); [b]*N*: number of ligands (number of repeating units in the polymeric scaffolds); [c]binding affinities of peptide–polymer conjugates; [d]binding affinities measured by ITC related to overall peptide concentrations.

the ligands based on polymethacrylamide displayed moderate enthalpic and almost negligible entropic contributions , all polyhydroxy-based peptide–polymer conjugates showed significantly stronger generation of heat through binding (enthalpy) together with a pronounced loss in entropy. Binding in all cases was driven mainly by enthalpy, which clearly outweighed the observed entropy loss. In the seven peptide–polymer conjugates investigated, increased loading density of ligands led consistently to increased affinity of the multivalent ligand (Table 1). The most significant difference between dextran and the two other polymer carriers was the stoichiometry of the formed peptide-polymer–protein complex. Inspection of the test solution revealed the formation of a colloidal suspension/dispersion both for pHPMA and for hPG-based peptide conjugates indicating the formation of insoluble aggregates possibly generated through crosslinking. Corresponding to the observed colloidal suspension/dispersion the stoichiometry of peptide ligands per protein receptor resulting from the ITC experiments was >2 for each of either pHPMA or hPG-based material, most pronounced for pHPMA with n = 2.6–2.8. Dextran-based conjugates displayed a ligand stoichiometry of 1.4 for the most potent multivalent ligand with a K_D of 1.2 μM, Dex-**2**. No correlation between ligand density and stoichiometry became evident from the recorded data, however, the observed correlation between low binding stoichiometry, increased binding affinity, and increased binding enthalpy seems to suggest the prevalence of a bivalent binding mode for the complex of Dex-**2** and tandem-WW-FBP21, which is supported also by the solubility of the non-crosslinked peptide-polymer–protein complex.

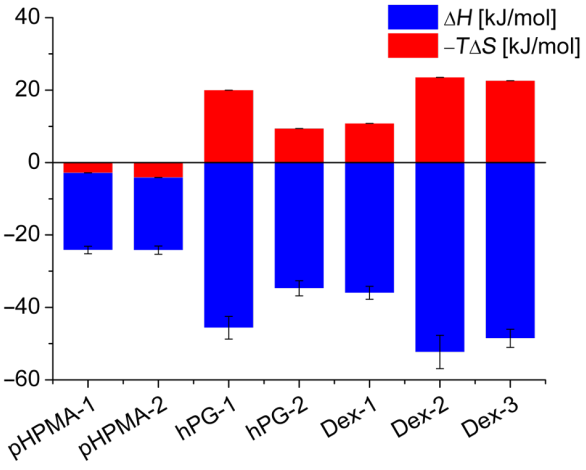

Figure 3: Enthalpic and entropic contributions to the free energy of binding processes of multivalent peptide-polymer conjugates and the tandem WW domain of protein FBP21 determined at 8 °C by ITC measurements.

Molecular dynamics simulations of multivalent ligands

In order to better understand our experimental observations regarding binding affinities, enthalpic/entropic energy contributions, and binding stoichiometries from a molecular point of view, the three polymer carriers were investigated using atomistic molecular dynamics simulations. Each polymer was represented by one model parameterized in accordance with the AMBER force field [22]. The concentration ratios of peptide ligands and monomeric units were fit to lab conditions such that each polymer was carrying three ligands. In contrast to the linear polymer models of dextran and pHPMA with 10 and 12 units between any two successive ligands, respectively, the hPG configuration was generated randomly with the aid of a probabilistic hPG building algorithm as described previously [23]. After some preparatory relaxation steps, each of the three polymers underwent three explicit solvent molecular dynamics

(MD) simulations of 100 ns length serving as production runs. The first 30% of the time steps were considered as an unrestricted equilibration phase and consequently omitted whereas from the remaining time series several promising structural and physical descriptors were determined. For all simulations and analytical calculations the Gromacs software suite was utilized [24]. Table 2 and Figure 4 show these theoretical results averaged over time as well as the three runs per polymer.

Structural properties and descriptors. Dividing the Euklidean distance between two successive peptide attachment points by the number of bonds in between (i.e., between the N-terminal nitrogen atoms of the cysteinylated peptide **P2** in the case of pHPMA, and the Cys-sulfur in the cases of both hPG and dextran) yields relative distances which indicate that the peptide ligands in pHPMA are further apart than in dextran and hPG, while the variance of the peptide positions in pHPMA is higher than in the two hydroxyl polymers (Table 2, Figure 4A). Next, we were interested in the distances between the C-terminal positions of the peptide ligands measured between the C-terminal amide nitrogens of the peptides (Table 2, Figure 4B). Here, the peptides on dextran were found to be closer (2.9 nm) to each other than in pHPMA (3.4) and hPG (3.7 nm). The larger distance in hPG might be related to the hypervalent morphology of this carrier, which possibly limits the proximity of attached ligands. Expected values of averaged (over time and atoms) radial distributions (correlating with normalized mean distances) of polymer atoms around peptide atoms clearly reveal a higher polymer-peptide proximity for the dextran system (1.23 nm) than for pHPMA (1.41 nm) and hPG (1.56 nm). Considering the statistical character of the underlying molecular ensemble, the time-averaged radial distribution function (rdf) values indicate a smaller ratio of the fraction of time steps with outstretched peptides (which are more accessible for binding with the tWW domain) and the fraction of time steps characterized by a contracted structure in case of peptides associated with the dextran polymer (Figure 4C). Thus, ligands attached to pHPMA or hPG are more often available for protein binding than those linked to dextran. As a consequence, multiple simultaneously outstretched peptides are even less likely to emerge in case of dextran in comparison with the other polymers. Moreover, after having bound the first protein and due to substantially smaller peptide end-to-end distances given with dextran, its next outstreched peptide will rather bind a free tWW domain of the same protein than of another one which clearly confirms the stoichiometric results. This binding mode is illustrated in Figure 5.

Another descriptor for the spatial arrangement that we denote as the peptide polymer's globularity was defined as the quotient of the volume under the multivalent ligand's solvent-accessible surface area (SASA) and the volume of the minimal sphere incorporating the entire molecule (Table 2). Not unexpectedly, the conformation of the peptide conjugate with the dendritic polymer hPG yields a significantly higher globularity (0.1) compared to those associated with pHPMA (0.04) or dextran (0.07). Regarding these two linear carriers only, the higher globularity of the dextran-based ligand is in good agreement with that material's peptide–polymer distance.

Thermodynamic properties. From a physical point of view, the significantly varying mean peptide–peptide and peptide–polymer distances are mainly attributed to molecular interactions between the involved atoms. For this reason we calculated non-bonded interaction energies between peptide atoms and both polymer and solvent atoms as the sum of van-der-Waals and electronic contributions (Table 2) While the interaction energies between peptides and solvents are, as expected, nearly identical for all three systems, the interaction of peptide atoms regarding polymer atoms amounts to substantially different values for the three carrier materials. With −913 kJ/mol dextran yielded the by far lowest energy compared with those peptides attached to the two high-stoichiometry polymers (−515 kJ/mol and −783 kJ/mol). Since lower energies

Table 2: Molecular dynamics simulations of the protein target and the multivalent polymeric ligands.

Polymeric scaffold	pHPMA	hPG	Dextran
Mean distance (expected value) rdf [nm][a]	1.41	1.56	1.23
Peptide distance at binding site [nm][b]	0,84	0,48	0,43
Peptide distance at the termination site [nm][c]	3,39	3,66	2,9
E(peptide-polymer) [kJ/mol][d]	−515,3	−783,3	−912,7
E(peptide-solution) [kJ/mol][e]	−3268,7	−3224,8	−3281,1
Globularity[f]	0,037	0,104	0,066

[a]Expected mean distance values (calculated by a radial distribution function); mean distance between two peptide ligands on a polymer chain measured between [b]the N-terminal sulfur atoms of the Cys-residues at their linking site and [c]the C-terminal nitrogen atoms of the Arg residue as the farthest distance between peptide and polymer backbone; average potential energy regarding [d]the affinity of the peptide to the polymer and [e]the solvation energy of the peptide; [f]ratio of the peptide-polymer conjugates volume and the appropriate sphere.

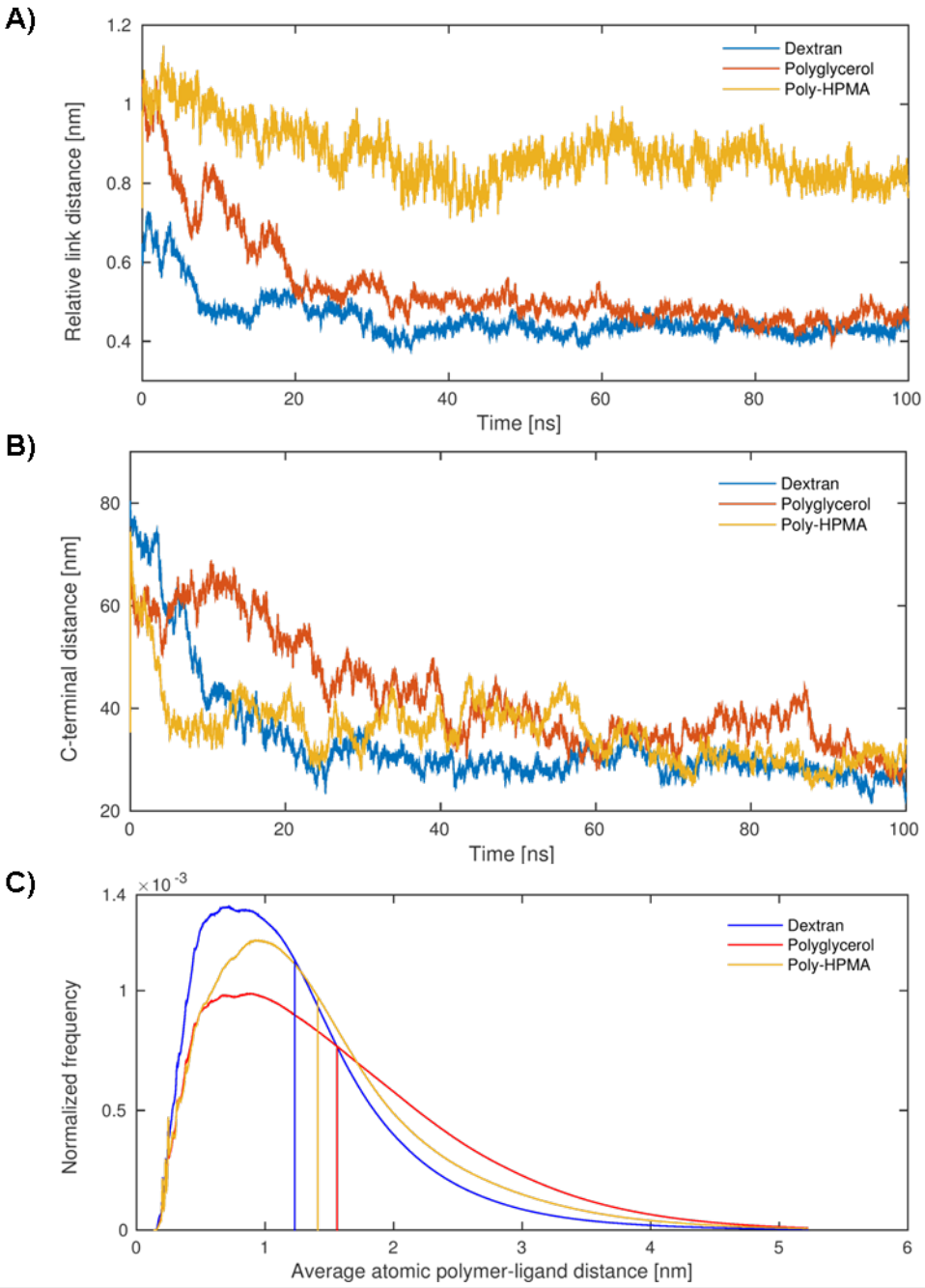

Figure 4: MD simulations over time (0–100 ns) yielding A) the mean sulfur distance between two peptides at their linking site, B) the mean nitrogen distance between two peptides at the farthest distance between peptide and polymer chain C) the frequency of observed peptide–polymer distances in dependence of the polymer backbone pHPMA, hPG and dextran, respectively.

correspond to preferential states, the interaction energy can be interpreted as a measure for a state's preference. In general, preferential states are characterized by (negative-signed) attractive forces dominating over (positive-signed) repulsive forces. Hence, according to these results, the peptide is more attracted by the dextran carrier than by the two others most likely causing the small expected polymer–peptide distance and possibly the small peptide end-to-end distances in case of dextran.

Finally, the molecular dynamics simulations of the peptide–polymer conjugates were compared with those of dimeric complexes with a bivalent binding mode in order to calculate the entropic loss of both the protein and of the peptide–polymer conjugates themselves (Table 3). Interestingly, in all three cases the major contribution to the entropic loss was on the side of the protein, the decrease in entropy on the polymer side was comparably small. Though bivalent binding

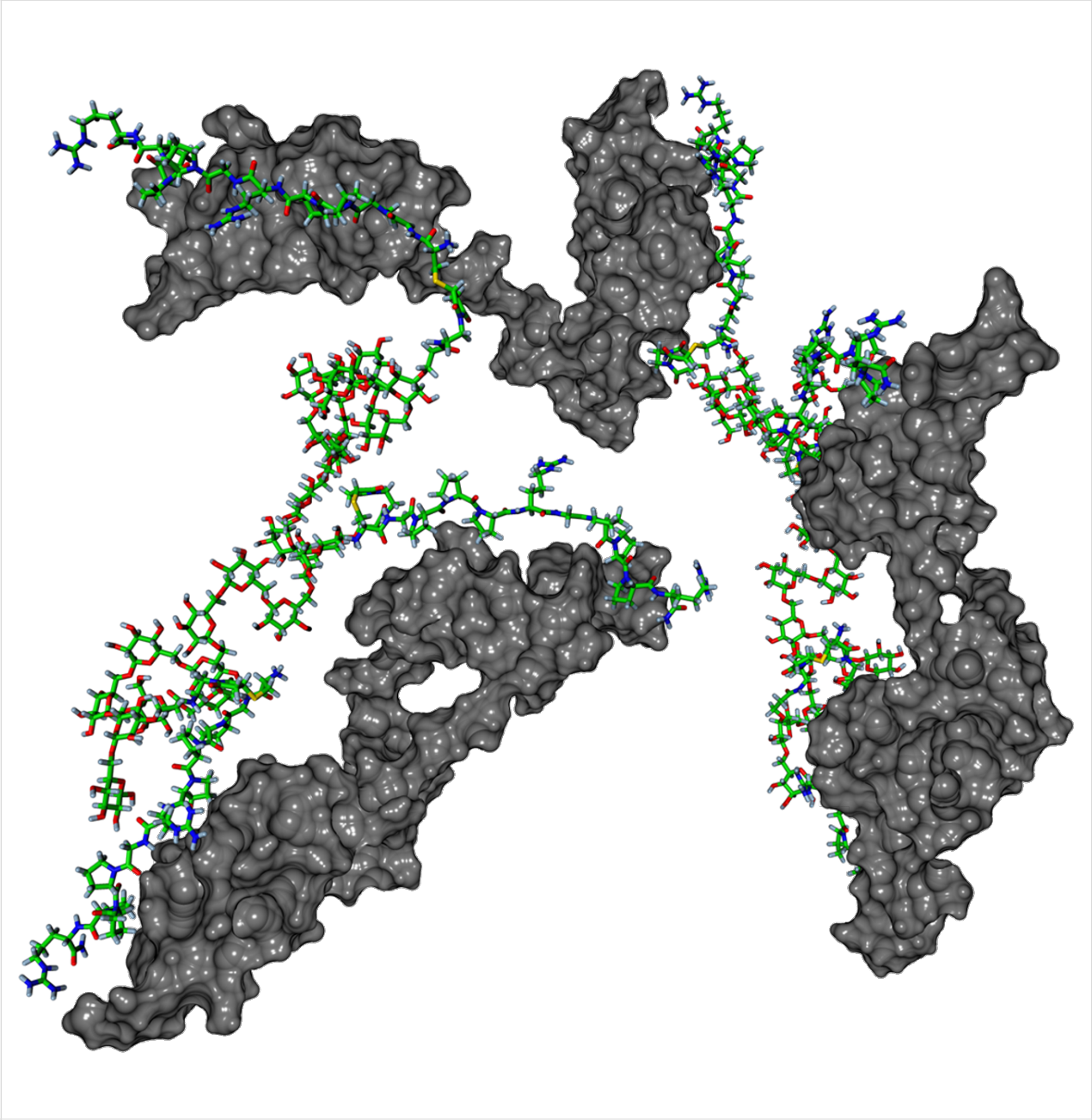

Figure 5: MD simulation image showing the interaction of two dextran–peptide conjugates with three tandem WW domains of FBP21 illustrating the intramolecular mode of binding.

modes are strongly favoured through enthalpic gain, the free energy gain is limited by the entropy loss, most likely caused by the flexibility of the linker and thus a larger number of alternative conformational states of the protein receptor.

Conclusion

All three investigated biocompatible polymers, namely linear poly(*N*-2-hydroxypropyl)methacrylamide (pHPMA), hyperbranched polyglycerol (hPG), and linear 2-carboxyethyldextran are suited for the construction of peptide–polymer conjugates,

Table 3: Calculated changes in entropy during binding of the multivalent polymeric ligands to the bivalent receptor by molecular dynamics simulations.

Binding partner	Entropy contribution $T\Delta S$ [kJ/mol]		
	pHPMA	hPG	dextran
Protein receptor	−14.91	−15.20	−14.74
Polymeric ligand	−0.67	−1.38	−0.92
Σ	−15.58	−16.58	−15.66

which can be used as potent multivalent ligands for a flexible protein–protein interaction site here exemplified by the tandem WW-domains of FBP-21. 2-Carboxyethyldextran furnished peptide–polymer conjugates with significantly higher binding affinity than the two other carriers. The observed binding modes of the three carriers were distinct. Dextran-based conjugates formed preferably bivalent, soluble complexes with a stoichiometry of <2 peptide ligands per protein binding site, while pHPMA and hPG formed colloidal suspensions/dispersions with stoichiometries >2 ligands per binding site. Molecular dynamics calculations suggested that conjugates with multivalently presented peptides on dextran occupy conformations in which two conjugated peptides are closer to each other and to the polymer backbone, corresponding to the calculated stronger peptide-polymer interaction. From the study it can be supposed that the simulated conformational space of the investigated peptide–polymer conjugates indeed correlates with the experimentally observed binding properties of the multivalent ligands. The construction and experimental investigation of further peptide–polymer conjugates will show, whether the results reported here will be helpful for the construction of even more potent multivalent and/or crosslinking ligands for protein–protein interaction sites and whether the ligands active in the protein binding assay can be further developed toward intracellularly delivered and intracellularly active PPI-inhibitors of the tandem WW-domain.

Supporting Information

Supporting Information File 1

Experimental.
[http://www.beilstein-journals.org/bjoc/content/supplementary/1860-5397-11-93-S1.pdf]

Acknowledgements

The authors gratefully acknowledge the support of this work by the DFG collaborative research center SFB 765 (Multivalency) with grants to MW, RH, CF and JR. We thank Dr. Kai Holland-Nell for technical support in synthesis of peptides.

References

1. Mammen, M.; Choi, S.-K.; Whitesides, G. M. *Angew. Chem., Int. Ed.* **1998,** *37,* 2754–2794. doi:10.1002/(SICI)1521-3773(19981102)37:20<2754::AID-ANIE2754>3.0.CO;2-3
2. Fasting, C.; Schalley, C. A.; Weber, M.; Seitz, O.; Hecht, S.; Koksch, B.; Dernedde, J.; Graf, C.; Knapp, E.-W.; Haag, R. *Angew. Chem., Int. Ed.* **2012,** *51,* 10472–10498. doi:10.1002/anie.201201114
3. Lauster, D.; Bandlow, V.; Memczak, H.; Bhatia, S.; Sieben, C.; Stöcklein, W.; Seitz, O.; Haag, R.; Herrmann, A. *Biophys. J.* **2014,** *106* (Suppl. 1), 647a. doi:10.1016/j.bpj.2013.11.3583
4. Eberhard, H.; Diezmann, F.; Seitz, O. *Angew. Chem., Int. Ed.* **2011,** *50,* 4146–4150. doi:10.1002/anie.201007593
5. Shimizu, H.; Burch, L. R.; Smith, A. J.; Dornan, D.; Wallace, M.; Ball, K. L.; Hupp, T. R. *J. Biol. Chem.* **2002,** *277,* 28446–28458. doi:10.1074/jbc.M202296200
6. Richter, M.; Chakrabarti, A.; Ruttekolk, I. R.; Wiesner, B.; Beyermann, M.; Brock, R.; Rademann, J. *Chem. – Eur. J.* **2012,** *18,* 16708–16715. doi:10.1002/chem.201202276
7. Ruttekolk, I. R.; Chakrabarti, A.; Richter, M.; Duchardt, F.; Glauner, H.; Verdurmen, W. P. R.; Rademann, J.; Brock, R. *Mol. Pharmacol.* **2011,** *79,* 692–700. doi:10.1124/mol.110.068296
8. Torchilin, V. P.; Lukyanov, A. N. *Drug Discovery Today* **2003,** *8,* 259–266. doi:10.1016/S1359-6446(03)02623-0
9. Copolovici, D. M.; Langel, K.; Eriste, E.; Langel, Ü. *ACS Nano* **2014,** *8,* 1972–1994. doi:10.1021/nn4057269
10. Koschek, K.; Dathe, M.; Rademann, J. *ChemBioChem* **2013,** *14,* 1982–1990. doi:10.1002/cbic.201300365
11. Duncan, R. *Curr. Opin. Biotechnol.* **2011,** *22,* 492–501. doi:10.1016/j.copbio.2011.05.507
12. Duro-Castano, A.; Conejos-Sánchez, I.; Vicent, M. J. *Polymers* **2014,** *6,* 515–551. doi:10.3390/polym6020515
13. Staub, O.; Rotin, D. *Structure* **1996,** *4,* 495–499. doi:10.1016/S0969-2126(96)00054-8
14. Sudol, M. Y.; Sliwa, K.; Russo, T. *FEBS Lett.* **2001,** *490,* 190–195. doi:10.1016/S0014-5793(01)02122-6
15. Sudol, M. *Prog. Biophys. Mol. Biol.* **1996,** *65,* 113–132. doi:10.1016/S0079-6107(96)00008-9
16. Huang, X.; Beullens, M.; Zhang, J.; Zhou, Y.; Nicolaescu, E.; Lesage, B.; Hu, Q.; Wu, J.; Bollen, M.; Shi, Y. *J. Biol. Chem.* **2009,** *284,* 25375–25387. doi:10.1074/jbc.M109.024828
17. Kofler, M.; Schuemann, M.; Merz, C.; Kosslick, D.; Schlundt, A.; Tannert, A.; Schaefer, M.; Lührmann, R.; Krause, E.; Freund, C. *Mol. Cell. Proteomics* **2009,** *8,* 2461–2473. doi:10.1074/mcp.M900191-MCP200
18. Klippel, S.; Wieczorek, M.; Schümann, M.; Krause, E.; Marg, B.; Seidel, T.; Meyer, T.; Knapp, E.-W.; Freund, C. *J. Biol. Chem.* **2011,** *286,* 38478–38487. doi:10.1074/jbc.M111.265710
19. Kato, Y.; Nagata, K.; Takahashi, M.; Lian, L.; Herrero, J. J.; Sudol, M.; Tanokura, M. *J. Biol. Chem.* **2004,** *279,* 31833–31841. doi:10.1074/jbc.M404719200
20. Sunder, A.; Mülhaupt, R.; Haag, R.; Frey, H. *Adv. Mater.* **2000,** *12,* 235–239. doi:10.1002/(SICI)1521-4095(200002)12:3<235::AID-ADMA235>3.0.CO;2-Y
21. Hassid, W. Z.; Barker, H. A. *J. Biol. Chem.* **1940,** *134,* 163–170.
22. Hornak, V.; Abel, R.; Okur, A.; Strockbine, B.; Roitberg, A.; Simmerling, C. *Proteins* **2006,** *65,* 712–725. doi:10.1002/prot.21123
23. Horn, H. W.; Swope, W. C.; Pitera, J. W.; Madura, J. D.; Dick, T. J.; Hura, G. L.; Head-Gordon, T. *J. Chem. Phys.* **2004,** *120,* 9655–9678. doi:10.1063/1.1683075
24. Hess, B.; Kutzner, C.; van der Spoel, D.; Lindahl, E. J. *J. Chem. Theory Comput.* **2008,** *4,* 435–447. doi:10.1021/ct700301q

License and Terms